



*Ministero dell'Istruzione
dell'Università e Ricerca*



**Università
degli Studi
di Palermo**

PhD in Molecular and Clinical Medicine
Department of Health Promotion, Mother and Child Care, Internal Medicine and Medical
Specialties
SSD MED/50

TOWARDS COLORECTAL CANCER STEM CELLS TARGETING: INVESTIGATING GENETIC AND EPIGENETIC LANDSCAPE

CANDIDATE

LAURA ROSA MANGIAPANE

COORDINATOR

PROF. ANTONINO TUTTOLOMONDO

TUTOR

PROF. MATILDE TODARO

CO-TUTOR

DR. VERONICA VESCHI

CYCLE: XXXIV
2020/2021

INDEX

1. INTRODUCTION

- 1.1 Colorectal cancer
- 1.2 Colon carcinogenesis
- 1.3 Stem cells and cancer stem cells

2. EPIGENETIC ALTERATIONS AS THERAPEUTIC TARGETS IN COLORECTAL CANCER STEM CELLS

- 2.1 Epigenetic alterations in cancer
- 2.2 Preliminary results
- 2.3 Conclusions
- 2.4 Materials and methods

3. THERAPEUTIC STRATEGIES TARGETING CANCER STEM CELLS AND THEIR MICROENVIRONMENT

Chapter 1: Targeting chemoresistant colorectal cancer via systemic administration of a BMP7 variant

Oncogene, 2020 Jan;39(5):987-1003

Chapter 2: PI3K-driven HER2 expression is a potential therapeutic target in colorectal cancer stem cells

Gut 2021, Jan 12;gutjnl-2020-323553

Chapter 3: Pharmacological targeting of the novel β -catenin chromatin-associated kinase p38 α in colorectal cancer stem cell tumorspheres and organoids

Cell Death & Disease, 2021 Mar 25;12(4):316

Chapter 4: CHK1 inhibitor sensitizes resistant colorectal cancer stem cells to nortopsentin

iScience, 2021 May 29;24(6):102664

Chapter 5: Nobiletin and Xanthohumol Sensitize Colorectal Cancer Stem Cells to Standard Chemotherapy

Cancers, 2021 Aug 4;13(16):3927

Chapter 6: Adipose stem cell niche reprograms the colorectal cancer stem cell metastatic machinery

Nature Communications, 2021 Aug 18;12(1):5006

4. CONCLUSIONS

5. REFERENCES

1. INTRODUCTION

1.1 Colorectal cancer

Colorectal cancer (CRC) is the third most commonly diagnosed cancer type in the world. It is the third most frequent cancer in men and the second in women, after breast cancer.

CRC is also the second most common cause of cancer death worldwide, causing almost 1 million deaths (Sung et al., 2021).

CRC arises within the mucosa, which consists of columnar epithelial cells that form crypt structures. The tumour then grows through the other layers of the bowel wall, invading surrounding vessels and eventually metastasizing to other organs and tissues. Classification of malignant tumours is based on the histotype, site of origin, morphologic grade, and spread of cancer throughout the body, according to the Tumour Node Metastasis (TNM) system (Carbone, 2020).

Survival is directly related to early detection, and outcome depends on the degree of local tissue invasion and presence of metastases.

A logical framework for understanding the biology of cancer is represented by the hallmarks of cancer, alterations in cell physiology that enable tumour growth and metastatic dissemination.

These alterations include: self-sufficiency in growth signals, insensitivity to growth-inhibitory signals, evasion of apoptosis, limitless replicative potential, sustained angiogenesis, tissue invasion and metastasis. Additionally, other consequential characteristics are the capability to modify, or reprogram, cellular metabolism, the evasion from immunological destruction, in particular by T and B lymphocytes, macrophages, and natural killer cells, genomic instability and tumour-promoting inflammation (Hanahan and Weinberg, 2000, Hanahan and Weinberg, 2011).

The choice of treatment depends on the stage at tumour presentation. Surgical resection is the main treatment of stage I CRC patients and no adjuvant therapy is offered to these patients.

Adjuvant therapy is recommended for patients diagnosed as stage II only if cancer has a higher risk of recurrence, and the main options include 5-FU and leucovorin, oxaliplatin, or capecitabine.

Patients diagnosed as stage III are, after surgery, adjuvantly treated with FOLFOX (5-FU, leucovorin, and oxaliplatin) or CAPOX (capecitabine and oxaliplatin) regimens but, in case of contraindication for these severe chemotherapeutic regimens, some patients may get 5FU with leucovorin or capecitabine alone. Some advanced colon cancers cannot be removed completely by surgery, thus neoadjuvant chemotherapy is given along with radiation.

Stage IV patients can be treated with chemotherapy with or without targeted therapy, in most cases surgery is unlikely to cure these cancers.

Targeted therapies include:

- monoclonal antibodies (mAb) that inhibit the vascular endothelial growth factor (VEGF), including bevacizumab, ramucirumab, ziv-aflibercept;
- mAb that target the epidermal growth factor receptor (EGFR), including cetuximab and panitumumab;
- kinase inhibitors, such as regorafenib;
- BRAF inhibitors, such as encorafenib, a drug specific for mutated BRAF.

Some of the most commonly used regimens include FOLFOX, CAPOX, FOLFIRI (5-FU, leucovorin and irinotecan), FOLFOXIRI (5-FU, leucovorin, oxaliplatin, and irinotecan), one of the above combinations plus a targeted drug, 5-FU and leucovorin, with or without a targeted drug, capecitabine, with or without a targeted drug, irinotecan, with or without a targeted drug (Benson et al., 2021).

These treatments have improved the response-rates for advanced CRC (Giacchetti et al., 2000).

However, resistance to chemotherapy arises in almost all patients and in the recent years a big effort has been made to identify new agents, specifically directed to cancer-specific pathways, promising to lead to a full and lasting tumour eradication.

1.2 Colon carcinogenesis

Colon cancer development is driven by accumulation of sequential mutations in oncogenes and tumor suppressor genes (Vogelstein et al., 1988).

According to this traditional stochastic model of carcinogenesis all cancer cells have the same tumorigenic potential and participate in tumour progression equally.

The most common early event associated to adenoma formation is the activation of the Adenomatous Polyposis Coli (APC)/ β -catenin pathway, altered in 80% of sporadic CRC cases (Powell et al., 1992). Germinal mutations in APC gene characterize individuals carrying Familial Adenomatous Polyposis (FAP), an inheritable genetic disease that accounts for only 2% of CRCs, that lead to development of non-invasive colonic adenomas (polyps).

APC is a negative regulator of Wnt signaling pathway, controlling the intracellular levels of β -catenin. Mutations in the APC gene lead to decrease in its tumour suppressor activity and result in activation of WNT signaling pathway. Therefore, β -catenin migrates to the nucleus, interacts with T-Cell Factor (TCF)/Lymphoid Enhancer-binding Factor (LEF) transcription factors, and induces transcription of target genes, including leucine rich repeat containing G protein-coupled receptor 5 (LGR5), Cyclin D1, and c-Myc. This leads to increased cell proliferation (Clevers, 2006).

APC mutations are not only important for tumour initiation but also for CRC maintenance (Dow et al., 2015).

Acquisition of new mutations is necessary for carcinogenesis progression. APC mutations are followed by activating mutations in the Kirsten rat sarcoma gene (KRAS). KRAS is one of the key players in the EGF pathway. Activating KRAS mutations result in constitutive activation of the mitogen activated protein kinase (MAPK) pathway, stimulating cell proliferation.

These mutations contribute to the transition from early to late adenoma and characterize the 30-50% of CRC patients (Cancer Genome Atlas, 2012, Fearon, 2011).

Other mutations identified in CRC affect tumour suppressor genes such as SMAD2 and SMAD4 (small mother against decapentaplegic 2-4), whose proteins mediate the signal of the transforming growth factor (TGF)-beta, and regulate multiple cellular processes, such as cell proliferation, apoptosis, and differentiation (Fleming et al., 2013).

Finally, inactivation of the tumour suppressor p53 contributes to the development of malignant carcinoma from late stage adenoma (Cancer Genome Atlas, 2012). Under physiological conditions, the p53 protein maintains genome integrity and induces apoptosis or senescence in cells irreparably damaged, regulating the expression of several genes involved in cell cycle control (Vogelstein et al., 2000). p53 is often inactivated by loss of heterozygosity (LOH) and its mutations are found in approximately 60% of CRC patients. It is important to mention that this proposed order in which mutations occur is not observed in all CRCs and can differ between patients.

In addition to the progression sequence discussed above, CRC is also characterized by epigenetic changes. Furthermore, tumours can be considered as multicellular models containing neoplastic cells, as well as infiltrating endothelial, immune, and stromal cells, including cancer-associated fibroblasts (CAFs). This tumour microenvironment (TME) enable and sustain the hallmarks of cancer (Hanahan and Coussens, 2012).

Collectively, genetics, epigenetics and TME contribute to intratumor heterogeneity, govern therapeutic resistance and tumour progression.

Another carcinogenesis model proposes that the development of the tumour is driven by a small subset of cells, cancer stem cells (CSCs), which is able to initiates and sustains tumour growth. Similarly to normal stem cells, these cells are able to both self-renewal and to generate a differentiated progeny (Barker et al., 2009).

1.3 Stem cells and cancer stem cells

The colon wall is composed of several layers: mucosa, submucosa, muscularis and serosa. The epithelial cells of the mucosa form a columnar cell monolayer organized into functional units called crypts of Lieberkühn. Multipotent stem cells reside at the base of the crypt and generate actively proliferating progenitors, which give rise to three main terminally differentiated colonic cell types: enterocytes, goblet cells and enteroendocrine cells (Blanpain et al., 2007).

These stem cells are responsible for the perpetual turn-over of the colonic epithelial cells during the whole lifetime of an individual. The first studies to identify the colonic stem cell population were based on the use of 3H-thymidine injection (Chang and Leblond, 1971). More recently, the expression of specific markers has been used as a tool to identify and locate cells with stem features within intestinal crypts. The two main models about the positioning of the intestinal stem cells (ISCs) are: the “+4 position” model, and the “stem cell zone” model. According to the first, ISCs are located at the +4 position above the Paneth cells at the base of the crypt. These cells are marked by the expression of the polycomb group protein B lymphoma Mo-MLV insertion region 1 homolog (BMI1) (Sangiorgi and Capecchi, 2008).

The “stem cell zone” model proposes that ISCs are interspersed between Paneth cells in the small intestine, or located at the very bottom of the crypt in the colon. These colon stem cells correspond to small and undifferentiated cycling cells, termed crypt base columnar (CBC) cells. Barker and colleagues identified *Lgr5* as a marker for ISCs (Barker et al., 2007).

The maintenance of stem niche is controlled by Wnt, bone morphogenetic protein (BMP), Notch and Hedgehog (Hh) pathways.

BMPs are members of the TGF- β family and regulate many fundamental biological processes, including proliferation, differentiation, and migration. BMPs bind both type I and type II receptors (BMPR1A, BMPR1B, and BMPR2), promoting the phosphorylation of SMAD1, 5, and 8 that, in association with SMAD4, regulates the expression of genes involved in the differentiation process (Chen et al., 1998, Gomez-Puerto et al., 2019). In healthy colon mucosa, BMPs are mainly located at the top of colon crypt, while BMP antagonists (gremlin and noggin) at the base (Kosinski et al., 2007). Furthermore, BMP signaling counteracts the Wnt pathway activity (He et al., 2004).

The loss of BMPR2 and SMAD4 expression has been reported in sporadic CRC, whereas germline mutations of BMPR1 and SMAD4 genes have been demonstrated to play a key role in CRC development (Kodach et al., 2008, Massague, 2008).

CSCs existence was first shown in 1997 by Bonnet and Dick, in acute myeloid leukemia (AML). They have isolated a CD34⁺/CD38⁻ cell population from bone marrow of patients with AML. This

fraction was able to reproduce the parental tumour phenotype if transplanted into immunodeficient non obese diabetic/severe combined immunodeficiency mice (NOD/SCID). Conversely, the more differentiated CD34+/CD38+ population lacked this ability (Bonnet and Dick, 1997, Lapidot et al., 1994).

Many reports have now described CSCs in several malignancies including head and neck (Prince et al., 2007), pancreas (Hermann et al., 2007), melanoma (Schatten et al., 2008), lung (Eramo et al., 2008), prostate (Collins et al., 2005) and colon tumours (Ricci-Vitiani et al., 2007).

In the recent years, interest in CSCs has increased due to their resistance to conventional anti-cancer therapies, generating the idea of combining these treatments with specific anti-CSCs therapies.

The CSCs capacity to survive to standard therapies is due to several characteristics including high expression of drugs transporters, cell cycle quiescence, high levels of DNA repair machinery, dysregulation of apoptosis and activation of some signalling pathways, such as EGFR, Wnt, Notch, phosphatidylinositol 3-kinase (PI3K)/protein kinase B (AKT) pathways, and to the effect of the microenvironment.

CSCs isolated from a variety of tumour types retain tumorigenic capacity and are responsible for the propagation, relapse and metastatic dissemination.

CSCs are identified using cell markers, some of these are commonly expressed by different types of cancer, others are tissue specific. It is possible, using different combination of these and through cell sorting, to obtain a cell population enriched in stem cells.

Colorectal-CSCs (CR-CSCs) can be identified by the expression of different surface markers, such as CD133, CD44, CD166, Lgr5, ALDH1 and EpCAM (O'Brien et al., 2007, Dalerba et al., 2007, Todaro et al., 2007, Du et al., 2008, Huang et al., 2009, Sato et al., 2009).

Furthermore, CD44v6 is a functional marker that confers to CR-CSCs the ability to migrate at distant sites and develop metastasis (Todaro et al., 2014).

The maintenance and survival of CSCs is regulated by different signaling pathways, which in recent years have emerged as prime targets.

EGFR is a member of the EGFR tyrosine kinase family, which consists of EGFR (ErbB1/HER1), HER2/neu (ErbB2), HER3 (ErbB3) and HER4 (ErbB4). These receptors are anchored in the cytoplasmic membrane and share a similar structure, that is composed of an extracellular ligand-binding domain, a short hydrophobic transmembrane region and an intracytoplasmic tyrosine kinase domain. The activation of these receptors is tightly regulated by the availability of ligands, including EGF, TGF- α , amphiregulin, betacellulin, heparin-binding epidermal growth factor, epiregulin and neuregulins (NRG1-4). Once these ligands bind to the extracellular domain, EGFR forms homo- or heterodimers with the other members of the family and induces

autophosphorylation of the intracellular domain and subsequent activation of downstream signalling pathways, including the MAPK, the PI3K/AKT and the Janus kinase 2/signal transducer and activator of transcription 3 (JAK2/STAT3) pathways, responsible for cancer cell proliferation, survival, invasion, metastasis formation and neo-angiogenesis.

EGFR is the most important actionable target identified so far in CRC. Small molecule tyrosine kinase inhibitors (TKIs), such as erlotinib, gefitinib and lapatinib, and mAbs against the extracellular domain of EGFR, cetuximab and panitumumab, are Food and Drug Administration (FDA)-approved for use in oncology. About 40% of patients with CRC are characterized by KRAS mutations at codons 12, 13, while less frequent mutations are located on codons 61, 146 and 154 (Cancer Genome Atlas, 2012).

These mutations lead the protein into a constitutively active state and make the cells independent from the EGFR signaling activation. The mutations in BRAF are rarer than KRAS mutations (8-15% of tumours) and are primarily (90%) V600E mutations (Davies et al., 2002).

Approximately 15%–20% of CRCs harbour activating mutations in PIK3CA exon 9 and/or exon 20 (Samuels et al., 2004). These mutations can be found in the same tumour along with KRAS and BRAF mutations. HER2 overexpression accounts for approximately 2% of all CRCs, increasing up to 5% in stage III or IV KRAS wild-type tumors (Valtorta et al., 2015, Ingold Heppner et al., 2014). Valtorta and colleagues defined specific immunohistochemistry (IHC)/ in situ hybridization (ISH) criteria to determine HER2 positivity in CRC. These criteria allowed selecting patients with HER2-positive, KRAS wild-type metastatic CRC (mCRC) for enrollment in the phase II HERACLES (HER2 Amplification for Colorectal Cancer Enhanced Stratification) trial of HER2-targeted therapy (Valtorta et al., 2015).

Several studies have shown the predictive and prognostic roles of these different gene mutations. Most patients undergo surgery of their primary tumour, thus samples are usually available for biomarker testing. However, this is not the case for ~20% of patients who present with metastatic disease. For these patients, biomarker testing is usually carried out using specimens from endoscopic biopsies or metastatic tumour (resected liver metastases or positive lymph nodes).

In other cases, both the primary tumour and metastatic tissue specimens may be available for mutation testing. An example of predictive biomarker for a specific therapy is HER2 in breast cancer (Cooke et al., 2001). HER2 amplification is also a negative predictor of response and cause of resistance to cetuximab in CRC (Bertotti et al., 2015, Yonesaka et al., 2011).

The combination of trastuzumab and lapatinib is active and well tolerated in HER2-positive metastatic colorectal patients resistant to previously received panitumumab or cetuximab (Sartore-Bianchi et al., 2016).

BRAF mutation is a negative prognostic marker for patients with mCRC (Tran et al., 2011).

BRAF V600E-mutated melanomas are sensitive to the BRAF-mutant inhibitor vemurafenib (Sosman et al., 2012), whereas CRCs harboring BRAF mutations are refractory (Kopetz et al., 2015). This lower response can be explained by a feedback reactivation of EGFR and downstream pathways (Corcoran et al., 2012, Prahallad et al., 2012). In a clinical trial the authors have tested targeted therapies in patients with metastatic BRAF mutant CRC, using combined BRAF (dabrafenib, D) and EGFR (panitumumab, P) inhibition with or without MEK inhibition (trametinib, T). The combinatorial treatment D+T+P achieves greater MAPK suppression and increase patients survival (Corcoran et al., 2018).

Several studies have shown that patients with mCRC, harboring activating mutations in KRAS exon 2 (codons 12/13), do not benefit from EGFR monoclonal antibody therapy with cetuximab and panitumumab (Amado et al., 2008, Karapetis et al., 2008, Van Cutsem et al., 2011).

Patients with KRAS exon 2 wild-type mCRC have significantly better outcomes from the addition of panitumumab to FOLFOX4 than those patients with RAS-mutant tumours (Douillard et al., 2013).

2. EPIGENETIC ALTERATIONS AS THERAPEUTIC TARGETS IN COLORECTAL CANCER STEM CELLS

2.1 Epigenetic alterations in cancer

Epigenetics can be defined as the study of heritable changes in gene expression or cell phenotype not caused by variations in the DNA sequence. In recent decades, knowledge regarding epigenetics has significantly expanded and it is now recognized that it plays an important role in the pathogenesis of various diseases, including cancer (Esteller, 2007). These changes reversibly affect gene activity. The best described epigenetic mechanism which contributes to CRC tumorigenesis is the alteration of CpG island methylation (Issa, 2004). During the process of methylation a methyl group (CH₃) is added on the carbon in position 5 of the cytosine residues. This leads to the formation of 5-methylcytosine. This methylation results in a closed chromatin structure that is correlated with decreased transcriptional activity (Baylin and Jones, 2011).

The CpG islands are genomic regions of at least 200 base pairs, preferentially located at the 5' end of the genes. They occupy about 70% of the promoters of human housekeeping and tissue-specific genes (Jones and Baylin, 2002).

The methylation is catalyzed by a class of enzymes, called DNA methyltransferase (DNMT), which use the cofactor S-adenosyl-methionine as a donor of the methyl group. The DNMT family consists of five members (DNMT1, DNMT2, DNMT3a, DNMT3b, DNMT3L) (Goll and Bestor, 2005).

DNMT1 plays the role of maintenance methyltransferase and carries methylation state from the parent cell to the daughter cells. DNMT1 is ubiquitously expressed in somatic cells, at high levels in proliferating cells. DNMT3a and 3b are instead responsible for *de novo* methylation (Okano et al., 1999). They establish methylation states early in embryonic development and in germ cells, and also play a role in maintaining DNA methylation in heterochromatic regions. Their expression is reduced in differentiated cells. DNMT3L is an inactive enzyme, which interacts with DNMT3a and 3b, stimulating their catalytic activity (Hata et al., 2002).

However, several studies show that the classification of DNMT3a/3b as *de novo* DNA methyltransferase and DNMT1 as maintenance DNA methyltransferase appears to be a simplification. Indeed, crescent evidence has revealed an important role of DNMT3a and DNMT3b in maintaining DNA methylation (Feng et al., 2010), while other studies have indicated *de novo* methylation activity of DNMT1 in specific loci (Jair et al., 2006). DNA methylation inhibits transcription through two distinct mechanisms. First, inhibiting the binding of transcription factors to promoter regions. Alternatively, methylated CpG sites can be recognized by a family of proteins, the MBP (Methyl Binding Proteins), which recruit repressor complexes, such as histone deacetylases, able to cause chromatin structural changes, which determine repression of gene expression.

Other mechanisms of epigenetic regulation are histone modifications and non-coding RNAs.

The N-terminal tails of histones can undergo different post-translational covalent modifications, such as methylation, acetylation, ubiquitination, sumoylation, biotinylation, ADP-ribosylation and phosphorylation (Kouzarides, 2007). These modifications lead to variations in the transcriptional accessibility of chromatin. Unlike DNA methylation, the modifications of the histone tails can determine both the activation and the repression of transcription. It depends on the modified residue and the type of modification present. For example, it is known that the trimethylation of lysine 4 in histone 3 (H3K4me3) makes the chromatin structure more open and therefore accessible to transcription factors, while the trimethylation of lysine 9 in histone 3 (H3K9me3) and of lysine 27 in histone 3 (H3K27me3) constitutes the main mechanism of transcription inhibition.

The histone acetylation consists in the transfer of an acetyl group on the lysine residues, by enzymes known as histone acetyltransferase (HAT). The histone acetylation neutralizes the lysine's positive charge, weakening the interactions between histones and DNA and causing the

decondensation of chromatin. Consequently, histone tails acetylation is associated with transcriptional activation. This mechanism can be reversed by histone deacetylase (HDAC).

Histones can be methylated on lysine and arginine residues. Methylation of lysines is catalyzed by lysine methyltransferase (KMT), methylation of arginine by proteins arginine methyltransferase (PRMT). Lysine side chains may be mono-, di- or tri-methylated, whereas the arginine side chains may be mono-methylated (symmetrically or asymmetrically).

SETD8 (also known as SET8, PR-Set7/9, KMT5A) is a member of the SET domain-containing methyltransferase family (Fang et al., 2002). It is the only known epigenetic enzyme responsible for the monomethylation of histone H4 lysine 20 (H4K20me1). SETD8 is involved in various biological processes, such as transcription modulation (Li et al., 2011), DNA replication (Tardat et al., 2007), maintenance of genome integrity (Oda et al., 2009), and cell cycle regulation (Wu et al., 2010). SETD8 also methylates lysine residues of non-histone proteins, such as PCNA (proliferating cell nuclear antigen) and p53 (Takawa et al., 2012). The methylation of p53 in lysine 382 (p53K382me1), determines an inhibition of its pro-apoptotic and cell growth arrest functions (Veschi et al., 2017, Shi et al., 2007).

Finally, non-coding RNAs (ncRNAs) are gene transcripts that do not undergo translation (Derrien et al., 2012). Among these are microRNAs (miRNAs), small non-coding RNAs that span between 18-24 nucleotides, which regulate gene expression through post-transcriptional silencing.

They bind to the untranslated regions (3' UTR) of the mRNA, inhibiting protein translation or favouring the destabilization or degradation of the mRNA (He and Hannon, 2004).

Their expression can be regulated by epigenetic mechanisms (Yao et al., 2019). MicroRNAs, in turn, can control the expression of epigenetic regulators, such as DNMT3a and DNMT3b or EZH2 (enhancer of zeste homolog 2) (Friedman et al., 2009, Ng et al., 2009). About 50% of the miRNA genes have a promoter containing CpG islands and the expression can be inhibited by DNA methylation. The reciprocal relationship between miRNAs and epigenetic regulation determines a feedback loop control (Lee et al., 2016).

Several CRCs are characterized by methylation of a wide variety of CpG islands, the so-called CpG island methylator phenotype (CIMP). CIMP tumours were defined as those with methylation of three or more of a small panel of genes (MINT1, MINT2, MINT31, CDKN2A, and MLH1).

High methylation phenotype CRC tumours (CIMP-H) have a high frequency of BRAF mutations (53% - 71%) and exhibit a relative lack of KRAS mutations (16%) and p53 mutations (11%) (Yagi et al., 2010, Shen et al., 2007). Microsatellite instability (MSI), primarily caused by hypermethylation of the MLH1 gene, is common in CIMP-H tumours (80%) (Weisenberger et al., 2006). MLH1 encodes for a DNA mismatch repair protein. Its silencing gives rise to tumours with

high mutation rate, high T-cell infiltration and a more mucinous presentation. Patients with these tumours are classified as microsatellite instable (Boland and Goel, 2010).

Patients who carry germline mutations in DNA repair genes (MLH1, MSH2, MSH6, PMS2, and EPCAM) develop the most common cause of hereditary CRC, the Lynch syndrome.

The use of drugs that interfere with chromatin-modifying enzymes, in particular HDACs and DNMTs, can have positive effects in the clinical treatment of cancer patients.

DNMTs inhibitors act with different mechanisms of action. Some of these compounds are phosphorylated and incorporated into the DNA double helix. When DNMTs bind to hemimethylated DNA, they immediately form irreversible covalent bonds with these drugs. This determines a cellular depletion of enzymes with methyltransferase activity (Egger et al., 2004).

The others, called "non-analogues of nucleotides", are not incorporated into the DNA, can inhibit DNMTs by binding to the catalytic site or they can associate with CpG islands by interfering with their methylation (Lee et al., 2005; Datta et al., 2009).

To date, the FDA has approved 5-azacytidine and decitabine (5-aza-2'-deoxycytidine), two DNMTs inhibitors analogues of the nucleotides, for the treatment of myelodysplastic syndrome (Kaminskas et al., 2005, Yoo et al., 2007).

Furthermore, HDAC and EZH2 inhibitors have also been approved by the FDA for the treatment of diverse malignancies and a wide range of epigenetic-based drugs are undergoing clinical trials (Nepali and Liou, 2021). These include: FK-228 and SAHA (HDAC inhibitors approved for the treatment of refractory cutaneous T-cell lymphoma), PXD101 (HDAC inhibitor approved for the treatment of refractory peripheral T cell lymphoma), LBH589 (HDAC inhibitor for the treatment of multiple myeloma) and tazemetostat (EZH2 inhibitor approved for the treatment of metastatic or locally advanced epithelioid sarcoma).

In many types of cancer, including CRC, there is a correlation between epigenetic mechanisms and the stem characteristics of cancer cells (Yi et al., 2008, Vedeld et al., 2014, van Vlerken et al., 2013, Avgustinova and Benitah, 2016).

Such epigenetic modifications are key factors during the normal development and differentiation of stem cells into specific cell subtypes. Mutations and/or alterations in the expression of epigenetic enzymes can lead to the loss of expression of specific genes of the differentiated state and to the restoration of the stem cells characteristics. Furthermore, it has been shown that the variability of response to pharmacological treatment may also depend on these epigenetic alterations (Shukla and Meeran, 2014).

2.2 Preliminary results

DNMT1 and SETD8 are overexpressed in CRC and p53^{K382me1} is highly expressed in CD44v6⁺CR-CSphCs present at the tumour front of invasion

Given the complex interplay between remodeling enzymes, histone modifiers and DNA methyltransferases (Cedar and Bergman, 2009), we examined the Cancer Genome Atlas Colon database, in order to identify epigenetic enzymes that may play a crucial function in the initiation and progression of CRC. Among these, we focused on those statistically significant and differentially expressed between healthy subjects and CRC patients (Fig. 1A). Overexpression of DNMT1 has been observed in several different tumour types (Wong, 2021, Wong, 2020, Colyn et al., 2021). We observed, through the analysis of the TCGA Colon Adenocarcinoma (TCGA-COAD) database, that DNMT1 expression is higher in colon cancer tissue compared to healthy mucosa (Fig. 1B). Furthermore, the immunohistochemical analysis of paraffin-embedded tissue sections of primary tumors derived from CRC patients showed that DNMT1 is over-expressed in tumour tissues compared with healthy mucosa (Fig. 1C). According to the analysis of TCGA-COAD database (Fig. 1A), we then focused on SETD8, a methyltransferase overexpressed in many tumors, which inactivates p53 through the methylation of its lysine 382 (p53K382me1). Western blot analysis showed that SETD8 and its histone target (H4K20me1) are variably expressed in our collection of CR-CSphCs, while its non-histone target (p53K382me1) follows a specific expression pattern (Fig. 1D). The 72% of CR-CSphCs (8/11) express p53K382me1 and at least 50% of these display a high p53K382me1/p53 ratio, as determined by densitometry (Fig. 1E). Interestingly, in colon cancer cell lines characterized by a more differentiated state, p53K382me1 is nearly undetectable, despite the high levels of total p53 protein (Fig. 1D). Accordingly, SETD8 protein levels are higher in colon cancer cell line HCT116 and in CR-CSphC#8, compared with normal colon cell lines (CRL-1790 and CRL-1831) (Fig. 1F). Analysis of the TCGA COAD database revealed higher SETD8 mRNA expression levels in colon cancer tissue compared to healthy mucosa, suggesting that SETD8 may play a critical role in CRC tumorigenesis (Fig. 1G). Consistently, immunohistochemical analysis in primary tumours derived from CRC patients showed that SETD8 is overexpressed in tumour tissues compared with healthy colon mucosa of healthy subjects. Of note, elevated levels of SETD8 are highly expressed in all CRC cells, compared to the healthy mucosa, while the p53K382me1 is specifically expressed in the CRC cells present at the tumour front of invasion and it is undetectable in the healthy mucosa epithelial cells

(Fig. 1H). Moreover, immunofluorescence analysis demonstrates that p53^{K382me1} is highly expressed in CD44v6-positive CR-CSphCs with metastatic potential (Fig. 1I).

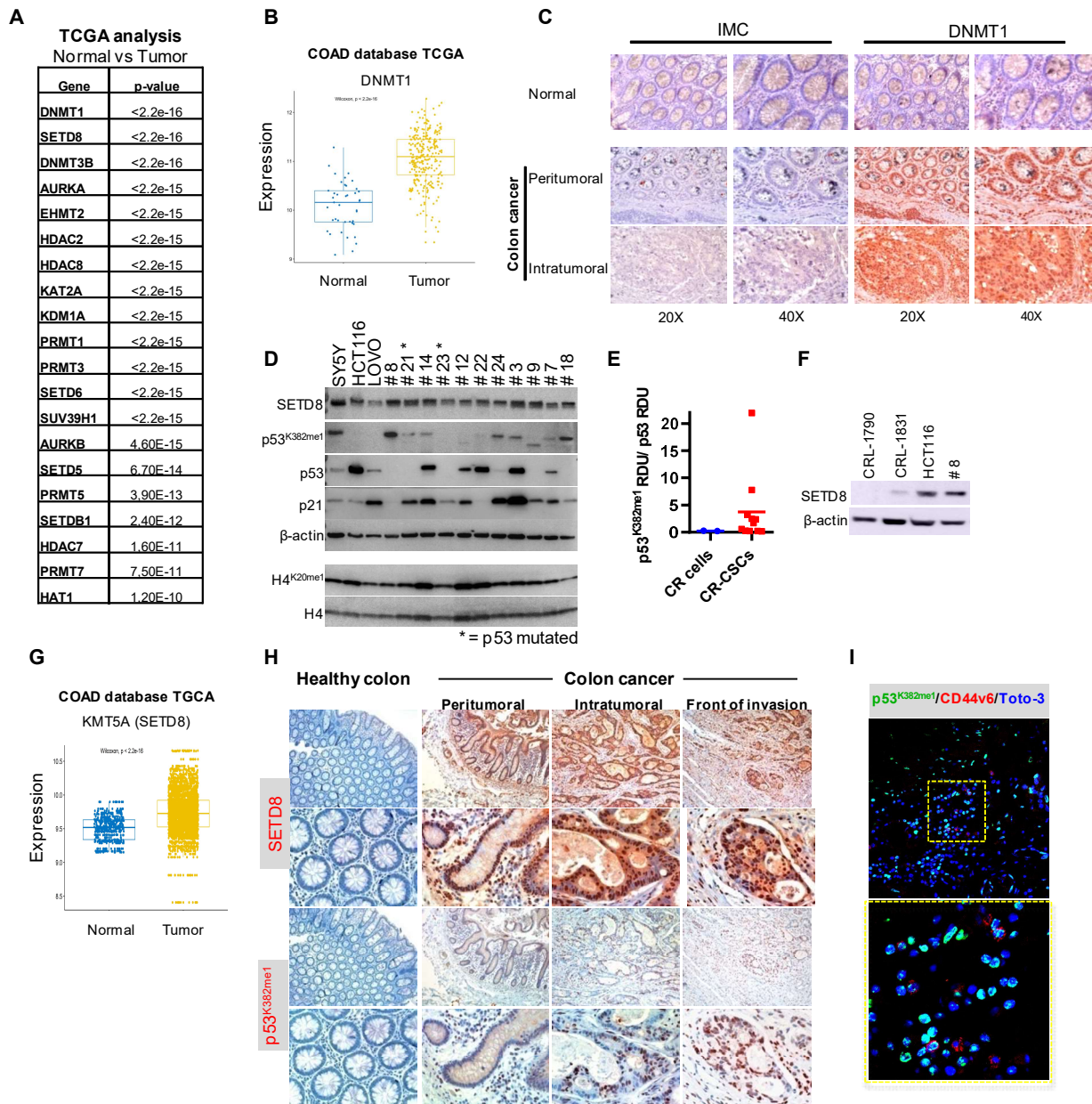


Fig.1: (A) List of epigenetic enzymes differentially upregulated in CRC patients compared to healthy subjects. (B) DNMT1 gene expression levels in normal and tumor tissue derived from colon cancer patients (TCGA COAD database). (C) Representative image of immunohistochemical analysis of DNMT1 and IMC (isotype matched control) on tumor and healthy tissues. (D) Immunoblot analysis of the indicated total and histone proteins in SY5Y neuroblastoma cell line (positive control), HCT116 and LOVO colon cancer cell lines, and 11 CR-CSphCs. β-actin and H4 were used as loading controls. (E) Densitometry analysis of p53^{K382me1} protein levels compared with p53 total protein levels measured as relative density units (RDU). (F) Immunoblot analysis of SETD8 in CRL-1790, CRL-1831, HCT116 cell lines and in CR-CSphC#8. β-actin was used as loading control. (G) TCGA analysis of *KMT5A* (SETD8) relative mRNA expression levels in normal and tumor tissue derived from colon cancer patients. (H) Immunohistochemical analysis of SETD8 and p53^{K382me1} on healthy colon mucosa of a healthy subject and on tumor tissue of a CRC patient. (I) Immunofluorescence analysis of p53^{K382me1} and CD44v6 in tumor tissue derived from a CRC patient. Nuclei were counterstained by Toto-3.

SETD8 inhibitor reduces cell viability and the clonogenic potential of CR-CSphCs in vitro, impairs tumour growth and prolongs mice survival in vivo

Treatment of six CR-CSphCs with the small molecule UNC0379, a specific substrate-competitive SETD8 inhibitor, impairs cell viability in a dose- and time-dependent manner. Interestingly, UNC0379 doesn't affect the viability of the human colon normal cell line CRL1831 (Fig 2A, B). Western blot analysis showed that UNC0379 treatment decrease p53K382me1 and H4K20me1 levels in CR-CSphCs, in a dose-dependent manner (Fig. 2C). The cell cycle analysis indicated that UNC0379 causes an increase in CR-CSphCs G0-G1 cell cycle phase and a reduction in S- and G2/M- cell cycle phases, while increasing the sub-G0 phase (Fig. 2D). Of note, exposure of CR-CSphCs to UNC0379 for 72 hours resulted in a reduction of their colony-forming capability (Fig. 2E).

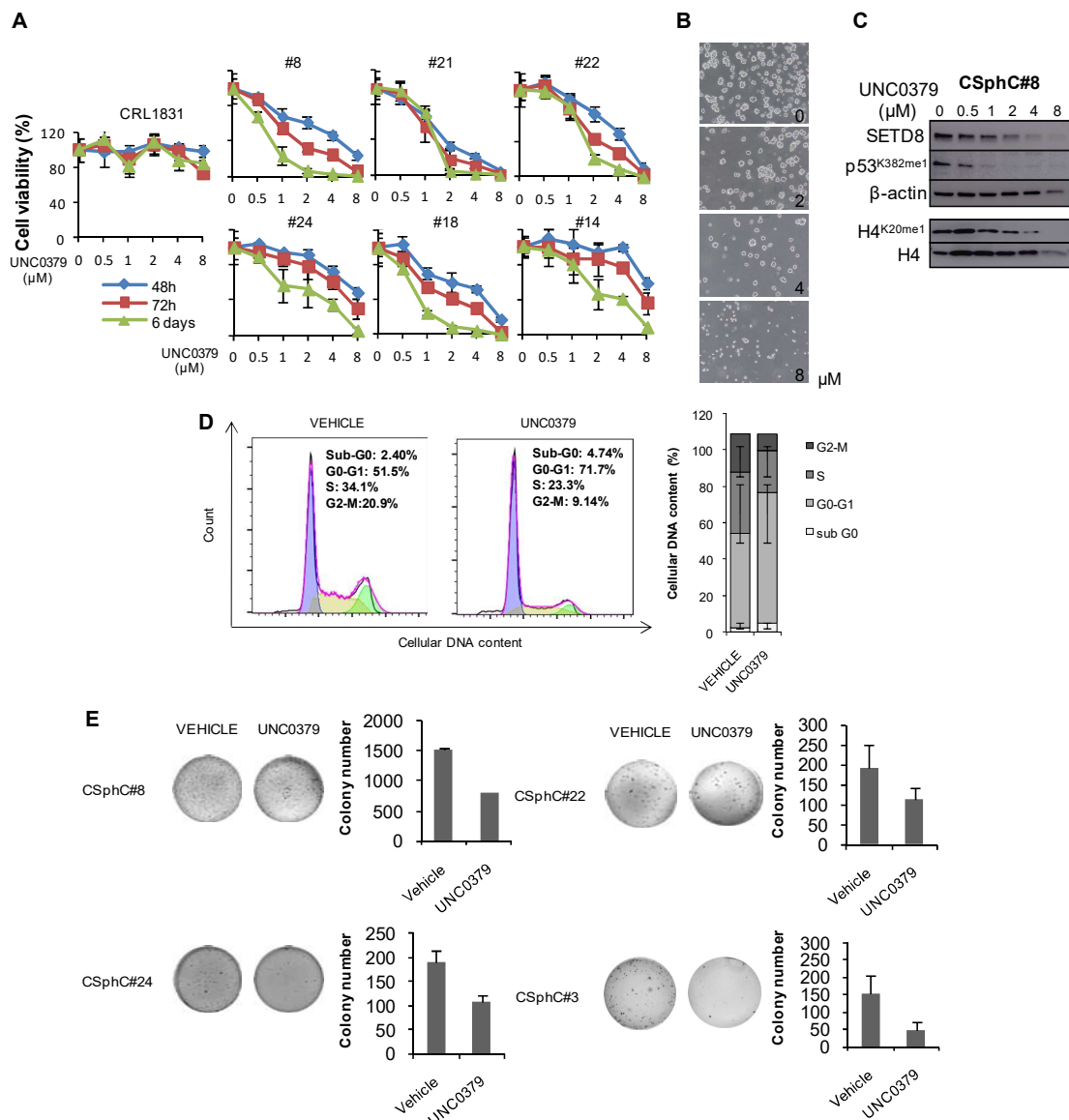


Fig.2: (A) Cell viability assay in 6 CR-CSphCs treated with UNC0379 at the indicated time and doses. (B) Representative optical microscope images of CR-CSphC#8 treated with UNC0379 at the indicated doses. (C) Immunoblot analysis of the indicated proteins in CR-CSphC#8 treated with UNC0379 for 48 hours at the indicated doses. β-actin and H4 were used as loading controls. (D) Cell cycle analysis of CR-CSphC#8 treated as in (A) for 24 hours, at a concentration of 4μM (blue color = G0-G1; yellow color = S; green color = G2-M). (right panel) Cell cycle analysis of CR-CSphC#8 treated as in (A) for 24 hours, at a concentration of 4μM. Data show percentage of cell number in sub G0, G0-G1, S, and G2-M phases. (E) Colony-forming assay of the indicated CR-CSphCs treated with vehicle or UNC0379 4μM, at 21 days.

SETD8 inhibition affects the CR-CSphC markers expression, including CD133, CD44v6, SOX-2 and NANOG (Fig. 3A). Among these, CD44v6 is a well-known functional biomarker involved in the main features of cancer progression. CR-CSphCs-expressing CD44v6 were efficiently targeted by UNC0379 and showed a higher activity of caspase 3 compared to the more differentiated counterpart (Fig. 3B). Therefore, these results demonstrated that this compound induces apoptosis in the subpopulation characterized by the more aggressive phenotype. We then evaluated the effects of UNC0379 treatment on tumour growth, performing an *ex-vivo* tumorigenicity assay. We exposed CR-CSphC to UNC0379 or control solvent for 24 hours *in vitro*, then we inoculated subcutaneously the cells into NSG (NOD/SCID/IL2 γ null) mice, monitoring tumour growth. Pharmacological inhibition of SETD8 showed decreased tumour growth and increased mice overall survival (Fig. 3C, D).

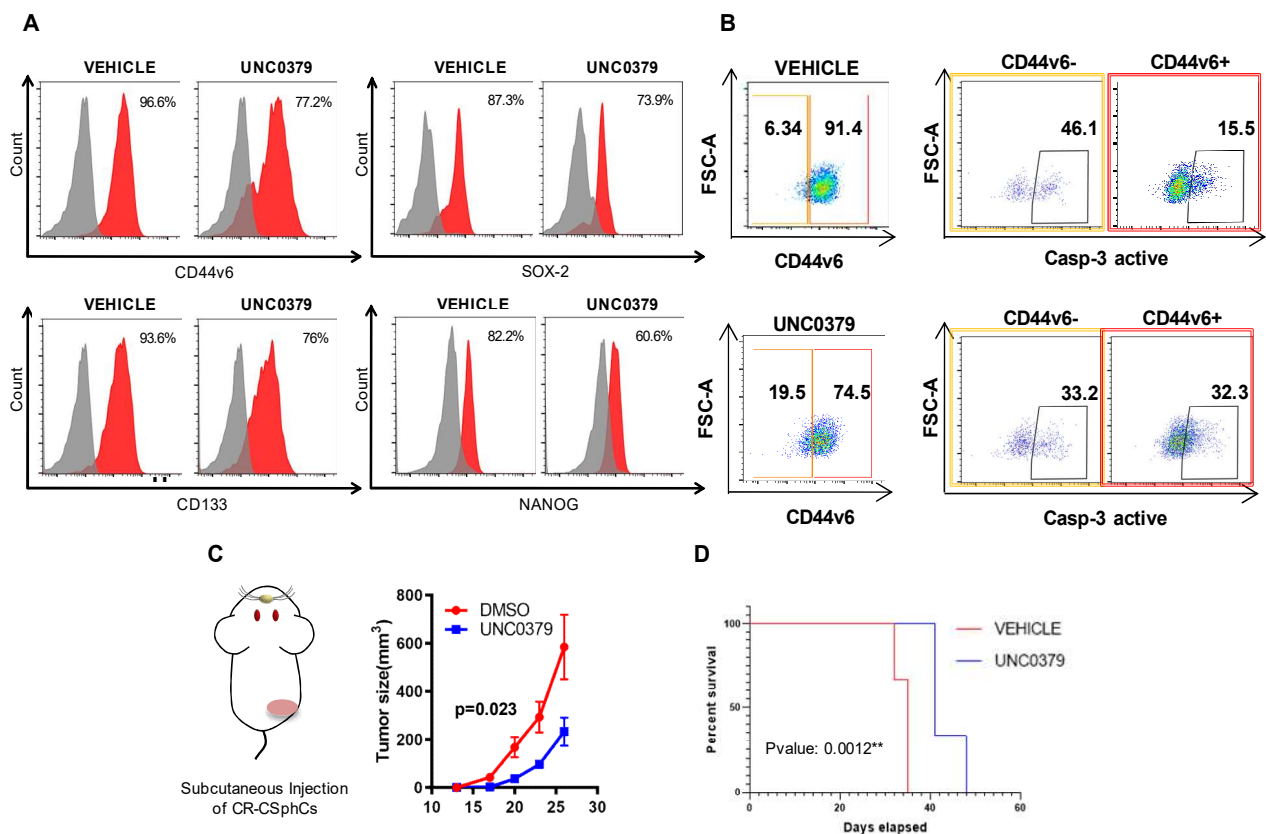


Fig.3: (A) Flow cytometry analysis of CD44v6, CD133, SOX-2 and NANOG on CR-CSphC#8. Grey color indicates cells stained with IMC. (B) Flow cytometry analysis of active Casp-3 positivity in CD44v6⁺ in CR-CSphC#8 treated with vehicle and UNC0379 4 μ M up to 72 hours. (*left panels*) Gating strategies of the expression of CD44v6 in CR-CSphC#8 treated as previously described. (C) CR-CSphC#8 was treated *ex-vivo* for 24 hours with UNC0379 4 μ M and then injected into NSG mice. (*right panel*) Subcutaneous size of tumor xenografts generated as previously described. (D) Survival curves of mice treated as in (C).

Genetic inhibition of SETD8 counteracts stemness features of CR-CSphCs and impairs in vivo tumour growth

We next investigated the effects of specific SETD8 targeting by its genetic inhibition. We transduced spheres with lentiviral vectors encoding for specific SETD8 small hairpin RNA (shRNA) sequences. SETD8 silencing reduces viable CR-CSphC number and the expression of CR-CSphCs markers (Fig. 4A, B), similarly to the pharmacologic inhibition. In order to evaluate the *in vivo* influence of this genetic silencing, CR-CSphCs transduced with inducible shSETD8 or with shRNA control (pTRIPZ) were injected orthotopically into the mouse caecum. SETD8 knockdown prevents tumour growth and abrogates tumour metastasis outgrowth (Fig. 4C, D). Immunohistochemical analysis of colon tumor sections derived from mice transduced with pTRIPZ showed elevated expression levels of SETD8 and CK20 (Fig. 4E). Then we proceeded to visualize polyps in the colon of mice in which we inoculated CR-CSphC transduced with shSETD8 and shRNA control, using methylene blue staining, as previously described (Wu et al., 2009).

As indicated by the yellow arrows in the figure 4F, the colon of PTRIPZ mice presents a condition of polyposic hyperplasia, not visible in presence of shSETD8. We also observe this marked hyperplasia in hematoxylin and eosin stained colon tumor sections of pTRIPZ mice (Fig. 4G). We next quantified the number and measured the size of polyps in each group of mice (Fig. 4H). Finally, we inoculated subcutaneously CR-CSphCs transduced with inducible shSETD8 or with shRNA control into NSG mice and monitored tumour growth. Genetic inhibition of SETD8 causes a significant reduction in tumor size, also visible through the macroscopic image of the tumors (Fig. 4I, J). Western blot analysis showed that the *in vivo* silencing of SETD8 decreases the expression of p53^{K382me1} (Fig. 4K).

Pharmacological and genetic inhibition of SETD8 reduces the expression of Wnt pathway-, EMT- and cell proliferation-related genes

In order to evaluate the differentially expressed genes related to epithelial to mesenchymal transition (EMT), tumor metastasis and Wnt signaling in CR-CSphCs in common between the pharmacological and genetic inhibition of SETD8, we performed a custom transcriptomic analysis (Fig. 5A). Specifically, we identified 21 the common downregulated genes by UNC0379 treatment and by the SETD8 silencing. Of note, gene set enrichment analysis (GSEA) and molecular signatures database (MSigDB) analysis of these 21 genes, revealed the inhibition of several pathways, including cell proliferation, cell communication and cell movement processes.

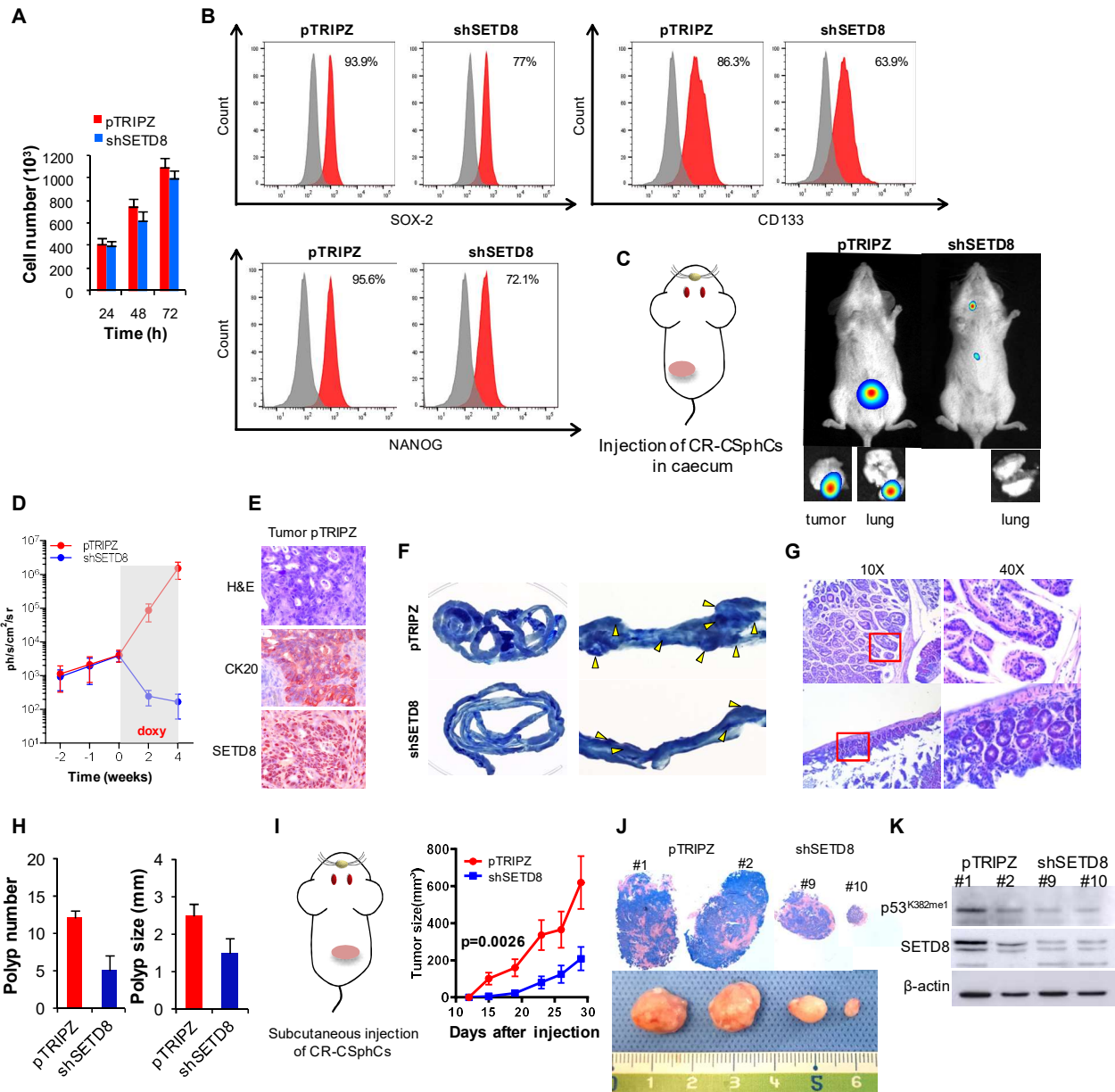


Fig.4: (A) Cell number of CR-CSphC#8 transduced with pTRIPZ and shSETD8 and treated with Doxycycline (Doxy) for the indicated hours. (B) Flow cytometry analysis of SOX-2, NANOG and CD133 on CR-CSphC#8 transduced with pTRIPZ and shSETD8 and treated with Doxy for 7 days. Grey color indicates cells stained with IMC. (C) CR-CSphC#8 transduced with Doxy inducible shSETD8 or with shRNA control (pTRIPZ) were injected orthotopically into the mouse caecum. (*right panel*) *In vivo* whole-body imaging analysis of mice at 4 weeks and the bioluminescence signals of primary tumor and lung metastasis. (D) Kinetics of tumor growth of mice as in (C) up to 4 weeks after starting Doxy treatment. CR-CSphC#8 transduced with pTRIPZ and shSETD8 were injected orthotopically 2 weeks before starting the Doxy treatment. (E) Representative image of H&E staining and immunohistochemical analysis of SETD8 and CK20 of tumor tissue of pTRIPZ mice. (F) Representative methylene blue staining of the entire intestine of mice treated as in (C). The yellow arrows indicate polyps. (G) Representative H&E staining of colon cancer section of mice treated as in (C). (H) Colon polyp number and size of mice treated as in (C). (I) CR-CSphC#8 transduced with pTRIPZ and shSETD8 were injected subcutaneously into NSG mice. (*right panel*) Subcutaneous size of tumor xenografts generated as previously described and monitored up to 30 days after injection. The treatment with the doxy started 12 days after the injection. (J) H&E staining and macroscopic images of tumors of mice treated as in (I). (K) Western Blot analysis of the indicated proteins of tumors of mice treated as in (I). β -actin was used as loading control.

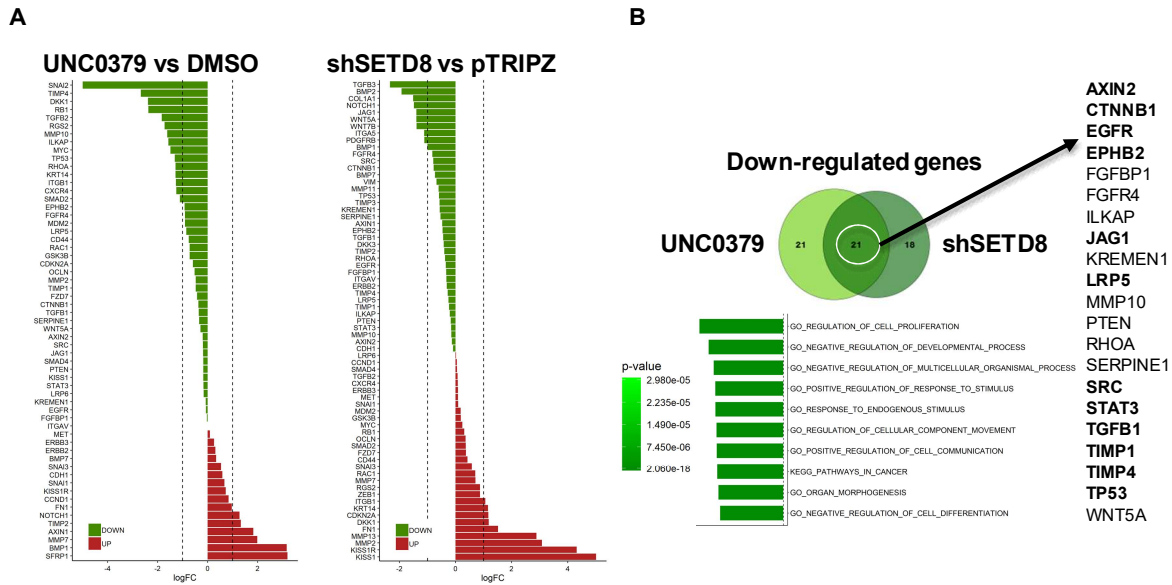


Fig.5: (A) Log fold change (logFC) values of differentially expressed related genes in CR-CSphC#8 treated with UNC0379 4 μ M and DMSO for 72 hours and in CR-CSphC#8 transduced with shSETD8 and pTRIPZ and treated with Doxy for 7 days. Dotted lines represent -1 and 1 logFC values. Upregulated genes are in red and downregulated genes in green (B) Venn diagram showing downregulated genes in CR-CSphC#8 treated with UNC0379 and transduced with inducible shSETD8. The black arrow indicates the common downregulated genes. Top ten significantly enriched gene sets selected by using Hallmark, KEGG, and GO, related to the indicated genes common in CR-CSphC#8 treated with UNC0379 and CR-CSphC#8 transduced with inducible shSETD8. P-values related to each enriched gene set are indicated.

2.3 Conclusions

DNA methyltransferase 1 and the lysine methyltransferase SETD8 play a critical role in the tumorigenesis of several tumours. Elevated levels of these epigenetic enzymes are observable in tissues derived from colon cancer patients compared to healthy subjects. Specifically, the methylation of the non-histone target p53 (p53K382me1) by SETD8 occurs mainly in the tumor front of invasion and is confined to CR-CSphCs CD44v6⁺, characterized by a tumorigenic and metastatic potential. Furthermore, elevated expression levels of SETD8 are associated with poor prognosis (Hervioui et al., 2021, Liu et al., 2021), representing a potential therapeutic target for advanced CRC patients that would benefit from its inhibition.

DNA-demethylating agents, azacitidine and decitabine, have been approved by FDA for the treatment of myelodysplastic syndrome and acute myeloid leukemia. Nevertheless, it's known that these compounds are not characterized by a stable pharmacokinetics because of their *in vivo* rapid deamination and spontaneous hydrolytic cleavage. Thus, for these reasons novel therapeutic strategies using the most recently developed epigenetic probes are urgently needed. Therefore, we focused on UNC0379, a substrate-competitive SETD8 inhibitor selectively targeting SETD8 among other 20 methyltransferase. Our studies demonstrate that SETD8 inhibition upon UNC0379 treatment results in reduced cell viability and an induction of apoptosis, which especially affects

CR-CSphCs CD44v6⁺. Here, we showed evidence that SETD8 knockdown results in a reduced expression of stem cell markers, including NANOG, SOX-2, CD133, CD44v6. These changes were accompanied by a functional decrease in cell ability to form colonies. Accordingly the specific targeting of SETD8 by a genetic inhibition affects the CR-CSphCs proliferation and their stem features. In pre-clinical xenograft CRC models, pharmacological and genetic inhibition of SETD8, displayed diminished tumour growth and conferred a significant survival advantage. In addition, SETD8 depletion was accompanied by reduced protein levels of p53K382me1. Transcriptomic analysis upon pharmacological and genetic inhibition of SETD8 revealed that among 21 common downregulated genes, the most significantly differentially expressed included genes related to Wnt pathway as AXIN-2, CTNBB1, and others EGFR, STAT3, TIMP1/4, LRP5, with a crucial role in cell proliferation, cell movement processes and stemness.

Collectively, our finding highlight the involvement of epigenetic modifiers in CRC tumorigenesis and underline SETD8 as a putative target, paving the way for a therapeutic strategy that could activate p53 functions.

2.4 Materials and methods

Isolation and treatment of CR-CSphCs

SY5Y, HCT116, LOVO, CRL-1790, CRL-1831 cell lines were obtained from ATCC and cultured at 37 °C in a humidified 5% CO₂ atmosphere as suggest by the supplier.

CR-CSphCs were purified from CRC patients undergoing colon resection, in accordance with the ethical standards regarding Human Experimentation (authorization CE9/2015, Policlinico Paolo Giaccone, Palermo), as previously described (Todaro et al., 2007).

CSphCs were cultured in ultra-low conditions, in stem cell medium (SCM) supplemented with EGF and b-FGF. Authentication of CSphC lines was routinely performed using a short tandem repeat DNA profiling kit (GlobalFiler™ PCR kit, Applied Biosystem) following the manufacturer's instructions and analyzed by ABI PRISM 3130 (Applied Biosystem).

Mycoplasma contamination was checked every 3 months using the Myco Alert™ Plus Mycoplasma Detection Kit (Lonza) according to the manufacturer's instructions.

CR-CSphCs cells were treated with UNC0379 (S7570, Selleckchem) at the indicated time and concentrations.

Immunohistochemistry and immunofluorescence

Immunohistochemical analysis was performed on 5- μ m-thick paraffin embedded xenograft and patients sections using antibody specific for DNMT1 (AB_2614950, clone 60B1220.1, mouse IgG, Active Motif), SETD8 (ab111691, rabbit IgG, abcam), p53K382me1 (rabbit polyclonal, described previously in Shi et al., 2007), CK20 (NCL-L-CK20, Ks20.8, IgG2a_k, Novocastra).

For intracellular epitope detection, tissue sections were permeabilized in ice-cold 0.1% TritonX-100 in PBS for 10 min. Stainings were revealed using biotin-streptavidin system (Dako) and detected with 3-amino-9-ethylcarbazole (AEC) or DAB (Dako). Nuclei were counterstained with aqueous hematoxylin (Sigma-Aldrich). H&E stainings were performed using standard protocols.

Immunofluorescence staining was performed on CRC tumour tissue fixed, permeabilized and incubated overnight with CD44v6 (2F10, mouse IgG1, R&D systems) and p53K382me1 (rabbit polyclonal, described previously in Shi et al., 2007). Cells were stained with Alexa Fluor-488 goat anti-rabbit and Rhodamine RedTM-X goat anti-mouse secondary antibodies (Life Technologies). Nuclei were counterstained using Toto-3 iodide (Life Technologies).

Western blot

CR-CSphCs were lysed in ice-cold lysis buffer (Tris-HCL 10 mM, NaCl 50 mM, sodium pyruvate 30 mM, NaF 50 nM, ZnCl₂ 5 μ M, triton 1, sodium orthovanadate 0.1 nM, sodium butyrate 10 mM and PMSF 1 mM) supplemented with protease and phosphatase inhibitors (Sigma-Aldrich). Proteins extracted were loaded in SDS-PAGE gels and blotted on nitrocellulose membranes. Membranes were blocked with a blocking solution (0.1% Tween 20 and 5% non-fat dry milk in PBS) for 1 hour at room temperature and then incubated with specific antibodies against SETD8 (ab111691, rabbit IgG, abcam), p53K382me1 (rabbit polyclonal, described previously in Shi et al., 2007), p53 (DO-1, mouse IgG2a, Santa Cruz Biotechnology), p21 (DCS60, mouse IgG2a, Cell Signaling Technology), H4K20me1 (AB_2615074, clone 5E10-D8, mouse IgG1k, Active Motif), H4 (AB_2636967, rabbit polyclonal, Active Motif) and β -actin (8H10D10, mouse, Cell Signaling Technology). Primary antibodies were revealed using anti-mouse or anti-rabbit HRP-conjugated (goat IgG, Thermo Fisher Scientific) for 1 hour at room temperature and detected with SuperSignalTM West Dura Extended Duration Substrate (Thermo Fisher Scientific) using Amersham imager 600 (GE Healthcare). Protein levels were normalized with β -actin and calculated by densitometric analysis using ImageJ software.

Cell viability and proliferation

CR-CSphCs viability was evaluated using the CellTiter 96 AQueous One Solution Cell Proliferation 369 Assay (MTS, Promega) following the manufacturer's instructions and examined with GDV MPT 370 reader (DV 990 BV6). Trypan Blue exclusion test is used to determine the number of viable cells and the proliferation rate of CR-CSphCs pTRIPZ and shSETD8.

Colony Forming Assay

CR-CSphCs were pretreated for 72 hours with UNC0379 or vehicle. Then they were plated at a clonal density of 2×10^3 cells/well on Agarose Sea Plaque Agar (Invitrogen). After 21 days, colonies were stained with 0.01% Crystal Violet and counted using ImageJ Software.

Flow cytometry and cell cycle analysis

To evaluate CD44v6 and CD133 expression, CR-CSphCs treated with vehicle or UNC0379 for 72 hours and CR-CSphCs transduced with pTRIPZ and shSETD8 were harvested, washed with PBS + 0.5% bovine serum albumin (BSA) and stained with CD44v6 (2F10 APC, mouse IgG1, R&D systems), CD133 (130-090-854, 293C3-APC, mouse IgG2b κ , Miltenyi) or with corresponding IMC for 1 hour at 4°C. Dead cells were excluded using the 7-AAD (0.25 μ g/ 1×10^6 cells, BD Biosciences).

For intracellular staining, cells were fixed in 2% paraformaldehyde, permeabilized with PBS + 1% Triton-X 100 and stained with SOX-2 (562139, clone O30-678, Alexa Fluor 647, mouse IgG1 κ , BD Biosciences) and NANOG (561300, clone N31-355, Alexa Fluor 647, mouse IgG1 κ , BD Biosciences) for 30 minutes at 4°C. Samples were analyzed by FACS Lyric (BD) flow cytometer.

In order to analyze the cell cycle, untreated and treated CR-CSphCs cell pellet was incubated, in the dark at 4°C overnight, with 1 ml of Nicoletti Buffer (0.1% of sodium citrate, 0.1% of Triton X-100, 50 μ g/ml of propidium iodide, 10 μ g/ml of RNase solution). The quantification of DNA content was performed using BD FACS Lyric flow cytometer (BD Clinical system, BD Bioscience).

Apoptotic cells upon UNC0379 treatment were identified by using the CaspGLOW™ Fluorescein Active Caspase-3 Staining Kit (Biovision), following the manufacturer's protocol. The caspase-3 activity was analyzed by flow cytometer. All the obtained data were analyzed by FlowJo software.

Cell transfection and lentiviral transduction

Lentiviral particles were generated by transfecting HEK-293T packaging cells with TRIPZ inducible shRNA control (ns shRNA, Dharmacon) or human SETD8 shRNA (shSETD8, Dharmacon) plasmids together with psPAX2 (Addgene, 12260) and pMD2.G (Addgene, 12259) in

DMEM 10% FBS supplemented with XtremeGENE HP DNA Transfection Reagent (Roche). Lentiviral supernatants were concentrated using the Lenti-X Concentrator reagent (Clontech) and 1×10^6 CR-CSphCs were transduced in presence of 8 $\mu\text{g}/\text{mL}$ of polybrene (Sigma-Aldrich). Transduced cells were treated with doxycycline (1 $\mu\text{g}/\text{ml}$, Sigma-Aldrich) for 7 days.

Animals and tumour models

6-8 weeks old male NSG mice were purchased by Charles River Laboratories. *In vivo* experiments were performed in accordance with the animal care committee guidelines of the University of Palermo (Italian Ministry of Health authorization n. 154/2017-PR).

Dissociated CR-CSphCs (5×10^3), treated *ex vivo* for 24 hours with UNC0379 and DMSO, were injected subcutaneously into the flank of NSG mice, in a total volume of 150 μl of SCM mixed with matrigel (BD) in a ratio of 1:1.

CR-CSphCs (5×10^3) transduced with shRNA control (pTRIPZ) or with shSETD8 were injected subcutaneously in NSG mice, as already described. On day 12 after the injection, doxycycline was added at 1 mg/ml to animal drinking water and replaced every 48 hours. For the orthotopic injection, CR-CSphCs (3×10^3) transduced with luciferase (LUC) and shSETD8 or shRNA control (pTRIPZ), were injected in mice caecum in 30 μl of 1:3 SCM/Matrigel solution. Two weeks after the injection, doxycycline was added at 1 mg/ml to animal drinking water and replaced every 48 hours.

The bioluminescence signal of CR-CSphCs was measured following i.p. administration of D-luciferin (150 mg/kg, Promega), 4 weeks after the induction with doxycycline, by using *in vivo* imaging system (IVIS Spectrum, PerkinElmer).

Tumours were measured twice per week by a digital caliper. Tumour size was calculated according to the formula: $(\pi/6) \times (\text{smaller diameter})^2 \times \text{larger diameter}$.

Once the endpoints were reached, animals were sacrificed accordingly to Directive 2010/63/EU guidelines (D.lgs 26/2016) and organs were collected for histopathological analysis.

Methylene Blue Staining

Mice were sacrificed and colon tissue was excised, cleaned with cold PBS, opened longitudinally, fixed in 10% neutral buffered formalin (3.7% formaldehyde, 1.2% methanol, 6.5 g/l sodium phosphate dibasic, 4 g/l sodium phosphate monobasic) at 25°C overnight and stained with 0.2% methylene blue solution. The polyps were then quantified and sized.

RNA isolation and Real-time PCR

The purification of RNA was carried out using TRIZOL™ Reagent (Thermo Fisher) protocol and 1 µg of total RNA, after the removal of genomic DNA, was retrotranscribed with the high-capacity c-DNA reverse Transcription kit (Applied Biosystem) and subjected to quantitative real-time PCR (qRT-PCR) with a custom PrimePCR panel (Bio-Rad) for 88 genes. Relative mRNA expression levels were normalized with the endogenous control (GAPDH) and calculated using the comparative Ct method ($2^{-\Delta\Delta C_t}$).

mRNA expression levels of EMT-, tumour metastasis-, and Wnt pathway-related genes were detected by RT2 profiler PCR array (PAHS-090, Qiagen) according to manufacturers' instructions. Data were analyzed using the R version 3.5.0 and plotted by the pheatmap version 1.0.10 and VennDiagram 1.6.20, gtools 3.8.1, and ggplot2 3.0.0. GSEA was performed by selecting the Kyoto Encyclopedia of Genes and Genomes, Gene Ontology and Hallmarks within MSigDB version 6.2.

Statistical analysis

The Wilcoxon test was used to compare the expression levels of *DNMT1*, *SETD8* and all the others epigenetic enzymes listed in Fig.1A in normal and tumorigenic samples from the The Cancer Genome Atlas (TCGA) colon adenocarcinoma (COAD) branch.

Student's t test was used to compare the tumor volume between UNC0379 or shSETD8 and non treatment groups and p values <0.05 were considered to be statistically significant. A paired t-test was used to compare the slopes of the growth rates. The analyses were carried out using the software GraphPad Prism 6.0. The Kaplan-Meier method was used to determine the probability of mice survival as a function of time. The statistical significance between two treatment groups was evaluated using a log-rank test (Mantel-Cox). All p values <0.05 were considered to be statistically significant. The analyses were carried out using the software GraphPad Prism 6.0.

3. THERAPEUTIC STRATEGIES TARGETING CANCER STEM CELLS AND THEIR MICROENVIRONMENT

The targeting of CSCs represents a novel approach in cancer treatment, so the identification of agents able to inhibit CSCs is currently a major challenge in cancer research field.

The different approaches that were clinically employed to target CSCs concern:

- Inhibition of signaling pathways used by CSCs
- Targeting the CSC microenvironment
- Targeting surface markers expressed by CSCs

Signaling pathways play an important role in the maintenance and survival of CSCs. However, a limitation of the efficacy and clinical impact of these therapeutic approaches is the fact that CSCs and normal stem cells share the expression of several genes and signaling pathways.

In clinical trials, several compounds have been used to target CSCs through the Wnt/ β -catenin signaling pathway. They can be grouped into four main categories: agents targeting proteins involved in Wnt signalling; porcupine inhibitors that hamper the processing and secretion of Wnt ligands; agents that activate caspases or inhibit tankyrase, promoting β -catenin degradation; inhibitors of downstream transcription (Clara et al., 2020).

Nicosamide has been approved by the FDA as a Wnt/ β -catenin pathway inhibitor, and its anticancer ability has been established by various studies. In a phase II trial, nicosamide was proved to safely and effectively treat CRC (Burock et al., 2018). It can inhibit the CSC population, and the self-renewal ability of CRC cells (Park et al., 2019). Additionally, there are many potential small-molecule compounds targeting CSCs through Wnt/ β -catenin signaling pathway in preclinical experiments, such as XAV939, which can abrogate CSC-mediated chemoresistance in colon cancer cells (Wu et al., 2016) and IC-2, which can reduce the expression of CSC markers and the sphere formation ability in CRC. Moreover, it can increase the sensitivity of 5-FU in the DLD-1 CRC cell line (Urushibara et al., 2017). Abnormal activity of another signalling pathway, the Notch signaling pathway, has been observed in CSCs. Notch pathway mainly consists of Notch receptors (Notch 1–4) and transmembrane ligands (Jagged 1, Jagged 2, delta-like ligand (DLL) -1, DLL-3, and DLL-4). When the receptors bind to the ligands, the Notch intracellular domain is released into the nucleus through proteolytic cleavage processes. The final cleavage is mediated by γ -secretase, which releases an intracellular fragment that can translocate to the nucleus and induce transcription of Notch target genes. There are three major clinical methods used to inhibit Notch signalling: γ secretase inhibition, Notch receptor or ligand antibodies, and combination therapy with chemotherapy agents.

A phase I clinical trial displays how RO4929097, a potent, selective, small molecule γ -secretase inhibitor, was well tolerated in advanced-stage solid tumours (Tolcher et al., 2012).

The hedgehog (Hh) signaling pathway regulates the self-renewal of CSCs and tissue homeostasis in cancer (McMillan and Matsui, 2012). When extracellular Hh ligands, Sonic hedgehog (SHh), Indian hedgehog (IH) or Desert hedgehog (Dhh), bind to the transmembrane receptors Patched 1 (PTCH1) and PTCH2, the inhibition of Smoothened (SMO), a downstream protein in the pathway, is decreased, leading to activation of the GLI transcription factors. SMO and GLI transcription factors are the three main targets of Hh pathway antagonists. Vismodegib is a selective inhibitor that blocks Hh signaling by binding to SMO and inhibiting activation of downstream target genes (Merchant and Matsui, 2010).

Additionally, vismodegib decreased the stem markers (such as CD44 and ALDH) of colon CSCs (Wu et al., 2017), and it was used to treat untreated metastatic CRC in a phase II trial (Berlin et al., 2013).

Another promising therapeutic strategy for the CSCs eradication is the targeting of the TME. Increasing evidence suggests that exists an interplay between CSCs and their TME, important in tumour development (Plaks et al., 2015). The CSC microenvironment is a highly heterogeneous complex comprised of stromal cells, such as CAFs and mesenchymal cells, immune cells, epithelial cells, vascular structures and a network of growth factors and cytokines, which supports cells within the extracellular matrix (EC). The interaction with these niches is necessary for the growth, maintenance and differentiation of CSC populations. Therefore, understanding the relationship between CSCs and their microenvironment could help in the development of efficient therapeutic strategies (Valkenburg et al., 2018).

Many signaling pathways have been explored broadly in CAF mediated cancer progression (Wu et al., 2021). They are regulated by various endogenous and exogenous factors, including biomarkers, cytokines, chemokines, miRNAs, and affect not only the biological behaviors of CAFs themselves but also the crosstalk between these and cancer cells.

For example, the activation of the PI3K pathway in CAFs regulates CAF-mediated cancer cell proliferation in several tumours (Zhou et al., 2020, Ma et al., 2019, Cacheux et al., 2019).

In CRC, CAFs increased the adhesion of cancer cells to endothelial cells and the tumour migration in liver or lung by upregulating CD44 through HGF/MET/AKT signal pathway (Zhang et al., 2019). There are mainly two major ways to decrease the CAFs number in TME: targeting specific CAFs markers or reverting the activated CAFs to quiescent phenotype.

Evidence suggests that the fibroblast-activated protein (FAP) is an excellent target for CAFs (Fitzgerald and Weiner, 2020). The simultaneous overexpression of the same molecular protein in

CAFs and cancer cells has the potential to be targeted as epithelial–mesenchymal common target (Meng et al., 2014). Alternatively, differentially expressed proteins in cancer cells and CAFs need an alternative approach, the targeting of CAFs to block the pro-tumour effect first and then cancer cells treatment. Finally, a novel therapeutic approach might involve the simultaneous target of two different components of one signalling cascade in cancer cells and CAFs. For instance, IL-6-neutralizing antibody for IL-6 produced by CAFs and the JAK inhibitor to inhibit the IL-6/JAK/STAT3 in cancer cells.

In 1909, Paul Ehrlich formulated the hypothesis that an intact immune system may prevent tumour development. Based on the understanding of cellular immune regulation, new methods for cancer treatment have emerged. Some of these are the immunologic checkpoint blocking or the chimeric antigen receptor T (CAR-T) cell therapies.

CSCs have been found to express high levels of the immune-checkpoint protein programmed cell death 1 ligand 1 (PD-L1), which inhibits T cell function through binding to its receptor, programmed cell death 1 (PD-1).

Some drugs that target the immune checkpoint receptors cytotoxic T-lymphocyte antigen 4 (CTLA-4) (Sakamuri et al., 2018), PD-1 (nivolumab, pembrolizumab and cemiplimab) (Meindl-Beinker et al., 2019, Cortese et al., 2019, Migden et al., 2018) and PD-L1 (avelumab, durvalumab and atezolizumab) (Motzer et al., 2019, Fujiwara et al., 2019, Sullivan et al., 2019) have also been in clinical trials. The use of Ipilimumab, a CTLA-4 antibody, is approved by the FDA for the treatment of metastatic melanoma (Hodi et al., 2010). For CAR-T cell therapy, CD19, CD20, CD22, CD123, EpCAM, and ALDH have been used for CSC-directed immunotherapy.

To achieve improved immune responses, the use of combination strategies for checkpoint inhibitors with other therapeutics have been assessed for an effective cancer treatment (Ruan et al., 2019).

The tumour microenvironment associated with obesity is a strong risk factor for cancer progression. Several retrospective studies analyzing large cohorts of cancer patients highlighted that obesity is a negative prognostic factor, including for CRC patients (Bhaskaran et al., 2018).

In obese individuals, mature adipocytes together with adipose stromal cells (ASCs) release inflammatory and angiogenic cytokines, including TNF- α and IL-6, which promote a chronic inflammatory state that creates a microenvironment able to sustain tumour progression (Rosen and Spiegelman, 2014, Park et al., 2011, Quail and Dannenberg, 2019). This activates in different types of cancer cell proliferation and a more aggressive behaviour (Ko et al., 2019).

Targeting the factors produced by adipose tissue in obese CRC patients could therefore represent a promising therapeutic strategy.

Finally, in the last few years there has been considerable interest toward developing monoclonal antibodies to target CSC-specific surface markers. A new recombinant, humanized monoclonal anti-CD44 antibody, RG7356, was well tolerated in a phase 1 study of 44 patients with acute myeloid leukaemia (Vey et al., 2016).

The therapeutic targeting of CD133 was evaluated for advanced cholangiosarcoma, in a phase 2 clinical trial (NCT02541370) using an immunotherapeutic approach based on CAR-T cells transduced with the anti-CD133 and anti-EGFR (Feng et al., 2017). EpCAM is another common CSC marker. Catumaxomab is a antibody anti-EpCAM/anti-CD3. Its administration demonstrated clinical benefit in malignant ascites secondary to epithelial cancers (Heiss et al., 2010). Adecatumumab, a recombinant human IgG1 monoclonal, tested in patients with metastatic breast cancer, resulted in a positive response in patients with higher expression of EpCAM (Schmidt et al., 2010).

Chapter 1


Targeting chemoresistant colorectal cancer via systemic administration of a BMP7 variant

Veronica Veschi, **Laura R. Mangiapane**, Annalisa Nicotra, Simone Di Franco, Emanuela Scavo, Tiziana Apuzzo, Davide S. Sardina, Micol Fiori, Antonina Benfante, Maria L. Colorito, Gianfranco Cocorullo, Felice Giuliante, Calogero Cipolla, Giuseppe Pistone, Maria Rita Bongiorno, Aroldo Rizzo, Courtney M. Tate, Xiaohua Wu, Scott Rowlinson, Louis F. Stancato, Matilde Todaro, Ruggero De Maria, Giorgio Stassi

Published in *Oncogene*, 2020



Targeting chemoresistant colorectal cancer via systemic administration of a BMP7 variant

Veronica Veschi¹ · Laura R. Mangiapane¹ · Annalisa Nicotra¹ · Simone Di Franco¹ · Emanuela Scavo¹ · Tiziana Apuzzo¹ · Davide S. Sardina¹ · Micol Fiori² · Antonina Benfante¹ · Maria L. Colorito¹ · Gianfranco Cocorullo¹ · Felice Giuliani^{3,4} · Calogero Cipolla¹ · Giuseppe Pistone⁵ · Maria Rita Bongiorno⁵ · Aroldo Rizzo⁶ · Courtney M. Tate⁷ · Xiaohua Wu⁷ · Scott Rowlinson⁷ · Louis F. Stancato⁷ · Matilde Todaro⁵  · Ruggero De Maria^{3,4} · Giorgio Stassi¹

Received: 10 April 2019 / Revised: 23 September 2019 / Accepted: 25 September 2019 / Published online: 7 October 2019
© The Author(s) 2019. This article is published with open access

Abstract

Despite intense research and clinical efforts, patients affected by advanced colorectal cancer (CRC) have still a poor prognosis. The discovery of colorectal (CR) cancer stem cell (CSC) as the cell compartment responsible for tumor initiation and propagation may provide new opportunities for the development of new therapeutic strategies. Given the reduced sensitivity of CR-CSCs to chemotherapy and the ability of bone morphogenetic proteins (BMP) to promote colonic stem cell differentiation, we aimed to investigate whether an enhanced variant of BMP7 (BMP7v) could sensitize to chemotherapy-resistant CRC cells and tumors. Thirty-five primary human cultures enriched in CR-CSCs, including four from chemoresistant metastatic lesions, were used for in vitro studies and to generate CR-CSC-based mouse avatars to evaluate tumor growth and progression upon treatment with BMP7v alone or in combination with standard therapy or PI3K inhibitors. BMP7v treatment promotes CR-CSC differentiation and recapitulates the cell differentiation-related gene expression profile by suppressing Wnt pathway activity and reducing mesenchymal traits and survival of CR-CSCs. Moreover, in CR-CSC-based mouse avatars, BMP7v exerts an antiangiogenic effect and sensitizes tumor cells to standard chemotherapy regardless of the mutational, MSI, and CMS profiles. Of note, tumor harboring *PIK3CA* mutations were affected to a lower extent by the combination of BMP7v and chemotherapy. However, the addition of a PI3K inhibitor to the BMP7v-based combination potentiates *PIK3CA*-mutant tumor drug response and reduces the metastatic lesion size. These data suggest that BMP7v treatment may represent a useful antiangiogenic and prodifferentiation agent, which renders CSCs sensitive to both standard and targeted therapies.

These authors contributed equally: Ruggero De Maria, Giorgio Stassi

Supplementary information The online version of this article (<https://doi.org/10.1038/s41388-019-1047-4>) contains supplementary material, which is available to authorized users.

✉ Ruggero De Maria
ruggero.demaria@unicatt.it

✉ Giorgio Stassi
giorgio.stassi@unipa.it

¹ Department of Surgical, Oncological and Stomatological Sciences (DICHIRONS), University of Palermo, 90127 Palermo, Italy

² Department of Oncology and Molecular Medicine, Istituto Superiore di Sanità, Rome, Italy

³ Istituto di Patologia Generale, Università Cattolica del Sacro

Introduction

Advanced colorectal cancer (CRC) is still a major challenge for clinical oncologists, being among the top causes of cancer-related death worldwide [1]. Cancer stem cells

Cuore, 00168 Rome, Italy

⁴ Fondazione Policlinico Universitario A. Gemelli—I.R.C.C.S., 00168 Rome, Italy

⁵ Department of Health Promotion Sciences, Internal Medicine and Medical Specialties (PROMISE), University of Palermo, 90127 Palermo, Italy

⁶ Pathology Unit, Ospedali Riuniti Villa Sofia-Cervello, Palermo, Italy

⁷ Lilly Research Laboratories, Lilly Corporate Center, Indianapolis, IN 46285, USA

(CSCs) are key players in tumor initiation and development of metastasis [2, 3]. In recent years, many studies investigating the biological behavior of CSCs inspired the design of innovative therapeutic strategies for CRC. Genetic and epigenetic changes, overexpression of anti-apoptotic proteins, and enhanced DNA repair machinery define the common traits of CSCs [4, 5]. The acquisition of an epithelial–mesenchymal transition (EMT) phenotype confers to CSCs the ability to invade and metastasize [6]. Among the most studied CSC markers, CD133 has been reported to identify CR-CSCs [7]. More recently, we determined that a splicing variant of CD44, CD44v6, is a functional marker expressed in CR-CSCs able to migrate and engraft at distant sites [8]. In line with the enhanced Wnt signaling observed in CR CD44v6⁺ cells, β -catenin activation induces CD44v6 expression in CR-CSCs. This pathway is sustained by the activation of the PI3K/AKT pathway, which promotes β -catenin activation through the inhibition of GSK3 β , a key component of its destruction complex [8]. According to the multistep model, the progressive acquisition of mutations in proto-oncogenes or tumor suppressor genes defines specific stages of CRC [9]. Aberrant alterations of principal components of pathways involved in intestinal stem cell self-renewal endorse the disruption of intestinal niche equilibrium [10]. In addition to Wnt, Notch, and Sonic hedgehog pathways, bone morphogenetic proteins (BMPs) finely regulate the intestinal niche homeostasis balancing self-renewal and differentiation [11, 12]. BMPs are members of the TGF- β superfamily and regulate many fundamental biological processes during development. BMPs bind both type I and type II receptors (BMPRI1A, BMPRI1B, and BMPRI2) to achieve a variety of cellular functions [13]. The activation of this pathway promotes the phosphorylation of SMAD1, 5, and 8 that in association with SMAD4 regulates the expression of genes involved in the differentiation process [14, 15]. BMP antagonists (gremlin and noggin) tightly modulate BMPs activity [16]. In healthy colon mucosa, the expression of BMPs and their antagonists is polarized. BMPs are mainly located at the top, while BMP antagonists at the base of colon crypt [17]. Alterations of BMP pathways can imbalance the homeostasis of the intestinal stem cell niche, thus favoring the development and progression of CRC. Indeed, the loss of BMPRI2 and SMAD4 expression has been reported in sporadic CRC, whereas germline mutations of *BMPRI1* and *SMAD4* genes have been demonstrated to enhance the susceptibility to develop juvenile polyposis, supporting that TGF- β signaling inactivation plays a key role in CRC development [18–22]. In intestinal stem cells, BMP signaling counteracts the Wnt pathway activity by impairing the nuclear accumulation of β -catenin through a PTEN-dependent AKT inhibition [23]. This antagonistic activity of BMP

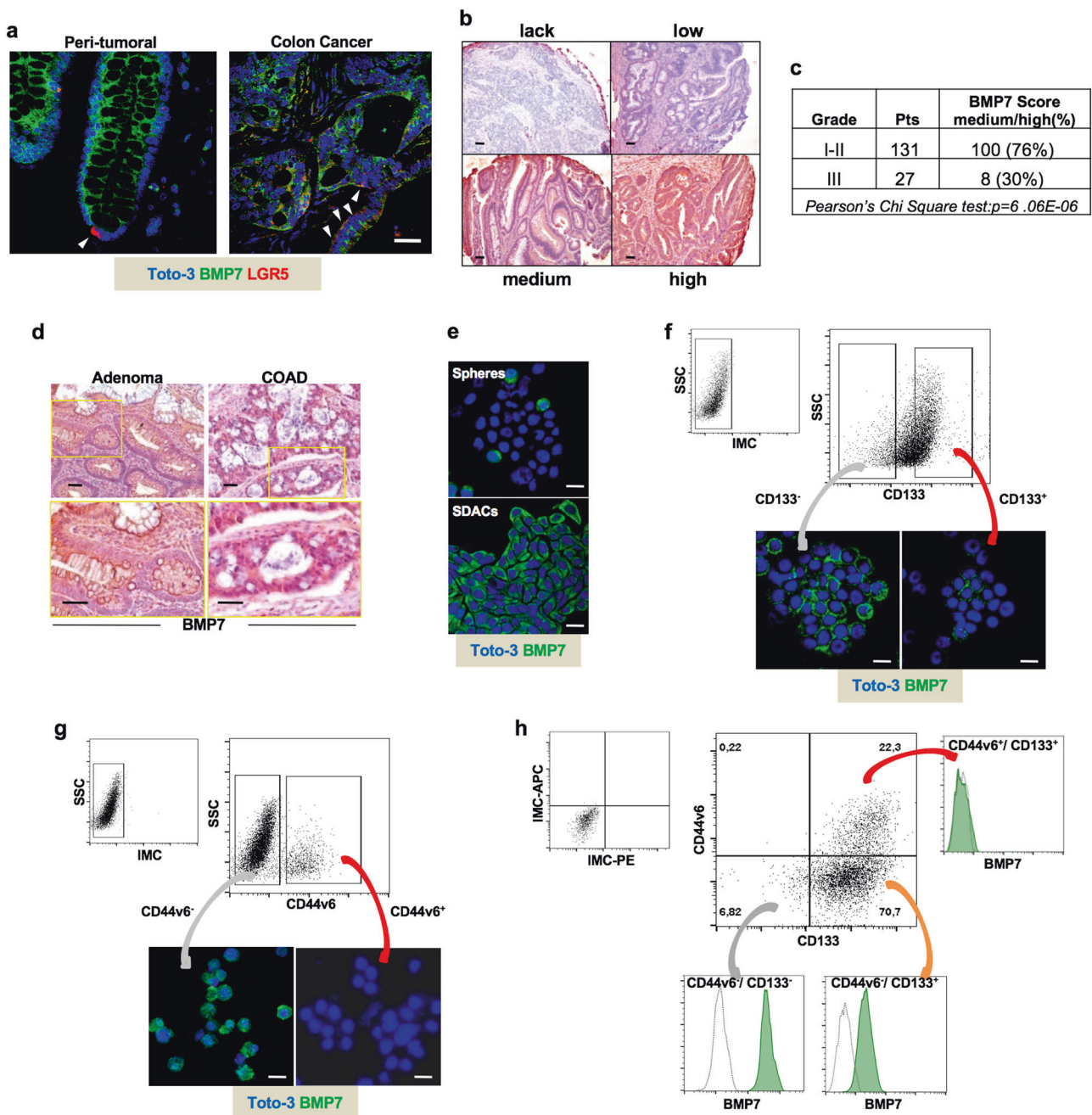
signaling against stem cells and Wnt pathway seems preserved in the cancer counterpart as indicated by the ability of BMP4 to promote differentiation and apoptosis of CR-CSCs [24].

BMP expression varies across tumor subtypes [25]. BMP7 is widely expressed in many tumors including breast, prostate, and colon cancer, and it is implicated in the regulation of cell proliferation [26–28]. However, its functional association with tumorigenicity and metastasis formation is still poorly understood. Recently, a human variant of BMP7 with enhanced stability and solubility (BMP7v) has been developed, by introducing mutations into the N terminus of BMP7 prodomain [29]. In glioblastoma stem-like cells, BMP7v impairs their proliferation and invasive capability by inducing differentiation [30] and significantly decreases angiogenesis. BMP7v, unlike BMP7, is not recognized by most of the BMP endogenous antagonists, such as noggin, gremlin, chordin, and chordin-like 2, due to reduced binding [31]. Disease progression in CRC is mostly due to the emergence of chemoresistant CSCs after therapeutic interventions [32]. Different mechanisms and biomarkers have been proposed so far to study and predict chemoresistance. Both microsatellite instability (MSI) and consensus molecular subtype (CMS) profiles correlate with the chemotherapy response in CRC. Specifically, MSI CRCs have been correlated with a better prognosis [33] but also with a lack of benefit from oxaliplatin (oxa) plus 5-fluorouracil (5-FU) therapy [34, 35]. CMS2 CRC is as the subset that most benefits from the chemotherapy, while the CMS4 results resistant to conventional therapy [36, 37]. We demonstrated that the activation of the PI3K/AKT pathway is essential for preserving the stem cell status in CRC CD44v6⁺ cells [8]. PI3K activation results in the onset of alternative signaling pathways, including Wnt- β -catenin axis activation that promotes CR-CSC survival, invasion, and development of metastases [38]. Using the BMP7v, here we have studied the possibility of targeting chemoresistant CRC through the induction of CSC differentiation. We provide evidence supporting the use of BMP7v in combination with chemotherapeutic compounds and/or PI3K inhibitors for CRC treatment.

Results

BMP7 is highly expressed in low-grade CRC patients

In accordance with the current literature, we found BMP7 abundantly expressed in CRC tissues, compared with peritumoral mucosa (Fig. 1a). BMP7 expression was limited to the apical part and absent in the LGR5⁺ stem



cells located at the very base of the cancer gland (Fig. 1a, left panel). Analysis of a cohort of 158 CRC patients showed a significant correlation between medium/high BMP7 expression and the low-grade (I-II) tumors, which was confirmed by the analysis of a cohort of CRC in R2 database (Fig. 1b, c and Supplementary Fig. 1a). Interestingly, BMP7 was found highly expressed in both colon adenoma and adenocarcinoma, suggesting this phenomenon as an early event in cancer (Fig. 1d). In line with the expression of BMP7 in the differentiated part of the colon gland, BMP7 was remarkably expressed in sphere-derived

adherent cells (SDACs), while it was present in few cells across CRC spheres, which are enriched in stem-like cells (Fig. 1e). Moreover, we found that CD133⁻ cells showed a higher percentage of BMP7-expressing cells as compared with the CD133⁺ compartment (Fig. 1f and Supplementary Fig. 1b, c). Interestingly, CD44v6⁺ cells lacked BMP7 expression, which was conversely confined to the CD44v6⁻ cell compartment (Fig. 1g and Supplementary Fig. 1d, e). In accordance with the immunofluorescence studies, flow cytometry analysis showed that BMP7 is expressed in CD133⁻/CD44v6⁻ cells and in a fraction of

◀ **Fig. 1** BMP7 is confined to differentiated CRC cells. **a** Immunofluorescence analysis of BMP7 (green color) and LGR5 (red color) on peritumoral mucosa and colon cancer paraffin-embedded tissues performed on CSC#8. One representative tumor from twenty different tumors examined is shown. Nuclei were counterstained by Toto-3 (blue color). White arrowheads indicate LGR5⁺ cells at the base of colon crypt. The scale bar represents 100 μ m. **b** Immunohistochemical analysis of BMP7 on CRC TMAs in lack, low, medium, and high staining intensity (red color). Nuclei were counterstained by aqueous hematoxylin (blue color). The scale bar represents 100 μ m. **c** Association of BMP7 expression with score medium/high and the pathological grading in CRC TMAs provided by TRISTAR technology group. **d** Immunohistochemical analysis of BMP7 (red color) in paraffin-embedded sections of colon adenomas and adenocarcinoma (COAD). Nuclei were counterstained by aqueous hematoxylin (blue color). The scale bar represents 100 μ m. **e** Immunofluorescence analysis of BMP7 (green color) in CRC sphere cells and their differentiated progeny SDACs. One representative of fifteen different CR-CSC lines (CSC#1–3, 5–7, 10, 11, 14–16, 18, 25, 33, and 40) is shown. Nuclei were counterstained by Toto-3 (blue color). The scale bars represent 20 μ m. **f** Representative flow cytometry analysis of CD133 in CRC sphere cells and its relative isotype-matched control (IMC) (upper panels) performed on CSC#4, 8, and 23–26. Immunofluorescence analysis of BMP7 (green color) in CD133⁺ and CD133⁻ enriched CRC sphere cell subpopulations (lower panels). Nuclei were counterstained by Toto-3 (blue color). The scale bars represent 20 μ m. **g** CD44v6 expression profiles of cells as described in **f** (upper panels). Expression of BMP7 (green color) in CD44v6⁺ and CD44v6⁻ enriched CRC sphere cell subpopulations assessed by immunofluorescence analysis (lower panels). Nuclei were counterstained by Toto-3 (blue color). The scale bars represent 20 μ m. **h** Flow cytometry analysis of BMP7 (green histograms) in enriched CD44v6⁻/CD133⁻, CD44v6⁻/CD133⁺, and CD44v6⁺/CD133⁺ CRC subpopulations performed as shown in **f**. Dotted line histograms indicate the relative IMC

CD133⁺ cell compartment, whereas it is nearly undetectable in enriched CD44v6⁺/CD133⁺ stem-like cells (Fig. 1h). These data demonstrate that BMP7 is predominantly expressed in differentiated CRC cell population, particularly in low-grade CRCs.

BMP7v affects CD44v6 expression in CR-CSCs

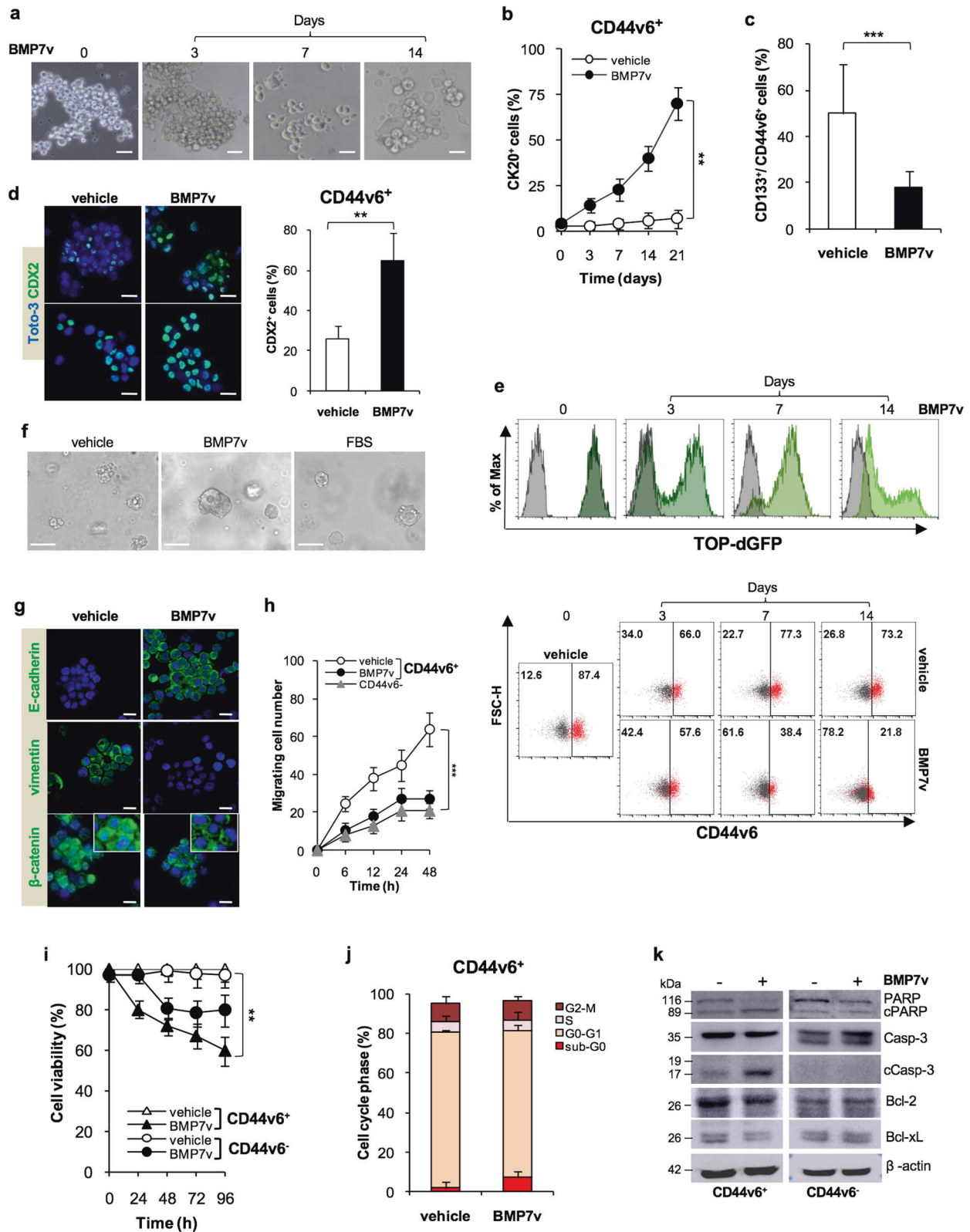
In order to define the potential of BMP7 as a prodifferentiation agent, we next evaluated whether the BMP signaling pathway components were conserved in a CRC model. We observed that type I and type II BMP receptors are expressed in both CD44v6⁺ and CD44v6⁻ fraction with more pronounced expression levels of BMPR2 in the CD44v6⁻ counterpart (Supplementary Fig. 2a, b). In order to investigate the effects of BMP7 on CR-CSCs, we used a modified BMP7 with enhanced stability and solubility (BMP7v) as previously described [30]. The dose concentration of 100 ng/ml of BMP7v corresponded to the IC50 and was also preferred for the in vitro ability to inhibit the colony forming capacity of CR-CSCs even in the presence of high doses of BMP antagonists, gremlin, and noggin (Supplementary Fig. 2c, d). CD44v6⁺ cells exposed

to BMP7v up to 21 days displayed a gradual morphological differentiation (Fig. 2a), paralleled by the acquisition of CK20 expression (Fig. 2b). In accordance, BMP7v significantly reduced the percentage of cells expressing the CD133/CD44v6 CSC markers and increased the number of CDX2⁺ cells within CRC spheres (Fig. 2c, d and Supplementary Fig. 2e, f). In a cohort of CRC patients, expression levels of CDX2 are inversely correlated with tumor grading (Supplementary Fig. 2g).

Interestingly, flow cytometry analysis of primary CRC sphere cells transduced with a β -catenin/TOP-dGFP reporter lentiviral vector showed that exposure to BMP7v was able to progressively decrease β -catenin activity and CD44v6 expression (Fig. 2e and Supplementary Fig. 2h). Moreover, BMP7v treatment caused the reduction of β -catenin activity and differentiation of CRC organoid, which was highlighted by lumen formation and cell polarization (Fig. 2f and Supplementary Fig. 2i). In the presence of BMP7v, CD44v6⁺ CRC sphere cells acquired E-cadherin expression, displayed loss of vimentin and reduction of nuclear β -catenin (Fig. 2g). A large cohort of CRC patients showed a positive correlation between the expression levels of BMP7 and E-cadherin (*CDH1*) (Supplementary Fig. 3a). In agreement, xenograft tumors generated by the injection of CR-CSCs (CSC# 1, 8, and 25), displayed a major number of cells expressing E-cadherin after BMP7v treatment (Supplementary Fig. 3b). Accordingly, the in vitro invasive capacity of CD44v6⁺ CR-CSCs was significantly impaired following treatment with BMP7v (Fig. 2h). Following 96 h of treatment, CD44v6⁺ fraction exhibited a more pronounced sensitivity to BMP7v-induced cell death than CD44v6⁻ cells (Fig. 2i). Although BMP7v treatment did not significantly affect G0/G1 to G2/M phase transition, it enhanced to a small extent the sub-G0 phase in CD44v6⁺ CR-CSCs (Fig. 2j and Supplementary Fig. 3c). In line with the induction of cell death, BMP7v treatment induced activation of both PARP and Caspase-3 and a downregulation of Bcl-2 and Bcl-xL in CD44v6⁺ cells (Fig. 2k and Supplementary Fig. 3d, e). These data indicate that BMP7v selectively targets the CD44v6⁺ CSC compartment by counteracting its Wnt pathway activity and antiapoptotic machinery.

BMP7v hampers the self-renewal capacity of CR-CSCs

We have already reported that BMP7v activity is resistant to the majority of BMP antagonists, such as noggin and chordin [31]. Given that only some cancers express high levels of gremlin and noggin [39, 40] we sought to investigate their inhibitory effects on both BMP4 and BMP7v. Although BMP4 was not able to accomplish its function in the presence of gremlin and noggin, BMP7v



reduced the colony forming capacity of CR-CSCs more efficiently than BMP4, even in the presence of BMP inhibitors (Fig. 3a). We have previously demonstrated that

CD44v6⁺ cells show upregulation of PI3K activity and EMT-related genes [8]. Differentially expressed EMT-, tumor metastasis- and Wnt signaling-related genes in

◀ **Fig. 2** BMP7v treatment promotes CR-CSC differentiation. **a** Phase-contrast microscopy analysis of CD44v6⁺ CRC sphere cells treated with BMP7v at the indicated time points. One representative of CSC#1, 2, 4, 5, 7, and 23–26 is shown. The scale bar represents 20 μm. **b** Percentage of CK20 positive cells in CD44v6⁺ CR-CSCs treated with vehicle or BMP7v up to 21 days evaluated by immunofluorescence analysis. Data are expressed as mean ± SD of experiments performed in 15 CRC sphere cell lines (CSC#1–3, 5–7, 10, 11, 14–16, 18, 25, 33, and 40). **c** Flow cytometry analysis of CD133/CD44v6 on CRC sphere cells treated with vehicle or BMP7v for 14 days. Data reported are mean ± SD of 15 CRC sphere cell lines analyzed (CSC#1–8, 10, 11, 14–16, 18, and 25). **d** (left panels) Immunofluorescence analysis of CDX2 on CR-CSCs upon 14 days of BMP7v treatment. One representative of CSC# 3, 9, and 21 is shown. Nuclei were stained with Toto-3 (blue color). The scale bars represent 20 μm. (right panel) Percentage of CDX2 positive cells in CD44v6⁺ CR-CSCs treated with vehicle or BMP7v up to 14 days evaluated by immunofluorescence analysis. Data are expressed as mean ± SD of experiments performed in CSC# 3, 9, and 21. **e** Flow cytometry analysis of TOP-dGFP or CD44v6 in enriched CD44v6⁺ sphere cells treated with BMP7v up to 14 days. One representative experiment of CSC#1, 2, 4, 7, and 10 is shown. **f** Phase-contrast microscopy analysis of TOP-dGFP CRC sphere cells grown in matrigel drops and treated with vehicle, BMP7v or FBS for 14 days. One representative of CSC# 8, 9, and 11 is shown. The scale bar represents 100 μm. **g** Immunofluorescence analysis of E-cadherin, vimentin, and β-catenin (green color) in CD44v6⁺ CRC cells exposed to vehicle or BMP7v for 14 days. One representative experiment performed in cells as in **e** is shown. Nuclei were stained with Toto-3 (blue color). The scale bars represent 20 μm. **h** Migrating CD44v6⁺ and CD44v6⁻ cells treated with vehicle or BMP7v up to 48 h. Data are shown as mean ± SD of three independent experiments performed in five CRC sphere cell lines (CSC#1, 5, 7, 10, and 12). **i** Cell viability percentage of enriched CD44v6⁺ and CD44v6⁻ cells treated with vehicle or BMP7v up to 96 h. Data are shown as mean ± SD of different experiments performed in CSC#1, 2, 4, 7, and 10. **j** Cell cycle analysis in CD44v6⁺ CR-CSCs exposed to vehicle or BMP7v for 72 h. The data show percentage of cell number in sub-G0, G0/G1, S, and G2/M phases. Data are expressed as mean ± SD of three independent experiments performed in five different CRC sphere cell lines as in **e**. **k** Immunoblot analysis of PARP, cleaved PARP (cPARP), Caspase-3 (Casp-3), cleaved Caspase-3 (cCasp-3), Bcl-2, Bcl-xL in CD44v6⁺, and CD44v6⁻ enriched cells treated as in **e** for 72 h. β-actin was used as loading control. One representative experiment performed in three different CRC sphere cell lines (CSC#1, 4, and 7)

CD44v6⁻ cell compartments (Fig. 3b) were comparable with those in CD44v6⁺ CRC cells treated with BMP7v (Fig. 3c), in line with the ability of this compound to turn CD44v6⁺ CSCs into CD44v6⁻ differentiated cells. Specifically, BMP7v induced the upregulation of 7 genes and the downregulation of other 48 genes in both CD44v6⁻ cells and CD44v6⁺ cell fractions. Of note, the gene set enrichment analysis (GSEA) performed with the molecular signatures database (MSigDB) revealed the activation of programs associated with differentiation and attenuation of EMT and metastatic biological processes (Fig. 3d, e and Supplementary Fig. 4a, b). The most relevant down-regulated and upregulated genes were further validated by RT-PCR (Fig. 3f). Thus, BMP7v forces CD44v6⁺ CR-CSCs towards a more differentiated phenotype.

BMP7v potentiates the effects of standard therapy in naive and chemoresistant CR-CSCs

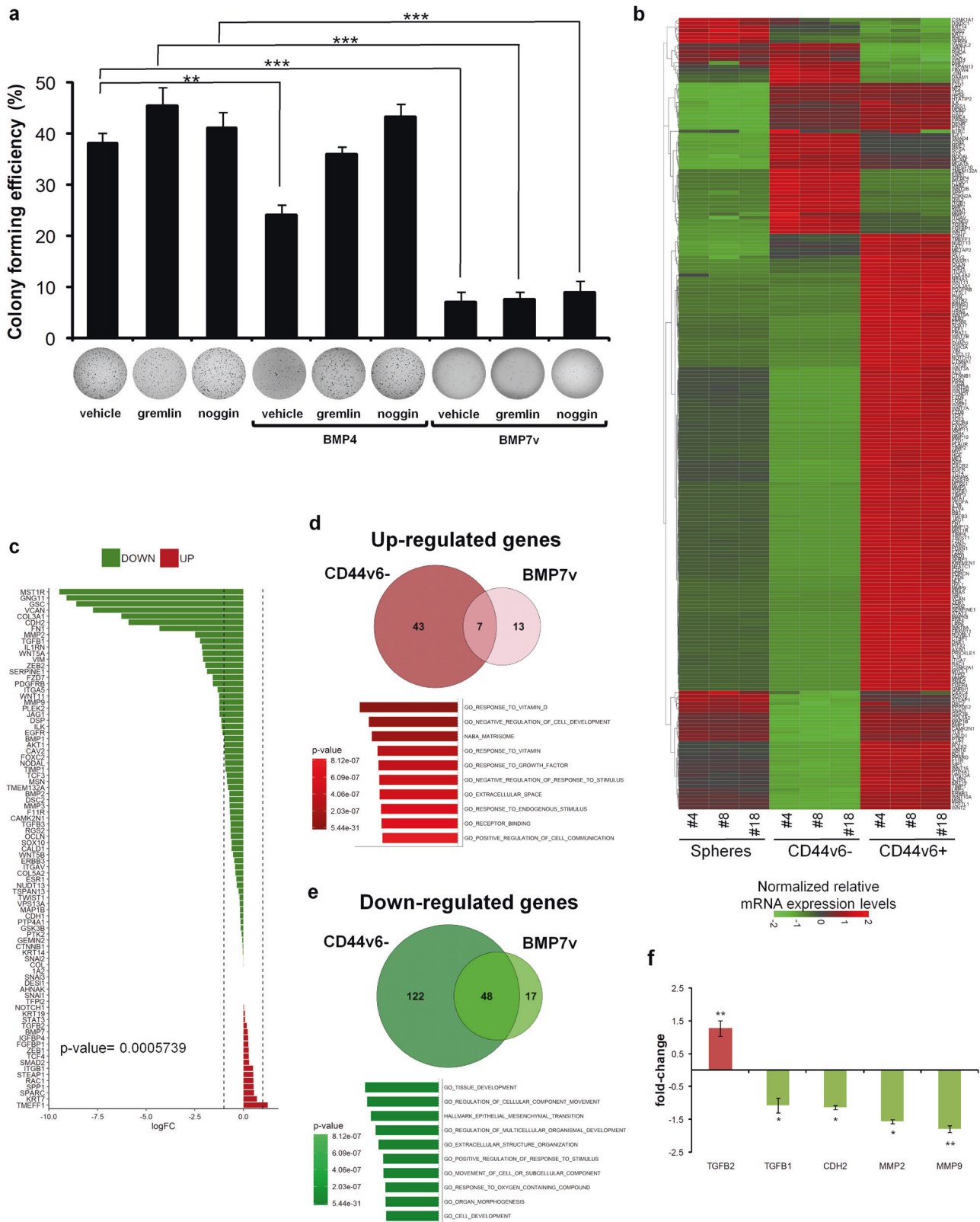
Following a dose-escalation delivery *in vivo*, we selected for subsequent studies the 50 μg/kg dose of BMP7v, which reduced significantly tumor growth while being well tolerated (Supplementary Fig. 5a). Of note, BMP7v alone exerted an antiangiogenic effect in xenograft tumors generated by the injection of CR-CSCs. Unlike BMP4, BMP7v treatment induced a fivefold increase in necrosis (Fig. 4a, b) and significantly reduced the number of microvessels in CR-CSC-based mouse avatars, as assessed by CD31 and VEGFR2 detection (Fig. 4c, d). In order to test whether BMP7v could sensitize CR-CSCs resistant to conventional therapy, we investigated the *in vitro* effect of BMP7v in combination with a standard chemotherapy regimen.

About half of the examined CR-CSC lines showed >50% survival after 24 h of *in vitro* treatment with oxa plus 5-FU (Fig. 4e). Based on the functional characterization of chemotherapy response, we selected four primary CR-CSC lines, derived from metastatic liver lesions of patients progressing after chemotherapy treatment (R1-R4), and three CR-CSC lines (CSC#1, 2, and 7) showing different degrees of chemoresistance. Of note, BMP7v was able to render R-CSCs sensitive to oxa plus 5-FU *in vitro* treatment, the same therapeutic regimen completely ineffective *in vivo* in the metastatic patients from which these cells were derived (Fig. 4f).

The ability to form colonies was significantly compromised in CR-CSCs in the presence of BMP7v in combination with oxa plus 5-FU *in vitro* (Fig. 4g). This treatment affected both the *in vitro* self-renewal and the *in vivo* tumorigenic capacity of subcutaneously injected CR-CSCs. While tumor xenografts generated by the injection of CSC#2 and 7 were sensitive to the combined treatment of BMP7v and chemotherapy, *PIK3CA*-mutant tumor xenografts derived from the implantation of CSC#1 delayed the outgrowth showing a kinetic trend similar to that of tumors treated with vehicle (Fig. 4h). Immunohistochemical analysis of xenograft tumors (CSC#7) treated with BMP7v and chemotherapy showed a reduction of CD44v6, nuclear β-catenin, and Ki67 expressing cells, together with a concomitant increase in CK20 positive cells (Fig. 4i). Interestingly, xenograft tumors treated with chemotherapy alone showed a significant increase of cells expressing CD44v6 and nuclear β-catenin accompanied with a decrease of Ki67 positive cells. Thus, BMP7v sensitizes both naive and chemoresistant CR-CSCs to standard therapies.

BMP7v enhances the therapeutic response to PI3K inhibitors and reduces the size of PIK3CA-mutant xenograft tumors

We next investigated whether the addition of PI3K inhibitors to BMP7v-based therapy could represent an



efficacious approach in the CD44v6⁺ cells, particularly in the presence of *PIK3CA* mutation. We first observed that in vitro BMP7v treatment attenuated the PI3K/AKT

pathway in CD44v6⁺ cells, whose expression levels became similar to those exhibited by CD44v6⁻ compartment (Fig. 5a and Supplementary Fig. 5b). Then we found

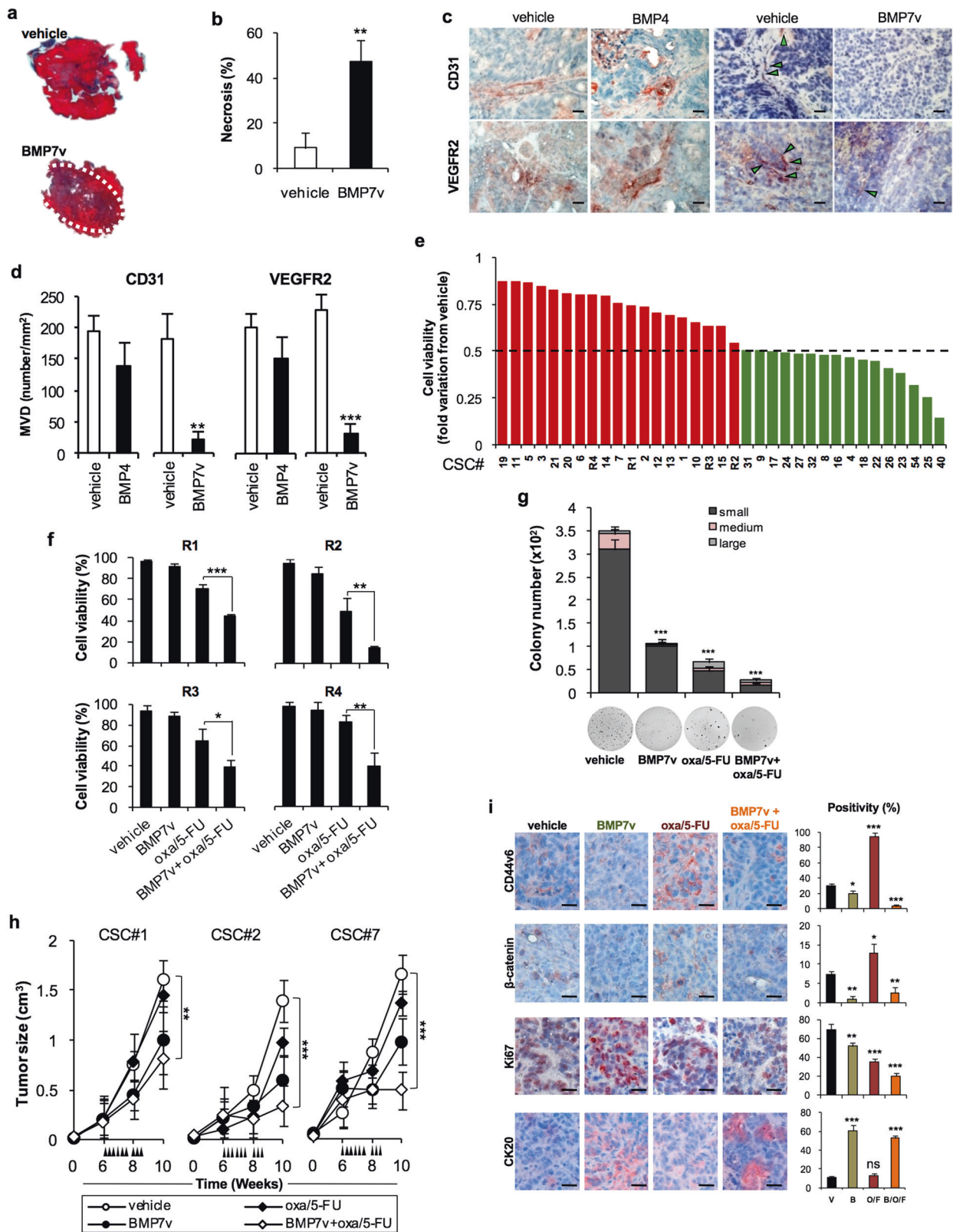
◀ **Fig. 3** BMP7v hampers the self-renewal and recapitulates a CD44v6⁻-like cell subpopulation profile. **a** Colony forming efficiency percentage of CD44v6⁺ CR-CSCs treated for 14 days with vehicle, gremlin or noggin alone or in combination with BMP4 or BMP7v. Data are reported as mean ± SD of five different CRC sphere cell lines analyzed (CSC#1, 2, 4, 7, and 10). Representative soft-agar analysis is shown in the lower part of graph. **b** Heat map of EMT-, tumor metastasis-, and Wnt pathway-related genes ($2^{-\Delta\Delta C_t}$ expression values) in spheres, CD44v6⁻ and CD44v6⁺ cells. Data are presented as normalized expression values of three different CRC sphere cell lines (CSC#4, 8, and 18). **c** Log fold change (logFC) values of differentially expressed related genes in enriched CD44v6⁺ cells treated with BMP7v for 3 days. Data are presented as the average of normalized mRNA expression levels of four different CR-CSC lines (CSC#1, 3, 5, and 7). Dotted lines represent -1 and 1 logFC values. *P* value indicates difference between normalized mRNA expression levels of untreated vs BMP7v treated samples. **d** Venn diagram showing upregulated (red) and **e** downregulated (green) genes in CD44v6⁻ and BMP7v treated cells. (Lower panels) Top ten significantly enriched gene sets (FDR *q* value ≤ 0.05), selected by using Hallmark, KEGG, and GO, related to the indicated 7 up- and 48 down-regulated genes common in CD44v6⁻ cells and CD44v6⁺ cells treated with BMP7v. *P* values related to each enriched gene set are indicated. **f** Fold change values of the differentially upregulated (red) and downregulated (green) genes further validated by RT-PCR in CR-CSCs upon treatment with BMP7v for 72 h. Data are expressed as mean ± SD of experiments performed in CSC# 1, 3, 9, and 21

that BMP7v combined with a PI3K inhibitor (taselisib) was also able to revert the intrinsic chemotherapy resistance of CR-CSCs in vitro (Fig. 5b). Following the integration of the dose-response and synergy score evaluation from Bliss and ZIP algorithms, 100 ng/ml of BMP7v and 1 μM of PI3K inhibitor (taselisib) were selected for in vitro therapeutic combination (Supplementary Fig. 5c). Thus, to render *PIK3CA*-mutant CR-CSCs-derived avatars more sensitive to the combination therapy, we decided to inhibit the PI3K activity concomitantly. As expected, BMP7v in combination with taselisib significantly reduced the size of tumor xenografts generated by the injection of *PIK3CA*-mutated CR-CSCs (Fig. 5c), suggesting the necessity to simultaneously add a PI3K inhibitor in the presence of enhanced activation of the PI3K/AKT pathway. To determine whether the addition of BMP7v to PI3K inhibitor, taselisib could also induce regression of the disease, metastatic mouse avatars generated by the injection of *PIK3CA*-mutated CR-CSCs into NOD-SCID mice spleen, were treated 4 weeks after the splenectomy once the metastatic lesions were detectable. The combination of PI3K and BMP7v significantly lessened the size of metastatic lesions of *PIK3CA*-mutated CR-CSCs, even 4 weeks after treatment suspension (Fig. 5d-f). The majority of CD44v6⁺ cells found in the liver and lung metastases of mice treated with the PI3Ki-BMP7v combination therapy underwent cell death, confirming the potential clinical application of this therapeutic approach in patients with metastatic CRC (Fig. 5g, h). Altogether, these findings

suggest that BMP7v can turn CD44v6⁺ cells into a therapy sensitive CD44v6⁻ differentiated phenotype. Although *PIK3CA*-mutated CR-CSCs are less sensitive to the pro-differentiation activity of BMP7 signaling, the addition of a PI3K inhibitor restores their sensitivity in established tumors (Fig. 6a).

Discussion

We previously demonstrated that CD44v6 is a functional receptor that identifies migrating CSCs able to develop CRC metastasis [8]. Here, we show that CD44v6 enriched CR-CSCs lack the expression of BMP7, which is conversely confined within the differentiated counterpart (CD44v6⁻ cells). The heterogeneous expression of BMP7 within the CD44v6⁻ compartment is likely due to the presence of progenitor cells (CD44v6⁻/CD133⁺ cells) endowed with residual β-catenin activation, which renders these cells reprogrammable by the microenvironmental cytokines [8]. Here, we show that BMP7 expression represents an early event in CRC as confirmed by its presence in colon adenoma and adenocarcinoma. Moreover, its expression inversely correlated with the pathological grading of CRCs, again supporting the association between this morphogen and differentiated tumor. In accordance with the reported effects in glioma stem cells [41], BMP7v induce the expression of differentiation markers in CR-CSCs, which gradually reduce their β-catenin activity and CD44v6 expression. We previously reported that BMP4 promotes differentiation and affects the self-renewal activity of CR-CSCs [24]. Through a *SMAD1/4*-mediated epigenetic mechanism, BMP4 leads to the recruitment of histone deacetylase HDAC1 and consequent transcriptional suppression of stemness genes [42]. Accordingly, targeting the Wnt pathway by BMP7v curtails the clonogenic activity of CD44v6⁺ CRC cells and leads to their terminal differentiation, as highlighted by the presence of PARP activation and downregulation of the antiapoptotic proteins Bcl-2 and Bcl-xL. The similar trend of cell viability in both CD44v6⁺ and CD44v6⁻ populations is likely due to the presence, in the CD44v6⁻ fraction, of progenitor cells that are affected by the BMP7v treatment. Tumor microenvironment reprograms cancer cells towards an EMT process leading them to acquire a more pronounced self-renewal and migratory phenotype [8, 43]. We have shown that cytokines released by cancer-associated fibroblasts are able to dedifferentiate CD44v6⁻ cells into CD44v6⁺ metastatic CR-CSCs, with the induction of a number of EMT genes [8]. BMP7v drives CR-CSCs to behave similarly to the differentiated CD44v6⁻ cells by downregulating the majority of EMT-related genes, which are needed by CD44v6⁺ cells to retain an



aggressive phenotype. We previously demonstrated that BMP4 induces PTEN upregulation and inhibition of PI3K/AKT [24], which sustains the stem-like cell properties of

CD44v6⁺ CR-CSCs [8]. BMP7v displays a similar inhibition on the PI3K/AKT pathway. Here, we have shown that even though PTEN increased moderately upon

◀ **Fig. 4** BMP7v exerts antiangiogenic effects and sensitizes chemoresistant CSCs to standard therapy. **a** Azan-Mallory staining on paraffin-embedded sections of xenografts derived from the injection of CRC sphere cells and treated for 4 weeks (6–9 weeks) with PBS (vehicle) or BMP7v. Data are representative of three independent experiments using different CRC sphere cell lines (CSC#2, 7, and 18). **b** Percentage of necrosis evaluated on paraffin-embedded sections of xenografts treated as in **a**. Data are shown as mean \pm SD of three independent experiments. **c** Immunohistochemical analysis of CD31 and VEGFR2 (red staining) on paraffin-embedded sections of xenografts generated by the injection of CRC sphere cell lines and treated with PBS (vehicle), BMP4, or BMP7v. Green arrowheads indicate microvessels expressing CD31 or VEGFR2. Images are representative of three independent experiments using cells as in **a**. Nuclei were revealed by hematoxylin staining (blue). The scale bar represents 20 μ m. **d** Number of microvessels positive for CD31 (left panel) and VEGFR2 (right panel) expression, evaluated on paraffin-embedded sections of xenografts treated as in **c**. Data are shown as mean \pm SD of cells. MVD = microvessel density. **e** Fold change of viable cells in 35 CR-CSC lines treated with oxaliplatin/5-FU for 24 h. Dotted line indicates the threshold between chemoresistant (red) and sensitive CR-CSCs (green). **f** Cell viability percentage in chemoresistant CR-CSCs (R1-R4) pretreated with BMP7 for 3 days and with oxaliplatin/5-FU (oxa/5-FU) for additional 24 h as indicated. Data are shown as mean \pm SD of three different experiments performed in the indicated R-CSCs. **g** Colony forming efficiency of CR-CSCs treated as in **f** and evaluated at 21 days. Representative soft-agar analyses are reported in the lower part of the graph. Bars show the mean \pm SD of seven different CRC sphere cell lines (CSC#1–3, 5, 7, 10, and 18). **h** Tumor size of subcutaneous growth of the indicated CR-CSCs. Mice were treated for 4 weeks (6–9 weeks) with vehicle, oxaliplatin/5-FU (oxa/5-FU) and BMP7v alone or in combination. Error bars show the mean \pm SD of tumor size measured in six mice/group. Black arrowheads indicate days of treatment. **i** Immunohistochemical analysis of CD44v6, β -catenin, Ki67, and CK20 (red color) in paraffin-embedded sections of CSC#7 xenografts treated as in **h**. Nuclei were counterstained by aqueous hematoxylin (blue color). The scale bar represents 20 μ m (left panels). Percentage of CD44v6, β -catenin, Ki67, and CK20 positive cells in paraffin-embedded sections of tumor xenografts treated with vehicle (V), BMP7v (B), oxaliplatin/5-FU (O/F), alone or in combination (B/O/F) for 72 h. Error bars are mean \pm SD of positive cell counts in three serial embedded-paraffin sections of six tumor xenografts per group derived from the injection of three different CRC sphere cells (CSC#1, 2, and 7) (right panels)

BMP7v treatment, PI3K protein expression, and AKT activation levels decreased significantly in CD44v6⁺ cells, which differentiate and revert to CD44v6⁻/PI3K^{low} cells. This mechanism is in line with the observation that the natural compound resveratrol inhibits the PI3K pathway by upregulating the BMP7 in human colon cancer cells [44]. The induction of differentiation may represent an alternative therapeutic approach to render CSCs sensitive to standard therapies [24, 45]. Differentiation therapy is currently in phase 2 clinical trial for the cure of acute promyelocytic leukemia [46]. The expression of anti-apoptotic genes and the upregulation of survival factors contribute to CSC resistance to conventional anticancer therapies [32].

BMP7v reduces the expression levels of anti-apoptotic proteins and makes *PIK3CA* wt CRC avatars sensitive to

standard chemotherapy. In addition, BMP7v enhances the therapeutic response even against CR-CSCs purified from metastatic lesions of patients who underwent chemotherapy. About 10–30% of CRCs exhibit PI3K activation sustained by *PIK3CA* mutations, which contribute to confer resistance to standard therapies and targeted agents [47]. *PIK3CA*-mutated tumor xenografts display resistance to the combination of BMP7v and chemotherapy. This is not surprising because it is likely that the increased β -catenin activation promoted by the constitutive activation of PI3K counteracts the inhibitory activity on the Wnt pathway induced by BMP signaling.

PI3K is a target for pharmacological drug design and therapeutic intervention in many cancers, including CRC [48]. Nowadays, although PI3K inhibitors have a limited effect as single agents in CRC, several clinical trials are exploring the efficacy of these inhibitors in different combinatorial treatments [47, 49]. Here we showed that BMP7v is able to sensitize chemoresistant CR-CSCs to PI3K inhibitors in vitro regardless their MSI and CMS profiles. Addition of a PI3K inhibitor to the combination of BMP7v and chemotherapy-induced tumor regression of *PIK3CA*-mutant tumor xenograft, further supporting the potential clinical application of this combination therapy. In line with our previous findings, PI3K inhibitors alone selectively target disseminating CR-CSCs [8], whereas in combination with BMP7v treatment induce disease regression by reducing the size of both primary tumors and established CRC liver metastasis.

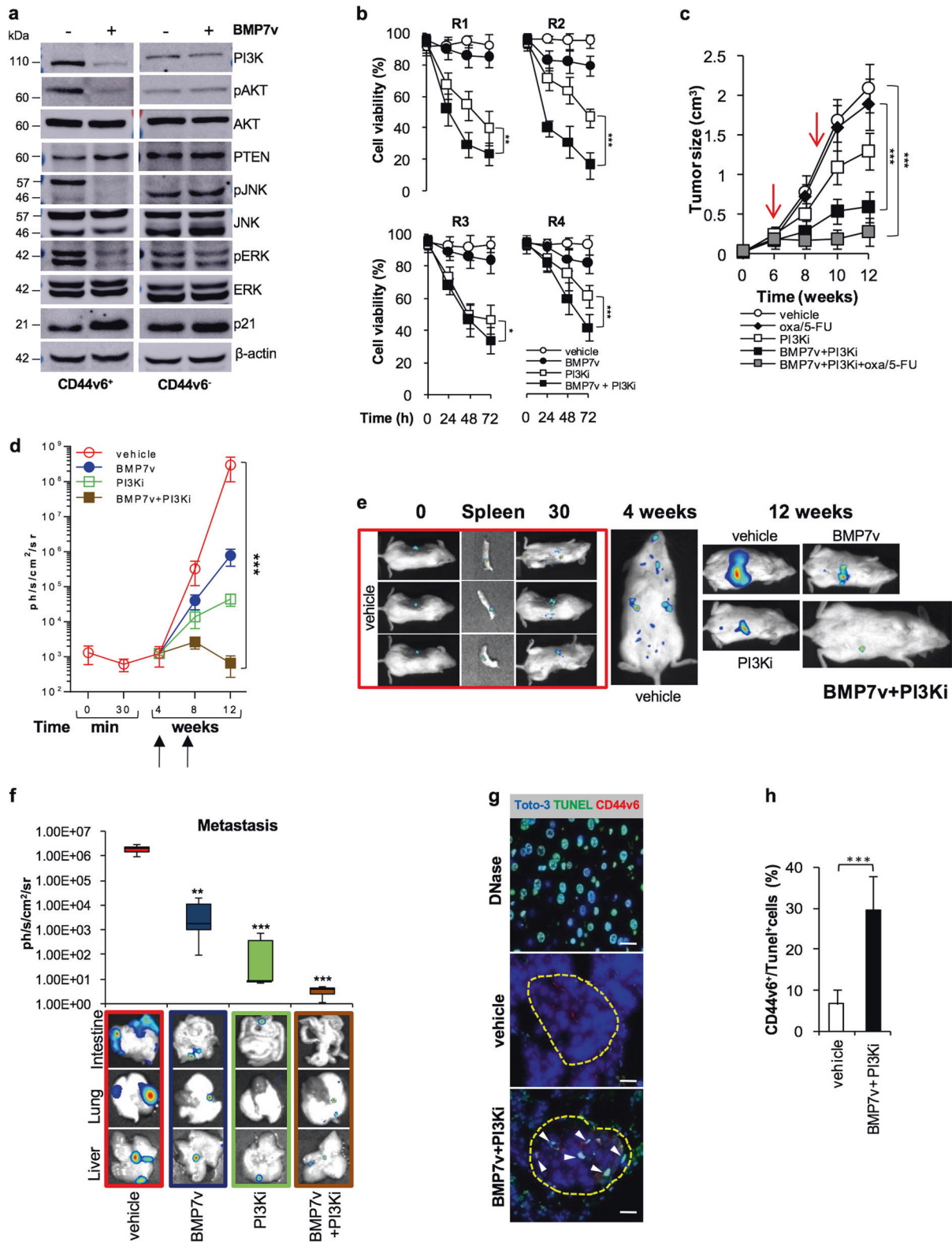
In conclusion, we have shown that BMP7v exerts a potent antitumor activity through the induction of differentiation of *PIK3CA* wt CR-CSCs. Although the presence of *PIK3CA* mutation reduces the therapeutic activity of BMP7v, we provide evidence that the addition of PI3K inhibitors may be sufficient to restore CR-CSC sensitivity to BMP7v. Unlike BMP4, BMP7v exerts a significant antiangiogenic effect and can be administered systemically, due to its solubility and prolonged half-life, which also facilitate its combination with standard chemotherapy or targeted agents. Further studies are needed to investigate the minimal residual disease upon the combination therapy based on BMP7v and PI3K inhibitor.

Because the efficacy of targeted therapy is limited by the presence of intratumor heterogeneity, this prodifferentiation approach coupled with such a considerable antiangiogenic activity may contribute to overcome the hurdles of dynamic tumor changes. Thus, BMP7v-based combination therapies may represent potential novel treatment options for CRC.

Materials and methods

Isolation and treatment of CR-CSCs

Human CRC tissues were obtained from 40 patients at the time of resection, in accordance with the ethical standards of



the Institutional Committee on Human Experimentation (authorization CE9/2015, Policlinico Paolo Giaccone, Palermo) after informed consent. Peritumoral mucosa was

recovered from the uninvolved surrounding tumor tissue. Clinical data of CRC patients from which CRC sphere cell lines were derived are reported in Supplementary Table 1.

Fig. 5 BMP7v in combination with PI3K inhibitor hampers tumor growth and reduces the metastatic lesion size. **a** Immunoblot analysis of PI3K, pAKT, AKT, PTEN, pJNK, JNK, pERK, ERK, and p21 in CD44v6⁺ and CD44v6⁻ cells treated with vehicle or BMP7v for 3 days. β -actin was used as loading control. One representative of three independent experiments (CSC#1, 4, and 7) is shown. **b** Cell viability percentage in R-CSCs treated with vehicle, BMP7v, PI3K inhibitor (PI3Ki), or BMP7v in combination with PI3K inhibitor (BMP7v + PI3Ki) up to 72 h. Data are shown as mean \pm SD of three different experiments performed with the indicated R-CSCs. **c** Tumor size of subcutaneous outgrowth of *PIK3CA*-mutated xenografts. Mice were treated with vehicle, PI3K inhibitor (PI3Ki), oxaliplatin/5-FU (oxa/5-FU), BMP7v in combination with PI3K inhibitor (BMP7v + PI3Ki) or BMP7v in combination with PI3K inhibitor and oxaliplatin/5-FU (BMP7v + PI3Ki + oxa/5-FU). Data are shown as mean \pm SD of tumor size of six mice/group using CSC#1, 18, and 25. Red arrows indicate the start and the end (from 6 to 9 weeks) of treatments. **d** Kinetics of metastasis formation detected by in vivo imaging analysis at the indicated time following spleen injection of CSC#1, 18, and 25 treated with vehicle, BMP7v, PI3K inhibitor (PI3Ki), or BMP7v in combination with PI3K inhibitor (BMP7v + PI3Ki) for 4 weeks. Black arrows indicate the start and end of treatments (from 4 to 7 weeks). Data are expressed as mean \pm SD of six mice analyzed. **e** In vivo whole-body imaging analysis of mice treated as in **d** and analyzed at the indicated time points after splenectomy. **f** Photons count of all metastatic sites (liver, lung, and intestine) in mice treated as in **d**. Error bars are reported as mean \pm SD of the xenografts analyzed as in **d** (upper panel). Representative in vivo imaging analysis of metastatic foci in the liver, lung, and intestine of mice treated as indicated (lower panels). **g** Immunofluorescence analysis of CD44v6 (red color) and TUNEL (green color) in paraffin-embedded sections of lung metastasis generated by the injection of CSC#25 in mice treated with vehicle or BMP7v + PI3K inhibitor (BMP7v + PI3Ki). White arrowheads indicate CD44v6⁺/Tunel⁺ CRC cells. Nuclei were counterstained with Toto-3 (blue color). Positive control was performed treating cells with DNase. The scale bars represent 20 μ m. **h** Percentage of CD44v6⁺/Tunel⁺ cells of lung metastasis treated with vehicle or BMP7v + PI3K inhibitor (BMP7v + PI3Ki). Data are mean \pm SD of xenografts derived from injection of three different cell lines (CSC#1, 18, and 25)

CRC sphere cells were isolated and propagated as previously described [8, 32]. Briefly, specimens were digested in DMEM medium supplemented with 10 μ g/ml of hyaluronidase (Sigma) and 0.6 mg/ml of collagenase (Gibco) for 1 h at 37 $^{\circ}$ C, resuspended in serum-free stem cell medium comprising EGF (Peprotech) and FGF2 (Peprotech) and cultured in ultra-low adhesion flasks. To generate SDACs, CR-CSCs were dissociated and then cultured in DMEM-high glucose supplemented with 10% FBS in adherent conditions up to 21 days [24]. Gradual morphological differentiation was determined by counting of cells in adherent conditions normalized with the number of CR-CSCs in suspension. To evaluate differentiation of CRC organoids, CR-CSCs were dissolved in a 1:10 stem cell medium/Matrigel solution, placed in a 24-well plate as a single drop covered by medium and monitored twice a week up to 21 days.

Authentication of CRC sphere cell lines was assessed by short tandem repeat (STR) DNA profiling (GlobalFiler™

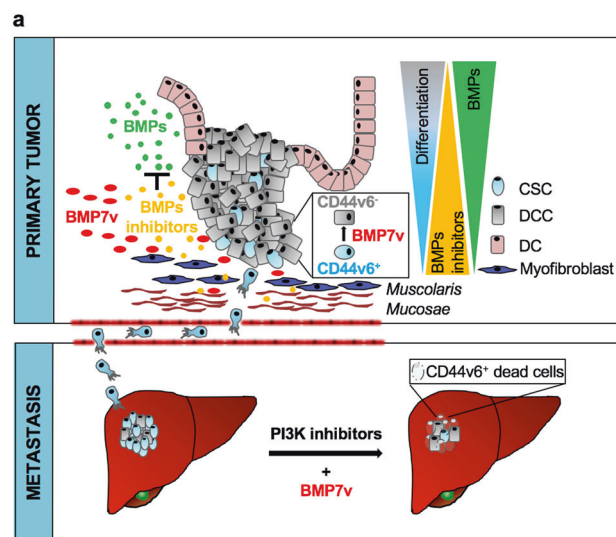


Fig. 6 Schematic model of BMP7v effects in primary and metastatic CRC. **a** In primary tumor the colon cancer crypt organization, which is physiologically maintained by BMPs/BMP inhibitor balance, is disrupted. The administration of BMP7v selectively counteracts the expansion of the CSC compartment by reducing CD44v6 expression. Moreover, BMP inhibitors (noggin, gremlin, and others), produced by myofibroblasts, are not able to inhibit BMP7v activity on promoting the differentiation of CSCs (upper panel). In metastatic tumor, BMP7v in combination with PI3K inhibitors reduces the number of CD44v6⁺ cells and hampers the tumor metastatic growth (bottom panel). CSC cancer stem cell, DCC differentiated cancer cell, DC differentiated cell

STR kit, Applied Biosystem) using the ABIPRISM 3130 genetic analyzer (Applied Biosystem) as recommended by the manufacturer's instructions. STR profiles of CRC sphere cells were matched with their relative patient-derived tumors. Primary cultures enriched in CSCs derived from chemoresistant metastatic liver lesions were obtained from patients undergoing hepatectomy with curative intent at the University Polyclinic A. Gemelli, Rome. Cell cultures were monitored for the presence of mycoplasma. CRC sphere cells and their enriched CD44v6⁺ and CD44v6⁻ fractions were treated with BMP7v (100 ng/ml produced by Eli Lilly as previously described) [30], gremlin (1 μ g/ml, R&D Systems), noggin (100 ng/ml, R&D Systems), BMP4 (100 ng/ml, R&D Systems), oxa (10 μ M, Selleckchem), 5-FU (10 μ M, Selleckchem), and taselesib (PI3Ki, 1 μ M GDC-0032, Chemiekt). Oxa was added to cell culture media 2 h before 5-FU treatment. All the compounds above described were added to cell culture media every 48 h. BMP7v dose was determined by the evaluation of colony forming efficiency in presence of different concentration of BMP inhibitors (gremlin and noggin), when in combination with PI3K inhibitor (taselesib) its effective dose was selected on the basis of CR-CSC viability. These experiments were conducted in SynergyFinder, including Bliss and ZIP, to calculate dose-response inhibition matrix and synergy scores [50].

Immunohistochemistry and Immunofluorescence

Immunohistochemistry analysis was performed on 5- μ m-thick paraffin-embedded sections of CRC tissues or CRC sphere cell-derived tumor xenografts. For intracellular epitope detection, tissue sections were permeabilized in ice-cold 0.1% TritonX-100 in PBS for 10 min. Tissue samples were exposed overnight at 4 °C to specific antibodies for BMP7 (MAB3541, mouse, IgG2_b, R&D system), E-cadherin (#3195, rabbit, IgG, CST), CD31 (M0823, clone JC70A, mouse IgG1_k, Dako), VEGFR2 (AF357, goat, IgG, R&D System), CD44v6 (BBA13, clone 2F10, mouse, IgG1, R&D system), β -catenin (sc-7199, rabbit, IgG, Santa Cruz Biotechnology), Ki67 (M7240, mouse, IgG1, DakoCytomation), and CK20 (NCL-L-CK20, mouse, IgG2_k, Novocastra Leica). Primary antibodies were revealed by biotin-streptavidin peroxidase LSAB 2 Kit (Dako). Stainings were detected by using 3-amino-9-ethylcarbazole chromogen. Nuclei were counterstained with aqueous hematoxylin (Sigma).

For Azan-Mallory, tissues were stained with azocarmine G (Sigma) and 5% of phosphoric acid. Then, sections were stained with a Mallory mix solution (Sigma). Staining was analyzed by using Imaging Analyzer Software.

Immunofluorescence staining was performed on paraffin-embedded sections, cells cytospun or cultured on coverslips. Cells were fixed in 2% paraformaldehyde for 20 min at 37 °C. Intracellular epitope detection was performed in cells permeabilized in 0.1% TritonX-100 in PBS for 10 min. Following blocking with 3% bovine serum albumin (BSA) for 30 min, cells were exposed overnight at 4 °C to BMP7 (MAB3541, mouse, IgG2_b, R&D system), LGR5 (GPR49, rabbit, IgG, Abgent), CDX2 (MAB3665, mouse, IgG1, R&D Systems), CK20 (NCL-L-CK20, mouse, IgG2_k, Novocastra Leica), E-cadherin (#3195, rabbit, IgG, CST), vimentin (#5741, rabbit, IgG, CST), β -catenin (MAB1329, mouse, IgG2_b, R&D Systems), CD44v6 (BBA13, clone 2F10, mouse, IgG1, R&D system), BMPR1A (MAB2406, mouse, IgG2_b, R&D Systems), BMPR1B (MAB505, mouse, IgG2_a, R&D Systems) and, BMPR2 (MAB811, mouse, IgG2_b, R&D Systems) antibodies or isotype-matched controls (IMCs). Primary antibodies were revealed using Alexa Fluor 488 or Rhodamine-conjugated anti-mouse or anti-rabbit secondary antibodies (Invitrogen) in the presence of RNase (40 μ g/ml, Sigma). Nuclei were counterstained using TOTO-3 iodide (Molecular Probes).

Cell quantitation was performed by ImageJ Software analysis. TUNEL assay was performed by using In Situ Cell Death Detection, AP Kit (Roche Diagnostics GmbH). DNA strand breaks were detected by 5-bromo-4-chloro-3-indolylphosphate (, Dako) substrate. DNase was used to perform the positive control.

TMAAs were provided by TriStar Technology group (*Tri*), LLC, 9700 Great Seneca Highway, Rockville, MD 20850.

Flow cytometry and cell cycle analysis

CD133 and CD44v6 positive and negative subpopulations were obtained using FACS cell sorter (BD). Cells were stained for 1 h at 4 °C with CD133-PE (130-090-851, 293C3, mouse IgG2_b, Miltenyi), CD44v6-APC (FAB3660A, clone 2F10, mouse, IgG1, R&D systems) or corresponding IMCs IgG2b-PE (#130-092-215, mouse, Miltenyi) or IgG1-APC (#IC002A, mouse, R&D systems). Before sorting, cells were resuspended in PBS supplemented with 2% BSA and 2 mM EDTA, and strained through a 70 μ m mesh to avoid cell hindrance. Dead cells were excluded with 7-AAD (BD). Quality of postsorting was verified by flow cytometry using specific antibodies against CD133 (170-070-702, CD133/1-APC, AC133, mouse IgG1_k, Miltenyi) or CD44v6 (#MA5-16966, CD44v6-FITC, VFF-7, mouse IgG1, Thermo Scientific). Cells were then washed twice in PBS, permeabilized with fixation/permeabilization solution (Cytofix/Cytoperm, BD) following the manufacturer's instructions and stained with BMP7-FITC (FCMAB135F, 2A10, mouse IgG1_k, Merck) or its IMC IgG1_k (#F6397, mouse, Sigma-Aldrich). For flow cytometry analysis of CD133 and CD44v6, PE-(293C3) or APC-conjugated (2F10) clone were used, respectively. Cell cycle analysis was performed by quantification of DNA content on dissociated cells. Cells were incubated overnight at 4 °C in a buffer containing 50 μ g/ml propidium iodide (Sigma-Aldrich), 0.1% sodium citrate (Sigma-Aldrich), 0.1% TritonX-100 and 10 μ g/ml RNase (Sigma-Aldrich). All data were analyzed using FlowJo software (Tree Star). The percentage of CD44v6⁺ cells has been assessed in all the 35 CRC sphere cell lines and indicated as low (<30%), medium (30–70%), and high (>70%) in Supplementary Table 2.

Lentiviral particles generation and CR-CSC transduction

To generate lentiviral particles, packaging cell line HEK-293T were transfected with second-generation packaging plasmids (PSPAX2 and pMD2.G plasmids Addgene) in association with p-TWEEN LUC or TOP-dGFP (Addgene # 35489) lentiviral vectors. Transfection was performed using X-tremeGENE HP DNA Transfection Reagent (Roche). Lentiviral supernatants were collected and concentrated with the Lenti-X Concentrator reagent (Clontech). 1×10^5 CRC sphere cells were transduced with concentrated viral supernatants for 24 h using 8 μ g/ml polybrene. Wnt pathway activity was monitored by flow cytometry analysis on the basis of the TOP-dGFP expression levels.

Cell viability, clonogenic, and invasion assay

The cell viability assay was performed using the CellTiter96[®] Aqueous One Solution Cell Proliferation Assay Kit (Promega) according to the manufacturer's instructions and examined with GDV programmable MPT reader (DV 990 BV6). For invasion assay, 2×10^3 dissociated CR-CSCs were plated into 8 μm pore size matrigel (BD)-coated transwell and treated with vehicle or BMP7v up to 48 h. Supernatant of NIH-3T3 cells cultured in serum-free medium was used as chemoattractant in the lower part of the transwell system. Migrating cells were examined and counted using an optical microscope. For clonogenicity, CR-CSCs were plated at a clonal density on Agarose Sea Plaque Agar (Invitrogen) and maintained up to 21 days. Colonies were stained with 0.01% Crystal Violet, evaluated based on their size (small 30–60 μm , medium 60–90 μm , and large >90 μm) and counted using ImageJ software.

Western blot analysis

Cell pellets were resuspended in ice-cold lysis buffer (50 mM Tris-HCL pH 8, 150 mM NaCl, 0.5% sodium deoxycholate, 0.1% SDS, 1% NP40, 1 mM EDTA) supplemented with a mix of protease and phosphatase inhibitors (Thermo Fisher Scientific). Equal amount of protein extracts was resolved on SDS-PAGE gels and blotted on nitrocellulose membranes. Membranes were exposed overnight at 4 °C to PARP (#9524, rabbit, IgG, CST), Caspase-3 (#9662, rabbit, IgG, CST), cleaved Caspase-3 (Asp175) (#9661, rabbit, IgG, CST), Bcl-2 (sc-7382, mouse, IgG, Santa Cruz), Bcl-xL (sc-8392, mouse, IgG, Santa Cruz), PI3K (p110 α) (#4249, C73F8, rabbit, IgG, CST), phospho-AKT (Ser473 XP) (#4060, D9E, rabbit, IgG, CST), AKT (#9272, rabbit, IgG, CST), PTEN (#9559, 138G6, rabbit, IgG, CST), phospho-JNK (Thr183/Tyr185) (#4668, 81E11, rabbit, IgG, CST), JNK (#9258, 56G8, rabbit, IgG, CST), phospho-ERK (sc-7383, E-4, mouse, IgG_{2a}, Santa Cruz), ERK (sc-94, rabbit, IgG, Santa Cruz), p21 (#2946, DCS60, mouse IgG_{2a}, CST), and β -actin (#3700, 8H10D10, mouse IgG_{2b}, CST). Primary antibodies were detected using specific secondary HRP-conjugated antibodies (Thermo Fisher Scientific) and chemiluminescence signals were revealed using Amersham imager 600 (GE Healthcare). Protein expression levels were measured by densitometry analysis using ImageJ software.

Mutation analysis and MSI profile

Total DNA was purified from CR-CSCs using the Blood and Tissue Kit (QIAGEN). The mutational status of *KRAS*,

BRAF, *PIK3CA*, and *SMAD4* genes was evaluated by the BigDye Terminator v3.1 Cycle Sequencing Kit (Applied Biosystems) using the following primers specific for *KRAS*^{G12/G13} (F-ATCGTCAAGGCACTCTTGCCCTAC, R-GTACTGGTGGAGTATTTGATAGTG), *BRAF*^{V600} (F-ACTCTAAGAGGAAAGATGAAG, R-GTGAATACTGGGAACTATGA), *PIK3CA*^{E545} (F-ATTGTTCACTACCATCCTC, R-TAATGTGCCAACTACCAATG) and *SMAD4*^{R361} (F-TGTGGAGTGCAGTGAAAGC, R-TCAATGGCTTCTGTCTGTG). Codon Code Aligner Software was used for sequence assembly and alignment. Assessment of MSI status of CR-CSCs was carried out using the GeneQuality CC-MSI kit (Analytica Advanced Biomedicine). Purified total DNA was subjected to a multiplex microsatellite PCR including mononucleotide repeats (BAT25, BAT26, BAT40, NR21, NR24, and TGF β RII) and dinucleotide repeats (D2S123, D17S250, D5S346, and D18S58). MSI analysis was carried out using GeneMapper 5.0 Software (Applied Biosystems). Samples were classified as MSI-high (four or more markers unstable), MSI-low (1–3 markers unstable), or MSS (microsatellite stable). Mutation and MSI profiles of CR-CSCs were performed on a Genetic Analyzer ABIPRISM 3130 (Applied Biosystems). COSMIC-reported mutations of *KRAS*, *BRAF*, *PIK3CA*, and *SMAD4* in the 35 CRC sphere cell lines used and their MSI profiles are indicated in Supplementary Table 2.

RNA isolation and Real-time PCR

Total RNA was obtained using the RNeasy Plus Mini Kit (Qiagen GmbH) according to the manufacturer's instructions. The yield of the extracted RNA was determined by Nanodrop ND-1000 (Nanodrop, Wilmington, DE). One microgram of total RNA was retro-transcribed using the High-Capacity cDNA Archive Kit (Applied Biosystems) following the standard protocol. Quantitative real-time PCR analysis was performed in SYBR Green PCR master mix (SuperArray Bioscience) containing primers for *BMP1A* (F-GTCATACGAAGATATGCCGTGAGGTTGT, R-ATGCTGTGAGTCTGGAGGCTGGATT), *BMP1B* (F-AAGGCTCAGATTTTCAGTGTCTGGGA, R-GGAGGCAGGTAGGGTGTAGGTCTTTATT), *BMP2* (F-GTGACTGGGTAAGCTCTTGCCGTCT, R-GCAGGTTTATAATGATCTCCTCGTGGT), *TGF β 1* (F-CTCGCCCTGTACAACAGCA, R-GGTTTCCACCATTAGCACGC), *TGF β 2* (ACAGACCCTACTTCAGAATTGTT, R-TGGGTTCTGCAAACGAAAGA) *CDH2* (F-GGAGAACCCATTGACATTGT, R-TGTTCCAGGCTTTGATCCCT), *MMP2* (TGGTGGGAACTCAGAAGGTG, R-CCACATCTTTCCGTCACTGC), *MMP9* (F-ACTACTGTGCCCTTTGAGTCC, R-CCAGTACTTCCCATCCTTGA), or *GAPDH* (F-GCTTCGCTCTCTGCTCCTCCTGT, R-

TACGACCAAATCCGTTGACTCCG). Relative mRNA expression levels were normalized with the endogenous control (*GAPDH*) and calculated using the comparative Ct method $2^{-\Delta\Delta C_t}$. mRNA expression levels of EMT-, tumor metastasis-, and Wnt pathway-related genes were detected by RT² profiler PCR array (PAHS-090, Qiagen) according to manufacturers' instructions. Data were analyzed using the R version 3.5.0 and plotted by the heatmap version 1.0.10 and VennDiagram 1.6.20, gtools 3.8.1, and ggplot2 3.0.0. GSEA was performed by selecting the Kyoto Encyclopedia of Genes and Genomes, Gene Ontology and Hallmarks within MSigDB version 6.2. Gene sets with a False Discovery Rate q value ≤ 0.05 were considered significantly enriched. CMS1–4 profile of CR-CSCs was based on the evaluation of RNA-seq data on matched specimens derived from primary lesions of CRC patients as reported in Linnekamp et al. [51]. Correlation analysis data were obtained using the “R2: Genomics Analysis and Visualization Platform” (<http://r2.amc.nl> <http://r2platform.com>) in CRC samples from the Expression Project for Oncology (GEO accession number GSE2109).

Animals and tumor models

Dissociated CRC sphere cells (5×10^5) were injected subcutaneously into the flank of 5–6-week-old male NOD-SCID mice (Charles River), in a total volume of 100 μ l of serum-free medium mixed with matrigel (BD) in a ratio of 1:1. The Replacement, Reduction, and Refinement (3Rs) principles were used to estimate the lowest sample size (six mice per group).

Mice were treated for four weeks with PBS (vehicle) or BMP7v (50 μ g/kg, 3 days/week) alone or in combination with oxa (0.25 mg/kg, once a week) and 5-FU (15 mg/kg, 2 days/week) by i.p. injection, and with taselisib (5 mg/kg, once daily) by oral gavage. Treatment with BMP4 was performed by intratumoral injection of 100 BMP4-coated beads once a week for 6 weeks. Heparin acrylic beads (Sigma) were incubated with BMP4 (0.65 μ g/ μ l) for 1 h at 37 °C and washed twice in PBS.

Tumor size was calculated according to the formula: $(\pi/6) \times (\text{smaller diameter})^2 \times \text{larger diameter}$.

For in vivo migration experiments, 3×10^5 luciferase (LUC)-transduced CD44v6⁺ CR-CSCs were resuspended in PBS and injected into the spleen of NOD/SCID mice. Following i.p. administration of D-luciferin (150 mg/kg, Promega), the bioluminescence signal of migrating cells was measured before and 30 min after the cell injection and immediately after splenectomy up to 12 weeks (every 4 weeks) by using Photon IMAGER instrument (Biospace). No randomization procedure was used. Investigators were not blinded during analysis.

Statistical analysis

The sample size was chosen to reach a power of 0.9, 0.05 error probability and a large effect size (>0.5) for our groups of treatments. Data were presented as mean \pm standard deviation. Statistical significance was estimated by Analysis of Variance (one way or two ways) with Bonferroni post test, or by unpaired *T* test. Results were referred to statistically significant as $P < 0.05$. * indicates $P < 0.05$, ** indicate $P < 0.01$, and *** indicate $P < 0.001$.

Study approval

This study was performed in accordance with the ethical standards of the Institutional Committee on Human Experimentation (authorization CE9/2015, Policlinico Paolo Giaccone, Palermo). All animal experiments were approved by the Institutional Italian Guidelines for Animal Welfare of the University of Palermo (D.L. n° 26 March 4, 2014, Authorization #154/2017-PR; Protocol 2B952.5).

Acknowledgements We are thankful to Alessandro Gorgone for technical support, Francesco Calo' for graphics and Tatiana Terranova for editing the manuscript. The research leading to these results has received funding from AIRC under 5x1000 (9979) project—P.I. SG and RDM.

Authors' contributions VV, GS, and RDM conceived and designed the experiments and wrote the manuscript; VV, LRM, AN, SDF, ES, TA, MF, AB, MLC and MT carried out the experiments, analyzed and elaborated data; DSS executed the bioinformatic analysis; GC, FG and CC provided colon cancer specimens; GP and MRB supplied scientific suggestions and critical review; AR provided paraffin-embedded sections of colon adenoma and additional colon cancer specimens; CMT, XW, SR and LFS provided the BMP7 variant (BMP7v) and critical comments to the manuscript. All authors revised the manuscript.

Conflict of interest Authors affiliated with Eli Lilly and Company have Eli Lilly and Company shares received via 401 (k) and bonus plans. RDM is an Advisory Board member of HiberCell. RDM and GS are recipients of grants from HiberCell. All other authors declare that they have no conflict of interest.

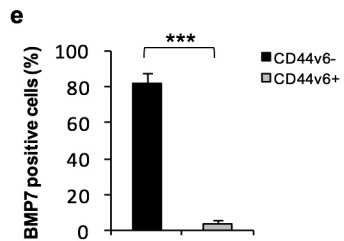
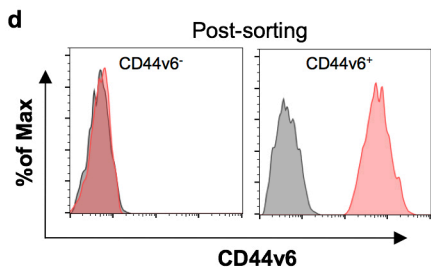
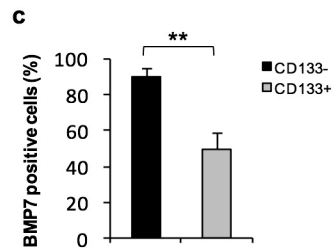
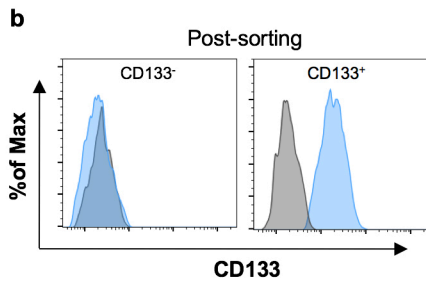
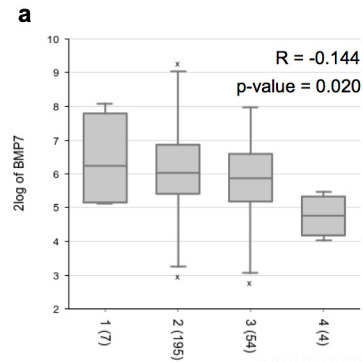
Publisher's note Springer Nature remains neutral with regard to jurisdictional claims in published maps and institutional affiliations.

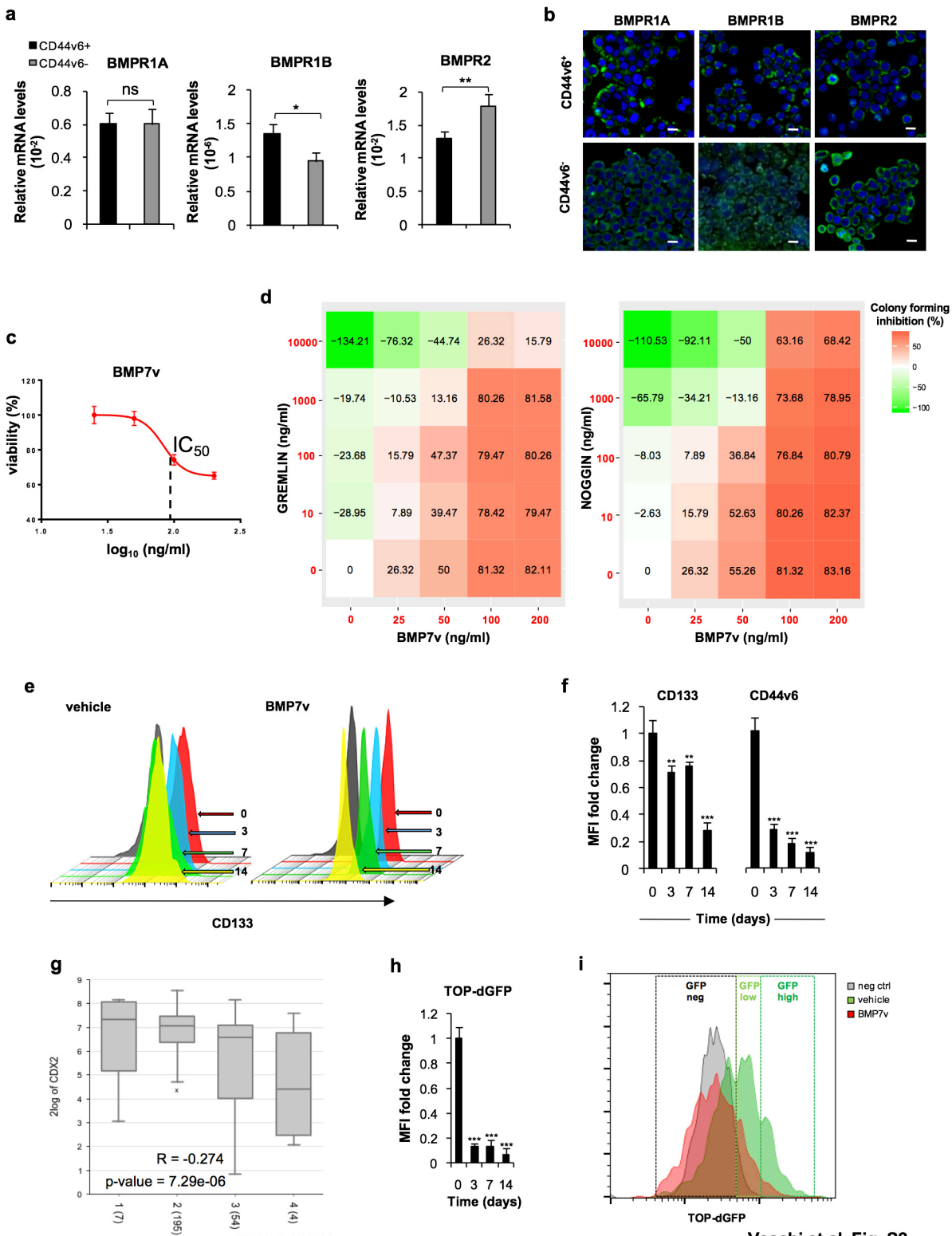
Open Access This article is licensed under a Creative Commons Attribution 4.0 International License, which permits use, sharing, adaptation, distribution and reproduction in any medium or format, as long as you give appropriate credit to the original author(s) and the source, provide a link to the Creative Commons license, and indicate if changes were made. The images or other third party material in this article are included in the article's Creative Commons license, unless indicated otherwise in a credit line to the material. If material is not included in the article's Creative Commons license and your intended use is not permitted by statutory regulation or exceeds the permitted use, you will need to obtain permission directly from the copyright holder. To view a copy of this license, visit <http://creativecommons.org/licenses/by/4.0/>.

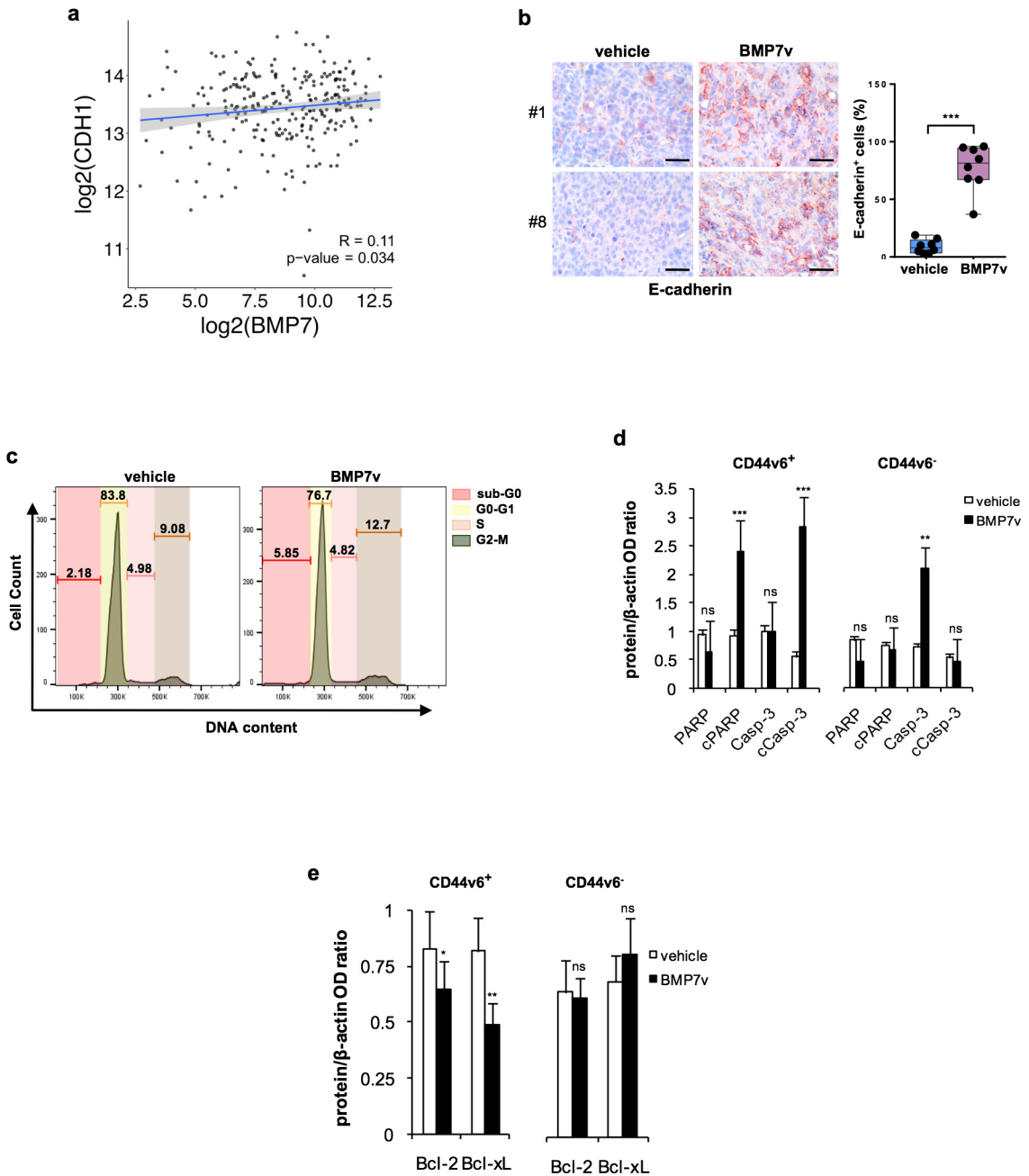
References

- Siegel RL, Miller KD, Fedewa SA, Ahnen DJ, Meester RGS, Barzi A, et al. Colorectal cancer statistics, 2017. *CA Cancer J Clin.* 2017;67:177–93.
- Zeuner A, Todaro M, Stassi G, De Maria R. Colorectal cancer stem cells: from the crypt to the clinic. *Cell Stem Cell.* 2014;15:692–705.
- Battle E, Clevers H. Cancer stem cells revisited. *Nat Med.* 2017;23:1124–34.
- Valent P, Bonnet D, De Maria R, Lapidot T, Copland M, Melo JV, et al. Cancer stem cell definitions and terminology: the devil is in the details. *Nat Rev Cancer.* 2012;12:767–75.
- Vitale I, Manic G, De Maria R, Kroemer G, Galluzzi L. DNA damage in stem cells. *Mol Cell.* 2017;66:306–19.
- Marcucci F, Stassi G, De Maria R. Epithelial-mesenchymal transition: a new target in anticancer drug discovery. *Nat Rev Drug Discov.* 2016;15:311–25.
- Ricci-Vitiani L, Lombardi DG, Pilozzi E, Biffoni M, Todaro M, Peschle C, et al. Identification and expansion of human colon-cancer-initiating cells. *Nature.* 2007;445:111–5.
- Todaro M, Gaggianesi M, Catalano V, Benfante A, Iovino F, Biffoni M, et al. CD44v6 is a marker of constitutive and reprogrammed cancer stem cells driving colon cancer metastasis. *Cell Stem Cell.* 2014;14:342–56.
- Arends JW. Molecular interactions in the Vogelstein model of colorectal carcinoma. *J Pathol.* 2000;190:412–6.
- Medema JP, Vermeulen L. Microenvironmental regulation of stem cells in intestinal homeostasis and cancer. *Nature.* 2011;474:318–26.
- Clevers H. The intestinal crypt, a prototype stem cell compartment. *Cell.* 2013;154:274–84.
- Vermeulen L, Snippert HJ. Stem cell dynamics in homeostasis and cancer of the intestine. *Nat Rev Cancer.* 2014;14:468–80.
- Chen D, Ji X, Harris MA, Feng JQ, Karsenty G, Celeste AJ, et al. Differential roles for bone morphogenetic protein (BMP) receptor type IB and IA in differentiation and specification of mesenchymal precursor cells to osteoblast and adipocyte lineages. *J Cell Biol.* 1998;142:295–305.
- Derynck R, Zhang YE. Smad-dependent and Smad-independent pathways in TGF-beta family signalling. *Nature.* 2003;425:577–84.
- Miyazono K, Kamiya Y, Morikawa M. Bone morphogenetic protein receptors and signal transduction. *J Biochem.* 2010;147:35–51.
- Rider CC, Mulloy B. Bone morphogenetic protein and growth differentiation factor cytokine families and their protein antagonists. *Biochemical J.* 2010;429:1–12.
- Kosinski C, Li VS, Chan AS, Zhang J, Ho C, Tsui WY, et al. Gene expression patterns of human colon tops and basal crypts and BMP antagonists as intestinal stem cell niche factors. *Proc Natl Acad Sci USA.* 2007;104:15418–23.
- Brosens LA, Langeveld D, van Hattem WA, Giardiello FM, Offerhaus GJ. Juvenile polyposis syndrome. *World J Gastroenterol.* 2011;17:4839–44.
- Haramis AP, Begthel H, van den Born M, van Es J, Jonkhoeer S, Offerhaus GJ, et al. De novo crypt formation and juvenile polyposis on BMP inhibition in mouse intestine. *Science.* 2004;303:1684–6.
- Massague J. TGFbeta in cancer. *Cell.* 2008;134:215–30.
- Thiagalingam S, Lengauer C, Leach FS, Schutte M, Hahn SA, Overhauser J, et al. Evaluation of candidate tumour suppressor genes on chromosome 18 in colorectal cancers. *Nat Genet.* 1996;13:343–6.
- Kodach LL, Wiercinska E, de Miranda NF, Bleuming SA, Musler AR, Peppelenbosch MP, et al. The bone morphogenetic protein pathway is inactivated in the majority of sporadic colorectal cancers. *Gastroenterology.* 2008;134:1332–41.
- He XC, Zhang J, Tong WG, Tawfik O, Ross J, Scoville DH, et al. BMP signaling inhibits intestinal stem cell self-renewal through suppression of Wnt-beta-catenin signaling. *Nat Genet.* 2004;36:1117–21.
- Lombardo Y, Scopelliti A, Cammareri P, Todaro M, Iovino F, Ricci-Vitiani L, et al. Bone morphogenetic protein 4 induces differentiation of colorectal cancer stem cells and increases their response to chemotherapy in mice. *Gastroenterology.* 2011;140:297–309.
- Irshad S, Bansal M, Guarnieri P, Davis H, Al Haj Zen A, Baran B, et al. Bone morphogenetic protein and Notch signalling crosstalk in poor-prognosis, mesenchymal-subtype colorectal cancer. *J Pathol.* 2017;242:178–92.
- Buijs JT, Henriquez NV, van Overveld PG, van der Horst G, Que I, Schwaninger R, et al. Bone morphogenetic protein 7 in the development and treatment of bone metastases from breast cancer. *Cancer Res.* 2007;67:8742–51.
- Kobayashi A, Okuda H, Xing F, Pandey PR, Watabe M, Hirota S, et al. Bone morphogenetic protein 7 in dormancy and metastasis of prostate cancer stem-like cells in bone. *J Exp Med.* 2011;208:2641–55.
- Beck SE, Jung BH, Fiorino A, Gomez J, Rosario ED, Cabrera BL, et al. Bone morphogenetic protein signaling and growth suppression in colon cancer. *Am J Physiol Gastrointest Liver Physiol.* 2006;291:G135–45.
- Swencki-Underwood B, Mills JK, Vennarini J, Boakye K, Luo J, Pomerantz S, et al. Expression and characterization of a human BMP-7 variant with improved biochemical properties. *Protein Expr Purif.* 2008;57:312–9.
- Tate CM, Pallini R, Ricci-Vitiani L, Dowless M, Shivanova T, D'Alessandris GQ, et al. A BMP7 variant inhibits the tumorigenic potential of glioblastoma stem-like cells. *Cell Death Differ.* 2012;19:1644–54.
- Tate CM, McEntire J, Pallini R, Vakana E, Wyss L, Blosser W, et al. A BMP7 variant inhibits tumor angiogenesis in vitro and in vivo through direct modulation of endothelial cell biology. *PLoS One.* 2015;10:e0125697.
- Todaro M, Alea MP, Di Stefano AB, Cammareri P, Vermeulen L, Iovino F, et al. Colon cancer stem cells dictate tumor growth and resist cell death by production of interleukin-4. *Cell Stem Cell.* 2007;1:389–402.
- Hemminki A, Mecklin JP, Jarvinen H, Aaltonen LA, Joensuu H. Microsatellite instability is a favorable prognostic indicator in patients with colorectal cancer receiving chemotherapy. *Gastroenterology.* 2000;119:921–8.
- Ribic CM, Sargent DJ, Moore MJ, Thibodeau SN, French AJ, Goldberg RM, et al. Tumor microsatellite-instability status as a predictor of benefit from fluorouracil-based adjuvant chemotherapy for colon cancer. *New Engl J Med.* 2003;349:247–57.
- Jover R, Castells A, Llor X, Andreu M. Predictive value of microsatellite instability for benefit from adjuvant fluorouracil chemotherapy in colorectal cancer. *Gut.* 2006;55:1819–20.
- Guinney J, Dienstmann R, Wang X, de Reynies A, Schlicker A, Soneson C, et al. The consensus molecular subtypes of colorectal cancer. *Nat Med.* 2015;21:1350–6.
- Song N, Pogue-Geile KL, Gavin PG, Yothers G, Kim SR, Johnson NL, et al. Clinical outcome from oxaliplatin treatment in stage II/III colon cancer according to intrinsic subtypes: secondary analysis of NSABP C-07/NRG oncology randomized clinical trial. *JAMA Oncol.* 2016;2:1162–9.

38. Tenbaum SP, Ordonez-Moran P, Puig I, Chicote I, Arques O, Landolfi S, et al. beta-catenin confers resistance to PI3K and AKT inhibitors and subverts FOXO3a to promote metastasis in colon cancer. *Nat Med.* 2012;18:892–901.
39. Sneddon JB, Zhen HH, Montgomery K, van de Rijn M, Tward AD, West R, et al. Bone morphogenetic protein antagonist gremlin 1 is widely expressed by cancer-associated stromal cells and can promote tumor cell proliferation. *Proc Natl Acad Sci USA.* 2006;103:14842–7.
40. Laurila R, Parkkila S, Isola J, Kallioniemi A, Alarmo EL. The expression patterns of gremlin 1 and noggin in normal adult and tumor tissues. *Int J Clin Exp Pathol.* 2013;6:1400–8.
41. Caja L, Tzavlaki K, Dadras MS, Tan EJ, Hatem G, Maturi NP, et al. Snail regulates BMP and TGF β pathways to control the differentiation status of glioma-initiating cells. *Oncogene.* 2018;37:2515–31.
42. Qi Z, Li Y, Zhao B, Xu C, Liu Y, Li H, et al. BMP restricts stemness of intestinal Lgr5(+) stem cells by directly suppressing their signature genes. *Nat Commun.* 2017;8:13824.
43. Mani SA, Guo W, Liao MJ, Eaton EN, Ayyanan A, Zhou AY, et al. The epithelial-mesenchymal transition generates cells with properties of stem cells. *Cell.* 2008;133:704–15.
44. Zeng YH, Zhou LY, Chen QZ, Li Y, Shao Y, Ren WY, et al. Resveratrol inactivates PI3K/Akt signaling through upregulating BMP7 in human colon cancer cells. *Oncol Rep.* 2017;38:456–64.
45. Gupta PB, Onder TT, Jiang G, Tao K, Kuperwasser C, Weinberg RA, et al. Identification of selective inhibitors of cancer stem cells by high-throughput screening. *Cell.* 2009;138:645–59.
46. Castaigne S, Chomienne C, Daniel MT, Ballerini P, Berger R, Fenaux P, et al. All-trans retinoic acid as a differentiation therapy for acute promyelocytic leukemia. I. Clinical results. *Blood.* 1990;76:1704–9.
47. Fruman DA, Chiu H, Hopkins BD, Bagrodia S, Cantley LC, Abraham RT. The PI3K pathway in human disease. *Cell.* 2017;170:605–35.
48. Liu P, Cheng H, Roberts TM, Zhao JJ. Targeting the phosphoinositide 3-kinase pathway in cancer. *Nat Rev Drug Discov.* 2009;8:627–44.
49. Rodon J, Dienstmann R, Serra V, Tabernero J. Development of PI3K inhibitors: lessons learned from early clinical trials. *Nat Rev Clinical Oncol.* 2013;10:143–53.
50. Ianevski A, He L, Aittokallio T, Tang J. SynergyFinder: a web application for analyzing drug combination dose-response matrix data. *Bioinformatics.* 2017;33:2413–5.
51. Linnekamp JF, Hooff SRV, Prasetyanti PR, Kandimalla R, Bui-khuisen JY, Fessler E, et al. Consensus molecular subtypes of colorectal cancer are recapitulated in in vitro and in vivo models. *Cell Death Differ.* 2018;25:616–33.





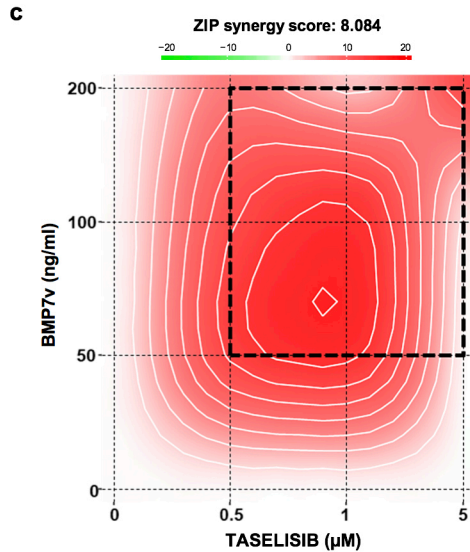
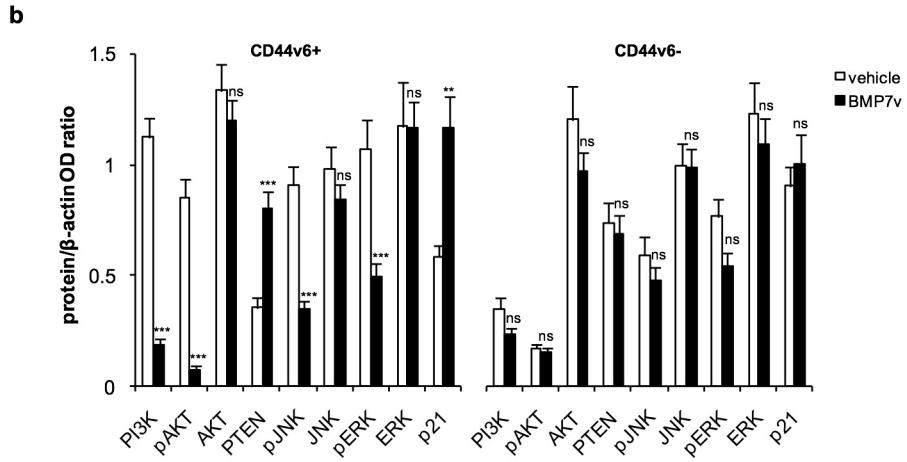
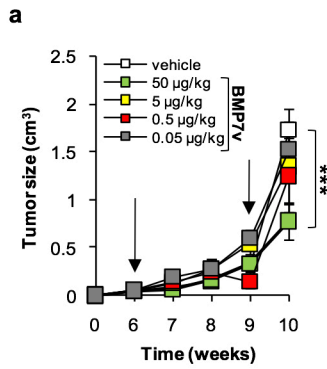


a**Gene/geneset overlap matrix of up-regulated genes**

Entrez Gene Id	Gene Symbol	GO_RESPONSE_TO_VITAMIN_D	GO_NEGATIVE_REGULATION_OF_CELL_DEVELOPMENT	NABA_IN_TISSUE	GO_RESPONSE_TO_VITAMIN	GO_RESPONSE_TO_GROWTH_FACTOR	GO_NEGATIVE_REGULATION_OF_RESPONSE_TO_STIMULUS	GO_EXTRACELLULAR_SPACE	GO_RESPONSE_TO_ENDOGENOUS_STIMULUS	GO_RECEPTOR_BINDING	GO_POSITIVE_REGULATION_OF_CELL_COMMUNICATION	Entrez Gene Description
655	BMP7											bone morphogenetic protein 7
6696	SPP1											secreted phosphoprotein 1
3688	ITGB1											integrin, beta 1 (fibronectin receptor, beta polypeptide, antigen CD29 includes MDF2, MSK12)
7042	TGFB2											transforming growth factor, beta 2
9982	FGFBP1											fibroblast growth factor binding protein 1
3487	IGFBP4											insulin-like growth factor binding protein 4
3855	KRT7											keratin 7

b**Gene/geneset overlap matrix of down-regulated genes**

Entrez Gene Id	Gene Symbol	GO_TISSUE_DEVELOPMENT	GO_REGULATION_OF_CELLULAR_COMPONENT_MOVEMENT	MALWARE_EPITHELIAL_MESENCHYMAL_TRANSITION	GO_REGULATION_OF_MULTICELLULAR_ORGANISMAL_DEVELOPMENT	GO_EXTRACELLULAR_STRUCTURE_ORGANIZATION	GO_POSITIVE_REGULATION_OF_RESPONSE_TO_STIMULUS	GO_MOVEMENT_OF_CELL_OR_SUBCELLULAR_COMPONENT	GO_RESPONSE_TO_OXYGEN_CONTAINING_COMPOUND	GO_ORGAN_MORPHOGENESIS	GO_CELL_DEVELOPMENT	Entrez Gene Description
7040	TGFB1											transforming growth factor beta 1
2335	FN1											fibronectin 1
3678	ITGA5											integrin, alpha 5 (fibronectin receptor, alpha polypeptide)
2303	FOXO2											forkhead box C2 (MFX-1, mesenchyme forkhead 1)
1281	COL3A1											collagen, type III, alpha 1
7076	TIMP1											TIMP metalloproteinase inhibitor 1
7474	WNT5A											wingless-type MMTV integration site family, member 5A
5159	PDGFRB											platelet-derived growth factor receptor, beta polypeptide
3611	ILK											integrin-linked kinase
2932	GSK3B											glycogen synthase kinase 3 beta
7481	WNT11											wingless-type MMTV integration site family, member 11
182	JAG1											Jagged 1
207	AKT1											v-akt murine thymoma viral oncogene homolog 1
7291	Twist1											twist homolog 1 (Drosophila)
4318	MMP9											matrix metalloproteinase 9 (gelatinase B, 92kDa gelatinase, 92kDa type IV collagenase)
1956	EGFR											epidermal growth factor receptor
2065	ERBB3											v-erb-b2 erythroblastic leukemia viral oncogene homolog 3 (avian)
4478	MSN											moesin
81029	WNT5B											wingless-type MMTV integration site family, member 5B
1832	DSP											desmoplakin
649	BMP1											bone morphogenetic protein 1
1000	CDH2											cadherin 2, type 1, N-cadherin (neuronal)
7431	VIM											vimentin
4313	MMP2											matrix metalloproteinase 2 (gelatinase A, 72kDa gelatinase, 72kDa type IV collagenase)
1499	CTNNB1											catenin (cadherin-associated protein), beta 1, 88kDa
9839	ZEB2											zinc finger E-box binding homeobox 2
6663	SOX10											SRY (sex determining region Y)-box 10
50848	F11R											F11 receptor
858	CAV2											caveolin 2
3054	SERPINE1											serpin peptidase inhibitor, clade E (nexin, plasminogen activator inhibitor type 1), member 1
5747	PTK2											PTK2, protein tyrosine kinase 2
7803	PTP4A1											protein tyrosine phosphatase type IVA, member 1
1824	DSC2											desmocollin 2
1290	COL5A2											collagen, type V, alpha 2
4314	MMP3											matrix metalloproteinase 3 (stromelysin 1, progelatinase)
1462	VCAM											vascular
800	CAD1											cadherin 1
7043	TGFB3											transforming growth factor beta 3
4131	MAP1B											microtubule-associated protein 1B
6929	TCF3											transcription factor 3 (E2A immunoglobulin enhancer binding factors E12/E47)
3557	IL1RN											interleukin 1 receptor antagonist
999	CDH1											cadherin 1, type 1, E-cadherin (epithelial)
4486	MST1R											macrophage stimulating 1 receptor (c-met-related tyrosine kinase)
55450	CANXN1											calcium/calmodulin-dependent protein kinase II inhibitor 1
10050658	OCLN											occludin
26499	PLEK2											pleckstrin 2
23230	VPS13A											vacuolar protein sorting 13 homolog A (S. cerevisiae)
25961	NUDT13											nucleoside diphosphate linked moiety X-type motif 13



Supplementary Figure Legends

Figure S1: CD44v6⁺ CR-CSCs lack BMP7 expression

a, Correlation analysis between *BMP7* mRNA expression levels and the pathological grading in CRC samples from R2 database (Tumor Colon EXPO 350). P-value indicates that the negative correlation coefficient is statistically significant. **b**, Post-sorting analysis of CD133 in CD133 enriched cells. One representative of CSC#4, 8, 23-26 is shown. Grey histograms show the isotype matched controls (IMC). **c**, Percentage of BMP7 positive cells in enriched CD133⁺ and CD133⁻ CRC sphere cells as in (b) assessed by immunofluorescence. Data are expressed as mean \pm SD of 6 different CRC sphere cell lines analyzed (CSC#4, 8, 23-26). **d**, CD44v6 expression on sorted CRC sphere cells as in (b) for CD44v6. **e**, Percentage of BMP7 positive cells evaluated by immunofluorescence analysis in CD44v6⁺ and CD44v6⁻ cells. Data are expressed as mean \pm SD as in (c).

Figure S2: BMP7v reduces the content of CD44v6⁺ CR-CSCs

a, Relative mRNA expression levels of *BMPRI1A*, *BMPRI1B* and *BMPRI2* in CD44v6⁺ and CD44v6⁻ cells. Data are expressed as mean \pm SD of 5 different CRC sphere cell lines analyzed (CSC#1, 2, 4, 7, 10). **b**, Immunofluorescence analysis of BMPRI1A, BMPRI1B and BMPRI2 (green color) in cells as in (a). Nuclei were counterstained with Toto-3 (blue color). The scale bars represent 20 μ m. **c**, Dose-response curve of BMP7v treatment based on cell viability % at 24 hours. IC₅₀ was calculated fitting a non linear regression algorithm. One representative experiment of CSC# 3, 7, 9, 21 is shown. **d**, Dose-response matrix indicating the inhibition percentage of CR-CSC colony forming efficiency following treatment with vehicle, gremlin (*left panel*) or noggin (*right panel*) alone or in combination with BMP7v for 14 days at the indicated dose concentrations. One representative experiment of CSC#1, 2, 7 is shown. **e**, Flow cytometry analysis of CD133 in CD44v6⁺ cells treated with vehicle or BMP7v up to 14 days. One representative experiment of CSC#1, 2, 4, 7, 10 is shown. **f**, Fold MFI change (over time 0) of CD133 and CD44v6 expression-in CD44v6⁺ CR-CSCs

treated with BMP7v up to 14 days. Data are expressed as mean \pm SD of 3 independent experiments performed in 5 different CRC sphere cell lines (CSC#1, 2, 4, 7, 10). **g**, Correlation analysis between *CDX2* mRNA expression levels and the pathological grading in CRC samples from R2 database (Tumor Colon EXPO 350). **h**, Fold MFI change (over time 0) of β -catenin activity (TOP-GFP) in CD44v6⁺ CR-CSCs treated with BMP7v up to 14 days. Data are expressed as mean \pm SD of 3 independent experiments performed as in (f). **i**, Flow cytometry analysis of CD44v6⁺ CR-CSCs transduced with TOP-GFP and treated with vehicle (green histogram) or BMP7v (red histogram) for 14 days. Negative control is indicated by the grey histogram. One representative experiment of CSC#8, 9, 11 is shown.

Figure S3: BMP7 expression levels are positively correlated with E-cadherin whereas inversely associated with pathological grading

a, Correlation analysis between *CDH1* (E-cadherin) and *BMP7* mRNA expression levels in CRC samples from TCGA-COAD and TCGA-READ. **b**, Immunohistochemical analysis of E-cadherin (red staining) in xenograft tumors derived from injection of CR-CSCs treated with vehicle or BMP7v for 4 weeks. Two representative experiments of CSC# 1, 8, 25 are shown. Nuclei were counterstained by aqueous hematoxylin (blue color). The scale bar represents 100 μ m (*left panels*). Box plot indicating the distribution of E-cadherin positive cell percentage measured in xenograft tumors treated as indicated in (b) *left panels*. Data are mean \pm SD of 3 different CRC sphere cell lines (CSC#1, 8, 25) (*right panel*). **c**, Representative flow cytometry analysis of cell cycle in CD44v6⁺ CR-CSCs (CSC#2) treated with vehicle or BMP7v for 72 hours. Plots show the percentage of cells in sub-G0 phase (red box), G0-G1 phase (light yellow box), S phase (pink box) and G2-M phase (brown box). **d** and **e**, Optical density ratio of PARP, c-PARP, Caspase-3 (Casp-3), cleaved Caspase-3 (cCasp-3), Bcl-2, Bcl-xL expression levels in CD44v6⁺ and CD44v6⁻ cells treated with vehicle or BMP7v for 72 hours. Data are mean \pm SD of 3 different CRC sphere cell lines (CSC#1, 4, 7).

Figure S4: BMP7v turns CD44v6⁺ into CD44v6⁻-like gene expression profile

a, Up- and **b** down-regulated genes and their relative involved gene sets, common in CD44v6⁻ cells and CD44v6⁺ cells treated with BMP7v, selected from Hallmark, KEGG and GO.

Figure S5: BMP7v potentiates the effects of chemotherapy and attenuates the activity of PI3K/AKT pathway in CR-CSCs

a, Tumor size of subcutaneous growth of CRC sphere cells treated for 4 weeks with vehicle or dose escalation of BMP7v. Arrows indicate the start and the end of treatment (from 6 to 9 weeks). Data represent mean \pm SD of tumor size of 6 tumors per group using 3 different sphere cell lines (CSC#2, 7, 18). **b**, Relative band densities of PI3K, pAKT, AKT, PTEN, pJNK, JNK, pERK, ERK and p21 in CD44v6⁺ (*left panel*) and CD44v6⁻ (*right panel*) cells treated with vehicle or BMP7v for 72 hours. Data are expressed as mean \pm SD of 3 independent experiments using different CRC sphere cell lines (CSC#1, 4, 7). **c**, Zip synergy score evaluation of BMP7v treatment alone or in combination with PI3K inhibitor (taselisib) in CR-CSCs for 24 hours at the indicated doses. Red area indicates doses of BMP7v and tasiselisib with synergistic effect. Dotted line indicates the highest synergistic area. One representative experiment of CSC# 3, 7, 9, 21 is shown.

Supplementary Table 1: Clinical data of CRC patients from which CRC sphere cell lines were derived.

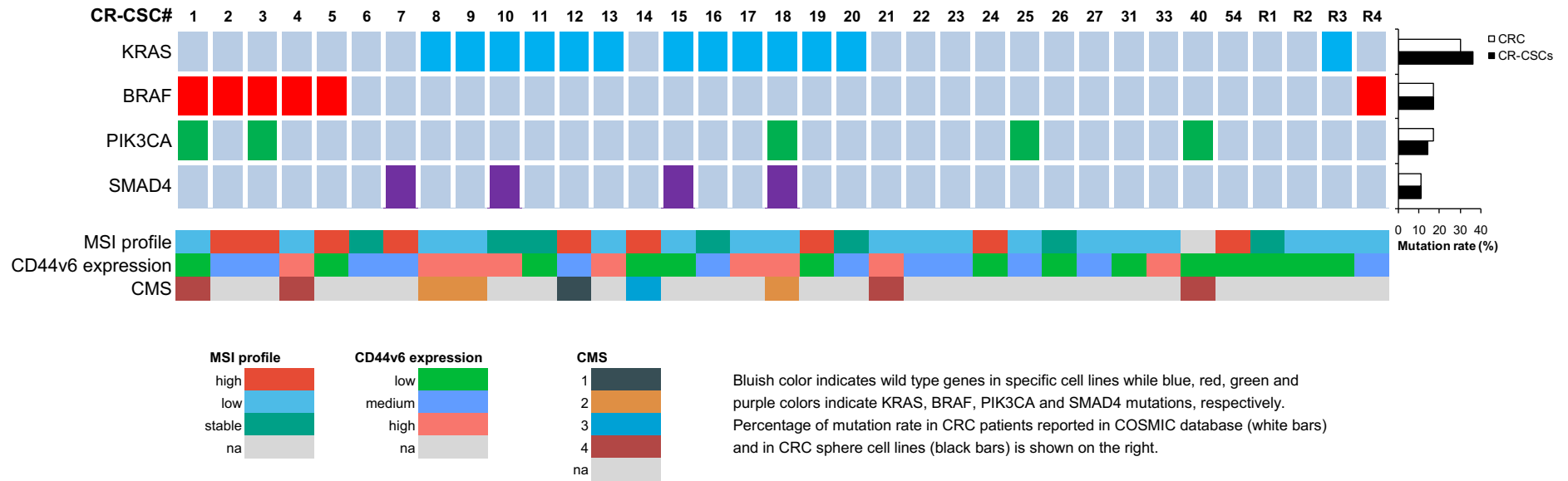
Supplementary Table 2: COSMIC-reported mutations of the indicated genes and MSI profile, CD44v6 expression, CMS in CR-CSC lines

Bluish color indicates wild type genes in specific cell lines while blue, red, green and purple colors indicate KRAS, BRAF, PIK3CA and SMAD4 mutations, respectively. Percentage of mutation rate in CRC patients reported in COSMIC database (white bars) and in CRC sphere cell lines (black bars) is shown on the right.

Supplementary Table 1: Clinical data of CRC patients from which CRC sphere cell lines were derived.

CR-CSC#	Age/Gender	Site	Grade	TNM classification	Stage	Ethnicity
1	68/M	sigma	G3	T2N1M0	IIIA	Caucasian
2	41/M	left	G3	T3N0M0	IIA	Caucasian
3	85/F	right-ileum	G3	T3N2M0	IIIC	Caucasian
4	59/F	right	G2	T3N0M0	IIA	Caucasian
5	68/M	right	G3	T4N1M0	IIIB	Caucasian
6	76/M	right	G2	T2N1M0	IIIA	Caucasian
7	62/M	right	G2	T3N1M0	IIIB	Caucasian
8	57/F	caecum	G3	T3N2M1	IV	Caucasian
9	53/F	recto-sigmoid	G2	T3N2M1	IV	Caucasian
10	69/M	left	G3	T4N3M1	IV	Caucasian
11	77/F	right	G2	T3N1M0	IIIB	Caucasian
12	76/M	right	G2	T3N2M0	IIIC	Caucasian
13	63/M	right	G3	T4N2M0	IIIC	Caucasian
14	47/F	right	G2	T3N0M0	IIA	Caucasian
15	69/M	left	G2	T3N1M1	IV	Caucasian
16	79/F	right	G2	T3N0M0	IIA	Caucasian
17	75/M	left	G2	T2N0M0	I	Caucasian
18	57/F	left	G3	T3N2M1	IV	Caucasian
19	63/F	sigma	G2	T4N2M1	IV	Caucasian
20	68/M	right	G2	T3N1M0	IIIB	Caucasian
21	60/F	right	G2	T3N1MX	IIIB	Caucasian
22	71/F	transverse	G2	T3N0M0	IIA	Caucasian
23	78/M	transverse	G2	T3N0M0	IIA	Caucasian
24	51/F	right	G2	T3N0M0	IIA	Caucasian
25	60/M	left	G2	T3N2M0	IIIC	Caucasian
26	58/F	recto-sigmoid	G2	T2N0MX	I	Caucasian
27	60/M	left	G3	T3N2M0	IIIC	Caucasian
31	67/M	right	G2	T3N1M0	IIIB	Caucasian
33	58/M	right	G2	T2N0M0	I	Caucasian
40	49/M	recto-sigmoid	G2	T2N1M0	IIIA	Caucasian
54	66/F	recto-sigmoid	G2	T2N1M0	IIIA	Caucasian
R1	65/M	liver metastasis	n.d.	T3N0M0	IIA	Caucasian
R2	61/F	liver metastasis	n.d.	T3N1M1	IV	Caucasian
R3	62/F	liver metastasis	n.d.	T3N1M0	IIIB	Caucasian
R4	38/M	liver metastasis	n.d.	T4N1M1	IV	Caucasian

Supplementary Table 2: COSMIC-reported mutations of *the indicated genes* and MSI profile, CD44v6 expression, CMS in CRC sphere cell lines.



Chapter 2

PI3K-driven HER2 expression is a potential therapeutic target in colorectal cancer stem cells

Laura Rosa Mangiapane, Annalisa Nicotra, Alice Turdo, Miriam Gaggianesi, Paola Bianca, Simone Di Franco, Davide Stefano Sardina, Veronica Veschi, Michele Signore, Sven Beyes, Luca Fagnocchi, Micol Eleonora Fiori, Maria Rita Bongiorno, Melania Lo Iacono, Irene Pillitteri, Gloria Ganduscio, Gaspare Gulotta, Jan Paul Medema, Alessio Zippo, Matilde Todaro, Ruggero De Maria, Giorgio Stassi

Published in *Gut*, 2021



OPEN ACCESS

Original research

PI3K-driven HER2 expression is a potential therapeutic target in colorectal cancer stem cells

Laura Rosa Mangiapane,¹ Annalisa Nicotra,¹ Alice Turdo ,² Miriam Gaggianesi,¹ Paola Bianca,¹ Simone Di Franco,¹ Davide Stefano Sardina,¹ Veronica Veschi,¹ Michele Signore ,³ Sven Beyes,⁴ Luca Fagnocchi ,⁴ Micol Eleonora Fiori ,⁵ Maria Rita Bongiorno,² Melania Lo Iacono,¹ Irene Pillitteri,¹ Gloria Ganduscio,¹ Gaspare Gulotta,¹ Jan Paul Medema,^{6,7} Alessio Zippo,⁴ Matilde Todaro,² Ruggero De Maria,^{8,9} Giorgio Stassi ¹

► Additional material is published online only. To view, please visit the journal online (<http://dx.doi.org/10.1136/gutjnl-2020-323553>).

For numbered affiliations see end of article.

Correspondence to

Professor Giorgio Stassi, Department of Surgical, Oncological and Stomatological Sciences, Università degli Studi di Palermo, Palermo, Italy; giorgio.stassi@unipa.it and Professor Ruggero De Maria, Institute of General Pathology, Università Cattolica del Sacro Cuore, Rome, Italy; ruggero.demaria@unicatt.it

LRM and AN contributed equally.

Received 8 November 2020

Revised 15 December 2020

Accepted 18 December 2020



© Author(s) (or their employer(s)) 2021. Re-use permitted under CC BY. Published by BMJ.

To cite: Mangiapane LR, Nicotra A, Turdo A, et al. *Gut* Epub ahead of print: [please include Day Month Year]. doi:10.1136/gutjnl-2020-323553

ABSTRACT

Objective Cancer stem cells are responsible for tumour spreading and relapse. Human epidermal growth factor receptor 2 (HER2) expression is a negative prognostic factor in colorectal cancer (CRC) and a potential target in tumours carrying the gene amplification. Our aim was to define the expression of HER2 in colorectal cancer stem cells (CR-CSCs) and its possible role as therapeutic target in CRC resistant to anti-epidermal growth factor receptor (EGFR) therapy.

Design A collection of primary sphere cell cultures obtained from 60 CRC specimens was used to generate CR-CSC mouse avatars to preclinically validate therapeutic options. We also made use of the ChIP-seq analysis for transcriptional evaluation of HER2 activation and global RNA-seq to identify the mechanisms underlying therapy resistance.

Results Here we show that in CD44v6-positive CR-CSCs, high HER2 expression levels are associated with an activation of the phosphatidylinositol 3-kinase (PI3K)/AKT pathway, which promotes the acetylation at the regulatory elements of the *ErbB2* gene. HER2 targeting in combination with phosphatidylinositol 3-kinase (PI3K) and mitogen-activated protein kinase kinase (MEK) inhibitors induces CR-CSC death and regression of tumour xenografts, including those carrying *Kras* and *Pik3ca* mutation. Requirement for the triple targeting is due to the presence of cancer-associated fibroblasts, which release cytokines able to confer CR-CSC resistance to PI3K/AKT inhibitors. In contrast, targeting of PI3K/AKT as monotherapy is sufficient to kill liver-disseminating CR-CSCs in a model of adjuvant therapy.

Conclusions While PI3K targeting kills liver-colonising CR-CSCs, the concomitant inhibition of PI3K, HER2 and MEK is required to induce regression of tumours resistant to anti-EGFR therapies. These data may provide a rationale for designing clinical trials in the adjuvant and metastatic setting.

INTRODUCTION

Despite major advances in terms of prevention and treatment, colorectal cancer (CRC) is one of the major causes of cancer-related death worldwide.¹ Diagnosis at stage IV and tumour progression after

surgery are very often lethal and require a substantial improvement of current therapeutic regimens. Over the past decade, the scientific community focused on different mechanisms found to be responsible for the development of therapy resistance, such as genetic heterogeneity and activation of alternative survival pathways.² Despite the availability of a large repertoire of new targeted therapeutics, there are not many options to treat patients with chemoresistant tumours, particularly if associated with activation of the signal pathway of rat sarcoma (RAS) or epidermal growth factor receptor (EGFR) resistance.

The expansion of resistant subclones due to tumour heterogeneity is now regarded as the major clinical hurdle in patient management.³ About 36%–40% of patients with CRC are characterised by *Kras*-activating mutation at codons 12, 13 and 61, while 8%–15% present mutations in the *Braf* gene. In advanced stages, the presence of either *Braf* or *Ras* mutations correlates with a particularly poor prognosis.⁴ Several studies have shown the predictive and prognostic roles of different gene mutations belonging to mitogen-activated protein kinase (MAPK) and phosphatidylinositol 3-kinase (PI3K)/AKT pathways, such as *Ras*, *Braf*, *Pik3ca* and *PTEN*.^{5,6} EGFRs are the most important actionable targets identified so far in CRC. Although the addition of EGFR-targeting antibodies to chemotherapy is the most effective current therapy for *Ras* wild-type (wt) metastatic CRC, the therapeutic response is temporary and restricted to a limited number of patients due to primary or acquired resistance.⁷ Repeated liquid biopsies accompanied by the analysis of tumour-associated genetic alterations would be needed to monitor the treatment responses and to adapt new targeted therapies.⁸ The heterogeneity in the clinical responses of these patients with *Kras*-wt CRC has pointed out the contribution of other genetic mutations or amplifications.⁹ For instance, beyond the *Ras* mutation, the activation of alternative or parallel downstream signalling inside or outside the MAPK pathways is involved in the anti-EGFR treatment inefficacy.^{7,10} Thus, simultaneous inhibition of the EGFR family members and alternative signalling pathways has been adopted to

Significance of this study

What is already known on this subject?

- ▶ Advanced colorectal cancer (CRC) remains essentially incurable, particularly in the presence of genomic alterations in the signalling pathway of rat sarcoma (RAS).
- ▶ Human epidermal growth factor receptor 2 (HER2) expression seems to correlate with the stage of disease and reduced survival in CRC.
- ▶ Targeting *ErbB2* amplification has a significant therapeutic activity in patients with CRC.
- ▶ The phosphatidylinositol 3-kinase (PI3K)/AKT pathway is constitutively activated in colorectal cancer stem cells (CR-CSCs) and sustains the expression of CD44v6, which drives the metastatic dissemination.

What are the new findings?

- ▶ The constitutive activation of PI3K/AKT is associated with high expression levels of HER2 in CD44v6-positive CR-CSCs.
- ▶ HER2, in combination with PI3K and mitogen-activated protein kinase kinase (MEK) inhibitors, leads to cancer stem cell death and tumour regression in CRC avatars resistant to anti-epidermal growth factor receptor (EGFR) therapy and to combinations of PI3K, BRAF and HER2 targeting.
- ▶ Liver disseminated CR-CSCs can be effectively killed by PI3K/AKT inhibitors in an experimental model of adjuvant therapy.
- ▶ Cytokines released by cancer-associated fibroblasts, particularly hepatocyte growth factor (HGF), stromal cell-derived factor-1 (SDF-1) and osteopontin (OPN), confer resistance to the targeting of the PI3K/AKT pathway and surrogate the protective effect of tumour microenvironment.

How might it impact on clinical practice in the foreseeable future?

- ▶ PI3K/AKT inhibitors could be effective in the adjuvant setting for CRC.
- ▶ Targeting HER2, MEK and PI3K may provide a valuable therapeutic strategy against anti-EGFR-resistant advanced CRCs.

overcome EGFR therapy resistance determined by the amplification of receptor tyrosine kinases.^{11 12} In contrast to melanoma, CRCs harbouring *Braf* mutations are refractory to BRAF inhibitors, such as vemurafenib.¹³ CRC resistance to BRAF inhibitors remains a major obstacle in clinical settings.¹⁴ This unresponsiveness is sustained by the activation of a feedback loop involving EGFR and downstream pathways.¹⁵ Although a recent phase II clinical study showed that addition of vemurafenib and cetuximab to chemotherapy prolonged the progression-free survival of metastatic patients with *Braf*-mutated tumours by 2.4 months, the prognosis of these patients remains poor.¹⁶ Moreover, another recent study reported that the combined BRAF, EGFR and mitogen-activated protein kinase kinase (MEK) inhibition in patients with *Braf*^{V600E}-mutant CRC could increase survival, even if patients experienced primary and acquired resistance due to a positive feedback regulation of MAPK pathway in tumour cells.¹⁷

Given that *Kras*-mutant CRCs display different resistance mechanisms to EGFR and MAPK inhibitors, many alternative strategies are currently under investigation.¹⁸ In addition to acquired genetic mutations, the activation of a positive human epidermal growth factor receptor 2 (HER2) and HER3 feedback loop seems to be one example of antitumour therapy escape.^{19 20} Accordingly, the combined treatment with MEK and

EGFR/HER2 dual inhibitors has shown a synergistic activity in preclinical models based on CRC cell lines bearing *Kras* mutation.²¹ The investigation on EGFR family members in CRC has been recently focused on HER2. *ErbB2* amplification occurs in approximately 3%–10% of patients with CRC and may promote resistance to EGFR inhibitors.^{22 23} Moreover, HER2 expression appears as a negative prognostic factor that correlates with the stage and survival in patients with CRC.²⁴ This hypothesis has been recently validated by the clinical trial Heracles, which showed that the combination of trastuzumab and lapatinib in *ErbB2*-amplified patients with CRC can induce the regression of tumours resistant to anti-EGFR therapies.²⁵ Constitutive expression of HER2 can be also driven by the degree of its enhancer and promoter activities.²⁶

Myc overexpression may contribute to promote therapy resistance in *Kras*-mutant CRCs.²⁷ While the MAPK effector promotes Myc stabilisation, its proteosomal degradation is mediated by GSK3 β .^{28 29} The role of Myc in the tumorigenesis programme is mediated by the upregulation of the miR-17–92 cluster, which is associated with a poor prognosis.³⁰

Colorectal cancer stem cells (CR-CSCs) are responsible for tumour development, spreading and resistance to chemotherapy.^{31 32} We have created a large collection of primary CRC cells growing as spheroids and able to reproduce the patients' tumour in mouse avatars. We have recently shown that CR-CSCs express CD44v6 and depend on the PI3K/AKT pathway for survival and spreading.^{31 33} Herein, we have studied the molecular pathways that should be targeted to kill CR-CSCs both in the adjuvant and metastatic settings. While targeting the PI3K/AKT pathway is sufficient to kill disseminating CR-CSCs, we found that HER2 is constitutively expressed in CR-CSCs and that the simultaneous targeting of HER2, PI3K and MEK neutralises the protective effect of tumour stroma and induces tumour regression, even in the presence of aggressive mutational backgrounds.

METHODS

A detailed description of the methods can be found in online supplemental information.

RESULTS**CD44V6-positive CRC cells express high levels of HER2 and are cetuximab resistant**

EGFR inhibitors promote an effective therapeutic response in about 50%–55% of the patients with *Ras/Braf*-wt CRC, whereas *Braf*- and *Kras*-mutant CRC cells are completely resistant.⁹ In accordance with clinical data, treatment with cetuximab affected the cell viability of about a half of the *Ras/Braf*-wt primary colorectal cancer sphere cells (CSphCs) and delayed the outgrowth of tumour xenografts (figure 1A, online supplemental figure 1A,B and online supplemental table 1).

Primary resistance to the EGFR blockade is mostly due to a constitutive activation of the RAS-MAPK signalling network.⁹ Accordingly, a global RNA-Seq transcriptome analysis of cetuximab-resistant versus sensitive *Ras/Braf*-wt CSphCs showed 252 differentially expressed genes (DEGs) (online supplemental figure 1C and online supplemental table 2). The gene set enrichment analysis (GSEA) computed with the Molecular Signatures Database displayed the enrichment of genes associated with activation of the MAPK-signalling pathway, including the negative feedback regulator DUSP4³⁴ (figure 1B and online supplemental

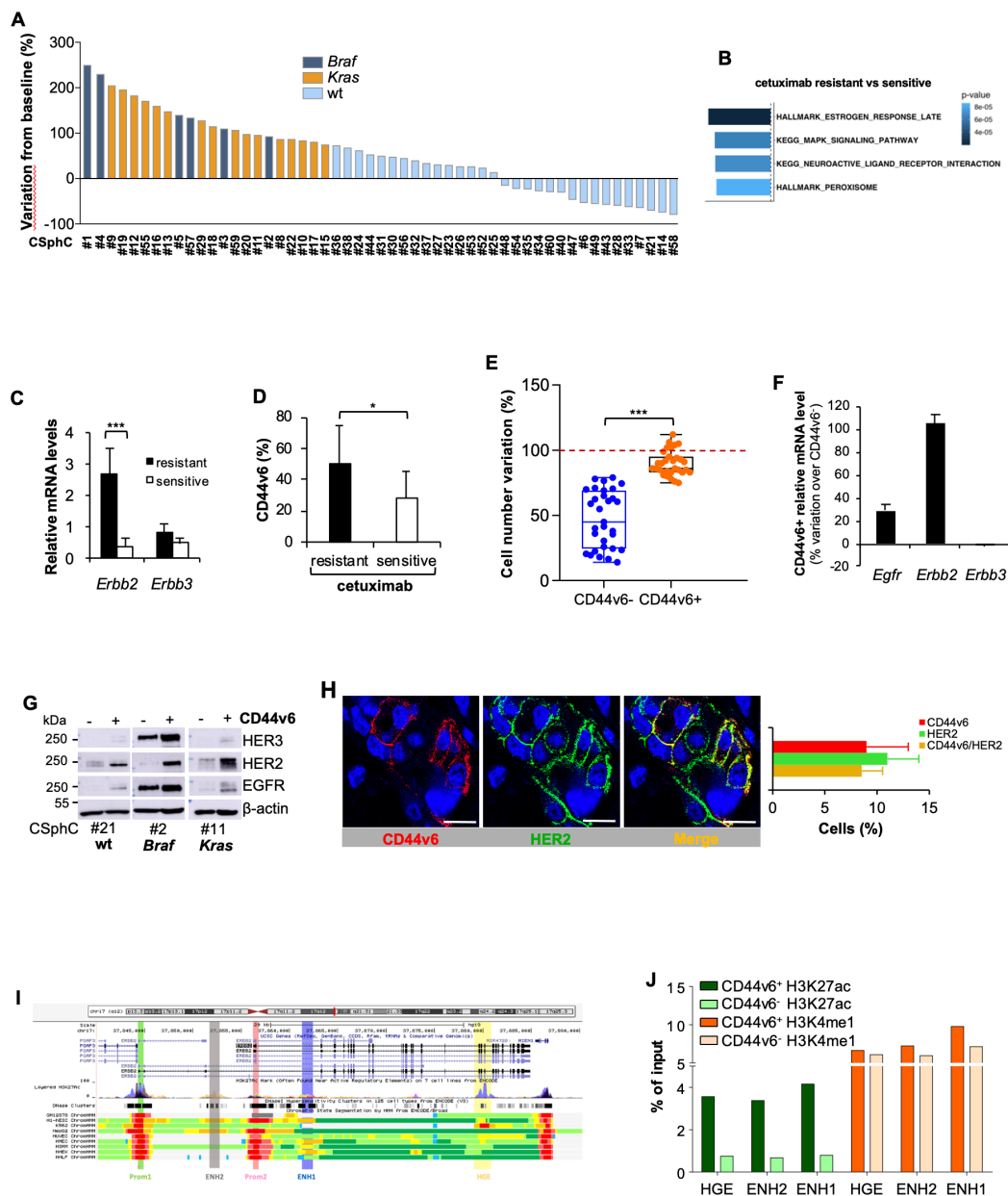


Figure 1 High expression of HER2 confers resistance to anti-epidermal growth factor receptor (EGFR) treatment in CD44v6-positive CR-CSCs. (A) Waterfall plot of cetuximab response in *Ras/Braf*-wt, *Braf*-mutant and *Kras*-mutant CSphC lines following 72 hours of treatment. (B) Top four significantly enriched gene sets in hallmark, canonical pathways MSigDB collections (false discovery rate (FDR) Q -value ≤ 0.05) identified through the analysis of differentially expressed genes between cetuximab resistant versus sensitive *Ras/Braf*-wt sphere cells. P values related to each enriched gene set are indicated. (C) *ErbB2* and *ErbB3* mRNA expression levels in *Ras/Braf*-wt sphere cells resistant and sensitive to cetuximab. *Gapdh* amplification was used as endogenous control. Data are represented as \pm SD of three experiments performed with 31 *Ras/Braf*-wt. (D) CD44v6 expression performed in cells as in (C). (E) Viable cell number variation in enriched CD44v6⁺ and CD44v6⁻ CD44v6-positive *Ras/Braf*-wt treated with cetuximab for 72 hours and normalised with the values of cells treated with vehicle (indicated as 100%, red dotted line). Boxes and whiskers represent mean \pm SD of six experiments performed with 15 resistant and 16 sensitive *Ras/Braf*-wt sphere cells. (F) Variation of *Egfr*, *ErbB2* and *ErbB3* mRNA expression levels in CD44v6-positive versus CD44v6⁻ cells. *Gapdh* amplification was used as endogenous control. Data are represented as mean \pm SD of nine experiments performed with three *Ras/Braf*-wt (CSphC#14, 21 and 33), three *Braf*-mutants (CSphC#1, 2 and 5) and three *Kras*-mutants (CSphC#10, 11 and 16). (G) Immunoblot analysis of HER3, HER2 and EGFR on purified CD44v6⁻ and CD44v6-positive *Ras/Braf*-wt (CSphC#21), *Braf*-mutant (CSphC#2) and *Kras*-mutant (CSphC#11) CR-CSPHC populations. β -Actin was used as loading control. (H, left panel) Representative immunofluorescence analysis of CD44v6 and HER2 on paraffin embedded sections from human CRC tissue specimen. Nuclei were counterstained with TOTO-3. Scale bars, 20 μ m. Percentages of CD44v6, HER2 and CD44v6/HER2 positivity in eight human CRC tissues are shown on the right panel. Data are mean \pm SD of eight different samples. (I) Browser view of the *ErbB2* locus, showing different isoforms of *ErbB2* and chromatin states (ChromHMM tracks). Two promoters and three potential enhancers are highlighted (Prom1, Prom2, ENH1, ENH2 and HGE). (J) ChIP-qPCR for the histone marks H3K27ac and H3K4me1 at the indicated enhancer regions (ENH1, ENH2 and HGE) in *Braf*-mutant cells positive or negative for CD44v6. Enrichment is indicated as % relative to the input. CR-CSC, colorectal cancer stem cell; CSphC, colorectal cancer sphere cell; ENH1, intron 1 enhancer; ENH2, intron 2 enhancer; HER2, human epidermal growth factor receptor 2; HGE, *HER2* gene body enhancer; MSigDB, Molecular Signatures Database; wt, wild type. * indicates $P < 0.05$ and *** indicates $P < 0.001$.

figure 1D). Besides the activation of signalling pathway of MAPK, *Ras/Braf*-wt CSphCs resistant to cetuximab showed higher mRNA expression levels of *ErbB2* compared with those sensitive (figure 1C). In line with literature,²³ our CSphC collection showed a 9.7% of *ErbB2* amplification (online supplemental table 1). We previously reported that while CD44v6 is a functional marker that identifies tumour-initiating CR-CSCs, the CD44v6-negative population represents the progenitor and differentiated fraction.^{31,33} A cohort of 31 out of 47 primary CSphC lines showed that the high percentage of CD44v6 expression levels resided in the *Ras/Braf*-wt cells resistant to cetuximab, even though these expression levels are similarly distributed between *Ras/Braf*-wt, *Braf*-mutated and *Kras*-mutated cell lines (figure 1D and online supplemental figure 1E). Because the CD44v6-positive population, within the *Ras/Braf*-wt cells, is resistant and increases after treatment with cetuximab (figure 1E and online supplemental figure 1F), we investigated whether the expression in signalling pathways associated with drug resistance may differ between the stem and differentiated cell compartments. Reverse phosphoproteomic analysis (RPPA) of CSphCs showed that, while MAPK pathways and HER2 are highly regulated, EGFR and HER3 are expressed in a lesser extent in the CD44v6-positive than in the CD44v6⁻ fraction (online supplemental figure 1G). The analysis at mRNA and protein levels confirmed an increased HER2 expression in the tumorigenic CD44v6-positive population of CRC cells, independently of the mutational background (figure 1F,G and online supplemental figure 1H,I). Accordingly, immunofluorescence analysis of patient tumour sections and tumour spheres indicated that the majority of CD44v6-positive cells coexpressed HER2 (figure 1H and online supplemental figure 1J).

We next investigated the transcriptional regulation of *ErbB2* expression in CD44v6-positive fraction by evaluating its 3' regulatory elements. Interestingly, H3K27 acetylation (H3K27ac) was enriched at the analysed regions of *HER2* gene body enhancer (HGE), intron 1 enhancer (ENH1) and intron 2 enhancer in CD44v6-positive compartment, whereas H3K4me1 enrichment was equally found in both CD44v6⁻ and CD44v6-positive cell fractions at all three enhancer regions (figure 1I,J and online supplemental figure 1K). These data indicate that the enhancers are poised in both cellular fractions but only fully activated in the CD44v6-positive compartment, suggesting that the activation of *ErbB2* transcription mediated by the increased acetylation is restricted to the CD44v6-positive CRC cell compartment.

PI3K/AKT pathway activation is associated with the transcriptional regulation of *ErbB2* in CD44v6-positive cells

The transcriptomic analysis of CD44v6^{high} versus CD44v6^{low} cells highlighted the presence of 173 DEGs (online supplemental figure 2A and online supplemental table 3). In CD44v6^{high} cells, the GSEA enriched for genes related to the activation of PI3K/AKT signalling pathway, such as NOS3³⁵ (figure 2A and online supplemental figure 2B). To investigate the role of PI3K in the transcriptional regulation of *ErbB2*, we induced an activating *Pik3ca* mutation into *Pik3ca*-wt low expressing HER2 CSphC lines by using CRISPR nuclease in combination with a specific donor DNA that introduced the *E545K* point mutation (online supplemental figure 2C and online supplemental table 1). The presence of a *Pik3ca*^{E545K} is associated with an increased expression of HER2 and phospho-AKT (figure 2B,C and online supplemental figure 2D). Interestingly, immunofluorescence analysis of primary tumour sections indicated that HER2-positive

cells were mainly prominent in the tumour invasion front and displayed activation of the PI3K/AKT pathway (figure 2D). The essential role of PI3K in the transcriptional regulation of *ErbB2* was further supported by ChIP-qPCR analysis showing that overexpression of the mostly represented *Pik3ca* activating mutation in breast cancer, the *Pik3ca*^{H1047R}, in mammary IMEC-MYC cells enhances the transcriptional activity of both *ErbB2* promoters (prom 1 and prom 2) and ENH1 and HGE (online supplemental figure 2E). Since the inhibition of the PI3K/AKT pathway hampers the cell viability of CD44v6-positive cells,³³ we evaluated whether the addition of a PI3K inhibitor to the combination therapy could affect the viability of both CD44v6-positive and CD44v6⁻ cells. To confirm the dependence of CR-CSCs on the PI3K activity, we tested an AKT (miransertib) and two PI3K (BKM120 and tasisib) inhibitors on several primary CSphC lines. Both miransertib and PI3K inhibitors reduced considerably the viability of CD44v6-positive cells in vitro regardless of the mutational background (online supplemental figure 2F–H), confirming that the PI3K/AKT pathway plays a key role on CR-CSC survival.

We previously showed that CRC development is sustained by cancer stem cells (CSCs), whose dissemination is responsible for CRC metastasis,³³ suggesting that targeting disseminated CR-CSCs may prevent tumour relapse and increase survival of patients with CRC.³¹ Thus, we investigated the ability of PI3K inhibitors to target disseminated sphere cells in the liver before they were able to make metastases in a model of adjuvant treatment. We found that the administration of tasisib in immunocompromised mice was able to prevent the formation of liver metastases after dissemination of CSphCs by spleen injection (figure 2E). These findings support the investigation of PI3K/AKT inhibitors in clinical trials aiming at killing disseminated metastasis-initiating CR-CSCs. The different survival properties of CD44v6 cells in vitro and in established tumours are likely due to the protective activity of the tumour microenvironment.³¹ Outside the protective tumour context, PI3K and AKT inhibitors can kill CR-CSCs. In contrast, the protective activity of cells and cytokines present in the tumour microenvironment may require the targeting of multiple pathways to overcome the enhanced survival of CR-CSCs. This hypothesis is supported by the significant therapeutic activity of PI3K inhibitors on micrometastases and small tumour lesions.³⁶ In order to identify some possible soluble mediators of such protective activity, we then measured the release of cytokines from cancer-associated fibroblasts (CAFs). Among the cytokines more abundantly produced by CAFs, we selected HGF, SDF-1 and OPN (figure 2F) to further investigation, based on their ability to support PI3K/AKT activity and stemness properties in CSphCs.³³ We next investigated whether the presence of CAFs would influence the survival of CSphCs exposed to the PI3K inhibitor. The coculture of GFP-labelled tumour spheres with CAFs protected cells from tasisib treatment (figure 2G), suggesting that CAFs could play a critical role in opposition to the killing activity of PI3K inhibitors in CRC. Moreover, neutralisation of HGF, SDF-1 and OPN completely prevented the protective activity of CAFs (figure 2H), indicating that these cytokines are responsible for delivering a survival signal in CR-CSCs that makes ineffective the PI3K targeting. Exposure of CSphCs, CD44v6-positive and CD44v6⁻ cell fractions to CAF-released cytokines enhanced the expression of *ErbB2* mRNA (figure 2I and online supplemental figure 2I). Interestingly, in the presence of tumour microenvironmental cytokines, *ErbB2* expression levels were not affected by the treatment with the PI3K inhibitor (online supplemental figure 2J–L). We also observed that HGF plays a major role in CAF-mediated protection of CSphCs treated with tasisib (figure 2J). Taken together, these data suggest that the tumour microenvironment protects CR-CSCs from the targeting of the PI3K/AKT pathway.

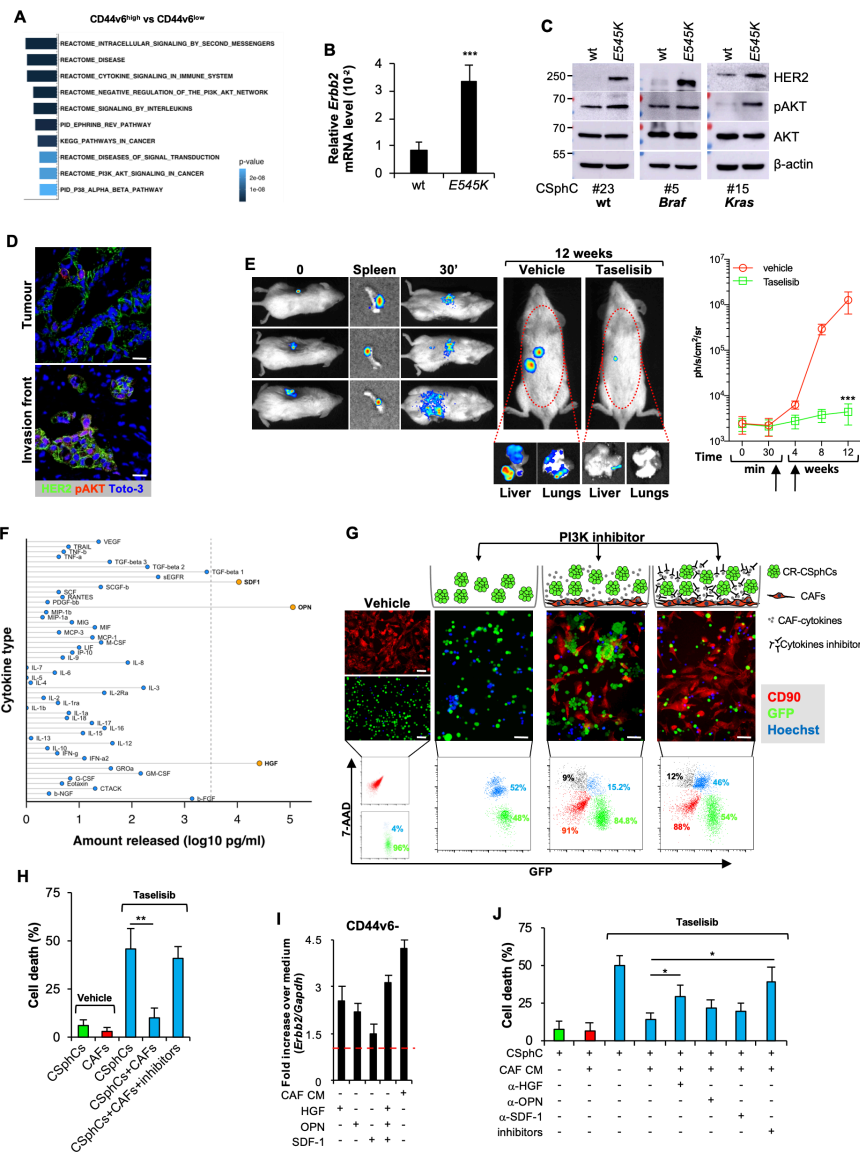


Figure 2 Activation of PI3K/AKT pathway is accompanied by elevated *ErbB2* expression levels in CD44v6-positive CRC cells. (A) Top 10 significantly enriched gene sets in hallmark, canonical pathways MSigDB collections (FDR Q-value \leq 0.05) computed by the analysis of differentially expressed genes between CD44v6^{high} and CD44v6^{low} cells. (B) mRNA relative levels of *ErbB2* in CSphCs and their corresponding CRISPR/Cas9-*Pik3ca*^{E545K} cells. Data are represented as mean \pm SD of six independent experiments performed with *Ras/Braf*-wt (CSphC#23), *Braf*-mutant (CSphC#5) and *Kras*-mutant (CSphC#15) cells and their corresponding CRISPR/Cas9-*Pik3ca*^{E545K} cells. (C) Immunoblot analysis of HER2, pAKT and AKT on *Ras/Braf*-wt (CSphC#23), *Braf*-mutant (CSphC#5) *Kras*-mutant (CSphC#15) cells. β -Actin was used as loading control. (D) Representative immunofluorescence analysis of HER2 and pAKT on paraffin-embedded sections from six human CRC tissue specimens. Nuclei were counterstained with TOTO-3. Scale bars, 20 μ m. (E, left panels) In vivo whole-body imaging analysis of mice at 0 and 30 min and 12 weeks injected with sphere cells into the spleen. Five days after cell injection, mice were treated daily with taselisib for 3 weeks. Signal within the red dotted area represents the bioluminescence quantification. Kinetics of metastasis formation at the indicated time points (right panels). Black arrows indicate the start and end of treatment (from day 6 to week 4). Data are mean \pm SD of four independent experiments of six mice per group using *Kras*-mutant (CSphC#8 and 11) sphere cell lines. (F) Lollipop plot representing the amount of cytokines released by immortalised CAFs. Data are mean of six independent experiments using cells purified from six different patients. (G) Cell death (blue colour) evaluated by immunofluorescence (upper panels) and flow cytometry (lower panels) in sphere cells (CSphC#8) transduced with GFP (green colour) cocultured with CAFs CD90 positive (red colour) and treated with a PI3K inhibitor (taselisib) for 72 hours in the presence or absence of hepatocyte growth factor (HGF), stromal cell-derived factor-1 (SDF-1) and osteopontin (OPN) blocking antibodies (inhibitors). Scale bars, 40 μ m. (H) Percentage of cell death in cells as in (G). Data are mean \pm SD of three independent experiments using *Ras/Braf*-wt (CSphC#14, 21 and 33), *Braf*-mutant (CSphC#1, 2 and 5) and *Kras*-mutant (CSphC#8, 10 and 11) sphere cell lines. (I) *ErbB2* mRNA expression levels in CD44v6⁻ enriched cells treated with CAF CM and the indicated cytokines. Data are mean \pm SD of three independent experiments performed with cells derived from *Ras/Braf*-wt (CSphC#14 and 33), *Braf*-mutant (CSphC#1 and 5) and *Kras*-mutant (CSphC#10 and 11) sphere cell lines. (J) Cell death in sphere cells exposed to CAF CM and treated with taselisib for 72 hours in the presence of cytokine neutralising antibodies as indicated. Data are mean \pm SD of three independent experiments performed with *Ras/Braf*-wt (CSphC#6, 14, 21 and 33), *Braf*-mutant (CSphC#1, 2, 4 and 5) and *Kras*-mutant (CSphC#8, 10, 11 and 17) sphere cell lines. CAF, cancer-associated fibroblast; CM, conditioned medium; CRC, colorectal cancer; CSphC, colorectal cancer sphere cell; HER2, human epidermal growth factor receptor 2; MSigDB, Molecular Signatures Database; wt, wild type. *indicates P<0.05, ** indicates P<0.01 and *** indicates P<0.001.

MEK sustains CR-CSCs resistance to the triple targeting of HER2, BRAF and PI3K

To further analyse the therapeutic potential of PI3K inhibitor in combination with MAPK pathway targeting, tumour xenografts, generated by the subcutaneous injection of CSphCs, were initially treated with either trastuzumab or cetuximab in combination with BRAF and PI3K inhibitors. These treatments were largely ineffective. We observed only a transient stabilisation of *Braf*-mutated tumours and a short delay in the disease progression of *Ras/Braf*-wt and *Kras*-mutated tumours (figure 3A and online supplemental figure 3A). These experiments allowed us to evaluate the potential mechanisms of acquired resistance to such triple combinations. CSphCs surviving the combinatorial treatment showed a significant phosphorylation of p235–236 S6 kinase (online supplemental figure 3B), which could follow the activation of RAS/ERK and mammalian target of rapamycin (mTOR) and result in the engagement of the Myc pathway.^{37,38} The activation of PI3K/AKT and MAPK pathways were confirmed by western blot in tumour specimen-derived subcutaneous xenograft treated with the triple combination (figure 3B and online supplemental figure 3C). This phenomenon was paralleled by a strong activation of the PI3K/AKT and MAPK pathways, particularly in the presence of *Braf* or *Kras* mutations (figure 3B). Moreover, cells surviving the combinatorial treatment showed high expression levels of the miR-17–92 cluster (online supplemental figure 3D), whose upregulation is associated with Myc expression.³⁹ Altogether, these findings indicate that PI3K and MEK promote CR-CSC resistance to the targeting of BRAF, HER2 and PI3K signalling pathways.

Replacement of BRAF targeting with a MEK inhibitor caused a marked reduction of the PI3K/AKT and MAPK pathway activation and a decrease of phosphorylation of S6 kinase (figure 3C and online supplemental figure 3E,F). Viability of CSphCs was severely affected by the use of trametinib combination regardless of the mutational status and remarkably diminished the Myc-regulated miRNAs in cells previously exposed to vemurafenib-based combination (online supplemental figure 3G,H).

We then investigated whether the MEK inhibitor-based combination is also able to overcome the protective effect mediated by the tumour microenvironment. Beside PI3K, CAF-released cytokines boosted MAPK pathway activation, which persisted after the treatment of CSphCs with vemurafenib-based combination therapy (figure 3D). Conversely, pharmacological targeting of MEK, instead of BRAF, promoted a considerable cell death, paralleled with a marked reduction of MEK/ERK, AKT activation and Myc expression in CSphCs, independently of the presence of *ErbB2* amplification and the exposure to CAF conditioned medium (figure 3D,E and online supplemental figure 3I). Of note, sphere cells able to survive to a prolonged exposure to the vemurafenib-based treatment remain sensitive to the triplet containing trametinib (online supplemental figure 3J). Altogether, these data suggest that the tumour microenvironment confers therapy resistance mediated by Myc through the activation of MAPK and PI3K–AKT pathways.

MEK inhibition-based therapy is synthetically lethal in CR-CSCs

In line with these results, we found that the replacement of vemurafenib with MEK inhibitors in the triple combination prevented the tumorigenic activity retained by sphere cells (figure 4A,B) and tumour progression when delivered in vivo, as indicated by the decrease in Ki67, CD44v6 and CK20 expression (figure 4C,D and online supplemental figure 4A–C). Of note, *Braf*-mutated or *Kras*-mutated xenograft tumours that recurred following the treatment with the vemurafenib-based triple combination, tumor xenografts resulted very sensitive to the trametinib-based combination therapy,

as shown by the massive tumour regression and lack of regrowth even 6 weeks after treatment suspension (figure 4E). Next, we examined whether this MEK-targeted triplet was effective on a large number of primary CSphC cultures of different mutational backgrounds and their corresponding tumour xenografts. To confirm the effectiveness of this treatment, we tested other MEK and PI3K inhibitors (cobimetinib and taselisib) in combination with trastuzumab. Importantly, tumour size generated by the subcutaneous injection of primary sphere cells was significantly hampered by the treatment with either trametinib in combination with trastuzumab and BKM120 or cobimetinib plus trastuzumab and taselisib, independently of the mutational status (figure 4A and online supplemental figure 4D,E). Of note, this latter combination remarkably reduced the CD44v6 expression level on xenograft-derived CRC cells (online supplemental figure 4F). Consistently, cobimetinib plus trastuzumab and taselisib induced the death of a conspicuous number of cells that were substituted by fibrosis, resulting in a considerable decrease in the amount of Ki67-positive and CK20-positive cells (online supplemental figure 4G). Thus, simultaneous MEK/HER2/PI3K inhibition exerted a potent antitumour activity in CRC xenografts regardless of the mutational status. Altogether these data demonstrate that the combination treatment with HER2, PI3K and MEK inhibitors is synthetically lethal for CRC cells (figure 4F).

DISCUSSION

The currently available targeted therapies for advanced CRC have a limited effect, particularly on the survival of patients carrying tumours with *Kras* mutation.⁵ We recently demonstrated that CD44v6-positive CR-CSCs are responsible for metastatic spreading and have a constitutive activation of the PI3K/AKT pathway that appears essential for their survival.³³ Here, we demonstrate that CR-CSCs express high levels of HER2, which are associated with a constitutive activation of the PI3K/AKT pathway. Inhibition of HER2, MEK and PI3K kills CR-CSCs and promotes a long-lasting regression of all the tumour xenografts tested, regardless of their mutational background.

Among the attempts to target the actionable mutations in CRC, the treatment with anti-HER2 in patients carrying *ErbB2* amplification has been successful in clinical trials, whereas patients with *Braf*^{V600E}-mutant CRC are poorly responsive to the administration of vemurafenib or dabrafenib.^{13,40}

Although the existence of synthetic lethality between BRAF and EGFR in *Braf*-mutated CRC cells would predict the potential therapeutic effect of a combined targeting, we found that CR-CSCs are resistant to the combination of anti-EGFR or anti-HER2 and BRAF inhibitors due to the constitutive activation of the PI3K/AKT pathway. This could be the reason why vemurafenib, in combination with irinotecan and cetuximab, showed a weak therapeutic effect in patients with metastatic CRC.⁴¹

Here, we found that the regulatory elements of *ErbB2* transcription are acetylated in CD44v6-positive cells. While this can explain why CR-CSCs are remarked by high HER2 expression, the potential ability of PI3K to promote a transcriptional activation of *ErbB2* corroborates the hypothesis that both of these oncogenic pathways should be targeted simultaneously. Since HER2 expression is lost on CR-CSC differentiation, it is likely that the specific expression of HER2 in the CD44v6-positive cell compartment results from the considerable reduction of the PI3K/AKT signalling pathway and β -catenin activity observed in their differentiated progeny.³³

Although sphere culture models mostly recapitulate the genetic landscape and the transcriptomic profile of parental tumour, representing valuable preliminary tools to identify potentially effective targeted therapies,^{42,43} it is fundamental to dissect the tumour

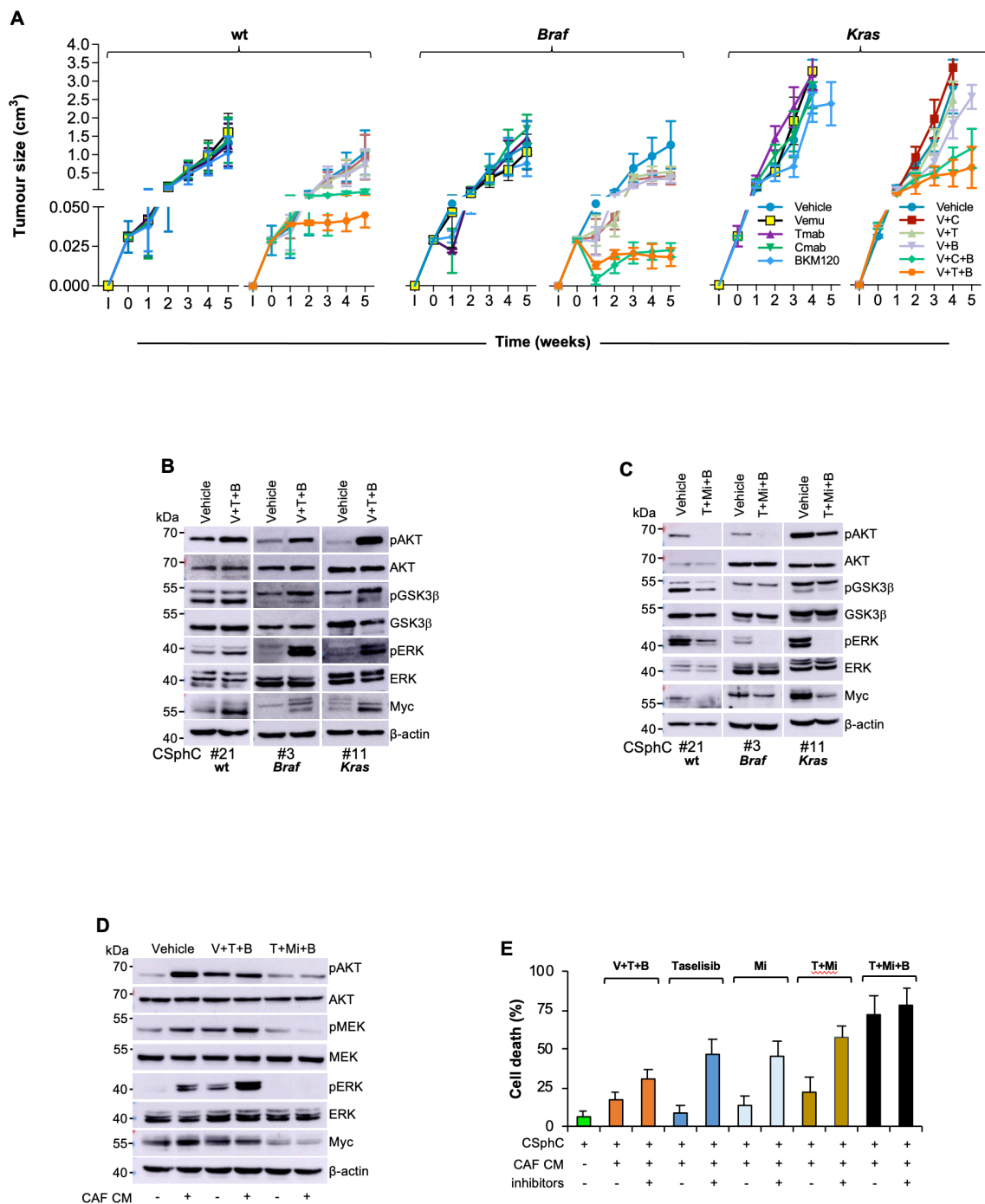


Figure 3 HER2/MEK/PI3K combinatorial targeting counteracts the protective effect of cytokines produced by CAF. (A) Size of xenograft tumours generated by subcutaneous injection of *Ras/Braf*-wt (CSphC#14, 21 and 33), *Braf*-mutant (CSphC#1, 2, 3 and 5) or *Kras*-mutant (CSphC#8, 11 and 16) sphere cells. Mice were treated for the first 4 weeks with vehicle (vehicle) or Vemu (or V), cetuximab (Cmab or C), Tmab (or T) and a PI3K inhibitor (B) alone or in combination as indicated. 'I' indicates the time of cell injection. Treatment was started at time 0. Data are mean values of six independent experiments ($n=6$ mice per group). (B) Immunoblot analysis of pAKT, AKT, pGSK3 β , GSK3 β , pERK, ERK and Myc on tumour xenograft-derived cells of mice injected with *RasBraf/Braf*-wt (CSphC#21), *Braf*-mutant (CSphC#3), *Kras*-mutant (CSphC#11) sphere cells. Mice were treated with vehicle or V in combination with T and B, and sacrificed 1 week after the treatment suspension (5 weeks). β -Actin was used as loading control. (C) Representative Western blot analysis of pAKT, AKT, pGSK3 β , GSK3 β , pERK, ERK and Myc in *Ras/Braf*-wt (CSphC#21), *Braf*-mutant (CSphC#3), *Kras*-mutant (CSphC#11) sphere cells treated for 24 hours with vehicle or T+Mi+B. β -Actin was used as loading control. (D) Immunoblot analysis of the indicated proteins in *Kras*-mutant (CSphC#9) sphere cells treated with vehicle or V in combination with T and B or T+Mi+B cultured in fetal bovine serum (FBS)-free Dulbecco's modified eagle medium (DMEM) or CAF CM for 24 hours. (E) Cell death percentage in CSphCs exposed to hepatocyte growth factor (HGF), stromal cell-derived factor-1 (SDF-1) and osteopontin (OPN) blocking antibodies (inhibitors) and treated as indicated for 72 hours. Data are mean \pm SD of three independent experiments performed with *Ras/Braf*-wt (CSphC#14, 21 and 33), *Braf*-mutant (CSphC#1, 2 and 5) and *Kras*-mutant (CSphC#8, 10 and 11) sphere cell lines. B, BKM120; CAF, cancer-associated fibroblast; CSphC, colorectal cancer sphere cell; T, trastuzumab; T+Mi+B, trastuzumab in combination with MEKi and BKM120; V, vemurafenib; V+T+B, vemurafenib in combination with trastuzumab and BKM120; wt, wild type; CM, conditioned medium.

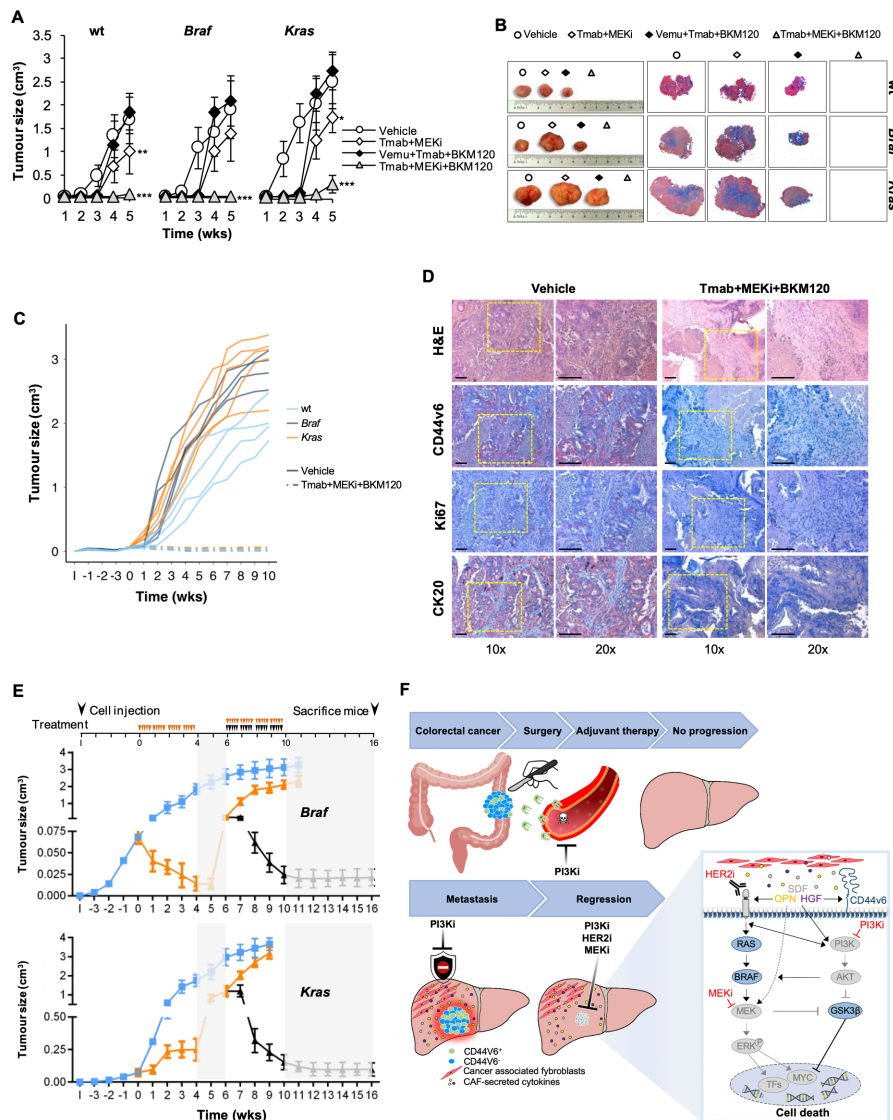


Figure 4 Therapeutic potential of HER2, PI3K and MEK targeting in CRC. (A) Size of tumours generated by subcutaneous injection of surviving *Ras/Braf*-wt (CSphC#14, 21 and 33), *Braf*-mutant (CSphC#1, 2 and 5) and *Kras*-mutant (CSphC#8, 11 and 16) sphere cells after 5 days of in vitro combination treatment as indicated. Data reported are mean \pm SD of tumour size for each cell lines ($n=6$ mice per group). (B) Representative macroscopic and Azan-Mallory analysis on tumour xenografts at 5 weeks treated as in (A). (C) Individual subcutaneous tumour volume plots of mice generated by the injection of four CSphC lines bearing the indicated different mutational background and treated for 4 weeks (0–4 weeks) with vehicle (vehicle) or Tmab plus MEKi plus BKM120. 'I' indicates the time of cell injection. Treatment was started at time 0. Data show kinetic growth of xenograft tumours generated by the injection of *Ras/Braf*-wt (CSphC#14, 21, 33 and 56), *Braf*-mutant (CSphC#1, 2, 3 and 5) and *Kras*-mutant (CSphC#8, 9, 11 and 16) CSphCs. (D) Representative H&E and immunohistochemical analysis of CD44v6, Ki67 and CK20 on tumour xenografts generated by the injection of *Kras*-mutant (CSphC#11) sphere cells treated as in (C) at the time of sacrifice (10 weeks). Scale bars, 200 μ m. (E) Tumour size of mice xenografted with *Braf*-mutant (CSphC#1–5) and *Kras*-mutant (CSphC#8, 9, 11, 13 and 16) mutant sphere cells. Mice were treated with vehicle (vehicle, blue lines) or sequential treatments. A combination of Vemu, Tmab, BKM120 (Vemu+Tmab+BKM120, orange line) was used as first line (0–4 weeks, orange arrowheads) and after 2 weeks off-treatments, Tmab in combination with MEKi and BKM120 (Tmab+MEKi+BKM120, black lines and arrowheads) or the same Vemu combination used in the first 4 weeks (orange arrowheads) was administered from weeks 6 to 10. Off-treatments are highlighted with grey regions. 'I' indicates the time of cell injection. Data are expressed as mean \pm SD of subcutaneously implanted CSphC lines for each mutational status ($n=6$ mice per group). (F) Scheme of the signalling axis illustrating the site of action of the triple combination therapy. Surgery is the main treatment for primary CRC followed by adjuvant therapy. PI3Ki has shown efficacy in targeting disseminating CRC cells, impeding tumour progression (upper panel). However, PI3Ki as single agents are unable to counteract the TME protective influence in metastatic lesions. Triple combination treatment (PI3Ki, HER2i and MEKi) induces tumour regression by overcoming CAF-secreted cytokine effect (lower left panel). In CD44v6-positive CR-CSCs characterised by high PI3K pathway activity, TME-derived cytokines upregulate HER2 and CD44v6 expression levels, activate mitogen-activated protein kinase (MAPK) pathway and increase Myc protein levels, jeopardising the potential therapeutic efficacy of PI3Ki. The additional targeting of HER2 and the Myc upstream kinase MEK achieves a synthetic lethal effect in CR-CSCs (lower right panel). HER2, BRAF, PI3K and MEK inhibitors are indicated as I. CAF, cancer-associated fibroblast; CRC, colorectal cancer; CR-CSC, colorectal cancer cancer stem cell; CSphC, colorectal cancer sphere cell; HER2, human epidermal growth factor receptor 2; MEKi, trametinib; PI3Ki, PI3K inhibitors; TF, transcriptional factor; Tmab, trastuzumab; TME, tumour microenvironment; Vemu, vemurafenib; wt, wild type. * indicates $P<0.05$, ** indicates $P<0.01$ and *** indicates $P<0.001$.

microenvironment contribution in mediating resistance of cancer cells to therapeutic drugs.

According to our previous observation, we found that tumour microenvironmental cytokines produced by CAFs contribute to recapitulate a protective effect against antitumour drugs expanding the CD44v6-positive compartment expressing HER2. We showed that HGF and to a lesser extent OPN and SDF-1 make CR-CSCs resistant to the targeting of the PI3K/AKT pathway, possibly explaining the disappointing results obtained in the clinical trials that evaluated the therapeutic effects of PI3K inhibitors in metastatic patients.⁴⁴ Such vulnerability of CR-CSCs in the absence of CAFs suggests that PI3K/AKT inhibitors can contribute to kill cells disseminated into the liver as part of adjuvant treatment due to the absence of a protective microenvironment. This hypothesis is strengthened by the observation that treatment with tasisib prevents the formation of liver metastases in mice receiving sphere cells by spleen injection.

In a subsequent set of experiments, we show that the addition of PI3K inhibitors to the combination of vemurafenib with trastuzumab or cetuximab induces a partial response of *Braf*-mutated tumours and a temporary stabilisation followed by a slower progression of *Ras/Braf*-wt and *Kras*-mutated tumours. Such transient therapeutic effect induces the rapid accumulation of tumour-initiating cells resistant to this triplet likely due to the presence of tumour microenvironmental cytokines.

The RPPA analysis in residual CSphCs spared by the HER2/BRAF/PI3K targeting allowed us to identify, through the regulation of S6 kinase phosphorylation, MEK and PI3K as major components of the resistance pathway. Accordingly, we observed increased levels of Myc in cells simultaneously exposed to agents targeting HER2, BRAF and PI3K. The concomitant activation of S6 kinase and MEK in sphere cells resistant to the vemurafenib-based triple combinations suggests that the failure to target both RAF and PI3K downstream pathways is responsible for maintaining activation of ERK and high Myc levels and promoting the pharmacological resistance of CR-CSCs to this triplet.

MEK is a key downstream element of the RAS-RAF pathway able to indirectly activate Myc.¹⁵ Replacement of vemurafenib with MEK inhibitors in the triple combination was able to significantly limit ERK activation and downregulate Myc expression while inducing a considerable therapeutic response in *Braf*-mutated and *Kras*-mutated tumours progressing after the vemurafenib-based combination. Of note, our data showed that MEK inhibition-based triplets were able to kill CR-CSCs in the presence of cytokines released by CAFs and to induce tumour regression in all CR-CSC-based xenografts tested, regardless of the mutational status and *ErbB2* amplification. Hence, HER2, PI3K and MEK appear as critical therapeutic targets in CR-CSCs, independently of the genomic abnormalities developed in patients' tumours. This combination appears the most active both in tumour xenografts and in the in vitro experiments designed in the presence of the CAF-released cytokines.

The advent of targeted therapies and the study of the associated resistance mechanisms revealed the presence of clonal heterogeneity in CRC.⁴⁵ Most of the current therapeutic strategies, including targeted combination treatments, affect differentiated cells and spare CSCs that eventually reinitiate tumour growth. It is therefore clear that the identification of the critical pathways responsible for the increase of survival and therapy resistance of CR-CSCs appears as a major priority to define possible effective treatments for patients with advanced CRC. This is particularly true for metastatic patients carrying oncogenic alterations in the RAS pathway, who have very limited therapeutic options. Our data show that MEK inhibition in association with PI3K and HER2 targeting can induce tumour regression even in tumours carrying mutations in the RAS pathway. Although targeted therapy is less toxic than standard chemotherapy,

EGFR inhibitors are commonly associated with adverse events, including the inhibition of the MEK/ERK signal pathway, which compromises the epidermis cell differentiation leading to skin lesions.⁴⁶ Given that HER2 inhibitors generally display minimal dermatological side effects as compared with those induced by EGFR inhibitors,²³ as shown by current clinical studies for the treatment of advanced CRC,²⁵ we foresee that triple targeting of HER2, MEK and PI3K may have a superior patient compliance and overall treatment outcome.

Here, we have shown that some biological features of CR-CSCs have the potential to be exploited in the clinics. The specific expression of HER2 in CR-CSCs, independently of gene amplification, suggests that HER2 should be regarded as key therapeutic target that deserves further preclinical and clinical investigations in CRC. The good therapeutic response, observed in clinical trial by HER2 targeting in patients with amplified tumours, increases the feasibility of this approach. Moreover, we provide evidence that targeting of the PI3K/AKT pathway could be exploited both in advanced disease and in the adjuvant setting. These findings may help define new therapeutic strategies based on CR-CSC targeting.

Author affiliations

¹Department of Surgical, Oncological and Stomatological Sciences, Università degli Studi di Palermo, Palermo, Italy

²Department of Health Promotion Sciences, Internal Medicine and Medical Specialties, Università degli Studi di Palermo, Palermo, Italy

³Core Facilities, Istituto Superiore di Sanità, Roma, Italy

⁴Department of Cellular, Computational, and Integrative Biology (CIBIO), University of Trento, Trento, Italy

⁵Department of Oncology and Molecular Medicine, Istituto Superiore di Sanità, Roma, Italy

⁶Laboratory for Experimental Oncology and Radiobiology, Center for Experimental and Molecular Medicine, University of Amsterdam, Amsterdam, Noord-Holland, The Netherlands

⁷Oncode Institute, University of Amsterdam, Amsterdam, Noord-Holland, The Netherlands

⁸Institute of General Pathology, Università Cattolica del Sacro Cuore Facoltà di Medicina e Chirurgia, Roma, Italy

⁹Policlinico A Gemelli, Roma, Lazio, Italy

Correction notice This article has been corrected since it published Online First. The funding statement has been amended.

Acknowledgements We thank Francesco Calò for graphic image editing and Alice Alferi for technical assistance. LRM is a student of the Molecular and Clinical Medicine PhD Program. AT and VV are research fellows funded by European Union-FESR FSE, PON Ricerca e Innovazione 2014–2020 (AIM line 1).

Contributors LRM, AN, RDM and GS conceived and designed the project. Experiments were conducted by LRM, AN, AT, MG, PB, SDF, VV, MS, SB, LF, MEF, MLI, IP, GGa and MT. Data provision and bioinformatic analysis were carried out by DSS, MS, SB, JPM and AZ. Pathology support, tissue provision and intellectual input were from MEF, MRB and GGu. RDM and GS wrote the manuscript.

Funding This work was supported by AIRC 5x1000 (9979) to GS and RDM, AIRC IG (22911) to AZ, RF2018-12367044 to MT and RDM, AIRC IG (21445) and PRIN (2017WINKSLR) to GS.

Competing interests None declared.

Patient consent for publication Not required.

Provenance and peer review Not commissioned; externally peer reviewed.

Data availability statement Data are available in a public, open access repository. All data relevant to the study are included in the article or uploaded as supplementary information. The data that support the findings of this study are available from the corresponding author (GS) upon reasonable request. RNA sequencing data of CR-CSPHs have been deposited in a public, open access GEO repository, under accession number GSE162104 (link to data: <https://www.ncbi.nlm.nih.gov/geo/query/acc.cgi?acc=GSE162104>).

Supplemental material This content has been supplied by the author(s). It has not been vetted by BMJ Publishing Group Limited (BMJ) and may not have been peer-reviewed. Any opinions or recommendations discussed are solely those of the author(s) and are not endorsed by BMJ. BMJ disclaims all liability and responsibility arising from any reliance placed on the content. Where the content includes any translated material, BMJ does not warrant the accuracy and reliability

of the translations (including but not limited to local regulations, clinical guidelines, terminology, drug names and drug dosages), and is not responsible for any error and/or omissions arising from translation and adaptation or otherwise.

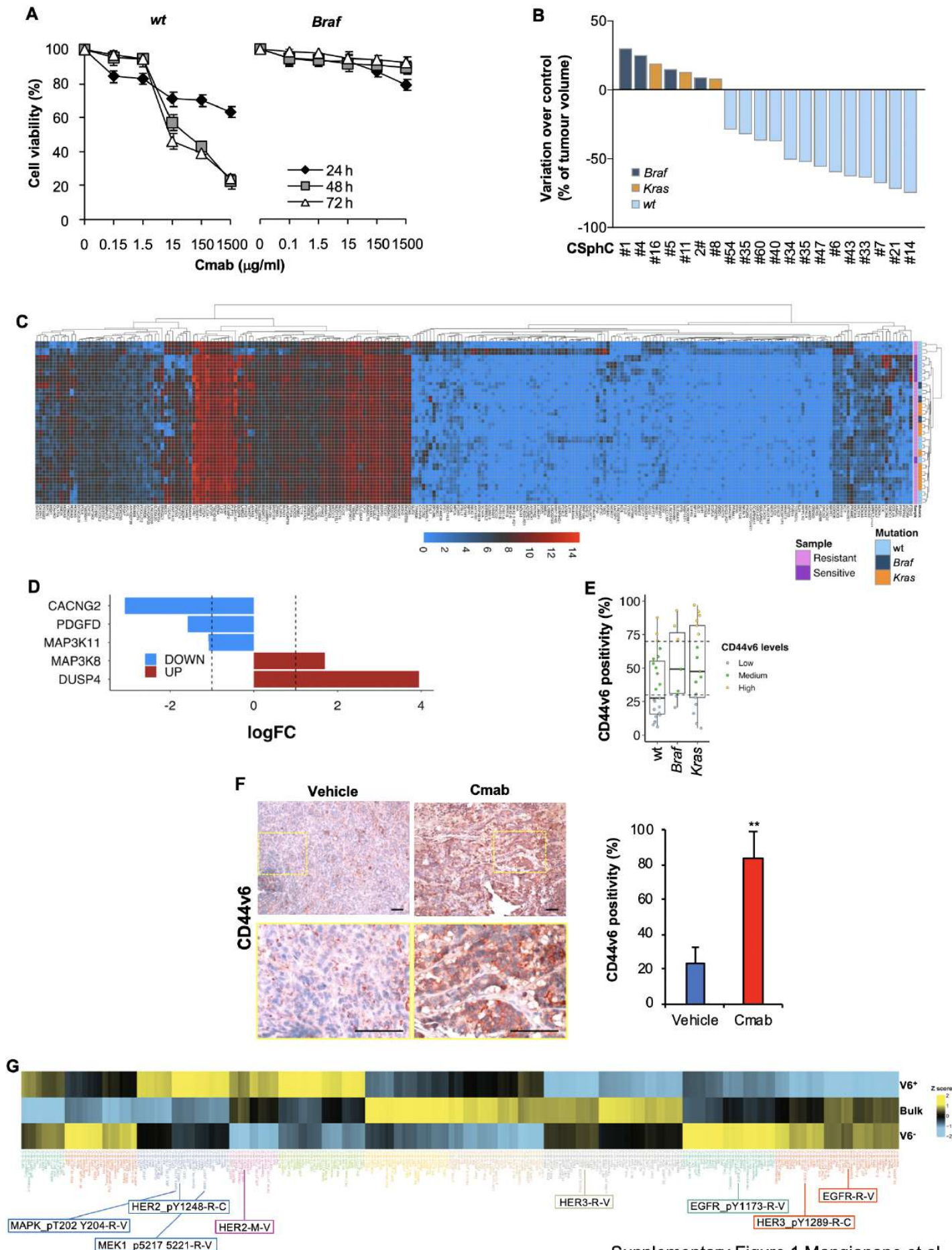
Open access This is an open access article distributed in accordance with the Creative Commons Attribution 4.0 Unported (CC BY 4.0) license, which permits others to copy, redistribute, remix, transform and build upon this work for any purpose, provided the original work is properly cited, a link to the licence is given, and indication of whether changes were made. See: <https://creativecommons.org/licenses/by/4.0/>.

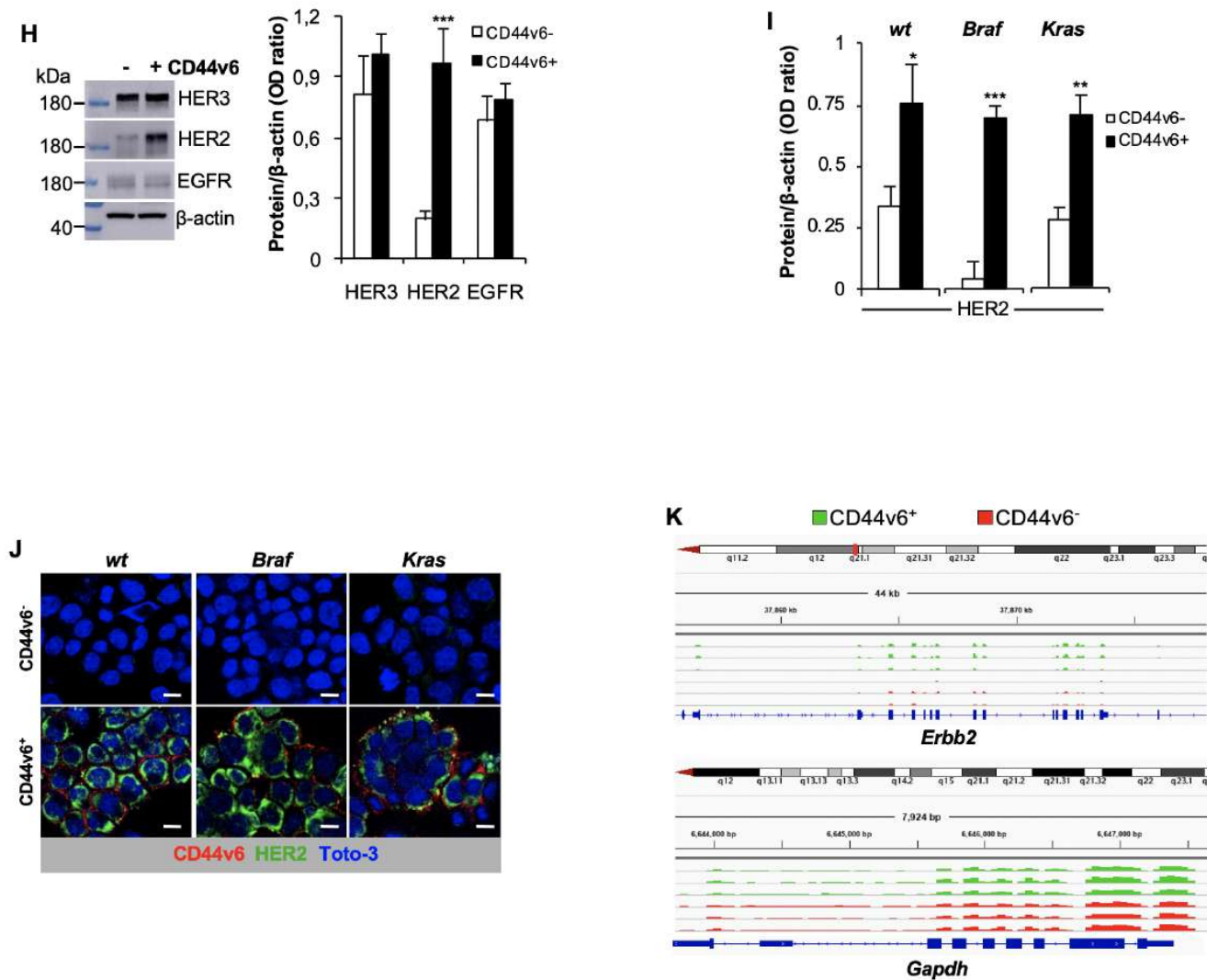
ORCID iDs

Alice Turdo <http://orcid.org/0000-0002-6152-4903>
 Michele Signore <http://orcid.org/0000-0002-0262-842X>
 Luca Fagnocchi <http://orcid.org/0000-0002-9551-5474>
 Micol Eleonora Fiori <http://orcid.org/0000-0002-1813-7035>
 Giorgio Stassi <http://orcid.org/0000-0002-1016-9059>

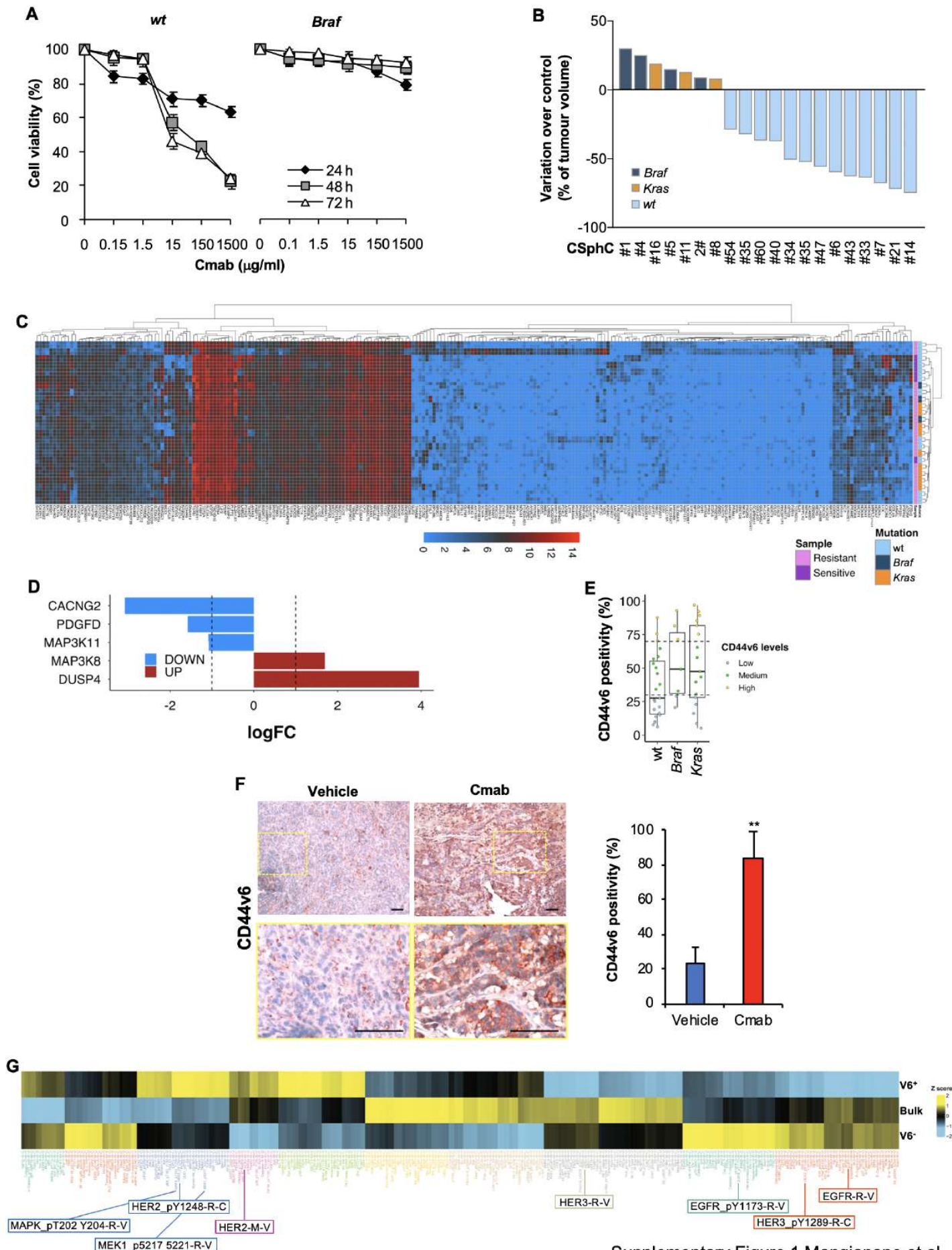
REFERENCES

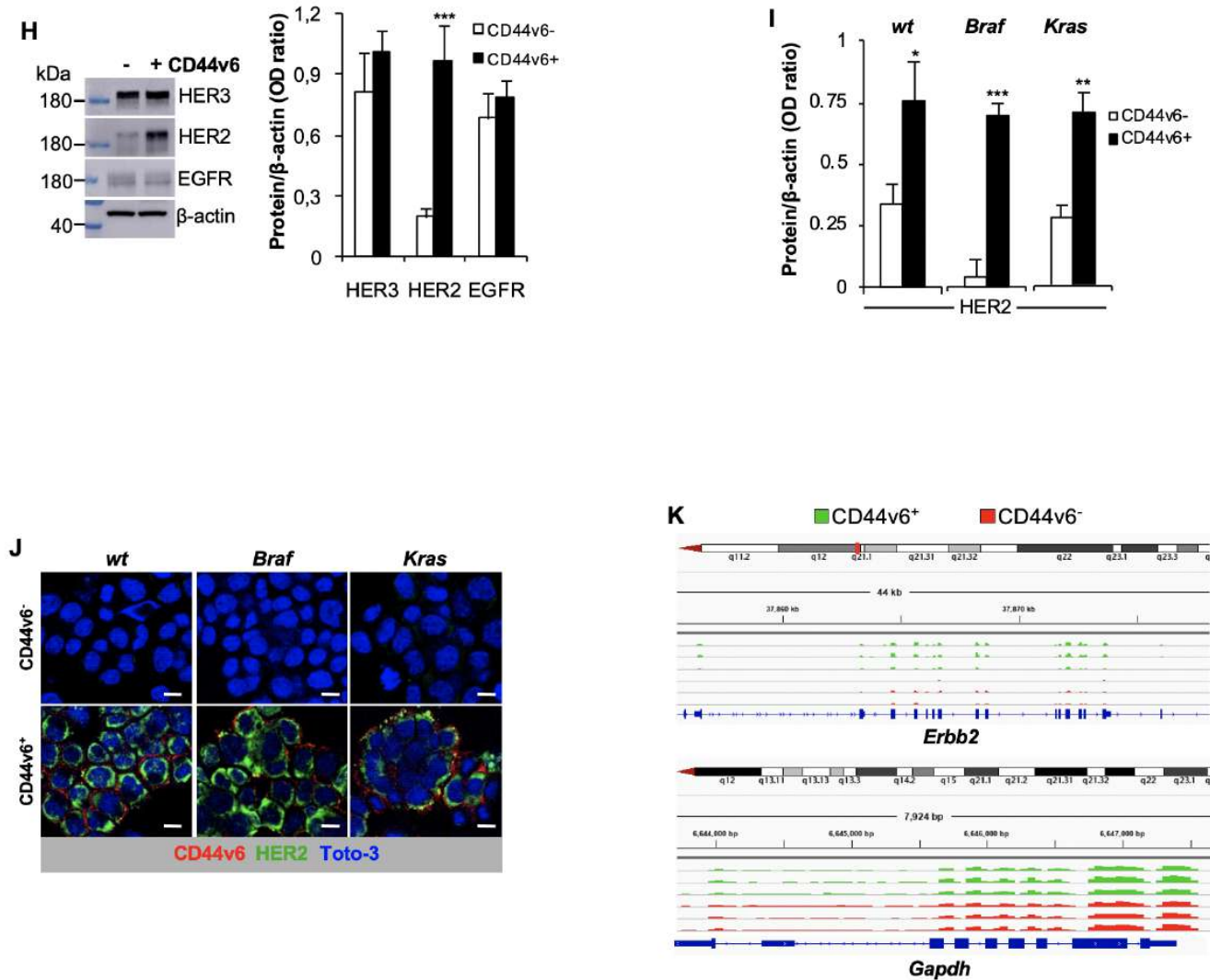
- Siegel RL, Miller KD, Jemal A. Cancer statistics, 2019. *CA: A Cancer Journal for Clinicians* 2019;69:7–34.
- Dagogo-Jack I, Shaw AT. Tumour heterogeneity and resistance to cancer therapies. *Nat Rev Clin Oncol* 2018;15:81–94.
- Russo M, Siravegna G, Blaszkowsky LS, et al. Tumor heterogeneity and lesion-specific response to targeted therapy in colorectal cancer. *Cancer Discov* 2016;6:147–53.
- Dienstmann R, Mason MJ, Sinicrope FA, et al. Prediction of overall survival in stage II and III colon cancer beyond TNM system: a retrospective, pooled biomarker study. *Ann Oncol* 2017;28:1023–31.
- Van Cutsem E, Cervantes A, Adam R, et al. ESMO consensus guidelines for the management of patients with metastatic colorectal cancer. *Annals of Oncology* 2016;27:1386–422.
- Mei ZB, Duan CY, Li CB, et al. Prognostic role of tumor PIK3CA mutation in colorectal cancer: a systematic review and meta-analysis. *Ann Oncol* 2016;27:1836–48.
- Misale S, Di Nicolantonio F, Sartore-Bianchi A, et al. Resistance to anti-EGFR therapy in colorectal cancer: from heterogeneity to convergent evolution. *Cancer Discov* 2014;4:1269–80.
- Siravegna G, Mussolin B, Buscarino M, et al. Erratum: clonal evolution and resistance to EGFR blockade in the blood of colorectal cancer patients. *Nat Med* 2015;21:827.
- De Roock W, Claes B, Bernasconi D, et al. Effects of KRAS, BRAF, NRAS, and PIK3CA mutations on the efficacy of cetuximab plus chemotherapy in chemotherapy-refractory metastatic colorectal cancer: a retrospective Consortium analysis. *Lancet Oncol* 2010;11:753–62.
- Tricker EM, Xu C, Uddin S, et al. Combined EGFR/MEK Inhibition Prevents the Emergence of Resistance in EGFR -Mutant Lung Cancer. *Cancer Discov* 2015;5:960–71.
- Arena S, Siravegna G, Mussolin B, et al. MM-151 overcomes acquired resistance to cetuximab and panitumumab in colorectal cancers harboring EGFR extracellular domain mutations. *Sci Transl Med* 2016;8:324ra14.
- Van Emburgh BO, Arena S, Siravegna G, et al. Acquired Ras or EGFR mutations and duration of response to EGFR blockade in colorectal cancer. *Nat Commun* 2016;7:13665.
- Kopetz S, Desai J, Chan E, et al. Phase II Pilot Study of Vemurafenib in Patients With Metastatic BRAF -Mutated Colorectal Cancer. *Journal of Clinical Oncology* 2015;33:4032–8.
- Ahronian LG, Sennott EM, Van Allen EM, et al. Clinical Acquired Resistance to RAF Inhibitor Combinations in BRAF -Mutant Colorectal Cancer through MAPK Pathway Alterations. *Cancer Discov* 2015;5:358–67.
- Prahallad A, Heynen GJJ, Germano G, et al. Ptpn11 is a central node in intrinsic and acquired resistance to targeted cancer drugs. *Cell Rep* 2015;12:1978–85.
- Kopetz S, McDonough SL, Morris VK, et al. Randomized trial of irinotecan and cetuximab with or without vemurafenib in BRAF -mutant metastatic colorectal cancer (SWOG 1406). *Journal of Clinical Oncology* 2017;35:520.
- Corcoran RB, André T, Atreya CE, et al. Combined BRAF, EGFR, and MEK Inhibition in Patients with BRAF^{V600E}-Mutant Colorectal Cancer. *Cancer Discov* 2018;8:428–43.
- Douillard J-Y, Oliner KS, Siena S, et al. Panitumumab-FOLFOX4 Treatment and RAS Mutations in Colorectal Cancer. *New England Journal of Medicine* 2013;369:1023–34.
- Kavuri SM, Jain N, Galimi F, et al. Her2 activating mutations are targets for colorectal cancer treatment. *Cancer Discov* 2015;5:832–41.
- Zhang L, Castanaro C, Luan B, et al. ERBB3/HER2 signaling promotes resistance to EGFR blockade in head and neck and colorectal cancer models. *Mol Cancer Ther* 2014;13:1345–55.
- Sun C, Hobor S, Bertotti A, et al. Intrinsic resistance to MEK inhibition in KRAS mutant lung and colon cancer through transcriptional induction of ErbB3. *Cell Rep* 2014;7:86–93.
- Personeni N, Fieus S, Piessevaux H, et al. Clinical Usefulness of EGFR Gene Copy Number as a Predictive Marker in Colorectal Cancer Patients Treated with Cetuximab: A Fluorescent *In situ* Hybridization Study. *Clinical Cancer Research* 2008;14:5869–76.
- Siena S, Sartore-Bianchi A, Marsoni S, et al. Targeting the human epidermal growth factor receptor 2 (HER2) oncogene in colorectal cancer. *Annals of Oncology* 2018;29:1108–19.
- Kapitanovic S, Radošević S, Kapitanovic M, et al. The expression of p185(HER-2/neu) correlates with the stage of disease and survival in colorectal cancer. *Gastroenterology* 1997;112:1103–13.
- Sartore-Bianchi A, Trusolino L, Martino C, et al. Dual-Targeted therapy with trastuzumab and lapatinib in treatment-refractory, KRAS codon 12/13 wild-type, HER2-positive metastatic colorectal cancer (HERACLES): a proof-of-concept, multicentre, open-label, phase 2 trial. *Lancet Oncol* 2016;17:738–46.
- Liu Q, Kulak MV, Borchering N, et al. A novel HER2 gene body enhancer contributes to HER2 expression. *Oncogene* 2018;37:687–94.
- Wang Q, Tan R, Zhu X, et al. Oncogenic K-ras confers SAHA resistance by up-regulating HDAC6 and c-myc expression. *Oncotarget* 2016;7:10064–72.
- Sears R, Nuckolls F, Haura E. Multiple Ras-dependent phosphorylation pathways regulate Myc protein stability. *Genes Dev* 2000;14:2501–14.
- Yeh E, Cunningham M, Arnold H, et al. A signalling pathway controlling c-myc degradation that impacts oncogenic transformation of human cells. *Nat Cell Biol* 2004;6:308–18.
- Diosdado B, van de Wiel MA, Terhaar Sive Droste JS, et al. Mir-17-92 cluster is associated with 13q gain and c-myc expression during colorectal adenoma to adenocarcinoma progression. *Br J Cancer* 2009;101:707–14.
- Zeuner A, Todaro M, Stassi G, et al. Colorectal cancer stem cells: from the crypt to the clinic. *Cell Stem Cell* 2014;15:692–705.
- Todaro M, Alea MP, Di Stefano AB, et al. Colon cancer stem cells dictate tumor growth and resist cell death by production of interleukin-4. *Cell Stem Cell* 2007;1:389–402.
- Todaro M, Gaggiani M, Catalano V, et al. Cd44V6 is a marker of constitutive and reprogrammed cancer stem cells driving colon cancer metastasis. *Cell Stem Cell* 2014;14:342–56.
- Cagnol S, Rivard N. Oncogenic KRAS and BRAF activation of the MEK/ERK signaling pathway promotes expression of dual-specificity phosphatase 4 (DUSP4/MKP2) resulting in nuclear ERK1/2 inhibition. *Oncogene* 2013;32:564–76.
- Lim K-H, Ancrile BB, Kashatus DF, et al. Tumour maintenance is mediated by eNOS. *Nature* 2008;452:646–9.
- Veschi V, Mangiapane LR, Nicotra A, et al. Targeting chemoresistant colorectal cancer via systemic administration of a BMP7 variant. *Oncogene* 2020;39:987–1003.
- Roux PP, Shahbazian D, Vu H, et al. Ras/Erk signaling promotes site-specific ribosomal protein S6 phosphorylation via RSK and stimulates cap-dependent translation. *J Biol Chem* 2007;282:14056–64.
- Gera JF, Mellingshoff IK, Shi Y, et al. AKT Activity Determines Sensitivity to Mammalian Target of Rapamycin (mTOR) Inhibitors by Regulating Cyclin D1 and c-myc Expression. *J Biol Chem* 2004;279:2737–46.
- He L, Thomson JM, Hemann MT, et al. A microRNA polycistron as a potential human oncogene. *Nature* 2005;435:828–33.
- Falchook GS, Long GV, Kurzrock R, et al. Dabrafenib in patients with melanoma, untreated brain metastases, and other solid tumours: a phase 1 dose-escalation trial. *The Lancet* 2012;379:1893–901.
- Hong DS, Morris VK, El Osta B, et al. Phase IB Study of Vemurafenib in Combination with Irinotecan and Cetuximab in Patients with Metastatic Colorectal Cancer with BRAF^{V600E} Mutation. *Cancer Discov* 2016;6:1352–65.
- Schütte M, Risch T, Abdavi-Azar N, et al. Molecular dissection of colorectal cancer in pre-clinical models identifies biomarkers predicting sensitivity to EGFR inhibitors. *Nat Commun* 2017;8:14262.
- Linnekamp JF, Hooff SRvan, Prasetyanti PR, et al. Consensus molecular subtypes of colorectal cancer are recapitulated in vitro and in vivo models. *Cell Death Differ* 2018;25:616–33.
- Vermeulen L, De Sousa E Melo F, van der Heijden M, et al. Wnt activity defines colon cancer stem cells and is regulated by the microenvironment. *Nat Cell Biol* 2010;12:468–76.
- Siravegna G, Mussolin B, Buscarino M, et al. Clonal evolution and resistance to EGFR blockade in the blood of colorectal cancer patients. *Nat Med* 2015;21:795–801.
- Segaert S, Van Cutsem E. Clinical signs, pathophysiology and management of skin toxicity during therapy with epidermal growth factor receptor inhibitors. *Annals of Oncology* 2005;16:1425–33.



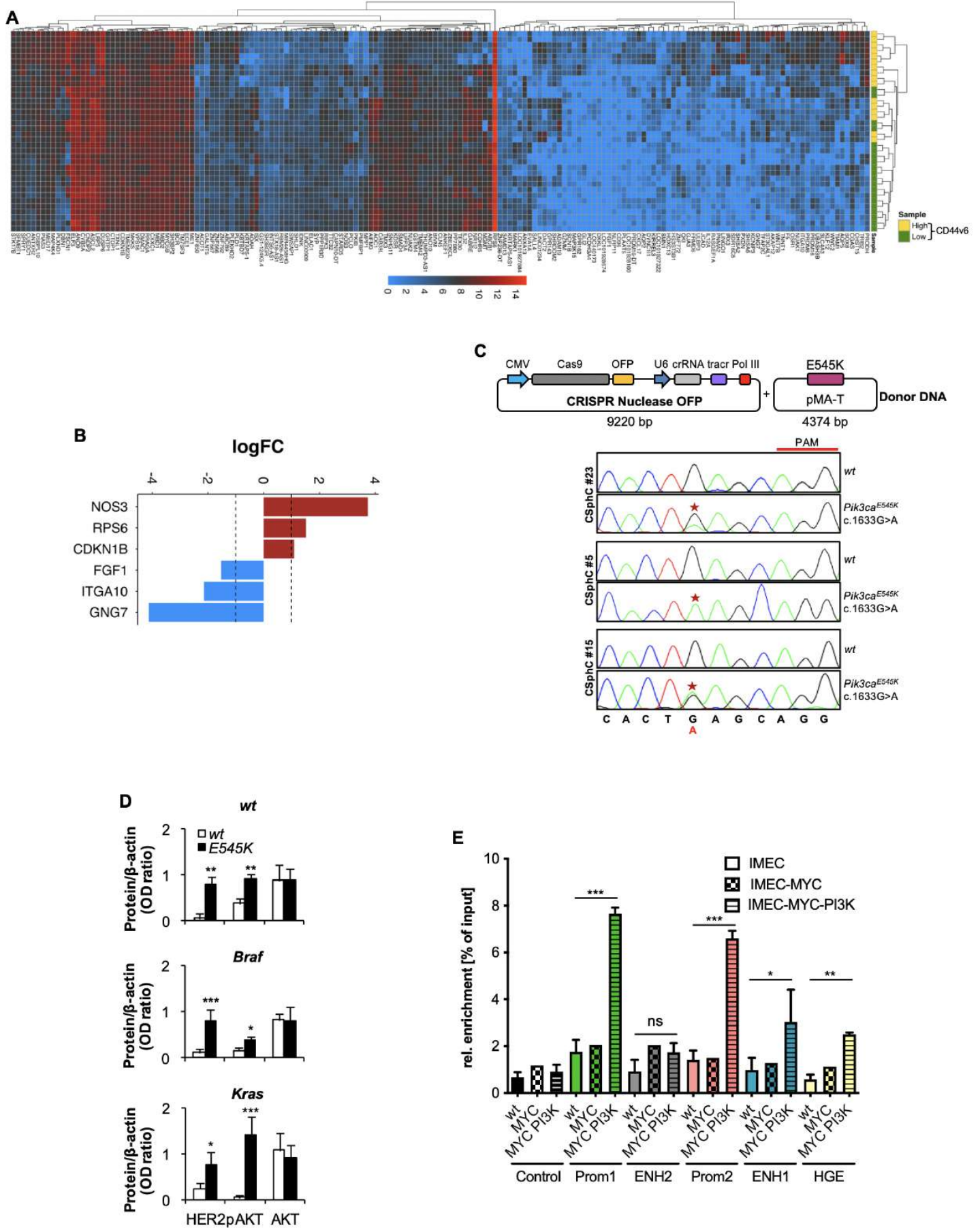


Supplementary Figure 1 Mangiapane et al.

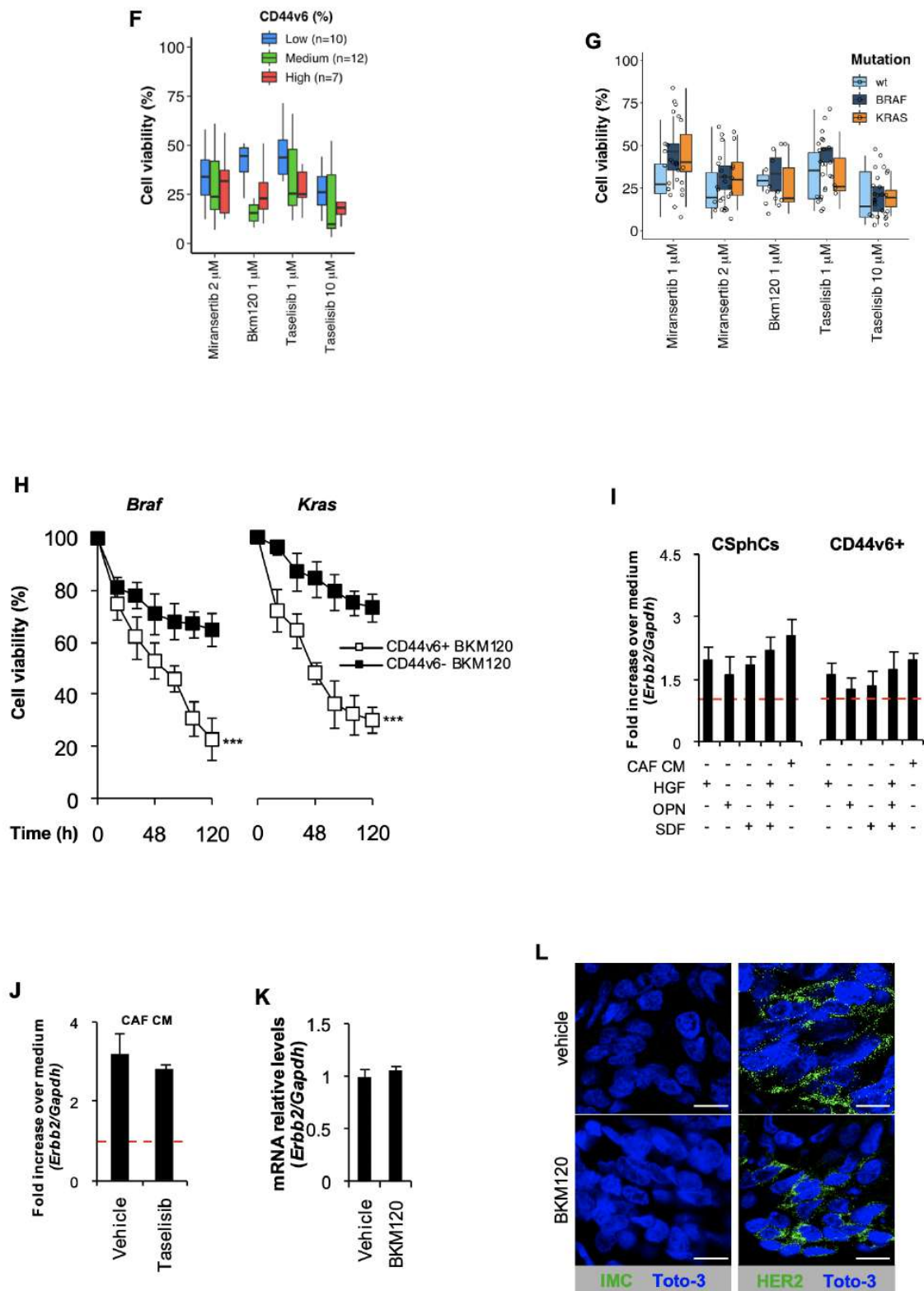




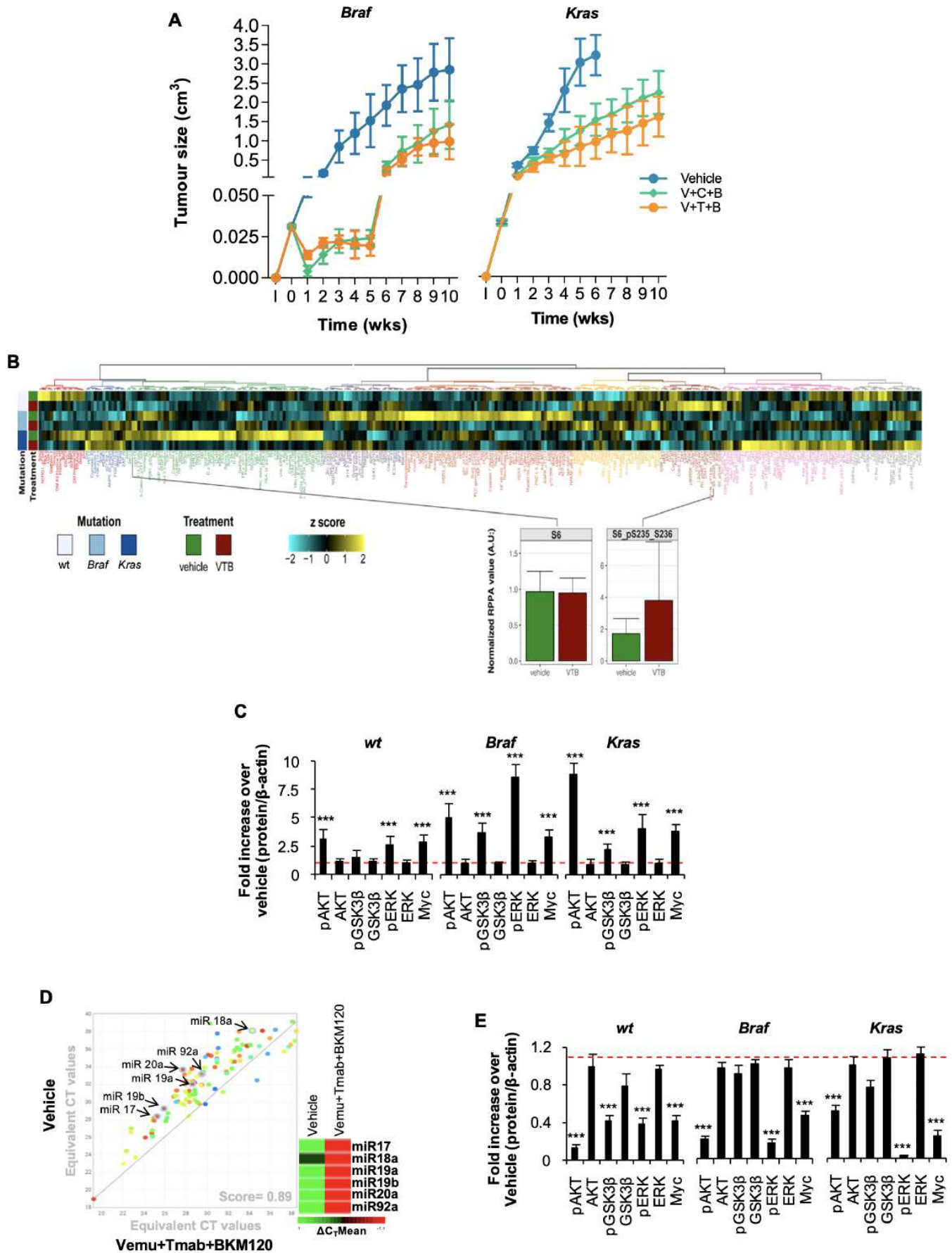
Supplementary Figure 1 Mangiapane et al.



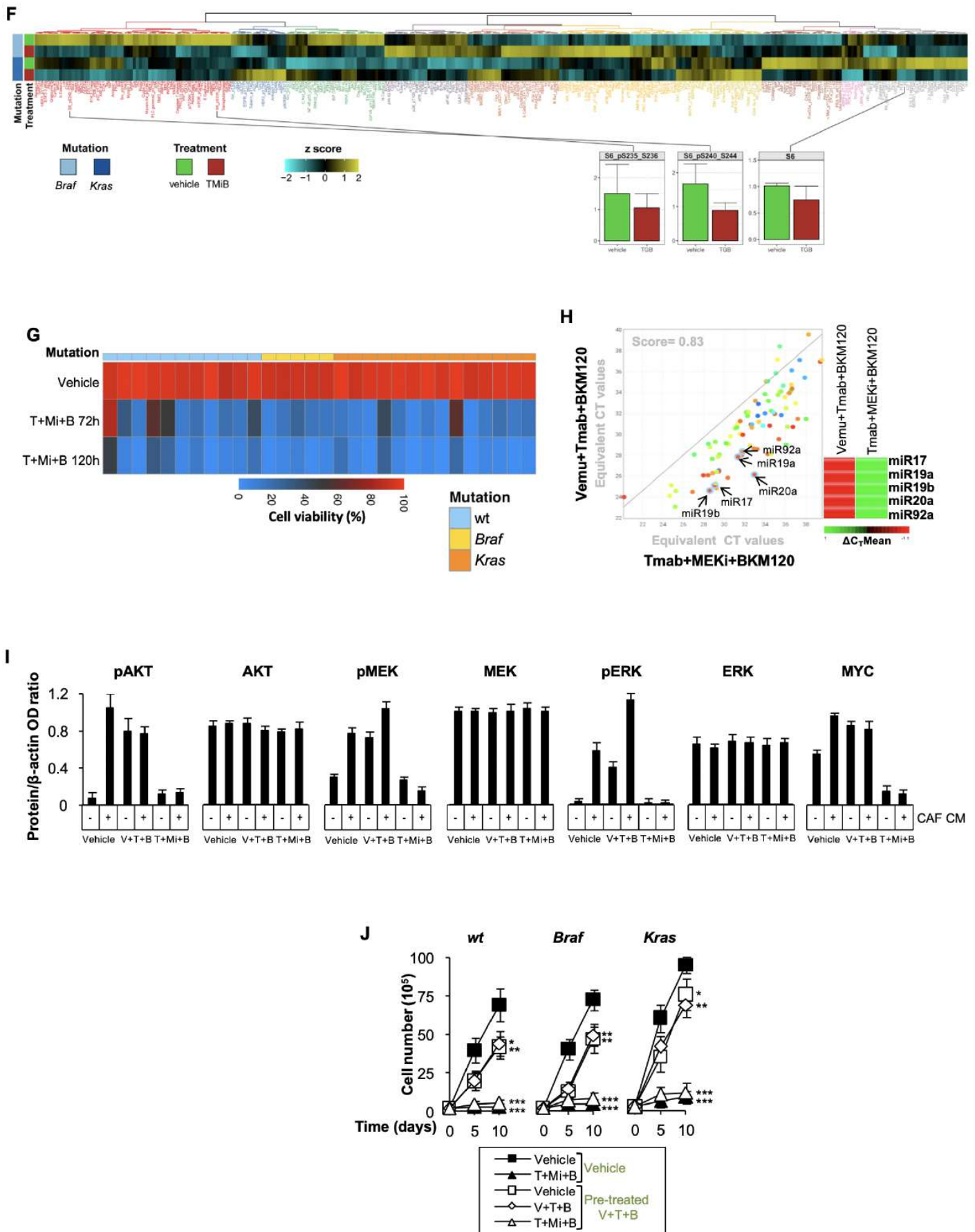
Supplementary Figure 2 Mangiapane et al.



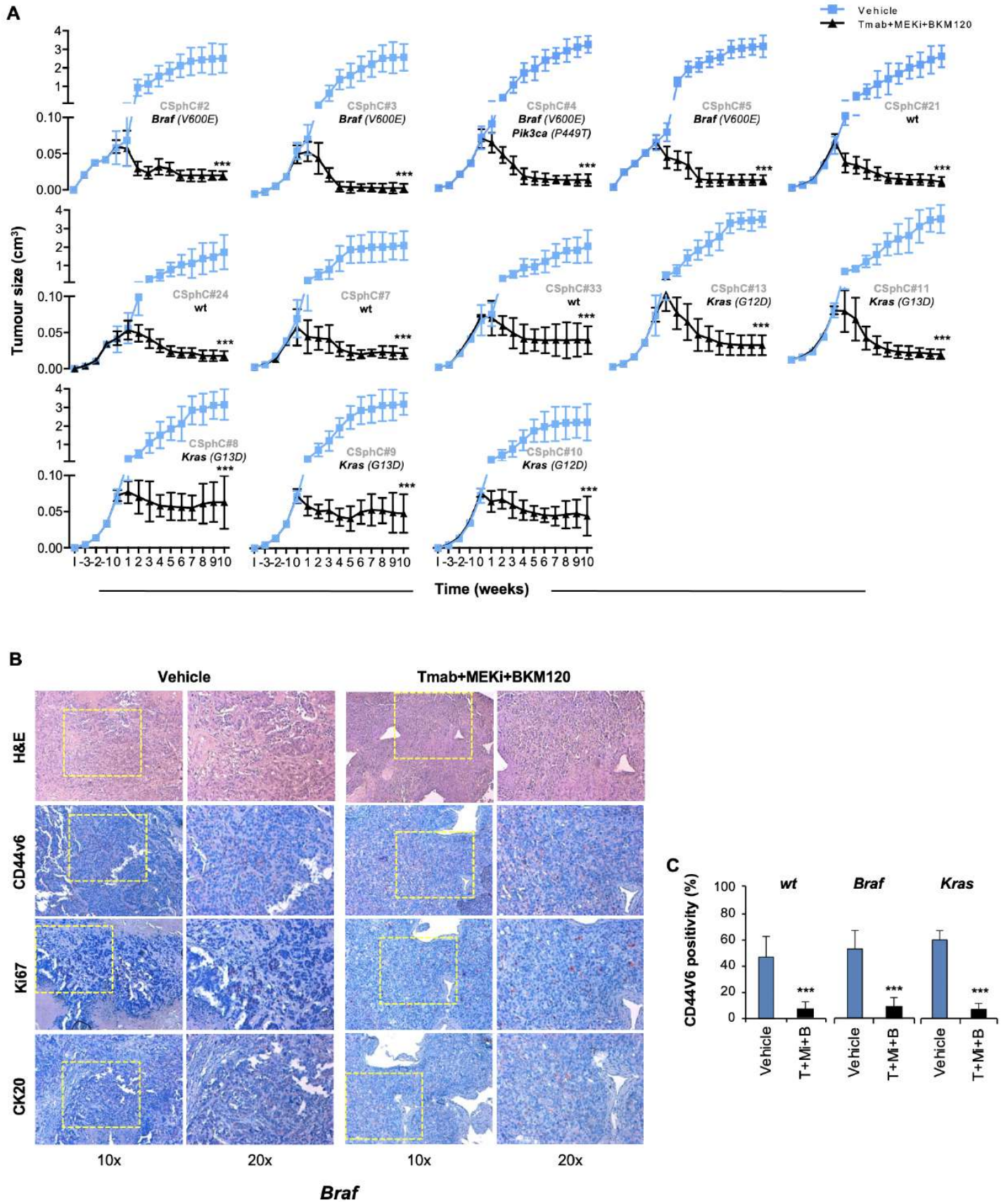
Supplementary Figure 2 Mangiapane et al.



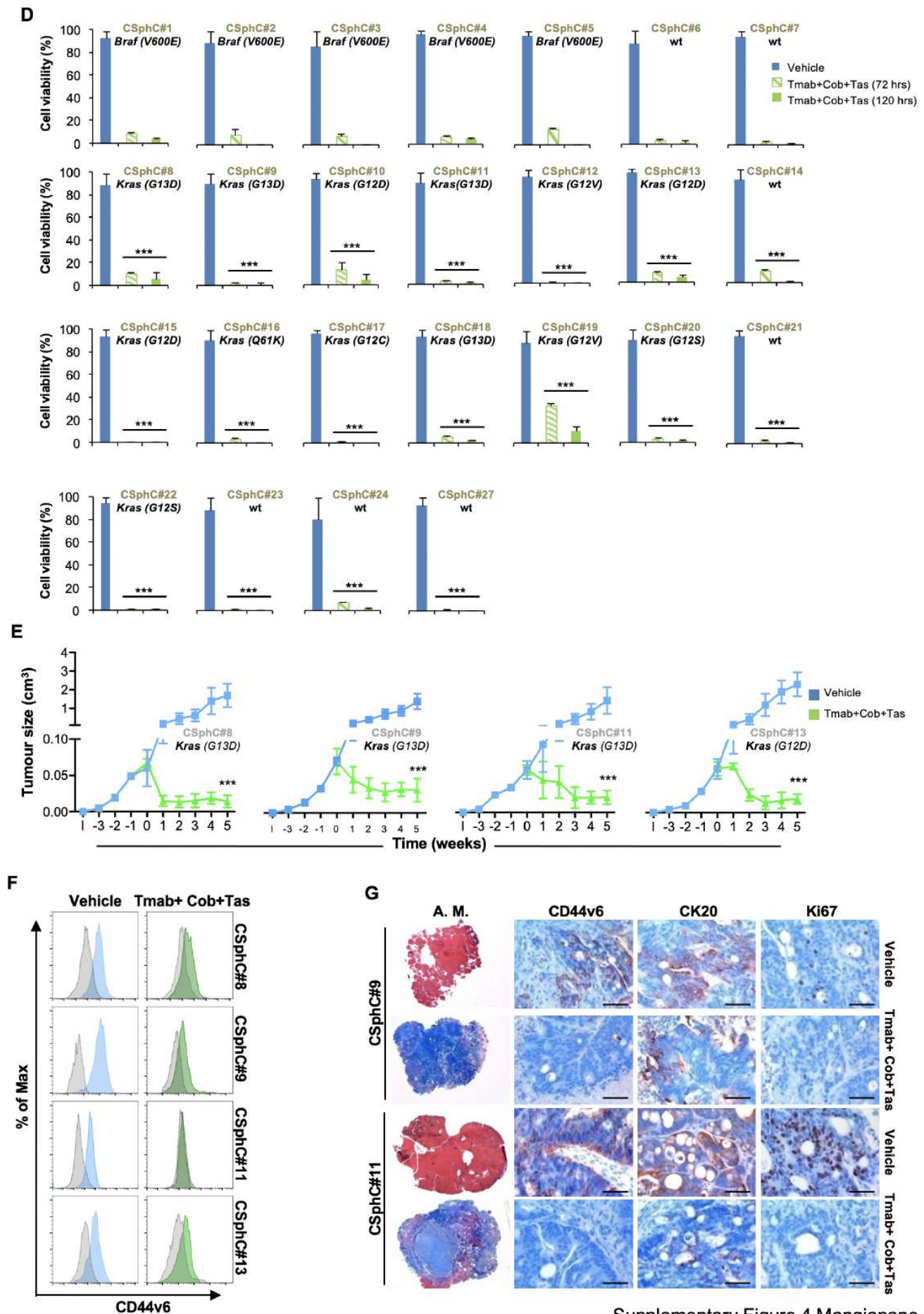
Supplementary Figure 3 Mangiapane et al.



Supplementary Figure 3 Mangiapane et al.



Supplementary Figure 4 Mangiapane et al.



Supplementary Figure 4 Mangiapane et al.

SUPPLEMENTAL INFORMATION

METHODS

CRC sphere cell culture

Purification and propagation of sphere cells was assessed as previously described¹ from 60 primary tumor specimens (age range 40–80 years) from CRC patients undergoing colon resection, in accordance with the ethical standards regarding Human Experimentation (authorization CE9/2015, Policlinico Paolo Giaccone, Palermo) (online supplemental table 1). CSphCs were cultured in serum-free stem cell medium (SCM) supplemented with EGF and b-FGF. Authentication of CSphC lines was routinely performed using a short tandem repeat DNA profiling kit (GlobalFiler™ PCR kit, Applied Biosystem) following the manufacturer's instructions and analyzed by ABI PRISM 3130 (Applied Biosystem). CSphC DNA profiles were matched with their relative patient tumor tissues. Mycoplasma presence was assessed with the MycoAlert™ Plus Mycoplasma Detection Kit (Lonza) every 3 months. To assess *ErbB2* copy number in CR-CSphCs we analyzed DNA samples using Digital Droplet PCR (Bio-Rad). After droplet generation and PCR amplification, plates were loaded in a Bio-Rad QX200 droplet reader and analyzed using the QuantaSoft v1.7.4 software (Bio-Rad) to evaluate droplets positive for *ErbB2* and/or *Rpp30*. Negative (no DNA) and positive (*ErbB2* amplified SKBR3 established cell line) controls were included in each plate. An *ErbB2/Rpp30* ratio < 1.25 identified non-amplified samples.^{2,3} The mutational profiles of the CSphCs were assessed by using a custom NGS panel and sequencing data were generated by MiSeq platform (Illumina).

CRC sphere cell treatment

CSphCs were treated with vemurafenib 1 μM (S1267, Selleckchem), cetuximab 20 μg/ml and trastuzumab 10 μg/ml (kindly provided by the Department of Central Hospital Services- Policlinico Paolo Giaccone), taselisib 0.5 μM (GDC-0032, Chemietek), BKM120 1 μM (S2247, Selleckchem), trametinib 100 nM (S2673, Selleckchem), cobimetinib 0.5 μM (S8041, Selleckchem) or miransertib 2 μM (S8339, Selleckchem). All the drugs were added in culture media every 48 hours.

The primary human CAF cell lines were isolated from CRC tissues obtained in accordance with the ethical policy of the University of Palermo Committee on Human Experimentation. For co-culture experiments, 1×10^5 immortalized CAFs (CAFs) were plated as monolayer into 12-well plates for 48 hours, until confluence was reached and subsequently 6×10^5 GFP-transduced CSphCs were seeded in presence or absence of HGF (1 μg/ml, MAB294, R&D), OPN (2 μg/ml, AF1433, R&D) and SDF-1 (50 μM, A5602, Sigma-Aldrich) neutralizing antibodies. After 48 hours cells were treated with 0.5 μM of taselisib for additional 72 hours. The preparation of CAF conditioned medium (CAF CM) was performed by culturing 1×10^6 cells in 5 ml of SCM for 48 hours. To analyze *ErbB2*

expression levels, CSphCs were exposed to CAF CM, HGF (100 ng/ml, PeproTech), OPN (1 µg/ml, Sigma-Aldrich) and SDF-1 (100 ng/ml, PeproTech) for 48 hours.

Cell survival

Cell proliferation and viability were evaluated by using CellTiter-Glo® Luminescent Cell Viability Assay Kit (Promega) according to the manufacturer's instructions and analyzed by Infinite® F500 (Tecan). Tripan blue exclusion test was accomplished to validate cell viability. CSphC death was assessed by adding Hoechst 33342 (Thermo Fisher Scientific) or 7-AAD (BD Pharmingen) and analyzed by a fluorescence microscope or flow cytometer, respectively.

Reverse-Phase Protein microArrays

The RPPA assay was carried out by the Functional Proteomics RPPA Core Facility by MD Anderson (Houston, TX, USA)⁴ on a service basis (online supplemental table 4). The data analysis was performed by our group. Briefly, cell pellets were lysed for protein extraction by resuspension in a buffer containing T-PER reagent (Thermo Fisher Scientific), 300 mM NaCl (J.T.Baker; Avantor Performance Materials, Center Valley, PA), protease and phosphatase inhibitor cocktails (Sigma-Aldrich), followed by 20 min incubation on ice. Following protein extraction, samples underwent centrifugation at 10,000xg for 10 minutes and, subsequently, supernatants were transferred to fresh tubes for quantification of total protein concentration (Bradford reagent method, Thermo Fisher Scientific). Before shipping for RPPA assay service, lysates were diluted to a final concentration of 0.5 µg/µl using 2X sodium dodecyl sulfate (SDS) buffer (Thermo Fisher Scientific) and 2-mercaptoethanol was added to a final concentration of 2.5%. Analysis of pre-normalized RPPA data was performed by means of the "R3.6" software and the following packages: 'base', 'coin', 'exactRankTests', 'gridExtra', 'grid', 'tidyverse', 'plyr', 'dendextend' and 'ComplexHeatmap'.

Western blot

Cell were lysed in presence of ice-cold buffer containing Tris-HCL 10 mM (Sigma-Aldrich), NaCl 50 mM (Sigma-Aldrich), sodium pyruvate 30 mM (Sigma-Aldrich), NaF 50 nM (Sigma-Aldrich), ZnCl₂ 5 µM (Sigma-Aldrich), triton 1% (Bio-Rad), protease inhibitor cocktail (Sigma-Aldrich), phosphatase inhibitor cocktail 2 and 3 (Sigma-Aldrich), sodium orthovanadate 0.1 nM (Sigma-Aldrich), sodium butyrate 10 mM (Sigma-Aldrich) and PMSF 1 mM (Sigma-Aldrich). Proteins extracted were loaded in SDS-PAGE gels and blotted on nitrocellulose membranes. After incubation with blocking solution (0.1% Tween 20 and 5% non-fat dry milk in PBS) for 1 hour at room

temperature, membranes were exposed overnight at 4°C to HER3/ErbB3 XP (D22C5, rabbit IgG, CST), HER2/ErbB2 XP (D8F12, rabbit IgG, CST), EGF receptor XP (D38B1, rabbit IgG, CST), phospho-AKT XP (Ser473; D9E, rabbit, IgG, CST), AKT (rabbit polyclonal, CST), phospho-GSK3 α/β (Ser21/9; D17D2, rabbit IgG, CST), GSK-3 β (27C10, rabbit IgG, CST), phospho-ERK 1/2 (Thr202/Tyr204; rabbit polyclonal, CST), ERK 1/2 (137F5, rabbit IgG, CST), Myc (rabbit polyclonal, CST), phospho-MEK1/2 (Ser217/221; 41G9, rabbit IgG, CST) or MEK1/2 (rabbit polyclonal, CST). β -actin (8H10D10, mouse, CST) was used as loading control to normalize protein expression. Primary antibodies were revealed using anti-mouse or anti-rabbit HRP-conjugated (goat H+L, Thermo Fisher Scientific) for 1 hour at room temperature and detected with SuperSignal™ West Dura Extended Duration Substrate (Thermo Fisher Scientific) using Amersham imager 600 (GE Healthcare). Protein levels were calculated by densitometric analysis using ImageJ software.

Cytokines quantification

CAF-released cytokines involved in tumor inflammation, cell proliferation and immune response processes were quantified using the Bio-Plex Pro™ Human Cytokine 21-plex and 27-plex Assay (Bio-Rad). HGF, OPN, SDF-1 and TGF- β production was assessed by using the Human Cancer Biomarker Panel 1 16-plex #171AC500M, Bio-Plex Pro Human Cytokine SDF-1 α Set #171B6019M, and Bio-Plex Pro™ TGF- β 3-plex Assay #171W4001M, respectively. Raw data were analyzed by Bio-Plex Software (Bio-Rad).

Flow cytometry and cell sorting

Cells were harvested, washed in PBS twice and stained for 1 hour at 4°C with conjugated antibodies CD44v6-APC (2F10, mouse IgG1, R&D systems) or isotype matched control (IC002A, mouse IgG1, R&D systems) and analyzed using both Accuri C6 Plus and FACSLyric (BD) flow cytometers. CD90 expression was assessed by using CD90 purified antibody (5E10, mouse IgG1k, BD) or isotype matched control (MOPC-21, mouse IgG1k, BD) and subsequent labeling with secondary antibodies Alexafluor 647 (goat anti-mouse IgG1, Thermo Fisher Scientific). Enrichment of CD44v6 or OFP expressing cells was accomplished by FACSMelody cell sorter. Prior to sorting, cells were washed with PBS containing 2% BSA and 2 mM EDTA and filtered with a 70 μ M mesh to prevent clogging. Post-sorting acquisition was performed in order to verify the population purity. Dead cells were excluded on the basis of the uptake of 7-AAD (0.25 μ g/1x10⁶ cells, BD Biosciences).

RNA Extraction, Real-Time PCR and RNASeq

Total RNA of CSphCs was isolated by using Trizol Reagent (Thermo Fisher) and retro-transcribed with the high-capacity c-DNA reverse Transcription kit (Applied Biosystem). Real-time PCR was performed by using the rotor gene probe PCR master mix (Qiagen) and the following primers: *ErbB2* (Hs01001580_m1), *ErbB3* (Hs00176538_m1), *Egfr* (Hs01076078_m1) and *Gapdh* (Hs02786624_g1) (Applied Biosystem). The relative mRNA level was normalized to *Gapdh* and calculated by using the comparative Ct method ($\Delta\Delta Ct$).

To evaluate the miRNA expression profiles of CSphCs untreated and exposed to different treatments, total RNA samples were retro-transcribed and real time PCR were performed using Megaplex pools kit (Applied Biosystem) specific for a set of 384 microRNAs (TaqMan Human MicroRNA Array A) as recommended by manufacturer's instructions. Collected data were analyzed with the Thermo FisherCloud software.

NEBNext Ultra Directional RNA Library Prep Kit for Illumina was used for the preparation of RNASeq samples following the manufacturer's instructions. mRNA was purified using oligo-dT magnetic beads from total RNA. Retrotranscribed cDNA was used for ligation with adapters and PCR amplification. Clustering and DNA sequencing was assessed using the Illumina NextSeq 500. Analysis was performed by using the Illumina data analysis pipeline RTA v2.4.11 and Bcl2fastq v2.17. Raw sequencing reads were aligned to Ensembl release 84 (GRCh38 assembly) using the HISAT2 2.1.0 pipeline. Data were analyzed using the R version 3.5.0 and plotted by the pheatmap version 1.0.10, gtools 3.8.1 and ggplot2 3.0.0. Gene set enrichment analysis (GSEA) was assessed by selecting Hallmarks and canonical pathways within molecular signatures database (MSigDB) version 7.0. False Discovery Rate q value ≤ 0.05 was used to identify significantly enriched gene sets.

Chromatin immunoprecipitation (ChIP) and ChIP-qPCR

Chromatin was isolated from both CD44v6⁺ and CD44v6⁻ CSphCs, IMEC, IMEC-MYC and IMEC-MYC-PI3K cells. Cells were fixed adding formaldehyde directly to the cell culture media to reach a final concentration of 1%, then were incubated for 10 min at room temperature (RT). The reaction was quenched adding glycine to a final concentration of 125 mM and incubated 5 min at RT. The medium was removed and cells were washed 3 times with cold, sterile PBS plus protease inhibitor, then cells were collected by centrifugation at 4°C for 5 min at 1200 rpm. ChIP experiments were performed as previously described.^{5, 6} Briefly, cell pellets were lysed in lysis buffer (50 mM Tris-HCl pH 8, 0.1% SDS, 10 mM EDTA pH 8, 1 mM PMSF (Sigma-Aldrich), protease inhibitor cocktail (Roche)) and chromatin was sonicated with a Bioruptor Pico sonicator

(Diagenode) for 25 cycles of 30 s, to reach an average fragment size of ~ 300 kb. Following quantification, 10 µg of sonicated chromatin were used in each immune-precipitation and incubated overnight at 4°C with 4 µg of indicated antibodies: anti- monomethyl histone H3 Lys4 (rabbit polyclonal, Abcam); anti-acethyl histone H3 Lys27 (rabbit polyclonal, Abcam). Concomitantly, protein G-coupled Dynabeads (Thermo Fisher Scientific) were blocked overnight at 4°C with 1 mg/ml sonicated salmon sperm DNA (Thermo Fisher Scientific) and 1 mg/ml BSA and then incubated with the ChIP reactions for 4 hours at 4°C. Magnetic beads were sequentially recovered and resuspended in RIPA buffer (10 mM Tris-HCl, pH 8, 0.1% SDS, 1 mM EDTA, pH 8, 140 mM NaCl, 1% DOC, 1% Triton, 1 mM PMSF, protease inhibitor cocktail), washed 5 times with ice-cold RIPA buffer, twice with ice-cold RIPA-500 buffer (10 mM Tris-HCl, pH 8, 0.1% SDS, 1 mM EDTA, pH 8, 500 mM NaCl, 1% DOC, 1% Triton, 1 mM PMSF, protease inhibitor cocktail), twice with ice-cold LiCl buffer (10 mM Tris-HCl, pH 8, 0.1% SDS, 1 mM EDTA, pH 8, 250 mM LiCl, 0.5% DOC, 0.5% NP-40, 1 mM PMSF, protease inhibitor cocktail) and once with TE buffer (10 mM Tris-HCl, pH 8, 1 mM EDTA, pH 8, 1 mM PMSF, protease inhibitor cocktail). Finally, the crosslinking was reversed in direct elution buffer (10 mM Tris-HCl, pH 8, 0.5% SDS, 5 mM EDTA, pH 8, 300 mM NaCl) at 65°C overnight and DNA was purified using Agencourt AMPure XP SPRI beads (Beckman, #A63882) and dissolved in 60 µl of Tris-HCl, pH 8. DNA was analyzed by quantitative PCR using the 2x SensiFAST SYBR No-ROX Mix (Bioline). The following oligos were used: Prom1 (fwd: CACCATCATGTGTGCGCCAAG / rev: GCAGGTTGGAAGAGGCAAAA), ENH2 (fwd: CAGTTTGTGGCCTGGACATC / rev: TACCTACTTCACCAGCCAGC), Prom2 (fwd: GGCTTGGGATGGAGTAGGAT / rev: AAATTCCCTAGGCTGCCACT), ENH1 (fwd: GACCACCAGAGTCCAGAGAG / rev: TCTCCGAACAAAAGGGACCA), HGE (fwd: GATCCGGAAGTACACGATGC / rev: GGCTGGGAGGACTTCACC), control (fwd: GATCAAGTCAGGCTGAATACACG / rev: TCTGTGCTCCTAGCTTGTCCT). All experimental values were shown as percentage of input. To take into account background signals, we subtracted the values obtained with a non-immune serum to the relative ChIP signals.

CRISPR editing and lentiviral transduction

CSphCs were transfected with 1 µg of all-in-one OFP vector system for CRISPR-based genome editing (Thermo Fisher Scientific) and 1 µg of pMA-T plasmid containing customized donor DNA for *Pik3ca*^{E545K} (Thermo Fisher Scientific), using the X-tremeGENE HP DNA Transfection Reagent (Roche) according to the manufacturer's instructions. DNA from control and transfected CSphCs was purified using the DNeasy Blood & Tissue Kit (Qiagen). The presence of *Pik3ca*^{E545K} mutation

was assessed using the HotStarTaq Plus Master Mix Kit (Qiagen) using the following primer set: F-ATTGTTCACTACCATCCTC; R-TAATGTGCCAACTACCAATG. Amplified products were then purified using the MinElute PCR Purification Kit (Qiagen). Purification and base pair sequence were prepared using the BigDye Terminator v3.1 Cycle Sequencing Kit and BigDye X-Terminator Purification Kit (Applied Biosystems), respectively. Capillary electrophoresis was performed on ABI PRISM 3130 Genetic Analyzer.

Lentiviral particles were generated by transfecting HEK-293T packaging cells with p-TWEEN LUC-GFP plasmids together with psPAX2 (Addgene, 12260) and pMD2.G (Addgene, 12259) in DMEM 10% FBS supplemented with XtremeGENE HP DNA Transfection Reagent (Roche). For stable cell transduction, concentrated lentiviral particles were added to 1×10^5 cells in culture medium in the presence of 8 $\mu\text{g/mL}$ of polybrene (Sigma-Aldrich). hTERT-immortalized human mammary epithelial cells (IMEC) were transduced with pMXs-c-Myc, PGK-Pik3ca H1047R, pBABE-puro-Ras V12, and MSCV-p53DD-iGFP vector, respectively as previously described.⁶ CAFs immortalization has been performed using a pLV-hTERT-IRES-hygro lentiviral plasmid (Addgene). Hygromycin (10 $\mu\text{g/ml}$; ant-hg-5, Invivogen) was used for selection of CAFs.

Animals and tumor models

6-8 weeks old male NOD/SCID mice were purchased by Charles River Laboratories and housed in the animal house at the Department of Biomedicine, Neuroscience and Advanced Diagnostics (Bi.N.D., University of Palermo). Mice were kept in a barrier facility for animals in a temperature-controlled system with a 12 hours dark/light cycle. Mice were given *ad libitum* access to pelleted chow [Special Diets Services-811900 VRF1 (P), Essex, UK] and to 0.45 mm filtered tap water in sterile drinking bottles. Each cage (1284L, Tecniplast S.p.A., Italy) provided with radiation-sterilized bedding (SAWI Research Bedding, JELU-WERK, Germany) has been used to house a maximum of 6 mice. Enrichment material such as soft paper and small red plastic houses (The Mouse House, ACRE011, Tecniplast) was used to meet animal welfare. All the surgical procedures have been performed during daytime, in accordance with the animal care committee guidelines of the University of Palermo (Italian Ministry of Health authorization n. 154/2017-PR). Subcutaneous xenografts were generated by injecting 2.5×10^5 CSphCs in the flank of NOD/SCID mice, in 150 μl of 1:1 SCM/Matrigel (BD) solution. After tumor appearance (0.03-0.06 cm^3), mice were randomized in control and treatment groups (6 mice/group). Mice were treated for 5 days/week, for 4 weeks, with vehicle, taselisib (5 mg/Kg, once-daily, oral gavage), vemurafenib (20 mg/Kg, twice-daily, oral gavage), trastuzumab (5 mg/Kg, once-weekly, *i.p.*), cetuximab (40 mg/Kg, twice-weekly, *i.p.*), BKM120 (20 mg/Kg, once-daily, oral gavage), trametinib (0.3 mg/Kg, once-daily, oral

gavage) or cobimetinib (5 mg/Kg, once-daily, oral gavage). Tumors were measured twice per week by a digital caliper. Tumor volume was calculated using the formula: largest diameter x (smallest diameter)² x $\pi/6$. Once the endpoints were reached (2 cm in tumor diameter or when mice showed signs of suffering), animals were sacrificed accordingly to Directive 2010/63/EU guidelines (D.lgs 26/2016) and organs were collected for subsequent analyses. For the adjuvant therapy experiments, 3×10^5 LUC-transduced *Kras*-mutant CSphCs resuspended in PBS were injected into the spleen of NOD/SCID mice. The migration of sphere cells was assessed at the time of cell injection and at 30 min immediately after splenectomy up to 12 weeks (every 4 weeks) following *i.p.* injection of VIVO GloTM Luciferin (150 mg/kg, Promega) by using *in vivo* imaging system (IVIS Spectrum, PerkinElmer). After 5 days of sphere cells injection, mice were treated for 3 weeks with vehicle or taselisib.

Immunofluorescence/Immunohistochemistry

Cytospun of CD44v6⁺ and CD44v6⁻ cell fractions were fixed and permeabilized as previously described.¹ Cells were exposed overnight at 4°C to specific antibodies to detect CD44v6 (2F10, mouse IgG₁, R&D systems) and HER2 (D8F12, rabbit IgG, CST). Subsequently, cells were labeled with secondary antibodies, Rhodamine Red-x Goat anti-Mouse IgG1 and Alexa Fluor-488 Goat anti-rabbit IgG (Life Technologies). Nuclei were counterstained using TOTO-3 iodide (Life Technologies). Cells were examined under a confocal microscope. For CAF-CSphC co-culture experiment, cells were labeled with CD90 (SE10, mouse IgG1, BD Pharmingen) and subsequently with Alexa Fluor-647 Goat anti-mouse IgG1 (Life Technologies). Nuclei were counterstained using Hoechst (33258, Thermofisher). Cell staining were examined by using EVOS Cell Imaging System (Life Technologies).

Immunohistochemical and immunofluorescence analysis were performed on 5- μ m-thick paraffin-embedded xenograft sections using antibody specific for CD44v6 (2F10, mouse IgG₁, R&D systems), HER2 (D8F12, rabbit IgG, CST), phospho-AKT XP (Ser473; D9E, rabbit, IgG, CST), Ki67 (T595, IgG1_k, Novocastra) and CK20 (Ks20.8, IgG2a_k, Novocastra). Stainings were then revealed using byotyne-streptavidine system (Dako) and detected with 3-amino-9-ethylcarbazole (AEC, Dako). Nuclei were counterstained with aqueous hematoxylin (Sigma-Aldrich). Azan-Mallory and H&E stainings were performed using standard protocols.

Statistical analysis

Results are shown as mean \pm SD for at least three repeated independent experiments for each group. The mean and SD were obtained by analyzing replicates using Prism 5 (GraphPad Software, La Jolla, CA, USA) applying ANOVA test (one-way or two-way) with Bonferroni multiple comparisons test. P-values less than 0.05 were considered statistically significant. *indicates $P < 0.05$, ** indicates $P < 0.01$ and ***indicates $P < 0.001$. RNA-seq data were normalized with log₂-counts per million transformation. Differential expression analyses between diverse conditions were conducted in R (v3.6.1) by using limma package. P-values for log₂ fold-change values are corrected with Benjamini-Hochberg procedure, only statistically significant differences were reported. ggplot2 and pheatmap packages were used for plotting the distributions and line plots, and heatmaps with clustergrams and sample annotations, respectively.

SUPPLEMENTAL FIGURE LEGENDS

Supplementary Figure 1. CD44v6 positive cells express high levels of HER2 and MAPK-ERK signaling molecules.

(A) Dose-response of cetuximab (Cmab) on *Ras/Braf*-wt (CSphC#14, 21) and *Braf*-mutant (CSphC#2, 5) sphere cell lines at the indicated time points. Data are mean \pm S.D. of 3 independent experiments. (B) Waterfall plot of cetuximab response in *Ras/Braf*-wt xenograft tumors from sensitive CSphCs treated for 4 weeks and analyzed 1 week after treatment suspension. *Braf*- and *Kras*-mutant xenografts served as control. (C) Unsupervised clustering of RNA-seq data from sphere cells sensitive and resistant to cetuximab and harboring the indicated mutations. (D) Log fold change (logFC) values of a subset of statistically differentially expressed genes, involved in the MAPK pathway, in sensitive versus resistant *Ras/Braf*-wt sphere cells to cetuximab, obtained by limma analysis. (E) Statistical distribution of CD44v6 positivity in 47 CSphC lines characterized by the indicated mutational background. Boxes and whiskers represent median \pm S.D. of 6 experiments. Dotted lines indicate high ($\geq 70\%$), medium (69%-31%) and low ($\leq 30\%$) CD44v6 levels. (F) (Left panel) Representative immunohistochemical analysis for CD44v6 on tumor xenografts generated by the injection of *Ras/Braf*-wt (CSphC#14) sphere cells and treated with cetuximab for 4 weeks. Scale bars, 200 μ m. (Right panel) Percentage of CD44v6 positivity in tumor xenografts generated by the injection of *Ras/Braf*-wt (CSphC#14, 21, 33) sphere cells. Data are mean \pm S.D. of 3 independent experiments. (G) RPPA analysis of CRC spheres (Bulk) and enriched CD44v6⁺ and CD44v6⁻ *Braf*- (CSphC#2) mutant cells. (H) Immunoblot analysis of HER3, HER2 and EGFR and their relative bar graphs on CD44v6⁻ and CD44v6⁺ cells derived from 10 different CR-CSphC lines with different mutational backgrounds (CSphC#1, #2, #3, #9, #11, #15, #16, #21, #33, #37). β -actin was used as loading control. Data are mean \pm S.D. of 3 independent experiments performed with 10 different sphere cell lines. (I) Bar graphs of immunoblot band densities for HER2 on enriched CD44v6⁺ and CD44v6⁻ *Ras/Braf*-wt, *Braf*- and *Kras*- mutant cells. Data are mean \pm S.D. of 3 independent experiments performed in *Ras/Braf*-wt (CSphC#14, 21, 33), *Braf*- (CSphC#1, 2, 3, 5) and *Kras*- (CSphC#8, 11, 16) mutant CD44v6 fractions. (J) Immunofluorescence analysis for HER2 and CD44v6 on CD44v6⁺ and CD44v6⁻ in *Ras/Braf*-wt (CSphC#21), *Braf*- (CSphC#2) and *Kras*- (CSphC#11) mutant cells. Nuclei were counterstained with TOTO-3. Data are representative of 2 independent experiments performed with *Ras/Braf*-wt (CSphC#14, 21), *Braf*- (CSphC#2, 5) and *Kras*- (CSphC#8, 11) mutant sphere cells. Scale bars, 10 μ m. (K) Browser view of RNA-seq analysis on *Braf*-mutant CD44v6 positive (green) and negative (red) CSphCs. The tracks of expression (RPKM normalized) for *ERRB2* (Upper panel) and *Gapdh* (Lower panel) are shown. For each cell type, tracks of three different biological replicates are shown.

Supplementary Figure 2. PI3K activation is associated with increased *ErbB2* transcription levels.

(A) Unsupervised clustering of RNA-seq data from CD44v6^{high} (>70%) and CD44v6^{low} (<30%) cells. (B) LogFC values of a subset of statistically differentially expressed genes, enriched for PI3K pathway, in CD44v6^{high} vs CD44v6^{low} cells. Data were computed by limma package in R. (C) (Upper panels) Schematic diagram of OFP CRISPR Nuclease and donor DNA (pMA-T) vectors. (Lower panels) Electropherograms showing the DNA sequence of *Pik3ca*-wt low expressing HER2 CR-CSphC lines (CSphC#23, 5, 15), following targeted genome editing. Red stars indicate the newly introduced point mutation (red letters G \rightarrow A). crRNA=CRISPR RNA; tracr=trans-activating crRNA; Pol III=terminator. (D) Bar graphs of immunoblot band densities for HER2, pAKT and AKT on *Ras/Braf*-wt (CSphC#6, 23), *Braf*- (CSphC#2, 5), *Kras*- (CSphC#10, 15) mutant cells and their corresponding CRISPR/Cas9-*Pik3ca*^{E545K} cells. Data are mean \pm S.D. of 3 independent experiments performed with the indicated CSphCs. (E) ChIP-qPCR for the histone marks H3K27Ac using amplicons for 2 promoters (Prom1 and Prom2), 3 potential enhancer regions (Enh1, Enh2, and HGE) and negative control (Control) in IMEC, IMEC-MYC and IMEC-MYC-PI3K cells. Enrichment is indicated as % of input. (F) Percentage of viable CD44v6 low ($\leq 30\%$),

medium (31-69%) and high ($\geq 70\%$) cells treated with miransertib, BKM120 and taselisib for 72 hours. Boxes and whiskers represent median \pm S.D. of 3 experimental replicates of 29 CR-CSphC lines. (G) Percentage of cell viability in 29 CR-CSphC lines, harboring the indicated mutations, exposed to different doses of PI3K and AKT inhibitors as indicated. Boxes and whiskers represent median \pm S.D. of 3 experimental replicates of 29 CR-CSphC lines. (H) Percentage of cell viability of CD44v6⁺ and CD44v6⁻ *Braf*⁻ (CSphC#2, 3, 4, 5) and *Kras*⁻ (CSphC#8, 9, 10, 11, 16) mutant sphere cells treated with BKM120. Data are mean \pm S.D. from 3 independent experiments. (I) mRNA expression levels of *ErbB2* in CSphCs and CD44v6⁺ enriched cells treated as indicated for 48 hours. Data are mean \pm S.D. of 3 independent experiments performed with *Ras/Braf*-wt (CSphC#14, 33), *Braf*⁻ (CSphC#1, 5) and *Kras*⁻ (CSphC#10, 11) mutant sphere cell lines. (J) *ErbB2* mRNA expression levels in CSphCs treated with vehicle or taselisib in presence of CAF CM. Data are mean \pm S.D. of 3 independent experiments using *Ras/Braf*-wt (CSphC#7, 27), *Braf*⁻ (CSphC#2, 3) and *Kras*⁻ (CSphC#12, 20) mutant sphere cell lines. (K) *ErbB2* mRNA expression levels in tumor xenografts treated with vehicle or BKM120 for 4 weeks. Mice were sacrificed 1 weeks after treatment suspension. Data are means \pm S.D. of 6 mice per group injected with *Ras/Braf*-wt (CSphC#14, 21, 33), *Braf*⁻ (CSphC#1, 2, 5) or *Kras*⁻ (CSphC#8, 11, 16) mutant sphere cells. (L) Representative immunofluorescence analysis for HER2 on tumor xenografts generated by the injection of *Braf*⁻ (CSphC#2) mutant sphere cells and treated as in K. Nuclei were counterstained with Toto-3 (blue color). Scale bars, 20 μ m.

Supplementary Figure 3. Triple targeting of HER2, MEK and PI3K overcomes the protective effect mediated by CAF-released cytokines. (A) Size of xenograft tumors generated by subcutaneous injection of *Braf*⁻ (CSphC#1, 2, 3, 5) and *Kras*⁻ (CSphC#8, 11, 16) mutant cells, treated for 4 weeks as indicated and monitored up to 10 weeks. "I" indicates the time of cell injection. Time-point 0 indicates the start of treatment. Data are mean \pm S.D. of 3 independent experiments (n=6 mice per group). (B) RPPA analysis of *Ras/Braf*-wt (CSphC#14), *Braf*⁻ (CSphC#2) and *Kras*⁻ (CSphC#11) mutant cells treated with vehicle or vemurafenib (Vemu) in combination with trastuzumab (Tmab) and PI3K inhibitor (BKM120) (VTB). Total and phosphorylated S6 are indicated. (C) Relative band densities of immunoblots for pAKT, AKT, pGSK, GSK3, pERK, ERK and Myc in tumor xenografts-derived cells of mice injected with *Ras/Braf*-wt (CSphC#14, 21, 33), *Braf*⁻ (CSphC#1, 2, 3), *Kras*⁻ (CSphC#8, 11, 16) mutant sphere cells treated with vehicle (Vehicle) or vemurafenib (Vemu) in combination with trastuzumab (Tmab) and PI3K inhibitor (BKM120) (V+T+B). Data are expressed as mean \pm S.D. of 3 subcutaneously implanted CSphC lines for each mutational status (n= 6 mice per group). (D) (Left panel) Representative average of miRNAs equivalent CT values on tumor xenograft-derived cells isolated from mice injected with *Kras*⁻ (CSC#8) mutant CR-CSphCs treated with vehicle (Vehicle) or vemurafenib in combination with trastuzumab plus PI3K inhibitor (Vemu+Tmab+BKM120). (Right panel) Clustergrams of miRNAs expression levels of those indicated with arrows in the correlation plot. Data are representative of 3 independent experiments performed with 3 different CR-CSphCs (CSC#8, 11, 16). (E) Bar graphs of immunoblot relative band densities for pAKT, AKT, pGSK, GSK, pERK, ERK and Myc in *Ras/Braf*-wt, *Braf*⁻ and *Kras*⁻ mutant sphere cells treated with vehicle (Vehicle) or trastuzumab (Tmab) in combination with trametinib (MEKi) and PI3K inhibitor (BKM120) (T+Mi+B). Data are mean \pm S.D. of 3 independent experiments performed with *Ras/Braf*-wt (CSphC#14, 21, 33), *Braf*⁻ (CSphC#1, 2, 3) and *Kras*⁻ (CSphC#8, 11, 16) mutant sphere cultures. (F) RPPA analysis of *Braf*⁻ (CSphC#2) and *Kras*⁻ (CSphC#11) mutant cells treated with vehicle or trastuzumab (Tmab) in combination with trametinib (MEKi) and PI3K inhibitor (BKM120) (TMiB) for 24 hours. Total and phosphorylated S6 expression levels are indicated. (G) Heatmap of viability percentage of cells with the indicated mutational background treated with vehicle (Vehicle) or trastuzumab in combination with MEKi and BKM120 (T+Mi+B) for 72 and 120 hours. Data are the mean of 3 experimental replicates performed on 30 cell lines. (H) (Left panel) Representative average of miRNAs equivalent CT values on *Kras*⁻ (CSC#11) mutant CR-

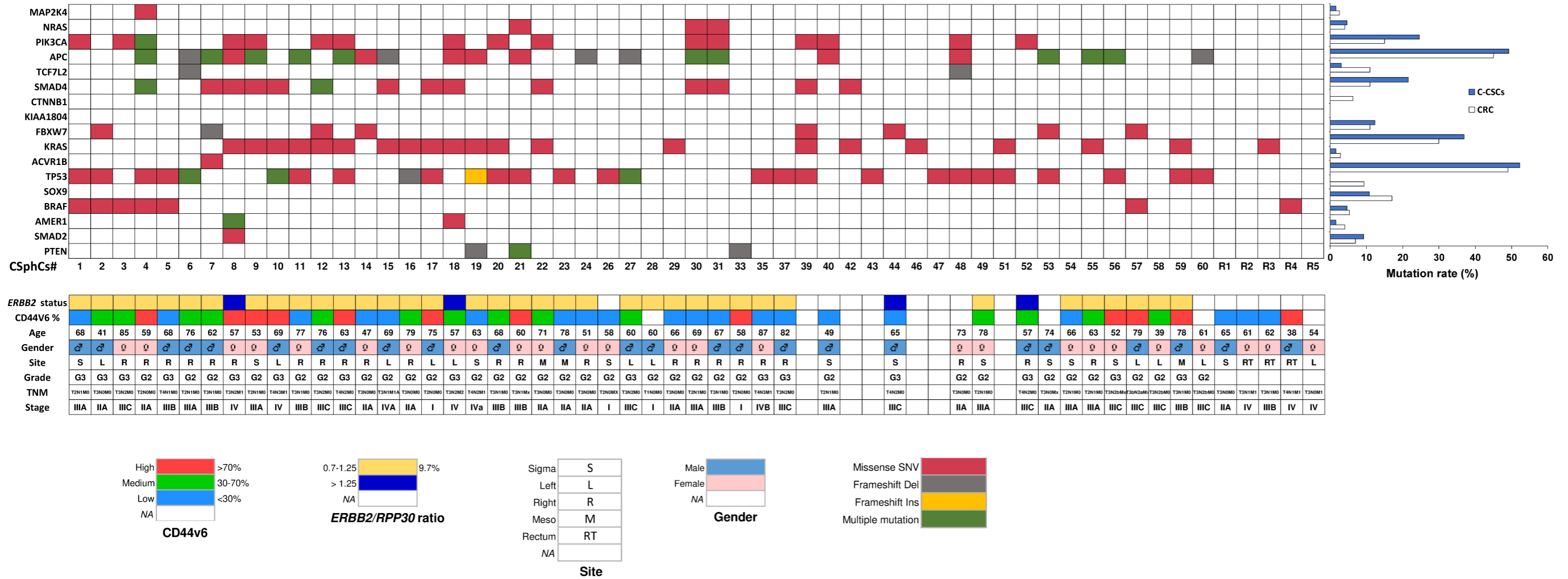
CSphCs, exposed to the indicated therapeutic regimen combinations. Before treating with trastuzumab in combination with MEK inhibitor and BKM120 (Tmab+MEKi+BKM120) for 24 hours, cells were pre-treated with vemurafenib in combination with trastuzumab and BKM120 for 5 days and maintained for 2 days off-drug period. (*Right panel*) Clustergrams of miRNAs expression levels, indicated with arrows in the correlation plot. Data are representative of 3 independent experiments performed with different CR-CSphCs (CSC#8, 11, 16). (**I**) Bar graphs of immunoblot relative band densities for pAKT, AKT, pMEK, MEK, pERK, ERK and Myc in *Braf*⁻ (#1, 2, 3) *Kras*⁻ (CSphC#8,11, 16) mutant sphere cells treated with vehicle (Vehicle) or vemurafenib (V) in combination with trastuzumab (T) and BKM120 (V+T+B) or trastuzumab in combination with MEKi and BKM120 (T+Mi+B) and cultured in FBS-free DMEM or CAF CM for 24 hours. Data are expressed as mean \pm S.D. of 3 independent experiments. (**J**) Growth of cells previously untreated (Vehicle) or treated with vemurafenib in combination with trastuzumab and BKM120 (Pre-treated V+T+B) for 5 days and exposed to trastuzumab in combination with MEKi and BKM120 (T+Mi+B) or V+T+B. Data are expressed as mean \pm S.D. of 4 independent experiments performed with 15 CR-CSphCs with different mutational backgrounds.

Supplementary Figure 4. The triple targeting of MEK, HER2 and PI3K induces regression of xenograft tumors generated by the injection of CR-CSCs. (**A**) Subcutaneous size of tumor xenografts generated by sphere cell lines bearing the indicated mutational background and treated as indicated. Time-point “I” indicates cell injection and 0 the start of treatment. Data are mean \pm S.D. of 3 independent experiments (n=6 mice per group). (**B**) H&E and immunohistochemical analysis of CD44v6, Ki67 and CK20 on tumor xenografts generated by the injection of *Braf*⁻ (CSphC#2) mutant sphere cells. Mice were treated for 4 weeks with vehicle (Vehicle) or trastuzumab (Tmab) plus trametinib (MEKi) plus BKM120 (BKM120). (**C**) Evaluation of CD44v6 positivity by flow cytometry in CR-CSphCs obtained from *Ras/Braf*-wt, *Braf*⁻ and *Kras*⁻ mutant xenografts treated as indicated, and analyzed 2 weeks after treatment suspension. Data are expressed as mean \pm S.D. of 3 independent experiments performed with *Ras/Braf*-wt (CSphC#21, 24, 33), *Braf*⁻ (CSphC#2, 3, 5) and *Kras*⁻ (CSphC#8, 11, 13) mutant cells. (**D**) Cell viability of the indicated sphere cells exposed for 72 and 120 hours to trastuzumab (Tmab) in combination with cobimetinib (Cob) and tselisib (Tas). Data are expressed as mean \pm S.D. of 4 independent experiments. (**E**) Subcutaneous outgrowth of *Kras*⁻ (CSphC#8, 9, 11, 13) mutant sphere cell-derived xenograft tumors at the indicated weeks and treated with vehicle (Vehicle) or trastuzumab (Tmab) in combination with cobimetinib (Cob) and tselisib (Tas) for 4 weeks. Data are means \pm S.D. of tumor size for each cell line (n= 6 mice per group). “I” indicates the time of cell injection and 0 the start of treatment. (**F**) CD44v6 flow cytometry analysis on cells dissociated from tumor xenografts treated as in (E). Grey histograms represent the relative isotype matched control. (**G**) Representative azan mallory staining and immunohistochemical analysis of CD44v6, CK20 and Ki67 on tumor xenografts obtained from the injection of *Kras*⁻ (CSphC#9, 11) mutant sphere cells treated as indicated. Scale bars, 100 μ m.

REFERENCES

- 1 Todaro M, Alea MP, Di Stefano AB, Cammareri P, Vermeulen L, Iovino F, *et al.* Colon cancer stem cells dictate tumor growth and resist cell death by production of interleukin-4. *Cell stem cell* 2007;**1**:389-402.
- 2 Gevensleben H, Garcia-Murillas I, Graeser MK, Schiavon G, Osin P, Parton M, *et al.* Noninvasive detection of HER2 amplification with plasma DNA digital PCR. *Clinical cancer research : an official journal of the American Association for Cancer Research* 2013;**19**:3276-84.
- 3 Takegawa N, Yonesaka K, Sakai K, Ueda H, Watanabe S, Nonagase Y, *et al.* HER2 genomic amplification in circulating tumor DNA from patients with cetuximab-resistant colorectal cancer. *Oncotarget* 2016;**7**:3453-60.
- 4 Li J, Zhao W, Akbani R, Liu W, Ju Z, Ling S, *et al.* Characterization of Human Cancer Cell Lines by Reverse-phase Protein Arrays. *Cancer cell* 2017;**31**:225-39.
- 5 Fagnocchi L, Cherubini A, Hatsuda H, Fasciani A, Mazzoleni S, Poli V, *et al.* A Myc-driven self-reinforcing regulatory network maintains mouse embryonic stem cell identity. *Nature communications* 2016;**7**:11903.
- 6 Poli V, Fagnocchi L, Fasciani A, Cherubini A, Mazzoleni S, Ferrillo S, *et al.* MYC-driven epigenetic reprogramming favors the onset of tumorigenesis by inducing a stem cell-like state. *Nature communications* 2018;**9**:1024.

Supplementary Table 1. Cancer sphere cells and their mutational profiles, ERBB2 status and CD44v6 expression.



COSMIC-reported mutation of the analyzed genes (*upper panel*). Mutation types (missense SNV, frameshift deletion or insertion, and multiple mutations) are indicated. Percentage of mutation rate in CRC patients reported in TCGA database (white bars) and in C-CSCs (blue bars) are indicated on the right. ERBB2 status and CD44v6 expression of CSphCs and clinical data related to CRC patients are reported (*lower panel*).

Chapter 3

Pharmacological targeting of the novel β -catenin chromatin-associated kinase p38 α in colorectal cancer stem cell tumorspheres and organoids


Martina Lepore Signorile, Valentina Grossi, Simone Di Franco, Giovanna Forte, Vittoria Disciglio, Candida Fasano, Paola Sanese, Katia De Marco, Francesco Claudio Susca, **Laura Rosa Mangiapane**, Annalisa Nicotra, Gabriella Di Carlo, Francesco Dituri, Gianluigi Giannelli, Giuseppe Ingravallo, Gianluca Canettieri, Giorgio Stassi and Cristiano Simone

Published in *Cell Death and Disease*, 2021

ARTICLE

Open Access

Pharmacological targeting of the novel β -catenin chromatin-associated kinase p38 α in colorectal cancer stem cell tumorspheres and organoids

Martina Lepore Signorile¹, Valentina Grossi¹, Simone Di Franco², Giovanna Forte¹, Vittoria Disciglio¹, Candida Fasano¹, Paola Sanese¹, Katia De Marco¹, Francesco Claudio Susca³, Laura Rosa Mangiapane², Annalisa Nicotra², Gabriella Di Carlo⁴, Francesco Dituri⁵, Gianluigi Giannelli⁵, Giuseppe Ingravallo⁴, Gianluca Canettieri⁶, Giorgio Stassi² and Cristiano Simone^{1,3} 

Abstract

The prognosis of locally advanced colorectal cancer (CRC) is currently unsatisfactory. This is mainly due to drug resistance, recurrence, and subsequent metastatic dissemination, which are sustained by the cancer stem cell (CSC) population. The main driver of the CSC gene expression program is Wnt signaling, and previous reports indicate that Wnt3a can activate p38 MAPK. Besides, p38 was shown to feed into the canonical Wnt/ β -catenin pathway. Here we show that patient-derived locally advanced CRC stem cells (CRC-SCs) are characterized by increased expression of p38 α and are “addicted” to its kinase activity. Of note, we found that stage III CRC patients with high p38 α levels display reduced disease-free and progression-free survival. Extensive molecular analysis in patient-derived CRC-SC tumorspheres and APC^{Min/+} mice intestinal organoids revealed that p38 α acts as a β -catenin chromatin-associated kinase required for the regulation of a signaling platform involved in tumor proliferation, metastatic dissemination, and chemoresistance in these CRC model systems. In particular, the p38 α kinase inhibitor ralimetinib, which has already entered clinical trials, promoted sensitization of patient-derived CRC-SCs to chemotherapeutic agents commonly used for CRC treatment and showed a synthetic lethality effect when used in combination with the MEK1 inhibitor trametinib. Taken together, these results suggest that p38 α may be targeted in CSCs to devise new personalized CRC treatment strategies.

Introduction

Colorectal cancer (CRC) is the third most frequent malignancy but the second leading cause of death for tumor worldwide¹. The survival rate of affected patients largely depends on the stage at which the tumor is diagnosed. About one-third of CRC patients have stage III

disease, which is characterized by spread to regional lymph nodes and absence of distant metastases². Stage III CRC patients are at high risk for tumor recurrence, and their overall prognosis, for which the N stage has been found to be a reliable indicator, remains unsatisfactory even with curative surgery and adjuvant chemotherapy³. Indeed, it is reported that more than one-third of stage III CRC patients will develop recurrence or metastasis within 5 years of systemic therapy⁴.

CRC stem cells (CRC-SCs) are involved in drug resistance, tumor recurrence, and metastasis after primary treatment. Indeed, conventional therapies wipe out bulk tumor populations, while CRC-SCs are resistant to chemotherapy and radiotherapy⁵. Therefore, new treatment

Correspondence: Valentina Grossi (grossi.labsimone@gmail.com) or Cristiano Simone (cristianosimone73@gmail.com)

¹Medical Genetics, National Institute for Gastroenterology, IRCCS ‘S. de Bellis’ Research Hospital, 70013 Castellana Grotte (Ba), Italy

²Cellular & Molecular Pathophysiology Laboratory, Department of Surgical & Oncological Sciences, University of Palermo, 90127 Palermo, Italy

Full list of author information is available at the end of the article

These authors contributed equally: Martina Lepore Signorile, Valentina Grossi
Edited by G. Blandino

© The Author(s) 2021



Open Access This article is licensed under a Creative Commons Attribution 4.0 International License, which permits use, sharing, adaptation, distribution and reproduction in any medium or format, as long as you give appropriate credit to the original author(s) and the source, provide a link to the Creative Commons license, and indicate if changes were made. The images or other third party material in this article are included in the article's Creative Commons license, unless indicated otherwise in a credit line to the material. If material is not included in the article's Creative Commons license and your intended use is not permitted by statutory regulation or exceeds the permitted use, you will need to obtain permission directly from the copyright holder. To view a copy of this license, visit <http://creativecommons.org/licenses/by/4.0/>.

approaches targeting CRC-SCs are needed in order to achieve complete tumor eradication⁶.

Several dysregulated signaling pathways confer to cancer stem cells (CSCs) a survival advantage over current therapies; among these pathways, the main driver controlling CSC fate is Wnt signaling⁷. During carcinogenesis, increasing amounts of β -catenin resulting from APC inactivation translocate into the nucleus and modulate the transcriptional activity of TCF/LEF transcription factors⁸. High levels of nuclear β -catenin lead to constitutive activation of the Wnt pathway, loss of normal cellular architecture, and neoplastic conversion⁹.

Previous reports indicate that p38 α , one of the four p38 isoforms (α , β , γ , δ), is highly expressed in colorectal neoplasms compared to normal mucosa¹⁰ and is the main p38 isoform in colorectal and ovarian cancer cells^{11–13}. Importantly, Wnts can activate p38 MAPKs. Indeed, Wnt3a was recently shown to stimulate p38 activation in mouse F9 teratocarcinoma cells. Of note, Wnt-induced p38 activation appears to regulate canonical Wnt/ β -catenin signaling⁸, and p38 was found to phosphorylate GSK3 β at Thr390, which inactivates GSK3 β kinase activity, leading to β -catenin accumulation¹⁴.

Our previous results indicate that p38 α is required for CRC cell proliferation and survival, and its inhibition induces growth arrest, autophagy, and cell death both in vitro and in vivo^{11,15–17}. Recently, we demonstrated the existence of a p38 α -ERK synthetic lethality crosstalk that is crucial for CRC therapy response. Indeed, combined inhibition of p38 α and MEK1 efficiently reduced the volume of xenografted tumors and colitis-associated orthotopic tumors in vivo^{10,12}. Besides, resistance to cisplatin (CDDP), irinotecan (CPT-11), and 5-fluorouracil (5-FU) chemotherapy has been shown to involve MAPK signaling, and recent studies identified p38 α MAPK as a mediator of resistance to various agents in CRC patients¹³. Our previous studies also revealed that p38 α inhibition sensitizes chemoresistant CRC cells to CDDP, with the combined treatment inducing Bax-dependent apoptosis in both chemosensitive and chemoresistant cells¹⁸.

p38 α is considered a prototypical chromatin-associated kinase. Indeed, it can associate with and phosphorylate several transcription factors and can recruit subunits of the SWI/SNF ATP-dependent remodeling complexes directly to the DNA, thereby modulating chromatin structure and transcription¹⁹. p38 α also phosphorylates MSK1, which in turn phosphorylates Ser10 on histone H3, inducing a transcriptional activation-permissive chromatin modification²⁰. Additionally, p38 α can physically interact with RNA polymerase II and promote the transcription elongation step²¹.

In recent years, a role has emerged for the p38 pathway in CSC regulation. Indeed, p38 seems to promote survival

in hypoxic and serum-starved CRC-SCs²² and mediates CSC drug resistance to oxaliplatin and anti-angiogenic agents²³. Moreover, p38-inhibited cells showed decreased expression of CSC markers and reduced sphere-forming ability in head and neck squamous cell carcinoma²⁴.

Here, we performed an extensive characterization of p38 α in patient-derived stage III CRC-SCs, identifying it as a direct interactor of β -catenin, the key element of the Wnt pathway. p38 α acts as a chromatin-associated kinase involved in the activation of β -catenin target gene transcription, and its pharmacological manipulation affects various cancer features. Importantly, we show that targeting p38 α may overcome chemoresistance in a CRC-SC model, with p38 α levels being a potential new marker of therapeutic efficacy in stage III CRC patients.

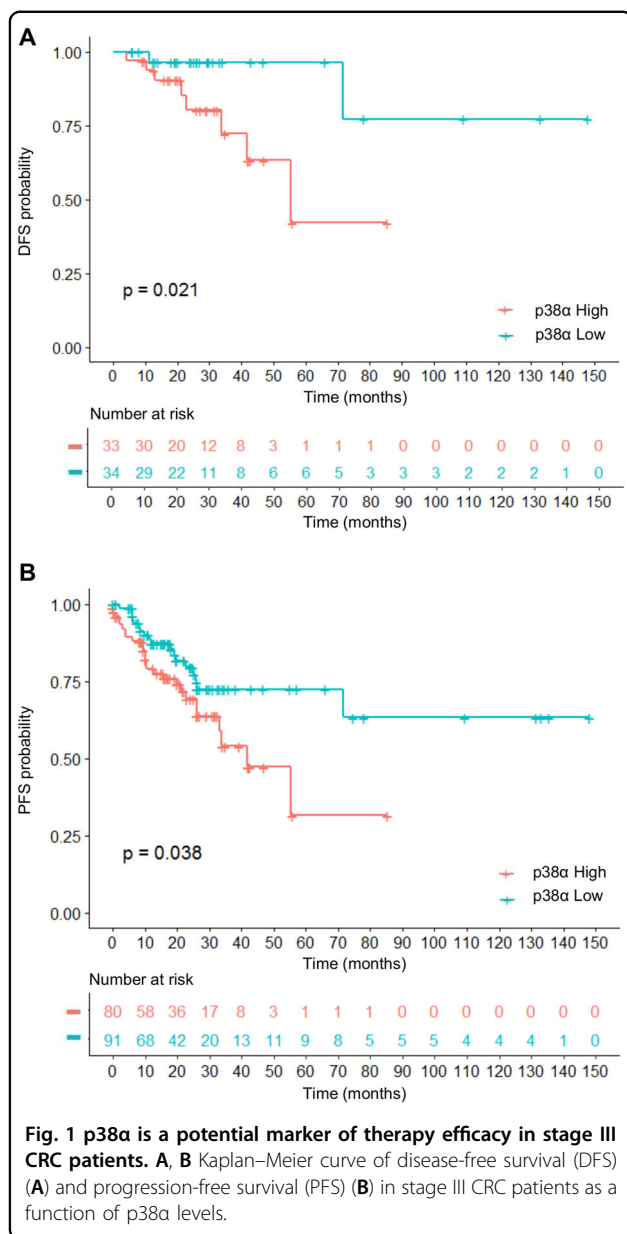
Results

p38 α is a potential marker of therapeutic efficacy in stage III CRC patients

Stage III CRC patients are eligible for adjuvant and combination therapies but still have a poor prognosis. In an attempt to identify potential targets for stage III disease therapy, we performed a meta-analysis on a cohort of colorectal tumor tissues retrieved from The Cancer Genome Atlas (TCGA) PanCancer Atlas. This dataset encompasses clinical data of 580 CRC patients with stage I–IV disease. We stratified the 171 stage III CRC patients based on p38 α mRNA level Z-score and classified them as p38 α high (80 patients) or p38 α low (91 patients) to investigate the association between p38 α expression and prognosis. We found that high expression of p38 α was associated with worse disease-free survival (DFS, p -value = 0.0209) and progression-free survival (PFS, p -value = 0.0382) (Fig. 1A, B).

Establishment and characterization of patient-derived stage III CRC-SCs

Patient-derived CRC-SCs are currently used as a model to evaluate drug response²⁵. We thus characterized various CRC cell lines established from stage III CRC patients and grown as tumorspheres by analyzing their mutation status, chromosomal and microsatellite instability (MSI), and expression of a group of surface markers (Fig. S1A, B). Immunoblot analysis showed increased amounts of c-Myc in patient-derived CRC cells compared to HCEC-1CT normal colonocytes and the CRC cell lines HCT116 and HT29. Notably, patient-derived CRC-SCs also proved rich in β -catenin, phospho-p38, and the stem cell markers CD44 and CD133, while expressing low levels of keratin 20, a major cellular protein found in mature enterocytes (Fig. S1B). All patient-derived CRC-SC lines (#8, #9, #21, and #40) used in this study were also found to express high levels of phospho-p38 α (p-p38 α , i.e., p38 α -active form) (Fig. S1C). In order



to characterize our CRC-SC-based pre-clinical model, we performed immunohistochemical analyses showing that CRC-SCs recapitulate parental tumor histological features and cellular heterogeneity in terms of p-p38 α expression and nuclear localization. Interestingly, p-p38 α expression is maintained in CRC-SCs even after the *in vivo* passage, as demonstrated by the analysis of tumor xenografts generated by subcutaneous injection of CRC-SCs (Fig. 2A). Importantly, our results also showed that most cells expressing CD44v6, an alternative splicing form of CD44 playing a major role in cancer progression, cell migration, and invasion²⁶, are characterized by nuclear localization of p-p38 α , thus suggesting that activation of p38 α is crucial for CRC-SCs (Fig. 2B).

p38 α is a new functional member of β -catenin complexes

In order to characterize the functional relationship between p38 α and the Wnt/ β -catenin pathway in CRC, we assessed p38 α and β -catenin protein localization in our colorectal model systems.

HCEC-1CT and HT29 cells were serum-starved to retain β -catenin in the cytoplasm and then switched to a serum-containing medium with or without LiCl, a well-established agonist of the Wnt/ β -catenin pathway. Immunoblot analysis confirmed that expression of β -catenin and its direct target gene *c-Myc* is barely detectable under serum starvation, while it increases substantially after serum stimulation. Interestingly, p38 α showed the same nuclear/cytoplasmic localization of β -catenin under all treatment conditions. Specifically, both were predominantly found in the nucleus in the CRC cell line, while they were primarily located in the cytoplasm in HCEC-1CT cells (Fig. S2A). These data were corroborated by immunofluorescence staining (Fig. S2B).

Experiments performed in patient-derived stage III CRC-SC tumorspheres cultured with or without a Wnt/ β -catenin pathway inhibitor (PRI-724) or activator (Wnt3a alone or in combination with LiCl) confirmed p38 α - β -catenin nuclear/cytoplasmic co-localization under all treatment conditions also in these cells (Fig. S2C).

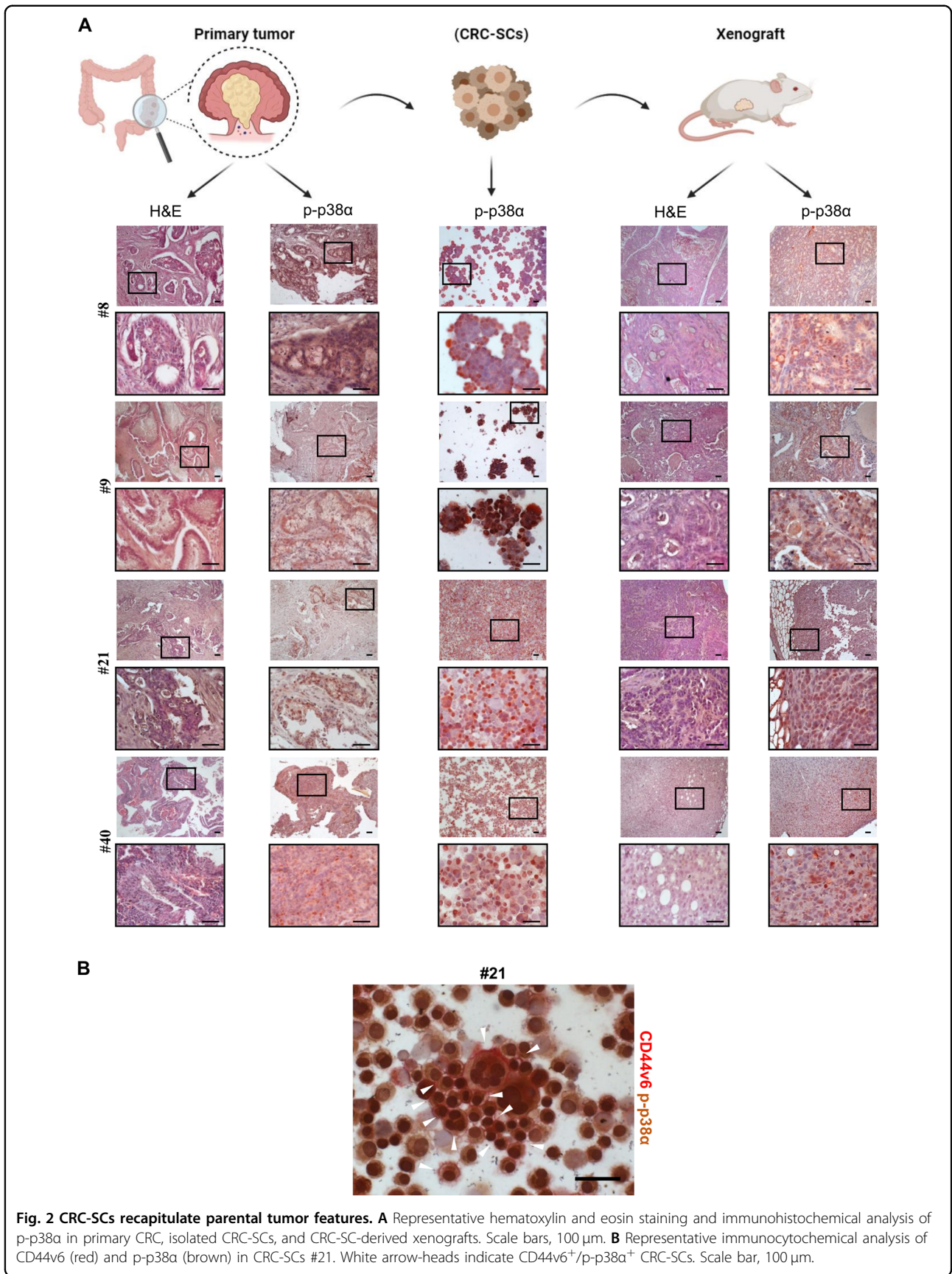
These results prompted us to ascertain whether p38 α directly interacts with β -catenin. We thus performed an *in vitro*-binding assay between a full-length His-tagged β -catenin recombinant protein and a GST-tagged p38 α fusion protein, using GST-p300-320-530 as a positive control²⁷, and found that p38 α directly interacts with β -catenin *in vitro* (Fig. 3A).

Of note, co-immunoprecipitation (Co-IP) experiments performed in HEK293 cells transiently transfected with HA-tagged p38 α and FLAG-tagged β -catenin confirmed that this interaction also occurs *in cellulo* (Fig. 3B).

Next, we evaluated whether endogenous p38 α is a partner of β -catenin complexes in our colorectal model systems. Immunoprecipitation of whole-cell lysates with an antiserum against p38 α or β -catenin, followed by immunoblotting, indicated that p38 α is a molecular partner of β -catenin complexes in these cells (Figs. 3C; S3A).

Further immunoprecipitation experiments in HCEC-1CT, HT29 cells, and patient-derived CRC-SCs subjected to a cellular fractionation protocol revealed that p38 α and β -catenin co-immunoprecipitate mainly in the cytoplasm in normal colonocytes but predominantly in the nucleus in CRC cells and patient-derived CRC-SCs (Fig. 3D, E; S3B).

To validate the results obtained *in cellulo*, we performed *in vivo* experiments in APC^{Min/+} mice, which are heterozygous for a missense mutation in the APC gene and model human familial adenomatous polyposis (FAP) as they develop multiple intestinal polyps that acquire carcinoma features after exposure to the carcinogen drug



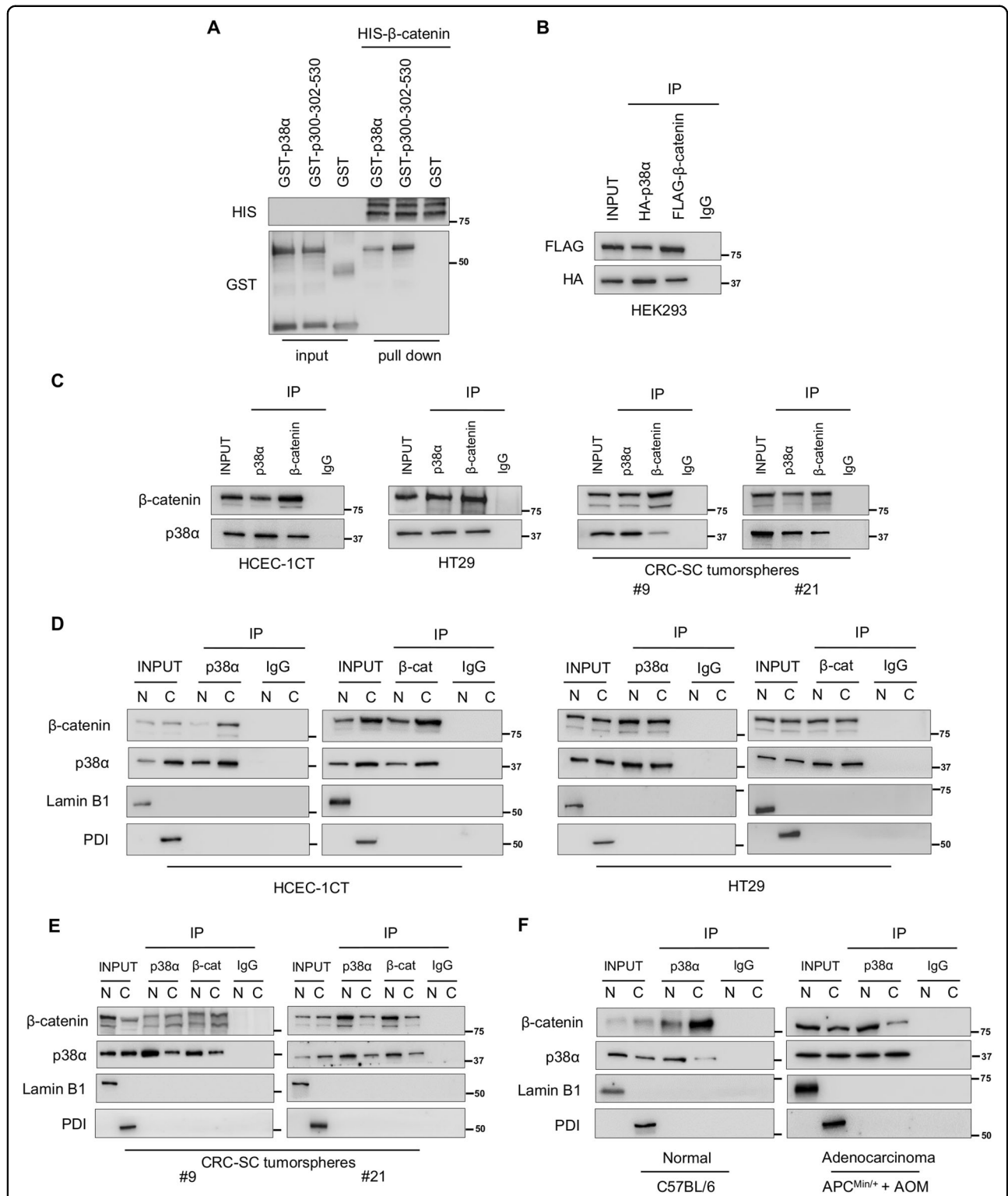


Fig. 3 Functional interaction between p38α and β-catenin in in vitro models of CRC. **A** In vitro binding assay between GST-p38α fusion protein and HIS-β-catenin. Bound proteins were analyzed by immunoblotting using anti-GST and anti-HIS antibodies. **B** Co-immunoprecipitation with anti-HA and anti-FLAG antibodies in HEK293 cells overexpressing HA-p38α or FLAG-β-catenin. **C** Co-immunoprecipitation of endogenous p38α and β-catenin in the indicated cells. **D** and **E** Co-immunoprecipitation of endogenous p38α and β-catenin in nuclear and cytoplasmic fractions of the indicated cells. **F** Co-immunoprecipitation of endogenous p38α and β-catenin in nuclear and cytoplasmic fractions from C57BL/6 mice normal colon tissue and AOM-treated APC^{Min/+} mice adenocarcinoma tissue. Input corresponds to 10% of the lysate. Anti-IgGs were used as negative controls. Lamin B1: nuclear loading control; PDI: cytoplasmic loading control; N = nucleus, C = cytoplasm, β-cat = β-catenin.

azoxymethane (AOM)²⁸. We found increased levels of p-p38, p-ERK, β -catenin, and c-Myc in mouse colon adenoma and adenocarcinoma compared to normal colon mucosa (Fig. S3C). Moreover, p38 α and β -catenin co-immunoprecipitated mainly in cytoplasmic fractions in normal colon mucosa but mostly in nuclear fractions in adenocarcinoma tissue (Figs. 3F; S3D).

p38 α is a novel β -catenin chromatin-associated kinase

Based on the above findings, it is reasonable to speculate that p38 α may be involved in β -catenin transcriptional activity in the nucleus of cancer cells. To confirm this hypothesis, we performed a dual-luciferase reporter assay on a c-Myc promoter-Luc construct²⁹. Intriguingly, overexpression of p38 α in HEK293 cells significantly enhanced transcriptional activity in a manner comparable to β -catenin overexpression. Moreover, concomitant overexpression of both proteins further increased c-Myc transcriptional activity (Fig. 4A).

To investigate the functional role of p38 α and β -catenin complexes in transcriptional regulation, we then evaluated p38 α and β -catenin co-occupancy of various β -catenin target gene promoters by chromatin immunoprecipitation (ChIP). HT29 cells were serum-starved to inhibit β -catenin activity in the nucleus and then switched to a serum-containing medium. ChIP assays revealed that serum mitogens dramatically stimulated β -catenin and p38 α recruitment to Wnt responsive elements (WREs) of several β -catenin target genes, including c-Myc, c-Met, Survivin, and CD44, which are all involved in CRC progression (Fig. 4B). Re-ChIP experiments were then performed to confirm β -catenin and p38 α co-occupancy, providing evidence that these proteins bind to the same chromatin regions after serum stimulation (Fig. 4B). Similar results were obtained in CRC-SCs, which showed co-recruitment of p38 α and β -catenin on β -catenin-binding motifs of all analyzed target genes. This occurred to an even higher extent when cells were cultured with the Wnt pathway activator Wnt3a. These data suggest that p38 α supports β -catenin in the activation of β -catenin target gene transcription in these cells (Figs. 4C; S3E).

Subsequently, we investigated the effect of p38 α pharmacological inhibition (with the selective inhibitor ralimetinib) or genetic ablation (with two specific siRNAs) on the regulation of β -catenin target gene expression. Real-time PCR experiments showed that treatment of HT29 cells with ralimetinib or specific siRNAs leads to the downregulation of β -catenin target genes, including CD44 and Cyclin D1 (cell cycle markers), Survivin (apoptosis inhibition), c-MET (migration and invasion), and SOX9 and TCF7 (CSC proliferation markers) (Fig. 4D). These data were confirmed in patient-derived CRC-SCs treated with Wnt3a and/or ralimetinib and/or the Wnt pathway inhibitor PRI-724, and suggest that p38 α is involved in the

activation of β -catenin target gene transcription in CRC cells and patient-derived CRC-SC tumorspheres (Fig. 4E).

β -catenin transcriptional activity is regulated by well-known phosphorylation signals in the N-terminus and C-terminus regions³⁰. We thus searched for novel β -catenin residues that could be directly phosphorylated by p38 α . Since 85% of the p38 α phosphorylation sites described so far are Ser-Pro or Thr-Pro motifs³¹, we performed an in silico phosphorylation prediction analysis with DISPHOS 1.3, NETPHOS 3.1, Phosida, iPTMnet, and Phosphosite Plus servers, focusing on serine and threonine residues. We identified eight putative phosphosites (S47, S129, S179, S222, T472, T547, S680, and S721) that were recognized by at least four prediction servers (Fig. S4). Of note, many of these residues have been described as being phosphorylated in vivo in different human cancers^{32,33}. These findings suggest that β -catenin may be a substrate of p38 α . To verify this hypothesis, we performed an in vitro kinase assay using purified proteins. Our results showed that active p38 α can efficiently phosphorylate β -catenin (Fig. 4F). Furthermore, we carried out Co-IP studies to ascertain whether activation of p38 α is required for the physical interaction with β -catenin in CRC-SC tumorspheres. Our results showed that p38 α active form (p-p38 α) interacts with β -catenin and p38 α pharmacological inhibition with ralimetinib does not prevent the formation of the complex (Fig. S5A–C).

p38 α inhibition downregulates CRC-SC markers in an in vivo model

We previously detected a significant reduction in tumor size in the small intestine and colon of APC^{Min/+} mice treated with the p38 α inhibitor SB202190¹¹. Moreover, we observed malignant regression, with foci of inflammatory cells replacing adenomatous glands, in tumors of treated animals¹⁰. Thus, to further explore the clinical potential of p38 α pharmacological inhibition for β -catenin target gene downregulation, we performed in vivo experiments in this murine model. Four-month-old animals were administered with AOM (14 mg/kg body weight) once a week for 5 weeks; one month later, they were subjected to daily intraperitoneal injections of SB202190 (0.05 μ mol/kg body weight) or DMSO for 14 days and then sacrificed (Fig. 5A). Analysis of hematoxylin and eosin-stained colon sections revealed the presence of several variably pedunculated adenomatous polyps in DMSO-treated APC^{Min/+} mice, with most glands showing irregular margins and stratified pencil-shaped nuclei of various sizes. In contrast, intestinal polyps detected in SB202190-treated animals were not pedunculated, and an overall regression of adenomatous morphology was observed (Fig. 5B). Immunohistochemical analysis of healthy colon sections from C57BL/6 control mice showed no nuclear p-p38 α or c-Myc staining, while cyclin D1 expression was limited to gland pits, and

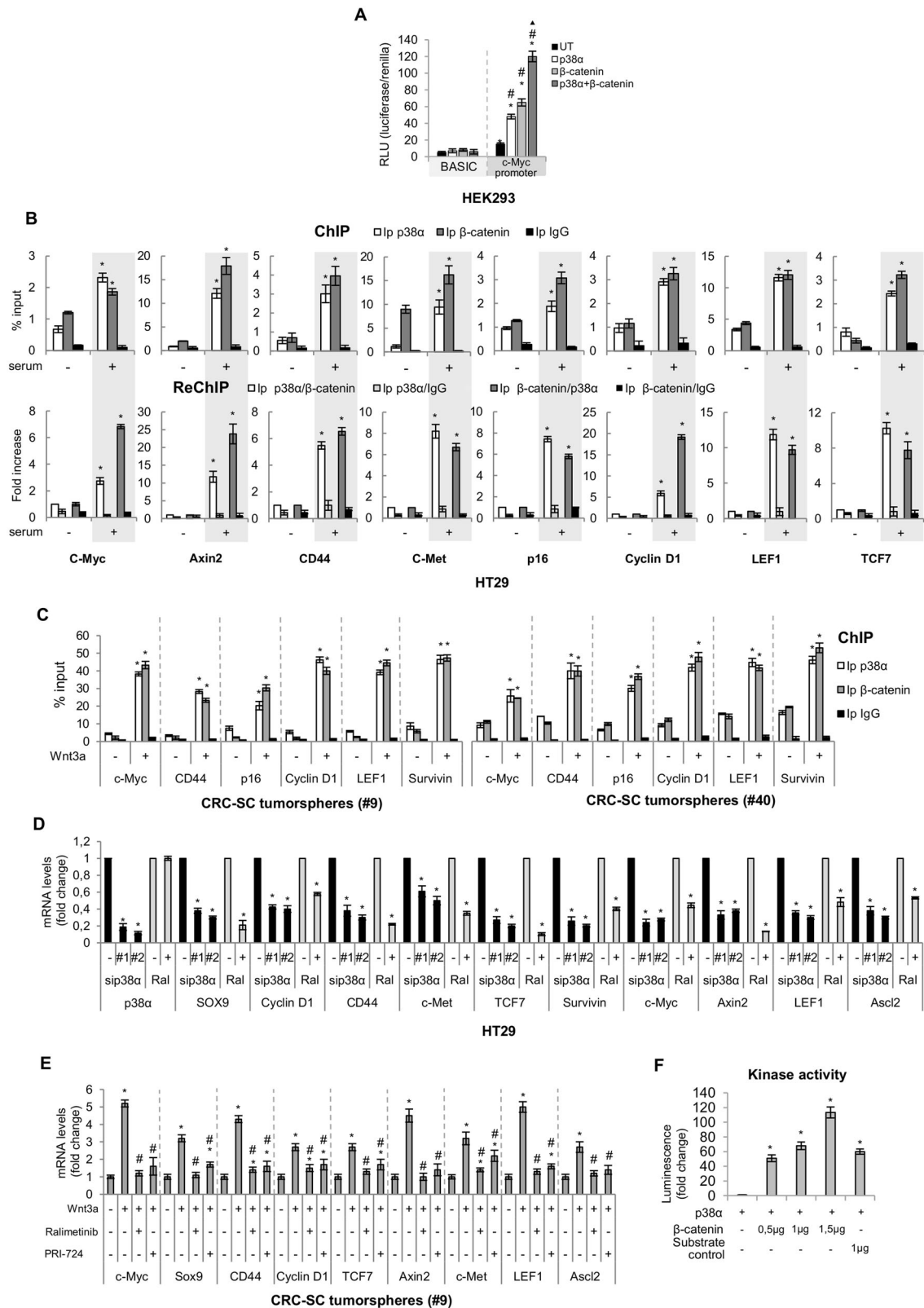


Fig. 4 (See legend on next page.)

(see figure on previous page)

Fig. 4 p38 α is a novel β -catenin chromatin-associated kinase. **A** Luciferase assay for c-Myc promoter activity. HEK293 cells were serum-starved for 24 h and transfected with either the empty vector (pcDNA) or pcDNA3.1-HAHA-p38 α and/or pcDNA- β -catenin expression constructs. **B** Chromatin immunoprecipitation (ChIP) and re-ChIP assays in HT29 cells. Cells were serum-starved for 48 h and then switched to a serum-containing medium for 4 h. In ChIP assays (upper panels), chromatin was pulled down with anti-p38 α and anti- β -catenin antibodies. In re-ChIP assays (lower panels), chromatin was pulled down with anti-p38 α antibodies and then re-immunoprecipitated with anti- β -catenin antibodies and vice versa. Anti-IgGs were used as negative controls. **C** ChIP with anti-p38 α and anti- β -catenin antibodies. CRC-SC tumorspheres were treated or not with Wnt3a (50 ng/ml) for 4 h. **B, C** Quantification was done using the % input method. **D** Real-time PCR analysis of β -catenin target genes in HT29 cells treated with ralimetinib (10 μ M) or two p38 α -specific siRNAs (sip38 α #1 and #2) for 48 h. **E** Real-time PCR analysis of β -catenin target genes in CRC-SC tumorspheres treated with Wnt3a (50 ng/ml) for 4 h with or without ralimetinib (10 μ M) or PRI-724 (25 nM) for 20 h. **D, E** Data are presented as mRNA fold change vs. control. **F** In vitro kinase assay showing β -catenin phosphorylation by p38 α . UT = untransfected. **A** * P < 0.05 vs. BASIC, # P < 0.05 vs. untransfected cells, Δ * P < 0.05 vs. p38 α -transfected or β -catenin-transfected cells. **B** * P < 0.05 vs. serum-starved cells. **C, E** * P < 0.05 vs. untreated cells, and # P < 0.05 vs. Wnt3a-treated cells. **D** * P < 0.05 vs. control (DMSO or control siRNA). **F** * P < 0.05 vs. active p38 α .

sporadic staining was detected for CD44v6. Conversely, in AOM-treated APC^{Min/+} mice colon sections, p-p38 α staining showed high nuclear positivity in vehicle-injected animals, whereas decreased expression was detected in epithelial cells of SB202190-treated animals. Importantly, considerable neoplastic regression was observed in SB202190-injected mice colon tumors. Histopathological analysis also revealed significantly detectable neutrophilic and lymphoid infiltrates in all tumors treated with the p38 α inhibitor. Moreover, nuclear c-Myc and cyclin D1 staining was detected in colon sections from vehicle-treated mice, while colon tumors from SB202190-injected animals showed faint cytoplasmic positivity with a stronger reduction in nuclear areas. In control tumor samples, staining for CD44v6 was observed at the bottom of intestinal crypts, where CRC-SCs reside, while no staining was detected in the crypts from tumors treated with SB202190 (Fig. 5C). These results confirmed that p38 α pharmacological inhibition induces the downregulation of CRC-SC markers, which likely reflects a reduction in the resistant tumor cell population. The above data further strengthen the potential of p38 α inhibition in CRC in vivo.

Targeting p38 α in patient-derived CRC-SCs to circumvent chemoresistance

CRC-SC cultures are heterogeneous and comprise variable amounts of differentiated and CSC populations²⁶. In order to evaluate the specific effect of p38 α inhibition on CSCs versus differentiated cells in CRC-SC cultures, cell samples enriched for the top 20% CD44v6^{high} or CD44v6^{low} subsets by cell sorting (Fig. S6) were treated with ralimetinib and scored for viability and clonogenic potential. Our results showed that pharmacological inhibition of p38 α reduces the proliferative capacity of both the CSC and the differentiated/progenitor cell compartments, identified as CD44v6^{high} and CD44v6^{low}, respectively (Fig. 6A, B). Importantly, our results also indicate that pharmacological inhibition of p38 α significantly reduced the clonogenic potential of both cell subsets (Fig. 6C).

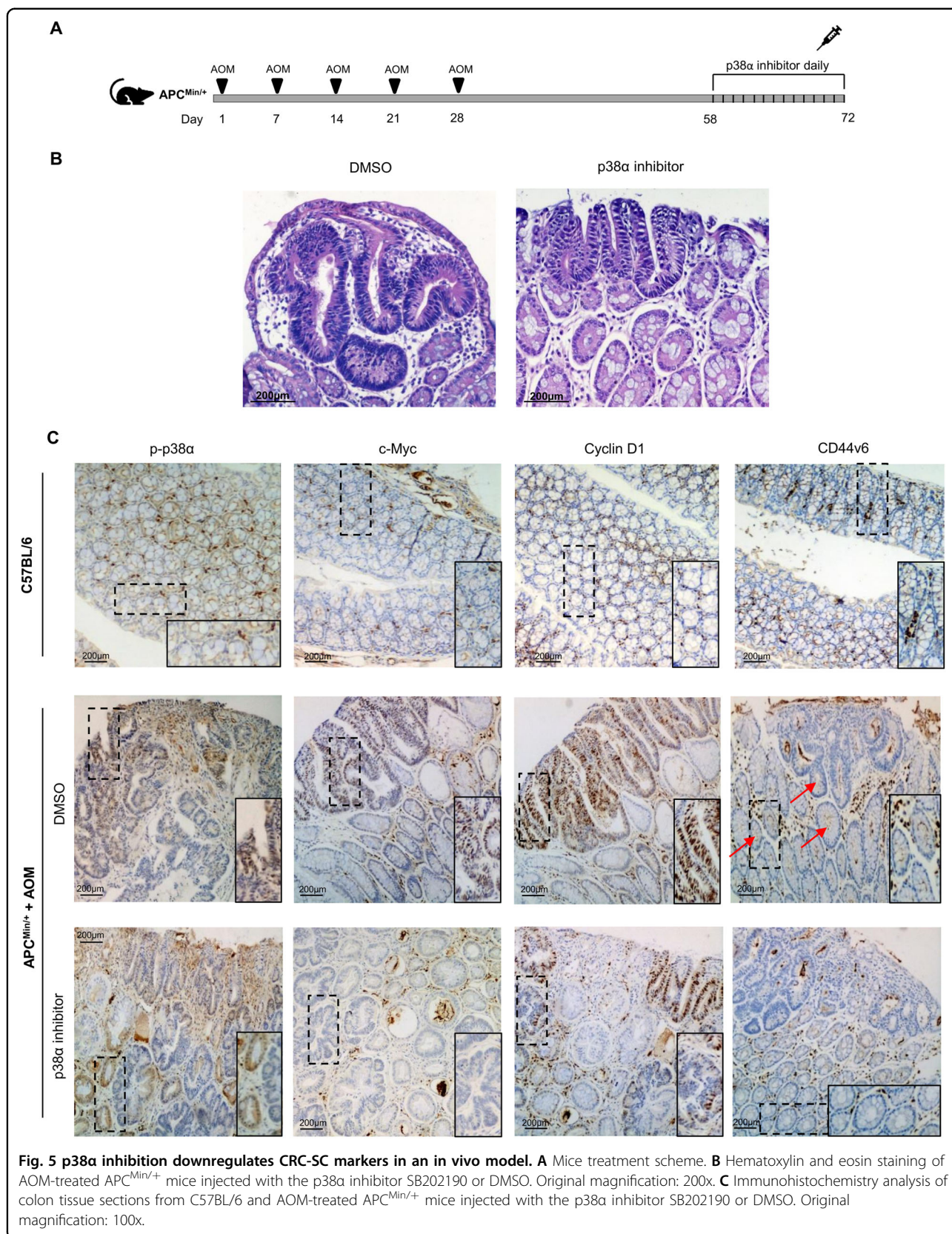
Since CSCs are involved in drug resistance and disease recurrence, we evaluated the potential of ralimetinib as a sensitizing agent in chemoresistant CRC-SCs as part of a synergistic approach with currently used chemotherapeutics (CHTs), such as 5-FU, CDDP, CPT-11, or trametinib, a MEK1 inhibitor that is already approved for clinical use (Fig. 6D).

To this end, CRC-SCs pre-treated with ralimetinib for 48 h were subsequently treated with CHTs/trametinib for 24 h. Our results revealed that the combined therapeutic strategy (ralimetinib + CHTs/trametinib) has nonlinear cumulative effects and is more effective than CHTs/trametinib alone. Indeed, pre-treatment with ralimetinib reduced CRC-SC proliferative index (Figs. 6E; S7A) and increased cell death (Figs. 6F; S7B). These data support the potential of p38 α inhibition to enhance sensitivity to CHTs.

Then, we performed a soft agar assay to assess the ability of patient-derived CRC-SCs to form colonies of anchorage-independent tumor cells. Our results showed that combined treatment with ralimetinib and CHTs or trametinib almost completely abolishes CRC-SC clonogenic activity compared to each single treatment (Figs. 6G; S7C).

Since patient-derived CRC-SCs grow as spheres, we also performed a spheroid-based migration assay to assess their invasive capacity. We found that co-treatment with ralimetinib and CHTs or trametinib leads to a remarkable decrease in CRC-SC migratory ability (Figs. 6H; S7D).

We further investigated the biological impact of co-treatment with ralimetinib and CHTs or trametinib on patient-derived CRC-SC fate by analyzing Ki67 expression and annexin V staining by flow cytometry. Ki67 is commonly used as a marker of cell proliferation; in addition, it is involved in the maintenance of the stem cell niche and thus can also be used as a CSC marker³⁴. Based on our results, pre-treatment with ralimetinib enhanced the growth-inhibitory activity of CHTs and trametinib (Figs. 7A; S7E), and this effect was associated with induction of apoptosis, while no necrosis was observed (Figs. 7B; S7F). Activation of the apoptotic pathway in co-treated CRC-



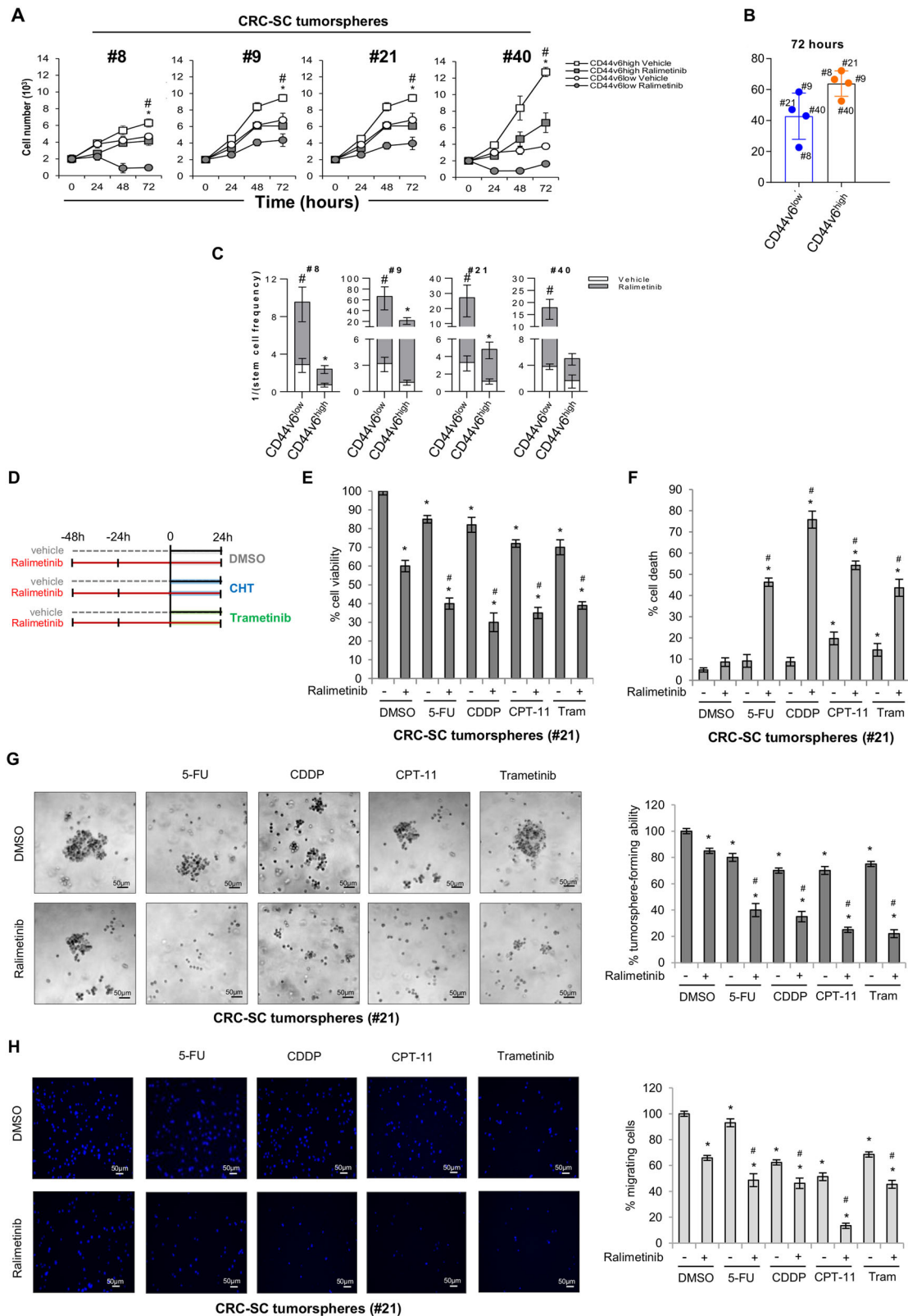


Fig. 6 (See legend on next page.)

(see figure on previous page)

Fig. 6 Targeting p38 α in patient-derived stage III CRC-SCs to circumvent chemoresistance. **A** Growth kinetics of CD44v6^{low}-enriched and CD44v6^{high}-enriched CRC-SCs treated with ralimetinib (10 μ M) or the vehicle for up to 72 h. **B** Viable cell number variation in CD44v6^{low}- and CD44v6^{high}-enriched CRC-SCs treated with ralimetinib (10 μ M) for 72 h. Values were normalized against those of vehicle-treated cells. **C** Limiting dilution assay performed on CD44v6^{low}-enriched and CD44v6^{high}-enriched CRC-SCs. The graph shows the clonogenic capacity of each cell subset. **A–C** CD44v6^{low} and CD44v6^{high} represent cell samples enriched for the top 20% cells with the lowest and highest expression of CD44v6, respectively. **A, C** * P < 0.05: CD44v6^{high} treated with ralimetinib vs. CD44v6^{high} treated with the vehicle; and # P < 0.05: CD44v6^{low} treated with ralimetinib vs. CD44v6^{low} treated with the vehicle. **D** Treatment scheme: CRC-SCs were pre-treated with ralimetinib (10 μ M) for 48 h and then treated with 5-FU (2 μ M), CDDP (30 μ M), CPT-11 (30 μ M), or trametinib (1 nM) for another 24 h in the presence of ralimetinib. **E** Quantification of cell viability by Cell Titer Glo in CRC-SCs #21 treated as described in **(D)**. **F** Quantification of cell death by trypan blue staining in CRC-SCs #21 treated as described in **(D)**. **G** Colony-forming ability of CRC-SCs #21 seeded onto double-layer soft agar and treated as described in **(D)**. Data represent the percentage of colonies relative to DMSO-treated cells. Original magnification: 100x. **H** Migratory ability of growth factor-starved CRC-SCs #21 placed in the inner chamber of transwell plates and treated with the indicated compounds for 16 h. Migrating cells were fixed and counted under a fluorescence microscope. Original magnification: 100x. Tram = trametinib. * P < 0.05: treatment vs. control (DMSO); and # P < 0.05: combined treatment vs. corresponding single treatments.

SCs was further confirmed by immunoblotting for cleaved PARP (Fig. 7C).

As additional evidence, a live/dead staining assay performed on patient-derived CRC-SC tumorspheres cultured in Matrigel showed a marked reduction in cell survival upon combined treatment with ralimetinib and CHTs or trametinib in this reconstituted 3D culture system (Fig. 7D).

Overall, these data indicate that p38 α inhibition makes chemoresistant patient-derived CRC-SCs more sensitive to 5-FU, CDDP, CPT-11, and trametinib, and prone to apoptosis.

Targeting p38 α as part of a synthetic lethality approach in APC^{Min/+} mice intestinal organoids

The above preclinical data, along with previous evidence showing the existence of a p38 α -ERK synthetic lethality crosstalk that is crucial for CRC therapy response^{10,12}, support further investigation of a CRC-SC-targeted synthetic lethality approach based on p38 α inhibition.

Budding organoids formed from adenoma crypt cells of APC^{Min/+} mice were thus used to assess the survivability of intestinal stem cells after treatment with ralimetinib and trametinib. Live/dead staining revealed the synthetic lethality effect of p38 α and MEK1 combined inhibition (Fig. 8A). These data were confirmed by the reduced number (Fig. 8B) and size (Fig. 8C) of organoids after treatment with both inhibitors.

Discussion

CRC is a leading cause of cancer-related death, with a 5-year survival rate of 5% in metastatic patients³. Recurrence and metastasis depend on a small subset of cells within the tumor, called CSCs⁵, which are exposed to selective pressure³⁵ and retain the potential for self-renewal, differentiation, and tumorigenicity³⁶. Indeed, current therapies are generally based on drugs that affect rapidly dividing cells, while CRC-SCs show a low proliferative potential³⁷. Furthermore, CRC-SCs display

alterations of DNA repair mechanisms and express high levels of proteins that are involved in CHT resistance³⁸. Hence, targeting this specific cell subpopulation may be an effective strategy to eradicate CRC and increase the survival of metastatic patients.

Several approaches focused on the CSC population are currently being evaluated, some of which successfully entered clinical trials (e.g., ClinicalTrials.gov ID NCT01190345, NCT01440127).

Here, we identified p38 α as a new druggable member of β -catenin chromatin-associated kinase complexes in colorectal model systems (normal colonocytes, CRC cell lines, and patient-derived CRC-SCs that recapitulate parental tumor histological features). Moreover, we showed that CRC cells and patient-derived CRC-SCs have higher levels of activated p38 α than normal colonocytes and are “addicted” to p38 α activity.

Interestingly, our meta-analysis on a cohort of colorectal tumors retrieved from TCGA PanCancer Atlas dataset correlated p38 α mRNA levels to stage III disease prognosis, with high p38 α expression being associated with worse DFS and PFS. Based on these findings, p38 α may be used as a marker of resistance and a predictor of therapy response in CRC.

We also demonstrated that p38 α acts as a β -catenin chromatin-associated kinase involved in tumor proliferation, metastatic dissemination, and chemoresistance. Indeed, our data suggest that p38 α serves as a regulator of gene expression by interacting with β -catenin-TCF/LEF transcriptional complexes that are recruited to WREs. The recruitment of protein kinases to promoter regulatory elements can have important functional consequences; in particular, these proteins may represent new therapeutic targets in cancer cell signaling.

Our analysis of p38 α recruitment on β -catenin target gene promoters using ChIP re-ChIP assays suggests that the Wnt signaling pathway likely converges on p38 α and β -catenin, which co-regulate target gene expression. Indeed, p38 α feeds into the Wnt pathway at least in two

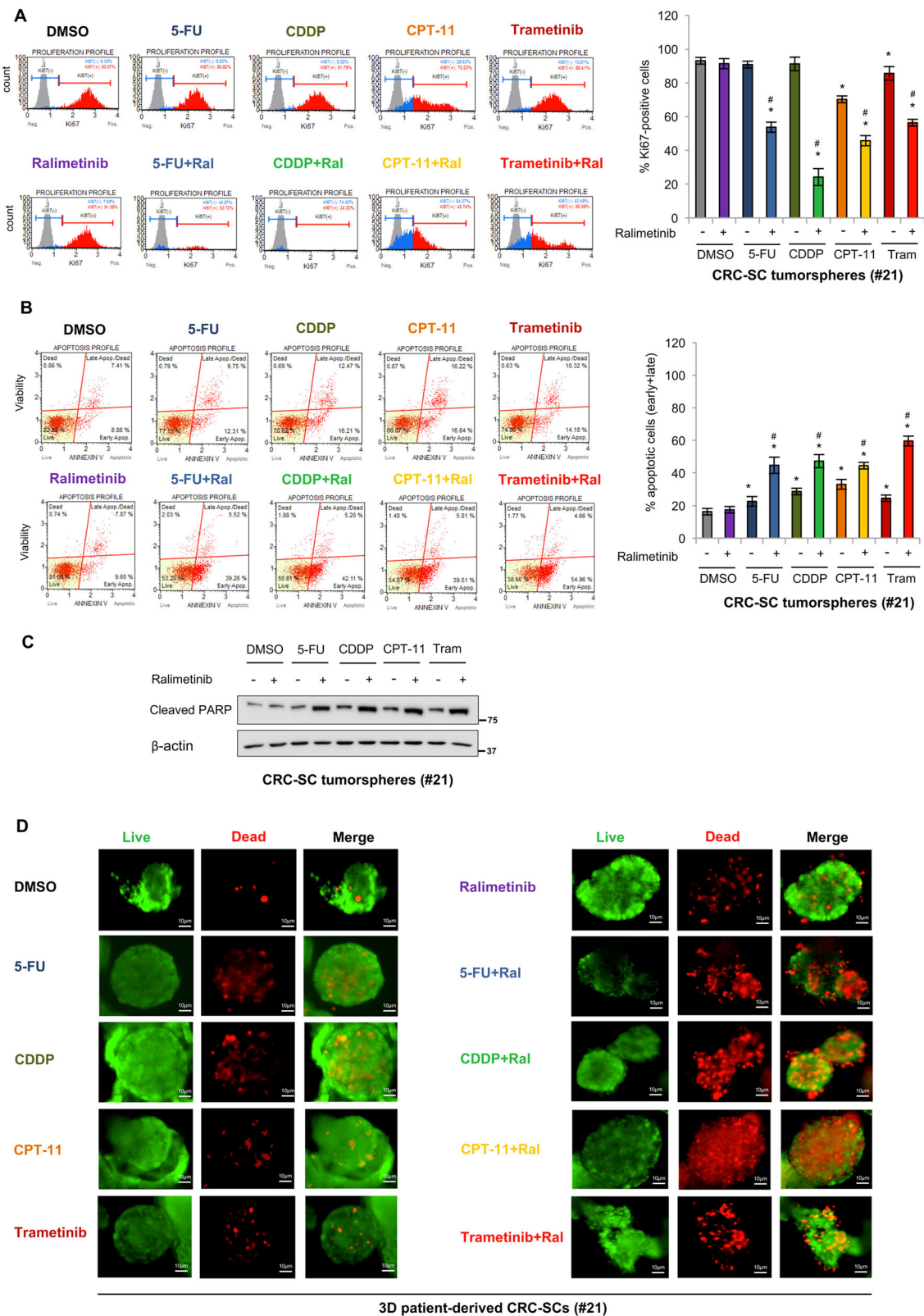


Fig. 7 (See legend on next page.)

(see figure on previous page)

Fig. 7 Combined treatment with ralimetinib and chemotherapeutics or trametinib has a synergistic cytotoxic effect. **A** Flow cytometry analysis of Ki67 expression in CRC-SCs #21 treated as described in Fig. 6D. Populations were gated identically using the unstained background populations shown in gray behind the Ki67-negative (blue) and Ki67-positive (red) populations. The graph on the right summarizes the percentage of Ki67-positive cells. **B** Flow cytometry analysis of annexin V staining in CRC-SCs #21 treated as described in Fig. 6D. The graph on the right summarizes the percentage of apoptotic cells (early + late). **C** Immunoblot analysis of cleaved PARP levels in CRC-SCs #21 treated as described in Fig. 6D. β -actin was used as a loading control. **D** Live/dead staining of CRC-SCs #21 grown as 3D cultures and treated as described in Fig. 6D. Tram = trametinib. Green: live cells; red: dead cells. * $P < 0.05$: treatment vs. control (DMSO); and # $P < 0.05$: combined treatment vs. corresponding single treatments.

different ways: one in the cytoplasm, at the level of GSK3 β , as demonstrated by Thornton and colleagues³⁷, and the other at the chromatin level, by interacting with and phosphorylating β -catenin on WREs, as shown by our data.

Activation of p38 α and nuclear β -catenin is observed in many tumors, and several genes targeted by these signaling pathways are crucial for cancer development and progression. For instance, it has been demonstrated that *c-Myc*, the main Wnt/ β -catenin target, is consistently overexpressed in CRC-SCs and its downregulation suppresses CRC-SC self-renewal and xenograft growth³⁹. Interestingly, we found that p38 α pharmacological inhibition does not prevent the formation of the p38 α - β -catenin complex but downregulates several β -catenin target genes, including *c-Myc*, in a manner comparable to the Wnt/ β -catenin inhibitor PRI-724, which is currently being evaluated in clinical trials (e.g., ClinicalTrials.gov ID NCT04351009). Moreover, our results revealed that both the CSC and the differentiated cell compartments of CRC-SC cultures are efficiently targeted by treatment with the p38 α kinase inhibitor ralimetinib.

In our model systems, the combined use of CHTs and ralimetinib proved more effective than CHTs alone.

In particular, ralimetinib promoted sensitization of patient-derived CRC-SCs to CHTs commonly used in CRC therapy, such as 5-FU, CDDP, and CPT-11, as shown by a reduction in Ki67-positive cells and induction of apoptosis. These combined treatments also affected key CRC-SC features that contribute to tumor aggressiveness and metastatization, including their colony-forming and migratory ability. Moreover, ralimetinib showed a synthetic lethality effect when used in combination with the MEK1 inhibitor trametinib in patient-derived CRC-SC tumorspheres, in a human 3D culture system, and in APC^{Min/+} mice organoids.

Overall, our results confirmed the crucial role of the p38 α - β -catenin axis in the regulation of intestinal tumorigenesis, suggesting that p38 α manipulation could be an effective therapeutic approach in stage III CRC patients. Indeed, it may be used to target CRC-SCs in addition to bulk tumor populations to counter uncontrolled proliferation, metastatic dissemination, and chemoresistance. Several p38 α inhibitors passed phase I

clinical trials and are currently in phase II or III for inflammatory diseases and cancer^{40–45}. In particular, ralimetinib displayed a tolerable safety profile, with preliminary evidence of antineoplastic activity in a recent phase I trial (ClinicalTrials.gov ID NCT01393990, completed in March 2020) in patients with advanced or metastatic cancer. Moreover, it is currently being tested in combination with other agents in an ongoing phase I study in CRC patients (ClinicalTrials.gov ID NCT02860780).

Altogether, our preclinical data support further clinical development of ralimetinib as a sensitizing agent to commonly used CHTs and suggest the potential of a synthetic lethality approach based on p38 α and MEK1 inhibition.

Materials and methods

Clinical data

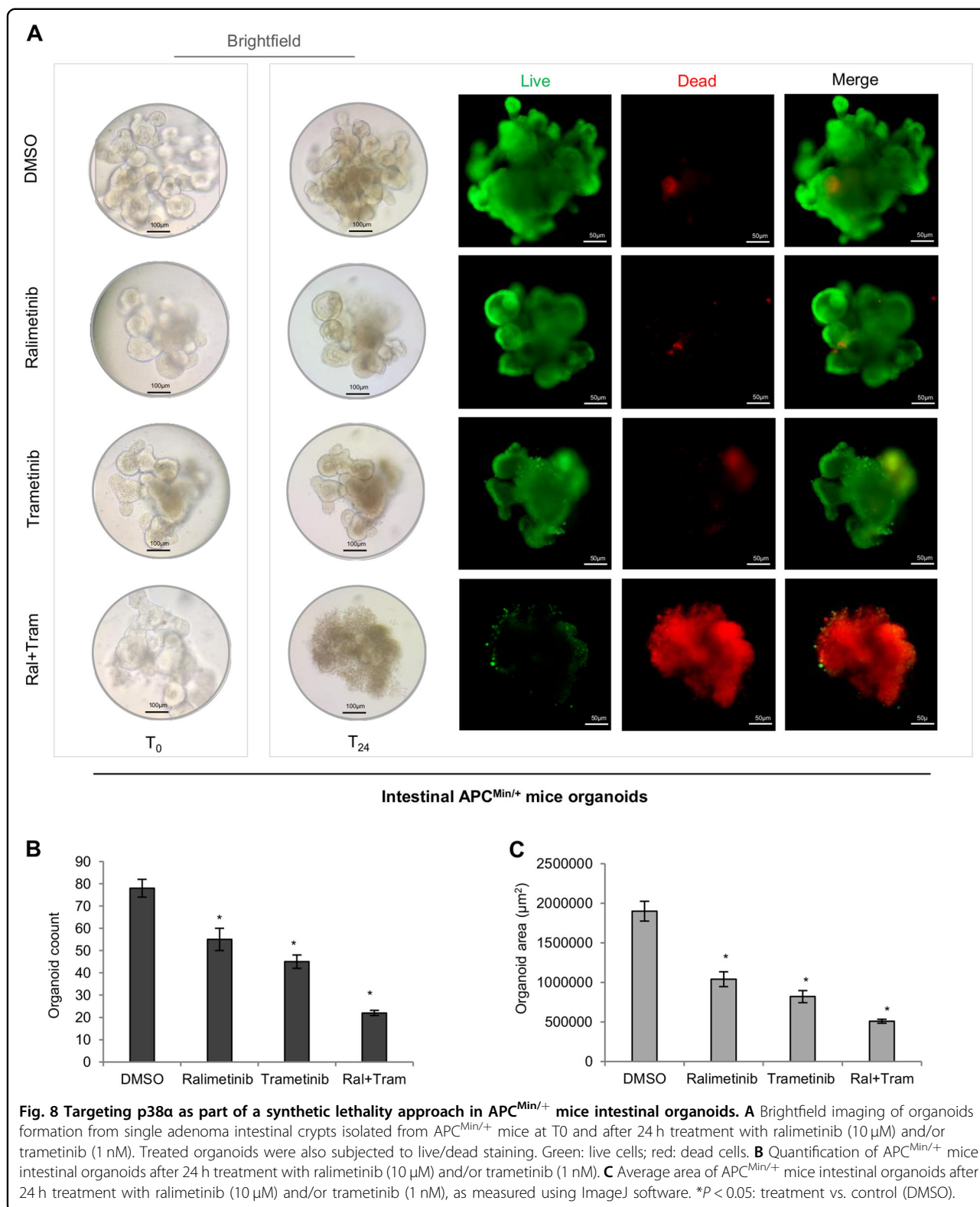
CRC tissues were obtained from four patients at the time of resection, in accordance with the ethical standards of the Institutional Committee on Human Experimentation (authorization CE9/2015, Policlinico P. Giaccone, Palermo) after informed consent.

Cell lines and intestinal 3D models

HCT116 and HT29 cells were cultured in DMEM (#11360-070, Gibco) with 10% FBS (#0270-106, Gibco) and 100 IU/ml penicillin–streptomycin (#15140-122, Gibco). HEK293 cells were supplemented with 1% pyruvate (#11360070, Gibco) and 1% NEAA (#11140, Sigma-Aldrich). HCEC-1CT cells were cultured in COLO-UP (Evercyte) medium supplemented with 100 IU/ml penicillin–streptomycin (#15140-122, Gibco). #8, #9, #21, and #40 cells were isolated and propagated from CRC patients as previously described³⁸. All cell lines were tested to be mycoplasma-free (#117048; Minerva Biolabs). Human intestinal 3D cultures were generated from CRC-SCs as previously described⁴⁶. Mouse intestinal organoids were generated from APC^{Min/+} male mice as previously described^{47,48}. All cell cultures were performed in a 37 °C and 5% CO₂ incubator.

Chemicals

5-FU (F6627), Wnt3a (H17001), LiCl (L9650), and Trypan blue (T8154) were purchased from Sigma-



Aldrich. Cisplatin (S1166), Ralimetinib (S1494), Trametinib (S2673), Irinotecan (S2217), PRI-724 (S8262), and SB202190 (S1077) were purchased from SelleckChem.

Cloning and plasmids

Efficiency DH5α Competent Cells (C2987H) and BL21 (DE3) Competent *E. coli* (C25271) were purchased from

New England Biolabs and were used for all cloning experiments. Cells were grown in standard LB media. Plasmids were generated as previously described⁴⁹. The pcDNA-human- β -catenin (#16828) plasmid was purchased from Addgene. Primer sequences are listed in Supplementary Table 1.

Cell transfection and RNA interference

HEK293 cells were transfected with mammalian expression plasmids using Lipofectamine 3000 (#L3000015, Thermo Fisher Scientific) according to the manufacturer's instruction. For RNA interference, HT29 cells were transfected with 50 nM validated siRNAs (Ambion) directed against MAPK14 using the HiPerfect reagent (#301704, QIAGEN) according to the manufacturer's instructions. siCTRL (Eurofins) was used as a non-silencing control. siRNA sequences are listed in Supplementary Table 1.

Recombinant protein expression/purification

BL21 competent cells, transformed with different constructs, were grown in LB medium with antibiotics and induced with IPTG. Cells were lysed with B-PER lysis buffer (#78248, Thermo Fisher Scientific). GST-fusion proteins were purified with Pierce Glutathione Magnetic Agarose Beads (TH269836, Thermo Fisher Scientific) according to the manufacturer's instructions. His-fusion proteins were purified with Dynabeads His-Tag Isolation and Pulldown (10104D, Thermo Fisher Scientific) according to the manufacturer's instructions.

Immunoblotting

Nuclear and cytoplasmic fractions were obtained by using the Nuclear Extraction Kit (#ab113474, Abcam) according to the manufacturer's instructions. Immunoblots were carried out as previously described¹⁰. Primary antibodies: anti- β -actin (#3700), anti-c-Myc (#9402), anti-p44/42 MAPK (Erk1/2) (#9102), anti-phospho p44/42 MAPK (Erk1/2) (Thr202/tyr204) (#9106S), anti-p38 MAPK (#9212), anti-p38 α MAPK (#9228), anti-phospho-p38 MAPK (Thr180/Tyr182) (#9211), anti-Lamin B1 (#12586), anti-Keratin20 (BK13063S), anti-PDI (#2446S), anti- β -catenin (#9562), anti-GST (#2625), anti-CD133 (#5860), anti-CD44 (#3570), anti-Musashi (#2154) all from Cell Signaling Technologies, anti-HIS-tag (H1029), anti-FLAG (F1804), anti-HA-tag (H3663) all from Sigma-Aldrich, anti-Igr5 (GPCR) (75732) from Abcam, HSP90 α/β (sc13119) from Santa Cruz Biotechnology, p-p38 MAPK α (Thr180, Tyr 182) (MA5-15177) from Invitrogen and anti-phospho-p38 α (MAB8691) from R&D Systems. Rabbit IgG HRP and Mouse IgG HRP (#NA934V and #NA931V, GE Healthcare, respectively) were used as secondary antibodies and revealed using the ECL-plus chemiluminescence reagent

(RPN2232, GE Healthcare). Densitometric evaluation was performed by ImageJ software.

Co-immunoprecipitation

Co-IP was carried out as previously described¹⁰. Cells were lysed with the Nuclear Extraction Kit (ab113474, Abcam) according to the manufacturer's instructions. Primary antibodies: p38 α (#8690, Cell Signaling), β -catenin (#9562, Cell Signaling), and p-p38 MAPK α (Thr180, Tyr 182) (MA5-15177, Invitrogen). IgG was used as a negative control.

Annexin V staining

2×10^4 cells/plate were stained with Muse Annexin V and Dead Cell Reagent (Luminex MCH100105) according to the manufacturer's instructions.

Immunofluorescence

Cells were seeded on glass coverslips, fixed in 4% paraformaldehyde, and permeabilized using 0.01–0.1% Triton X-100. Coverslips were incubated with the indicated primary antibodies and then with Alexa Fluor 488 (#A-11094, Thermo Fisher Scientific) and 647 (#A-32728) secondary antibodies; nuclei were counterstained using DAPI (D9542, Sigma-Aldrich). Slides were sealed using Vectashield Mounting Medium (#H1000, Vector Laboratories). Images were acquired using a Zeiss fluorescence microscope. Primary antibodies: p38 α (#8690, Cell Signaling) and β -catenin (#9562, Cell Signaling).

Quantitative real-time PCR

RNA extraction and real-time PCR were performed as previously described¹⁰. Primer sequences are listed in Supplementary Table 1.

Histology and immunohistochemistry

Tissue specimens were formalin-fixed in 4% buffered formalin, embedded in paraffin, sectioned at 4 mm thickness, and stained with hematoxylin and eosin. Additional sequential sections (3–5 μ m) were cut and used for immunohistochemical analysis. Sections were dewaxed and rehydrated in dH₂O. Endogenous peroxidase activity was blocked by incubation in 3% hydrogen peroxide for 10 min. Antigen retrieval was conducted in 10 mM sodium citrate buffer (pH 6.0) for 30 min. Sections were incubated overnight with the primary antibodies: p-p38 α (1:100, MA5-15177, Thermo Fisher Scientific), β -catenin (1:400, 9562, Cell Signaling), c-Myc (1:100, #9402, Cell Signaling), cyclin D1 (1:50, #2978, Cell Signaling), and CD44v6 (1:250, AB2080, Merck Millipore). Then, they were incubated with secondary biotinylated antibodies and subsequently with streptavidin–biotin–peroxidase (Envision + System HRP anti-rabbit and anti-mouse, K8002, Agilent). Samples were developed with DAB and mounted with permanent

mounting media. Negative controls were used in each experiment. p-p38 α , β -catenin, c-Myc, Cyclin D1, and CD44v6 immunoreactivity was evaluated by a semi-quantitative approach by two independent pathologists, in a blinded manner, who scored the percentage of positive-stained cells and the intensity of the staining (0: absent, 1: mild and focal, 2: moderate, 3: intense and diffuse).

Immunocytochemical analysis was performed on cytopins using p-p38 MAPK α (Thr180, Tyr 182) (MA5-15177) (1:100) from Invitrogen. Single staining was revealed using a biotin–streptavidin system (Dako) and detected with 3-amino-9-ethylcarbazole (Dako). Nuclei were counterstained with aqueous hematoxylin (Sigma).

Chromatin immunoprecipitation

Chromatin isolated from HT29 cells and CRC-SCs was subjected to chromatin immunoprecipitation using the MAGnify Chromatin Immunoprecipitation System (492024, Thermo Fisher Scientific) according to the manufacturer's instructions. Chromatin was sonicated to a fragment length of about 200–500 bp and immunoprecipitated with 1 μ g of rabbit IgG: p38 α (#8690, Cell Signaling) and β -catenin (#9562, Cell Signaling). For re-ChIP, immune complexes were eluted with elution buffer (TE buffer, 10 mM DTT) for 30 min at 37 °C, diluted with the dilution buffer provided in the kit, and subjected to immunoprecipitation with a second antibody of interest. Primer sequences are listed in Supplementary Table 1.

In vitro pull-down assay

His- β -catenin recombinant human protein was incubated with GST-p38 α fusion protein. p300 (302-530)-GST fusion protein was used as a positive control. Fusion proteins were precipitated with Dynabeads His-Tag Isolation and Pull-down (10104D, Thermo Fisher Scientific) according to the manufacturer's instructions. Primary antibodies: poly-Histidine (H1029, Sigma-Aldrich) and GST (#2625, Cell Signaling). Rabbit IgG HRP and Mouse IgG HRP (#NA934V, #NA931V, GE Healthcare, respectively) were used as secondary antibodies and revealed using the ECL-plus chemiluminescence reagent (RPN2232, GE Healthcare).

Cell sorting

For CRC-SC sorting, cells were collected, washed in PBS, and stained for 1 h at 4 °C with conjugated antibodies specific for CD44v6 (2F10 APC, mouse IgG1; R&D Systems) or a corresponding isotype-matched control (IMC). Dead cell exclusion was performed by using 7-AAD (0.25 μ g/ 1×10^6 cells, BD Biosciences). Cells were washed with 2% BSA and 2 mM EDTA in PBS and filtered with a 70 μ m mesh to prevent cell clogging. Isolation of CD44v6^{low} and CD44v6^{high} cells was performed by using the FACSMelody cell sorter. Post-sorting analysis was performed to verify the purity of sorted populations.

Karyotyping protocol

CRC-SCs were seeded at high density (2×10^6 cells/ml). After 24 h, colcemid-treated CRC-SCs were incubated in a hypotonic solution, fixed in a chilled fixative solution, and then washed extensively. Chromosomes were counted using an Olympus microscope.

Mutation analysis

For targeted deep DNA re-sequencing, the sequencing library was prepared as previously described²⁵. MSI analysis was performed with a reference panel of five fluorescent dye-labeled microsatellite primers (NR-21, BAT-25, MONO-27, NR-24, BAT-26) using the MSI Analysis System kit (MD1641, Promega). Amplified fragments were detected by loading the PCR products for capillary electrophoresis using an ABI Prism 3500 Genetic Analyser and the POP-4 polymer (4393710, Applied Biosystems) according to the manufacturer's instructions. MSI status was determined upon analysis with GeneMapper software, Version_4.1 (Applied-Biosystems).

Cellular assays

For cell viability assays, viability was assessed using the CellTiter-Glo Luminescent Cell Viability Assay Kit (G7570, Promega) according to the manufacturer's instructions. The luminescent signal was read using a SPECTROstar Omega microplate reader (BMG Labtech). The CellTiter 96[®] AQueous One Solution Cell Proliferation Assay (G3580, Promega) (MTS) was performed according to the manufacturer's instructions and analyzed by using the GDV MPT reader (DV 990 BV6).

For cell death assays, cell death was assessed by cell counting as previously described¹⁷. Human intestinal 3D cultures and APC^{Min/+} mouse intestinal organoids were stained using the LIVE/DEAD[®] Cell Imaging Kit (R37601, Thermo Fisher Scientific) according to the manufacturer's instructions.

For clonogenic assays, dissociated CRC-SCs were plated in triplicate at 500 cells/well suspended in 0.3% agarose over a layer of 0.5% agarose and treated as indicated.

For motility assays, 1×10^4 control or treated CRC-SCs were suspended in 200 μ l of non-supplemented stem cell medium and plated into the upper wells of Matrigel-coated Boyden chambers containing 8 μ m diameter polycarbonate membranes (CLS3422-48EA, Corning). Lower wells contained 600 μ l of stem cell medium supplemented with 20 ng/ml EGF and 10 ng/ml basic FGF and the relevant drugs.

For proliferation assays, CRC-SCs treated as indicated were analyzed to determine the percentage of proliferating cells based on Ki67 expression using the Muse Ki67 Proliferation Kit (MCH100114, Merck Millipore) according to the manufacturer's instructions.

For the luciferase assay, HEK293 cells were lysed with 100 μ l Passive Lysis (E1910, Promega) and the assay was performed according to the manufacturer's instructions.

Analysis of p38 α kinase activity was performed using the ADP-Glo Kinase Assay (V6930, Promega) according to the manufacturer's instructions. p38 α active protein (25 ng, V2701, Promega) was assayed in a kinase reaction buffer with 50 μ M ATP and varying concentrations of human recombinant β -catenin (0.5, 1, and 1.5 μ g). 1 μ g of p38 peptide substrate was used as a control. The generated luminescence was measured using a luminometer (SPECTROstar Omega microplate reader, BMG Labtech).

ELDA

CD44v6^{low}- and CD44v6^{high}-enriched cells were plated at 1, 2, 4, 8, 16, 32, 64, and 128 cells per well in 96-well plates. Clonal frequency was calculated using the extreme limiting dilution analysis (ELDA) tool (<http://bioinf.wehi.edu.au/software/elda/index.html>).

In vivo studies

For in vivo studies, normal, adenoma, and adenocarcinoma colon mucosa tissues were obtained from C57BL/6 mice ($n = 12$), APC^{Min/+} mice ($n = 12$), and APC^{Min/+} mice ($n = 24$) treated with 14 mg/kg of AOM (A5486, Sigma-Aldrich), respectively. Four-month-old APC^{Min/+} male mice were administered with AOM (14 mg/kg body weight) once a week for 5 weeks; one month later, they were subjected to daily intraperitoneal injections of the p38 α inhibitor SB202190 (0.05 μ mol/kg body weight) or DMSO for 14 days and then sacrificed. Body weight was recorded daily. Procedures involving animals and their care were conducted in conformity with the institutional guidelines that comply with national and international laws and policies.

TCGA PanCancerAtlas data source and meta-analysis

To study the association between p38 α mRNA expression levels and CRC aggressiveness, RNA-seq gene expression data (Z -scores) of 592 CRC patients and TNM stage clinical data of 580/592 patients were obtained from TCGA PanCancerAtlas through the cBioPortal website⁵⁰. Patients were stratified based on p38 α mRNA Z -score into two groups with high (>median, $n = 296/592$) or low (\leq median, $n = 296/592$) p38 α mRNA expression. Statistical analysis was performed using R (version 3.6.2), an open-source freely available software environment for statistical computing and graphics. Survival curves of stage III CRC patients ($n = 171$) were assessed according to the Kaplan–Meier method, and DSF and PFS were used as the endpoint. Differences between stage III CRC patients with high p38 α mRNA ($n = 80/171$) and low

p38 α mRNA ($n = 91/171$) were assessed using the log-rank test and R packages “*survival*” and “*survminer*”^{51–53}.

In silico prediction analysis

In silico prediction analysis was performed using DISPHOS 1.3, NETPHOS 3.1, Phosida, iPTMne, and Phosphosite Plus servers.

Quantification and statistical analysis

The statistical significance of the results was analyzed using the Student's t -tail test, and $P < 0.05$ was considered statistically significant. Results are representative of at least three independent experiments.

Acknowledgements

We thank Dr. Giusy Bianco and Vito Spilotro for the animal care assistance. We thank Dr. Francesco Paolo Jori for his helpful discussion during the preparation of the manuscript and editorial assistance.

Author details

¹Medical Genetics, National Institute for Gastroenterology, IRCCS ‘S. de Bellis’ Research Hospital, 70013 Castellana Grotte (Ba), Italy. ²Cellular & Molecular Pathophysiology Laboratory, Department of Surgical & Oncological Sciences, University of Palermo, 90127 Palermo, Italy. ³Medical Genetics, Department of Biomedical Sciences and Human Oncology (DIMO), University of Bari Aldo Moro, 70124 Bari, Italy. ⁴Department of Emergency and Organ Transplantation, Operating Unit of Pathological Anatomy, University of Bari Aldo Moro, 70124 Bari, Italy. ⁵Personalized Medicine, National Institute for Gastroenterology, IRCCS ‘S. de Bellis’ Research Hospital, 70013 Castellana Grotte (Ba), Italy. ⁶Department of Molecular Medicine, Sapienza University of Rome, 00161 Rome, Italy

Funding

This work was supported by the Italian Ministry of Health ‘Ricerca Corrente 2018–2020; 2019–2021’ to C.S. and ‘Starting Grant’ SG-2019-12371540 to P.S., PRIN—Research Projects of National Relevance (PRIN 2017, no. 2017WVNSLR-LS4) from the Italian MIUR to C.S. and G.S., AIRC IG-23794 2020-2024 to C.S.

Data availability

All data are available upon request to the corresponding author.

Conflict of interest

The authors declare no competing interests.

Publisher's note

Springer Nature remains neutral with regard to jurisdictional claims in published maps and institutional affiliations.

Supplementary information The online version contains supplementary material available at <https://doi.org/10.1038/s41419-021-03572-4>.

Received: 6 October 2020 Revised: 22 February 2021 Accepted: 1 March 2021

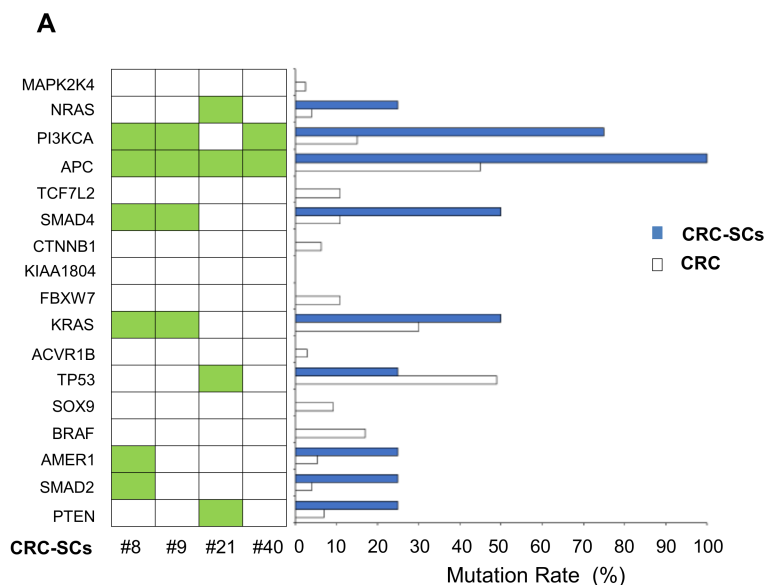
Published online: 25 March 2021

References

- Keum, N. & Giovannucci, E. Global burden of colorectal cancer: emerging trends, risk factors and prevention strategies. *Nat. Rev. Gastroenterol. Hepatol.* **16**, 713–732 (2019).
- Lieu, C. et al. Duration of oxaliplatin-containing adjuvant therapy for Stage III colon cancer: ASCO Clinical Practice Guideline. *J. Clin. Oncol.* **37**, 1436–1447 (2019).

3. Li, C. et al. Survival nomograms for stage III colorectal cancer. *Medicine* **97**, e13239 (2018).
4. Sheth, K. R. & Clary, B. M. Management of hepatic metastases from colorectal cancer. *Clin. Colon Rectal Surg.* **18**, 215–223 (2005).
5. Zhou, Y. et al. Cancer stem cells in progression of colorectal cancer. *Oncotarget* **9**, 33403–33415 (2018).
6. Szaryńska, M., Olejniczak, A., Kobiela, J., Psychalski, P. & Kmieć, Z. Therapeutic strategies against cancer stem cells in human colorectal cancer. *Oncol. Lett.* **14**, 7653–7668 (2017).
7. Yang, L. et al. Targeting cancer stem cell pathways for cancer therapy. *Signal Transduct. Target. Ther.* **5**, 1–35 (2020).
8. Bienz, M. & Clevers, H. Linking colorectal cancer to Wnt signaling. *Cell* **103**, 311–320 (2000).
9. Bikkavilli, R. K., Feigin, M. E. & Malbon, C. C. p38 mitogen-activated protein kinase regulates canonical Wnt-beta-catenin signaling by inactivation of GSK3beta. *J. Cell Sci.* **121**, 3598–3607 (2008).
10. Chiacchiera, F. et al. Blocking p38/ERK crosstalk affects colorectal cancer growth by inducing apoptosis in vitro and in preclinical mouse models. *Cancer Lett.* **324**, 98–108 (2012).
11. Chiacchiera, F. et al. p38alpha blockade inhibits colorectal cancer growth in vivo by inducing a switch from HIF1alpha- to FoxO-dependent transcription. *Cell Death Differ.* **16**, 1203–1214 (2009).
12. Grossi, V. et al. Sorafenib inhibits p38a activity in colorectal cancer cells and synergizes with the DFG-in inhibitor SB202190 to increase apoptotic response. *Cancer Biol. Ther.* **13**, 1471–1481 (2012).
13. Grossi, V., Peserico, A., Tezil, T. & Simone, C. p38a MAPK pathway: a key factor in colorectal cancer therapy and chemoresistance. *World J. Gastroenterol.* **20**, 9744–9758 (2014).
14. Thornton, T. M. et al. Phosphorylation by p38 MAPK as an alternative pathway for GSK3beta inactivation. *Science* **320**, 667–670 (2008).
15. Comes, F. et al. A novel cell type-specific role of p38alpha in the control of autophagy and cell death in colorectal cancer cells. *Cell Death Differ.* **14**, 693–702 (2007).
16. Simone, C. Signal-dependent control of autophagy and cell death in colorectal cancer cell: the role of the p38 pathway. *Autophagy* **3**, 468–471 (2007).
17. Madia, F., Grossi, V., Peserico, A. & Simone, C. Updates from the intestinal front line: autophagic weapons against inflammation and cancer. *Cells* **1**, 535–557 (2012).
18. Germani, A. et al. Targeted therapy against chemoresistant colorectal cancers: Inhibition of p38a modulates the effect of cisplatin in vitro and in vivo through the tumor suppressor FoxO3A. *Cancer Lett.* **344**, 110–118 (2014).
19. Simone, C. et al. p38 pathway targets SWI-SNF chromatin-remodeling complex to muscle-specific loci. *Nat. Genet.* **36**, 738–743 (2004).
20. Soloaga, A. et al. MSK2 and MSK1 mediate the mitogen- and stress-induced phosphorylation of histone H3 and HMG-14. *EMBO J.* **22**, 2788–2797 (2003).
21. Alepuz, P. M., de Nadal, E., Zapater, M., Ammerer, G. & Posas, F. Osmostress-induced transcription by Hot1 depends on a Hog1-mediated recruitment of the RNA Pol II. *EMBO J.* **22**, 2433–2442 (2003).
22. Lin, S.-P. et al. Survival of cancer stem cells under hypoxia and serum depletion via decrease in PP2A activity and activation of p38-MAPKAPK2-Hsp27. *PLoS ONE* **7**, e49605 (2012).
23. Chen, S.-F. et al. Quercetin suppresses drug-resistant spheres via the p38 MAPK-Hsp27 apoptotic pathway in oral cancer cells. *PLoS ONE* **7**, e49275 (2012).
24. Roy, S. et al. Role of p38 MAPK in disease relapse and therapeutic resistance by maintenance of cancer stem cells in head and neck squamous cell carcinoma. *J. Oral Pathol. Med.* **47**, 492–501 (2018).
25. Manic, G. et al. CHK1-targeted therapy to deplete DNA replication-stressed, p53-deficient, hyperdiploid colorectal cancer stem cells. *Gut* **67**, 903–917 (2018).
26. Todaro, M. et al. CD44v6 is a marker of constitutive and reprogrammed cancer stem cells driving colon cancer metastasis. *Cell Stem Cell* **14**, 342–356 (2014).
27. Sun, Y. et al. Regulation of beta-catenin transformation by the p300 transcriptional coactivator. *Proc. Natl Acad. Sci. USA* **97**, 12613–12618 (2000).
28. Suzui, M., Okuno, M., Tanaka, T., Nakagama, H. & Moriwaki, H. Enhanced colon carcinogenesis induced by azoxymethane in min mice occurs via a mechanism independent of beta-catenin mutation. *Cancer Lett.* **183**, 31–41 (2002).
29. He, T. C. et al. Identification of c-MYC as a target of the APC pathway. *Science* **281**, 1509–1512 (1998).
30. Hornbeck, P. V., Zhang, B., Murray, B., Kornhauser, J. M. & Latham, V. Skrzypek E. PhosphoSitePlus, 2014: mutations, PTMs and recalibrations. *Nucleic Acids Res.* **43**, D512–D520 (2015).
31. Trempeole, N., Dave-Coll, N. & Nebreda, A. R. Snapshot: p38 MAPK substrates. *Cell* **152**, 924–924e1 (2013).
32. Mertins, P. et al. Proteogenomics connects somatic mutations to signalling in breast cancer. *Nature* **534**, 55–62 (2016).
33. Stuart, S. A. et al. A phosphoproteomic comparison of B-RAFV600E and MKK1/2 inhibitors in melanoma cells. *Mol. Cell. Proteom.* **14**, 1599–1615 (2015).
34. Cidado, J. et al. Ki-67 is required for maintenance of cancer stem cells but not cell proliferation. *Oncotarget* **7**, 6281–6293 (2016).
35. Merlo, L. M. F., Pepper, J. W., Reid, B. J. & Maley, C. C. Cancer as an evolutionary and ecological process. *Nat. Rev. Cancer* **6**, 924–935 (2006).
36. Feitelson, M. A. et al. Sustained proliferation in cancer: mechanisms and novel therapeutic targets. *Semin. Cancer Biol.* **35**, S25–S54 (2015).
37. Paldino, E., Tesori, V., Casalbone, P., Gasbarrini, A. & Puglisi, M. A. Tumor initiating cells and chemoresistance: which is the best strategy to target colon cancer stem cells? *BioMed. Res. Int.* **2014**, 859871 (2014).
38. Todaro, M. et al. Colon cancer stem cells dictate tumor growth and resist cell death by production of interleukin-4. *Cell Stem Cell* **1**, 389–402 (2007).
39. Roy, S. & Majumdar, A. P. Signaling in colon cancer stem cells. *J. Mol. Signal.* **7**, 11 (2012).
40. Lee, M. R. & Dominguez, C. MAP kinase p38 inhibitors: clinical results and an intimate look at their interactions with p38alpha protein. *Curr. Med. Chem.* **12**, 2979–2994 (2005).
41. Scott, L. J. Tofacitinib: a review of its use in adult patients with rheumatoid arthritis. *Drugs* **73**, 857–874 (2013).
42. Alten, R. Intracellular targets: current data on effectiveness and safety profile. *Z. Rheumatol.* **72**, 867–872 (2013).
43. Bühler, S. & Laufer, S. A. p38 MAPK inhibitors: a patent review (2012–2013). *Expert Opin. Ther. Pat.* **24**, 535–554 (2014).
44. Patnaik, A. et al. A First-in-Human Phase I study of the Oral p38 MAPK Inhibitor, Ralimetinib (LY2228820 Dimesylate), in patients with advanced cancer. *Clin. Cancer Res.* **22**, 1095–1102 (2016).
45. Cienas, J., Zalyte, E., Bairoch, A. & Gaudet, P. Kinases and cancer. *Cancers* **10**, (2018). <https://doi.org/10.3390/cancers10030063>.
46. Cammareri, P. et al. Isolation and culture of colon cancer stem cells. *Methods Cell Biol.* **86**, 311–324 (2008).
47. Sato, T. & Clevers, H. Growing self-organizing mini-guts from a single intestinal stem cell: mechanism and applications. *Science* **340**, 1190–1194 (2013).
48. Joosten, S. P. J. et al. MET signaling mediates intestinal crypt-villus development, regeneration, and adenoma formation and is promoted by stem cell CD44 isoforms. *Gastroenterology* **153**, 1040–1053.e4 (2017).
49. Nakatani, Y. & Ogryzko, V. Immunoaffinity purification of mammalian protein complexes. *Methods Enzymol.* **370**, 430–444 (2003).
50. Gao, J. et al. Integrative analysis of complex cancer genomics and clinical profiles using the cBioPortal. *Sci. Signal.* **6**, pl1 (2013).
51. Hornik, K. The comprehensive R archive network. *WIREs Comput. Stat.* **4**, 394–398 (2012).
52. Therneau T. A Package for Survival Analysis in R. <https://cran.r-project.org/web/packages/survival/vignettes/survival.pdf> (2020).
53. Kassambara A, Kosinski M, Bieček, P. & Fabian, S. *Drawing Survival Curves Using ggplot2?* <https://cran.r-project.org/web/packages/survminer/survminer.pdf> (2020).

Figure S1



CIN	Yes	Yes	Yes	Yes
MSI	No	Yes	Yes	No
Age	57	53	60	49
Gender	F	F	F	M
Site	R	S	R	S
Grade	G3	G2	G2	G2
TNM	T3N2 M1	T2N1 M0	T3N1 Mx	T2N1 M0
Stage	IV	IIIA	IIIB	IIIA
	#8	#9	#21	#40

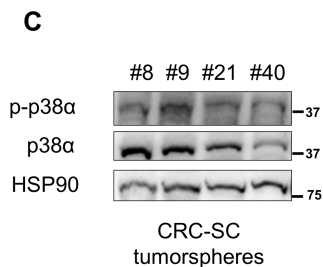
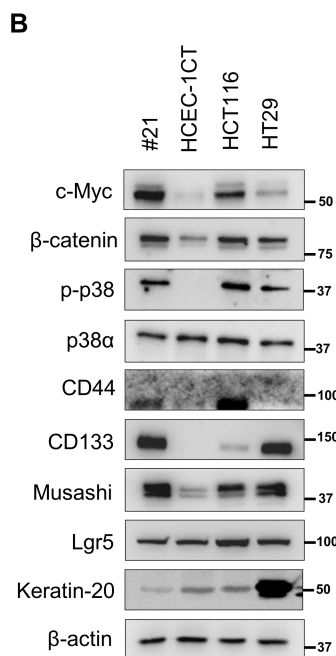


Figure S2

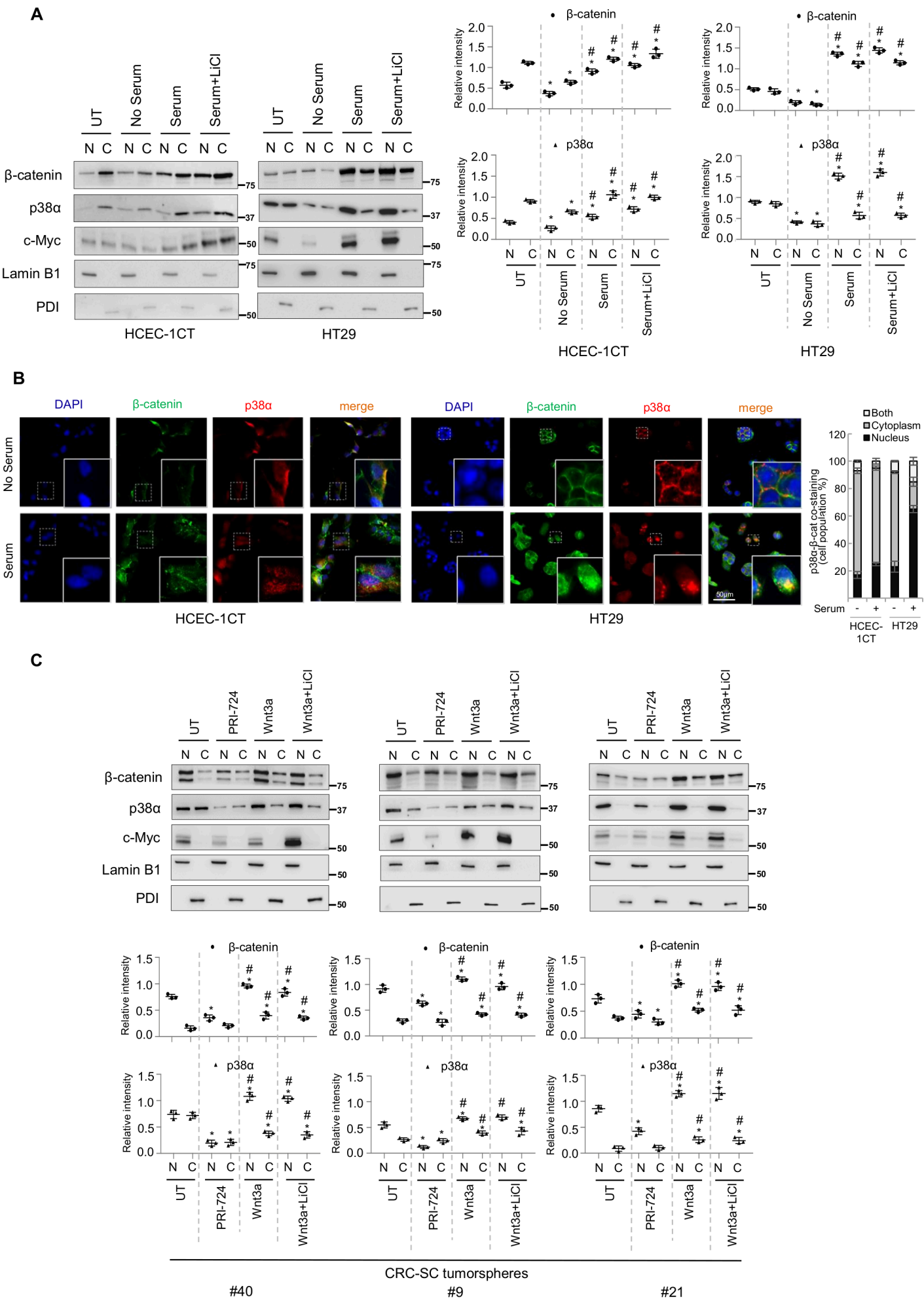


Figure S3

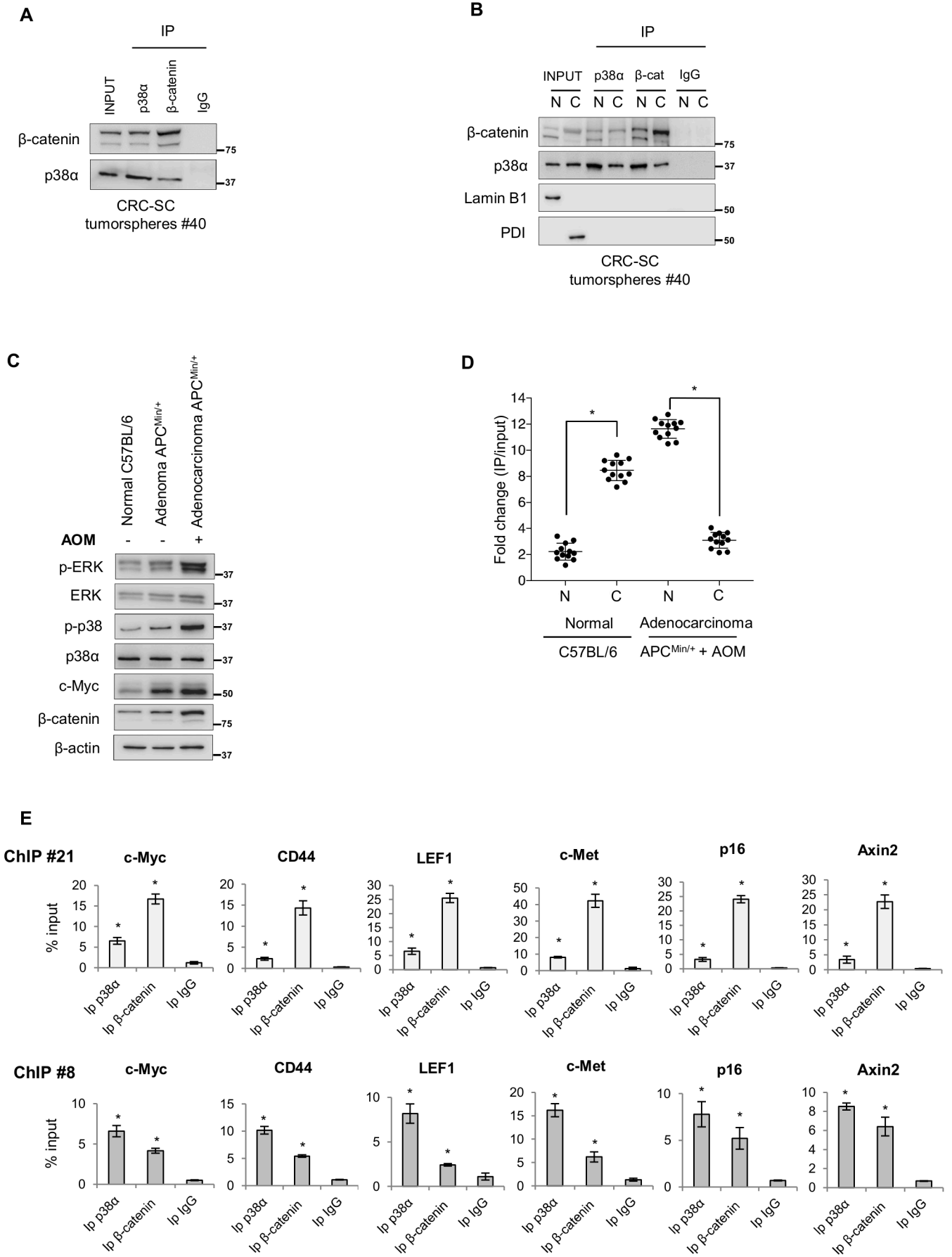
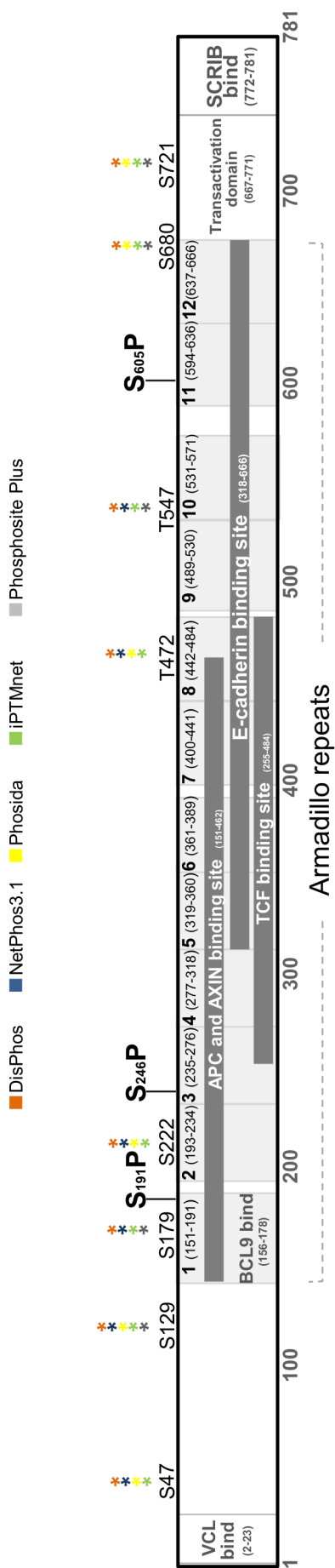
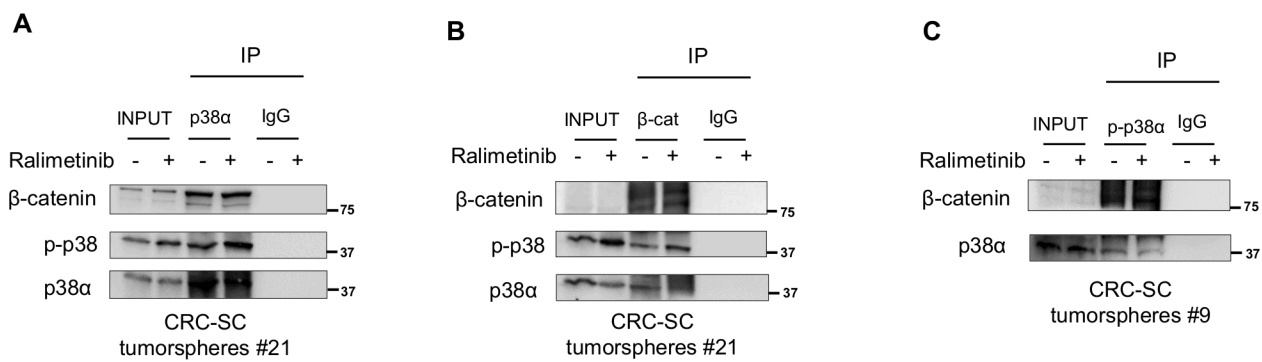
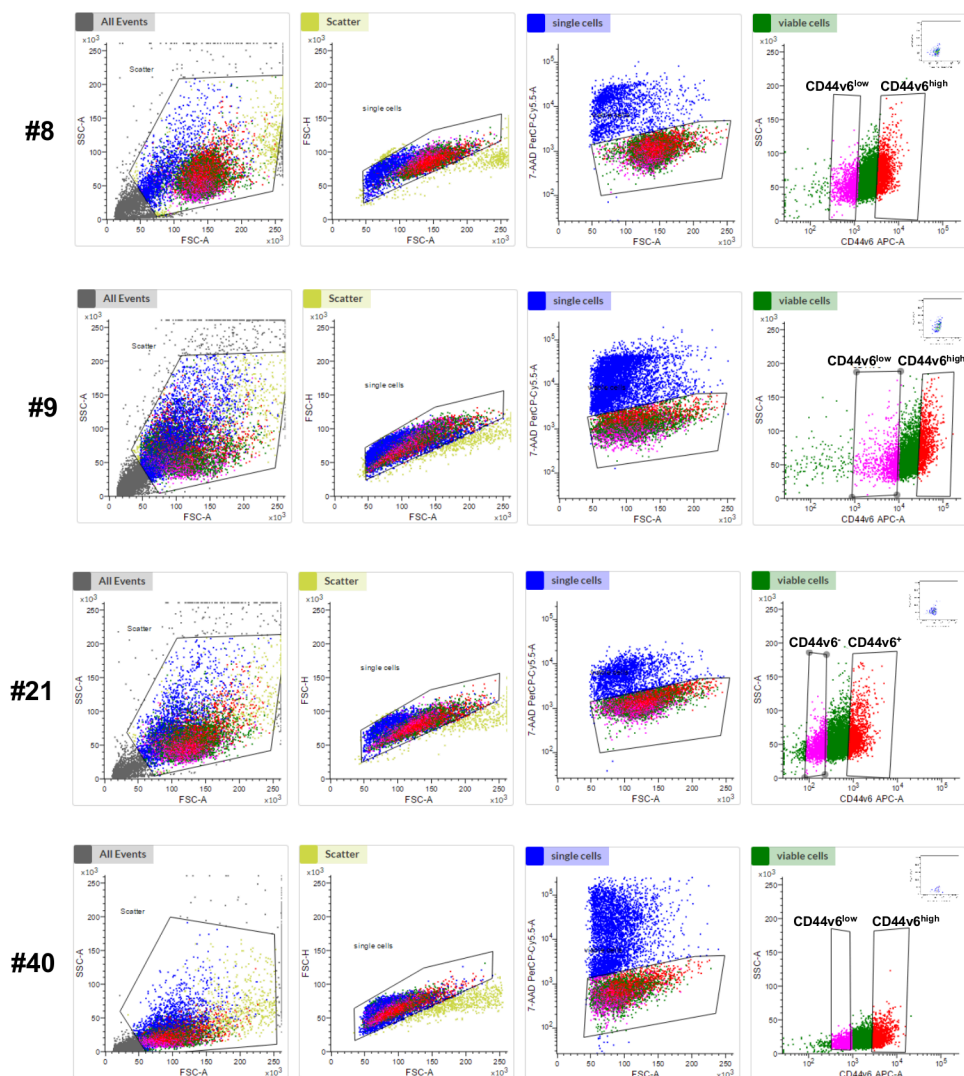
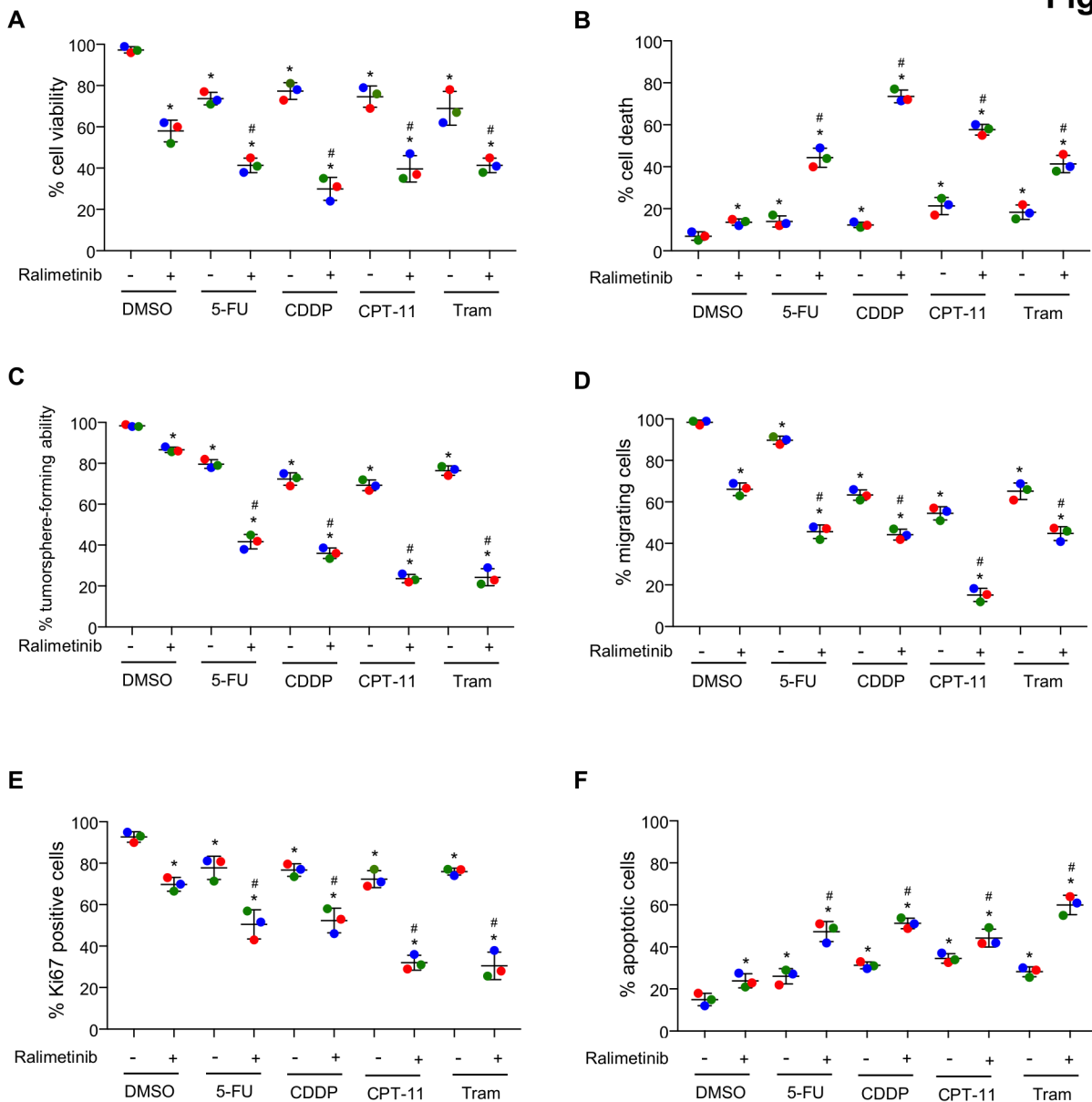


Figure S4









1 **Supplementary figure legends**

2 **Supplementary Figure 1. Characterization of patient-derived stage III CRC-SCs**

3 (A) Mutation, chromosomal (CIN) and microsatellite instability (MSI) analysis of patient-
4 derived stage III CRC-SCs (#40, #8, #21, #9) F=female; M=male; R=rectum; S=sigmoid.

5 (B) Immunoblot analysis showing the expression of several stem cell markers in CRC-SCs
6 #21, HCEC-1CT normal colonocytes, HCT116 and HT29 CRC cell lines. β -actin was used
7 as a loading control.

8 (C) Immunoblot analysis showing p-p38 α levels in CRC-SCs. HSP90 was used as a
9 loading control.

10

11 **Supplementary Figure 2. p38 α and β -catenin subcellular co-localization**

12 (A) Left panels: Immunoblot analysis showing p38 α and β -catenin subcellular localization
13 in HCEC-1CT and HT29 cells under different culture conditions. Cells were serum-starved
14 for 48 h and then switched to a serum-containing medium with or without LiCl (10 mM)
15 for 4 h. Right panels: Densitometric analysis of the indicated proteins normalized against
16 the loading control.

17 (B) Left panels: Immunofluorescence analysis showing p38 α and β -catenin subcellular
18 localization in HCEC-1CT and HT29 cells under serum starvation and after serum
19 addition. Right panel: Quantification of p38 α and β -catenin co-staining.

20 (C) Upper panels: Immunoblot analysis showing p38 α and β -catenin subcellular
21 localization in CRC-SCs #40, #9, and #21 treated with PRI-724 (1 μ M) for 24 h or with
22 Wnt3a (50 ng/ml) and/or LiCl (10 mM) for 4 h. Lower panels: Densitometric analysis of
23 the indicated proteins normalized against the loading control.

24 (A, C) Lamin B1: nuclear loading control; PDI: cytoplasmic loading control.

25 UT=untreated; N=nucleus; C=cytoplasm; LiCl=lithium chloride.

26 Statistical analysis was performed using Student's t-tail test; *P<0.05 vs UT; #P<0.05 vs.
27 serum-starved cells was considered statistically significant.

28

29 **Supplementary Figure 3. Functional interaction between p38 α and β -catenin in**
30 **patient-derived stage III CRC-SCs and mouse models**

31 (A) Co-immunoprecipitation of endogenous p38 α and β -catenin in patient-derived stage III
32 CRC-SCs #40.

33 (B) Co-immunoprecipitation of endogenous p38 α and β -catenin (β -cat) in nuclear and
34 cytoplasmic fractions of patient-derived stage III CRC-SCs #40. Lamin B1: nuclear
35 loading control; PDI: cytoplasmic loading control.

36 (C) Immunoblot analysis of the indicated proteins in C57BL/6 mice and in APC^{Min/+} mice
37 treated or not with azoxymethane.

38 (D) Densitometric analysis of co-immunoprecipitated p38 α and β -catenin in nuclear and
39 cytoplasmic fraction from colon tissues isolated from 12 C57BL/6 mice and 12 AOM-
40 treated APC^{Min/+} mice.

41 (E) ChIP with anti-p38 α and anti- β -catenin antibodies in CRC-SCs #21 and #8.
42 Quantification was done using the % input method.

43 N=nucleus; C=cytoplasm, AOM=azoxymethane. Statistical analysis was performed using
44 Student's t-tail test; *P<0.05 was considered statistically significant.

45

46 **Supplementary Figure 4. Prediction analysis of phosphorylation sites on β -catenin**
47 **amino acid sequence**

48 Schematic representation of the human β -catenin protein highlighting functional domains
49 and binding sites of the main interactors. *In silico* prediction analysis was performed using
50 five different servers: DISPHOS 1.3, NETPHOS 3.1, Phosida, iPTMnet, and Phosphosite
51 Plus.

52

53 **Supplementary Figure 5. Involvement of p38 α active form in p38 α - β -catenin**
54 **complexes**

55 (A) Immunoprecipitation of whole-cell lysates with an antiserum against p38 α followed by
56 immunoblotting with anti- β -catenin and anti-p-p38 antibodies in CRC-SCs #21.

57 (B) Immunoprecipitation of whole-cell lysates with an antiserum against β -catenin
58 followed by immunoblotting with anti-p38 α and anti-p-p38 antibodies in CRC-SCs #21.

59 (C) Immunoprecipitation of whole-cell lysates with an antiserum against p-p38 α followed
60 by immunoblotting with anti- β -catenin and anti-p38 α antibodies in CRC-SCs #9.

61 (A-C) Input corresponds to 10% of the lysate.

62

63 **Supplementary Figure 6. CRC-SC sorting of CD44v6^{low}- and CD44v6^{high}-enriched**
64 **populations**

65 Flow cytometry gating strategy (single cells/viable cells gates) and cell sorting of top 20%
66 CD44v6^{low} versus CD44v6^{high} CRC-SCs #8, #9, #21, and #40. Insets indicate the specific
67 isotype-matched control (IMC).

68

69 **Supplementary Figure 7. p38 α inhibition sensitizes patients-derived stage III CRC-**
70 **SCs to chemotherapeutics**

71 (A) Quantification of cell viability by Cell Titer Glo in CRC-SCs #40, #8, and #9 pre-
72 treated with ralimetinib (10 μ M) for 48 h and then treated with 5-FU (2 μ M), CDDP (30
73 μ M), CPT-11 (30 μ M), or trametinib (1 nM) for another 24 h in the presence of
74 ralimetinib.

75 (B) Quantification of cell death by trypan blue staining in CRC-SCs #40, #8, and #9
76 treated as described in (A).

77 (C) Colony-forming ability of CRC-SCs #40, #8, #9 seeded onto double-layer soft agar
78 and treated as described in (A). Data represent the percentage of colonies relative to
79 DMSO-treated cells.

80 (D) Migratory ability of growth factor-starved CRC-SCs #40, #8, and #9 placed in the
81 inner chamber of transwell plates and treated with the indicated compounds for 16-20 h.
82 Migrating cells were fixed and counted under a fluorescence microscope.

83 (E) Graph summarizing the percentage of Ki67-positive cells detected by flow cytometry
84 analysis in CRC-SCs #40, #8, and #9 treated as described in (A).

85 (F) Graph summarizing the percentage of apoptotic cells (early + late) detected by flow
86 cytometry analysis of annexin V staining in CRC-SCs #40, #8, and #9 treated as described
87 in (A).

88 Blue dots: #40; red dots: #9; green dots: #8. 5-FU=5-fluorouracil; CDDP=cisplatin; CPT-
89 11=irinotecan; Tram=trametinib. Statistical analysis was performed using Student's t-tail
90 test; *P<0.05: treatments vs. control (DMSO); and #P<0.05: combined treatment vs.
91 corresponding single treatments.

Chapter 4

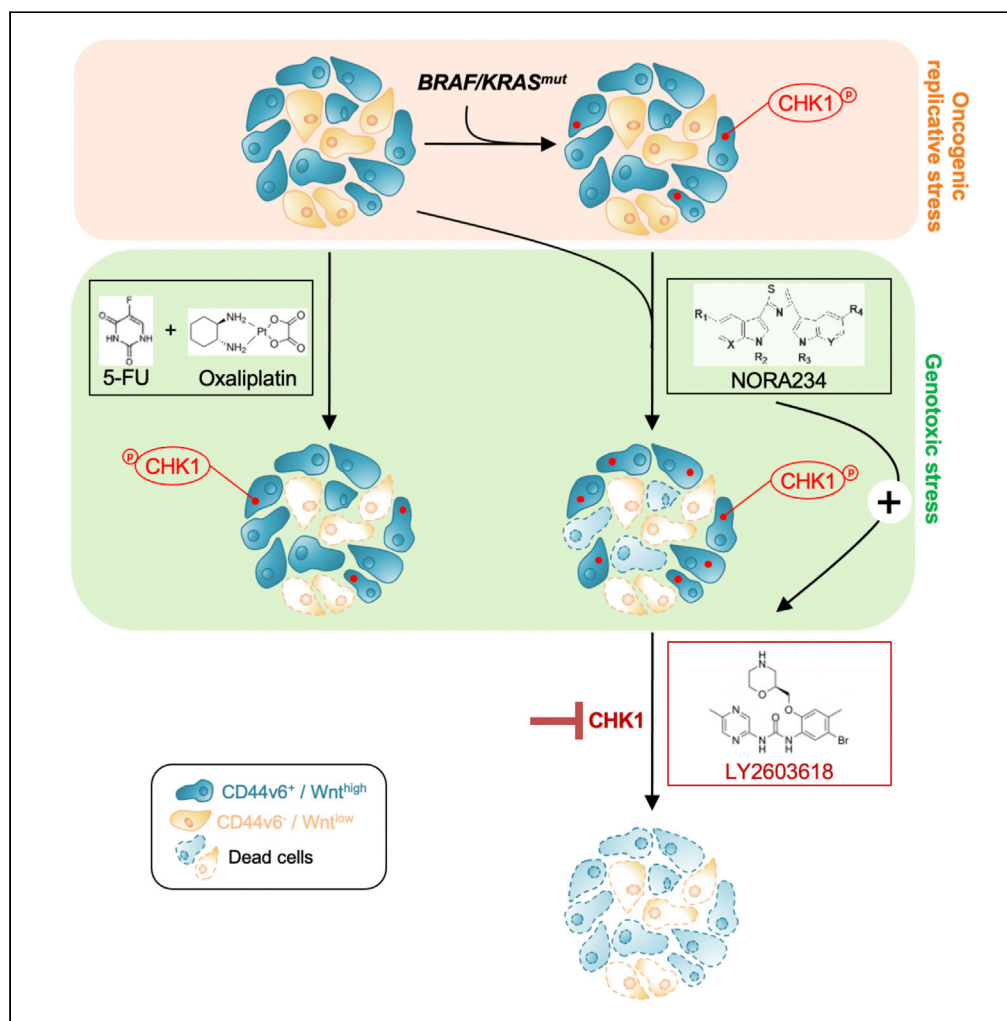
CHK1 inhibitor sensitizes resistant colorectal cancer stem cells to nortopsentin

Simone Di Franco, Barbara Parrino, Miriam Gaggianesi, Vincenzo Davide Pantina, Paola Bianca, Annalisa Nicotra, **Laura Rosa Mangiapane**, Melania Lo Iacono, Gloria Ganduscio, Veronica Veschi, Ornella Roberta Brancato, Antonino Glaviano, Alice Turdo, Irene Pillitteri, Lorenzo Colarossi, Stella Cascioferro, Daniela Carbone, Camilla Pecoraro, Micol Eleonora Fiori, Ruggero De Maria, Matilde Todaro, Isabella Screpanti, Girolamo Cirrincione, Patrizia Diana, and Giorgio Stassi

Published in *iScience*, 2021

Article

CHK1 inhibitor sensitizes resistant colorectal cancer stem cells to nortopsentin



Simone Di Franco,
Barbara Parrino,
Miriam
Gaggianesi, ...,
Girolamo
Cirrincione,
Patrizia Diana,
Giorgio Stassi

giorgio.stassi@unipa.it

Highlights

CR-CSCs acquire a long-term resistance to the NORA234 treatment

Replicative and genotoxic stress induces the activation of CHK1

Adaptive response to NORA234 is associated with high expression levels of CHK1

NORA234 together with targeting of CHK1 leads to depletion of CR-CSC compartment

Di Franco et al., iScience 24, 102664
June 25, 2021 © 2021 The Author(s).
<https://doi.org/10.1016/j.isci.2021.102664>



Article

CHK1 inhibitor sensitizes resistant colorectal cancer stem cells to nortopsentin

Simone Di Franco,^{1,9} Barbara Parrino,^{2,9} Miriam Gaggianesi,^{1,9} Vincenzo Davide Pantina,¹ Paola Bianca,¹ Annalisa Nicotra,¹ Laura Rosa Mangiapane,¹ Melania Lo Iacono,¹ Gloria Ganduscio,¹ Veronica Veschi,¹ Ornella Roberta Brancato,³ Antonino Glaviano,¹ Alice Turdo,³ Irene Pillitteri,¹ Lorenzo Colarossi,⁴ Stella Cascioferro,² Daniela Carbone,² Camilla Pecoraro,² Micol Eleonora Fiori,⁵ Ruggero De Maria,^{6,7} Matilde Todaro,³ Isabella Screpanti,⁸ Girolamo Cirrincione,² Patrizia Diana,² and Giorgio Stassi^{1,10,*}

SUMMARY

Limited therapeutic options are available for advanced colorectal cancer (CRC). Herein, we report that exposure to a neo-synthetic bis(indolyl)thiazole alkaloid analog, nortopsentin 234 (NORA234), leads to an initial reduction of proliferative and clonogenic potential of CRC sphere cells (CR-CSphCs), followed by an adaptive response selecting the CR-CSphC-resistant compartment. Cells spared by the treatment with NORA234 express high levels of CD44v6, associated with a constitutive activation of Wnt pathway. In CR-CSphC-based organoids, NORA234 causes a genotoxic stress paralleled by G2-M cell cycle arrest and activation of CHK1, driving the DNA damage repair of CR-CSphCs, regardless of the mutational background, microsatellite stability, and consensus molecular subtype. Synergistic combination of NORA234 and CHK1 (rabusertib) targeting is synthetic lethal inducing death of both CD44v6-negative and CD44v6-positive CRC stem cell fractions, aside from Wnt pathway activity. These data could provide a rational basis to develop an effective strategy for the treatment of patients with CRC.

INTRODUCTION

Notwithstanding the recent advances in cancer research and therapy, in terms of early diagnosis and treatment options, colorectal cancer (CRC) represents the second-leading cause of cancer-related death, owing to the phenomena of primary and acquired resistance to antitumor therapy, as well as the onset of recurrence and metastatic disease (Dillekas et al., 2019; Siegel et al., 2020). All these biological mechanisms have been recently demonstrated to be driven by a specific cancer cell subset, called cancer stem cells (CSCs), which is endowed with peculiar features shared with healthy stem cells responsible for tumor initiation, promotion, and progression (Puglisi et al., 2009; Todaro et al., 2014; Turdo et al., 2019). CSCs are characterized by several hallmarks that render them resistant to conventional therapy and able to disseminate to distant organs, including slow cycling, stemness/differentiative capacity, high expression of adenosine-triphosphate-binding cassette transporters, antiapoptotic proteins, and DNA damage repair machinery (Di Franco et al., 2014; Saigusa et al., 2009). Despite the advent of targeted therapies for the treatment of cancer, the resistance phenomenon and, in most cases, the low specificity are the key challenges. Thus, there is an urgent need to design innovative antitumor therapies that can efficiently target CRC stem cells (CR-CSCs) and, at the same time, reduce conventional treatment side effects (Veschi et al., 2020). We showed that activated CR-CSCs express CD44v6 and depend on the PI3K/AKT and Wnt pathway for their survival and spreading (Todaro et al., 2014; Vermeulen et al., 2010). Importantly from a clinical perspective, we have recently demonstrated that the expression of CD44v6, as well as the regulation of Wnt pathway, is a highly dynamic process during tumor progression, which is finely modulated by the tumor microenvironment (Lemos et al., 2018).

Recent findings have shown the promising use, as potential adjuvant, of natural compounds of different sources (Nobili et al., 2009). Although natural compounds need high doses for the completion of their biological activity, the low toxicity and capability of inhibiting multiple pathways represent a resourceful long-term strategy to boost standard anticancer therapeutic regimens (Lodi et al., 2017). In this context,

¹Department of Surgical, Oncological and Stomatological Sciences, University of Palermo, Università degli Studi di Palermo, Palermo, Italy

²Department of Biological, Chemical and Pharmaceutical Sciences and Technologies (STEBICEF), University of Palermo, Palermo, Italy

³Department of Health Promotion Sciences, Internal Medicine and Medical Specialties (PROMISE), University of Palermo, Palermo, Italy

⁴Pathology Unit, Mediterranean Institute of Oncology, Viagrande, Catania, Italy

⁵Department of Oncology and Molecular Medicine, Istituto Superiore di Sanità, Rome, Italy

⁶Institute of General Pathology, Università Cattolica del Sacro Cuore Facoltà di Medicina e Chirurgia, Roma, Italy

⁷Policlinico A Gemelli, Lazio, Roma, Italy

⁸Department of Molecular Medicine, Sapienza University, Rome, Italy

⁹These authors contributed equally

¹⁰Lead contact

*Correspondence: giorgio.stassi@unipa.it
<https://doi.org/10.1016/j.isci.2021.102664>



alkaloids, being characterized by a nitrogen atom within a heterocyclic ring, interact with a wide spectrum of molecules and have been recently recognized as an important source for cancer treatment (Carbone et al., 2020; Cascioferro et al., 2020a, 2020b; Habli et al., 2017; Jung et al., 2019; Kumar and Agnihotri, 2019; Lu et al., 2012). Among alkaloids, particular attention was given to nortopsentin, whose analogs showed good antiproliferative activity against several human tumor cell lines (Cascioferro et al., 2019; Kumar et al., 2011). We have reported that nortopsentin analogs effectively inhibit the *in vitro* activity of CDK1, causing a block in the G2/M cell cycle phase increasing the apoptotic events of pancreatic cancer cells (Carbone et al., 2015). Based on the significant functional effects of natural derivative compounds toward cancer (Habli et al., 2017; Moudi et al., 2013; Nobili et al., 2009), it is reasonable to hypothesize that CSCs could represent an elective target.

Importantly, in addition to the targeting of multiple intracellular pathways (Millimouno et al., 2014), alkaloids have been demonstrated to trigger DNA damage response (DDR) in cancer cells (Ehrhardt et al., 2013; Habli et al., 2017). After DNA damage, specific kinases such as ataxia telangiectasia mutated (ATM) and ataxia telangiectasia and Rad3 related (ATR) are recruited and activated, thus leading to activation of downstream effectors, including CHK1 (Walker et al., 2009). The activation of the ATR/CHK1 axis, which was highly detected in CRC, is pivotal for the cell cycle arrest in G2/M phases and activation of the DDR pathway (Gralewska et al., 2020; Zhang and Hunter, 2014). This hallmark enhances the capability of CSCs to activate DDR and induce resistance to anticancer therapy. CHK1 inhibitors are currently under clinical trial aiming to sensitize cancer cells to genotoxic agents (Hong et al., 2018; Rogers et al., 2020). In particular, the CHK1 inhibitor LY2603618 (rabusertib) displays a potent effect and a highly selective CHK1 inhibitor activity, without targeting CHK2 (King et al., 2014; Klaeger et al., 2017; van Harten et al., 2019).

Considering the potent antitumor activity of bis-indole neo-synthetic alkaloid compounds (Gul and Hamann, 2005), herein, we evaluate the biological activity of the bis-indole neo-synthetic alkaloid NORA234, as an anticancer agent that efficiently targets CR-CSCs.

RESULTS

CRC sphere cells possess intrinsic resistance to conventional chemotherapy

Taking advantage of our broad collection of primary cell lines, which recapitulate the main characteristics of parental cancer cells including the genomic and transcriptomic survey, we sought to explore the molecular mechanisms underlying the resistance of CRC sphere cells (CR-CSphCs) to standard chemotherapeutic regimen. Regardless from mutational status, CR-CSphCs displayed a stable proliferation after treatment with 5-fluorouracil (5-FU) in combination with oxaliplatin (Figure 1A). Of note, treated CR-CSphCs underwent a block on S phase, likely owing to the occurrence of DNA damage in the replication phase at early time point (Figure 1B).

Given that CR-CSphCs represent a heterogeneous cell compartment, characterized by the presence of cells at different stage of differentiation, such as progenitor and terminally differentiated cells, we investigated which cell fraction is spared by the chemotherapy treatment taking over and gaining a proliferative advantage. Among CR-CSphCs transduced with a GFP Wnt reporter gene, we observed that the GFP-negative fraction was sensitive to chemotherapy-induced cell death, whereas exposure to 5-FU in combination with oxaliplatin for 5 days led to a significant increase of survival of GFP⁺ CR-CSphCs, paralleled by a β -catenin activation (Figure 1C) (Vermeulen et al., 2010). We formerly provided evidence that while CD44v6 is a functional marker that pinpoints CRC cells endowed with the ability to *in vivo* generate and recapitulate the parental tumor, CD44v6-negative compartment is constituted by the transit-amplifying and differentiated cells (Todaro et al., 2014). As observed for Wnt pathway activity, chemotherapy did not efficiently target CD44v6-positive fraction (Figure 1D), thus confirming that standard antitumor therapy is able to only target differentiated CRC cells. Mouse avatars generated by subcutaneous injection of CR-CSphCs, treated with 5-FU in combination with oxaliplatin, showed a growth similar to treatment with a vehicle (Figure 1E). This poor effect on cancer cells was also associated with a significant decrease of the cell viability of healthy cells, already at a short term of exposure (Figure 1F). These data indicate the possibility that resistant tumorigenic cells can emerge and expand after the chemotherapy treatment.

NORA234 reduces CR-CSphCs proliferation and clonogenic potential

Because CR-CSphCs become resistant to the chemotherapy, we evaluated whether neo-synthetic alkaloid compounds could be exploited as innovative antitumor agents. Of six alkaloid derivatives tested,

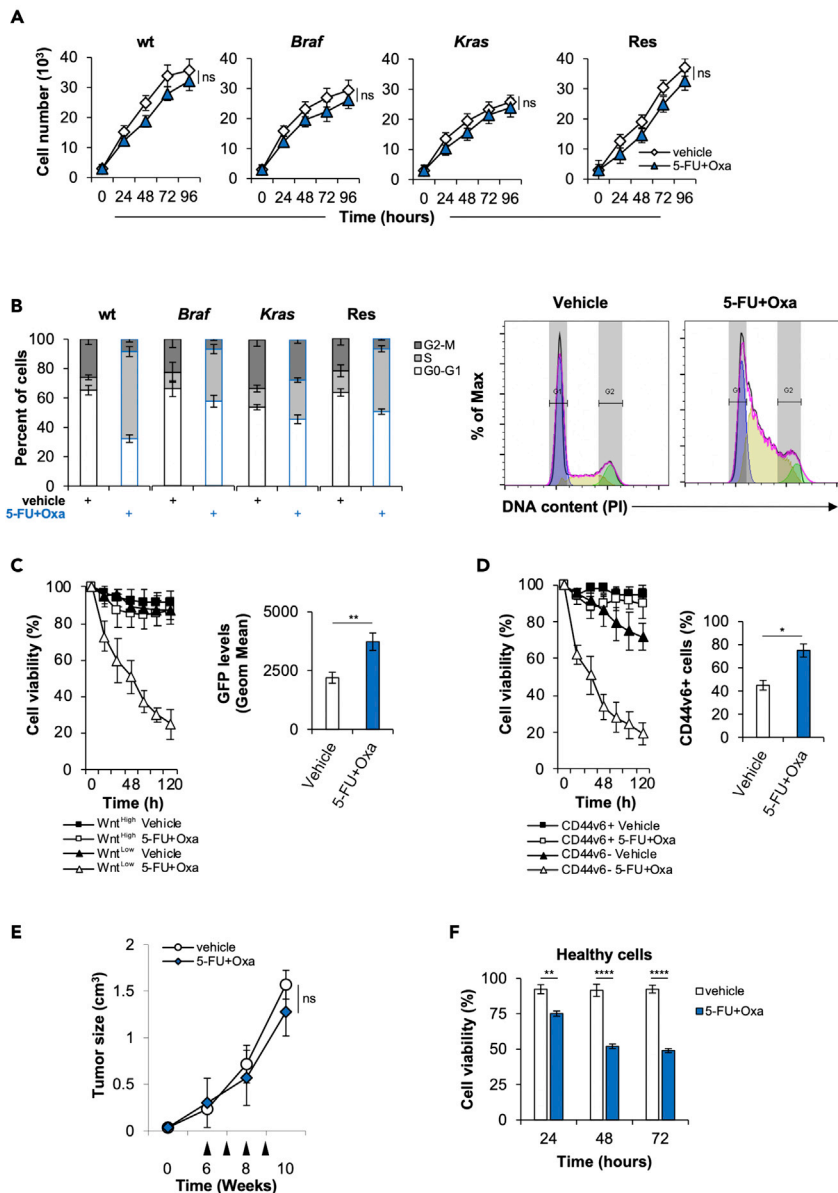


Figure 1. CR-CSphCs are endowed with innate chemoresistance

(A) Cell growth kinetics of CR-CSphCs treated with a vehicle or 5-FU in combination with oxaliplatin, up to 4 days. Data represent the mean \pm SD (n = 3) using 2 different CR-CSphC lines for each subgroup (wt, #7 and #21; Braf, #3 and #5; Kras #8 and #9; Res #R3 and #R4). Statistical significance between 2 groups was determined by unpaired Student's t-test (2-tailed). ns, nonsignificant.

(B) Cell cycle analysis in CR-CSphCs treated as in (A) for 24 h. Data show percentage of cell number in G0–G1, S, and G2–M phases. Data are expressed as mean \pm SD of three independent experiments performed in CR-CSphCs isolated from patients with wt (#7 and #21), Braf (#3 and #5), Kras (#8 and #9) and chemoresistant (#R3 and #R4) CRC. (Right panels) Representative cell cycle analysis of CR-CSphCs treated with a vehicle or 5-FU in combination with oxaliplatin, for 24 h (blue color = G0-G1; yellow color = S; green color = G2-M).

(C) Percentage of viability in flow-cytometry-sorted TOP-GFP CR-CSphCs, treated as in (A) up to 120 h. Data are expressed as mean \pm SD of three independent experiments performed using two different CR-CSphC lines (#8, #9). (Right panel) Representative flow cytometry analysis of TOP-GFP expression in spared CR-CSphCs, at 5 days. Statistical significance between 2 groups was determined by unpaired Student's t-test (2-tailed). **p \leq 0.01.

(D) Cell viability percentage of CR-CSphCs enriched for CD44v6 expression and treated with vehicle or 5-FU in combination with oxaliplatin up to 120 h. Data are expressed as mean \pm SD of three independent experiments performed using four different CR-CSphCs lines (#3, #9, #21, #R4). (Right panel) Representative flow cytometry analysis of the

Figure 1. Continued

percentage of CD44v6 positivity in spared CR-CSphCs, at 5 days. Statistical significance between 2 groups was determined by unpaired Student's t-test (2-tailed). * $p \leq 0.05$.

(E) Tumor size of CR-CSphCs subcutaneously injected into immunocompromized mice, treated for 4 weeks (from sixth to ninth week) with vehicle or 5-FU in combination with oxaliplatin. Data represent the mean \pm SD of tumor size measured in six mice per group, using 2 different CR-CSphC lines (#8, #21). Black arrowheads indicate weeks of treatment. Statistical significance between 2 groups was determined by unpaired Student's t-test (2-tailed). ns, nonsignificant.

(F) Cell viability analysis of healthy cells (IMEC and AD-MSCs) treated as in (D), for 3 days. Data are expressed as mean \pm SD of three independent experiments. Statistical significance between 2 groups was determined by unpaired Student's t-test (2-tailed).** $p \leq 0.01$; **** $p \leq 0.0001$. See also [Figure S1](#).

NORA234 showed a great antiproliferative effect on both established CRC cell lines and primary CR-CSphCs, in a time- and concentration-dependent manner ([Figures S1A–S1C](#)). Given the importance of mutational profile ([Domingo et al., 2018](#)), microsatellite instability (MSI) ([Fornasarig et al., 2000](#); [Ward et al., 2001](#)), consensus molecular subtype (CMS) ([Guinney et al., 2015](#)), and CD44v6 expression ([Todaro et al., 2014](#)) in the response to standard and targeted therapies, we investigated the ability of NORA234 to target CR-CSphCs on each of these subgroups.

Treatment with NORA234 reduced the cell viability of CR-CSphCs, regardless of their mutational/MSI status, CMS, and basal expression levels of CD44v6 ([Figures S1D–S1G](#)). Although NORA234 treatment alone led to delayed proliferation rate of CR-CSphCs unrelated to the mutational status, after 48 h, cells acquired resistance and started regrowing ([Figure 2A](#) and [Table S1](#)).

In addition, while NORA234 mainly targeted the Wnt^{low} cell compartment, only the 30% of CR-CSCs endowed with high Wnt pathway activity, highlighted by β -catenin-driven GFP expression, resulted affected ([Figures 2B](#) and [S1H](#)). In line with this phenomenon, 65% of CD44v6-positive CR-CSCs survived, whereas the differentiated fraction exhibited a pronounced sensitivity to NORA234 treatment ([Figures 2C](#) and [S1I](#)). These data indicate that this alkaloid derivative selectively target CD44v6-negative cells, sparing most CD44v6-positive CR-CSCs.

Of note, while long-term exposure to NORA234, by selecting the treatment-resistant cell clones, showed a stability of clonogenic potential, healthy cells did not show any significant toxicity ([Figures 2D](#) and [S1J–S1L](#)).

Acquired resistance to NORA234 is mediated by activation of DDR pathways driven by CHK1

To explore the molecular mechanisms involved in the adaptive response of CR-CSphCs, we evaluated whether NORA234 could induce a genotoxic defect that is repaired during the DNA replication. CR-CSphCs in response to NORA234 showed an increase G2-M phase, thus indicating that cell cycle arrest induced by DNA damage is required for the triggering of DDR machinery ([Figure 3A](#)). Proteomic analysis of DNA damage biomarkers exhibited increased expression levels of γ -H2AX and cleaved PARP, paralleled by upregulation of the homologous recombination repair protein RAD51 in CR-CSphCs after exposure to NORA234 ([Figure 3B](#)). Such treatment led to an induction of DNA damage and consequent cell death, which is more pronounced in wt CR-CSphCs ([Figures S2A–S2C](#)). Moreover, transcriptomic analysis revealed that CR-CSphCs respond to NORA234 treatment, regardless the mutational background, by increasing the expression of CHK1-related proteins, which are restored to basal levels on drug washout ([Figure 3C](#)). This phenomenon could be driven by genotoxic stress ([Figures 3D, 3E, S2D, and S2E](#)). Of note, CR-CSphCs bearing *Braf* or *Kras* oncogenic mutation displayed higher basal activation levels of CHK1, likely owing to the replicative stress induced by a dysregulated proliferative pathway ([Figures 3F, 3G, and S2F](#)) ([Colomer et al., 2019](#); [Manic et al., 2018](#)). Accordingly, analysis of a large cohort of patients with cancer showed a significant upregulation of CHK1 at both RNA and protein levels in CRC compared with healthy mucosa ([Figures S2F–S2H](#)) ([Madoz-Gurpide et al., 2007](#)). Altogether, these data suggest that CR-CSphCs are highly dependent on CHK1-mediated DDR in the resistance to genotoxic stress agents including NORA234.

NORA234 in combination with CHK1 inhibitor abrogates the CR-CSC compartment

We next investigated the role of CHK1 in the acquired resistance to NORA234 treatment of CR-CSCs. In accordance with literature, inducible silencing of CHK1 led to a block in S phase of the cell cycle and stabilization of CR-CSphCs proliferation ([Figures S3A–S3D](#)). After CHK1 downregulation, while the expression

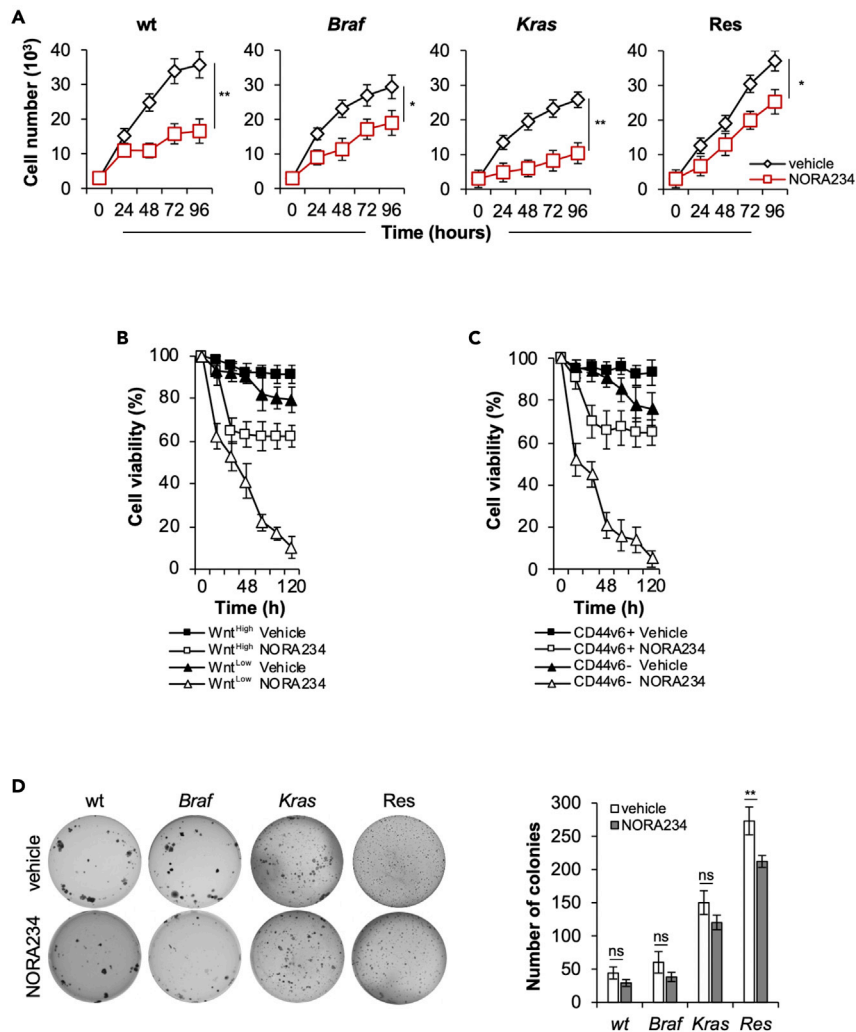


Figure 2. CD44v6⁺ CR-CSCs acquire resistance to NORA234 treatment

(A) Kinetics of cell growth of CR-CSpHCs treated with vehicle or NORA234, up to 4 days. Data represent the mean \pm SD ($n = 3$) using CR-CSpHCs isolated from wt (#7 and #21), *Braf* (#3 and #5), *Kras* (#8 and #9) and chemoresistant (#R3 and #R4) CRC patients. Statistical significance between 2 groups was determined by unpaired Student's t-test (2-tailed). * $p \leq 0.05$; ** $p \leq 0.01$.

(B) Viability percentage of low and high TOP-GFP cell fraction treated as in (A) up to 120 h. Data are expressed as mean \pm SD of three independent experiments performed using two different CR-CSpHC lines (#8, #9).

(C) Viability percentage of CR-CSpHCs enriched for CD44v6 expression and treated as in (A) up to 120 h. Data are expressed as mean \pm SD of three independent experiments performed using four different CR-CSpHC lines (#3, #9, #21, #R4).

(D) Colony-forming assay of CR-CSpHCs treated with a vehicle or NORA234, at 21 days. The number of colonies represents mean \pm SD of 3 independent experiments performed with cells isolated from 4 different patients with CRC (CR-CSpHCs #3, #9, #21, #R4). Statistical significance between 2 groups was determined by unpaired Student's t-test (2-tailed). ns, nonsignificant; ** $p \leq 0.01$. See also Figure S1.

γ -H2AX highly increased, a reduction of DDR response, highlighted by RAD51 expression, was observed in CR-CSpHCs. As consequence, CR-CSpHCs, harboring silenced CHK1, slightly enhanced apoptotic events (Figures S3E and S3F). Interestingly, after NORA234 treatment, downregulation of CHK1 sensitized CR-CSpHCs to induced cell death, associated with a significant decrease of cell proliferation and clonogenicity regardless the mutational background (Figures 4A–4C). Notwithstanding blockade of CHK1, by pharmacological inhibition with rabusertib (LY2603618), in combination with NORA234, had a limited toxic effect on healthy cells, CR-CSCs-expressing CD44v6, endowed with high activity of Wnt pathway and marked by

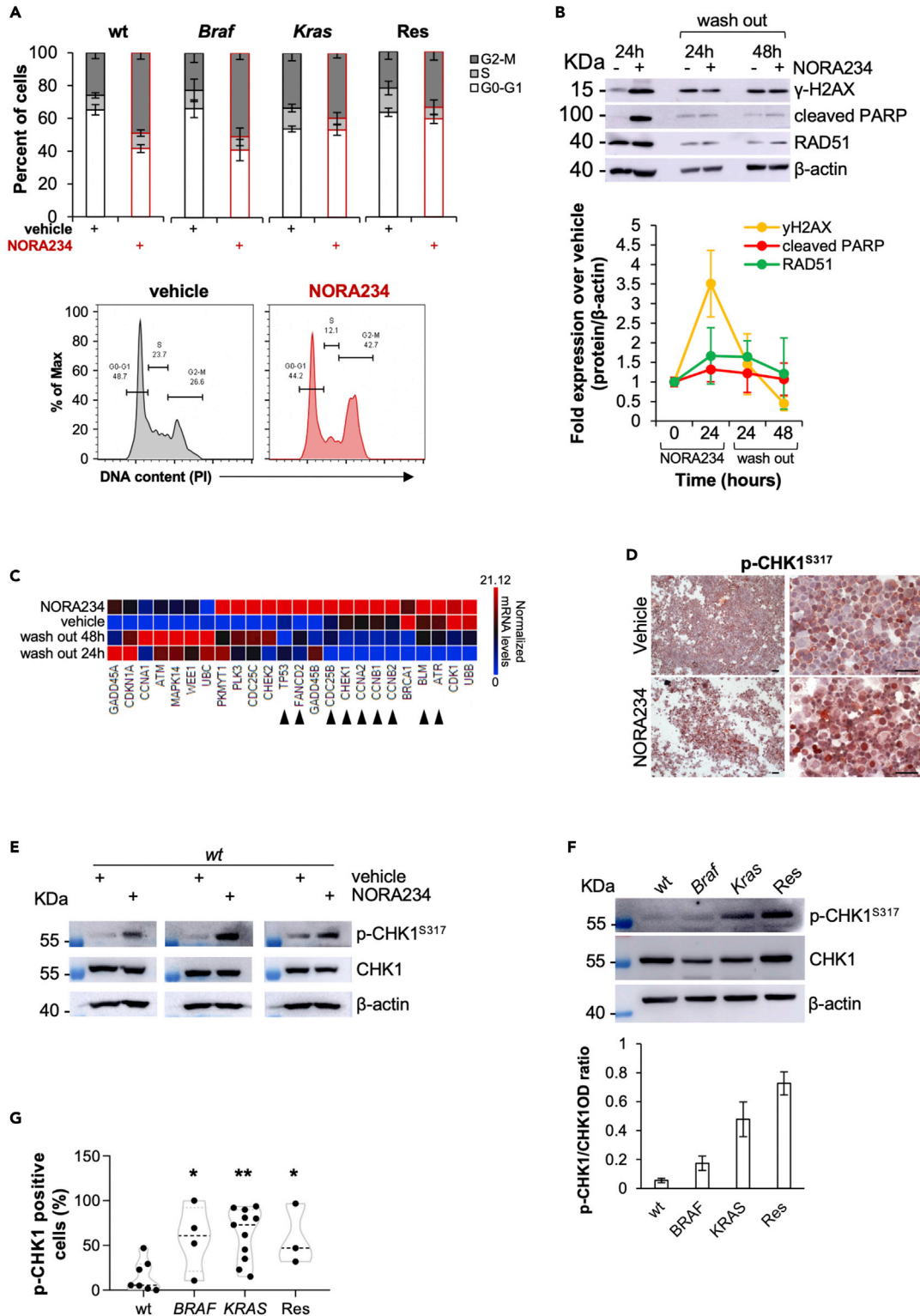


Figure 3. CR-CSphCs resistance to NORA234 is mediated by increased activity of CHK1-mediated DDR

(A) Cell cycle analysis in CR-CSphCs treated with a vehicle or NORA234 (red bars), for 24 h. The data show percentage of cell number in G0–G1, S, and G2–M phases. Data are expressed as mean \pm SD of three independent experiments performed with cells isolated from 4 different patients with CRC (CR-CSphCs #3, #9, #21, #R4). (Lower panels) Representative cell cycle analysis of CR-CSphCs (#R3) treated with vehicle or NORA234, for 24 h.

Figure 3. Continued

(B) Representative immunoblot analysis and quantification of DNA damage (γ -H2AX), apoptosis (cleaved PARP), and DDR (RAD51) markers expression in CR-CSphCs treated with vehicle or NORA234 at the indicated time points. β -actin was used as loading control. Data are presented as mean \pm S.D. of 2 independent experiments performed with cells isolated from 4 different patients with CRC (CR-CSphCs #3, #9, #21, #R4).

(C) Heatmap of DNA damage – ATM/ATR regulation of G2-M-checkpoint-related genes ($2^{-\Delta\Delta Ct}$ expression values) in CR-CSphCs treated as in (B). Data are presented as normalized expression values of cells isolated from 4 different CRC patients (CR-CSphCs #3, #9, #21, #R4). Black arrow heads indicate genes upregulated upon 24 h of treatment with NORA234, which values are restored to basal levels after 48 h of drug washout.

(D) Representative immunocytochemistry analysis of nuclear p-CHK1, in CR-CSphCs (#21) treated with a vehicle, 5-FU in combination with oxaliplatin, or NORA234, at 24 h. Scale bars, 100 μ m.

(E) Immunoblot analysis of p-CHK1 and CHK1 in wt CR-CSphCs (CSphC #21, #24, and #33) treated as indicated for 24 h. β -actin was used as a loading control.

(F) Immunoblot and its relative OD ratio analysis of p-CHK1 and CHK1 in wt, *Braf*, *Kras*, or chemoresistant CR-CSphCs. β -actin was used as a loading control. Data are presented as mean \pm S.D. of 2 independent experiments performed with cells isolated from 4 different patients with CRC (CR-CSphCs #21, #3, #9, #R4).

(G) Box and violin plot of p-CHK1 positivity, evaluated by flow cytometry, in wt (CR-CSphCs #7, #14, #24, #35, #37, #58), *Braf* (CR-CSphCs #1, #2, #3, #4), *Kras* (CR-CSphCs #8, #9, #10, #11, #12, #15, #16, #20, #22, #57, #59), or chemoresistant CR-CSphCs (CR-CSphCs #R2, #R3, #R4). Data are expressed as mean \pm SD of three independent experiments. Statistical significance between 2 groups was determined by unpaired Student's t-test (2-tailed). * $p \leq 0.05$; ** $p \leq 0.01$. See also [Figure S2](#).

nuclear β -catenin, were efficiently targeted (Todaro et al., 2014; Vermeulen et al., 2010) (Figures 4D–4F and S4A–S4F).

Notably, the combinatorial treatment based on the use of NORA234 and CHK1 inhibitor showed a synergistic effect possibly driven by the concomitant induction of DNA damage followed by the inhibition of DDR molecular machinery (Figure S4G).

These data indicate that inhibition of CHK1 together with a genotoxic stress may be considered as promising synthetic lethal antitumor regimen for patients with CRC regardless the mutational status.

DISCUSSION

Treatment of CRC is currently based on chemotherapy regimen and EGFR- or VEGF-based targeted therapies. These treatments are unable to target CR-CSCs expressing CD44v6, which acquire an adaptive therapy resistance owing to the constitutive activation of PI3K and Wnt pathway (Mangiapan et al., 2021; Todaro et al., 2014). CR-CSphCs exposed to NORA234 led to an initial decrease of proliferative capacity and clonogenicity, which was followed by the regrowth of resistant subclones, characterized by high expression levels of CD44v6 and β -catenin activity. The block in G2-M of CR-CSphCs induced by NORA234-driven genotoxic stress is likely paralleled with the inhibition of ATM-regulated DNA damage checkpoint. However, the adaptive response to NORA234 led to a restore of genome integrity mediated by RAD51 and highlighted by the reduction of γ -H2AX, thus giving evidence of an alternative DDR mechanism. Transcriptomic and proteomic analysis showed that the transient effect induced by NORA234 was followed by accumulation of a cell fraction endowed with highly activation of CHK1-mediated DDR machinery. In presence of replication stress (RS), CHK1 directly interacts with ATR (Chen and Poon, 2008; Madoz-Gurpide et al., 2007), by playing a crucial role in DNA replication, response to RS, and cell cycle progression (Zeman and Cimprich, 2014; Zhang and Hunter, 2014).

Here, we show that CR-CSphCs are highly dependent on CHK1-mediated DDR in the resistance to genotoxic stress induced by alkaloid derivate, NORA234, probably reducing the genomic instability, sustained by RS (Aguilera and Garcia-Muse, 2013; Cancer Genome Atlas, 2012; Gorgoulis et al., 2005; Pearl et al., 2015). Proliferative cancer cells are highly dependent on cell cycle checkpoints controlled by CHK1 posing this mechanism as the "Achilles' heel" (Dietlein et al., 2015). Blockade of CHK1 activity inhibits cancer cell replication and cell cycle checkpoints, thus leading CR-CSphCs to apoptosis regardless of their mutational status (Manic et al., 2018, 2021). On these premises, CHK1 inhibitors have been recently exploited in clinical studies to block RS-induced pathways in cancer cells endowed with DDR defects (NCT01341457, NCT01296568, NCT00415636) (Reilly et al., 2019). Treatment with CHK1 inhibitor (LY2603618) in combination with gemcitabine and pemetrexed reported adverse effects (NCT01139775) (Wehler et al., 2017). Although the results obtained using CHK1-based double combinations showed acceptable safety and pharmacokinetics, the response of patients with cancer was below expectation (Calvo et al., 2016; Gorecki et al., 2021; Weiss et al., 2013). Thus, all together these findings point out the urgent need to improve patient selection criteria (i.e., mutational profile) and design a new combinatorial treatment strategy.

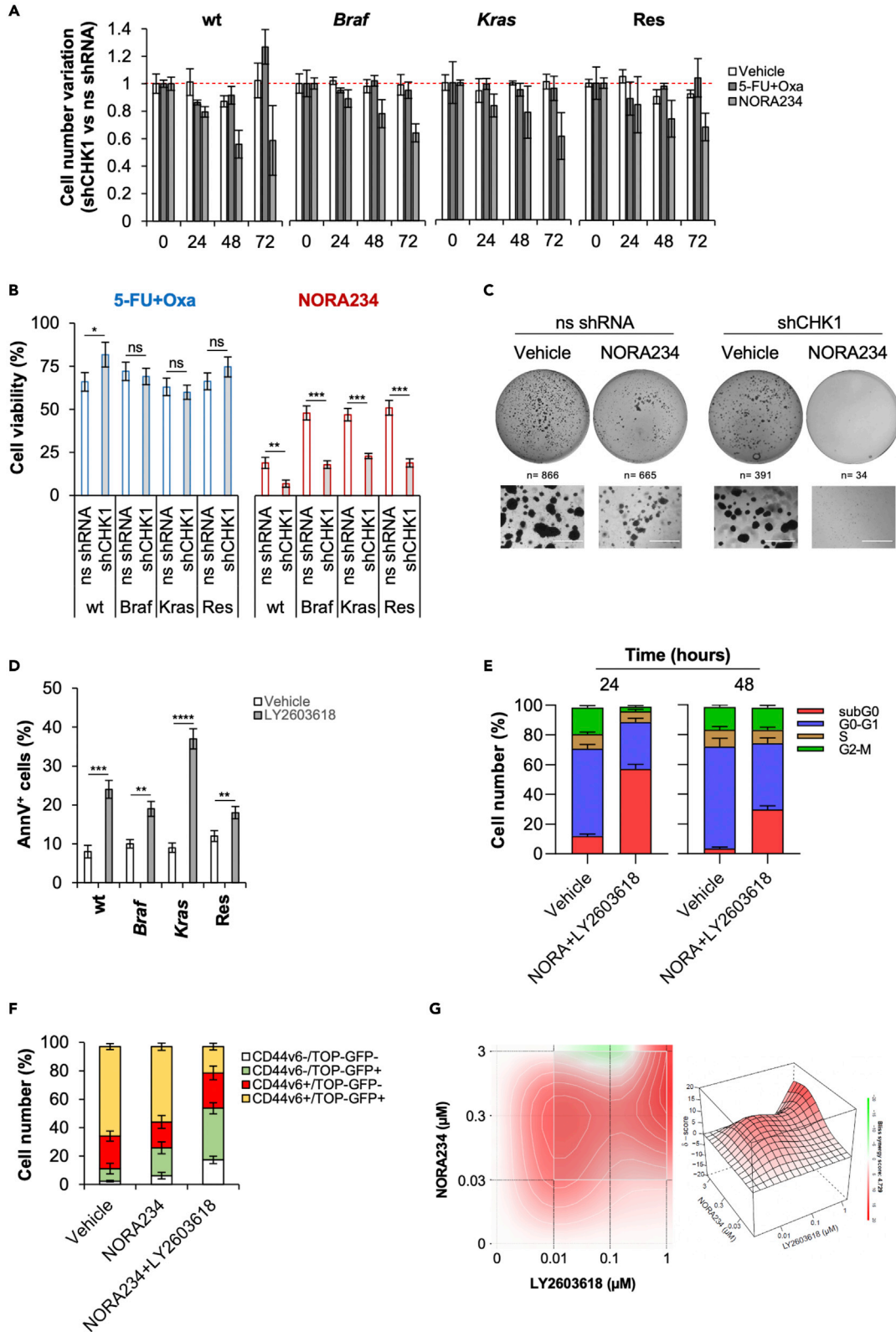


Figure 4. Inhibition of CHK1 activity sensitized CR-CSphCs to NORA234 by synthetic lethality

(A) Fold variation of cell number in CR-CSphCs transduced with shCHK1 or ns shRNA and treated with vehicle, 5-FU in combination with oxaliplatin, or NORA234, up to 72 h. Data are mean \pm S.D. of 3 independent experiments performed with cells isolated from patients with wt (#21), *Braf* (#3), *Kras* (#9), or chemoresistant (#R4) CRC.

(B) Cell viability analysis of cells treated as in (A) for 72 h. Data are mean \pm S.D. of 3 independent experiments performed with cells isolated from 4 different CRC patients (CR-CSphCs #3, #9, #21, #R4). Statistical significance between 2 groups was determined by unpaired Student's t-test (2-tailed). ns, nonsignificant; * $p \leq 0.05$; ** $p \leq 0.01$; *** $p \leq 0.001$.

(C) Representative colony forming assay of CR-CSphCs (R#4) transduced with shCHK1 or ns shRNA and treated with vehicle or NORA234, at 21 days. *n* represents the number of colonies. Scale bars, 1000 μm .

(D) Percentage of Annexin V positivity in CR-CSphCs treated with vehicle or rabusertib (LY2603618), for 24 h. Data represent mean \pm S.D. of 3 independent experiments performed with cells isolated from patients with wt (#21), *Braf* (#3), *Kras* (#9) or chemoresistant (#R4) CRC. Statistical significance between 2 groups was determined by unpaired Student's t-test (2-tailed). ** $p \leq 0.01$; *** $p \leq 0.001$; **** $p \leq 0.0001$.

(E) Cell cycle analysis in CR-CSphCs treated with vehicle or NORA234 in combination with Rabusertib (LY2603618), for 48 h. Data show percentage of cell number in subG0 (red color), G0–G1 (blue color), S (brow color), and G2–M (green color) cell cycle phase. Data are expressed as mean \pm SD of three independent experiments using cells isolated from 4 different patients with CRC (CR-CSphCs #3, #9, #21, #R4).

(F) Flow cytometry analysis of GFP and CD44v6 positivity percentage in CR-CSphCs transduced with TOP-GFP and treated with a vehicle, NORA234, alone or in combination with rabusertib (LY2603618), for 48 hr. Data are expressed as mean \pm SD of three independent experiments using cells isolated from 2 different patients with CRC (CR-CSphCs #8, #9).

(G) 3D synergy map of viability in CR-CSphCs treated alone or in combination with NORA234 and rabusertib (LY2603618) at the indicated doses, for 48 h. Data are mean of 3 independent experiments using cells isolated from patients with wt (#21), *Braf* (#3), *Kras* (#9) or chemoresistant (#R4) CRC. See also Figures S3 and S4.

Addition of CHK1 inhibitor to the NORA234 treatment was able to synergistically target CR-CSphCs, regardless of their mutational background, having a limited toxic effect on healthy cells. Of note, the double combination led to a marked apoptotic induction in the CSC compartment, as highlighted by the reduction of CD44v6⁺/Wnt^{high} cells, and the concurrent abrogation of CR-CSphCs proliferation and clonogenicity. Such treatment overcame the acquired resistance mechanisms dictated by chemotherapy and targeted therapies, which mostly affect the more differentiated CD44v6-negative cell compartment (Mangiapane et al., 2021; Siravegna et al., 2015).

Our results provide evidence that CR-CSphCs circumvent the genotoxic stress and induction of apoptosis driven by NORA234 by hijacking toward the activation of CHK1. Accordingly, the inhibition of CHK1, by both genetic and pharmacological approach, sensitizes CR-CSphCs to NORA234, thus suggesting that the pharmacological inhibition of two DDR effectors, such as ATM and CHK1, might be exploited in pre-clinical models (Mauri et al., 2020; Rundle et al., 2017).

DDR is a key mechanism whose molecular components are finely regulated during CRC progression, thus conferring a selective advantage in the acquisition of genetic alterations and chemoresistance. A major limitation in the use of genotoxic antitumor drugs is represented by the presence of CSCs, which are endowed with innate chemoresistance. Here, we demonstrate that nortopsentin analog, NORA234, targets CR-CSphCs, which acquire an adaptive resistance by upregulating CHK1-driven DDR pathways. The combinatorial treatment based on the use of NORA234 and CHK1 inhibitor was sufficient to abrogate CR-CSCs proliferative and clonogenic potential, regardless the mutational status.

Although further advances are needed to elucidate the clinical relevance of presented findings, our results demonstrate that NORA234 displays a synthetic lethality effect with the deficiency of CHK1-mediated DDR mechanisms, thus suggesting its putative exploitation in clinical setting as adjuvant therapy to sensitize CR-CSCs to targeted therapy.

Limitations of the study

Although our *in vitro* analyses clearly demonstrated that CR-CSCs are targeted by the combination treatment based on the use of nortopsentin analog and CHK1 inhibitor, its exploitation in adjuvant clinical setting should be previously validated in a metastatic preclinical study.

Resource availability**Lead contact**

Further information and requests for resources and reagents should be directed to and will be fulfilled by the lead contact, Giorgio Stassi (giorgio.stassi@unipa.it). This study led to the generation of new unique reagents.

Materials availability

All the reagents and data generated in this study will be made available on request. A payment and/or a completed Materials Transfer Agreement could be required if there is potential for commercial application.

Data and code availability

This study did not generate/analyze data sets/codes.

STAR★METHODS

Detailed methods are provided in the online version of this paper and include the following:

- **KEY RESOURCE TABLE**
- **EXPERIMENTAL MODELS AND SUBJECT DETAILS**
 - Colorectal cancer cells isolation and culture
 - Animals and tumor models
- **METHODS DETAILS**
 - *In vitro* treatment of CR-CSphCs
 - Synthesis of nortopsentin analog compounds
 - Cell viability, proliferation, and clonogenic assay
 - Flow cytometry, cell sorting, and cell cycle analysis
 - Cell transfection and lentiviral transduction
 - Immunohistochemistry and immunofluorescence
 - Real-time polymerase chain reaction
 - Western blot
- **QUANTIFICATION AND STATISTICAL ANALYSIS**
 - Database and statistical analysis

SUPPLEMENTAL INFORMATION

Supplemental information can be found online at <https://doi.org/10.1016/j.isci.2021.102664>.

ACKNOWLEDGMENTS

AT and VV are research fellows funded by European Union FESR FSE, PON Ricerca e Innovazione 2014–2020 (AIM line 1). This work was supported by Italian Association of Cancer Research Investigator Grant (21445) and PRIN (2017WNKSLR) to G.S., RF2018-12367044 to R.D.M. and M.T., and PON ARS01_00432 to R.D.M., I.S., P.D., and G.S.

AUTHOR CONTRIBUTIONS

Conceptualization and visualization: S.D.F., B.P., M.G., and G.S.; Methodology, S.D.F., B.P., M.G., V.D.P., P.B., A.N., L.R.M., M.L.I., G.G., V.V., A.G., A.T., I.P., and M.T.; Software and formal analysis: S.D.F., B.P., M.G., and A.T.; Writing – original draft: S.D.F., B.P., M.G., P.D., and G.S.; Writing – review & editing: S.D.F., M.G., M.T., R.D.M., P.D., and G.S.; Resources: B.P., L.C., S.C., D.C., C.P., M.E.F., G.C., P.D., and G.S.; Supervision: M.T., R.D.M., I.S., P.D., and G.S.; Funding acquisition: R.D.M., M.T., I.S., P.D., and G.S.

DECLARATION OF INTERESTS

The authors have no conflicts of interests to declare.

INCLUSION AND DIVERSITY

The author list of this paper includes contributors from the location where the research was conducted who participated in the data collection, design, analysis, and/or interpretation of the work.

Received: February 22, 2021

Revised: May 3, 2021

Accepted: May 26, 2021

Published: June 25, 2021

REFERENCES

- Aguilera, A., and Garcia-Muse, T. (2013). Causes of genome instability. *Annu. Rev. Genet.* 47, 1–32.
- Calvo, E., Braiteh, F., Von Hoff, D., McWilliams, R., Becerra, C., Galsky, M.D., Jameson, G., Lin, J., McKane, S., Wickremsinhe, E.R., et al. (2016). Phase I study of CHK1 inhibitor LY2603618 in combination with gemcitabine in patients with solid tumors. *Oncology* 91, 251–260.
- Cancer Genome Atlas, N. (2012). Comprehensive molecular characterization of human colon and rectal cancer. *Nature* 487, 330–337.
- Carbone, A., Parrino, B., Di Vita, G., Attanzio, A., Spano, V., Montalbano, A., Barraja, P., Tesoriere, L., Livrea, M.A., Diana, P., et al. (2015). Synthesis and antiproliferative activity of thiazolyl-bis-pyrrolo[2,3-b]pyridines and indolyl-thiazolyl-pyrrolo[2,3-c]pyridines, nortopsentin analogues. *Mar. Drugs* 13, 460–492.
- Carbone, D., Parrino, B., Cascioferro, S., Pecoraro, C., Giovannetti, E., Di Sarno, V., Musella, S., Auriemma, G., Cirrincione, G., and Diana, P. (2020). 1,2,4-Oxadiazole topsentin analogs with antiproliferative activity against pancreatic cancer cells, targeting GSK3beta kinase. *ChemMedChem* 16, 537–554.
- Cascioferro, S., Attanzio, A., Di Sarno, V., Musella, S., Tesoriere, L., Cirrincione, G., Diana, P., and Parrino, B. (2019). New 1,2,4-oxadiazole nortopsentin derivatives with cytotoxic activity. *Mar. Drugs* 17, 35.
- Cascioferro, S., Li Petri, G., Parrino, B., El Hassouni, B., Carbone, D., Arizza, V., Perricone, U., Padova, A., Funel, N., Peters, G.J., et al. (2020a). 3-(6-Phenylimidazo [2,1-b][1,3,4]thiadiazol-2-yl)-1H-indole derivatives as new anticancer agents in the treatment of pancreatic ductal adenocarcinoma. *Molecules* 25, 329.
- Cascioferro, S., Petri, G.L., Parrino, B., Carbone, D., Funel, N., Bergonzini, C., Mantini, G., Dekker, H., Geerke, D., Peters, G.J., et al. (2020b). Imidazo [2,1-b][1,3,4]thiadiazoles with antiproliferative activity against primary and gemcitabine-resistant pancreatic cancer cells. *Eur. J. Med. Chem.* 189, 112088.
- Chen, Y., and Poon, R.Y. (2008). The multiple checkpoint functions of CHK1 and CHK2 in maintenance of genome stability. *Front Biosci.* 13, 5016–5029.
- Colomer, C., Margalef, P., Villanueva, A., Vert, A., Pecharroman, I., Sole, L., Gonzalez-Farre, M., Alonso, J., Montagut, C., Martinez-Iniesta, M., et al. (2019). IKKalpha kinase regulates the DNA damage response and drives chemo-resistance in cancer. *Mol. Cell* 75, 669–682.e65.
- Di Franco, S., Todaro, M., Dieli, F., and Stassi, G. (2014). Colorectal cancer defeating? Challenge accepted! *Mol. Aspects Med.* 39, 61–81.
- Dietlein, F., Kalb, B., Jokic, M., Noll, E.M., Strong, A., Tharun, L., Ozretic, L., Kunstlinger, H., Kambartel, K., Randerath, W.J., et al. (2015). A synergistic interaction between Chk1- and MK2 inhibitors in KRAS-mutant cancer. *Cell* 162, 146–159.
- Dillekas, H., Rogers, M.S., and Straume, O. (2019). Are 90% of deaths from cancer caused by metastases? *Cancer Med.* 8, 5574–5576.
- Domingo, E., Camps, C., Kaisaki, P.J., Parsons, M.J., Mouradov, D., Pentony, M.M., Makino, S., Palmieri, M., Ward, R.L., Hawkins, N.J., et al. (2018). Mutation burden and other molecular markers of prognosis in colorectal cancer treated with curative intent: results from the QUASAR 2 clinical trial and an Australian community-based series. *Lancet Gastroenterol. Hepatol.* 3, 635–643.
- Ehrhardt, H., Pfeiffer, S., Schrems, D., Wachter, F., Grunert, M., and Jeremias, I. (2013). Activation of DNA damage response by antitumor therapy counteracts the activity of vinca alkaloids. *Anticancer Res.* 33, 5273–5287.
- Fornasarig, M., Viel, A., Valentini, M., Capozzi, E., Sigon, R., De Paoli, A., Della Puppa, L., and Boiocchi, M. (2000). Microsatellite instability and MLH1 and MSH2 germline defects are related to clinicopathological features in sporadic colorectal cancer. *Oncol. Rep.* 7, 39–43.
- Gorecki, L., Andrs, M., and Korabecny, J. (2021). Clinical candidates targeting the ATR-CHK1-WEE1 Axis in cancer. *Cancers (Basel)* 13, 795.
- Gorgoulis, V.G., Vassiliou, L.V., Karakaidos, P., Zacharatos, P., Kotsinas, A., Liloglou, T., Venere, M., Dittullo, R.A., Jr., Kastrinakis, N.G., Levy, B., et al. (2005). Activation of the DNA damage checkpoint and genomic instability in human precancerous lesions. *Nature* 434, 907–913.
- Gralewska, P., Gajek, A., Marczak, A., and Rogalska, A. (2020). Participation of the ATR/CHK1 pathway in replicative stress targeted therapy of high-grade ovarian cancer. *J. Hematol. Oncol.* 13, 39.
- Guinney, J., Dienstmann, R., Wang, X., de Reynies, A., Schlicker, A., Soneson, C., Marisa, L., Roepman, P., Nyamundanda, G., Angelino, P., et al. (2015). The consensus molecular subtypes of colorectal cancer. *Nat. Med.* 21, 1350–1356.
- Gul, W., and Hamann, M.T. (2005). Indole alkaloid marine natural products: an established source of cancer drug leads with considerable promise for the control of parasitic, neurological and other diseases. *Life Sci.* 78, 442–453.
- Habli, Z., Toumeh, G., Fatfat, M., Rahal, O.N., and Gali-Muhtasib, H. (2017). Emerging cytotoxic alkaloids in the battle against cancer: overview of molecular mechanisms. *Molecules* 22, 250.
- Hong, D.S., Moore, K., Patel, M., Grant, S.C., Burris, H.A., 3rd, William, W.N., Jr., Jones, S., Meric-Bernstam, F., Infante, J., Golden, L., et al. (2018). Evaluation of Prexasertib, a checkpoint kinase 1 inhibitor, in a phase Ib study of patients with squamous cell carcinoma. *Clin. Cancer Res.* 24, 3263–3272.
- Ianevski, A., He, L., Aittokallio, T., and Tang, J. (2017). SynergyFinder: a web application for analyzing drug combination dose-response matrix data. *Bioinformatics* 33, 2413–2415.
- Jung, Y.Y., Shanmugam, M.K., Narula, A.S., Kim, C., Lee, J.H., Namjoshi, O.A., Blough, B.E., Sethi, G., and Ahn, K.S. (2019). Oxymatrine attenuates tumor growth and deactivates STAT5 signaling in a lung cancer xenograft model. *Cancers (Basel)* 11, 49.
- King, C., Diaz, H., Barnard, D., Barda, D., Clawson, D., Blosser, W., Cox, K., Guo, S., and Marshall, M. (2014). Characterization and preclinical development of LY2603618: a selective and potent Chk1 inhibitor. *Invest New Drugs* 32, 213–226.
- Klaeger, S., Heinzlmeir, S., Wilhelm, M., Polzer, H., Vick, B., Koenig, P.A., Reinecke, M., Ruprecht, B., Petzoldt, S., Meng, C., et al. (2017). The target landscape of clinical kinase drugs. *Science* 358, eaan4368.
- Kumar, D., Kumar, N.M., Chang, K.H., Gupta, R., and Shah, K. (2011). Synthesis and in-vitro anticancer activity of 3,5-bis(indolyl)-1,2,4-thiadiazoles. *Bioorg. Med. Chem. Lett.* 21, 5897–5900.
- Kumar, S., and Agnihotri, N. (2019). Piperlongumine, a piper alkaloid targets Ras/PI3K/Akt/mTOR signaling axis to inhibit tumor cell growth and proliferation in DMH/DSS induced experimental colon cancer. *Biomed. Pharmacother.* 109, 1462–1477.
- Lenos, K.J., Miedema, D.M., Lodestijn, S.C., Nijman, L.E., van den Bosch, T., Romero Ros, X., Lourenco, F.C., Lecca, M.C., van der Heijden, M., van Neerven, S.M., et al. (2018). Stem cell functionality is microenvironmentally defined during tumour expansion and therapy response in colon cancer. *Nat. Cell Biol* 20, 1193–1202.
- Lodi, A., Saha, A., Lu, X., Wang, B., Sentandreu, E., Collins, M., Kolonin, M.G., DiGiovanni, J., and Tiziani, S. (2017). Combinatorial treatment with natural compounds in prostate cancer inhibits prostate tumor growth and leads to key modulations of cancer cell metabolism. *NPJ Precis Oncol.* 1, 18.
- Lu, J.J., Bao, J.L., Chen, X.P., Huang, M., and Wang, Y.T. (2012). Alkaloids isolated from natural herbs as the anticancer agents. *Evid. Based Complement Alternat Med.* 2012, 485042.
- Madoz-Gurpide, J., Canamero, M., Sanchez, L., Solano, J., Alfonso, P., and Casal, J.I. (2007). A proteomics analysis of cell signaling alterations in colorectal cancer. *Mol. Cell Proteomics* 6, 2150–2164.
- Mangiapane, L.R., Nicotra, A., Turdo, A., Gaggianesi, M., Bianca, P., Di Franco, S., Sardina, D.S., Veschi, V., Signore, M., Beyes, S., et al. (2021). PI3K-driven HER2 expression is a potential therapeutic target in colorectal cancer stem cells. *Gut*.
- Manic, G., Musella, M., Corradi, F., Sistigu, A., Vitale, S., Soliman Abdel Rehim, S., Mattiello, L., Malacaria, E., Galassi, C., Signore, M., et al. (2021). Control of replication stress and mitosis in colorectal cancer stem cells through the interplay of PARP1, MRE11 and RAD51. *Cell Death Differ.*
- Manic, G., Signore, M., Sistigu, A., Russo, G., Corradi, F., Siteni, S., Musella, M., Vitale, S., De Angelis, M.L., Pallocca, M., et al. (2018). CHK1-targeted therapy to deplete DNA replication-stressed, p53-deficient, hyperdiploid colorectal cancer stem cells. *Gut* 67, 903–917.

- Mauri, G., Arena, S., Siena, S., Bardelli, A., and Sartore-Bianchi, A. (2020). The DNA damage response pathway as a land of therapeutic opportunities for colorectal cancer. *Ann. Oncol.* **31**, 1135–1147.
- Millimouno, F.M., Dong, J., Yang, L., Li, J., and Li, X. (2014). Targeting apoptosis pathways in cancer and perspectives with natural compounds from mother nature. *Cancer Prev. Res. (Phila)* **7**, 1081–1107.
- Moudi, M., Go, R., Yien, C.Y., and Nazre, M. (2013). Vinca alkaloids. *Int. J. Prev. Med.* **4**, 1231–1235.
- Nobili, S., Lippi, D., Witort, E., Donnini, M., Bausi, L., Mini, E., and Capaccioli, S. (2009). Natural compounds for cancer treatment and prevention. *Pharmacol. Res.* **59**, 365–378.
- Pearl, L.H., Schierz, A.C., Ward, S.E., Al-Lazikani, B., and Pearl, F.M. (2015). Therapeutic opportunities within the DNA damage response. *Nat. Rev. Cancer* **15**, 166–180.
- Puglisi, M.A., Sgambato, A., Saulnier, N., Rafanelli, F., Barba, M., Boninsegna, A., Piscaglia, A.C., Lauritano, C., Novi, M.L., Barbaro, F., et al. (2009). Isolation and characterization of CD133+ cell population within human primary and metastatic colon cancer. *Eur. Rev. Med. Pharmacol. Sci.* **13** (Suppl 1), 55–62.
- Reilly, N.M., Novara, L., Di Nicolantonio, F., and Bardelli, A. (2019). Exploiting DNA repair defects in colorectal cancer. *Mol. Oncol.* **13**, 681–700.
- Rogers, R.F., Walton, M.I., Cherry, D.L., Collins, I., Clarke, P.A., Garrett, M.D., and Workman, P. (2020). CHK1 inhibition is synthetically lethal with loss of B-family DNA polymerase function in human lung and colorectal cancer cells. *Cancer Res.* **80**, 1735–1747.
- Rundle, S., Bradbury, A., Drew, Y., and Curtin, N.J. (2017). Targeting the ATR-CHK1 Axis in cancer therapy. *Cancers (Basel)* **9**, 41.
- Saigusa, S., Tanaka, K., Toiyama, Y., Yokoe, T., Okugawa, Y., Ioue, Y., Miki, C., and Kusunoki, M. (2009). Correlation of CD133, OCT4, and SOX2 in rectal cancer and their association with distant recurrence after chemoradiotherapy. *Ann. Surg. Oncol.* **16**, 3488–3498.
- Siegel, R.L., Miller, K.D., and Jemal, A. (2020). Cancer statistics, 2020. *CA Cancer J. Clin.* **70**, 7–30.
- Siravegna, G., Mussolin, B., Buscarino, M., Corti, G., Cassingena, A., Crisafulli, G., Ponzetti, A., Cremolini, C., Amatu, A., Lauricella, C., et al. (2015). Clonal evolution and resistance to EGFR blockade in the blood of colorectal cancer patients. *Nat. Med.* **21**, 827.
- Todaro, M., Gaggianesi, M., Catalano, V., Benfante, A., Iovino, F., Biffoni, M., Apuzzo, T., Sperduti, I., Volpe, S., Cocorullo, G., et al. (2014). CD44v6 is a marker of constitutive and reprogrammed cancer stem cells driving colon cancer metastasis. *Cell Stem Cell* **14**, 342–356.
- Turdo, A., Veschi, V., Gaggianesi, M., Chinnici, A., Bianca, P., Todaro, M., and Stassi, G. (2019). Meeting the challenge of targeting cancer stem cells. *Front Cell Dev Biol* **7**, 16.
- van Harten, A.M., Buijze, M., van der Mast, R., Rooimans, M.A., Martens-de Kemp, S.R., Bachas, C., Brink, A., Stigter-van Walsum, M., Wolthuis, R.M.F., and Brakenhoff, R.H. (2019). Targeting the cell cycle in head and neck cancer by Chk1 inhibition: a novel concept of bimodal cell death. *Oncogenesis* **8**, 38.
- Vermeulen, L., De Sousa, E.M.F., van der Heijden, M., Cameron, K., de Jong, J.H., Borovski, T., Tuynman, J.B., Todaro, M., Merz, C., Rodermond, H., et al. (2010). Wnt activity defines colon cancer stem cells and is regulated by the microenvironment. *Nat. Cell Biol* **12**, 468–476.
- Veschi, V., Mangiapane, L.R., Nicotra, A., Di Franco, S., Scavo, E., Apuzzo, T., Sardina, D.S., Fiori, M., Benfante, A., Colorito, M.L., et al. (2020). Targeting chemoresistant colorectal cancer via systemic administration of a BMP7 variant. *Oncogene* **39**, 987–1003.
- Walker, M., Black, E.J., Oehler, V., Gillespie, D.A., and Scott, M.T. (2009). Chk1 C-terminal regulatory phosphorylation mediates checkpoint activation by de-repression of Chk1 catalytic activity. *Oncogene* **28**, 2314–2323.
- Ward, R., Meagher, A., Tomlinson, I., O'Connor, T., Norrie, M., Wu, R., and Hawkins, N. (2001). Microsatellite instability and the clinicopathological features of sporadic colorectal cancer. *Gut* **48**, 821–829.
- Wehler, T., Thomas, M., Schumann, C., Bosch-Barrera, J., Vinolas Segarra, N., Dickgreber, N.J., Dalhoff, K., Sebastian, M., Corral Jaime, J., Alonso, M., et al. (2017). A randomized, phase 2 evaluation of the CHK1 inhibitor, LY2603618, administered in combination with pemetrexed and cisplatin in patients with advanced nonsquamous non-small cell lung cancer. *Lung Cancer* **108**, 212–216.
- Weiss, G.J., Donehower, R.C., Iyengar, T., Ramanathan, R.K., Lewandowski, K., Westin, E., Hurt, K., Hynes, S.M., Anthony, S.P., and McKane, S. (2013). Phase I dose-escalation study to examine the safety and tolerability of LY2603618, a checkpoint 1 kinase inhibitor, administered 1 day after pemetrexed 500 mg/m² every 21 days in patients with cancer. *Invest New Drugs* **31**, 136–144.
- Zeman, M.K., and Cimprich, K.A. (2014). Causes and consequences of replication stress. *Nat. Cell Biol* **16**, 2–9.
- Zhang, Y., and Hunter, T. (2014). Roles of Chk1 in cell biology and cancer therapy. *Int. J. Cancer* **134**, 1013–1023.

STAR★METHODS

KEY RESOURCE TABLE

REAGENT or RESOURCE	SOURCE	IDENTIFIER
Antibodies		
Human CD44 v6 APC-conjugated Antibody	R&D system	Cat#FAB3660A; AB_621925
Mouse IgG1 APC-conjugated Antibody	R&D system	Cat#IC002A; AB_357239
Phospho-Histone H2A.X (Ser139) (20E3)	Cell Signaling Technology	Cat# 9718; AB_2118009
Rabbit (DA1E) mAb IgG XP® Isotype Control	Cell Signaling Technology	Cat# 3900; AB_1550038
Rad51 (D4B10)	Cell Signaling Technology	Cat# 8875; AB_272110
Phospho-Chk1 (Ser345) (133D3)	Cell Signaling Technology	Cat# 2348; AB_331212
Chk1 (2G1D5)	Cell Signaling Technology	Cat# 2360; AB_2080320
β-actin (8H10D10)	Cell Signaling Technology	Cat# 3700; AB_2242334
Chk2 (1C12)	Cell Signaling Technology	Cat# 3440; AB_2229490
p53 Antibody	Cell Signaling Technology	Cat# 9282; AB_331476
Histone H2A.X	Cell Signaling Technology	Cat# 2595; AB_10694556
Cleaved PARP (Asp214)	Cell Signaling Technology	Cat# 9541; AB_331426
Phospho-Chk1 (Ser317) (D12H3)	Cell Signaling Technology	Cat# 12302; AB_2783865
Cdk1 (POH1)	Cell Signaling Technology	Cat# 9116; AB_2074795
Phospho-cdk1 (Tyr15) (10A11)	Cell Signaling Technology	Cat# 4539; AB_560953
Alexa Fluor 488 goat anti-rabbit	ThermoFisher Scientific	Cat# A11008; AB_143165
Goat anti-rabbit HRP-linked	ThermoFisher Scientific	Cat# 31460; AB_228341
Biological samples		
Subcutaneous CRC xenografts	This paper	N/A
CR-C53H lines	Mangiapane et al. (2021)	N/A
Chemicals, peptides, and recombinant proteins		
Collagenase, Type II	ThermoFisher Scientific	Cat# 17101015
Hyaluronidase	Sigma-Aldrich	Cat# H4272
StemPro Accutase Cell Dissociation Reagent	ThermoFisher Scientific	Cat# A1110501
Rabusertib (LY2603618)	Selleckchem	Cat# S2626
NORA234		
5-FU	Selleckchem	Cat# S1209
Oxaliplatin	Sigma	Cat# O9512
Polybrene	Sigma-Aldrich	Cat# H9268
Puromycin	Sigma-Aldrich	Cat# A1113803
Doxycycline	Sigma-Aldrich	Cat# D9891
TOTO-3 Iodide	ThermoFisher Scientific	Cat# T3604
DAPI	ThermoFisher Scientific	Cat# D1306
7-AAD	BD Pharmingen	Cat# 559925
SeaPlaque Agarose	Lonza	Cat# 50101
Propidium Iodide	Sigma-Aldrich	Cat# P4170
TRIzol™ Reagent	Thermo Fisher	Cat# 15596026
Critical commercial assays		
iScript gDNA Clear cDNA Synthesis Kit	BIO-RAD	Cat# 1725034
SsoAdvanced Universal SYBR Green Supermix	BIO-RAD	Cat# 1725271

(Continued on next page)

Continued

REAGENT or RESOURCE	SOURCE	IDENTIFIER
DNA damage-ATM ATR regulation of G2 M checkpoint	BIO-RAD	Cat# 10030616
CaspGLOW™ Fluorescein Active Caspase-3 Staining Kit	Biovision	Cat# K183
CaspGLOW™ Red Active Caspase-3 Staining Kit	Biovision	Cat# K193
FITC Annexin V Apoptosis Detection Kit I	BD	Cat#556547
Experimental models: cell lines		
Adipose-Derived Mesenchymal Stem Cells	ATCC	PCS-500-011
hTERT immortalized IMECs	Alessio Zippo	N/A
Experimental models: organisms/strains		
NOD/SCID mice	Charles River Laboratories	Cat# 634
Recombinant DNA		
psPAX2	Addgene	Cat# 12260
pMD2.G	Addgene	Cat# 12259
TRIPZ inducible Lentiviral Non-silencing shRNA control	Dharmacon	Cat# RHS4743
TRIPZ Inducible Lentiviral Human CHEK1 shRNA	Dharmacon	Cat# RHS4696-200700465
TOP-GFP	Addgene	Cat# 35489
Software and algorithms		
Graphpad Prism 8	GraphPad Software	http://www.graphpad.com/scientificsoftware/prism/
R version 3.6.1	R software	https://www.r-project.org/
FlowJo_v10.7.1	BD	https://www.flowjo.com/solutions/flowjo
Fiji	ImageJ software	https://imagej.net/Fiji/Downloads

EXPERIMENTAL MODELS AND SUBJECT DETAILS

Colorectal cancer cells isolation and culture

CRC specimens were provided by the University Hospital “P. Giaccone,” in accordance with the ethical policy of the Institutional Committee for Human Experimentation (authorization CE9/2015, Policlinico Paolo Giaccone, Palermo). Human samples were digested with collagenase (0.6 mg/mL) and hyaluronidase (10 µg/mL), and cell suspension was cultured in ultralow adhesion using serum-free stem cell medium (SCM) supplemented with EGF and b-FGF (Todaro et al., 2014). Chemoresistant CR-CSphCs line was obtained from metastatic liver lesions of patients receiving chemotherapy who have undergone hepatectomy at the University Polyclinic A. Gemelli, Rome (Table S1). CR-CSphCs lines and the related tumor tissues were routinely authenticated by short tandem repeat (STR) analysis using a multiplex PCR assay (GlobalFiler™ STR kit, Applied Biosystem) and analyzed by ABIPRISM 3130 genetic analyzer (Applied Biosystems) (Mangiapane et al., 2021). The presence of mycoplasma contamination was checked by using the MycoAlert™ Plus Mycoplasma Detection Kit (Lonza) as per the manufacturer’s instructions every 3 months. All the experiments were performed with early passage cultures and the expression of stem-like markers was regularly assessed. Adipose-derived mesenchymal stem cells (PCS-500-011) and hTERT immortalized mammary epithelial cells (kindly provided by Prof. Alessio Zippo) were cultured as per the manufactures’ instructions and used for cell viability assay as healthy control cells.

Animals and tumor models

Six- to 8-week-old male NOD/SCID mice were purchased by Charles River Laboratories, and *in vivo* experiments were performed as per the ARRIVE and Animal Care Committee Guidelines of the University of Palermo (Italian Ministry of Health authorization n. 154/2017-PR). 2.5×10^5 CR-CSphCs were subcutaneously injected in the flank of NOD/SCID mice, in 150 µl of 1:1 SCM/Matrigel (BD) solution. Mice were treated for 4 weeks (weeks 6–9) by intraperitoneal (i.p.) injection with phosphate-buffered saline (PBS) (vehicle)

with 5-FU (15 mg/kg, 2 days/week) in combination with oxaliplatin (0.25 mg/kg, once a week). Tumor volume was calculated using the formula: largest diameter \times (smallest diameter)² \times $\pi/6$. To evaluate possible toxic effects of NORA234, mice were treated for 3 weeks with a vehicle (PBS) or NORA234 (8 mg/kg, 2 days/week) by i.p. injection. At the end of treatment, animals were sacrificed accordingly to Directive 2010/63/EU guidelines (D.lgs 26/2016), and the liver, colon, kidney, spleen, lungs and pancreas were collected for histopathological examination.

METHODS DETAILS

In vitro treatment of CR-CSphCs

CR-CSphCs were treated with 5-fluorouracil 10 μ M (Selleckchem) and oxaliplatin 10 μ M (Sigma-Aldrich), NORA234 (0.3 μ M), and LY2603618 0.1 μ M (rabusertib, Selleckchem) alone or in combination. All the compounds were replenished in culture media every 48 h. To determine the IC50 or drug-combination efficiency of LY2603618 and NORA234, 6×10^3 CR-CSphCs were seeded in 96-well plates and, after 24 h, treated with different concentrations (vehicle, 0.01 μ M, 0.1 μ M, 1 μ M, 10 μ M) up to 96 h. For drug screening, CR-CSphCs were treated with vehicle or different neo-synthetic alkaloid compounds at the indicated concentrations (Vehicle, 0.03 μ M, 0.3 μ M, 3 μ M).

Synthesis of nortopsentin analog compounds

To carry out the synthesis of nortopsentin analog compounds, a suspension of the appropriate carbothioamide (5.0 mmol) and holo-acetyl compounds (5.0 mmol) in ethanol (3.0 ml) was heated under reflux for 30 min–3 h. The resulting precipitate was filtered off, dried, and recrystallized from ethanol to afford the pure compounds (Cascioferro et al., 2019).

Cell viability, proliferation, and clonogenic assay

CR-CSphCs viability was assessed using the CellTiter 96® Aqueous One Solution Cell Proliferation 369 Assay (MTS, Promega) as per the manufacturer's instructions and analyzed by the GDV MPT 370 reader (DV 990 BV6). To evaluate cell proliferation, Cell Titer-Glo Luminescent Cell Viability Assay Kit (Promega) was used as per the manufacturer's instruction, and luminescence was measured by using Infinite F500 (Tecan). Bliss synergistic score was calculated by using SynergyFinder (Ianevski et al., 2017). For colony-formation assay, CR-CSphCs were seeded at a clonal density on 0.3% Agarose SeaPlaque Agar (Invitrogen) and cultured up to 21 days. Colonies were stained with 0.01% crystal violet and counted using ImageJ software.

Flow cytometry, cell sorting, and cell cycle analysis

CR-CSphCs were harvested, washed with PBS, and stained with CD44v6 (2F10 APC, mouse IgG1, R&D systems), p-CHK1 (Ser345, 133D3, Rabbit IgG, Cell Signaling Technology), or corresponding IMC for 1 h at 4°C. The dead cells were excluded with 7-AAD (0.25 μ g/1 \times 10⁶ cells, BD Biosciences).

For intracellular staining, cells were fixed in 4% paraformaldehyde, permeabilized with 100% ice-cold methanol and stained with Phospho-Histone H2A.X (γ -H2AX, Ser139) (20E3, rabbit IgG, Cell signaling technology) and isotype-matched control (DA1E) (rabbit mAb IgG, Cell signaling technology) for 1 h at room temperature. After incubation with secondary antibody goat-anti-rabbit IgG (H+L), AlexaFluor-488 (ThermoFisher), CR-CSphCs were washed with PBS and incubated with RNase A (10 μ g/mL, Qiagen Cat# 19101) and propidium iodide (5 μ g/mL, Sigma-Aldrich) for 20 min at 4°C. Samples were analyzed by flow cytometer. Apoptotic cells were identified by using the CaspGLOW Fluorescein or Red Active Caspase 3 Staining Kit (Biovision) or the FITC Annexin V Apoptosis Staining Kit (BD Bioscience) as per the manufacturer's protocol. The caspase 3 activity and the percentage of early and late apoptotic cells were analyzed by flow cytometry.

To enrich Wnt- and CD44v6-expressing cells, CR-CSphCs were resuspended in PBS supplemented with 2% bovine serum albumin and 2mM ethylenediaminetetraacetate and filtered with a 70- μ m mesh to avoid cell sorter (FACSMelody, BD Bioscience) plugging. To verify the purity of sorted cells, a postsorting acquisition was performed.

For cell cycle analysis, CR-CSphCs were centrifuged, and cell pellet was incubated with 1 ml of Nicoletti Buffer (0.1% of sodium citrate, 0.1% of Triton x-100, 50 μ g/ml of propidium iodide, 10 μ g/ml of RNase

solution) in the dark at 4°C overnight. DNA content was evaluated by BD FACSLyric flow cytometer (BD Clinical system, BD Bioscience).

The overall obtained data were analyzed by FlowJo software.

Cell transfection and lentiviral transduction

To generate lentiviral particles, packaging cell line HEK-293T was transfected with TOP-dGFP-reporter (Addgene, 35489), TRIPZ inducible lentiviral nonsilencing shRNA control (ns shRNA, Dharmacon), or human CHK1 shRNA (shCHK1, Dharmacon) plasmids in association with psPAX2 (Addgene, 12260) and pMD2.G (Addgene, 12259) in OPTIMEM (Gibco) supplemented with XtremeGENE HP DNA transfection reagent (Roche).

Lentiviral supernatants were concentrated using the Lenti-X Concentrator reagent (Clontech) and CR-CSphCs were transduced in presence of 8 µg/mL of polybrene (Sigma-Aldrich). Transduced clones were selected by using puromycin (1 µg/ml, Sigma-Aldrich). shCHK1 was induced treating transduced cells with doxycycline (1 µg/ml, Sigma-Aldrich) for 5–10 days.

Immunohistochemistry and immunofluorescence

Immunohistochemical analysis was performed on cytopins, using phospho-CHK1 (S317, D12H3; Cell Signaling Technology). Single staining was revealed using biotin-streptavidin system (Dako) and detected with 3-amino-9-ethylcarbazole (AEC, Dako). Double staining was performed using antibodies against CD44v6 (2F10 APC, mouse IgG1, R&D systems) and p-CHK1 (Ser345, 133D3, Rabbit IgG, Cell Signaling Technology), revealed by the MACH 2 double stain 2 kit conjugated goat antimouse polymer horseradish peroxidase (HRP) and the conjugated goat antirabbit polymer alkaline phosphatase (Biocare Medical), and detected by DAB and Vulcan Fast Red chromogen. Nuclei were counterstained with aqueous hematoxylin (Sigma-Aldrich). Hematoxylin and eosin stainings were performed using standard protocols.

Cytospun of CR-CSphCs untreated or treated with NORA234 were fixed, permeabilized, and incubated overnight with RAD51 (D4B10, cell signaling technology). To reveal, primary antibody cells were stained with Alexa Fluor-488 Goat antirabbit IgG (Life Technologies) secondary antibody. Nuclei were counterstained using Toto-3 iodide (Life Technologies) or DAPI (33258, Thermofisher).

Real-time polymerase chain reaction

Total RNA was obtained using the TRIzol™ Reagent (Thermo Fisher) protocol, and 1 µg of total RNA, after the removal of genomic DNA, was retrotranscribed as per the manufacturer's instructions. The expression analysis of genes involved in DNA damage signaling pathway was evaluated using a PrimePCR designed panel (Bio-Rad). Relative mRNA expression levels were normalized with the endogenous control (GAPDH) and calculated using the comparative Ct method ($2^{-\Delta\Delta Ct}$).

Western blot

CR-CSphCs were lysed in ice-cold lysis buffer (Tris-HCl 10 mM, NaCl 50 mM, sodium pyruvate 30 mM, NaF 50 nM, ZnCl₂ 5 µM, Triton 1, sodium orthovanadate 0.1 nM, sodium butyrate 10 mM and PMSF 1 mM) supplemented with protease and phosphatase inhibitors (Sigma-Aldrich). Whole-cell lysates were loaded in sodium dodecyl sulfate-polyacrylamide-gel electrophoresis gels and blotted on nitrocellulose membranes. Membranes were blocked with a 5% nonfat dry milk and 0.1% Tween 20 PBS solution for 1 h at room temperature and then incubated with specific antibodies against γ-H2AX (Ser139, 20E3, Rabbit IgG, Cell Signaling Technology), cleaved PARP (Asp214, D64E10, Rabbit IgG, Cell Signaling Technology), RAD51 (D4B10, rabbit IgG, Cell Signaling Technology), CHK1 (2G1D5, Mouse IgG1, Cell Signaling Technology), CHK2 (1C12, Mouse IgG2b, Cell Signaling Technology), P53 (Rabbit, Cell Signaling Technology), H2AX (Rabbit, Cell Signaling Technology), pCHK1 (Ser345, 133D3, Rabbit IgG, Cell Signaling Technology), p-CDK1 (Tyr15, 10A11, Rabbit, Cell Signaling Technology), CDK1 (POH1, Mouse IgG2a, Cell Signaling Technology), and β-actin (8H10D10, mouse IgG2b, Cell Signaling Technology). Primary antibodies were revealed using antimouse or antirabbit HRP-conjugated (goat IgG; Thermo Fisher Scientific) and detected by Amersham imager 600 (GE Healthcare). Protein levels were normalized with β-actin and calculated by densitometric analysis using ImageJ software.



QUANTIFICATION AND STATISTICAL ANALYSIS

Database and statistical analysis

Transcriptomic data of healthy and tumor tissues have been collected by using the Gene Expression Profile Interactive Analysis (GEPIA) database (<http://gepia.cancer-pku.cn/>), by matching TCGA normal and GTEx data. Data were shown as mean \pm standard deviation. Statistical significance was estimated by unpaired t-test. Results were referred to statistically significant as $p < 0.05$. * indicates $p < 0.05$, ** indicate $p < 0.01$, *** indicate $p < 0.001$, and **** indicate $p < 0.0001$.

Supplemental information

CHK1 inhibitor sensitizes resistant colorectal cancer stem cells to nortopsentin

Simone Di Franco, Barbara Parrino, Miriam Gaggianesi, Vincenzo Davide Pantina, Paola Bianca, Annalisa Nicotra, Laura Rosa Mangiapane, Melania Lo Iacono, Gloria Ganduscio, Veronica Veschi, Ornella Roberta Brancato, Antonino Glaviano, Alice Turdo, Irene Pillitteri, Lorenzo Colarossi, Stella Cascioferro, Daniela Carbone, Camilla Pecoraro, Micol Eleonora Fiori, Ruggero De Maria, Matilde Todaro, Isabella Screpanti, Girolamo Cirrincione, Patrizia Diana, and Giorgio Stassi

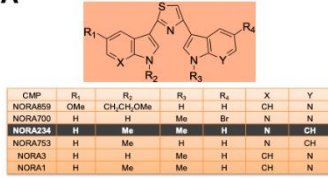
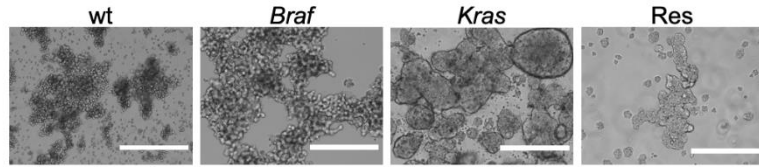
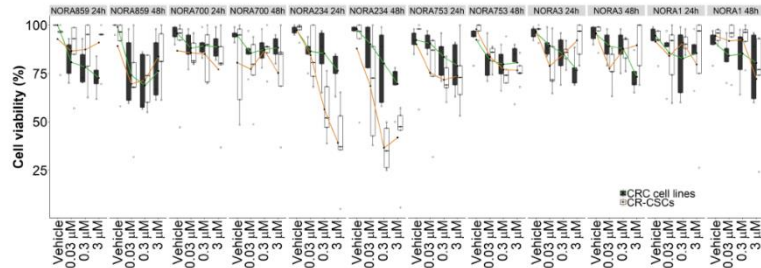
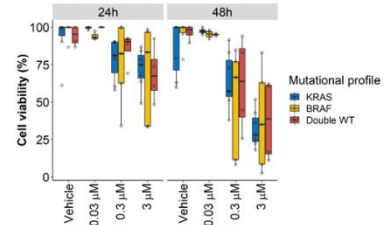
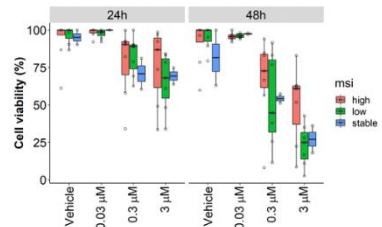
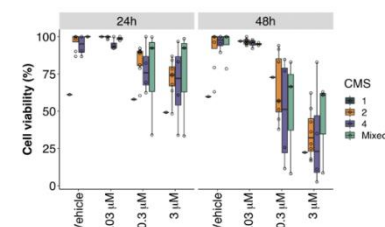
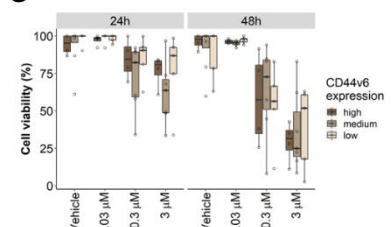
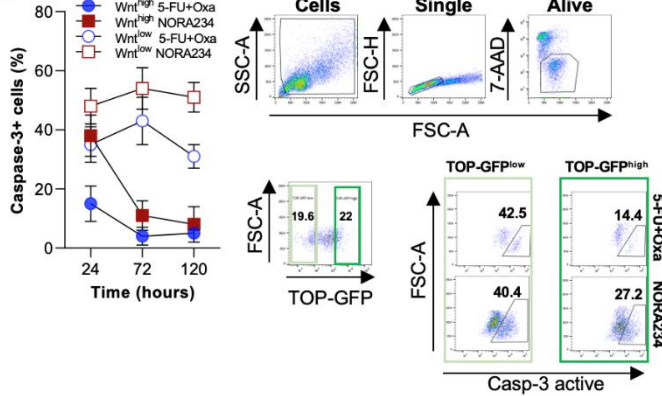
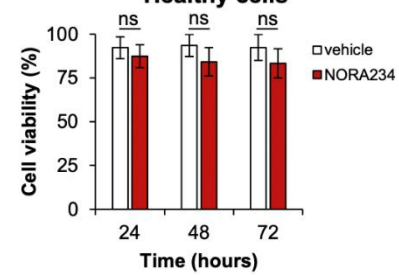
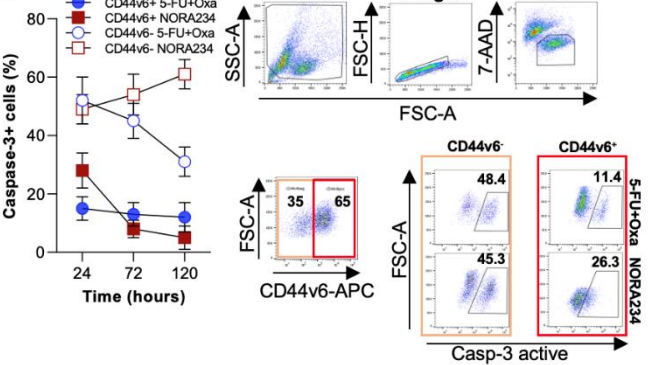
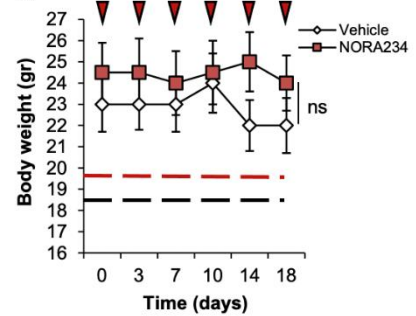
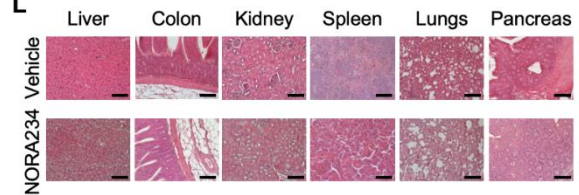
A**B****C****D****E****F****G****H****J****I****K****L**

Figure S1: NORA234 treatment impaired CRC cell proliferation, sparing healthy cells, Related to Figure 1 and Figure 2.

(A) Chemical structure of synthetic nortopsentin analogs. (*lower panel*) Table of the chemical group substitutions present in the six alkaloid derivatives.

(B) Representative contrast phase images of CR-CSphCs isolated from 4 different CRC patients (CR-CSphCs #3, #9, #21, #R4). Scale bars, 400 μm .

(C) Cell viability percentage of CRC cell lines and CR-CSphCs treated with vehicle, or the indicated concentration of NORA859, NORA700, NORA234, NORA753, NORA3 and NORA1, up to 48 hours.

(D-G) Cell viability analysis of in 29 CR-CSphC lines clustered according to the indicated mutational background (D), MSI status (E), CMS profile (F), or CD44v6 expression (low $\leq 30\%$, medium 31-69% and high $\geq 70\%$) (G), treated with vehicle or the indicated concentration of NORA234 for 48 hours.

(H-I) Representative flow cytometry analysis of active Casp-3 positivity in TOP-GFP^{high/low} (H), or CD44v6^{+/-} (I), CR-CSphCs treated with vehicle, 5-FU in combination with oxaliplatin, or NORA234, up to 120 hours. (*right panels*) Representative gating strategies for the analysis of active Casp-3 positive cells in TOP-GFP^{high/low} (H), or CD44v6^{+/-} (I) CR-CSphCs, treated as previously described, for 120 hours.

(J) Cell viability percentage of healthy cells (IMEC and AD-MSCs) treated as in (D-G), up to 72 hours. Statistical significance between 2 groups (n=6) was determined by unpaired Student's t-test (2-tailed).ns, non-significant.

(K) Weight of mice treated with vehicle or NORA234 (8 mg/kg) at the indicated time points (red arrow heads) up to 18 days. Data are mean \pm S.D (n=3 mice for group). Statistical significance between 2 groups was determined by unpaired Student's t-test (2-tailed).ns, non-significant.

(L) Representative H&E staining of liver, colon, kidney, spleen, lungs, and pancreas of mice treated as in (K). Scale bars, 200 μm .

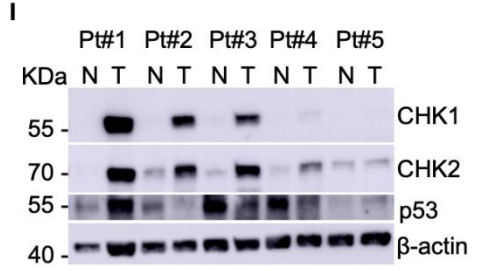
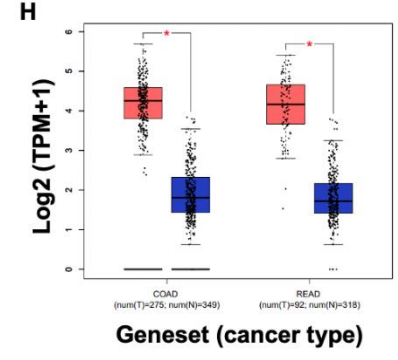
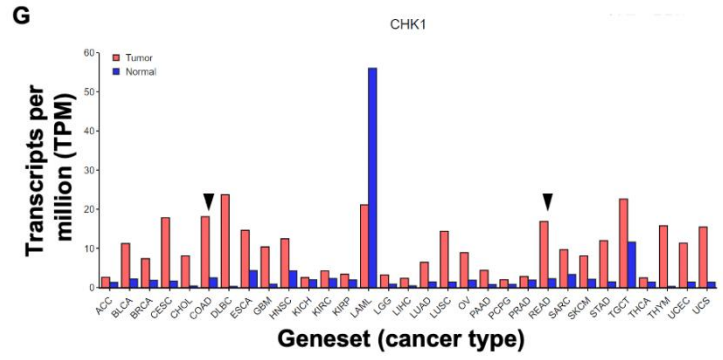
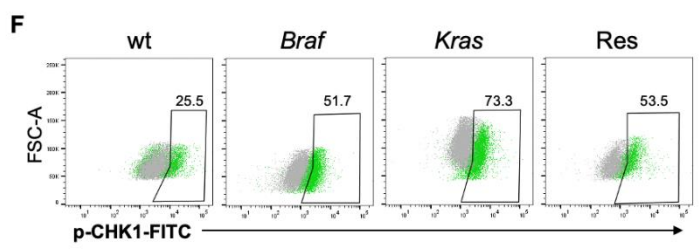
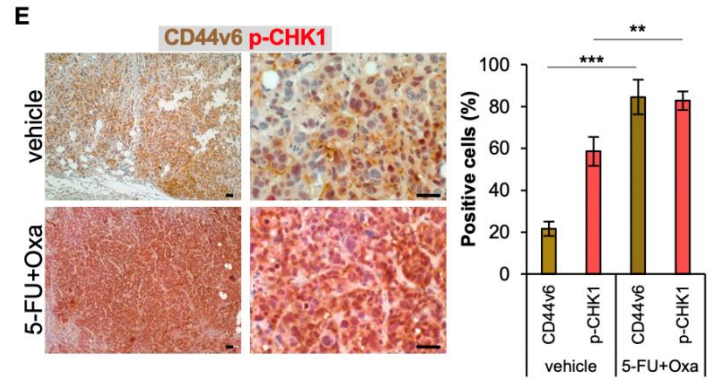
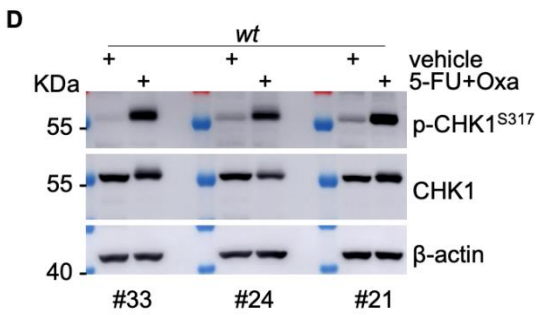
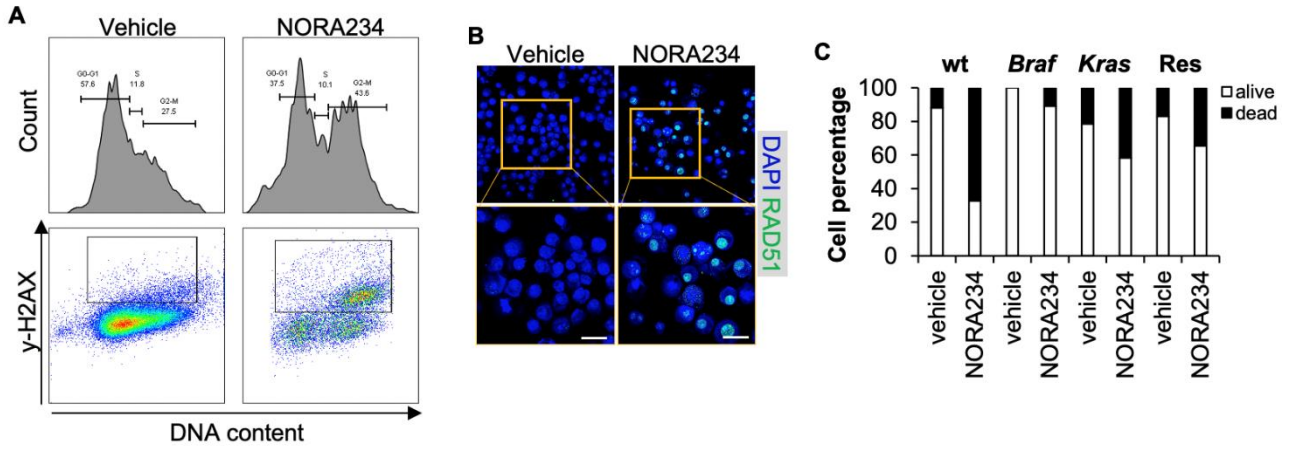


Figure S2: CHK1 is highly expressed in CRC, Related to Figure 3.

(A) Representative cell cycle analysis in CR-CSphCs (#21) treated with vehicle or NORA234 for 24 hours. The percentage of cells in G0-G1, S and G2-M cell cycle phase is indicated. (*lower panel*) Representative flow cytometry analysis of γ -H2AX positivity in cells (CR-CSphC#21) treated for 24 hours as previously described and stained with PI.

(B) Representative immunofluorescence analysis of RAD51 in CR-CSphCs (#21) treated with vehicle or NORA234 for 48 hours. Nuclei were counterstained with DAPI. Scale bars, 20 μ m.

(C) Cell percentage of alive and dead CR-CSphCs isolated from wt (#21), *Braf* (#3), *Kras* (#9) or chemoresistant (#R4) CRC patients, treated with vehicle or NORA234 for 48 hours.

(D) Immunoblot analysis of p-CHK1 and CHK1 in wt CR-CSphCs (CSphC #21, #24, and #33) treated for 24 hours, as indicated. β -actin was used as loading control.

(E) Immunohistochemical analysis of CD44v6 (brown) and p-CHK1 (red) on paraffin-embedded sections of tumor xenografts generated by subcutaneous injection of wt CR-CSphCs (#21), treated for 4 weeks (from 6th to 9th week) with vehicle or 5-FU in combination with oxaliplatin. (*right panel*) Percentage of CD44v6 and p-CHK1 positive cells. Data are mean \pm S.D (n=6 mice for group). Statistical significance between 2 groups was determined by unpaired Student's t-test (2-tailed). ** p \leq 0.01; *** p \leq 0.001.

(F) Representative flow cytometry analysis of p-CHK1 on wt (#58), *Braf* (#3), *Kras* (#11) and chemoresistant (#R2) CR-CSphCs. Grey color indicates cells stained with IMC.

(G) Transcriptomic analysis, expressed as transcripts per million (TPM), of CHK1 in different datasets of normal and tumor tissue from GEPIA database.

(H) Boxplot analysis of CHK1 expression in colon (COAD) and rectal (READ) cancer datasets of normal and tumor tissue from GEPIA database.

(I) Immunoblot analysis of CHK1, CHK2 and p53 in 5 representative colorectal tumor specimens (T) and adjacent-normal counterparts (N). β -actin was used as loading control.

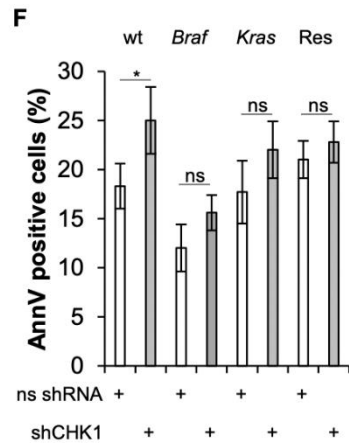
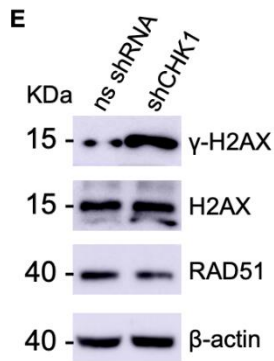
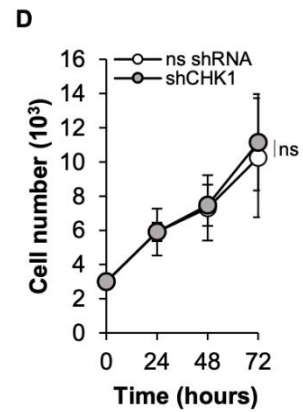
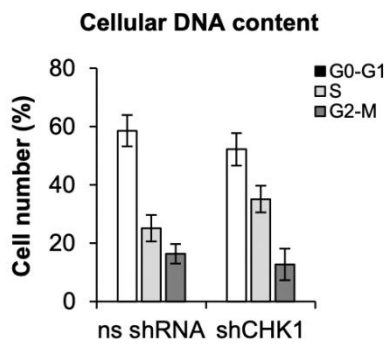
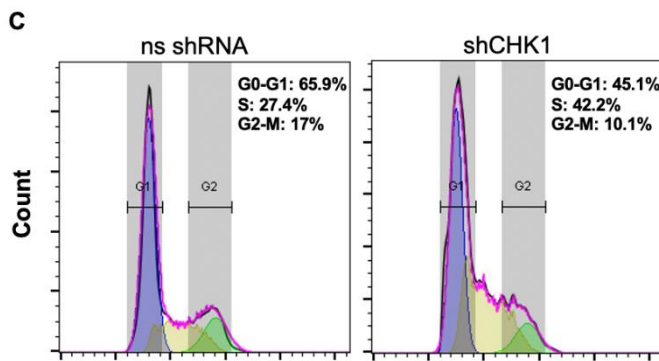
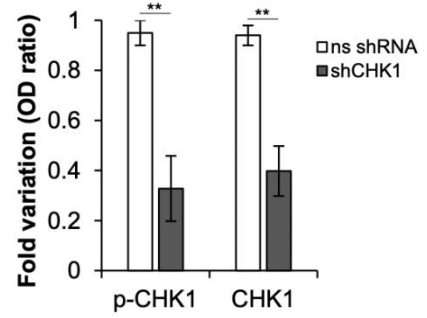
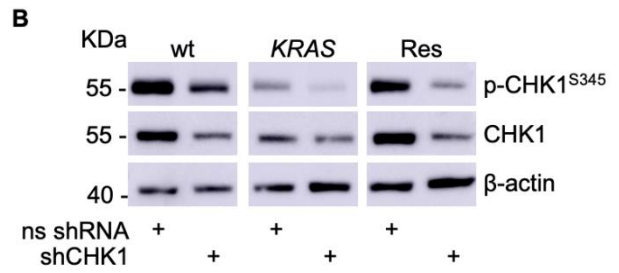
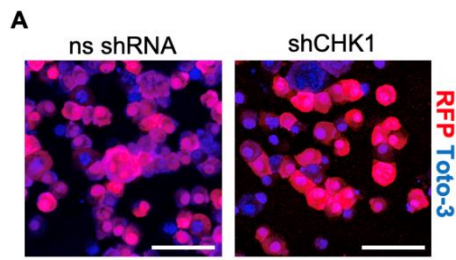


Figure S3: Silencing of CHK1 promotes the acquisition of DNA damage in CR-CSphCs, Related to Figure 4.

(A) Representative fluorescence analysis of CR-CSphCs (#21) transduced with ns shRNA control or shCHK1. Nuclei were counterstained with Toto-3. Scale bars, 100 μ m.

(B) Representative immunoblot analysis and quantification of p-CHK1^{S345} and CHK1 expression in CR-CSphCs transduced as in (A). β -actin was used as loading control. Data are expressed as mean \pm SD of three independent experiments using cells isolated from 3 different CRC patients (CR-CSphCs #9, #21, #R4). Statistical significance between 2 groups was determined by unpaired Student's t-test (2-tailed). ** $p \leq 0.01$.

(C) Representative cell cycle analysis in CR-CSphCs (#3) transduced as in (A). Data show percentage of cell number in G0-G1 (blue color), S (yellow color), and G2-M (green color) cell cycle phase. Data are expressed as mean \pm SD of three independent experiments using cells isolated from 4 different CRC patients (CR-CSphCs #3, #9, #21, #R4).

(D) Cell growth kinetics of CR-CSphCs transduced as in (A), up to 3 days. Data represent the mean \pm SD of three independent experiments using 4 different CR-CSphCs (#3, #9, #21, #R4). Statistical significance between 2 groups was determined by unpaired Student's t-test (2-tailed). ns, non-significant.

(E) Representative immunoblot analysis and quantification of γ -H2AX, H2AX and RAD51 expression in CR-CSphCs (#21) transduced as in (A). β -actin was used as loading control.

(F) Percentage of AnnexinV positivity in CR-CSphCs transduced as in (A). Data represent mean \pm S.D. of 3 independent experiments performed with cells isolated from wt (#21), *Braf* (#3), *Kras* (#9) or chemoresistant (#R4) CRC patients. Statistical significance between 2 groups was determined by unpaired Student's t-test (2-tailed). ns, non-significant; * $p \leq 0.05$.

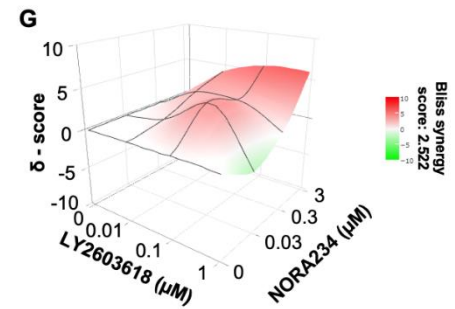
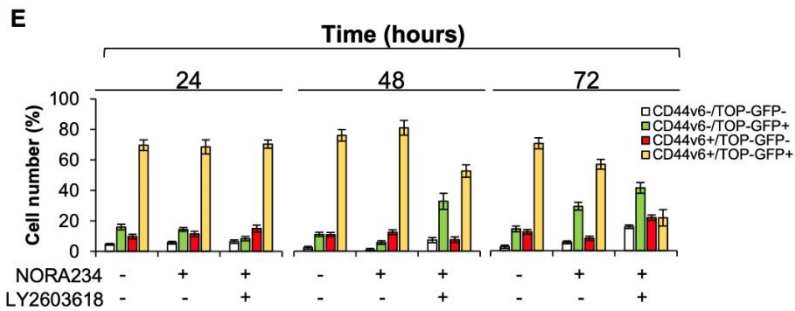
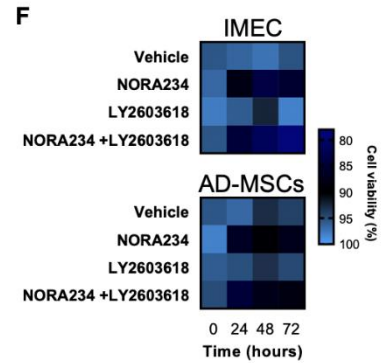
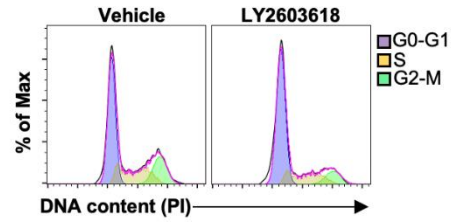
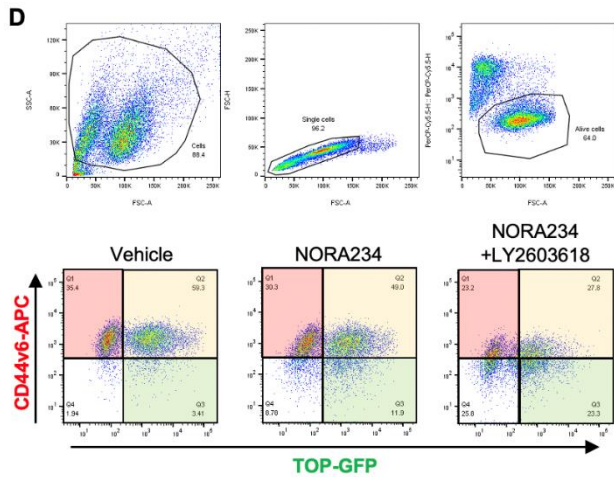
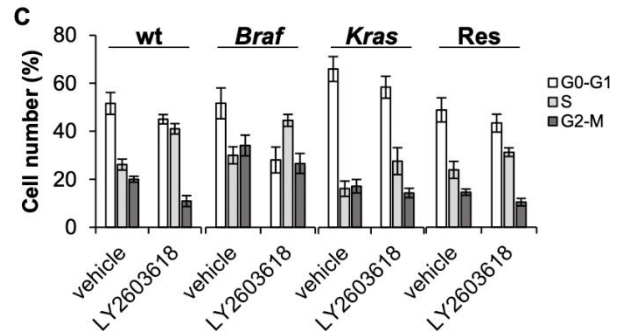
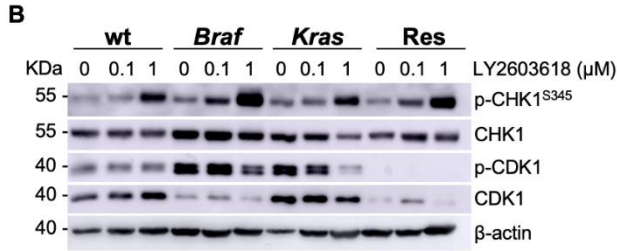
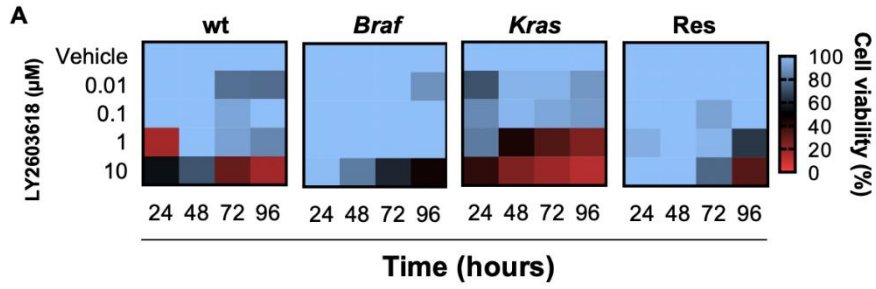


Figure S4: CHK1 inhibition in combination with NORA234 targets CD44v6 positive CRC cells, Related to Figure 4.

(A) Viability heatmap of cells treated with vehicle or Rabusertib (LY2603618), up to 96 hours. Data are expressed as mean of three independent experiments using 4 different CRC patients (CR-CSphCs#3, #9, #21, #R4).

(B) Representative immunoblot analysis of pCHK1^{S345}, CHK1, pCDK1 and CDK1 on 4 different CR-CSphCs isolated from wt (#21), *Braf* (#3), *Kras* (#9) or chemoresistant (#R4) CRC patients treated with the indicated concentration of LY2603618 for 48 hours. β -actin was used as loading control.

(C) Cell cycle analysis in CR-CSphCs treated with vehicle or LY2603618, for 24 hours. The graph represents the percentage of cell number in G0-G1, S, and G2-M phases. Data are expressed as mean \pm SD of three independent experiments performed using 4 different CRC patients (CR-CSphCs#3, #9, #21, #R4). (*lower panels*) Representative cell cycle analysis of CR-CSphCs treated with vehicle or LY2603618, for 24 hours.

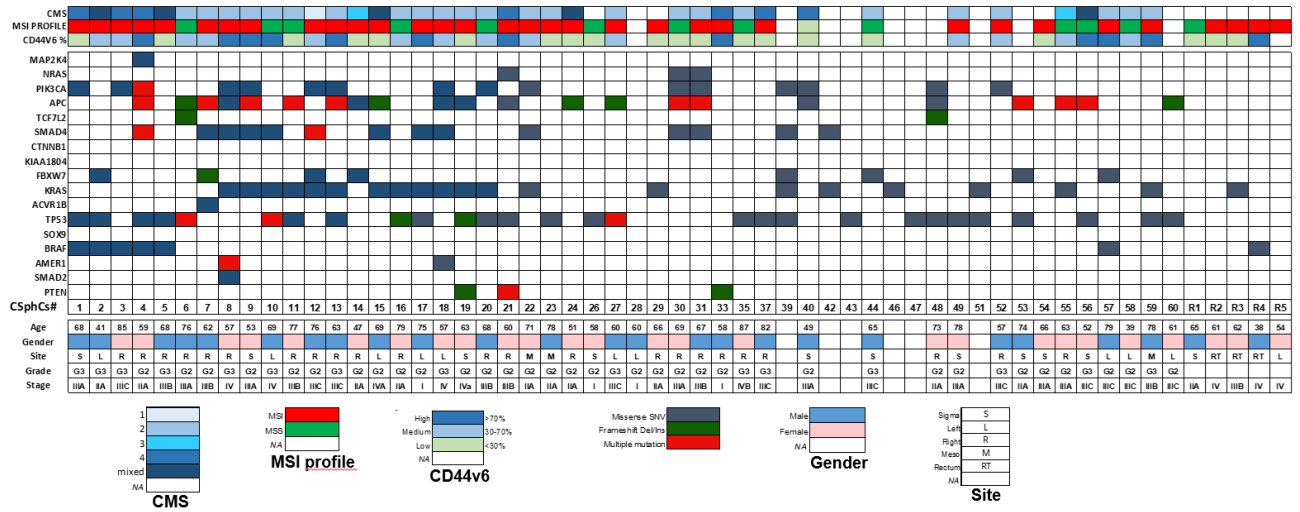
(D) Gate strategies for flow cytometry analysis of CR-CSphCs treated with vehicle or NORA234, alone and in combination with LY2603618, for 48 hours. (*lower panels*) Representative flow cytometry analysis of CD44v6 positivity in CR-CSphCs (#8, #9) transduced with TOP-GFP and treated as previously described.

(E) Cell number percentage of CD44v6/TOP-GFP positivity of CR-CSphCs treated as in (D). Data are expressed as mean \pm SD of three independent experiments performed using 2 different CR-CSphCs (#8, #9).

(F) Cell viability percentage of healthy cells treated alone or in combination with NORA234 and Rabusertib (LY2603618), up to 72 hours. Data are expressed as mean of six independent experiments using IMEC or AD-MSCs.

(G) 3D synergy map of cell viability of Bliss score in cells treated as in (F), at the indicated doses, for 48 hours. Data are expressed as mean of three independent experiments using IMEC and AD-MSCs.

Supplementary Table S1. CR-CSCs and their CMS, MSI profile, CD44v6 expression and mutational profiles, Related to Figure 1-4.



Chapter 5









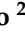

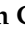




Nobiletin and Xanthohumol Sensitize Colorectal Cancer Stem Cells to Standard Chemotherapy

Alice Turdo , Antonino Glaviano , Giacomo Pepe , Federica Calapà, Stefania Raimondo, Micol Eleonora Fiori, Daniela Carbone , Manuela Giovanna Basilicata, Veronica Di Sarno, Carmine Ostacolo, Barbara Parrino, Stella Cascioferro, Camilla Pecoraro, Simone Di Franco, Diana Bellavia, Miriam Gaggianesi, Veronica Veschi, Melania Lo Iacono, Gloria Ganduscio, Vincenzo Davide Pantina, **Laura Rosa Mangiapane**, Maria Rita Bongiorno, Riccardo Alessandro, Matilde Todaro, Ruggero De Maria, Patrizia Diana, Pietro Campiglia, and Giorgio Stassi

Published in *Cancers*, 2021

Article

Nobiletin and Xanthohumol Sensitize Colorectal Cancer Stem Cells to Standard Chemotherapy

Alice Turdo ^{1,†}, Antonino Glaviano ^{2,†}, Giacomo Pepe ³, Federica Calapà ⁴, Stefania Raimondo ⁵, Micol Eleonora Fiori ⁶, Daniela Carbone ⁷, Manuela Giovanna Basilicata ³, Veronica Di Sarno ³, Carmine Ostacolo ⁸, Barbara Parrino ⁷, Stella Cascioferro ⁷, Camilla Pecoraro ⁷, Simone Di Franco ², Diana Bellavia ⁹, Miriam Gaggianesi ², Veronica Veschi ², Melania Lo Iacono ², Gloria Ganduscio ², Vincenzo Davide Pantina ², Laura Rosa Mangiapane ¹, Maria Rita Bongiorno ¹, Riccardo Alessandro ⁵, Matilde Todaro ¹, Ruggero De Maria ^{4,10}, Patrizia Diana ⁷, Pietro Campiglia ^{3,*} and Giorgio Stassi ^{2,*}

- ¹ Department of Health Promotion, Mother and Child Care, Internal Medicine and Medical Specialties (PROMISE), University of Palermo, 90127 Palermo, Italy; alice.turdo@unipa.it (A.T.); laurarosa.mangiapane@unipa.it (L.R.M.); mariarita.bongiorno@unipa.it (M.R.B.); matilde.todaro@unipa.it (M.T.)
- ² Department of Surgical, Oncological and Stomatological Sciences (DICHIRONS), University of Palermo, 90127 Palermo, Italy; antonino.glaviano@unipa.it (A.G.); simone.difranco@unipa.it (S.D.F.); miriam.gaggianesi@unipa.it (M.G.); veronica.veschi@unipa.it (V.V.); melania.loiacono@unipa.it (M.L.I.); gloria.ganduscio@unipa.it (G.G.); vincenzodavide.pantina@community.unipa.it (V.D.P.)
- ³ Department of Pharmacy, University of Salerno, 84084 Fisciano, SA, Italy; gipepe@unisa.it (G.P.); mbasilicata@unisa.it (M.G.B.); vdisarno@unisa.it (V.D.S.)
- ⁴ Fondazione Policlinico A. Gemelli, 00168 Rome, Italy; federica.calapa@guest.policlinicogemelli.it (F.C.); ruggero.demaria@unicatt.it (R.D.M.)
- ⁵ Department of BioMedicine, Neuroscience and Advanced Diagnostics (Bi.N.D), Biology and Genetics Section, University of Palermo, 90133 Palermo, Italy; stefania.raimondo@unipa.it (S.R.); riccardo.alessandro@unipa.it (R.A.)
- ⁶ Department of Oncology and Molecular Medicine (OMM), Istituto Superiore di Sanità (ISS), 00161 Rome, Italy; micol.fiori@iss.it
- ⁷ Department of Biological, Chemical and Pharmaceutical Sciences and Technologies (STEBICEF), University of Palermo, Via Archirafi 32, 90123 Palermo, Italy; daniela.carbone@unipa.it (D.C.); barbara.parrino@unipa.it (B.P.); stellamaria.cascioferro@unipa.it (S.C.); camilla.pecoraro@unipa.it (C.P.); patrizia.diana@unipa.it (P.D.)
- ⁸ Department of Pharmacy, University of Naples Federico II, 80131 Napoli, Italy; carmine.ostacolo@unipa.it
- ⁹ Department of Molecular Medicine, Sapienza University, 00189 Rome, Italy; diana.bellavia@uniroma1.it
- ¹⁰ Università Cattolica del Sacro Cuore, Istituto di Patologia Generale, 00168 Rome, Italy
- * Correspondence: pcampiglia@unisa.it (P.C.); giorgio.stassi@unipa.it (G.S.); Tel.: +39-089-969242 (P.C.); +39-091-23890813 (G.S.)
- † These authors contributed equally to this work.



Citation: Turdo, A.; Glaviano, A.; Pepe, G.; Calapà, F.; Raimondo, S.; Fiori, M.E.; Carbone, D.; Basilicata, M.G.; Di Sarno, V.; Ostacolo, C.; et al. Nobiletin and Xanthohumol Sensitize Colorectal Cancer Stem Cells to Standard Chemotherapy. *Cancers* **2021**, *13*, 3927. <https://doi.org/10.3390/cancers13163927>

Academic Editor: Michael Kahn

Received: 15 June 2021

Accepted: 30 July 2021

Published: 4 August 2021

Publisher's Note: MDPI stays neutral with regard to jurisdictional claims in published maps and institutional affiliations.



Copyright: © 2021 by the authors. Licensee MDPI, Basel, Switzerland. This article is an open access article distributed under the terms and conditions of the Creative Commons Attribution (CC BY) license (<https://creativecommons.org/licenses/by/4.0/>).

Simple Summary: Colorectal cancer stem cells (CR-CSCs) play a pivotal role in the therapy resistance and relapse of CRC patients. Herein we demonstrate that new treatment approaches comprising polymethoxyflavones and prenylflavonoids extracted from *Citrus sinensis* and *Humulus lupulus*, respectively, hamper the viability of CR-CSCs as well as synergizing with 5-fluorouracil and oxaliplatin (FOX)-based chemotherapy. Extract fractions containing Nobiletin and Xanthohumol, in combination with chemotherapy, decreased stemness properties of CR-CSCs and restrained the outgrowth of chemoresistant metastatic CR-CSCs. These data pinpoint Nobiletin and Xanthohumol as efficacious anti-cancer compounds in metastatic settings.

Abstract: Colorectal cancer (CRC) mortality is mainly caused by patient refractoriness to common anti-cancer therapies and consequent metastasis formation. Besides, the notorious toxic side effects of chemotherapy are a concurrent obstacle to be tackled. Thus, new treatment approaches are needed to effectively improve patient outcomes. Compelling evidence demonstrated that cancer stem cells (CSCs) are responsible for treatment failure and relapse. New natural treatment approaches showed capabilities to selectively target the CSC subpopulation by rendering them targetable by standard cytotoxic compounds. Herein we show the anti-cancer properties of the polymethoxyflavones

and prenylflavonoids extracted from *Citrus sinensis* and *Humulus lupulus*, respectively. The natural biofunctional fractions, singularly and in combination, reduced the cell viability of CRC stem cells (CR-CSCs) and synergized with 5-fluorouracil and oxaliplatin (FOX) chemotherapy. These phenomena were accompanied by a reduced S and G2/M phase of the cell cycle and upregulation of cell death-related genes. Notably, both phytoextracts in combination with FOX thwarted stemness features in CR-CSCs as demonstrated by the impaired clonogenic potential and decreased Wnt pathway activation. Extracts lowered the expression of CD44v6 and affected the expansion of metastatic CR-CSCs in patients refractory to chemotherapy. Together, this study highlights the importance of polymethoxyflavones and prenylflavonoids as natural remedies to aid oncological therapies.

Keywords: flavonoids; nobiletin; xanthohumol; anti-cancer therapy; cancer stem cells; colorectal cancer; natural biofunctional molecules

1. Introduction

Colorectal cancer (CRC) is the third most common cancer worldwide and the second most deadly cancer with a mortality rate of 600,000 deaths every year [1]. Most importantly, the 5-year survival rate ranges from 90 to 10% for stage I and stage IV patients, respectively [2]. The current clinical practice of cancer treatment mainly relies on surgery, chemotherapy, and radiotherapy. These approaches may be helpful to patients to some extent; however, more in-depth research is urgently needed to establish an unmet resolving therapy. The threatening fact of CRC is that despite some initial responses to currently available treatments, most patients with advanced stages could succumb to the disease due to therapy resistance and metastasis formation [3]. Therefore, determining the molecular mechanism of CRC resistance is crucial for designing new effective strategies.

Notably, a subpopulation of CRC cells, commonly identified by the expression of cell surface markers CD133 and CD44v6, are endowed with stemness properties, and thus defined as CRC stem cells (CR-CSCs) [4,5]. Remarkably, these cells play a critical role in the metastasis and relapse of CRC since they feature intrinsic properties of tumorigenesis, invasion, metastasis formation, and therapy resistance [5,6]. The underlying mechanism of CR-CSC resistance to treatment includes the activation of stemness signaling pathways, such as Wnt/ β -catenin [7], Hedgehog [8], Notch [9], Hippo/Yap [10], and PI3K/AKT [5], as well as the high activity of detoxifying enzymes, and the increase of drug efflux pump levels [11] and anti-apoptotic factors [12].

During the last century, we have witnessed the use of chemotherapy as a synthetic drug-based treatment of cancer, which has improved the overall quality and extension of patients' lives [13]. The addition of the third-generation platinum derivative oxaliplatin to a regimen of 5-FU and leucovorin (folinic acid) (FOLFOX), has become the mainstay of therapy in postoperative patients and metastatic CRC [14]. The FOLFOX regimen has been shown in multiple trials to improve progression-free survival (PFS) and overall survival (OS), compared with 5-FU and leucovorin alone, with more than 50% of response rates [15]. Of note, the non-chemotherapeutic drug leucovorin increases the anti-cancer effects of fluorouracil, while reducing the side effects caused by fluorouracil plus oxaliplatin (FOX) [16].

Notwithstanding the fact that chemotherapy is one of the major pharmacological therapy for cancer [17], toxicity to normal cells have hampered its current efficacy [18]. Side effects firstly reduce patient's quality of life and also compromise therapy efficacy due to drug discontinuation and dose reduction [19]. Inevitably, the most common adverse effects reported for FOLFOX are tiredness and fatigue, organ toxicity, myelosuppression, and elevated liver transaminase levels [20]. Hence, due to the aforementioned reasons, reducing the undesired toxicity by selective protection of healthy cells without compromising the killing of transformed cells represents the only promising strategy to enhance CRC treatment.

Interestingly, regular consumption of fruits and vegetables is known to be protective against the risk of numerous cancers [21]. In line with this, during the last decades, there has been growing evidence of an inverse association between citrus fruit intake [22], as well as hop intake [23], and risk of cancer. Consequently, there has been an increasing interest in exploiting the potential role of citrus and hop in preventing or treating cancer [24], along with their possible use in combination with oncological therapies [25].

The tumor preventive effect of orange and hop is mainly exerted by biologically active polyphenols, such as flavonoids, which display antioxidant activity, control cell cycle progression, and modulate the activation of oncogenic pathways [26]. Among flavonoid subgroups, two well-known anticancer molecules derived from orange and hop are respectively Nobiletin [27] and Xanthohumol [28]. In CRC cell lines, the polymethoxyflavone Nobiletin inhibits proliferation, induces cellular apoptosis, limits angiogenesis, sensitizes cells to chemotherapy, and prevents tumor formation [29]. Similarly, the prenylflavonoid Xanthohumol inhibits cell proliferation, induces DNA damages and apoptosis, and sensitizes CRC cell lines to chemotherapy [30]. However, the use of polyphenols in clinical practice has been limited by a lack of knowledge regarding their long-lasting anti-cancer properties and the therapeutic doses avoiding cytotoxicity against normal cells. Moreover, purification of Nobiletin and Xanthohumol from the phytocomplexes or its chemical synthesis remains quite expensive, and multi-kilograms-scale production is far to come [31,32], thus new strategies should be implemented to achieve potential therapeutic use of these molecules. Bioactivity-based fractionation of natural extracts represents a time- and cost-saving approach [33,34] and it is particularly relevant from the point of view of a sustainable economy, allowing waste recovery [35,36].

Herein we show that selected fractions from *Citrus sinensis* and *Humulus lupulus* extracts, containing Nobiletin (NCF) and Xanthohumol (XCF) as the main components, respectively, decrease the cell viability of primary cells isolated from CRC patients and CRC cell lines, causing reduced and negligible cytotoxicity toward healthy cells at therapeutic concentrations. In addition, these fractionated extracts, either singularly or in combination, may synergize with FOX-based chemotherapy to increase apoptosis, impair the sphere-forming capability, reduce the S phase and the G2/M phase of the cell cycle, and decrease the activation of the Wnt pathway as well as the expression of the metastatic CR-CSC marker CD44v6. Notably, both fractions exerted a cytotoxic effect against CR-CSCs isolated from liver metastasis of chemoresistant patients, sensitizing them toward standard chemotherapy.

This study implies that the strategy of rational fractionation of natural extracts may represent a promising forefront remedy to improve future CRC chemotherapy, by both enhancing drug efficacy to reduce CSC survival as well as decreasing drug cytotoxicity.

2. Materials and Methods

2.1. Sample Preparation

Hand-squeezed juice of *Citrus sinensis* var. Tarocco was centrifuged at $15,000\times g$ for 15 min at $25\text{ }^{\circ}\text{C}$ to remove fibers, then lyophilized for 24 h at $-52\text{ }^{\circ}\text{C}$ (LyoQuest-55, Telstar Technologies, Terrassa, Spain). The powder thus obtained was extracted with MeOH (Sigma-Aldrich, St. Louis, MO, USA) and the procedure was repeated three times for the complete recovery of a polyphenolic fraction [37].

Hop pellets were converted to powder with a mortar and treated with hexane for 10 min and then extracted with MeOH for 10 min ($\times 3$) [38].

The methanolic extracts were combined, evaporated to dryness under vacuum at $40\text{ }^{\circ}\text{C}$ in a rotary evaporator, dissolved in MeOH:water 50:50 (*v/v*) to a concentration of 1 mg mL^{-1} , filtered on a $0.45\text{ }\mu\text{m}$ nylon membrane (Merck Millipore, Milan, Italy), and finally analyzed by reverse phase (RP)-ultra-high performance liquid chromatography (UHPLC) coupled to diode array detection (DAD) and mass/mass spectrometry (MS/MS).

2.2. LCMS–IT-TOF Conditions

UHPLC-ESI-IT-TOF analyses were performed on a Shimadzu Nexera UHPLC system coupled online to an LCMS–IT-TOF mass spectrometer through an ESI source (Shimadzu, Kyoto, Japan). LC-MS data elaboration was performed by the LCMSsolution[®] software (Version 3.50.346, Shimadzu). LC-MS analysis of polyphenolic compounds was carried out on a Kinetex[™] EVO C18 150 × 2.1 mm × 2.6 μm (100 Å) column thermostated at 40 °C (Phenomenex, Bologna, Italy), monitoring the chromatograms at 330 and 370 nm. Mobile phases consisted of 0.1% (v/v) CH₃COOH/H₂O (A) and 0.1% (v/v) CH₃COOH/ACN (B). Analysis was performed in gradient elution as follows: 0–25 min, 15–90%B; 25–27.0 min, isocratic to 90%B; then five minutes for column re-equilibration. MS detection of polymethoxyflavones (*Citrus sinensis*) and prenylflavonoids (*Humulus lupulus*) was operated in positive ionization and a negative mode, respectively, with the following parameters: Detector voltage, 1.55 kV; CDL (curve desolvation line) temperature, 250 °C; block heater temperature, 250 °C; nebulizing gas flow (N₂), 1.5 L min^{−1}; drying gas pressure, 110 kPa. Full scan MS data were acquired in the range of 150–2000 *m/z* and MS/MS experiments were conducted in a data-dependent acquisition, while precursor ions were acquired in the range 150–1000 *m/z*.

Molecular formulas of identified compounds were calculated by the Formula Predictor software (Version 1.12, Shimadzu). The following online databases were also consulted: ChemSpider (<http://www.chemspider.com>, accessed on 12 May 2021), SciFinder Scholar (<https://scifinder.cas.org>, accessed on 12 May 2021) and Phenol-Explorer (www.phenol-explorer.eu, accessed on 12 May 2021).

2.3. Semiprep-RPHPLC-UV/Vis

The purification of polymethoxyflavones and prenylflavonoids was carried out by semi-preparative reversed-phase liquid chromatography employing a Shimadzu Semiprep-HPLC system consisting of two LC20AP pumps, a SIL20AP autosampler, a fraction collector FRC10A, a UV detector SPD20AV equipped with a preparative cell, and a system controller CBM 20A.

The separation was carried out on a Kinetex[™] C18 150 × 21.2 mm × 5 μm (100 Å), employing water (A) and acetonitrile (B) as mobile phases, both acidified by 0.1% (v/v) CH₃COOH setting the flow rate at 20 mL min^{−1}. The analysis was performed in gradient elution as follows:

Citrus sinensis gradient: 0–30 min, 10–70%B; 30–35 min, 70–10%B; 35–40 min, isocratic to 10%B.

Humulus lupulus gradient: 0–15 min, 5–30%B; 15–20 min, 30–70%B; 20–22 min, 70–100%B; 22–27 min, isocratic to 100%B; then five minutes for column re-equilibration.

2.4. Cell Culture

The purification and culture of CSphCs, from 6 primary tumor specimens and 6 liver metastasis of patients diagnosed with CRC, were performed as described in [39], in accordance with the ethical standards of Human Experimentation (authorization CE9/2015, Policlinico “Paolo Giaccone”, Palermo and authorization AIRC IG 2015, 17621, 2016, Fondazione Policlinico A Gemelli IRCCS, Rome, Italy). The authentication of CR-CSphCs is routinely performed by the short tandem repeat (STR) DNA profiling kit (GlobalFiler[™] STR kit, Applied Biosystem, Thermo Fisher Scientific, Waltham, MA, USA) followed by sequencing analysis on ABIPRISM 3130 (Applied Biosystem, Thermo Fisher Scientific Waltham, MA, USA). Mycoplasma infection is constantly monitored with the MycoAlert[™] Plus Mycoplasma Detection Kit (Lonza, Houston, TX, USA). DNA profiles of patient tumor tissues were matched with the corresponding CR-CSphCs.

HCT116 and RKO CRC cell lines were purchased by ATCC (Manassas, VA, USA) and cultured in DMEM (Sigma-Aldrich, St. Louis, MO, USA) supplemented with 10% FBS (Corning, Corning, NY, USA). HUVEC and HS-5 cell lines were purchased by ATCC (Manassas, VA, USA) and cultured in the Vascular Cell Basal Medium supplemented with

the Vascular Endothelial Cell Growth Kit-VEGF (ATCC, Manassas, VA, USA) and in DMEM (ATCC, Manassas, VA, USA) supplemented with 10% FBS, respectively.

CRC cells were treated with 5-fluorouracil (Selleckchem, Houston, TX, USA) plus oxaliplatin (Sigma-Aldrich, St. Louis, MO, USA). Oxaliplatin was administered 3 h before 5-fluorouracil.

2.5. Cell Viability

Cell viability was determined by adding the CellTiter 96 AQueous One Solution Reagent (Promega, Madison, WI, USA) to untreated and treated CR-CSCs and CRC cell lines. The solution was incubated for 2 h at 37 °C and the 490 nm absorbance was assessed by using the Programmable MPT plate reader (GVD).

Cell viability was assessed with the MTT (3-(4,5-dimethylthiazol-2-yl)-2,5-diphenyltetrazolium bromide) in the two normal cell lines, HUVEC and HS5. Twenty-four hours after seeding, the cells were treated with 5–10 and 25 µg/mL of orange fractionated extract, hop fractionated extract, and mix extract. After 24 or 48 h treatment, MTT was added to each well and the plate was incubated for 3 h at 37 °C. After the addition of isopropanol, the plate was read at 540 nm.

2.6. Drug Combination Study

Drug combination studies have been assessed by using the Chou–Talalay method, which is based on the median effect and the combination index (CI) equations in order to determine the quantization of drug interactions. The CI, computed in CompuSyn using the Chou–Talalay method, calculated on cell proliferation following the treatment with different FOX and Nobiletin dose pairs. CI < 1 represented synergism (slight, moderate, strong, very strong); otherwise, it indicated additivity (CI = 1) or antagonism (CI > 1) between two drugs [40].

2.7. Transfection of Cells, Lentiviral Particle Production, and Cell Transduction

In order to produce lentiviral particle HEK-293T, packaging cells were transfected with TOP-GFP (Addgene, Watertown, MA, USA), psPAX2 (Addgene), and pMD2.G (Addgene) using XtremeGENE HP DNA Transfection Reagent (Roche, Basel, Switzerland). Lentiviral particles were subsequently concentrated by using the Lenti-X Concentrator reagent (Clontech, Takara Bio, San Jose, CA, USA). CR-CSpHCs were transduced with the lentiviral particle and 8 µg/mL of polybrene (Sigma-Aldrich, St. Louis, MO, USA).

2.8. Clonogenic and Sphere Forming Assay

CR-CSpHCs were pretreated for 48 h with NCF, XCF, Mix, and FOX chemotherapy and subsequently plated as single cells per well in a 96-well plate. Wells containing 1, 2, 3, 4, or 5 cells were included in the analysis. CR-CSpHCs clonogenic potential was calculated with the Extreme Limiting Dilution Analysis (ELDA) 'limdil' function (<http://bioinf.wehi.edu.au/software/elda>, accessed on 2 April 2021).

In order to assess the sphere-forming capability of CR-CSCs, single cells, pretreated for 48 h with NCF, XCF, Mix, and FOX chemotherapy, were plated in ultra-low 6-well plates at 5,000 and 10,000 cells/mL density [41]. The sphere counts were performed after 48 h by using ImageJ software. The dense and tightly compacted structures were considered spheres. Sphere-forming efficiency was calculated with the formula (number of spheres/number of seeded cells) × 100.

2.9. RNA Isolation and Gene Expression Analysis

The purification of RNA was carried out using TRIZOL (Thermo Fisher Scientific, Waltham, MA, USA) protocol. For gene expression analysis, the total RNA (1 µg) was retrotranscribed and subjected to quantitative real-time PCR (qRT-PCR) with a custom PrimePCR panel (Bio-Rad, Hercules, CA, USA) for 88 genes involved in cell death, stemness, and the epithelial-to-mesenchymal transition according to the manufacturer's instructions.

Single gene assays were also performed using an SYBR green PCR mastermix (Qiagen, Hilden, Germany) and the following primers: *DKK1* (forward: 5'- GGT ATT CCA GAA GAA CCA CCT TG -3'; reverse: 5'- CTT GGA CCA GAA GTG TCT AGC AC -3'); *WNT5B* (forward: 5'- CAA GGA ATG CCA GCA CCA GTT C -3'; reverse: 5'- CGG CTG ATG GCG TTG ACC ACG -3'); *WNT3A* (forward: 5'- ATG AAC CGC CAC AAC AAC GAG G -3'; reverse: 5'- GTC CTT GAG GAA GTC ACC GAT G -3'); *WNT7B* (forward 5'- AGA AGA CCG TCT TCG GGC AAG A -3'; reverse 5'- AGT TGC TCA GGT TCC CTT GGC T -3'). The mRNA level was normalized to *GAPDH* (forward: GCT TCG CTC TCT GTC CCT CCT GT; reverse: TAC GAC CAA ATC CGT TGA CTC CG) housekeeping gene and calculated using the CT comparative method ($\Delta\Delta Ct$ method).

2.10. Flow Cytometry

CR-CSCs were washed in PBS twice, and stained for 1 h at 4 °C with conjugated antibodies CD44v6-APC (2F10, mouse IgG1, R&D systems, Minneapolis, MN, USA) or isotype-matched control (IC002A, mouse IgG1, R&D systems, Minneapolis, MN, USA). Dead cells were excluded based on the uptake of 7-AAD (BD Biosciences, Franklin Lakes, NJ, USA).

For cell cycle analysis, untreated and treated CR-CSC were washed with PBS and centrifuged at 1300 rpm for 5 min. After removing the supernatant, the cell pellet was resuspended in 1 mL of Nicoletti Buffer (0.1% of Sodium citrate 0.01% of Tritox-100, 50 µg/mL of Propidium Iodide, 10 µg/mL of Rnase solution) and incubated in the dark at 4 °C for 16 h.

Apoptotic cells were detected by using the CaspGlow Fluorescein Active Caspase 3 Staining kit (Biovision, Milpitas, CA, USA) and Brilliant Violet 421 Annexin V apoptosis staining kit (Biolegend, San Diego, CA, USA) according to the manufacturer's protocol. CR-CSCs were then analyzed using the FACSLyric flow cytometer (BD Biosciences, Franklin Lakes, NY, USA).

3. Results

3.1. Nobiletin and Xanthohumol Hamper CR-CSphCs Viability While Sparing Healthy Cells

Our group and others have previously demonstrated that CR-CSCs possess the capability to withstand chemotherapy and guide disease recurrence [39]. We sought to investigate to what extent the standard anti-cancer approach based on chemotherapy counteracted the viability of our CRC spheroid cells (CR-CSphCs) collection, which are heterogeneous cell populations composed of CSC, transit-amplifying, and differentiated cells (Table S1) [42].

Following exposure to increasing concentrations of 5-fluorouracil and oxaliplatin (FOX)-based therapy, by mimicking the clinically used schedule and doses for FOX [15,43], CR-CSphCs showed higher resistance to this therapeutic regimen as compared to established CRC cell lines (Figure 1A). Although both cell types exhibited a similar pattern of diminished cell proliferation, CR-CSphCs showed a 3.9-fold increase in the half-maximal inhibitory concentration (IC50) (Figure 1A).

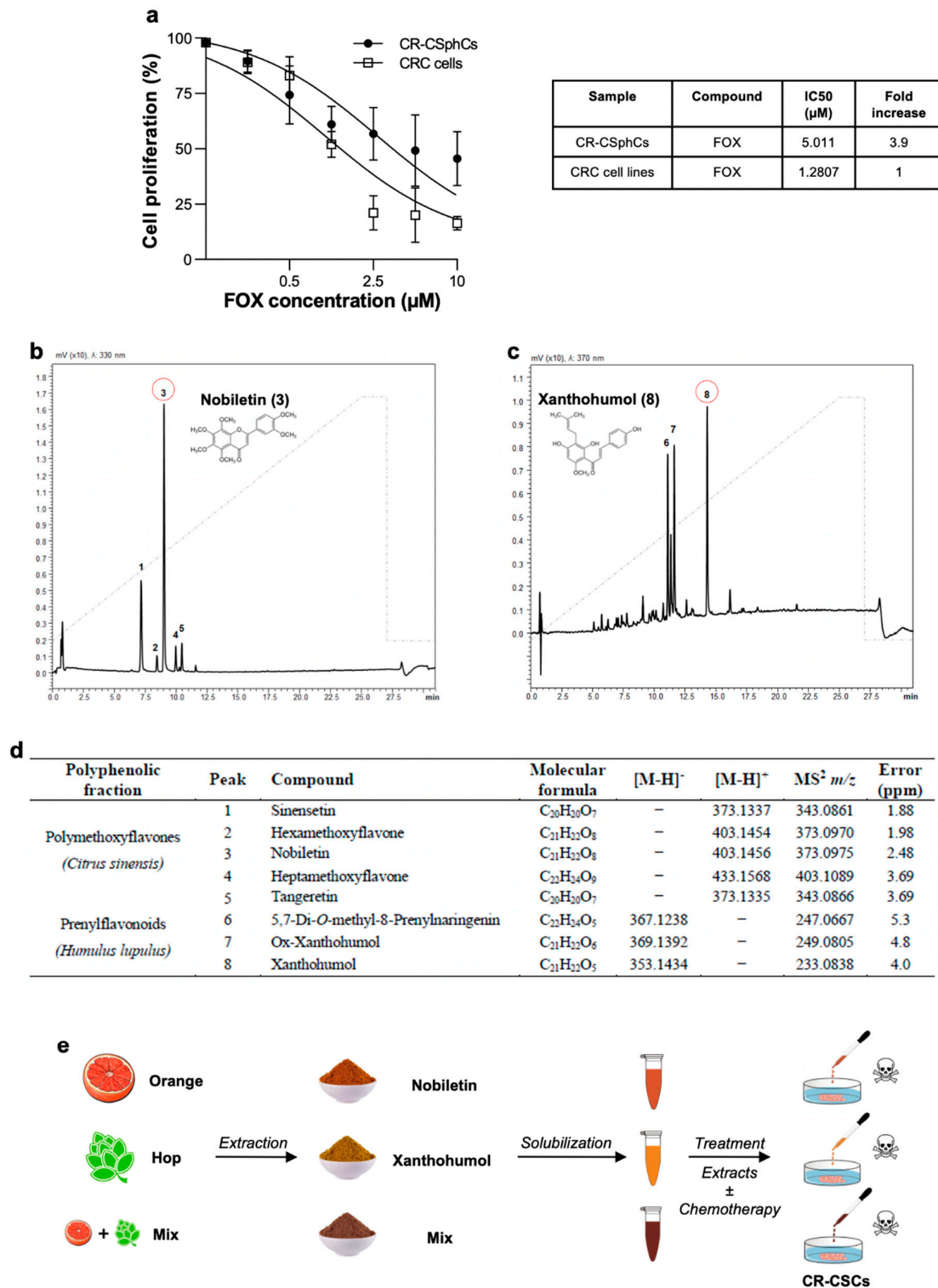


Figure 1. CR-CSphCs are resistant to chemotherapy. (a) Cell proliferation percentage of CR-CSphCs (#3, #8, and #59) and CRC cell lines (HCT116 and RKO) treated with 0.1 µM, 0.5 µM, 1 µM, 2.5 µM, 5 µM, and 10 µM of FOX chemotherapy for 48 h. Data are represented as mean ± SD of three independent experiments. IC50 values are indicated in the right panel; (b) chromatographic profiles of polymethoxyflavones and chemical structure of Nobiletin, isolated from *Citrus sinensis*; (c) chromatographic profiles of prenylflavonoids and chemical structure of Xanthohumol, isolated from *Humulus lupulus*; (d) qualitative profile of isolated polyphenolic fractions; (e) NCF, XCF, and Mix (50% NCF plus 50% XCF) were firstly extracted through lyophilization and then solubilized in methanol. CR-CSphCs and CRC cell lines were exposed to extracts, either singularly or in combination with FOX chemotherapy.

These results mirror the difficulties in targeting the CR-CSphCs subpopulation with therapeutically relevant doses of standard anti-cancer compounds that, in the meantime, comply with tolerability.

Given that high chemotherapy concentrations are required to induce significant inhibition of cell proliferation of CR-CSphCs, we sought to examine the anti-cancer effect of natural fractionated extracts of *Citrus sinensis* and *Humulus lupulus*, obtained from waste recovery by a time- and cost-saving method and containing Nobiletin and Xanthohumol as main components, respectively.

Thus, we performed class-specific isolation through reversed-phase semi-preparative liquid chromatography. As can be appreciated from Figure 1B–D, we collected polymethoxyflavones and prenylflavonoids from citrus and hop extracts, respectively. The identity of isolated metabolites was assessed by UHPLC-MS/MS analysis and supported by their retention times, comparing UV spectra and MS/MS data with those present in the literature.

In detail, the characteristic fragment ions of polymethoxyflavones were obtained by the loss of 31 Da corresponding to the CH₃O group. Among them, compounds 3 and 5 were unambiguously identified as Nobiletin and Tangeretin, respectively, by comparison with the reference standards. Compound 1 was characterized as pentamethoxyflavone and identified as sinensetin while the chromatographic peaks 2 and 4 were identified as hexa- and heptamethoxyflavone, respectively. Compounds 6, 7, and 8, showed at m/z 367, m/z 369, and m/z 353 [M-H]⁻ fragmentation ions at m/z 247, m/z 249, and at m/z 233 corresponding the product ions with the negative charge retained on the A-rings, following retro-Diels-Alder fragmentation [M-H-C₈H₈O]⁻.

Before assessing the effects of the Nobiletin-containing fraction (NCF), the Xanthohumol-containing fraction (XCF), and their combination (Mix) on tumor cells, we studied their impact on the viability of two healthy cell lines. The human stromal cells, HS-5, and the human umbilical vein endothelial cells, HUVEC, have been extensively described as reliable models to estimate and predict the side effects of anti-cancer drugs on healthy cells [44–46]. The two cell lines were treated with increasing concentrations of the two fractions for 24 and 48 h and only mild effects on cell viability were observed, supporting the absence of significant toxicity of Nobiletin and Xanthohumol (Figure S1A,B).

Together, these data indicate that NCF and XCF could serve as potential adjuvants of standard anti-cancer compounds, while minimizing the occurrence of side effects.

3.2. Phytoextracts Sensitize CR-CSphCs to Chemotherapy

In order to assess the potential use of either NCF, XCF, or their combination as chemosensitizing agents, we studied the potential synergistic effects of these natural compounds with FOX.

Multiple lines of chemotherapy, after an initial tumor shrinkage, led to the selection and expansion of the CSC compartment with consequent tumor recurrence. We took advantage of our collection of CR-CSphCs isolated from both naïve primary CRC and liver metastasis of patients who were refractory to chemotherapy (Table S1). These cells represent a solid pre-clinical model, able to reproduce a patient's sensitivity to drugs. Specifically, we selected three concentrations of extracts, 12.5 µg/mL, 25 µg/mL, and 40 µg/mL, to test their effects on CR-CSphCs proliferation. The administration of NCF, XCF, and their combination (Mix) significantly reduced the proliferation of CR-CSphCs, including chemotherapy-resistant cells (Figure 2A–D and Figure S2). Combined exposure to NCF and FOX reduced the viability of six CR-CSphCs (#8, #24, #R1, #R2, #R3, and #R4), while treatment with FOX in combination with XCF significantly reduced the viability of four CR-CSphCs (#R7p, #24, #37, and #R2) (Figure S2A–C). Likewise, the combination index (CI) analysis, calculated by the Chou–Talalay method, highlighted the synergistic effects of Nobiletin and Mix plus FOX in reducing CR-CSphC#8 viability (Figure 2C and Figure S2A). These results were also validated on CRC cell lines, which showed a remarkable decrease in cell proliferation following the administration of the combined treatments (Figure S2E,F).

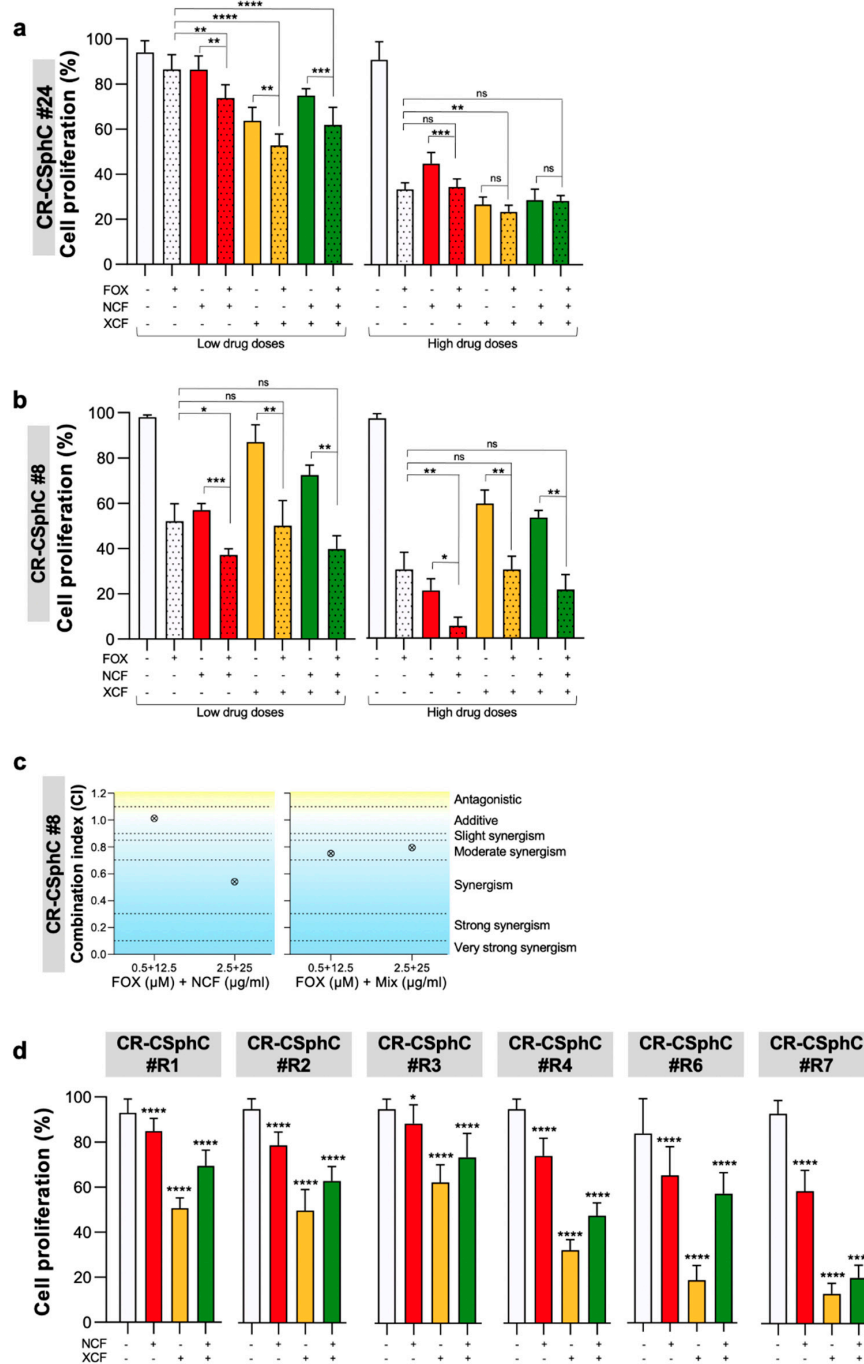


Figure 2. Combination of NCF plus chemotherapy hampers the proliferation of CR-CSphCs. **(a)** Cell proliferation percentage of CR-CSphCs (#24) treated with 25 or 40 µg/mL of NCF, XCF, or Mix extracts alone or in combination with 1.25 or 5 µM FOX for 48 h. Data are represented as mean ± SD of three independent experiments. Comparisons between two groups were made using a two-tailed Student’s *t*-test: ns, not significant, ** $p \leq 0.01$, *** $p \leq 0.001$, **** $p \leq 0.0001$; **(b)** cell proliferation percentage of CR-CSphCs (#8) treated with 12.5 or 25 µg/mL of NCF, XCF, or Mix extracts alone or in combination with 0.5 or 2.5 µM FOX for 48 h. Data are represented as mean ± SD of three independent experiments. Comparisons between two groups were made using a two-tailed Student’s *t*-test: ns, not significant, * $p \leq 0.05$, ** $p \leq 0.01$, *** $p \leq 0.001$; **(c)** synergy plot representing the combination index (CI), computed in CompuSyn by using the Chou–Talalay method, calculated from cell proliferation data of CR-CSphCs (#8) treated with different FOX and NCF and Mix dose pair at 48 h; **(d)** cell viability of metastatic CR-CSCs exposed for 72 h to 40 µg/mL NCF, XCF, or both extracts (Mix), as compared to control (vehicle). * $p \leq 0.05$, **** $p \leq 0.0001$.

3.3. Nobiletin and Xanthohumol Induce Apoptosis of CR-CSphCs in Combination with Chemotherapy

The genotoxic stress dictated by the extracts plus chemotherapy caused a reduction in CR-CSphCs S- and G2/M- cell cycle phases and substantially increased the G0/G1 and sub-G0 phase (Figure 3A and Figure S3A). The cytostatic effect caused by the combined treatment is conceivably induced by the short-term exposure of 48 h, which concomitantly allows early events of apoptosis. Thus, these data suggest that long-term treatments are required to definitively commit cells to apoptosis [29].

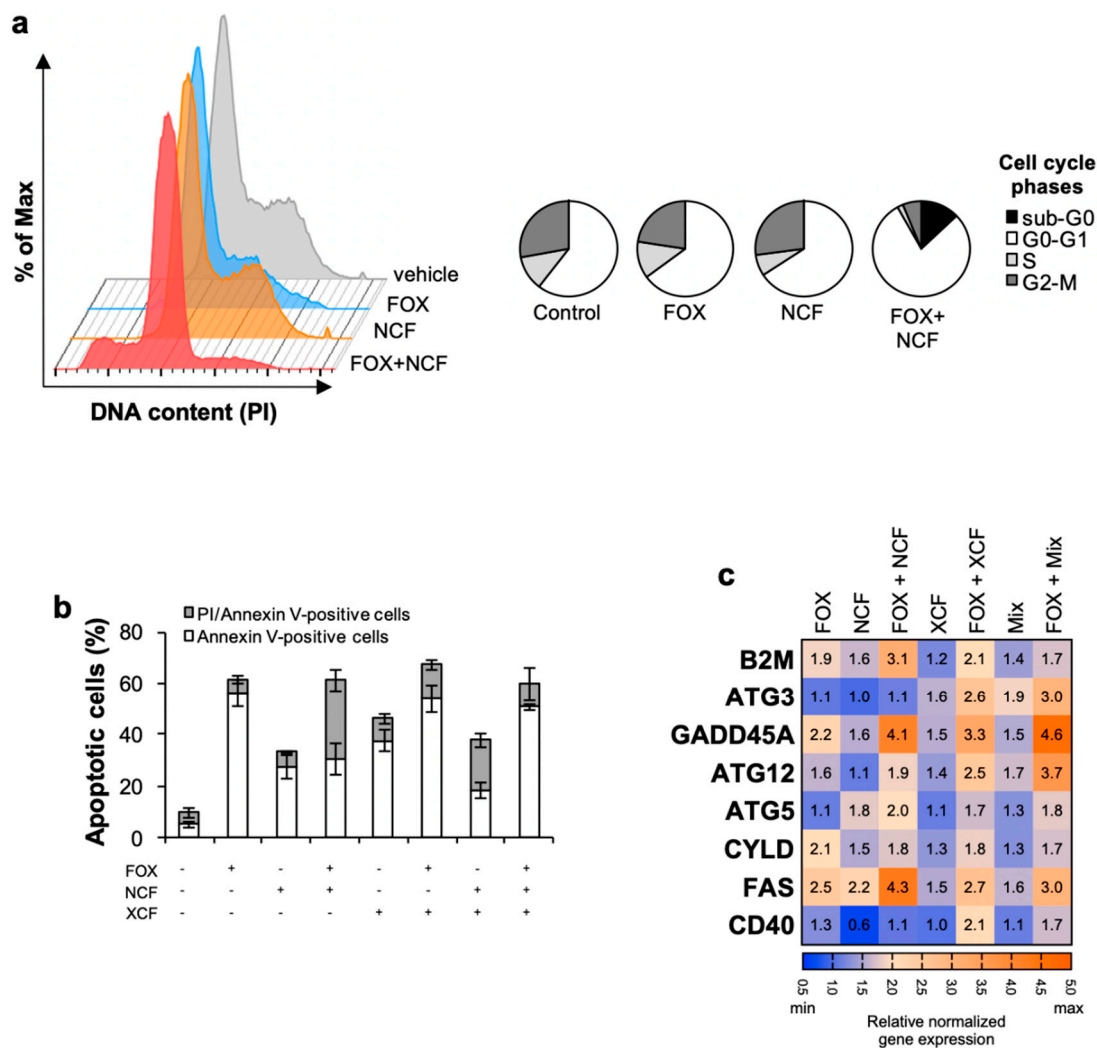


Figure 3. Flavonoids extracts plus chemotherapy induce apoptosis in CR-CSphCs. (a) Phase Representative flow cytometry analysis of cell cycle phases distribution in CR-CSphCs (#8) exposed to 0.5 μ M FOX and 12.5 μ g/mL NCF, alone or in combination, for 48 h. DNA content was assessed by propidium iodide (PI) staining; (b) percentage of apoptotic CR-CSphCs (#8) treated with 0.5 μ M FOX and 12.5 μ g/mL NCF, XCF, or both extracts, alone or in combination, for 48 h. The analysis was performed by flow cytometry on CR-CSphCs labeled with propidium iodide (PI) and Annexin-V; (c) gene expression analysis of pro-apoptotic genes in CR-CSphCs (#8) after exposure to 0.5 μ M FOX and 12.5 μ g/mL NCF, XCF, or both extracts (Mix), as compared to control (vehicle) for 48 h. Data are expressed as $2^{-\Delta\Delta Ct}$ expression values normalized to *GAPDH* and *HPRT* genes.

Accordingly, the combination of treatments induced the apoptotic events in CR-CSphCs, as demonstrated by the increased number of AnnexinV-positive cells (Figure 3B and Figure S3B).

To further confirm that NCF, XCF, and Mix are required to induce programmed cell death in combination with chemotherapy in CR-CSphCs, we analyzed the expression of

genes related to apoptosis and autophagy. Gene expression analysis revealed enhanced expression of eight proapoptotic genes, ATG3, ATG5, ATG12, B2M, CD40, CYLD, FAS, and GADD45A, up-regulated in CR-CSphCs treated with each of the extracts and chemotherapy (Figure 3C). Flavonoids induce apoptosis at early events, which was paralleled with an increase in the expression of genes associated with apoptosis without determining a significant increase in Caspase-3 activity (Figure S3B), likely due to a caspase-3 independent apoptosis phenomenon.

These results suggest that fractionated extracts lessen the common dose of chemotherapeutic drugs, thereby reducing their side effects and rendering the therapeutic regimen more acceptable.

3.4. NCF and XCF Counteract Stemness Features of CR-CSCs

We and others demonstrated that standard chemotherapy efficaciously kills differentiated cells while sparing cells with stemness features [39]. Thus, we hypothesized that the addition of the flavonoid extracts to FOX chemotherapy could affect the stem compartment of CR-CSphCs.

Therefore, we assessed the sphere-forming potential of CR-CSphCs as a functional approach to study CSCs self-renewal. Interestingly, following a short time exposure, we observed that FOX plus NCF, and to a lesser extent XCF and Mix, were able to suppress CR-CSCs sphere formation (Figure 4A and Figure S4A,B). In addition, we performed an in vitro limiting dilution assay to evaluate the residual self-renewal activity of cells previously exposed to 48 h of treatment. Consistent with previous results, the administration of extracts and chemotherapy hampered the clonogenic potential of CR-CSphC (Figure 4B).

We previously demonstrated that CD44v6 is a marker of CR-CSCs endowed with metastatic potential, and thereby responsible for disease progression [5]. After 48-h exposure to the combination of NCF, XCF, and Mix plus FOX, CR-CSCs showed a significantly lower expression of CD44v6 (75.6%, 84.1%, and 74.3%, respectively) compared to the control (96.5%) (Figure 4C and Figure S4C,D).

Wnt pathway activity is a functional biomarker that defines the CR-CSC population [7], and it is associated with poor prognosis in CRC patients [47]. Wnt/ β -catenin activity is mostly associated with high expression levels of CD44v6, which significantly correlates with the overall survival probability of CRC patients [5]. Moreover, besides the well-known role of the Wnt pathway in the mechanisms that establish the stemness, Wnt gene targets were found involved at various levels in drug resistance [48]. To corroborate the role of flavonoid-based therapies in counteracting Wnt pathway activation, we analyzed the expression of Wnt pathway inhibitors and effectors. This therapeutic approach, which combines chemotherapy plus NCF and/or XCF was able to boost the gene expression levels of the major inhibitor of the Wnt pathway, DKK1, and lower the expression of the Wnt pathway effectors WNT3A, WNT5B, and WNT7B (Figure S4E,F) [49–51].

The activity of the Wnt pathway was validated by transducing CR-CSphCs with a Wnt reporter construct, which encodes for GFP when β -catenin binds to TCF/LEF promoter [7]. Wnt-high (GFP-positive) cells were sensitive to FOX in combination with extracts (Figure 4D). We also noticed an increase of Wnt-low early apoptotic cells positive for Annexin V. Thus, flavonoids treatment leads to a significant decrease of CD44v6 expression along with a reduced number of CR-CSCs bearing activation of the Wnt pathway.

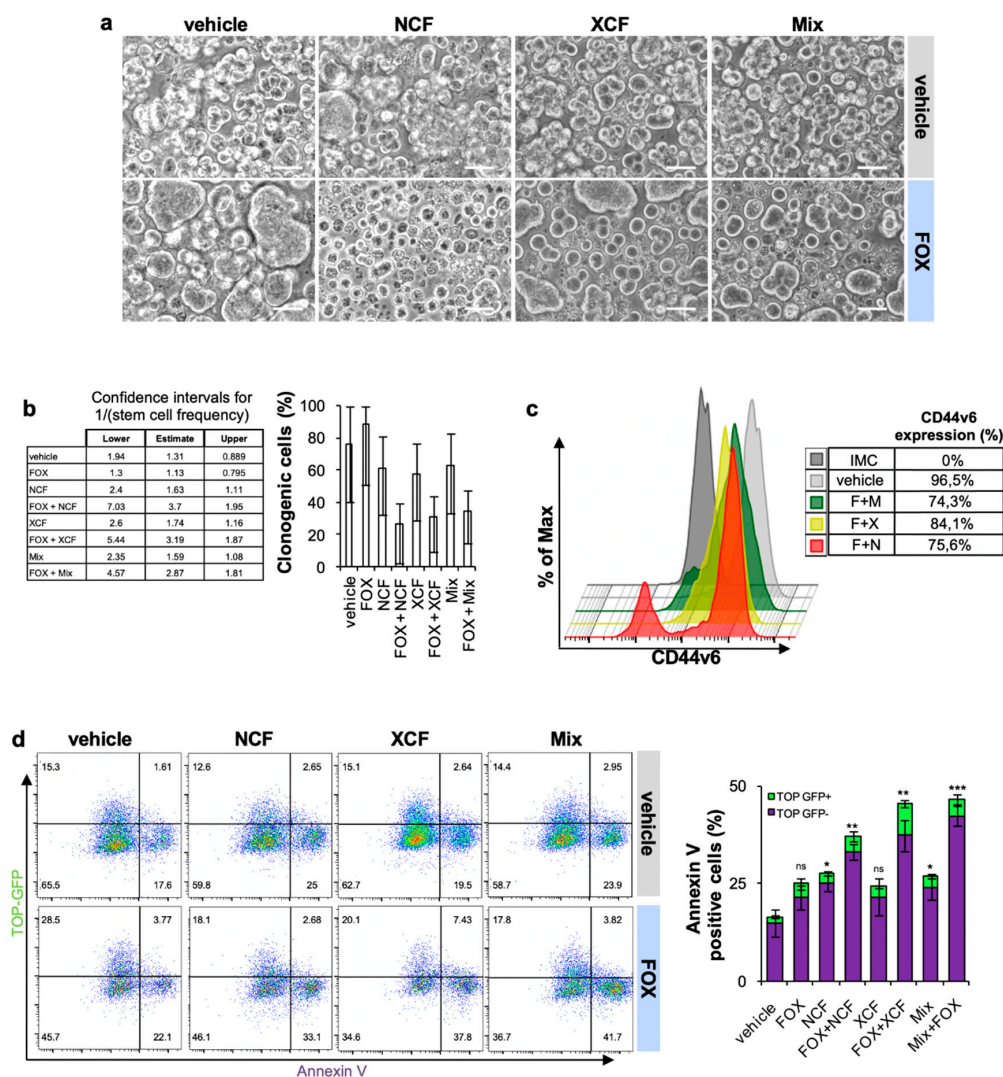


Figure 4. Flavonoids extracts plus chemotherapy decreased the stemness features of CR-CSphC. (a) Phase contrast image showing the sphere forming capability of CR-CSphCs treated with 0.5 μ M FOX in combination with 12.5 μ g/mL NCF, XCF, or both extracts (Mix), for 48 h; (b) clonogenic capability, evaluated by ELDA software, of CR-CSphCs. Pre-treated for 48 h as in (a); (c) representative flow cytometry analysis of CD44v6 expression on CR-CSCs following 48 h treatment as in (a); (d) representative flow cytometry analysis of Annexin V on CR-CSphCs (#8) transduced with TOP-GFP and treated as in A (left panel) and relative percentage of Annexin V positive CR-CSphCs (#8) (right panel). Data are expressed as mean \pm SD of three independent experiments. Comparisons between two groups were made using a two-tailed Student's *t*-test: ns, not significant, * $p \leq 0.05$, ** $p \leq 0.01$, *** $p \leq 0.001$.

4. Discussion

The pharmacological use of chemotherapy as a cancer remedy has been limited by its notorious side effects caused by toxicity to normal cells [17]. Thus, avoiding the undesired toxicity without compromising the targeting of cancer cells represents the main goal to be achieved in cancer treatment. Natural biofunctional molecules are known to exert their tumor-preventive effects by antioxidant polyphenols such as flavonoids [27,28]. Flavonoids, as natural compounds, play a crucial role in preventing intestinal barrier damage by preserving its integrity and the mucosal architecture [52], suggesting that they may not have any side effects on normal intestinal stem cells.

Both chemotherapy and targeted therapy, if not successful in eradicating the disease, may result in the reappearance of even more aggressive cancers. CR-CSCs expansion can

occur during or after therapy interruption due to microenvironmental cues and/or the accumulation of genetic aberrations that nullify the effect of therapy [4].

Nobiletin and Xanthohumol, either singularly or 50% mixed with each other, synergize with FOX-based chemotherapy in order to reduce cell CR-CSphCs viability, the cell cycle S phase and G2/M phase, the sphere-forming capability, and clonogenic potential. Notably, flavonoids treatment lowers the number of CR-CSCs expressing high levels of Wnt and CD44v6, which together with the Wnt pathway activity is the most accurate functional biomarker that identifies a CR-CSC population endowed with metastatic potential [5].

Nobiletin has been reported to sensitize cells to chemotherapy and promote apoptosis in CRC cell lines [53]. Likewise, Xanthohumol has also been reported to sensitize CRC cells to chemotherapy by inhibiting cell proliferation and induce DNA damage and apoptosis in CRC cells [30]. In accordance, NCF and XCF in combination with FOX determine upregulation of pro-apoptotic genes, as well as downregulation of anti-apoptotic genes. Furthermore, given that several of the pro-apoptotic genes induced by flavonoids and the FOX combined treatment, such as ATG3, ATG5, and ATG12, play a critical role in the autophagic process [54,55], we hypothesize that CR-CSphCs exposed to the combined treatment experience severe intra-cellular stress, leading to apoptosis that may follow an autophagic process. Interestingly, we observed that both NCF and XCF, albeit showing cytotoxic effects toward cancer cells, are well tolerated by normal cells. This phenomenon is still not thoroughly understood and could be explained by the presence of altered metabolism or activation of molecular pathways exclusively in cancer cells.

The underlying mechanisms of Nobiletin and Xanthohumol in reducing the viability of CR-CSphCs refractory to chemotherapy is possibly related to the downregulation of stemness programs, such as the Wnt pathway. Indeed, it has already been demonstrated that chemotherapy, for example, 5-FU, induces the activation of the Wnt pathway in CRC cells to mediate treatment escape [56].

Notably, beyond Wnt pathway activation, other stemness and survival pathways specific for CSCs have been described to be involved in the anticancer activity of Nobiletin and Xanthohumol [57,58]. Flavonoids decrease the expression of drug efflux transporters in CRC, which is a well-described mechanism of drug resistance in CSCs [59,60]. This could represent a potential mechanism for the specific targeting of the CR-CSC subset.

In summary, we investigated how NCF and XCF interfere with cell proliferation and apoptosis, by possibly targeting stemness pathways involved in the onset and progression of cancer. Interestingly, we found that these plant derived-natural compounds, either singularly or in combination, are beneficial as additive molecules to chemotherapy, possibly limiting anti-cancer cytotoxicity towards normal cells. The novelty of our research relies on the synergistic/additive effect of the Nobiletin/Xanthohumol treatment in combination with chemotherapy, which affects the viability of CR-CSCs purified and propagated from CRC liver metastasis of patients treated with chemotherapy. In conclusion, flavonoids could serve as a promising strategy for anti-cancer treatment, which preserves patients' quality of life.

5. Conclusions

Here we investigated the potential effects of natural flavonoids, both polymethoxyflavones and prenylflavonoids, as potential adjuvants in CRC therapy. The results obtained showed how specific fractions from natural extracts are able to improve the efficacy of chemotherapy, at the same time reducing cancer cell survival and chemotherapeutics cytotoxicity. Specifically, these fractions are characterized by the presence of active compounds that have been previously characterized for their anticancer potential, namely Nobiletin from *Citrus sinensis* and Xanthohumol from *Humulus lupulus*. The obtained results will pave the way for further investigations about the use of fractionated natural extracts as adjuvants in chemotherapy in the form of functional or fortified foods and/or dietary supplements.

Supplementary Materials: The following are available online at <https://www.mdpi.com/article/10.3390/cancers13163927/s1>, Figure S1: NCF and XCF do not affect non-transformed cells. Figure S2:

NCF and XCF sensitize cancer cells to chemotherapy. Figure S3: NCF and XCF plus chemotherapy induce apoptosis in CR-CSphCs. Figure S4: NCF and XCF plus chemotherapy counteract the stemness potential of CR-CSCs. Table S1: CR-CSphCs characterization, CD44v6 expression, MSI profile, and *KRAS*, *BRAF*, *APC*, and *PIK3CA* gene mutation profile.

Author Contributions: Conceptualization, A.T., A.G., G.P., P.C., and G.S.; methodology, F.C., S.R., M.E.F., D.C., M.G.B., V.D.S., C.O., B.P., S.C., C.P., S.D.F., D.B., M.G., V.V., M.L.I., G.G., V.D.P., and L.R.M.; validation, A.T. and M.E.F.; formal analysis, A.T., A.G., G.P., F.C., and M.E.F.; writing—original draft preparation, A.T., A.G., G.P., F.C., S.R., and M.E.F.; writing—review and editing, R.A., M.T., R.D.M., P.D., P.C., and G.S.; supervision, M.R.B., R.A., M.T., R.D.M., P.D., P.C., and G.S.; funding acquisition, R.A., M.T., R.D.M., P.D., P.C., and G.S. All authors have read and agreed to the published version of the manuscript.

Funding: This work was supported by the following grants: PRIN (Prot.No.2017E84AA4) and Regione Campania-PON Campania FESR 2014–2020 “Combattere la resistenza tumorale: piattaforma integrate multidisciplinare per un approccio tecnologico innovativo alle oncoterapie-Campania Oncoterapie (Project N. B61G18000470007) to P.C. RF2018-12367044 to M.T. and R.D.M. PRIN (Prot.No.2017WKNKSLR) to G.S. European Union 2014–2020 PON Ricerca e Innovazione grant from the Italian Ministry of Education, University and Research, entitled “PROGEMA-Processi Green per l’Estrazione di Principi Attivi e la Depurazione di Matrici di Scarto e Non” (ARS01_00432) to R.A., R.D.M., P.D., P.C. and G.S.

Institutional Review Board Statement: The study was conducted according to the guidelines of the Declaration of Helsinki and approved by the Institutional Ethics Committee of University of Palermo (authorization CE9/2015, Policlinico “Paolo Giaccone”, 14.10.2015, Palermo) and Fondazione Policlinico A Gemelli IRCCS, Rome (authorization AIRC IG 2015/17621, 2016, Fondazione Policlinico A Gemelli IRCCS, Rome, Italy).

Informed Consent Statement: Informed consent was obtained from all subjects involved in the study.

Data Availability Statement: Data related to the study are included in the article or uploaded as supplementary information. Data are available from the corresponding authors (P.C. and G.S.) upon reasonable request.

Acknowledgments: A.T., S.R., and V.V. are research fellows funded by the European Union- FESR FSE, PON Ricerca e Innovazione 2014–2020 (AIM line 1). L.R.M. is a PhD student of the Molecular and Clinical Medicine program. We thank Francesco Calò for image editing.

Conflicts of Interest: The authors declare no conflict of interest.

References

1. Sung, H.; Ferlay, J.; Siegel, R.L.; Laversanne, M.; Soerjomataram, I.; Jemal, A.; Bray, F. Global cancer statistics 2020: GLOBOCAN estimates of incidence and mortality worldwide for 36 cancers in 185 countries. *CA Cancer J. Clin.* **2021**, *71*, 209–249. [[CrossRef](#)]
2. Brenner, H.; Kloor, M.; Pox, C.P. Colorectal cancer. *Lancet* **2014**, *383*, 1490–1502. [[CrossRef](#)]
3. Song, R.; Gu, D.; Zhang, L.; Zhang, X.; Yu, B.; Liu, B.; Xie, J. Functional significance of Hippo/YAP signaling for drug resistance in colorectal cancer. *Mol. Carcinog.* **2018**, *57*, 1608–1615. [[CrossRef](#)]
4. Ricci-Vitiani, L.; Lombardi, D.G.; Pilozzi, E.; Biffoni, M.; Todaro, M.; Peschle, C.; De Maria, R. Identification and expansion of human colon-cancer-initiating cells. *Nature* **2007**, *445*, 111–115. [[CrossRef](#)] [[PubMed](#)]
5. Todaro, M.; Gaggianesi, M.; Catalano, V.; Benfante, A.; Iovino, F.; Biffoni, M.; Apuzzo, T.; Sperduti, I.; Volpe, S.; Cocorullo, G.; et al. CD44v6 is a marker of constitutive and reprogrammed cancer stem cells driving colon cancer metastasis. *Cell Stem Cell* **2014**, *14*, 342–356. [[CrossRef](#)] [[PubMed](#)]
6. Dalerba, P.; Dylla, S.J.; Park, I.K.; Liu, R.; Wang, X.; Cho, R.W.; Hoey, T.; Gurney, A.; Huang, E.H.; Simeone, D.M.; et al. Phenotypic characterization of human colorectal cancer stem cells. *Proc. Natl. Acad. Sci. USA* **2007**, *104*, 10158–10163. [[CrossRef](#)] [[PubMed](#)]
7. Vermeulen, L.; De Sousa, E.M.F.; van der Heijden, M.; Cameron, K.; de Jong, J.H.; Borovski, T.; Tuynman, J.B.; Todaro, M.; Merz, C.; Rodermond, H.; et al. Wnt activity defines colon cancer stem cells and is regulated by the microenvironment. *Nat. Cell Biol.* **2010**, *12*, 468–476. [[CrossRef](#)] [[PubMed](#)]
8. Usui, T.; Sakurai, M.; Umata, K.; Elbadawy, M.; Ohama, T.; Yamawaki, H.; Hazama, S.; Takenouchi, H.; Nakajima, M.; Tsunedomi, R.; et al. Hedgehog signals mediate anti-cancer drug resistance in three-dimensional primary colorectal cancer organoid culture. *Int. J. Mol. Sci.* **2018**, *19*, 1098. [[CrossRef](#)]
9. Huang, R.; Wang, G.; Song, Y.; Tang, Q.; You, Q.; Liu, Z.; Chen, Y.; Zhang, Q.; Li, J.; Muhammand, S.; et al. Colorectal cancer stem cell and chemoresistant colorectal cancer cell phenotypes and increased sensitivity to Notch pathway inhibitor. *Mol. Med. Rep.* **2015**, *12*, 2417–2424. [[CrossRef](#)]

10. Touil, Y.; Igoudjil, W.; Corvaisier, M.; Dessein, A.F.; Vandomme, J.; Monte, D.; Stechly, L.; Skrypek, N.; Langlois, C.; Grard, G.; et al. Colon cancer cells escape 5FU chemotherapy-induced cell death by entering stemness and quiescence associated with the c-Yes/YAP axis. *Clin. Cancer Res.* **2014**, *20*, 837–846. [[CrossRef](#)]
11. Turdo, A.; Veschi, V.; Gaggianesi, M.; Chinnici, A.; Bianca, P.; Todaro, M.; Stassi, G. Meeting the challenge of targeting cancer stem cells. *Front. Cell Dev. Biol.* **2019**, *7*, 16. [[CrossRef](#)]
12. Francescangeli, F.; Contavalli, P.; De Angelis, M.L.; Careccia, S.; Signore, M.; Haas, T.L.; Salaris, F.; Baiocchi, M.; Boe, A.; Giuliani, A.; et al. A pre-existing population of ZEB2(+) quiescent cells with stemness and mesenchymal features dictate chemoresistance in colorectal cancer. *J. Exp. Clin. Cancer Res.* **2020**, *39*, 2. [[CrossRef](#)]
13. Weeks, J.C.; Catalano, P.J.; Cronin, A.; Finkelman, M.D.; Mack, J.W.; Keating, N.L.; Schrag, D. Patients' expectations about effects of chemotherapy for advanced cancer. *N. Engl. J. Med.* **2012**, *367*, 1616–1625. [[CrossRef](#)] [[PubMed](#)]
14. Giacchetti, S.; Perpoint, B.; Zidani, R.; Le Bail, N.; Faggiuolo, R.; Focan, C.; Chollet, P.; Llory, J.F.; Letourneau, Y.; Coudert, B.; et al. Phase III multicenter randomized trial of oxaliplatin added to chronomodulated fluorouracil-leucovorin as first-line treatment of metastatic colorectal cancer. *J. Clin. Oncol.* **2000**, *18*, 136–147. [[CrossRef](#)]
15. de Gramont, A.; Figuer, A.; Seymour, M.; Homerin, M.; Hmissi, A.; Cassidy, J.; Boni, C.; Cortes-Funes, H.; Cervantes, A.; Freyer, G.; et al. Leucovorin and fluorouracil with or without oxaliplatin as first-line treatment in advanced colorectal cancer. *J. Clin. Oncol.* **2000**, *18*, 2938–2947. [[CrossRef](#)] [[PubMed](#)]
16. Wang, S.; Wang, L.; Zhou, Z.; Deng, Q.; Li, L.; Zhang, M.; Liu, L.; Li, Y. Leucovorin enhances the anti-cancer effect of bortezomib in colorectal cancer cells. *Sci. Rep.* **2017**, *7*, 682. [[CrossRef](#)] [[PubMed](#)]
17. Johnstone, R.W.; Ruefli, A.A.; Lowe, S.W. Apoptosis: A link between cancer genetics and chemotherapy. *Cell* **2002**, *108*, 153–164. [[CrossRef](#)]
18. Rajagopalan, S.; Politi, P.M.; Sinha, B.K.; Myers, C.E. Adriamycin-induced free radical formation in the perfused rat heart: Implications for cardiotoxicity. *Cancer Res.* **1988**, *48*, 4766–4769. [[PubMed](#)]
19. Berg, D. Managing the side effects of chemotherapy for colorectal cancer. *Semin. Oncol.* **1998**, *25*, 53–59. [[PubMed](#)]
20. Jansman, F.G.; Sleijfer, D.T.; de Graaf, J.C.; Coenen, J.L.; Brouwers, J.R. Management of chemotherapy-induced adverse effects in the treatment of colorectal cancer. *Drug Saf.* **2001**, *24*, 353–367. [[CrossRef](#)] [[PubMed](#)]
21. Key, T.J.; Schatzkin, A.; Willett, W.C.; Allen, N.E.; Spencer, E.A.; Travis, R.C. Diet, nutrition and the prevention of cancer. *Public Health Nutr.* **2004**, *7*, 187–200. [[CrossRef](#)]
22. Song, J.K.; Bae, J.M. Citrus fruit intake and breast cancer risk: A quantitative systematic review. *J. Breast Cancer* **2013**, *16*, 72–76. [[CrossRef](#)]
23. Jiang, C.H.; Sun, T.L.; Xiang, D.X.; Wei, S.S.; Li, W.Q. Anticancer activity and mechanism of xanthohumol: A prenylated flavonoid from hops (*Humulus lupulus* L.). *Front. Pharmacol.* **2018**, *9*, 530. [[CrossRef](#)] [[PubMed](#)]
24. Harikumar, K.B.; Kunnumakkara, A.B.; Ahn, K.S.; Anand, P.; Krishnan, S.; Guha, S.; Aggarwal, B.B. Modification of the cysteine residues in IkappaBalpha kinase and NF-kappaB (p65) by xanthohumol leads to suppression of NF-kappaB-regulated gene products and potentiation of apoptosis in leukemia cells. *Blood* **2009**, *113*, 2003–2013. [[CrossRef](#)] [[PubMed](#)]
25. Cirmi, S.; Maugeri, A.; Ferlazzo, N.; Gangemi, S.; Calapai, G.; Schumacher, U.; Navarra, M. Anticancer potential of citrus juices and their extracts: A systematic review of both preclinical and clinical studies. *Front. Pharmacol.* **2017**, *8*, 420. [[CrossRef](#)] [[PubMed](#)]
26. Clere, N.; Faure, S.; Martinez, M.C.; Andriantsitohaina, R. Anticancer properties of flavonoids: Roles in various stages of carcinogenesis. *Cardiovasc. Hematol. Agents Med. Chem.* **2011**, *9*, 62–77. [[CrossRef](#)] [[PubMed](#)]
27. Morley, K.L.; Ferguson, P.J.; Koropatnick, J. Tangeretin and nobiletin induce G1 cell cycle arrest but not apoptosis in human breast and colon cancer cells. *Cancer Lett.* **2007**, *251*, 168–178. [[CrossRef](#)]
28. Gerhauser, C.; Alt, A.; Heiss, E.; Gamal-Eldeen, A.; Klimo, K.; Knauff, J.; Neumann, I.; Scherf, H.R.; Frank, N.; Bartsch, H.; et al. Cancer chemopreventive activity of Xanthohumol, a natural product derived from hop. *Mol. Cancer Ther.* **2002**, *1*, 959–969.
29. Goh, J.X.H.; Tan, L.T.; Goh, J.K.; Chan, K.G.; Pusparajah, P.; Lee, L.H.; Goh, B.H. Nobiletin and derivatives: Functional compounds from citrus fruit peel for colon cancer chemoprevention. *Cancers* **2019**, *11*, 867. [[CrossRef](#)]
30. Scagliarini, A.; Mathey, A.; Aires, V.; Delmas, D. Xanthohumol, a prenylated flavonoid from hops, induces DNA damages in colorectal cancer cells and sensitizes SW480 cells to the SN38 chemotherapeutic agent. *Cells* **2020**, *9*, 932. [[CrossRef](#)]
31. Asakawa, T.; Sagara, H.; Kanakogi, M.; Hiza, A.; Tsukaguchi, Y.; Ogawa, T.; Nakayama, M.; Ouchi, H.; Inai, M.; Kan, T. Practical synthesis of polymethylated flavones: Nobiletin and its desmethyl derivatives. *Org. Process Res. Dev.* **2019**, *23*, 595–602. [[CrossRef](#)]
32. Khupse, R.S.; Erhardt, P.W. Total synthesis of xanthohumol. *J. Nat. Prod.* **2007**, *70*, 1507–1509. [[CrossRef](#)]
33. Carrizzo, A.; Basilicata, M.G.; Pepe, G.; Sorensen, K.K.; Ciccarelli, M.; Sarno, V.D.; Damato, A.; Venturini, E.; Borrelli, A.; Musella, S.; et al. A novel vasoactive peptide “PG1” from buffalo ice-cream protects from angiotensin-evoked high blood pressure. *Antioxidants* **2021**, *10*, 441. [[CrossRef](#)]
34. Basilicata, M.G.; Pepe, G.; Adesso, S.; Ostacolo, C.; Sala, M.; Sommella, E.; Scala, M.C.; Messori, A.; Autore, G.; Marzocco, S.; et al. Antioxidant properties of buffalo-milk dairy products: A beta-Lg peptide released after gastrointestinal digestion of buffalo ricotta cheese reduces oxidative stress in intestinal epithelial cells. *Int. J. Mol. Sci.* **2018**, *19*, 1955. [[CrossRef](#)] [[PubMed](#)]
35. Deng, G.F.; Shen, C.; Xu, X.R.; Kuang, R.D.; Guo, Y.J.; Zeng, L.S.; Gao, L.L.; Lin, X.; Xie, J.F.; Xia, E.Q.; et al. Potential of fruit wastes as natural resources of bioactive compounds. *Int. J. Mol. Sci.* **2012**, *13*, 8308–8323. [[CrossRef](#)]
36. Barbosa-Pereira, L.; Pocheville, A.; Angulo, I.; Paseiro-Losada, P.; Cruz, J.M. Fractionation and purification of bioactive compounds obtained from a brewery waste stream. *Biomed. Res. Int.* **2013**, *2013*, 408491. [[CrossRef](#)]

37. Pepe, G.; Pagano, F.; Adesso, S.; Sommella, E.; Ostacolo, C.; Manfra, M.; Chieppa, M.; Sala, M.; Russo, M.; Marzocco, S.; et al. Bioavailable Citrus sinensis extract: Polyphenolic composition and biological activity. *Molecules* **2017**, *22*, 623. [[CrossRef](#)] [[PubMed](#)]
38. Salviati, E.C.E.; Sommella, E.; Montella, F.; Bertamino, A.; Ostacolo, C.; Parrino, B.; Rubino, R.; Vecchione, C.; Puca, A.; Novellino, E.; et al. Immunomodulatory activity of Humulus lupulus bitter acids fraction: Enhancement of natural killer cells function by NKp44 activating receptor stimulation. *J. Funct. Foods* **2019**, *61*, 103469. [[CrossRef](#)]
39. Todaro, M.; Alea, M.P.; Di Stefano, A.B.; Cammareri, P.; Vermeulen, L.; Iovino, F.; Tripodo, C.; Russo, A.; Gulotta, G.; Medema, J.P.; et al. Colon cancer stem cells dictate tumor growth and resist cell death by production of interleukin-4. *Cell Stem Cell* **2007**, *1*, 389–402. [[CrossRef](#)]
40. Chou, T.C. Theoretical basis, experimental design, and computerized simulation of synergism and antagonism in drug combination studies. *Pharmacol. Rev.* **2006**, *58*, 621–681. [[CrossRef](#)] [[PubMed](#)]
41. Lo, P.K.; Kanojia, D.; Liu, X.; Singh, U.P.; Berger, F.G.; Wang, Q.; Chen, H. CD49f and CD61 identify Her2/neu-induced mammary tumor-initiating cells that are potentially derived from luminal progenitors and maintained by the integrin-TGFbeta signaling. *Oncogene* **2012**, *31*, 2614–2626. [[CrossRef](#)]
42. Zeuner, A.; Todaro, M.; Stassi, G.; De Maria, R. Colorectal cancer stem cells: From the crypt to the clinic. *Cell Stem Cell* **2014**, *15*, 692–705. [[CrossRef](#)] [[PubMed](#)]
43. Sorbye, H.; Glimelius, B.; Berglund, A.; Fokstuen, T.; Tveit, K.M.; Braendengen, M.; OGREID, D.; Dahl, O. Multicenter phase II study of Nordic fluorouracil and folinic acid bolus schedule combined with oxaliplatin as first-line treatment of metastatic colorectal cancer. *J. Clin. Oncol.* **2004**, *22*, 31–38. [[CrossRef](#)] [[PubMed](#)]
44. May, J.E.; Donaldson, C.; Gynn, L.; Morse, H.R. Chemotherapy-induced genotoxic damage to bone marrow cells: Long-term implications. *Mutagenesis* **2018**, *33*, 241–251. [[CrossRef](#)]
45. Cao, Y.; Gong, Y.; Liu, L.; Zhou, Y.; Fang, X.; Zhang, C.; Li, Y.; Li, J. The use of human umbilical vein endothelial cells (HUVECs) as an in vitro model to assess the toxicity of nanoparticles to endothelium: A review. *J. Appl. Toxicol.* **2017**, *37*, 1359–1369. [[CrossRef](#)]
46. Henrique, T.; Zanon, C.F.; Girol, A.P.; Stefanini, A.C.B.; Contessoto, N.S.A.; da Silveira, N.J.F.; Bezerra, D.P.; Silveira, E.R.; Barbosa-Filho, J.M.; Cornelio, M.L.; et al. Biological and physical approaches on the role of piplartine (piperlongumine) in cancer. *Sci. Rep.* **2020**, *10*, 22283. [[CrossRef](#)] [[PubMed](#)]
47. Zhan, T.; Rindtorff, N.; Boutros, M. Wnt signaling in cancer. *Oncogene* **2017**, *36*, 1461–1473. [[CrossRef](#)] [[PubMed](#)]
48. Martin-Orozco, E.; Sanchez-Fernandez, A.; Ortiz-Parra, I.; Ayala-San Nicolas, M. WNT signaling in tumors: The way to evade drugs and immunity. *Front. Immunol.* **2019**, *10*, 2854. [[CrossRef](#)]
49. Shen, C.; Nayak, A.; Melendez, R.A.; Wynn, D.T.; Jackson, J.; Lee, E.; Ahmed, Y.; Robbins, D.J. Casein kinase 1alpha as a regulator of Wnt-driven cancer. *Int. J. Mol. Sci.* **2020**, *21*, 5940. [[CrossRef](#)] [[PubMed](#)]
50. Schatoff, E.M.; Goswami, S.; Zafra, M.P.; Foronda, M.; Shusterman, M.; Leach, B.I.; Katti, A.; Diaz, B.J.; Dow, L.E. Distinct colorectal cancer-associated APC mutations dictate response to tankyrase inhibition. *Cancer Discov.* **2019**, *9*, 1358–1371. [[CrossRef](#)]
51. Huang, S.M.; Mishina, Y.M.; Liu, S.; Cheung, A.; Stegmeier, F.; Michaud, G.A.; Charlat, O.; Wiellette, E.; Zhang, Y.; Wiessner, S.; et al. Tankyrase inhibition stabilizes axin and antagonizes Wnt signalling. *Nature* **2009**, *461*, 614–620. [[CrossRef](#)]
52. Wen, X.; Zhao, H.; Wang, L.; Wang, L.; Du, G.; Guan, W.; Liu, J.; Cao, X.; Jiang, X.; Tian, J.; et al. Nobiletin attenuates DSS-induced intestinal barrier damage through the HNF4alpha-claudin-7 signaling pathway. *J. Agric. Food Chem.* **2020**, *68*, 4641–4649. [[CrossRef](#)]
53. Zheng, Q.; Hirose, Y.; Yoshimi, N.; Murakami, A.; Koshimizu, K.; Ohigashi, H.; Sakata, K.; Matsumoto, Y.; Sayama, Y.; Mori, H. Further investigation of the modifying effect of various chemopreventive agents on apoptosis and cell proliferation in human colon cancer cells. *J. Cancer Res. Clin. Oncol.* **2002**, *128*, 539–546. [[CrossRef](#)]
54. Zhuang, L.; Ma, Y.; Wang, Q.; Zhang, J.; Zhu, C.; Zhang, L.; Xu, X. Atg3 overexpression enhances bortezomib-induced cell death in SKM-1 cell. *PLoS ONE* **2016**, *11*, e0158761. [[CrossRef](#)]
55. Yousefi, S.; Perozzo, R.; Schmid, I.; Ziemiecki, A.; Schaffner, T.; Scapozza, L.; Brunner, T.; Simon, H.U. Calpain-mediated cleavage of Atg5 switches autophagy to apoptosis. *Nat. Cell Biol.* **2006**, *8*, 1124–1132. [[CrossRef](#)]
56. He, L.; Zhu, H.; Zhou, S.; Wu, T.; Wu, H.; Yang, H.; Mao, H.; SekharKathera, C.; Janardhan, A.; Edick, A.M.; et al. Wnt pathway is involved in 5-FU drug resistance of colorectal cancer cells. *Exp. Mol. Med.* **2018**, *50*, 1–12. [[CrossRef](#)] [[PubMed](#)]
57. Ko, Y.C.; Choi, H.S.; Liu, R.; Kim, J.H.; Kim, S.L.; Yun, B.S.; Lee, D.S. Inhibitory effects of tangeretin, a citrus peel-derived flavonoid, on breast cancer stem cell formation through suppression of Stat3 signaling. *Molecules* **2020**, *25*, 2599. [[CrossRef](#)] [[PubMed](#)]
58. Liu, M.; Yin, H.; Qian, X.; Dong, J.; Qian, Z.; Miao, J. Xanthohumol, a prenylated chalcone from hops, inhibits the viability and stemness of doxorubicin-resistant MCF-7/ADR cells. *Molecules* **2016**, *22*, 36. [[CrossRef](#)] [[PubMed](#)]
59. Lee, S.H.; Kim, H.J.; Lee, J.S.; Lee, I.S.; Kang, B.Y. Inhibition of topoisomerase I activity and efflux drug transporters' expression by xanthohumol from hops. *Arch. Pharm. Res.* **2007**, *30*, 1435–1439. [[CrossRef](#)]
60. Ma, W.; Feng, S.; Yao, X.; Yuan, Z.; Liu, L.; Xie, Y. Nobiletin enhances the efficacy of chemotherapeutic agents in ABCB1 overexpression cancer cells. *Sci. Rep.* **2015**, *5*, 18789. [[CrossRef](#)]

Nobiletin and Xanthohumol Sensitize Colorectal Cancer Stem Cells to Standard Chemotherapy

Alice Turdo, Antonino Glaviano, Giacomo Pepe, Federica Calapà, Stefania Raimondo, Micol Eleonora Fiori, Daniela Carbone, Manuela Giovanna Basilicata, Veronica Di Sarno, Carmine Ostacolo, Barbara Parrino, Stella Cascioferro, Camilla Pecoraro, Simone Di Franco, Diana Bellavia, Miriam Gaggianesi, Veronica Veschi, Melania Lo Iacono, Gloria Ganduscio, Vincenzo Davide Pantina, Laura Rosa Mangiapane, Maria Rita Bongiorno, Riccardo Alessandro, Matilde Todaro, Ruggero De Maria, Patrizia Diana, Pietro Campiglia and Giorgio Stassi

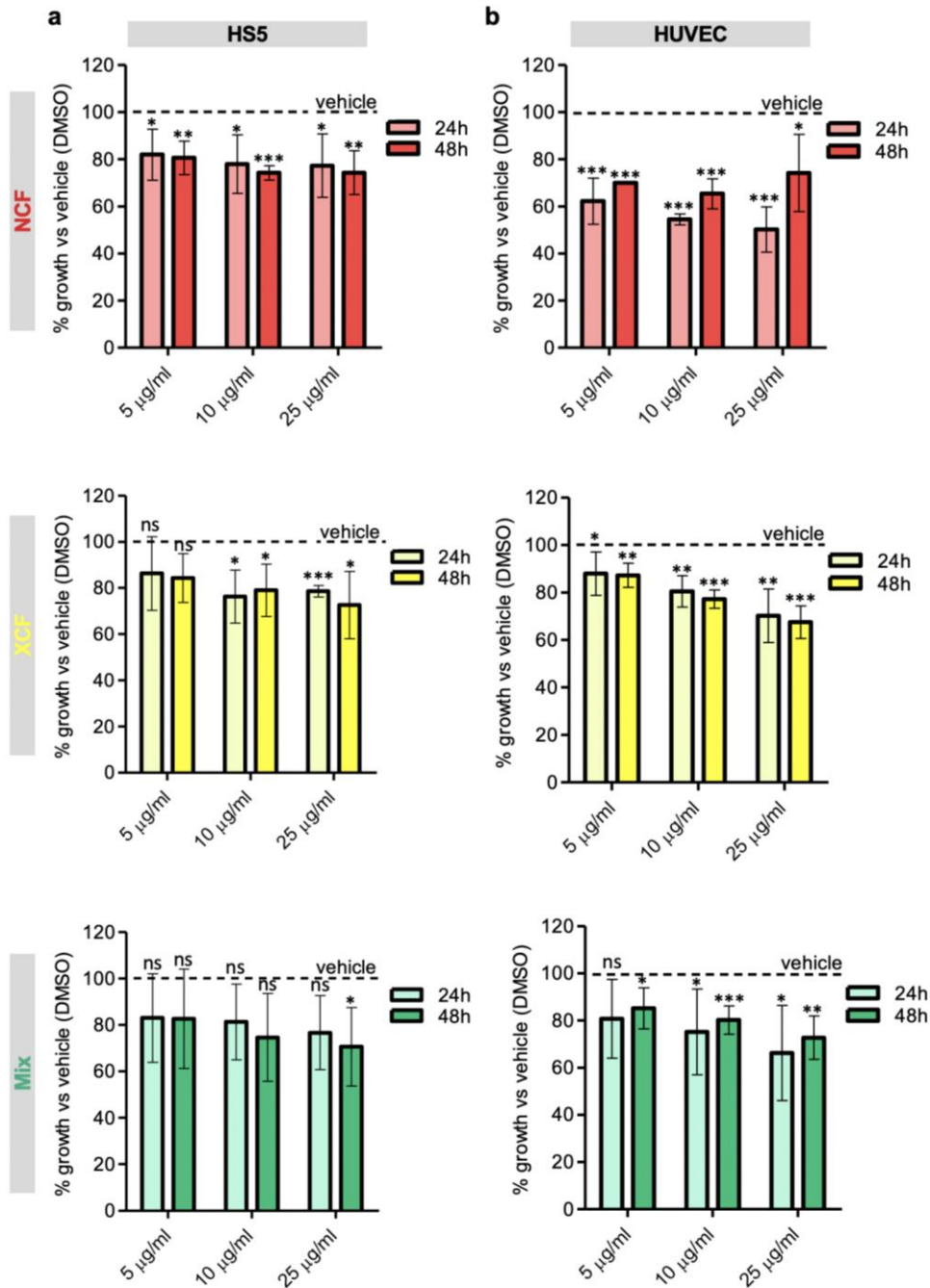
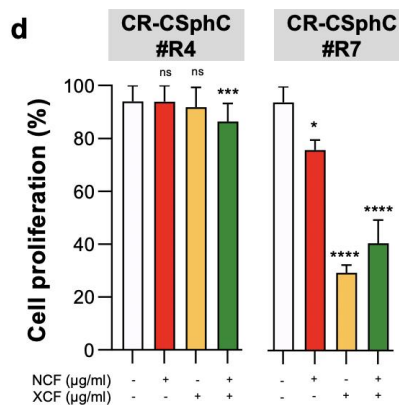
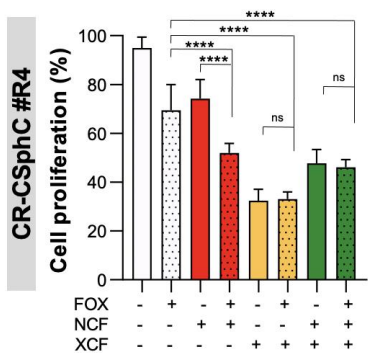
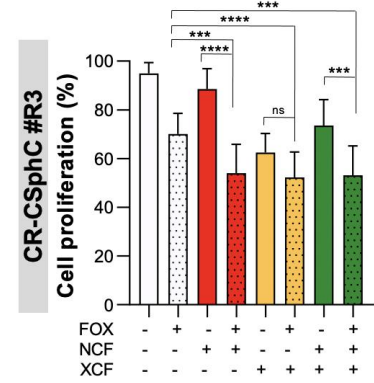
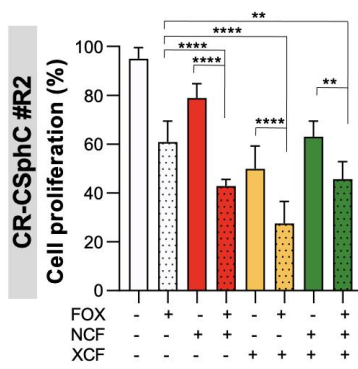
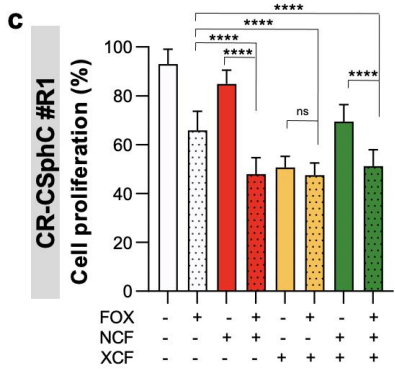
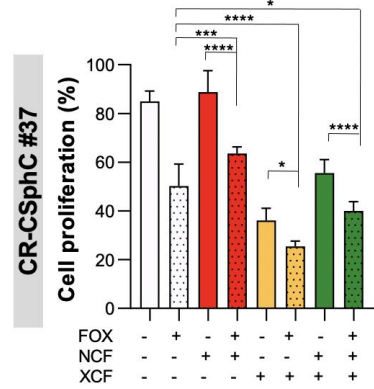
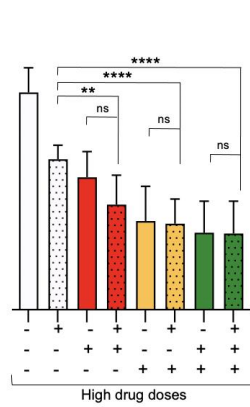
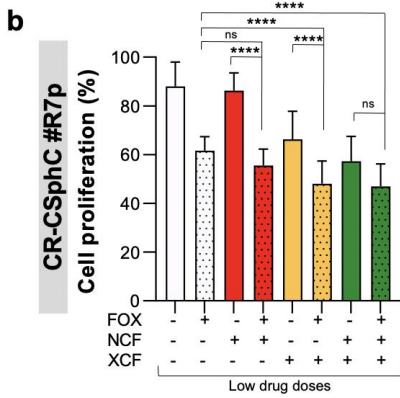
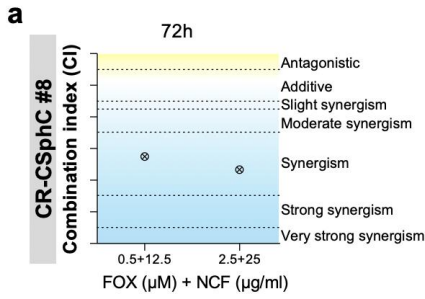


Figure S1. NCF and XCF do not affect non-transformed cells. Percentage of growth of HS5 (a) and HUVEC (b) cell lines treated with 5, 10, and 25 µg/ml of NCF, XCF, or the Mix of extracts for 24 and 48 hours. Values are plotted as the percentage of 5 growth versus the vehicle (DMSO, dotted line). Data are represented as means ± SD. Comparisons between two groups (cells treated with the extracts vs cells treated with the vehicle) were made using a two-tailed Student's t-test: * $p \leq 0.05$, ** $p \leq 0.01$, *** $p \leq 0.001$.



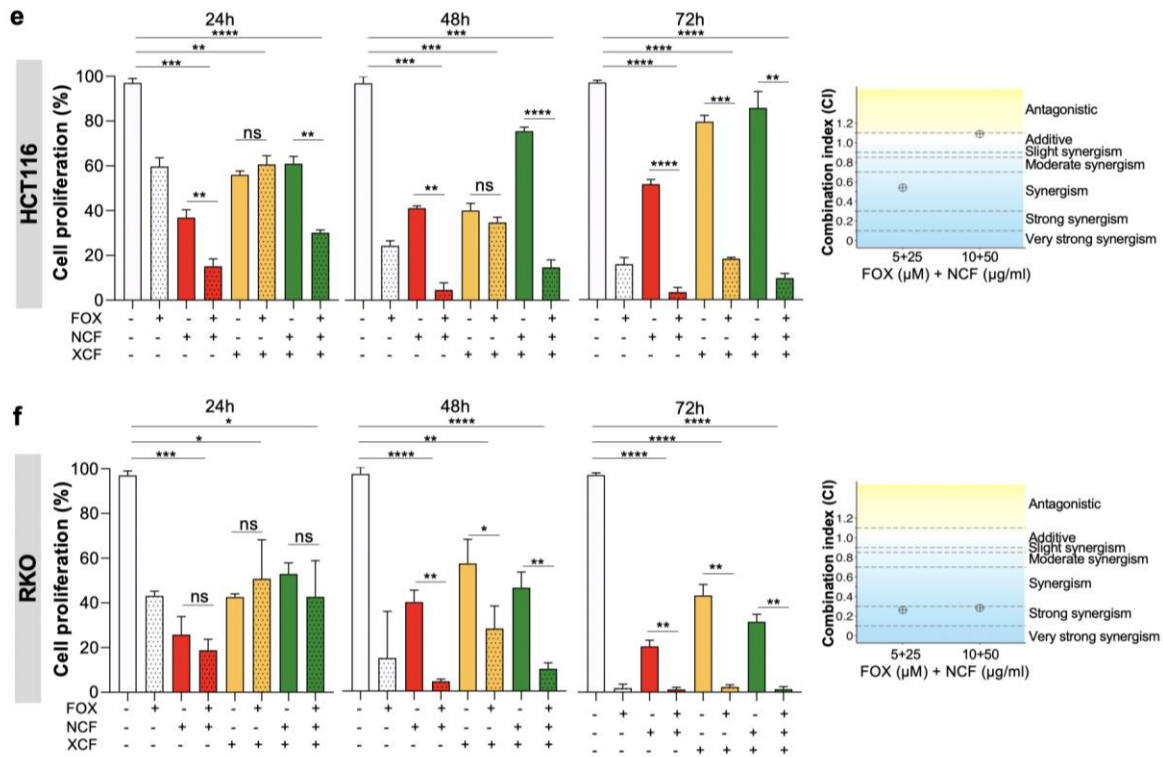


Figure S2. NCF and XCF sensitize cancer cells to chemotherapy (a) Synergy plot representing the combination index (CI), computed in CompuSyn by using Chou-Talalay method, calculated from cell proliferation data of CR-CSphCs (#8) treated with different FOX and NCF dose pair at 72 hours; (b) Cell proliferation percentage of primary CR-CSphCs (#R7p) treated with 25 and 40 μg/ml of NCF, XCF or Mix extracts alone or in combination with 5 μM FOX for 72 hours (left panel) and CR-CSphCs (#37) treated with 25 μg/ml of NCF, XCF or Mix extracts alone or in combination with 1.25 μM FOX for 72 hours (right panel); (c) Cell proliferation percentage of CR-CSC #R1, #R2, #R3, #R4 treated with 40 μg/ml of NCF, XCF or Mix extracts alone or in combination with 5 μM FOX for 72 hours; (d) Cell proliferation percentage of CR-CSC #R4 and #R7 treated with 25 μg/ml of NCF, XCF or Mix extracts for 72 hours; (e,f) Cell viability of CRC cell lines (HCT116 and RKO) treated with 25 μg/ml of NCF, XCF or Mix extracts alone or in combination with 5 μM FOX at the indicated time points (left panel). Synergy plot representing the combination index (CI), computed in CompuSyn by using Chou-Talalay method, calculated from cell proliferation data of CRC cell lines treated with different FOX and NCF dose pair at 48 hours (right panel). Data are represented as mean ± SD of three independent experiments. Percentage of untreated control (vehicle) is shown. Comparisons between two groups were made using a two-tailed Student's t-test: ns, not significant, * $p \leq 0.05$, ** $p \leq 0.01$, *** $p \leq 0.001$, **** $p \leq 0.0001$.

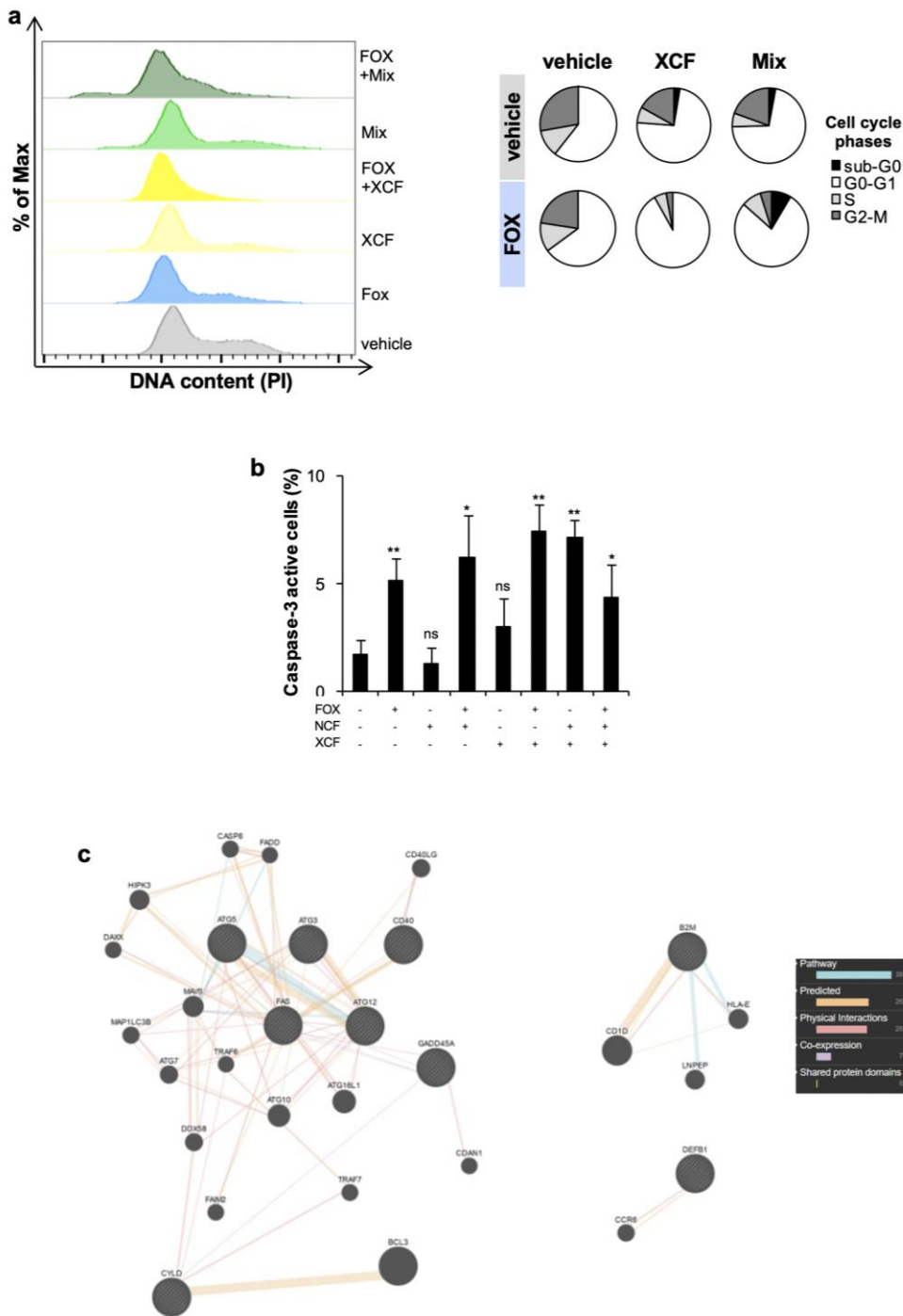


Figure S3. NCF and XCF plus chemotherapy induce apoptosis in CR-CSphCs (a) Representative flow cytometry analysis of cell cycle phases distribution in CR-CSphCs (#8) exposed to 0.5 μ M FOX and 12.5 μ g/ml Xanthohumol or Mix, alone or in combination, for 48 hours. DNA content was assessed by propidium iodide (PI) staining; (b) Percentage of cells treated as in (a) showing caspase-3 activity assessed by flow cytometry analysis; (c) Network integration of multiple genes showed in Figure 3C calculated by geneMANIA software.

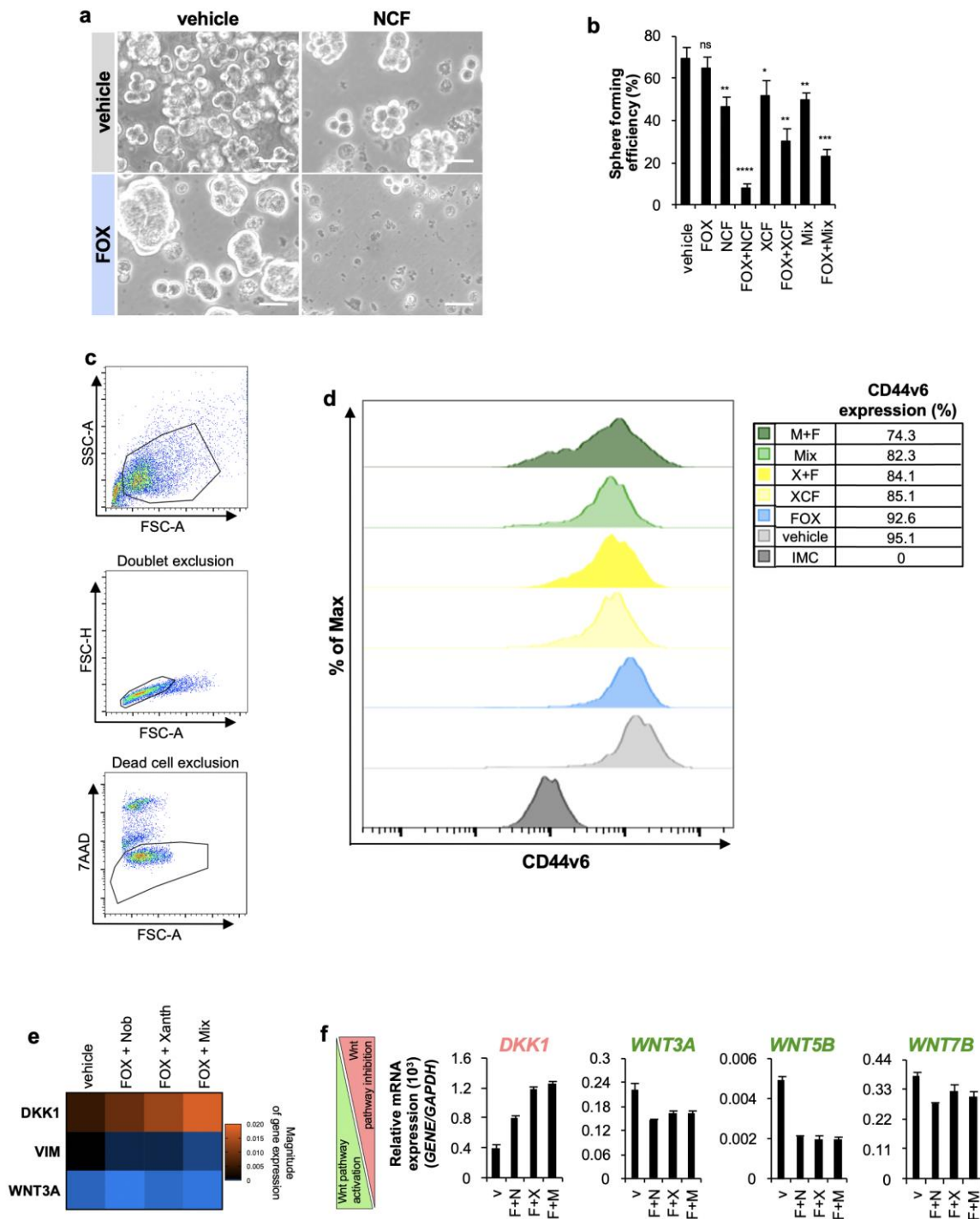


Figure S4. NCF and XCF plus chemotherapy counteract the stemness potential of CR-CSCs (a) Phase contrast image showing the sphere forming capability of CR-CSCs, cultured at low cell density, treated with 0.5 μ M FOX and 12.5 μ g/ml NCF, alone or in combination, for 48 hours, scale bar represents 25 μ m; (b) Sphere forming efficiency of CR-CSCs treated with 0.5 μ M FOX and 12.5 μ g/ml NCF, alone or in combination, for 48 hours (c) Representative flow cytometry analysis showing the gating strategies of CR-CSPhC shown in Figure 3D; (d) Representative flow cytometry analysis of CD44v6 expression on CR-CSCs following 48 hours treatment with 12.5 μ g/ml of NCF, XCF or Mix extracts alone or in combination with 0.5 μ M FOX for 72 hours; (e) Gene expression analysis of genes involved in stemness and EMT in CR-CSPhCs after exposure to 0.5 μ M FOX and 12.5 μ g/ml NCF, XCF or Mix, as compared to control (vehicle) for 48 hours. Data are expressed as $2^{-\Delta\Delta Ct}$ expression values normalized to *GAPDH* and *HPRT* genes; (f) Relative mRNA expression levels of genes involved in Wnt pathway activation (*DKK1*, *AXIN1*, *AXIN2*, *CK1*) and inhibition (*WNT3A*, *WNT5B*, *WNT7B*). *GAPDH* was used as control.

	#	Age	Gender	Site	Stage	Grading	TNM classification	MSI clinical relevant	CD44v6 (%)	KRAS	BRAF	APC	PIK3CA
CR-CSphC	3	85	F	colon (right site)	IIIC	G3	T3N2M0	MSI	33	wt	mut	wt	mut
	8	57	F	colon (right site)	IV	G3	T3N2M1	MSS	92.3	mut	wt	mut	mut
	24	51	F	colon (right site)	IIA	G2	T3N0M0	MSI	9.96	wt	wt	mut	wt
	37	82	M	colon (right site)	IIIC	G3	T3N2M0	MSI	46	wt	wt	mut	wt
	59	78	M	colon	IIIB	G3	T3N1M0	MSS	85.4	mut	wt	wt	wt
	R7p	70	M	colon (left side)	NA	NA	NA	NA	NA	wt	mut	NA	wt
Chemoresistant CR-CSphC	R1	65	M	liver metastasis of colon cancer (sigmoid)	IIA	NA	T3N0M0	MSS	13.7	wt	wt	NA	NA
	R2	61	F	liver metastasis of colon cancer (rectum)	IV	NA	T3N1M1	MSS	19.1	wt	wt	NA	NA
	R3	62	F	liver metastasis of colon cancer (rectum)	IIIB	NA	T3N1M0	MSS	22.8	mut	wt	NA	NA
	R4	38	M	liver metastasis of colon cancer (rectum)	IV	NA	T4N1M1	MSS	93	wt	mut	NA	NA
	R6	69	F	liver metastasis of colon cancer (left site)	NA	NA	NA	NA	NA	wt	wt	NA	wt
	R7	70	M	liver metastasis of colon cancer (left site)	NA	NA	NA	NA	NA	wt	mut	NA	wt

Table S1. CR-CSphCs characterization, CD44v6 expression, MSI profile, and *KRAS*, *BRAF*, *APC* and *PIK3CA* gene mutational profile. TNM classification is referred to the time of initial diagnosis. Wt, wild-type; mut, mutated; NA, data not available.











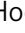








Chapter 6

Adipose stem cell niche reprograms the colorectal cancer stem cell metastatic machinery

Simone Di Franco, Paola Bianca, Davide Stefano Sardina, Alice Turdo, Miriam Gaggianesi, Veronica Veschi, Annalisa Nicotra, **Laura Rosa Mangiapane**, Melania Lo Iacono, Irene Pillitteri, Sander van Hooff, Federica Martorana, Gianmarco Motta, Eliana Gulotta, Vincenzo Luca Lentini, Emanuele Martorana, Micol Eleonora Fiori, Salvatore Vieni, Maria Rita Bongiorno, Giorgio Giannone, Dario Giuffrida, Lorenzo Memeo, Lorenzo Colarossi, Marzia Mare, Paolo Vigneri, Matilde Todaro, Ruggero De Maria, Jan Paul Medema, Giorgio Stassi

Published in *Nature Communications*, 2021

Adipose stem cell niche reprograms the colorectal cancer stem cell metastatic machinery

Simone Di Franco ¹, Paola Bianca ², Davide Stefano Sardina ², Alice Turdo ², Miriam Gaggianesi ¹, Veronica Veschi ¹, Annalisa Nicotra ², Laura Rosa Mangiapane ², Melania Lo Iacono ¹, Irene Pillitteri ¹, Sander van Hooff³, Federica Martorana ⁴, Gianmarco Motta ⁴, Eliana Gulotta⁵, Vincenzo Luca Lentini ⁶, Emanuele Martorana ⁷, Micol Eleonora Fiori ⁸, Salvatore Vieni¹, Maria Rita Bongiorno², Giorgio Giannone⁹, Dario Giuffrida⁹, Lorenzo Memeo ⁹, Lorenzo Colarossi ⁹, Marzia Mare^{9,10}, Paolo Vigneri ¹¹, Matilde Todaro², Ruggero De Maria^{12,13}, Jan Paul Medema^{3,14} & Giorgio Stassi ¹✉

Obesity is a strong risk factor for cancer progression, posing obesity-related cancer as one of the leading causes of death. Nevertheless, the molecular mechanisms that endow cancer cells with metastatic properties in patients affected by obesity remain unexplored.

Here, we show that IL-6 and HGF, secreted by tumor neighboring visceral adipose stromal cells (V-ASCs), expand the metastatic colorectal (CR) cancer cell compartment (CD44v6+), which in turn secretes neurotrophins such as NGF and NT-3, and recruits adipose stem cells within tumor mass. Visceral adipose-derived factors promote vasculogenesis and the onset of metastatic dissemination by activation of STAT3, which inhibits miR-200a and enhances ZEB2 expression, effectively reprogramming CRC cells into a highly metastatic phenotype. Notably, obesity-associated tumor microenvironment provokes a transition in the transcriptomic expression profile of cells derived from the epithelial consensus molecular subtype (CMS2) CRC patients towards a mesenchymal subtype (CMS4). STAT3 pathway inhibition reduces ZEB2 expression and abrogates the metastatic growth sustained by adipose-released proteins. Together, our data suggest that targeting adipose factors in colorectal cancer patients with obesity may represent a therapeutic strategy for preventing metastatic disease.

¹Department of Surgical Oncological and Stomatological Sciences (DICHIRONS), University of Palermo, Palermo, Italy. ²Department of Health Promotion Sciences, Internal Medicine and Medical Specialties (PROMISE), University of Palermo, Palermo, Italy. ³Laboratory for Experimental Oncology and Radiobiology, Center for Experimental and Molecular Medicine, Cancer Center Amsterdam, Amsterdam UMC, University of Amsterdam, Amsterdam, The Netherlands. ⁴Department of Clinical and Experimental Medicine, A.O.U. Policlinico-Vittorio Emanuele, Division of Medical Oncology, University of Catania, Catania, Italy. ⁵Reconstructive Plastic Surgery, ARNAS Ospedali Civico Di Cristina e Benfratelli, Palermo, Italy. ⁶Pathology Unit, Ospedali Riuniti Villa Sofia-Cervello, Palermo, Italy. ⁷IOM (Mediterranean Institute of Oncology) Ricerca, Viagrande, Catania, Italy. ⁸Department of Oncology and Molecular Medicine, Istituto Superiore di Sanità, Rome, Italy. ⁹Department of Experimental Oncology, Mediterranean Institute of Oncology, Viagrande, Catania, Italy. ¹⁰Department of Clinical and Experimental Medicine, University of Messina, “G.Martino” Hospital, Messina, Italy. ¹¹Department of Clinical and Experimental Medicine, A.O.U. Policlinico-Vittorio Emanuele, Center of Experimental Oncology and Hematology, University of Catania, Catania, Italy. ¹²Istituto di Patologia Generale, Università Cattolica del Sacro Cuore, Rome, Italy. ¹³Fondazione Policlinico Universitario “A. Gemelli” - I.R.C.C.S, Rome, Italy. ¹⁴Onco Institute, Amsterdam UMC, University of Amsterdam, Amsterdam, The Netherlands. ✉email: giorgio.stassi@unipa.it

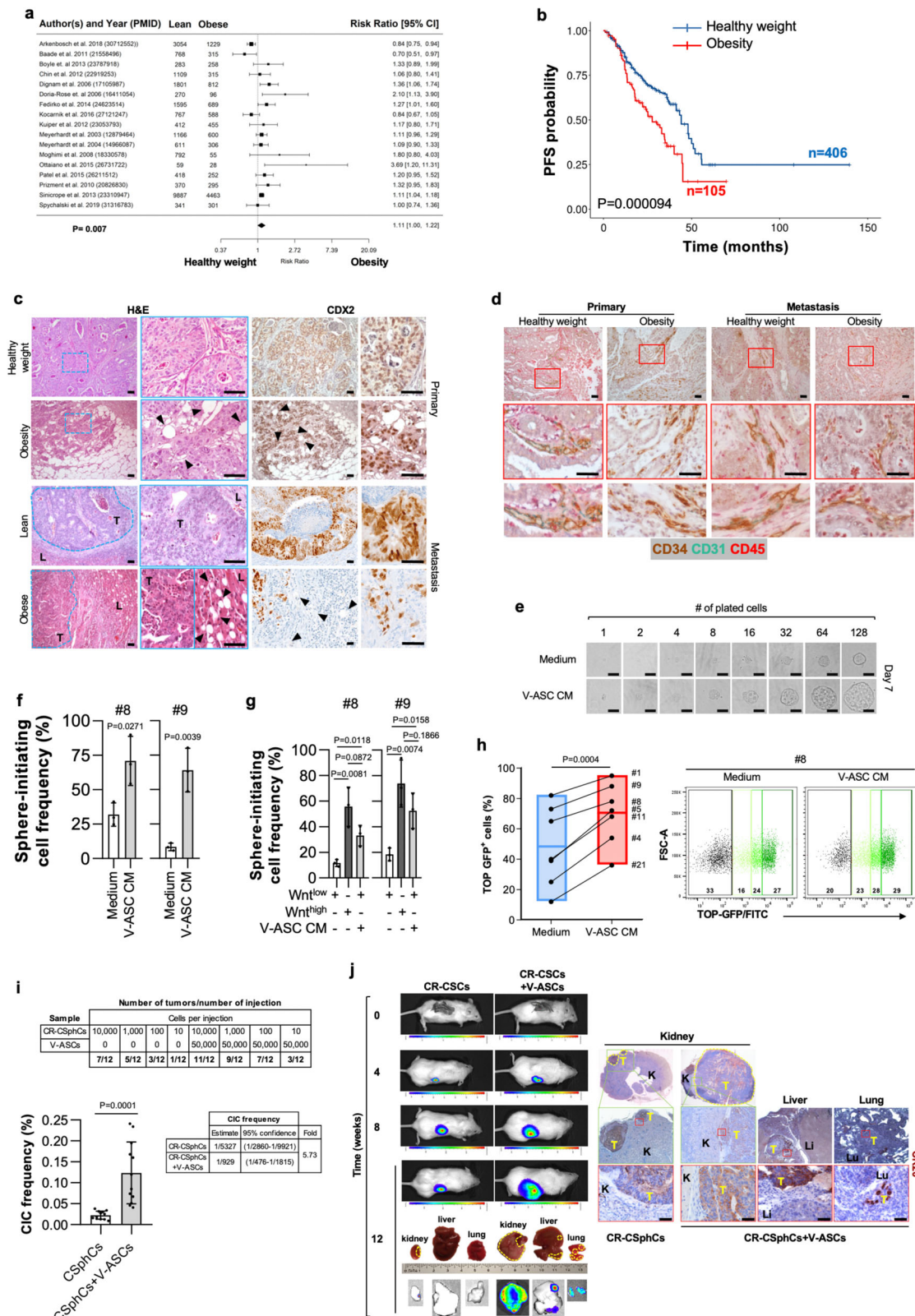
Colorectal cancer (CRC) is the third most common cause of cancer-related death worldwide¹. Despite the great effort made in the study of CRC, the molecular mechanisms underlying the metastatic process are still poorly defined. It is becoming increasingly clear that obesity, whose prevalence is raising worldwide², is associated with cancer incidence and contributes to up to 20% of cancer-related deaths^{3,4}. Adipose tissue (AT) is an endocrine organ subdivided into two compartments. White AT, prevalently distributed subcutaneously and surrounding bowels, and brown AT, present in the cervical and supraclavicular area, are endowed with fat storage and thermogenic function, respectively⁵. White AT is characterized by a marked cell variety, which includes adipocytes, immune cells, vascular, and progenitor cells⁶. In obesity state, both the subcutaneous and visceral white adipose tissues expand by hypertrophy of pre-existing adipocytes. Recent evidence showed that visceral fat, in high-fat diet-induced obese mouse models, determines a hyperplastic response, which is driven by adipose precursor cells, identified as $\text{Lin}^-/\text{Sca1}^+/\text{CD29}^+/\text{CD34}^+$ ⁷. This phenomenon could be due to the different embryological origin of subcutaneous and visceral adipose tissue, and/or by the presence of specific resident factors, as highlighted by lineage tracing experiment performed in adult Wt1-GFP knock-in mice⁸. In particular, mature adipocytes are postmitotic cells, suggesting that hyperplasia arises from the expansion and differentiation of adipocyte precursors^{9,10}. Mature adipocytes together with adipose stromal cells (ASCs) influence the surrounding cell populations through the release of a plethora of inflammatory and angiogenic cytokines^{5,7,11,12}. In individuals affected by obesity, adipose-released proteins, including $\text{TNF-}\alpha$, IL-6, and monocyte chemoattractant protein1 (MCP1), promote a chronic inflammatory state that creates a microenvironment able to sustain tumor progression^{13,14}. In the presence of obesity-released protein, various types of cancers activate cell proliferative processes and behave more aggressively^{15–22}. Several retrospective studies analyzing large cohorts of cancer patients highlighted that obesity has a significant impact on overall survival, positing this indicator as a significant negative prognostic factor, including for CRC patients^{23–25}. Furthermore, Bhaskaran and colleagues showed that while in CRC patients, characterized by a BMI from 15 to 25 kg/m^2 , the mortality risk does not vary, it linearly increases in those with BMI from 25 to 50 kg/m^2 ²⁵. An increase of VAT governs the expansion of intestinal stem cells and proliferation of progenitors by activating $\text{GSK-3}\beta$ and contributing to β -catenin accumulation in canonical WNT signaling pathway^{26,27}. It has been established that cancers, including colon, originate by a small subset of cells with stem-like features called cancer stem cells (CSCs), whose phenotype and behavior can be modulated by the tumor microenvironment (TME)^{28–30}. More recently, TME cytokines, such as IL-6 and HGF, were demonstrated to have clinical relevance and induce cancer cell stemness concomitantly enhancing the epithelial-to-mesenchymal transition (EMT), cell migration, and metastatic potential^{31–33}. The interaction between the CRC cells and their TME is fundamental for addressing cancer cell fate, which characterizes the tumor biological behavior³⁴. In agreement, CRC can be stratified into four consensus molecular subtypes (CMS) according to their molecular signature, which in part depends on the composition of the TME and predicts clinical outcome³⁵. Specifically, CMS1 displays an immune system signature, CMS2 represents an epithelial-like cancer characterized by the activation of Wnt and *c-Myc* signaling pathways, CMS3 shows a metabolic deregulation, and CMS4 displays a mesenchymal phenotype. Of note, 14% of all CRCs represents a transition or mixed phenotype. The dynamic CRC microenvironment that induces a CMS plasticity shaping the clinical outcome, has been poorly investigated.

In this work, we have investigated the paracrine effect of VAT in the mesenchymal phenotype modulation of CRC cells, by reprogramming the CMS. We show that in CRC patients affected by obesity, tumor-infiltrating ASCs are key elements of cancer progression. CRC cell-released NGF and VEGF induce ASC recruitment and transdifferentiation in endothelial cell phenotype. Moreover, we provided evidence that IL-6 and HGF, enhance the tumorigenic and metastatic potential of CRC cells. Our data indicate microenvironmental cytokines as essential prognostic molecules that predict the tumor behavior of obesity-associated cancer patients.

Results

Visceral adipose stromal cells promote tumorigenic and metastatic activity of CR-CSphCs. To confirm the clinical impact of obesity on the biological behavior of cancer cells, we first evaluated the potential role of adipose tissue in CRC progression, correlating recurrence and survival in CRC patients with a healthy weight ($18.50 < \text{BMI} < 25$) or affected by obesity ($\text{BMI} > 30$). A meta-analysis of a large cohort of CRC patients revealed that obesity is negatively associated with survival probability (Fig. 1a). Importantly, this correlation was also confirmed by the progression-free survival (PFS) analysis on a large cohort of CRC patients, positing BMI as a negative prognostic factor independent of stage and treatment (Fig. 1b, and Supplementary Fig. 1a, b). Obesity is characterized by a chronic low-grade inflammation, which relies on the presence of a heterogeneous cell population, including lymphocytes, endothelial cells, macrophages, progenitor, and mature adipose cells³⁶. Intriguingly, immunohistochemical analysis of tumor sections from CRC patients with obesity highlighted that adipose cells, marked by high expression of adiponectin, were located at tumor invasive front and interspersed among tumor cells expressing CDX2 and covering the 28% of the entire tumor mass (Fig. 1c and Supplementary Fig. 1c, d). Likewise, CRC liver metastasis of patients affected by obesity displayed a prominent presence of adipose cells at metastatic lesion edge, in the proximity of peritumoral budding. This phenomenon was not observable in primary and metastatic CRC tissues from lean patients (Fig. 1c and Supplementary Fig. 1c, d). As the obesity inflammatory environment is strongly sustained by the paracrine activity of mature adipocytes and adipose-derived vascular stromal cells³⁷, including adipose stem cells, we next investigated whether this cell subset is present in the tumor area and could influence cancer cell phenotype. By immunohistochemical analysis, we found that a high percentage of cells within tumor-neighboring and -infiltrating adipose tissue of patients with obesity are $\text{CD34}^+/\text{CD45}^-$, while lacking the expression of CD31, indicating their ASC identity in both primary and metastatic CRC. Tumor specimens of lean CRC patients displayed the presence of cells expressing $\text{CD34}^+/\text{CD31}^+/\text{CD45}^-$ ascribable to an endothelial phenotype (Fig. 1d and Supplementary Fig. 1e).

Whereas ASCs isolated from subcutaneous AT (S-ASCs) are enriched in CD10 positive cells, visceral ASCs (V-ASCs) show high expression of CD200 and WT1^{8,38} (Supplementary Fig. 1f, g and Supplementary Table 1). Following exposure to adipogenic differentiation medium, S-ASCs and V-ASCs were equally inclined to differentiate in vitro toward adipocytes, as displayed by AdipoRed staining (Supplementary Fig. 1h, i)^{39,40}. Conditioned medium (CM) from V-ASCs boosted both the colony-forming capacity of CRC sphere cells (CR-CSphCs) and the in vivo tumor growth, which was sustained by the high number of cells expressing Ki67 observed in tumor xenografts generated by the co-injection of CR-CSphCs and V-ASCs (Supplementary Fig. 1j–l and Supplementary Table 2). We next investigated



whether the adipogenic niche could impact the self-renewal activity of CRC cells. The in vitro limiting-dilution assay showed that treatment with V-ASC-released factors enhances the sphere-initiating cell frequency of bulk and enriched Wnt^{low} CR-CSphCs, recapitulating the clonogenic potential of Wnt^{high} cells (Fig. 1e–g). This phenomenon was paralleled by the conversion of $Wnt^{inactive}$ (GFP⁻) to Wnt^{active} (GFP⁺) cells, confirming the

crucial role of the Wnt signaling pathway in the CRC stemness-associated reprogramming (Fig. 1h).

To explore the role of ASCs more in detail, we investigated their effect in the clonal tumor initiation of CR-CSphCs. V-ASCs co-injected into the subrenal capsule of mice with a limiting-dilution series of CR-CSphCs increased the frequency of cancer-initiating cells (5.73-fold; $p < 0.0001$) (Fig. 1i). These data indicate

Fig. 1 Tumor-infiltrating VAT boosts the metastatic potential of CR-CSphCs. **a** Forest plot of survival changes in high (>30, obesity) versus low (≥ 18.5 and <25, lean) BMI CRC patients. Data represent the risk ratio \pm 95% CI. Statistical significance was calculated by a Random-effect meta-analysis model. **b** Kaplan–Meier of progression-free survival (PFS) curve in a cohort of 511 CRC patients, based on BMI status. Healthy weight indicates $18.5 < \text{BMI} < 30$, and obesity $\text{BMI} > 30$. Statistical significance was calculated using the log-rank (Mantel–Cox) test. **c** H&E analysis and CDX2 expression on primary and liver metastasis in CRC patients with healthy weight or affected by obesity. Black arrow heads indicate tumor-infiltrating adipose cells. Li: liver; T = tumor. **d** Immunohistochemical analysis of CD34 (brown color), CD31 (green color), and CD45 (red color) in tissues as in **c**. For **c**, **d** one representative of 9 independent experiments is shown. **e** Phase-contrast analysis of CMS2 cells (CSphC #9) treated with medium or V-ASC CM. For **(c–e)** scale bars, 100 μm . One representative of three independent experiments is shown. **f** ELDA software analysis of the clonogenic activity in CMS2 CR-CSphCs following treatment with medium or V-ASC CM. **g** Clonogenic assay of CMS2 CR-CSphC lines TOP–GFP^{high} and TOP–GFP^{low} (15% highest/lowest TOP–GFP levels) treated with medium or V-ASC CM. For **(f–g)** statistical significance was calculated using the two-tailed t test and data are mean \pm standard error of three independent experiments performed with CR-CSphCs isolated from three different CRC patients (CSphC #8, #9). **h** Percentage of TOP–GFP positive cells, in CMS2 cells treated with medium or V-ASC CM (*left panel*). Box plots show min-to-max values, with line indicating the mean value. Flow cytometry analysis of TOP–GFP (black color indicates Wnt⁺ cells; green color scale indicates low, intermediate, and high Wnt⁺ cells) (*right panel*). Statistical significance was calculated using the paired two-tailed t test. Data are mean \pm standard error of independent experiments performed with different CR-CSphCs (#1, #4, #5, #8, #9, #11, #21). **i** Number of mouse tumor xenografts generated by subrenal capsule injection of 10, 100, 1000, or 10,000 CR-CSphCs, alone or in combination with 50,000 V-ASCs (*upper panel*). Percentage of cancer-initiating cell (CIC) and its fold increase of cells (lower panels). Data are mean \pm standard error (95% confidence interval) of 12 independent experiments performed with CR-CSphCs injected as described above. Statistical significance was calculated by ELDA software (<http://bioinf.wehi.edu.au/software/elda/>). **j** In vivo imaging and CK20 immunohistochemistry analysis of xenograft tumor formation obtained by subrenal capsule injection of 100 CR-CSphCs alone or together with V-ASCs at the indicted time points. Photon signal of all metastatic sites (kidney, liver, and lungs) at 12 weeks. A yellow dotted line indicates a tumor xenograft lesion. Tumor (T), kidney (K), liver (Li), and lung (Lu) are indicated. One representative of 12 independent experiments is shown. Scale bars, 100 μm .

that CRC spheres retain cells endowed with stem cell properties, which are significantly expanded in presence of adipose microenvironment stimuli.

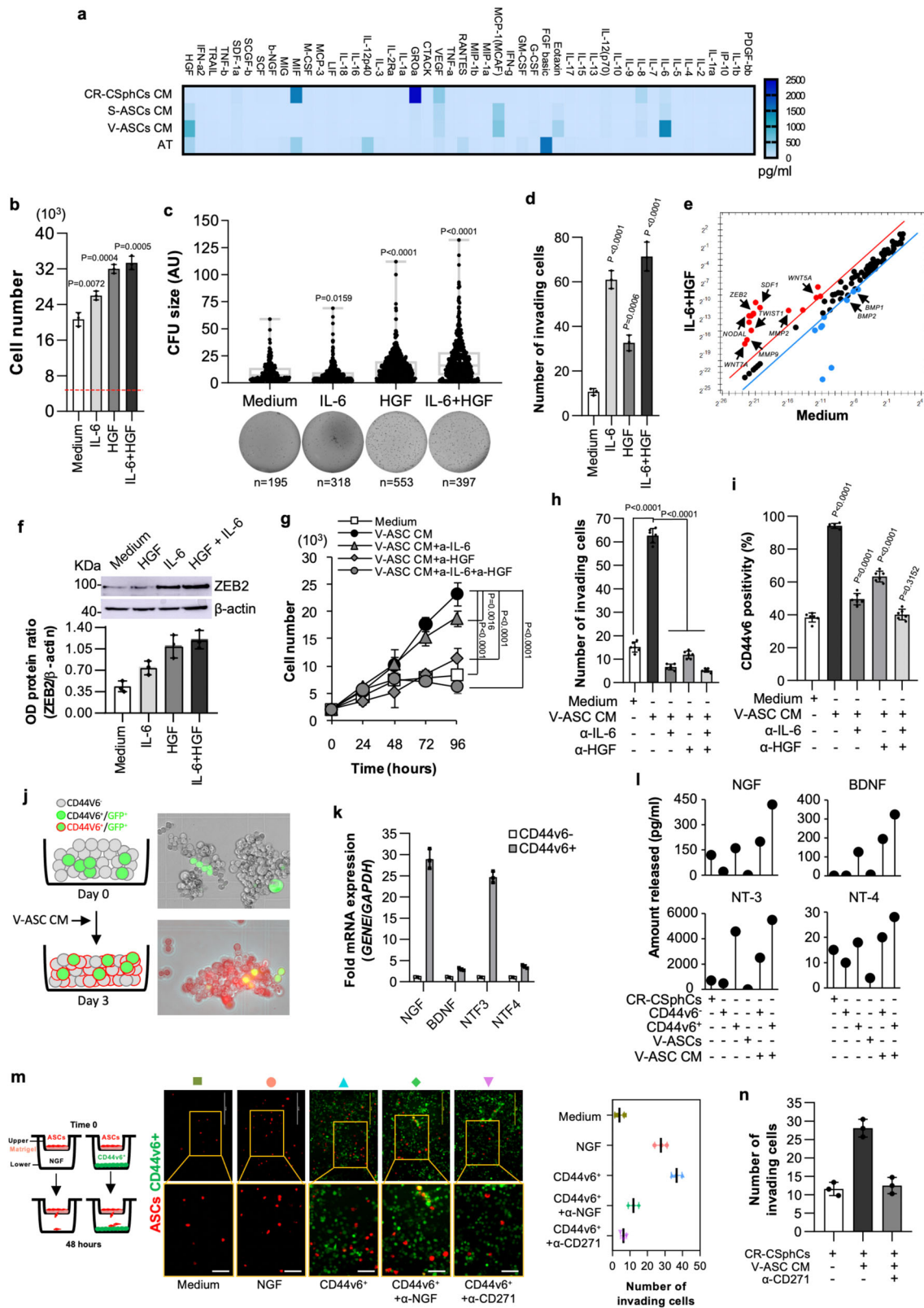
Interestingly, V-ASC is endowed with migration capacity (Supplementary Fig. 1n, o). Their CM significantly enhanced in vitro cell invasion of CR-CSphCs (Supplementary Fig. 1m). In line with the more pronounced invasive potential, in vivo limiting-dilution assay, in presence of V-ASCs, showed that CMS2 CR-CSphCs acquire the ability to generate metastatic lesions into the liver and lungs even when a small number of cells is transplanted (Fig. 1j). While S-ASCs were unable to influence the liver and lung colonization, V-ASCs potentiate the migratory capacity and the engraftment of CR-CSphCs in distant sites (Supplementary Fig. 1p, q). These data indicate a crosstalk between ASCs and CRC cells in supporting cancer progression.

IL-6 and HGF expand the number of CD44v6 + CR-CSCs, which produce NGF and favor the migration capacity and endothelial transdifferentiation of visceral ASCs. To identify the key players of metastasis promoted by VAT, we next investigated whether cytokines released by V-ASCs would influence the metastatic properties of CR-CSphCs. According with reported literature, V-ASCs, isolated from CRC patients with obesity, produce more abundant IL-6 and HGF as compared with S-ASCs, CR-CSphCs, and primary adipose tissue cells (AT) (Freese et al., 2015) (Fig. 2a). CR-CSphCs and their differentiated counterpart (sphere-derived adherent cells, SDACs), obtained as previously described⁴¹ and characterized respectively by high and low expression of active β -catenin⁴² (Supplementary Fig. 2a), constitutively expressed IL-6R and c-MET (Supplementary Fig. 2b, c). The presence of IL-6 and/or HGF enhanced the proliferative capacity and colony-forming potential of CR-CSphCs (Fig. 2b, c), which concomitantly acquire an invasive phenotype together with the expression of stemness and metastasis-related genes such as *WNT5A*, *WNT5B*, *WNT7A*, *MMP2*, *MMP9*, *TWIST*, *NODAL*, *SDF1* and *ZEB2* (Fig. 2d, e and Supplementary Fig. 2d). IL-6 and HGF increased ZEB2 protein expression, in line with the upregulation of its mRNA levels (Fig. 2f). Moreover, blockade of IL-6 and/or HGF abrogated cell proliferation and migratory activity of CR-CSphCs induced by V-ASCs-released proteins (Fig. 2g, h). Accordingly, V-ASC-derived IL-6 and HGF released into V-ASC CM significantly boosted the

expression of CD44v6 (Fig. 2i), a marker that identifies CRC cells characterized by a robust metastatic potential⁴³, and even induced CD44v6⁺ sphere cells to acquire CD44v6 expression (Fig. 2j and Supplementary Fig. 2e).

Because ASCs are characterized by the expression of CD271^{44–46}, we evaluated the involvement of its ligands, produced by CSCs, in the recruitment of ASCs. CD44v6 + cells express high levels of nerve growth factor (NGF) and NTF3 mRNA as compared with the other CD271 ligand family members, BDNF and NTF4 (Fig. 2k) and secrete NGF and NT-3, while these neurotrophins are barely released by CD44v6⁺ cells, unless exposed to CM of V-ASC (Fig. 2l). This phenomenon is likely due to the enhancement of neurotrophins production and the reprogramming of CD44v6⁺ into CD44v6 + cells, mediated by HGF/c-MET signaling pathway^{43,47}. The CD44v6 + cell-released NGF and NT-3 promote ASCs recruitment, which is completely prevented by a CD271 neutralizing antibody, compared with the weaker effects of NGF neutralizing antibody (Fig. 2m). Moreover, CR-CSphCs exposed to V-ASC CM were also able to attract ASCs (Fig. 2m, n). Notably, the analysis of a cohort of 289 CRC patients showed a significant negative correlation between relapse-free survival (RFS) and CD271 expression (Supplementary Fig. 2f, g). Thus, these data suggest that ASC-derived IL-6 and HGF can reprogram CD44v6⁺ progenitors into CD44v6 + cells, which can increase their metastatic potential by secreting NGF and recruiting ASCs within tumor mass.

Because CD44v6 + cells express and produce high levels of VEGF, which augments the proliferation rate of ASCs (Fig. 3a, b and Supplementary Fig. 3a), we hypothesized that its release could also promote angiogenesis and vasculogenesis. A global RNA-Seq transcriptomic analysis and functional enrichment of differentially expressed genes (DEGs) computed by Panther of CD44v6 + versus CD44v6⁺ cells highlighted enrichment in biological processes associated with extracellular matrix (ECM) remodeling (Supplementary Fig. 3b). The majority of CD271 + ASCs express VEGFR (Fig. 3c), suggesting that CD44v6 + cell-derived VEGF may trigger an angiogenic signal on ASCs. The paracrine activity of CD44v6 + cells induced the transdifferentiation of enriched CD34 + /CD31⁺ ASCs toward endothelial-like cells expressing CD31 (Fig. 3d and Supplementary Fig. 3c). Moreover, exposure to CM released by CD44v6 + cells led HUVEC endothelial cells to develop vascular



tubules likewise those formed following treatment with VEGF (Fig. 3e and Supplementary Fig. 3d). In line with the more pronounced vascular density, associated with a preferential localization of CD44v6 + cells at the vascular front and observed in CRC xenografts generated by co-injection of CR-CSphCs and V-ASCs (Fig. 3f), these findings suggest the involvement of the

CSC compartment in the neo-angiogenesis and angiogenic sprouting of pre-existing capillaries.

Visceral released proteins induce EMT of CR-CSphCs. Next, we sought to investigate whether the presence of ASCs within tumor mass could lead to the acquisition of a transcriptional signature

Fig. 2 Adipose-derived factors expand CD44v6⁺ cell fraction that secretes NGF and potentiates the migration capacity of ASCs. **a** Cytokines secreted by CR-CSphCs ($n = 4$: #1, #8, #9, #21), S-ASCs ($n = 6$: #3, #5, #6, #8, #14, #20), V-ASCs ($n = 6$: #3, #5, #6, #8, #14, #18), or primary adipose tissue (AT) ($n = 4$). Data are the mean of 3 independent experiments. **b** Cell growth of CR-CSphCs treated for 5 days with IL-6 and HGF alone or in combination. The dotted red line shows the cell number at day 0. **c** Colony size of CR-CSphCs treated as indicated. n represents the number of colonies. Statistical significance was calculated using the two-tailed t test. **d** Invasion assay of CR-CSphCs pretreated with the indicated cytokines for 48 h. For **b–d** data show mean \pm S.D. of three independent experiments using four different CR-CSphCs (CSphC #1, #8, #9, #21). **e** mRNA expression levels of CSC-related genes in CMS2 CR-CSphCs (CSphC #8, 9) exposed to vehicle (Medium) or IL-6 in combination with HGF for 48 h. **f** Immunoblot analysis of ZEB2 in CMS2 CR-CSphCs (CSphC #8) treated as indicated. Data are mean \pm S.D. of three independent experiments using two different CSphCs (CSphC #8, #9). Samples were run on the same gel and images were cropped only for the purpose of this figure. Source data are provided as a Source Data file. **g** Kinetic growth of CR-CSphCs treated as indicated. **h** Number of invading CR-CSphCs at 48 h, pretreated with V-ASC CM and the indicated neutralizing antibodies for 48 h. **i** Flow cytometry analysis of CD44v6 positivity in CR-CSphCs treated as indicated, for 48 h. For **g–i** data are mean \pm S.D. of six independent experiments performed with 2 different CR-CSphC lines (#8 and #9). For (b–d and g–i) statistical significance was calculated using the unpaired two-tailed t test. **j**, CD44v6 expression in CD44v6⁻ and GFP-transduced CD44v6⁺ cells after 3 days of exposure to V-ASC CM. One representative of 6 independent experiments is shown. **k** NGF, BDNF, NTF3, and NTF4 mRNA expression levels on CD44v6⁻ and CD44v6⁺ cells. Results show mean \pm S.D. of three independent experiments performed with enriched cells from two different CR-CSphC lines (CSphC #8, #9). **l** Lollipop plot showing NGF, BDNF, NT-3, and NT-4 production by the indicated cells treated as indicated. **m**, Invasion assay of RFP transduced ASCs, using the indicated cells/media as chemoattractant agents. Scale bars, 100 μ m. **n** Number of invading ASCs in presence of the indicated cells/media as chemoattractant agents. For **l–n** data are mean \pm SD of three independent experiments using CR-CSphCs from different patients (CSphC #1, #8, #9, #21).

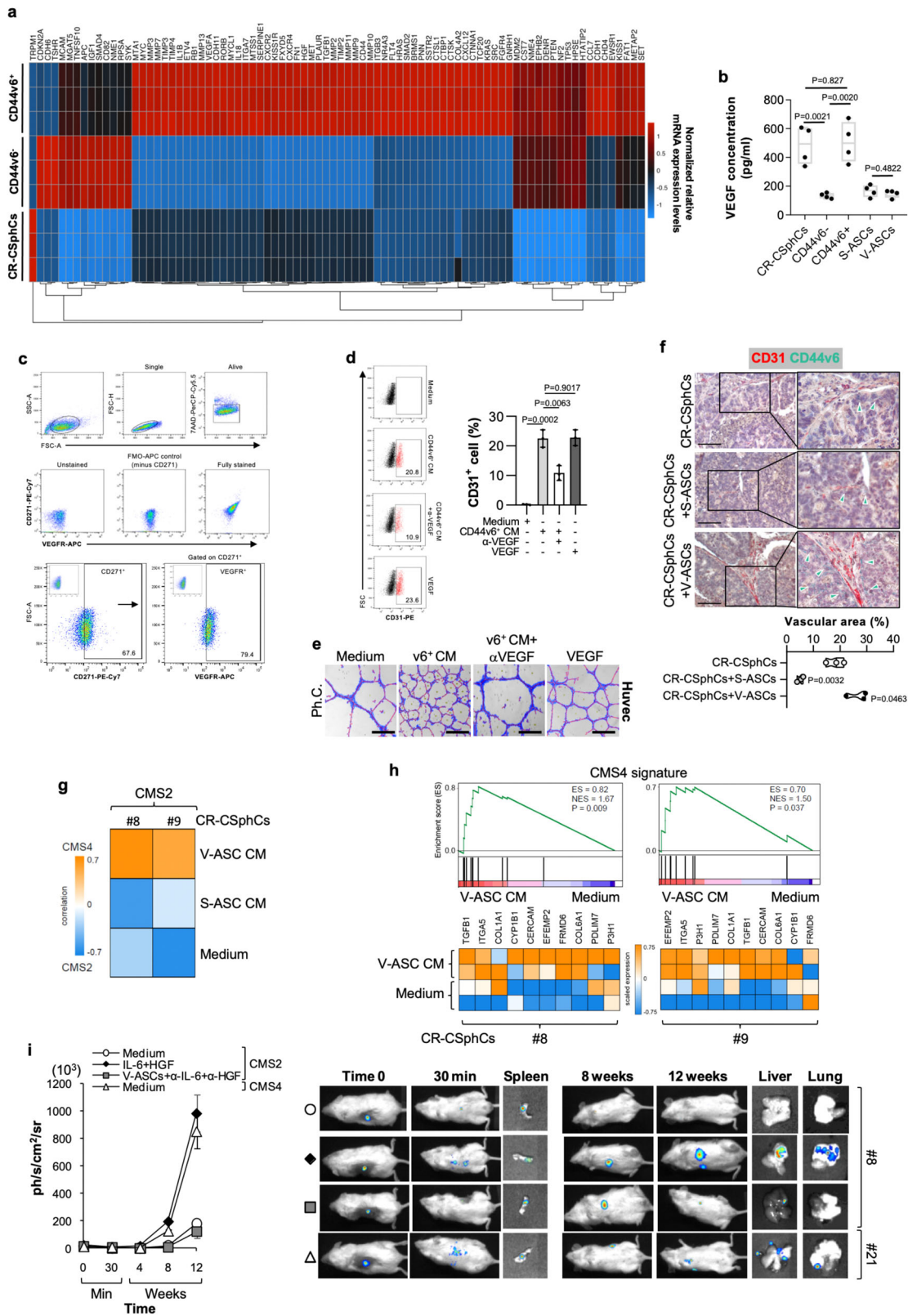
related to a CMS associated with a metastatic potential. Confirming the prominent role of released proteins in triggering metastasis pathways, exposure of CR-CSphCs to V-ASC CM turned the transcriptomic profile from an epithelial/CMS2 pattern into a phenotype that resembles the mesenchymal CMS4 (Fig. 3g). Likewise, a global RNA-Seq transcriptome analysis of CR-CSphCs treated with V-ASC CM or medium alone showed 10 DEGs, associated with a CMS4 signature (Fig. 3h). Accordingly, IL-6 and HGF promoted the downregulation of epithelial (*CDX2*, *E-cadherin*), and upregulation of mesenchymal (*CXCR4*, *SLUG*, *TWIST*, *ZEB1*, *ZEB2*) markers. Moreover, in CMS2 cells treated with V-ASC CM, targeting of both IL-6 and HGF restored the basal levels of EMT-related genes (Supplementary Fig. 3e). In addition, the treatment of CMS2 CR-CSphCs with IL-6 and/or HGF recapitulated the invasive scenario observed in CMS4 CR-CSphCs, which display a great ability to colonize the liver and lung. Conversely, IL-6 and HGF targeting abolished the metastatic activity induced by VAT, restoring the nonmetastatic phenotype of CMS2 CR-CSphCs (Fig. 3i). Thus, these data lay the groundwork for a critical consideration of released proteins in the regulation of the molecular machinery involved in metastasis. Taken together our results demonstrate that the paracrine activity of V-ASCs drives the transition of CRC sphere cells toward a mesenchymal-like phenotype, endowing them with a metastatic potential.

VAT governs the EMT through regulation of ZEB2 expression.

We next explored the metastatic molecular events enhanced by V-ASCs. Based on a global RNA-Seq transcriptome analysis of CR-CSphCs exposed to V-ASC CM compared to those treated with medium alone, the gene set enrichment analysis (GSEA) performed with the molecular signatures database (MSigDB) showed negative enrichment of genes associated with metabolic pathways, and positive enrichment for genes related to EMT program (Fig. 4a). About 50% of EMT-related DEGs in CMS2 CR-CSphCs exposed to V-ASC CM are similar to those expressed in CMS4 CR-CSphCs. This includes upregulation of zinc finger E-box binding homeobox (ZEB) transcription factors *ZEB1* and *ZEB2* in line with the capacity of released proteins to reprogram CMS2 CR-CSphCs toward a pro-metastatic phenotype (Fig. 4b). In particular, 15 genes were upregulated while six downregulated in both the CMS4 and CMS2 CR-CSphCs treated with V-ASC CM (Fig. 4c). GSEA based on the differentially expressed genes from qPCR computed by MSigDB displayed an enrichment of terms associated with tumorigenesis, cell proliferation, EMT

signaling pathways, and cancer stemness (Supplementary Fig. 3f). *ZEB1* and *ZEB2*, whose upregulation is induced both at mRNA and protein levels by V-ASCs cytokines (Fig. 4d, e), have been reported to modulate miR-200 family members expression and regulate EMT in CRC⁴⁸.

Analysis of a large spectrum of miRNAs expression reveals that miRNA-200 family members, and particularly miR-200a, are downregulated in CMS2 CR-CSphCs following treatment with V-ASC CM, showing similar miRNA levels exhibited by CMS4 CR-CSphCs (Fig. 4f and Supplementary Fig. 3g). In CR-CSphCs treated with V-ASCs CM, analysis of the network of most differentially expressed miRNAs and their targets showed that ASC-released proteins regulate a plethora of genes that converge on miR-200a/ZEB members axis involved in the EMT process (Fig. 4g). These data suggest that obesity-released proteins, through the modulation of miR-200a, could play a crucial role in determining the switch from an epithelial- to a mesenchymal-like phenotype, ultimately providing a considerable impact on disease progression. In line with this hypothesis, blockade of IL-6 and HGF restored the basal levels of miR-200a expression in CMS2 CR-CSphCs treated with V-ASC CM (Supplementary Fig. 3h). Moreover, CMS2 cells transfected with antagomiR-200a significantly increased their invasive capacity, whereas synthetic miR-200a led to a reduced number of invasive CMS4 cells despite their intrinsic mesenchymal-like phenotype (Supplementary Fig. 3i, j). To assess the effect of miR-200a in CR-CSphC behavior, we transduced CMS4 cells with miR-200a. CMS4 CR-CSphCs overexpressing miR-200a showed abrogation of *ZEB2* expression coupled with a significant reduction of both the basal as well as IL-6 and HGF-induced clonogenic and invasive potential (Supplementary Fig. 3k–o). Thus, we evaluated whether *ZEB1* and *ZEB2*, under the control of V-ASCs secreted proteins, could contribute to the induction of EMT in CR-CSphCs. Both *ZEB1* and *ZEB2* are known to actively participate in the metastatic process and to be regulated by the miR-200 family through a negative feedback loop⁴⁹. Importantly, the expression of both *ZEB1* and *ZEB2* have been associated with poor prognosis in CRC^{50,51}. We therefore explored whether the expression of these EMT-inducing transcription factors influenced the metastatic capacity of CMS2 CR-CSphCs. *ZEB2* protein expression levels in CMS2 cells exposed to V-ASC CM were similar to those detected in CMS4 cells (Fig. 4h). Moreover, exogenous expression of *ZEB2* fostered expression of both vimentin and CD44v6 and enhanced the tumor spreading into distant organs (Fig. 4i, j, and Supplementary Fig. 4a–c), indicating that *ZEB2* may act as a



functional marker of CRC cells endowed with metastatic properties⁵². In accordance with these data, the analysis of a cohort of 37 tissue samples displayed a positive correlation between CD44v6 expression and CRC patients affected by obesity (Supplementary Fig. 4d). Knock-down of ZEB2 in CMS4 CR-CSphCs led to downregulation of vimentin and EMT-related genes and impaired the metastatic potential of these cells

(Supplementary Fig. 4e-i). Altogether, these results posit ZEB2 as a functional biomarker for CRC endowed with a metastatic potential.

IL-6/HGF blockade reduces the metastasis formation induced by VAT. To further define the signaling pathway involved in the regulation of miR-200a by pro-metastatic factors, we analyzed the

Fig. 3 VEGF induces endothelial differentiation of ASCs, which activate the EMT program of CRC sphere cells. **a** Clustergram of tumor microenvironment-related genes in CR-CSphCs (CSphC #1, #8, #9, #21) and CD44v6⁻ or CD44v6⁺ enriched cells. Data are presented as normalized expression values. **b** VEGF production in cells as indicated. Data are mean \pm SD of 4 independent experiments. Box and whiskers show min-to-max values, with line indicating the mean value. **c**, Gating strategy of CD271/VEGFR expression on ASCs (upper panels). Dot-plots of CD271/VEGFR staining with or without the indicated antibody (FMO-APC control, minus CD271-PE-Cy7) (middle panel). Flow cytometry analysis of CD271 and VEGFR in ASCs. Data are representative of 3 independent experiments performed with 10 different ASC lines (lower panel). **d**, Percentage of CD31 positivity, by flow cytometry analysis, on CD34⁺/CD31⁺/CD45⁻ enriched ASCs exposed to vehicle (Medium), CD44v6⁺ + CR-CSCs CM (CSC #1, #8, #9, #21), in presence or absence of VEGF neutralizing antibody, or VEGF for 14 days. Data are mean \pm SD of three independent experiments using 3 different ASC cultures. **e** Phase-contrast micrographs of capillary-like tubular structures of HUVEC cells treated as indicated for 16 h. Scale bars, 500 μ m. One representative of 3 independent experiments is shown. **f** Immunohistochemical analysis of CD31 (red) and CD44v6 (green) on tumor xenografts generated by subcutaneous injection of CR-CSphCs alone or in combination with S-ASCs or V-ASCs (upper panel). Percentage of vascular surface area, based on CD31 positivity, in tumor xenografts (lower panel). Scale bars, 200 μ m. Data are representative of 3 independent experiments. For **b**, **d**, and **f** statistical significance was calculated using the unpaired two-tailed *t* test. **g** Transcriptomic profile correlation between CMS2 CR-CSphCs (CSphC #8, #9) treated with S-ASCs or V-ASC conditioned medium (CM) and CMS4-associated gene signature. **h** GSEA of CMS4-associated gene signature in CMS2 CR-CSphCs (CSphC #8, #9) treated with V-ASC CM (upper panel). Top ten significantly up- and downregulated CMS4 signature genes in treated cells (lower panel). Statistical significance between two groups was determined by unpaired Student's *t* test (2-tailed). **i**, Kinetics and whole-body *in vivo* imaging analysis of mice (*n* = 6) intrasplenically injected with LUC-GFP CMS4, or CMS2 CR-CSphCs alone or co-injected with V-ASCs and treated as indicated. Data are mean \pm S.D. of independent experiments performed with CR-CSphCs isolated from two different CMS2 (CSphC #8, #9) and CMS4 (#1, #21) CRC patients.

transcriptomic and the post-translational reprogramming of CR-CSphCs in presence of V-ASC CM. GSEA revealed that V-ASC-released factors promoted the enrichment of genes associated with STAT3-activated pathways in CR-CSphCs (Fig. 5a). Immunoblot analysis showed that both V-ASC CM and IL-6/HGF activate STAT3 pathway in CMS2 cells by enhancing the phosphorylation of STAT3 in tyrosine and serine residues (Fig. 5b). In accordance, immunohistochemical analysis of colon tumor sections indicated that activation of STAT3, highlighted by nuclear staining, is mainly located in proximity to adipose tissue of CRC patients with obesity. While cancer cells in contact with tumor stroma in lean patients displayed a weak presence of nuclear p-STAT3 (Fig. 5c). C188-9, an inhibitor of STAT3 phosphorylation, reduced the activation of STAT3, sustained by IL-6 together with HGF (Fig. 5d and Supplementary Fig. 5a). Moreover, in presence of IL-6 and HGF, C188-9 significantly lessened the cell proliferation rate, together with the clonogenic activity, and restored both miR-200a and ZEB2 expression levels in treated CR-CSphCs (Fig. 5e–h). Likewise, CMS2 CR-CSphCs, exposed to IL-6 and HGF, changed their cell morphology acquiring a distinctive polarization associated with an elongated shape, which is attenuated by the exposure to C188-9 (Fig. 5i). These results suggest that adipose microenvironmental cytokines, via STAT3/miR-200a/ZEB1/2 axis, drive epithelial-associated CMS2 CR-CSphCs to acquire a mesenchymal phenotype.

To circumvent this potentially detrimental activity of adipose tissue, we next analyzed whether therapeutic targeting of adipose-released proteins could prevent metastasis formation. Given that CR-CSphCs express IL-6R and c-MET, we focused on the currently available clinical compounds tocilizumab and crizotinib, which target the IL-6 and HGF pathway, respectively (Supplementary Fig. 6a). Importantly, the combinatorial treatment with tocilizumab and crizotinib was able to revert the impact of V-ASC CM on CR-CSphCs proliferation and colony-forming capacity (Fig. 6a, b). Furthermore, this dual-target therapy impeded the V-ASC-induced downregulation of miR-200a, thus reducing the expression of both ZEB1 and ZEB2, and the acquired invasive behavior of CMS2 CR-CSphCs (Fig. 6c–e). To determine whether tocilizumab, in combination with crizotinib, could be employed in an adjuvant setting and prevent metastasis formation induced by visceral adiposity, metastatic mouse avatars were generated by co-injection of CMS2 CR-CSphCs and V-ASCs into mice spleen. Five days after the splenectomy, mice were treated three times a week for 3 weeks (Fig. 6f). This optimized combinatorial drug dosage does not

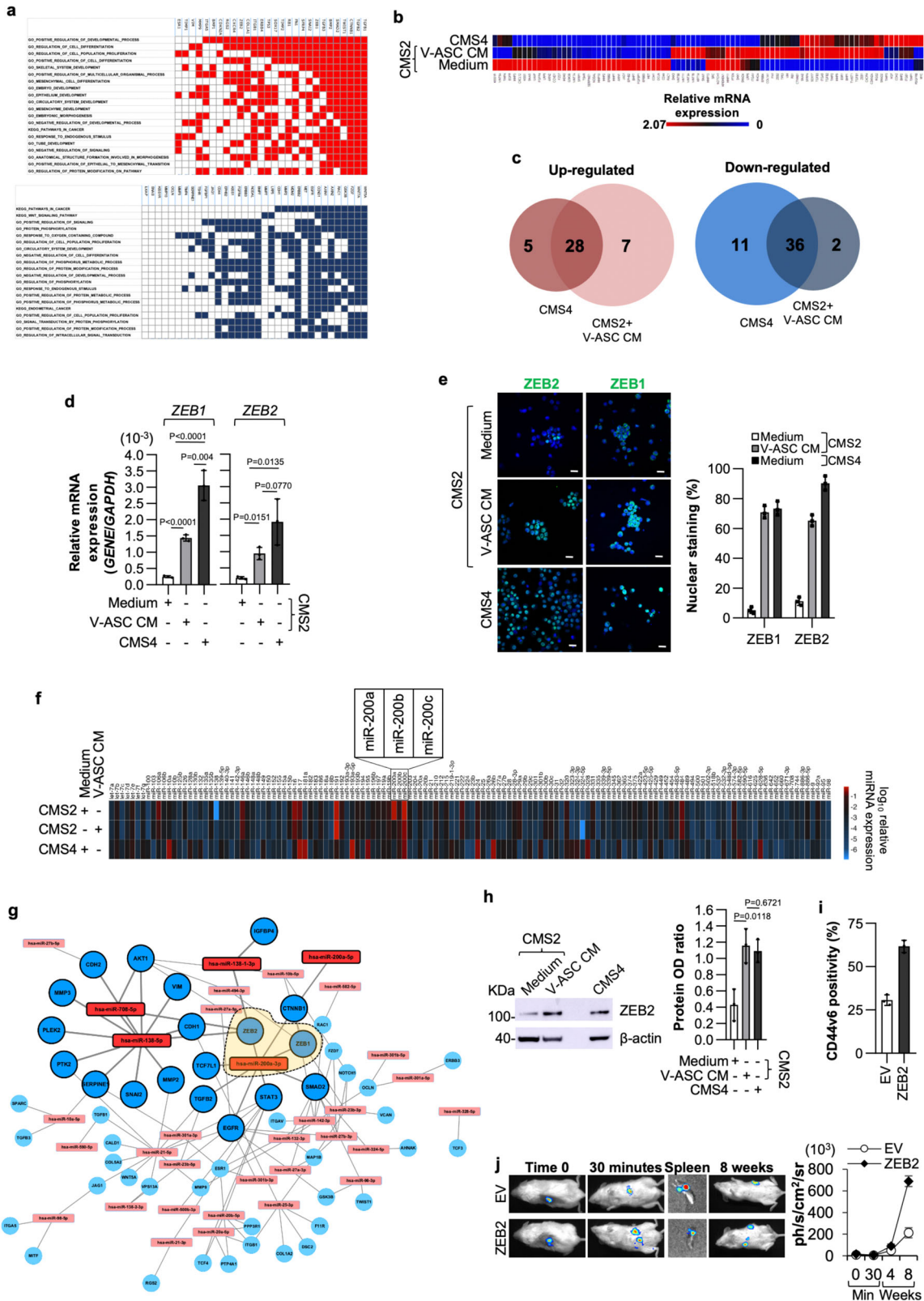
provoke preclinical signs of toxicity as evidenced by the absence of significant body weight oscillations (Supplementary Fig. 6b). Strikingly, this therapeutic regimen significantly reduced the metastatic engraftment frequency of V-ASC-stimulated CMS2 cells, even 8 weeks after treatment suspension (Fig. 6g and Supplementary Fig. 6c, d). Moreover, in line with our *in vitro* data, we observed that most CRC cells found in metastatic lesions of mice co-injected with CR-CSphCs and V-ASCs showed mesenchymal traits highly expressing p-STAT3 and ZEB2 (Supplementary Fig. 6e). Furthermore, the analysis of a cohort of 112 CMS2 CRC patients showed a significant negative correlation between ZEB2 expression and RFS probability (Fig. 6h, i), suggesting that ZEB2 is a putative prognostic factor that could be relevant in cancer patients affected by obesity.

Discussion

Here, we describe the paracrine role of VAT that through the activation of ZEB2 confers to CRC cells, endowed with an epithelial phenotype, a mesenchymal-like trait coupled with the ability to migrate and engraft at the distant site. CMS classification of CRC, based on gene expression analysis, has been recently proposed as a clinical tool to stratify patients according to the biological tumor behavior³⁵. Among the distinct cancer subtypes, as a consequence of transition phenotype or tumor heterogeneity, a relevant fraction is represented by indeterminate or mixed nonconsensus samples³⁵. Chronic adipose-derived proteins released in TME of patients with obesity, reprogram CMS2 CRC cells into a cell phenotype that is characterized by the partial expression of genes associated with CMS4 signature, likely reflecting a transient CMS2/CMS4 subtype. This phenomenon is in line with the presence of CRC patients classified as mixed, whose clinical outcome remains undefined and transcriptomic profile may reside in that category named “hybrid,” “partial,” or “reversible” epithelial-mesenchymal (E/M) phenotype^{53,54}. Induction of E/M state ensures the reaction of cancer cells to microenvironmental stimuli preserving cancer stemness and tumor initiation abilities⁵⁵.

We predict that the future availability of integrated transcriptomic and clinical data may allow to define a new signature specific for CRC patients affected by obesity and to determine the prognostic impact of obesity in CMS2 CRC patients.

Our data reveal that V-ASCs are prominently present in a primary and metastatic lesion of CRC from patients with obesity. These cells release IL-6 and HGF, which in turn induce EMT up-regulating STAT3 phosphorylation and ZEB2 and increase the



number of cells expressing CD44v6, the cell population able to colonize the liver and produce CRC metastases⁴³. CD44v6 + cells produce NGF and NFT3, which in turn recruit ASCs promoting a paracrine loop that increase the tumor cell aggressiveness. The presence of adipose tissue in liver CRC metastasis is likely due to recruitment from disseminated CD44v6 cells and the migration capacity of V-ASCs in patients affected by obesity. In parallel with

metastatic dissemination, VEGF released by CD44v6 + CRC cells likely contributes to increase tumor angiogenesis via the trans-differentiation of ASCs in endothelial cells and angiogenic sprouting of pre-existing vessels, thus sustaining the remodeling of tumor vasculature^{56–58} (Fig. 6j). Although both IL-6 and HGF activate STAT3 and induce ZEB2, they seem to play a different role in tumor progression. HGF promotes cancer stemness and

Fig. 4 V-ASCs enhance the expression of ZEB2 sustaining the metastatic activity of CR-CSphCs. **a** Up- (red) and down- (blue) regulated genes and their relative top twenty significantly enriched gene sets (FDR q value ≤ 0.05), common in CMS4 CR-CSphCs (CSphC #1, #21) and CMS2 cells (CSphC #8, #9) treated with V-ASC CM, selected from all gene sets within MSigDB (H, CP Biocarta, CP Kegg, MIR, CGN, CM, BP, CC, MF, C6, C7). **b** Heatmap of EMT-related genes in CMS2 (CSphC #8, #9) and CMS4 (CSphC #1, #21) CR-CSphCs treated for 48 h as indicated. **c**, Venn diagrams of up- and downregulated genes in untreated CMS4 (CSphC #1, #21) and V-ASC CM-treated CMS2 (CSphC #8, #9) CR-CSphCs, compared to untreated CMS2 cells. **d** ZEB1 and ZEB2 mRNA expression levels in CMS4 and CMS2 CR-CSphCs treated as indicated. **e** Immunofluorescence analysis of CR-CSphCs expressing nuclear ZEB1 and ZEB2 (CMS2 #8, CMS4 #21) treated as indicated. Nuclei were counterstained with TOTO-3. Scale bars, 20 μm . For **d** and **e** data represent mean \pm S.D. of three independent experiments using CMS2 (#8, #9) and CMS4 (#1, #21) CR-CSphC lines. **f** Global gene expression profile of miRNAs in CMS4 (CSphC #1, #21) and CMS2 (#8, #9) CR-CSphCs treated as indicated. **g** Network of most differentially expressed miRNAs and their targets inferred from miRTarBase in CMS2 CR-CSphCs (CSphC #8, #9) treated with V-ASCs CM for 48 h. Bold colors represent miRNAs with a fold-change >8 . Orange area within dashed line highlights ZEB1 and ZEB2 as direct targets of miR-200a. **h** Immunoblot analysis of ZEB2 in CMS4 (CSphC #1, #21) and CMS2 (CSphC #8, #9) CR-CSphCs treated as indicated. Data are mean \pm S.D. of three independent experiments performed with CR-CSphCs isolated from 2 different CMS2 (CSphC #8, #9) and CMS4 (CSphC #1, #21) CRC patients. Samples were run on the same gel and images were cropped only for the purpose of this figure. Source data are provided as a Source Data file. For (d and h) statistical significance was calculated using the two-tailed t test. **i** Flow cytometry analysis of CD44v6 in CMS2 CR-CSphCs (CSphC #8, #9) transduced with empty vector (EV) or ZEB2 synthetic gene. Bars represent means \pm S.D. of three independent experiments using two CR-CSphCs. **j** In vivo whole-body imaging analysis of mice ($n = 6$) following intrasplenic injection of CR-CSphCs transduced as in **i** at 30 min and 8 weeks after splenectomy (left panel). Luciferase signal measured as ph/s/cm²/sr (right panel). Data are mean \pm S.D. of independent experiments performed with two CMS2 CR-CSphCs (#8, #9).

increases the clonogenicity, whereas IL-6 mainly contributes to enhance the invasion of CMS2 CR-CSphCs. In accordance with recent findings, the GSEA shows that the enrichment for genes associated with EMT and metastatic signature is dictated by the presence of VAT-released factors⁵⁹.

CMS2 CRC cells in contact with VAT-proteins activate STAT3 and up-regulate ZEB2 along with a decrease of miR-200a expression levels. Notably, over-expression of miR-200a hampers the invasive ability of CRC cells with a CMS4 signature, indicating that their constitutive metastatic behavior relies on signaling regulated by miR-200a/ZEB2 axis⁶⁰ (Fig. 6i). ZEB2 and miR-200a act through a mutual inhibitory feedback loop, which has been reported to be involved in the establishment of E/M cancer phenotype^{55,61}. ZEB2 emerges as a prognostic predictive biomarker for CMS2 CRC, as confirmed by the inverse correlation between relapse-free survival and ZEB2 expression, which could be also relevant to identify cancers endowed with E/M traits and associated with high aggressiveness⁵⁵. Thus, evaluation of ZEB2 expression levels could ameliorate CRC patient stratification for adjuvant therapy.

Despite the excess of AT accumulation directly influences tumor response to standard therapies due to augmented clearance and altered pharmacokinetics⁶², the decreased overall survival of cancer patients with obesity could be also dependent on the molecular mechanisms governed by microenvironmental adipose-released proteins. Here we show that targeting the activation of the JAK/STAT pathway, by inhibiting STAT3 (C188-9), IL-6R (tocilizumab), or c-MET (crizotinib), impairs the VAT-driven metastasis promoting activity of CMS2 CR-CSphCs (Fig. 6i). Thus, because adipose-released factors fuel CRC microenvironment by determining a chronic inflammatory state and increasing the risk of distant metastasis formation⁶³, the clinical availability of these drugs could be taken into consideration for an adjuvant setting strategy in obesity-related cancer patients.

Methods

Tissue collection, isolation, and culture of cancer and adipose cells. Colorectal cancer and adipose specimens were collected from CRC patients who underwent surgical resection, in accordance with the ethical policy of the University of Palermo Committee on Human Experimentation. Isolation and propagation of CR-CSphCs and ASCs were performed as previously reported^{43,64}. CR-CSphC lines #1, #8, #9, and #21 were isolated from lean CRC patients. Adipose stromal cells from VAT and SAT were obtained from the greater omentum and subcutaneous anterior abdominal wall, respectively. The study received ethical approval for the purification and culture of CR-CSphC and ASCs, by Ethics

Committee 1 board, University of Palermo - Azienda Ospedaliera Universitaria "Paolo Giaccone" (authorization CE 6/2015). The study complied with all the ethical regulations for work with human participants, including obtaining the informed consent for both CRC patients with healthy weight, and affected by obesity.

Human samples were crosscut into small pieces and grinded using scalpels and surgical scissors and digested at 37 °C for 30 min in DMEM medium supplemented with 0.6 mg/ml of collagenase (Gibco) and 10 $\mu\text{g}/\text{ml}$ of hyaluronidase (Sigma). The cell pellet was resuspended: i. for CRC, in serum-free stem cell medium (SCM) supplemented with EGF and b-FGF; ii. for adipose tissue, in mesenchymal stem cell medium (ThermoFisher Scientific), in ultra-low attachment cell culture flasks, leading to cell growth as spheroids. When cancer and adipose spheroids reached approximately 80% of confluence, cells were mechanically and enzymatically disaggregated, using Accutase (ThermoFisher Scientific). ASCs were routinely frozen and stored in liquid nitrogen at early passages to maintain their pluripotency (passage 1–12). Differentiated adipose cells were obtained by exposing ASCs, for up to 28 days, to adipogenesis differentiation medium (ThermoFisher Scientific). Differentiation efficiency was evaluated by AdipoRed assay (Lonza). Colorectal cancer sphere-derived adherent cells (SDACs) were obtained by culturing cells in adherent condition, in presence of 10% FBS, as previously described^{41,65}. Huvec cells prescreened for angiogenesis were purchased by Lonza (C2519AS) and cultured according to the manufacturer's instructions.

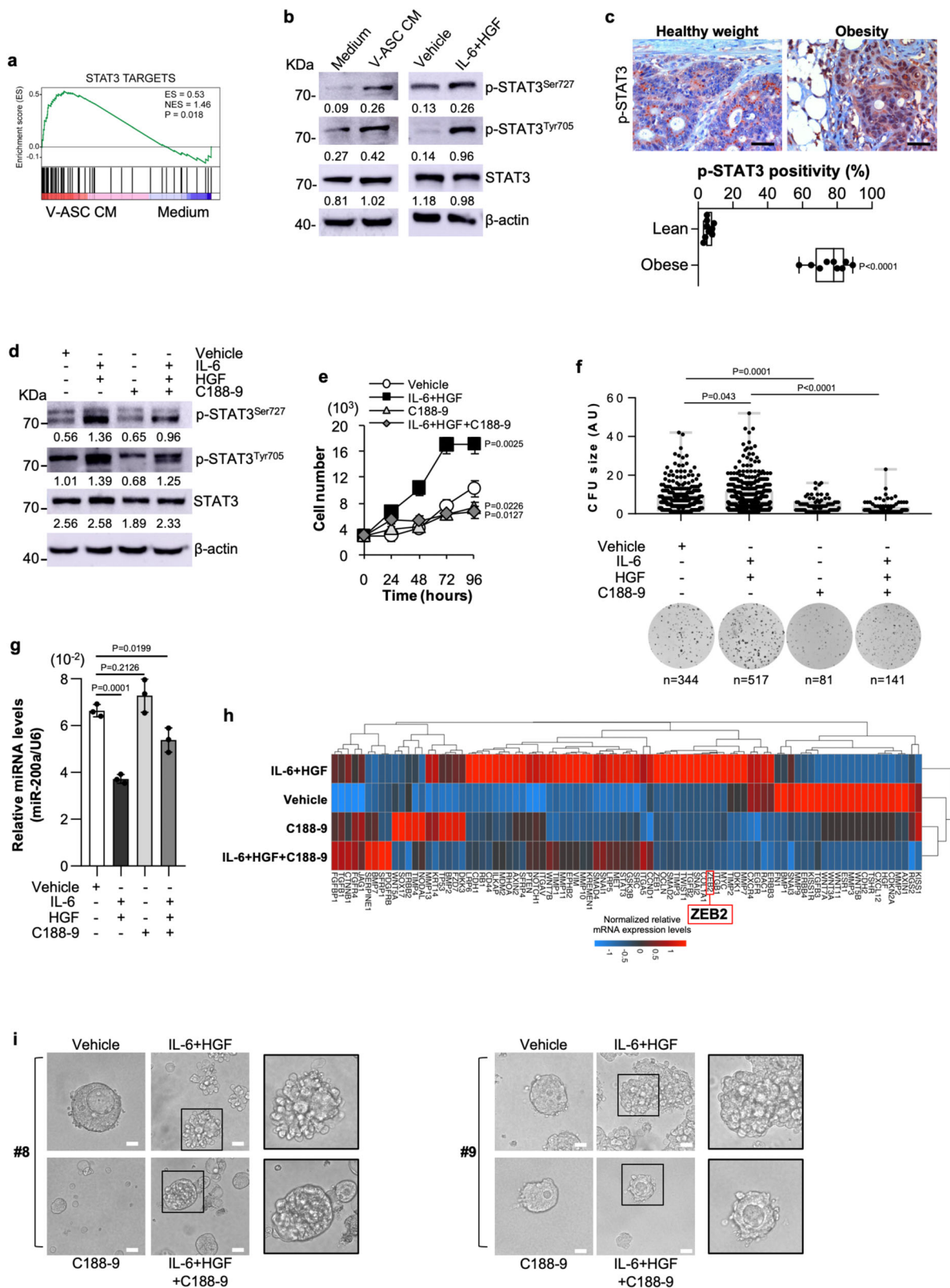
CR-CSphC and ASC lines were routinely authenticated by short tandem repeat (STR) analysis using a multiplex PCR assay, including a set of 24 loci (GlobalFiler™ STR kit, Applied Biosystem), by comparing them to the parental patient tissues⁶⁶. Conditioned medium was collected 48 h after cells reached subconfluence in SCM. The viability of CR-CSphC culture, which is routinely estimated by trypan blue and 7-AAD, is 93 \pm 7%.

CR-CSphCs were treated with recombinant IL-6 (2 ng/ml; Novus), HGF (10 ng/ml; Peprotech), VEGF (10 ng/ml; Novus) and exposed to neutralizing antibodies against IL-6 (100 ng/ml; R&D), HGF (200 ng/ml; R&D), NGF (0.2 $\mu\text{g}/\text{ml}$; R&D), CD271 (0.5 $\mu\text{g}/\text{ml}$; Merck), and VEGF (10 ng/ml; R&D), tocilizumab (10 $\mu\text{g}/\text{ml}$; Selleckchem) or crizotinib (30 nM; Selleckchem), or to STAT3 inhibitor C188-9 (10 μM ; Selleckchem). CM, cytokines, and neutralizing antibodies were added every 48 h to the cell culture.

Cell viability assay was performed using the CellTiter 96® Aqueous One Solution Cell Proliferation Assay (MTS) according to the manufacturer's instructions and analyzed by using the GDV MPT reader (DV 990 BV6). To monitor the acquisition of epithelial versus a mesenchymal phenotype, 5×10^3 viable CR-CSphCs were embedded in 1:10 SCM/Matrigel solution and seeded as a single drop in a pre-warmed 24 well plate. Following matrigel polymerization, 500 μl of SCM were overlaid to each well and 3D organoid formation was followed up to 21 days.

ELISA cytokines quantification. Tumor inflammation, cell proliferation, and immune response cytokines, produced by cancer and adipose cells, were quantified by using the Bio-Plex Pro™ Human Cytokine 21-plex and 27-plex Assay (Bio-Rad), or by customized Luminex Assay specific for VEGF, NGF, BDNF, NT-3, NT-4 (R&D). Raw data were analyzed by Bio-Plex Manager Software 6.2 (Bio-Rad).

Cell transfection and lentiviral transduction. 1×10^6 viable CR-CSphCs were transfected with 8 μg of antagomiR-200a (ABM), or synthetic miR-200a (ABM), using the X-tremeGENE HP DNA Transfection Reagent (Roche) according to the manufacturer's instructions. Lentiviral particles were generated by transfecting



HEK-293 (ATCC, CRL-1573) packaging cells with TOP-GFP (Addgene), p-TWEEN LUC-GFP, pLenti-GIII-CMV-RFP-2A-Puro (ABM), ZEB2-RFP (ABM), nonsilencing shRNA control (Dharmacon), TRIPZ Human ZEB2 shRNA (Dharmacon), pLenti-III-mir-GFP-Blank (ABM) or LentimiRa-GFP-hsa-mir-200a (ABM) plasmids, together with psPAX2 (Addgene), and pMD2.G (Addgene) in OPTIMEM (Gibco) supplemented with XtremeGENE HP DNA Transfection Reagent (Roche). Cell transduction was fulfilled in presence of 8 µg/ml of polybrene (Sigma-Aldrich). Selection of resistant clones, where suitable, was performed by

treating cells with puromycin (1 µg/ml) for 5-10 days. Inducible gene expression was obtained by treating cells for 72 h with Doxycycline (1 µg/ml; Sigma).

Immunohistochemistry/immunofluorescence and flow cytometry. Immunohistochemical analysis was performed on 4 µm-thick paraffin-embedded tumor sections, cytopins, or cells grown on glass coverslip, using a mix made by 100 µl of Antibody Diluent (Dako, S3022) and specific antibody against CDX2 (AMT28;

Fig. 5 IL-6 and HGF induce a mesenchymal phenotype by activation of STAT3. **a** GSEA of STAT3 targets gene signature in CMS2 CR-CSphCs (CSphC #8, #9) exposed to V-ASC CM. Statistical significance was calculated as described in Subramanian et al. (doi: 10.1073/pnas.0506580102). **b** Immunoblot analysis of phosphorylated STAT3 (p-STAT3^{SER727/TYR705}) and STAT3 in CMS2 CR-CSphCs (CSphC #9) treated as indicated. β -actin was used as a loading control. Samples were run on the same gel and images were cropped only for the purpose of this figure. Source data are provided as a Source Data file. One representative of three independent experiments is shown. **c** Immunohistochemical analysis of p-STAT3 on paraffin-embedded sections of CRC patients with healthy weight or affected by obesity. One representative experiment of nine is shown. Scale bars, 100 μ m. Box and whiskers show min-to-max values, with a line indicating the mean value. **d** Immunoblot analysis of CMS2 CR-CSphCs (CSphC #9) treated as indicated. β -actin was used as a loading control. One representative of four independent experiments is shown. Samples were run on the same gel and images were cropped only for the purpose of this figure. Source data are provided as a Source Data file. **e** Proliferation rate of CMS2 CR-CSphCs exposed to the indicated treatment. Data are mean \pm S.D. of three independent experiments using two different CR-CSphC lines (CSphC #8, #9). **f** Colony-forming analysis of CR-CSphCs treated as indicated, at 21 days. Boxes and whiskers represent mean \pm S.D. of colony size performed in four independent experiments using four different CR-CSphC lines (CSphC #1, #8, #9, #21). *n* represents the number of colonies. **g** miR-200a expression levels in CMS2 cells treated as indicated using two different CR-CSphC lines (CSphC #8, #9). U6 was used as housekeeping control gene. Histograms represent mean \pm S.D. of three independent experiments. For (c and e-g) statistical significance was calculated using the two-tailed *t* test. **h** Clustergram of stemness-related genes in CMS2 CR-CSphCs (CSphC #8, #9) treated for 48 h as indicated. *GAPDH* and *HPRT1* were used as housekeeping control genes. **i** Phase-contrast analysis of CMS2 CR-CSphCs grown in matrigel and treated as indicated at 10 days. One representative of four independent experiments carried out with two different CR-CSphC lines (CSphC #8, #9) is shown. Scale bars, 20 μ m. For (d-i) STAT3 inhibitor C188-9 was used at 10 μ M concentration.

mouse IgG_{1k}, Novocastra, 1:50 dilution), Adiponectin (19F1; mouse IgG, ThermoFisher, 1:500 dilution), CK20 (Ks20.8, mouse IgG_{2a/ks}, Novocastra, 1:50 dilution), p-STAT3 (Tyr705; 9145, rabbit IgG, CST, 1:50 dilution), STAT3 (9139, mouse IgG_{2a}, CST, 1:300 dilution), and ZEB2 (E-11, mouse IgG_{2a}, Santa Cruz, 1:100 dilution). Single staining was revealed using biotiny-streptavidin system (Dako) and detected with 3-amino-9-ethylcarbazole (Dako). Double staining was performed using antibodies against CD31 (AB28364, rabbit IgG, Abcam, 1:50 dilution) and CD44v6 (2F10, mouse IgG1, R&D systems, 1:100 dilution), or using antibodies against CK20 and ki67 (D3B5, rabbit IgG, CST, 1:100 dilution), revealed by the MACH 2 double stain 2 kit conjugated goat antimouse polymer horseradish peroxidase (HRP) and the conjugated goat antirabbit polymer alkaline phosphatase (AP) (Biocare Medical), and detected by DAB or Vina Green, and Vulcan Fast Red chromogen. Triple staining was performed using antibodies against CD34 (IC0115, mouse IgG₁, CST, 1:50 dilution), CD31 (JC70A, mouse IgG_{1k}, Dako, 1:50 dilution), and CD45 (D9M8I, rabbit IgG, CST, 1:200 dilution), revealed by specific secondary antibodies, and detected by DAB, Vina Green and Vulcan Fast Red chromogen, respectively. For paraffin-embedded sections of primary CRC, the staining was detected using the Fast Red/Diaminobenzidine (DAB) substrates, while Fast Red/Vina Green were used in liver metastasis to avoid the intrinsic brown color background. Nuclei were counterstained with aqueous hematoxylin (Sigma). H&E stainings were performed using standard protocols. The adipose tissue and the vascular area were evaluated by calculating the area covered by Adiponectin⁺ and CD31⁺ cells, respectively (ImageJ, Colour deconvolution plugin). “Cell counter” plugin (ImageJ 1.8.0_172) was used to determine the number of cells expressing CD34/CD31/CD45, CK20/ki67, or p-STAT3. The analysis was assessed on five tumor sections of primary and metastatic tissue, for each experimental condition.

Retrospective immunohistochemistry score of CD44v6 expression in CRC patients with healthy weight and affected by obesity has been measured as quick score (Q), by multiplying the percentage of positive cells (P) by the intensity (I).

For immunofluorescence, cells were cytospun or grown on glass coverslips, fixed, permeabilized, and exposed overnight at 4 °C to a mix made by 100 μ l of 3% BSA 0,05% Tween-20 PBS and specific antibodies against ZEB2, ZEB1 (H-102, rabbit IgG, Santa Cruz, 1:100 dilution), WT1 (83535, rabbit IgG, CST, 1:100 dilution), IL-6R (PA5-47209, goat IgG, ThermoFisher Scientific, 1:50 dilution), c-Met (95106, mouse IgG₁, R&D, 1:100 dilution), or isotype-matched control (IMC), as previously described⁴³. Primary antibody staining was detected by using antirabbit, antigoat, or antimouse secondary antibodies conjugated with Alexa Fluor-488 or Rhodamine Red-x (Life Technologies). Nuclei were counterstained using Toto-3 iodide (Life Technologies), or DAPI (ThermoFisher Scientific). Lipid droplets were stained using the Oil Red O (Sigma).

For flow cytometry analysis, following antibody titration, 1×10^5 cells were collected, washed in PBS and stained for 1 h at 4 °C with conjugated antibodies specific for CD44v6 (2F10 APC, mouse IgG₁, R&D systems, 5 μ l/sample), CD271 (C40-1457 PE-Cy7, mouse IgG1k, BD, 12 μ l/sample), VEGFR (89106 APC, mouse IgG₁, R&D, 10 μ l/sample), CD31 (WM59 PE, mouse IgG_{1k}, BD, 5 μ l/sample), CD34 (581 APC, mouse IgG_{1k}, BD, 20 μ l/sample), CD45 (5H9, mouse IgG_{1k}, BD, 5 μ l/sample), CD90 (5E10 PE, mouse IgG_{1k}, BD, 10 μ l/sample), CD105 (166707 APC, mouse IgG₁, R&D, 10 μ l/sample), CD73 (AD2, mouse IgG_{1k}, BD, 5 μ l/sample), CD10 (97C5 APC, mouse IgG_{1k}, Miltenyi Biotech, 5 μ l/sample), CD200 (MRC OX-104 APC, mouse IgG_{1k}, BD, 20 μ l/sample), CD36 (CLB-IVC7, mouse IgG_{1k}, BD, 5 μ l/sample), CD106 (51-10C9, mouse IgG_{1k}, BD, 5 μ l/sample), or corresponding IMC. Dead cells' exclusion was performed by using 7-AAD (0.25 μ g/1 $\times 10^6$ cells, BD Biosciences).

Isolation of TOP-GFP^{high/low} and CD44v6⁺/⁻ CR-CSphCs, or CD34⁺/⁻ CD31⁺/CD45⁺ ASCs was performed by using the FACSMelody cell sorter. Cells were washed with 2% BSA and 2 mM EDTA PBS and filtered with a 70 μ M mesh to

prevent cell clogging. Postsorting analysis was performed to verify the purity of the sorted population. Dead cells' exclusion was performed by staining cells with 7-AAD.

Clonogenesis, colony forming, and invasion assay. Clonogenicity of bulk or enriched Wnt^{high/low} CR-CSphCs, was determined by plating 1, 2, 4, 8, 16, 32, 64, 128 cells per well, in medium or V-ASC CM, and analyzed with the Extreme Limiting Dilution Analysis (ELDA) ‘limdil’ function (<http://bioinf.wehi.edu.au/software/elda/index.html>).

CR-CSphCs were seeded as dissociated cells (2×10^4 viable cells) in 0.3% agar (SeaPlaque Agarose; Lonza) and cultured up to 21 days. Colony-forming potential was assessed by staining cells with 0.01% crystal violet in 1% methanol. Colonies were counted using ImageJ software based on the size (small <7 pixels, medium 7–13 pixels, and large >13 pixels).

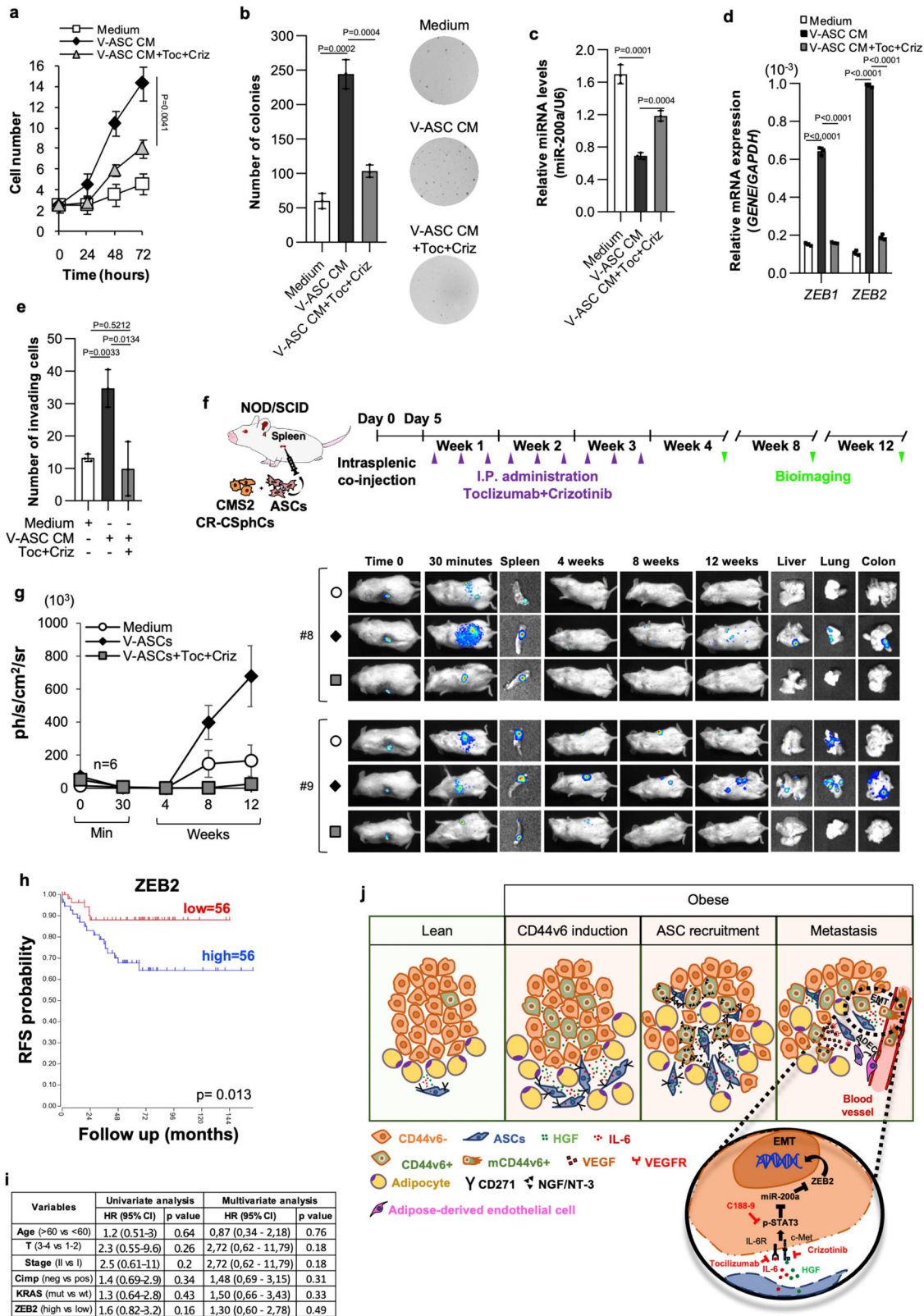
The invasive potential was evaluated by seeding 2×10^3 viable CR-CSphCs in 200 μ l of SCM into 8 μ m pore size transwell coated with 30 μ l of 1:6 Matrigel/SCM solution (BD Biosciences). SCM supplemented with 10% human serum was used as chemoattractant, alone or in combination with NGF (10 ng/ml; Peprotech), NGF neutralizing antibody (0.2 μ g/ml; R&D), or CD271 neutralizing antibody (ME20.4, mouse IgG1, Merck). To study the paracrine role of CD44v6⁺ cells in the induction of an invasive phenotype on ASCs, 1×10^5 enriched viable cells were seeded in the lower chamber of 24 well plate until confluence was reached.

Animal models and Treatments. Six weeks old male NOD-SCID mice were purchased by Charles River Laboratories and housed at the University of Palermo in accordance to institutional guidelines of the Italian animal welfare (D.L. n° 26 March 4, 2014) and authorization n. 951/2015-PR. Mice were maintained in a temperature-controlled system (22 °C, 50% humidity) with a 12 h dark/light cycle, with *ad libitum* access to pelleted chow (Special Diets Services-811900 VRF1 (P)) and to 0.45 μ m filtered water in sterile drinking bottles, in cages (Tecniplast) with radiation-sterilized bedding (SAWI Research Bedding, JELU-WERK).

CIC capacity was evaluated by injecting 50 μ l of 1:3 Matrigel/SCM containing luciferase LUC/GFP-transduced CR-CSphCs (10, 100, 1000, or 10,000), alone or in combination with V-ASCs (50,000), in the subrenal capsule of NSG mice. Following i.p. injection of VivoGlo Luciferin (150 mg/kg), tumor growth and metastasis formation were monitored by evaluation of bioluminescence emission, which was detected by the whole-body imaging system (IVIS Lumina III, PerkinElmer). CIC frequency was analyzed with the Extreme Limiting Dilution Analysis (ELDA) ‘limdil’ function (<http://bioinf.wehi.edu.au/software/elda/index.html>).

Subcutaneous xenografts were generated by injecting 150 μ l of 1:1 Matrigel/SCM solution containing 2.5×10^5 viable CR-CSphCs, alone or in combination with S-ASCs or V-ASCs (1.25×10^5 viable cells). After tumor appearance (0.03–0.06 cm³), mice were monitored twice a week and tumors were measured by using a digital caliper. Tumor volume was calculated using the formula largest diameter \times (smallest diameter)² $\times \pi/6$. Once the endpoints were reached, with subcutaneous tumors having the largest diameter = 2 cm, or when mice showed signs of suffering, animals were sacrificed accordingly to Directive 2010/63/EU guidelines (D.lgs 26/2014).

In vivo metastatic potential of CR-CSphCs was assessed by intrasplenic injection of 30 μ l of PBS solution in presence of 3×10^5 luciferase LUC/GFP-transduced cells, alone or in combination with 1.25×10^5 V-ASCs. To ascertain the in vivo migratory/engraftment potential, 1.25×10^5 LUC-GFP-transduced ASCs were injected into NOD-SCID mice spleen. The spleen was removed 30 min after cell injection. Where indicated, mice were treated i.p. with tocilizumab (10 mg/kg) in combination with crizotinib (5 mg/kg) 3 days/week for 3 weeks. At 12 weeks,



after mouse sacrifice, organs were harvested, macroscopically analyzed, and fixed in formalin for histological analysis.

Tube formation assay. Huvec cells were plated on matrigel coated wells (200 μ l/cm²) at 80,000 cells/cm² seeding density with 170 μ l/cm² of EGM-2 growth medium, in presence or absence of 10 ng/ml VEGF, or CD44v6 + CR-CSphCs' CM. Plates were incubated for 16 h at 37 °C in humidified incubator 5% CO₂, before microscopy observation. Phase-contrast images of Huvec-derived tubes were

captured using the EVOS microscope (AMG) at x4 magnification. Image analysis for the evaluation of tubule characteristics (tubules covered area (%), tubules length, total number of tubules, mean of tubules length) was performed using the Wimasis software (<https://www.wimasis.com/en/>).

Real-time PCR and RNAseq. RNA was retrotranscribed using the High-Capacity cDNA Archive Kit (Applied Biosystems). Quantitative Real-time PCR (qRT-PCR) was accomplished in a SYBR Green PCR master mix (Qiagen) containing primers

Fig. 6 IL-6 and HGF targeting hampers the VAT-induced metastatic capacity of CR-CSphCs. **a** Growth kinetics of CMS2 CR-CSphCs treated with V-ASC CM, alone or in combination with tocilizumab (Toc) and crizotinib (Criz). **b** Colony-forming assay of CR-CSphCs following the indicated treatment, at 21 days. **c**, miR-200a expression in CMS2 CR-CSphCs treated as indicated for 48 h. U6 was used as housekeeping control gene. **d** ZEB1 and ZEB2 expression levels in cells treated for 72 h as indicated. GAPDH was used as housekeeping control gene. **e** Number of invading CMS2 CR-CSphCs pretreated as indicated for 48 h. Statistical significance between two groups was determined by unpaired Student's *t* test (2-tailed). For (a–e) data are mean \pm S.D. of three independent experiments using two different CR-CSphC lines (CSphC #8, #9). Statistical significance was calculated using the two-tailed *t* test. **f** Schematic model of intrasplenic injection of CR-CSphCs showing time points of treatments and in vivo bioluminescence detection. **g** Kinetics and whole-body imaging analysis of mice ($n = 6$) following intrasplenic injection of LUC-GFP-transduced CMS2 CR-CSphCs alone or co-injected with V-ASCs untreated or treated with the indicated pharmaceutical compounds. Insets represent spleen collected 30 min after cell injection, and liver, lung, and bowel collected at the time of sacrifice. Data are mean \pm S.D. of independent experiments using two different CR-CSphC lines (CSphC #8, #9), and 2 S- (#3, #6) or V-ASC (#5, #14) lines. **h** RFS rate of CMS2/MSS/Stage1-2 CRC patients according to ZEB2 expression levels. Statistical significance was calculated using the log-rank (Mantel-Cox) test. **i** Univariate and Multivariate analysis of relapse-free survival (RFS) according to regression Cox model in CRC patients as in **h**. Statistical significance was calculated using the Wald test. **j** Schematic representation of bidirectional crosstalk between ASCs and CRC cells. Visceral adipose factors enhance the expression of CD44v6; CD44v6 + -released NGF/NT-3 drives the intra-tumor recruitment of ASCs; adipose-released proteins induce EMT of CRC cells through the activation of STAT3; CD44v6 + -released VEGF promotes the endothelial transdifferentiation of ASCs. Clinically available drugs targeting HGF and IL-6 are highlighted in red.

for NGF, BDNF, NTF3, NTF4, ZEB1, ZEB2, CDX2, E-CADHERIN, CXCR4, FRMD6, N-CADHERIN, SLUG, SNAIL, TWIST, and VIMENTIN. GAPDH was used as endogenous control. Primers sequences are included in Supplementary Table 3.

mRNA expression levels of EMT- (PAHS-090Z, Qiagen) and tumor metastasis-related genes (PAHS-028Z, Qiagen) were detected by RT₂ profiler PCR array. The gene expression profile of EMT-, Wnt- and CSCs-related gene expression was evaluated by using the PrimePCR Custom Panel (Bio-Rad) according to manufacturer's instructions. To evaluate miRNA expression levels, total RNA was retrotranscribed by using miScript reverse Transcription Kit (Qiagen). miRNA expression profile was determined using Megaplex pools kit (Applied Biosystem) specific for a set of 384 microRNAs (TaqMan Human MicroRNA Array A) as recommended by manufacturer's instructions. Collected data were analyzed with the Thermo FisherCloud software. miR-200a, miR-200b, and miR-200c expression levels were evaluated by qRT-PCR using specific primers (Qiagen). miRNA expression levels were normalized with endogenous RNU-6 (Qiagen) control and calculated using the comparative Ct method ($2^{-\Delta\Delta C_t}$). For measuring mRNA expression, the NEBNext Ultra Directional RNA Library Prep Kit for Illumina was used to process the samples. The sample preparation was performed according to the protocol 'NEBNext Ultra Directional RNA Library Prep Kit for Illumina' (NEB). Briefly, mRNA was isolated from total RNA using the oligo-dT magnetic beads. After the fragmentation of the mRNA, a cDNA synthesis was performed. This was used for ligation with the sequencing adapters and PCR amplification of the resulting product. The quality and yield after sample preparation were measured with the Fragment Analyzer. The size of the resulting products was consistent with the expected size distribution (a broad peak between 300 and 500 bp). Clustering and DNA sequencing using the Illumina NextSeq 500 was performed according to the manufacturer's protocols. A concentration of 1.6 pM of DNA was used. NextSeq control software 2.0.2 was used. Image analysis, base calling, and quality check were performed with the Illumina data analysis pipeline RTA v2.4.11 and Bcl2fastq v2.17. Raw sequencing reads were aligned to Ensembl release 84 (GRCh38 assembly) using the HISAT2 2.1.0 pipeline⁶⁷ and counts were summarized per gene using the summarizeOverlaps function in the GenomicsAlignment R package⁶⁸. Gene counts were normalized to reads per million and log₂ transformed. The CMS signature was derived from the TCGA dataset⁶⁹, which expression data were downloaded from the FIREHOSE repository (<https://gdac.broadinstitute.org/>). This included RNAseq expression data generated by the Illumina HiSeq ($N = 326$) and Genome Analyzer ($N = 172$) platforms (RSEM normalized data). After log₂ transformation, data from both platforms were combined into a single dataset ($N = 498$), correcting platform-specific effects with the ComBat algorithm⁷⁰ as implemented in the sva R package⁷¹. As a first step toward defining a CMS signature, genes were selected with at least one read per gene in all 12 cell line expression profiles ($N = 10,949$). This set of genes was further filtered based on a correlation of correlations approach³⁵ comparing the TCGA dataset with the cell line expression data and retaining genes with a correlations of correlation score ≥ 0.1 ($N = 4481$). CMS labels for the TCGA samples were obtained from Guinney et al.³⁵ (134 CMS2, 81 CMS4) and differential gene expression (CMS4 versus CMS2) was determined using the limma R package⁷². The CMS signature was constructed using the log₂ fold changes of the 10 most significantly upregulated and 10 most significantly downregulated genes. This signature was used to calculate the Pearson correlation coefficient with the cell line expression profiles, averaging the treatment replicates and mean-centering within the cell line (both gene-wise). GSEA⁷³ using the CMS4 signature, as well as the tumor stemness and STAT3 targets gene sets, was performed using the GSEA software (<http://software.broadinstitute.org/gsea/index.jsp>).

Gene set enrichment analysis was accomplished in R with fgsea package by considering all gene sets from MSigDB collections (msigdb.v6.2.symbols) with

sample permutation (1,000 permutations). A differential expression analysis was performed with limma package.

Western blot. Cells were lysate in ice-cold buffer, loaded in SDS-PAGE gels, and blotted on nitrocellulose membranes. Membrane were pre-incubated with blocking buffer (0.1% Tween 20 and 5% nonfat dry milk in PBS) for 1 h at room temperature and then exposed to a mix made by 5% BSA 0.05% Tween-20 PBS and specific antibodies (1:1000 dilution) against ZEB2 (E-11, mouse IgG_{2a}, Santa Cruz), p-STAT3 (Ser727) (rabbit, CST), p-STAT3 (Tyr705) (9145, rabbit IgG, CST), STAT3 (9139, mouse IgG_{2a}, CST), active β -catenin (Ser33/37/Thr41) (D13A1, rabbit IgG, CST), β -catenin (D10A8, rabbit IgG, CST), vimentin (R28, rabbit, CST), or β -actin (8H10D10, mouse, CST). Primary antibodies were revealed using anti-mouse or anti-rabbit HRP-conjugated (goat H + L, ThermoFisher Scientific, 1:2000 dilution in blocking buffer) and detected by Amersham imager 600 (GE Healthcare). Protein levels were calculated by densitometric analysis using ImageJ software v1.8.0_172.

Statistical analysis. The meta-analysis was conducted after the selection of all the relevant studies on PubMed database related to BMI and survival of CRC patients. The studies were classified by year and population size, and the relative Hazard Ratio (HR), Risk Ratio, and Odds Ratio values were collected. In order to account for the missing confidence intervals (CI) for the estimate of effect in a study we used the method as proposed in Altman et al.⁷⁴. Meta-analysis was conducted by using metafor package in R and choosing the default Restricted Maximum-likelihood Estimator (REML) estimation to fit the model.

Survival results were obtained from an internal database of medical records or using the "R2: Genomics Analysis and Visualization Platform (<http://r2.amc.nl> <http://r2platform.com>)" and analyzed with a log-rank (Mantel-Cox) test and expressed as Kaplan-Meier survival curves.

Clinical data for progression-free survival, univariate and multivariate analysis, were obtained from Istituto Oncologico del Mediterraneo ($n = 393$), and Azienda Ospedaliero Universitaria "Policlinico Vittorio Emanuele" ($n = 441$). Univariate and multivariate analysis were performed in R (v R-4.1.0) with "survival" package by fitting a Cox proportional hazards regression model to evaluate the risk of Progression-Free Survival (PFS) associated with each covariate. PFS was calculated with right-censored data and the event of distant recurrence for each patient.

Data were shown as mean \pm standard deviation. Following Kolmogorov-Smirnov test to assess the samples distribution, statistical significance was estimated by unpaired *T* test, or by two-tailed Mann-Whitney test. Results were referred to statistically significant as $p < 0.05$. * indicates $p < 0.05$, ** indicate $p < 0.01$, *** indicate $p < 0.001$, and **** indicate $p < 0.0001$.

Reporting summary. Further information on experimental design is available in the Nature Research Reporting Summary linked to this paper.

Data availability

All data relevant to the study are included in the article or uploaded as supplementary information. Uncropped western blots are included in the Source Data file. The data that support the findings of this study are available from the corresponding author (GS) upon reasonable request. RNA sequencing data of CR-CSphCs treated with control medium, S-ASC or V-ASC CM generated in this study have been deposited in a public, open-access GEO repository, under accession number [GSE162561](https://www.ncbi.nlm.nih.gov/geo/query/acc.cgi?acc=GSE162561) (link to data:). The CMS signature was derived from the TCGA dataset, which expression data were downloaded from the FIREHOSE repository (<https://gdac.broadinstitute.org/>). CMS labels for the TCGA samples were obtained from Guinney et al. and are available at the website:

<https://www.synapse.org/#!Synapse:syn2623706/files/>, following login in. Source data are provided with this paper.

Received: 4 September 2020; Accepted: 3 August 2021;

Published online: 18 August 2021

References

- Siegel, R. L., Miller, K. D., Fuchs, H. E. & Jemal, A. Cancer statistics, 2021. *CA Cancer J. Clin.* **71**, 7–33 (2021).
- Blüher, M. Obesity: global epidemiology and pathogenesis. *Nature reviews Endocrinology*. **15**, 288–298 (2019).
- Lauby-Secretan, B. et al. Body fatness and cancer—viewpoint of the IARC working group. *N. Engl. J. Med.* **375**, 794–798 (2016).
- Bhaskaran, K. et al. Body-mass index and risk of 22 specific cancers: a population-based cohort study of 5.24 million UK adults. *Lancet*. **384**, 755–765 (2014).
- Rosen, E. D. & Spiegelman, B. M. What we talk about when we talk about fat. *Cell*. **156**, 20–44 (2014).
- Lengyel, E., Makowski, L., DiGiovanni, J. & Kolonin, M. G. Cancer as a matter of fat: the crosstalk between adipose tissue and tumors. *Trends Cancer*. **4**, 374–384 (2018).
- Jeffery, E., Church, C. D., Holtrup, B., Colman, L. & Rodeheffer, M. S. Rapid depot-specific activation of adipocyte precursor cells at the onset of obesity. *Nat. Cell Biol.* **17**, 376–385 (2015).
- Chau, Y. Y. et al. Visceral and subcutaneous fat have different origins and evidence supports a mesothelial source. *Nat. Cell Biol.* **16**, 367–375 (2014).
- Rodeheffer, M. S., Birsoy, K. & Friedman, J. M. Identification of white adipocyte progenitor cells in vivo. *Cell* **135**, 240–249 (2008).
- Cristancho, A. G. & Lazar, M. A. Forming functional fat: a growing understanding of adipocyte differentiation. *Nat. Rev. Mol. Cell Biol.* **12**, 722–734 (2011).
- Fasshauer, M. & Bluher, M. Adipokines in health and disease. *Trends Pharmacol. Sci.* **36**, 461–470 (2015).
- Park, J., Euhus, D. M. & Scherer, P. E. Paracrine and endocrine effects of adipose tissue on cancer development and progression. *Endocr. Rev.* **32**, 550–570 (2011).
- O’Sullivan, J., Lysaght, J., Donohoe, C. L. & Reynolds, J. V. Obesity and gastrointestinal cancer: the interrelationship of adipose and tumour microenvironments. *Nat. Rev. Gastroenterol. Hepatol.* **15**, 699–714 (2018).
- Quail, D. F. & Dannenberg, A. J. The obese adipose tissue microenvironment in cancer development and progression. *Nat. Rev. Endocrinol.* **15**, 139–154 (2019).
- Kucerova, L., Matuskova, M., Hlubinova, K., Altanerova, V. & Altaner, C. Tumor cell behaviour modulation by mesenchymal stromal cells. *Mol. Cancer*. **9**, 129 (2010).
- Kucerova, L. et al. Interaction of human adipose tissue-derived mesenchymal stromal cells with breast cancer cells. *Neoplasma*. **58**, 361–370 (2011).
- Strong, A. L. et al. Obesity associated alterations in the biology of adipose stem cells mediate enhanced tumorigenesis by estrogen dependent pathways. *BCR*. **15**, R102 (2013).
- Theriau, C. F., Sauve, O. S., Beaudoin, M. S., Wright, D. C. & Connor, M. K. Proliferative endocrine effects of adipose tissue from obese animals on MCF7 cells are ameliorated by resveratrol supplementation. *PLoS ONE*. **12**, e0183897 (2017).
- Ji, S. Q. et al. Adipose tissue-derived stem cells promote pancreatic cancer cell proliferation and invasion. *Braz. J. Med. Biol. Res.* **46**, 758–764 (2013).
- Nowicka, A. et al. Human omental-derived adipose stem cells increase ovarian cancer proliferation, migration, and chemoresistance. *PLoS ONE*. **8**, e181859 (2013).
- Klopp, A. H. et al. Omental adipose tissue-derived stromal cells promote vascularization and growth of endometrial tumors. *Clin. Cancer Res.* **18**, 771–782 (2012).
- Ko, J. H. et al. Conditioned media from adipocytes promote proliferation, migration, and invasion in melanoma and colorectal cancer cells. *J. Cell. Phys.* **234**, 18249–18261 (2019).
- Murphy, T. K., Calle, E. E., Rodriguez, C., Kahn, H. S. & Thun, M. J. Body mass index and colon cancer mortality in a large prospective study. *Am. J. Epidemiol.* **152**, 847–854 (2000).
- Campbell, P. T. et al. Impact of body mass index on survival after colorectal cancer diagnosis: the Cancer Prevention Study-II Nutrition Cohort. *J. Clin. Oncol.* **30**, 42–52 (2012).
- Bhaskaran, K., Dos-Santos-Silva, I., Leon, D. A., Douglas, I. J. & Smeeth, L. Association of BMI with overall and cause-specific mortality: a population-based cohort study of 3.6 million adults in the UK. *Lancet Diabetes Endocrinol.* **6**, 944–953 (2018).
- Mao, J. et al. Overnutrition stimulates intestinal epithelium proliferation through beta-catenin signaling in obese mice. *Diabetes*. **62**, 3736–3746 (2013).
- Chen, D. et al. Paracrine factors from adipose-mesenchymal stem cells enhance metastatic capacity through Wnt signaling pathway in a colon cancer cell co-culture model. *Cancer Cell Int.* **15**, 42 (2015).
- Valent, P. et al. Cancer stem cell definitions and terminology: the devil is in the details. *Nat. Rev. Cancer*. **12**, 767–775 (2012).
- Medema, J. P. Targeting the colorectal cancer stem cell. *N. Engl. J. Med.* **377**, 888–890 (2017).
- Lytle, N. K., Barber, A. G. & Reya, T. Stem cell fate in cancer growth, progression and therapy resistance. *Nat. Rev. Cancer*. **18**, 669–680 (2018).
- Ebbing, E. A. et al. Stromal-derived interleukin 6 drives epithelial-to-mesenchymal transition and therapy resistance in esophageal adenocarcinoma. *Proc. Natl Acad. Sci. USA*. **116**, 2237–2242 (2019).
- Jimenez, G. et al. Mesenchymal stem cell’s secretome promotes selective enrichment of cancer stem-like cells with specific cytogenetic profile. *Cancer Lett.* **429**, 78–88 (2018).
- Rokavec, M. et al. IL-6R/STAT3/miR-34a feedback loop promotes EMT-mediated colorectal cancer invasion and metastasis. *J. Clin. Invest.* **124**, 1853–1867 (2014).
- Lenos, K. J. et al. Stem cell functionality is microenvironmentally defined during tumour expansion and therapy response in colon cancer. *Nat. Cell Biol.* **20**, 1193–1202 (2018).
- Guinney, J. et al. The consensus molecular subtypes of colorectal cancer. *Nat. Med.* **21**, 1350–1356 (2015).
- Reilly, S. M. & Sattiel, A. R. Adapting to obesity with adipose tissue inflammation. *Nat. Rev. Endocrinol.* **13**, 633–643 (2017).
- Ouchi, N., Parker, J. L., Lugus, J. J. & Walsh, K. Adipokines in inflammation and metabolic disease. *Nat. Rev. Immunol.* **11**, 85–97 (2011).
- Ong, W. K. et al. Identification of specific cell-surface markers of adipose-derived stem cells from subcutaneous and visceral fat depots. *Stem Cell Rep.* **2**, 171–179 (2014).
- Baglioni, S. et al. Functional differences in visceral and subcutaneous fat pads originate from differences in the adipose stem cell. *PLoS ONE*. **7**, e36569 (2012).
- Ritter, A. et al. Subcutaneous and visceral adipose-derived mesenchymal stem cells: commonality and diversity. *Cells*. **8**, 1288 (2019).
- Lombardo, Y. et al. Bone morphogenetic protein 4 induces differentiation of colorectal cancer stem cells and increases their response to chemotherapy in mice. *Gastroenterology*. **140**, 297–309 (2011).
- Vermeulen, L. et al. Wnt activity defines colon cancer stem cells and is regulated by the microenvironment. *Nat. Cell Biol.* **12**, 468–476 (2010).
- Todaro, M. et al. CD44v6 is a marker of constitutive and reprogrammed cancer stem cells driving colon cancer metastasis. *Cell Stem Cell*. **14**, 342–356 (2014).
- Barilani, M. et al. Low-affinity nerve growth factor receptor (CD271) heterogeneous expression in adult and fetal mesenchymal stromal cells. *Sci. Rep.* **8**, 9321 (2018).
- Esteve, D. et al. Lobular architecture of human adipose tissue defines the niche and fate of progenitor cells. *Nat. Commun.* **10**, 2549 (2019).
- Beckenkamp, L. R. et al. Comparative characterization of CD271(+) and CD271(-) subpopulations of CD34(+) human adipose-derived stromal cells. *J. Cell Biochem.* **119**, 3873–3884 (2018).
- Nan, L. et al. Pancreatic stellate cells facilitate perineural invasion of pancreatic cancer via HGF/c-met pathway. *Cell Transpl.* **28**, 1289–1298 (2019).
- Brabletz, S. & Brabletz, T. The ZEB/miR-200 feedback loop—a motor of cellular plasticity in development and cancer? *EMBO Rep.* **11**, 670–677 (2010).
- Park, S. M., Gaur, A. B., Lengyel, E. & Peter, M. E. The miR-200 family determines the epithelial phenotype of cancer cells by targeting the E-cadherin repressors ZEB1 and ZEB2. *Genes Dev.* **22**, 894–907 (2008).
- Trinh, A. et al. Practical and robust identification of molecular subtypes in colorectal cancer by immunohistochemistry. *Clin. Cancer Res.* **23**, 387–398 (2017).
- Sreekumar, R. et al. Assessment of nuclear ZEB2 as a biomarker for colorectal cancer outcome and TNM risk stratification. *JAMA*. **1**, e183115 (2018).
- Li, M. Z. et al. ZEB2 promotes tumor metastasis and correlates with poor prognosis of human colorectal cancer. *Am. J. Transl. Res.* **9**, 2838–2851 (2017).
- Gupta, P. B., Pastushenko, I., Skibinski, A., Blanpain, C. & Kuperwasser, C. Phenotypic plasticity: driver of cancer initiation, progression, and therapy resistance. *Cell Stem Cell*. **24**, 65–78 (2019).
- Denisov, E. V. & Perelmuter, V. M. A fixed partial epithelial-mesenchymal transition (EMT) triggers carcinogenesis, whereas asymmetrical division of hybrid EMT cells drives cancer progression. *Hepatology*. **68**, 807–810 (2018).
- Jolly, M. K. et al. Implications of the hybrid epithelial/mesenchymal phenotype in metastasis. *Front. Oncol.* **5**, 155 (2015).
- Bago, J. R., Alieva, M., Soler, C., Rubio, N. & Blanco, J. Endothelial differentiation of adipose tissue-derived mesenchymal stromal cells in glioma tumors: implications for cell-based therapy. *Mol. Ther.* **21**, 1758–1766 (2013).

57. Traktuev, D. O. et al. Robust functional vascular network formation in vivo by cooperation of adipose progenitor and endothelial cells. *Circ. Res.* **104**, 1410–1420 (2009).
58. Fukumura, D. et al. Paracrine regulation of angiogenesis and adipocyte differentiation during in vivo adipogenesis. *Circ. Res.* **93**, e88–e97 (2003).
59. Su, F., Ahn, S., Saha, A., DiGiovanni, J. & Kolonin, M. G. Adipose stromal cell targeting suppresses prostate cancer epithelial-mesenchymal transition and chemoresistance. *Oncogene*. **38**, 1979–1988 (2019).
60. Fessler, E. et al. A multidimensional network approach reveals microRNAs as determinants of the mesenchymal colorectal cancer subtype. *Oncogene*. **35**, 6026–6037 (2016).
61. He, P., Qiu, K. & Jia, Y. Modeling of mesenchymal hybrid epithelial state and phenotypic transitions in EMT and MET processes of cancer cells. *Sci. Rep.* **8**, 14323 (2018).
62. Lyman, G. H. & Sparreboom, A. Chemotherapy dosing in overweight and obese patients with cancer. *Nat. Rev. Clin. Oncol.* **10**, 451–459 (2013).
63. Weidinger, C., Ziegler, J. F., Letizia, M., Schmidt, F. & Siegmund, B. Adipokines and Their Role in Intestinal Inflammation. *Front. Immunol.* **9**, 1974 (2018).
64. Virzi, F. et al. Combined platelet-rich plasma and lipofilling treatment provides great improvement in facial skin-induced lesion regeneration for scleroderma patients. *Stem Cell Res. Ther.* **8**, 236 (2017).
65. Todaro, M. et al. Colon cancer stem cells dictate tumor growth and resist cell death by production of interleukin-4. *Cell Stem Cell*. **1**, 389–402 (2007).
66. Veschi, V. et al. Targeting chemoresistant colorectal cancer via systemic administration of a BMP7 variant. *Oncogene*. **39**, 987–1003 (2020).
67. Kim, D., Langmead, B. & Salzberg, S. L. HISAT: a fast spliced aligner with low memory requirements. *Nat. Methods*. **12**, 357–360 (2015).
68. Lawrence, M. et al. Software for computing and annotating genomic ranges. *PLoS Computational Biol.* **9**, e1003118 (2013).
69. Cancer Genome Atlas, N. Comprehensive molecular characterization of human colon and rectal cancer. *Nature*. **487**, 330–337 (2012).
70. Johnson, W. E., Li, C. & Rabinovic, A. Adjusting batch effects in microarray expression data using empirical Bayes methods. *Biostatistics* **8**, 118–127 (2007).
71. Leek, J. T., Johnson, W. E., Parker, H. S., Jaffe, A. E. & Storey, J. D. The sva package for removing batch effects and other unwanted variation in high-throughput experiments. *Bioinformatics*. **28**, 882–883 (2012).
72. Ritchie, M. E. et al. Limma powers differential expression analyses for RNA-seq and microarray studies. *Nucleic Acids Res.* **43**, e47 (2015).
73. Subramanian, A. et al. Gene set enrichment analysis: a knowledge-based approach for interpreting genome-wide expression profiles. *Proc. Natl Acad. Sci. USA*. **102**, 15545–15550 (2005).
74. Altman, D. G. & Bland, J. M. How to obtain the confidence interval from a P value. *Bmj*. **343**, d2090 (2011).

Acknowledgements

We are thankful to Francesco Calo' for graphics. The research leading to these results has received funding from AIRC under 5 × 1000 (9979) project to Giorgio Stassi and Ruggero De Maria; ONCODE, Transcan-2 grant Tactic, Dutch Cancer Society (KWF) Grants

UvA2015-7587 and 10150 to Jan Paul Medema; AIRC IG (21445) and PRIN 2017WVKSLR to Giorgio Stassi, RF2018-12367044 to Matilde Todaro and Ruggero De Maria.

Alice Turdo and Veronica Veschi are research fellows funded by European Union-FESR FSE, PON Ricerca e Innovazione 2014–2020 (AIM line 1).

Author contributions

S.D.F. and G.S. conceived and designed the experiments; S.D.F., P.B., A.T., M.G., V.V., A.N., L.R.M., M.L.I., I.P., M.E.F., L.C., and M.T. carried out the experiments, analyzed and elaborated data; S.D.F., D.S.S., S.V.H., and E.M. executed the bioinformatics analysis; M.R.B., R.D.M., and J.P.M. supplied scientific suggestions and critical review; F.M., G.M., L.L., G.G., D.G., L.M., M.M., and P.V. provided clinical data of CC patients; M.T., R.D.M., J.P.M., and G.S. provided critical comments to the manuscript; S.D.F. and G.S. wrote the manuscript; R.D.M., J.P.M., and G.S. provided funds.

Competing interests

The authors declare no competing interests.

Additional information

Supplementary information The online version contains supplementary material available at <https://doi.org/10.1038/s41467-021-25333-9>.

Correspondence and requests for materials should be addressed to G.S.

Peer review information *Nature Communications* thanks Hector Palmer and the other, anonymous, reviewer(s) for their contribution to the peer review of this work. Peer reviewer reports are available.

Reprints and permission information is available at <http://www.nature.com/reprints>

Publisher's note Springer Nature remains neutral with regard to jurisdictional claims in published maps and institutional affiliations.

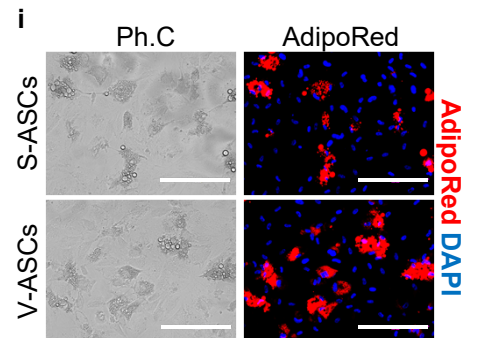
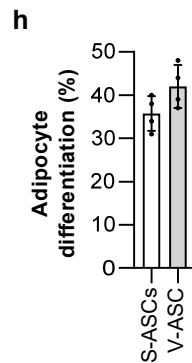
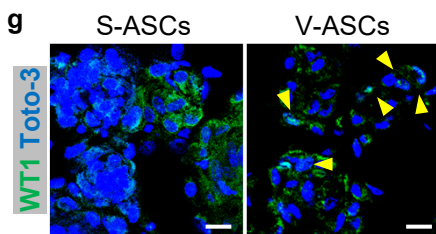
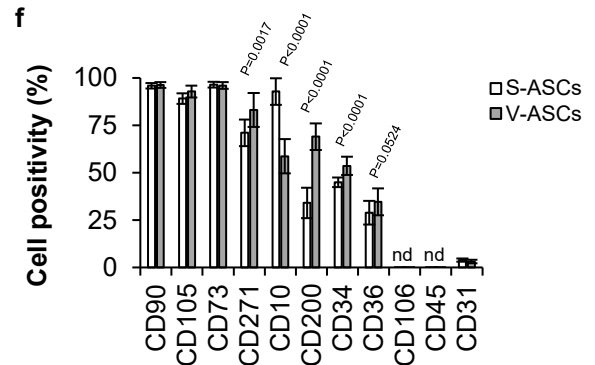
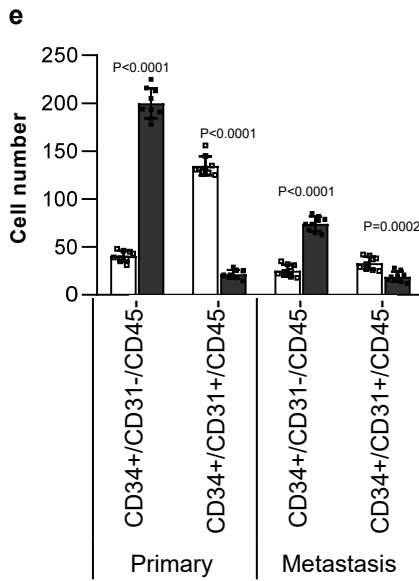
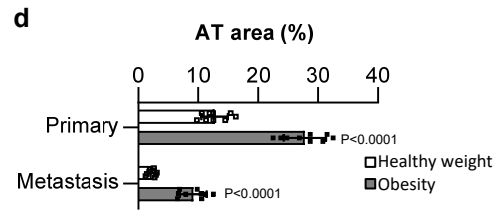
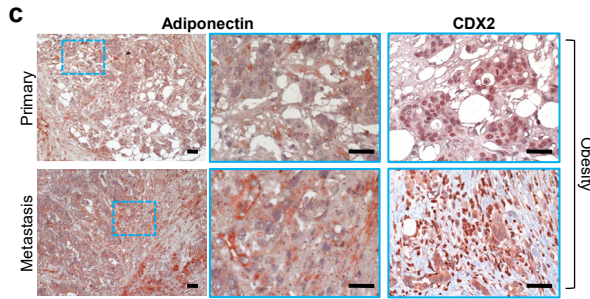
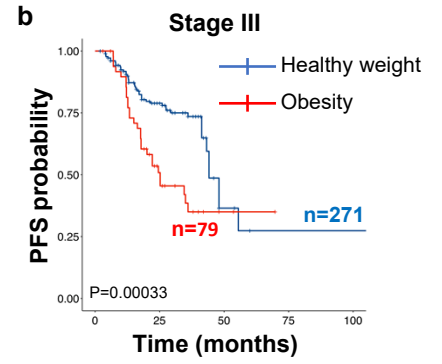


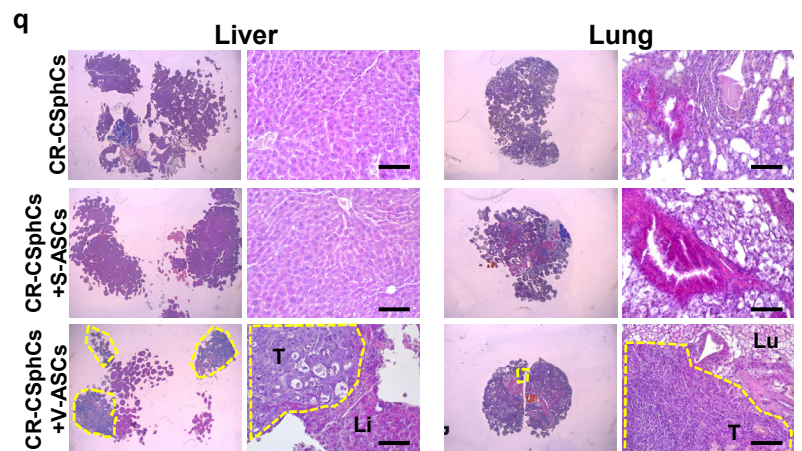
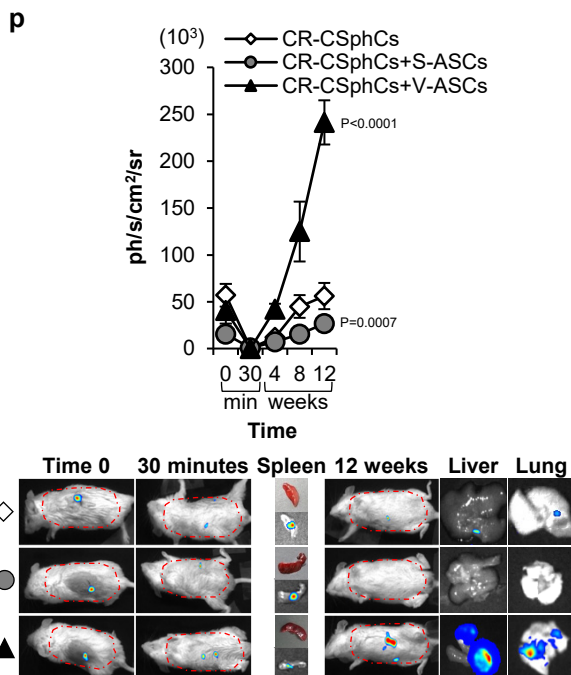
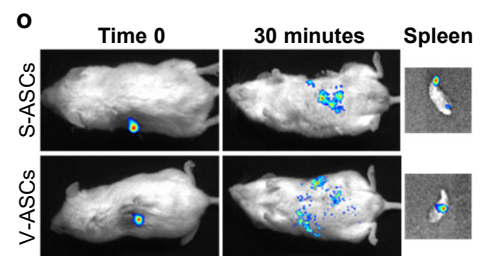
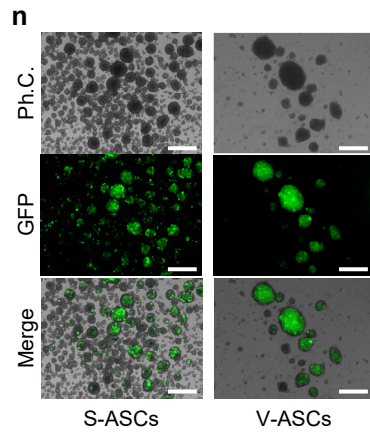
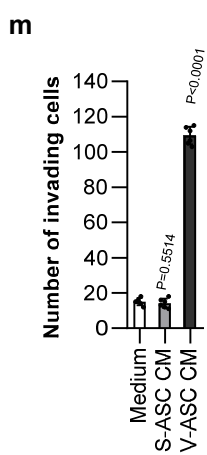
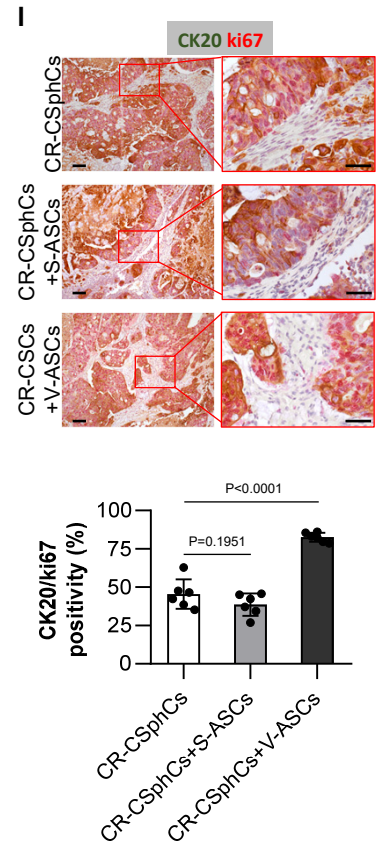
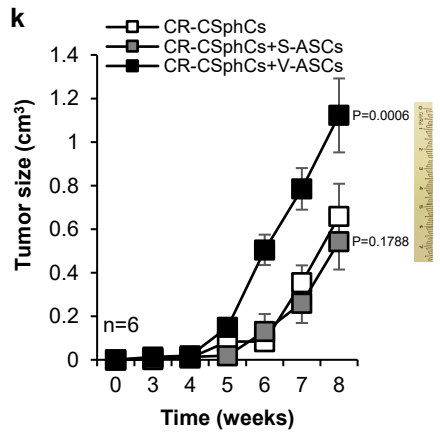
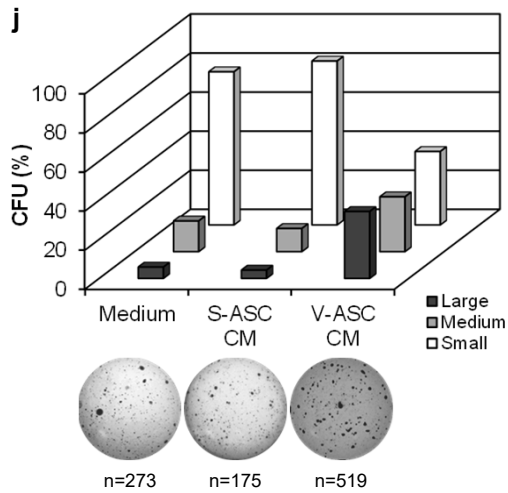
Open Access This article is licensed under a Creative Commons Attribution 4.0 International License, which permits use, sharing, adaptation, distribution and reproduction in any medium or format, as long as you give appropriate credit to the original author(s) and the source, provide a link to the Creative Commons license, and indicate if changes were made. The images or other third party material in this article are included in the article's Creative Commons license, unless indicated otherwise in a credit line to the material. If material is not included in the article's Creative Commons license and your intended use is not permitted by statutory regulation or exceeds the permitted use, you will need to obtain permission directly from the copyright holder. To view a copy of this license, visit <http://creativecommons.org/licenses/by/4.0/>.

© The Author(s) 2021

a

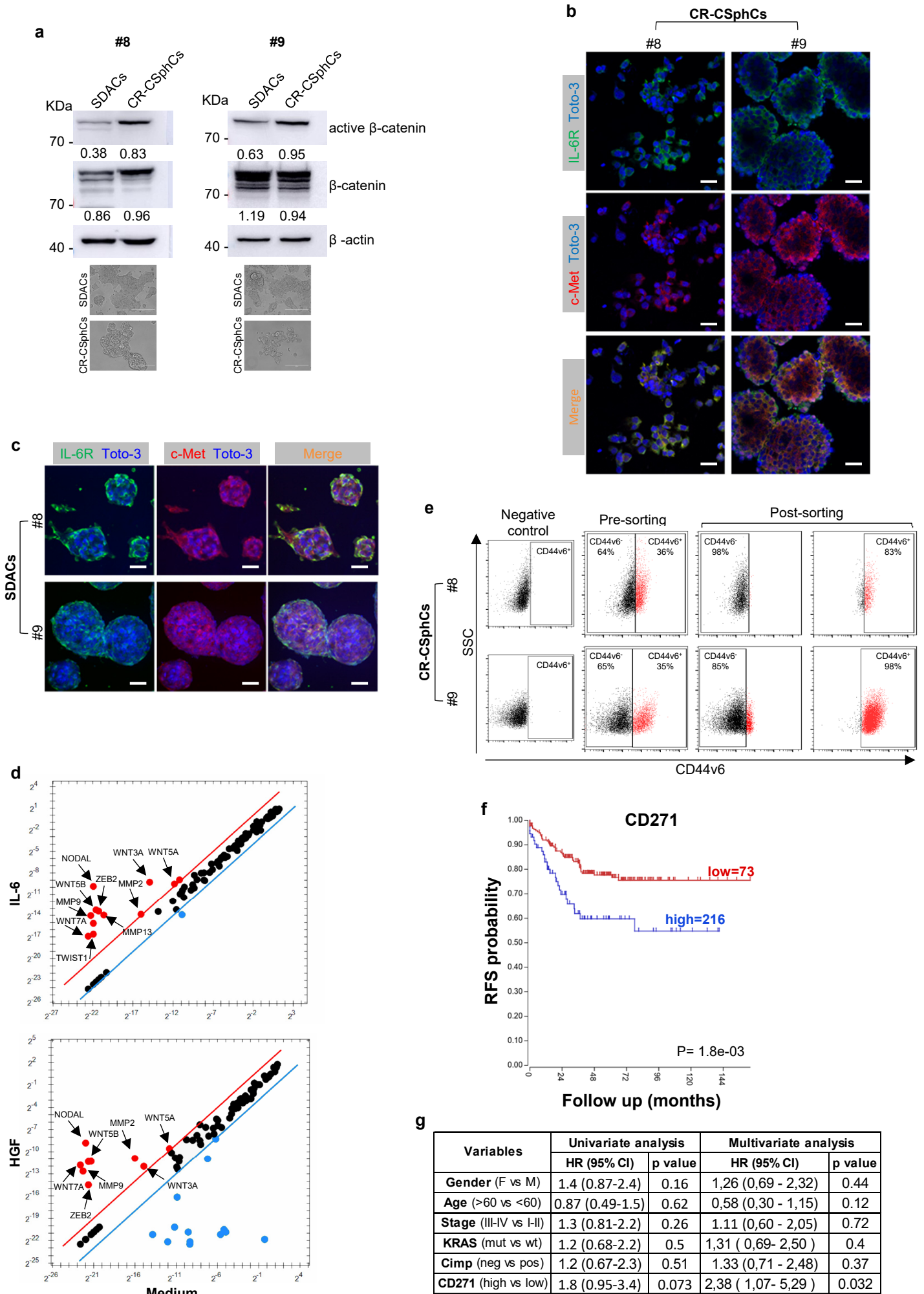
Variables	Univariate analysis			Multivariate analysis		
	Patients #	HR (95% CI for HR)	p value	Patients #	HR (95% CI for HR)	p value
BMI (>=30 vs >18.5 & <30)	511	1.8 (1.3-2.4)	0.00012	341	1.82 (1.3 - 2.6)	0.00094
Stage (3-4 vs 1-2)	488	2.3 (1.7-3.1)	3.10E-07		3 (2.1 - 4.4)	8.50E-09
Curative Surgery (1 vs 0)	360	0.19 (0.1-0.36)	5.20E-07		0.109 (0.055 - 0.21)	1.80E-10
Adjuvant Regimen (1 vs 0)	356	1.3 (0.95-1.8)	0.097		0.887 (0.62 - 1.3)	0.51





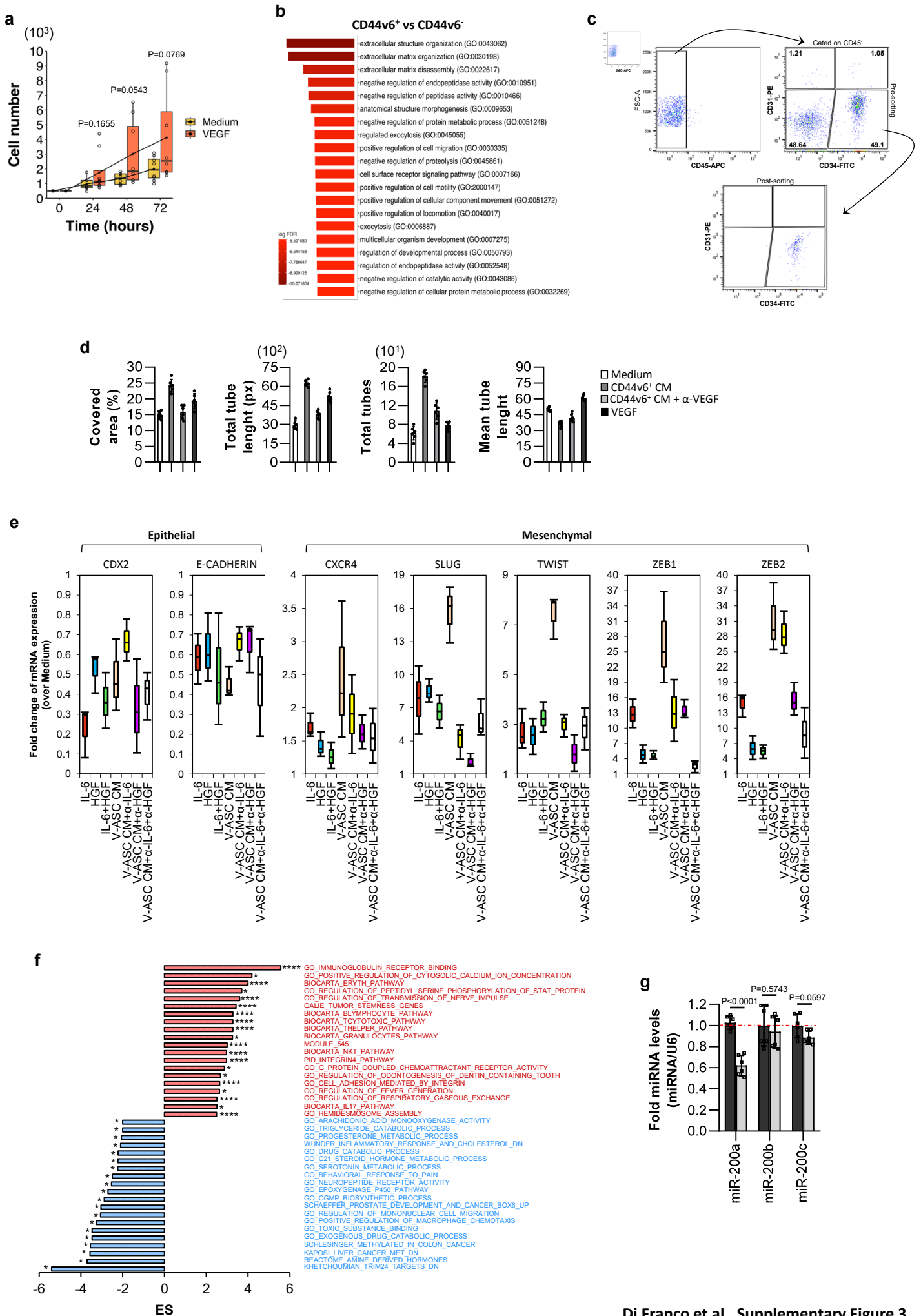
Supplementary Fig. 1. V-ASCs sustain the metastatic potential of CR-CSphCs.

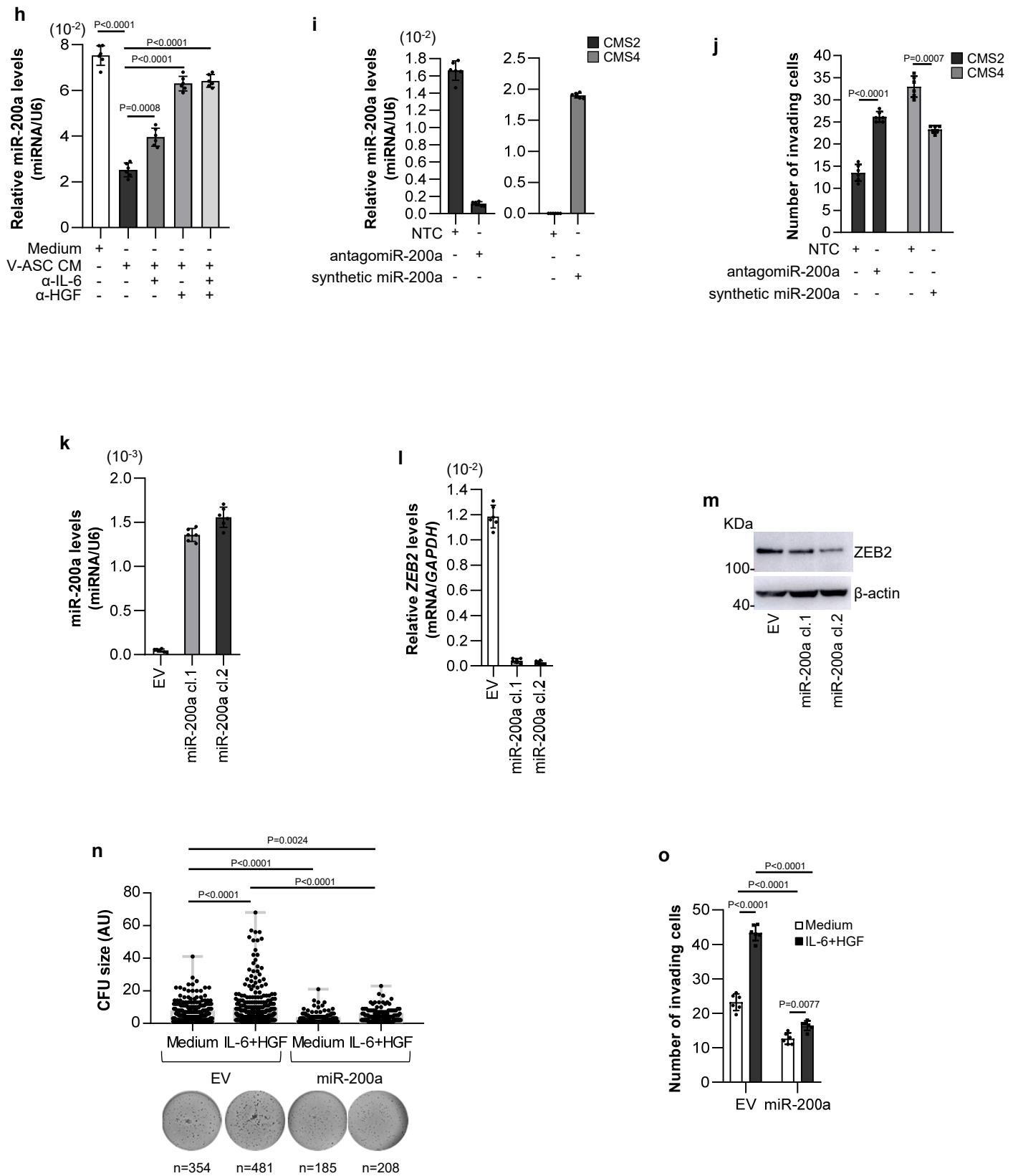
a, Univariate and multivariate analysis of progression free survival (PFS) according to regression Cox model in CRC patients. Statistical significance was calculated using the Wald test. **b**, Kaplan-Meier PFS curves in stage III CRC patients, based on BMI status. Healthy weight indicates $18,5 < \text{BMI} < 30$, and obesity $\text{BMI} > 30$. Statistical significance was calculated using the log-rank (Mantel–Cox) test. **c**, Immunohistochemical analysis of adiponectin and CDX2 on primary and liver metastasis tissue specimens from CRC patients with obesity. One representative of 9 independent experiments is shown. Scale bars, 100 μm . **d**, Percentage of adipose tissue (AT) area based on adiponectin positivity, evaluated in primary tumor and liver metastasis as in (c). **e**, Number of $\text{CD34}^+/\text{CD31}^-/\text{CD45}^-$ and $\text{CD34}^+/\text{CD31}^+/\text{CD45}^-$ cells on primary and liver metastasis CRC from patients with healthy weight or affected by obesity. For (d, e) data are mean \pm standard error of 9 independent experiments. **f**, Mesenchymal stem cell and endothelial (CD31, CD34) marker expression in ASCs isolated from subcutaneous (S-ASCs; $n=13$) and visceral (V-ASCs; $n=10$) adipose tissue. **g**, Immunofluorescence analysis of WT1 expression in S-ASCs or V-ASCs. Yellow arrow heads indicate ASCs with nuclear localization of WT1. Scale bars, 40 μm . Data are representative of experiments performed in 12 S-ASCs and 10 V-ASCs. **h**, Adipocyte differentiation of S-ASCs or V-ASCs. Data are mean \pm S.D. of 4 independent experiments using 3 different S-ASC and V-ASC cultures. **i**, Phase contrast and fluorescence analysis of lipid droplets content in cells as indicated. Scale bars, 100 μm . One representative of 4 independent experiments is shown. **j**, Colony forming assay of CR-CSphCs treated as indicated. n represents number of colonies. **k**, Size of subcutaneous tumor xenografts at the indicated time points generated by injection of CR-CSphCs alone or together with S-ASC or V-ASCs. **l**, Immunohistochemical analysis of CK20 (brown) and ki67 (red) of tumor xenografts generated by subcutaneous injection of cells as in (k) (*upper panel*). Percentage of $\text{ki67}^+/\text{CK20}^+$ cells in tumor xenografts. **m**, Invasion assay of CR-CSphCs treated as indicated for 48 hours (*lower panel*). **n**, GFP expression of transduced LUC-GFP S-ASCs and V-ASCs. Scale bars, 500 μm . One representative of 3 independent experiments is shown. **o**, Whole body *in vivo* imaging analysis 30 minutes after intrasplenic injection of ASCs transduced with LUC-GFP. **p**, Kinetics of *in vivo* whole-body imaging analysis of metastasis formation following intrasplenic injection of LUC-GFP transduced CR-CSphCs alone and together with S-ASCs or V-ASCs at the indicated time points. Bioluminescence signal of isolated organs was detected after splenectomy at the indicated time. Red dotted line indicates the area of photons quantification. For (j-m, and p) data are mean \pm SD of 6 independent experiments using 4 different CR-CSphC lines (#1, #8, #9 and #21). **q**, H&E analysis of liver and lung metastases derived from tumor xenografts generated by intrasplenic injection of indicated cells. Scale bars, 200 μm . Li: liver; Lu: lungs; T: tumor. For (o-q) one representative of 6 independent experiments is shown. Statistical significance between 2 groups was determined by unpaired Student's t-test (2-tailed).



Supplementary Fig. 2. CRC spheres and their derived adherent cells express IL-6R and c-Met.

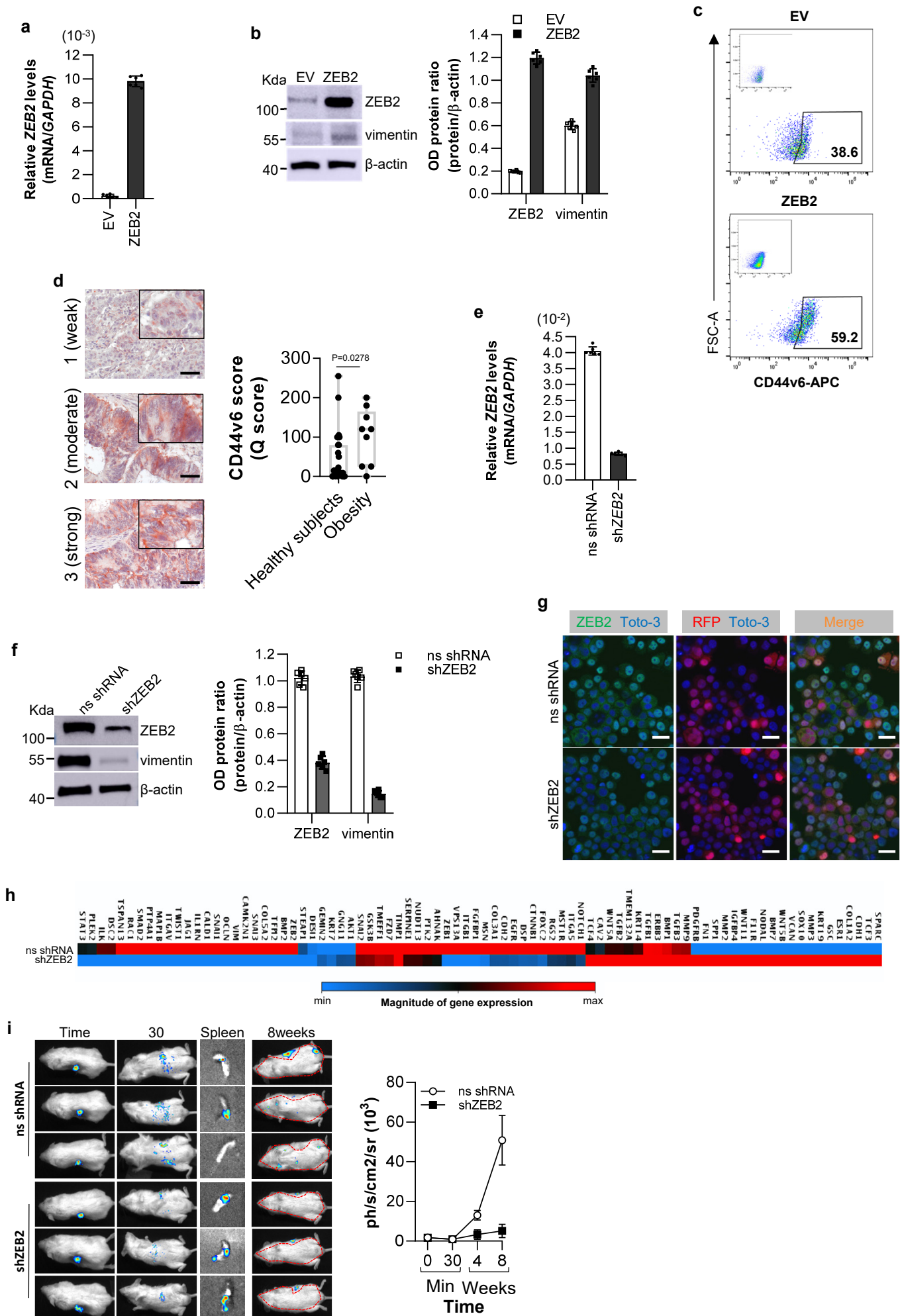
a, Immunoblot analysis of non phospho active and total β -catenin in CMS2 CR-CSphCs (#8 and #9) and sphere-derived adherent cells (SDACs). β -actin was used as loading control (*upper panel*). Samples were run on the same gel and images were cropped only for the purpose of this figure. Source data are provided as a Source Data file. Representative phase contrast analysis of cell morphology in CMS2 CR-CSphCs (#8 and #9) and sphere-derived adherent cells (SDACs). Scale bars, 200 μ m (*lower panel*). **b**, Immunofluorescence analysis of IL-6R and c-Met in CMS2 CR-CSphCs (CSphC #8, #9). Nuclei were counterstained with Toto-3. **c**, Immunofluorescence analysis of IL-6R and c-Met in CMS2 SDACs (#8, #9). For (a-c) data are representative of 4 independent experiments. For (b-c) scale bar, 40 μ m. **d**, Stemness-related genes in CMS2 CR-CSphCs (#8, #9) treated with vehicle (Medium), IL-6 or HGF for 48 hours. Black arrows indicate up- (red) and down- (blue) regulated genes. *GAPDH* and *HPRT1* were used as housekeeping control genes. **e**, Flow cytometry profiles of CD44v6 in CD44v6⁻ and CD44v6⁺ sorted CR-CSphCs (CSphC #8, #9). Gating strategy to sort CD44v6⁻ and CD44v6⁺ CR-CSphCs used on the *in vitro* assays presented on Fig. 2j-m. **f**, Relapse-free survival (RFS) rate of CMS2 CRC patients according to CD271 expression levels. Statistical significance was calculated using the log-rank (Mantel–Cox) test. **g**, Univariate and multivariate analysis of relapse free survival (RFS) according to regression Cox model in CRC patients as in (f). Statistical significance was calculated using the Wald test.





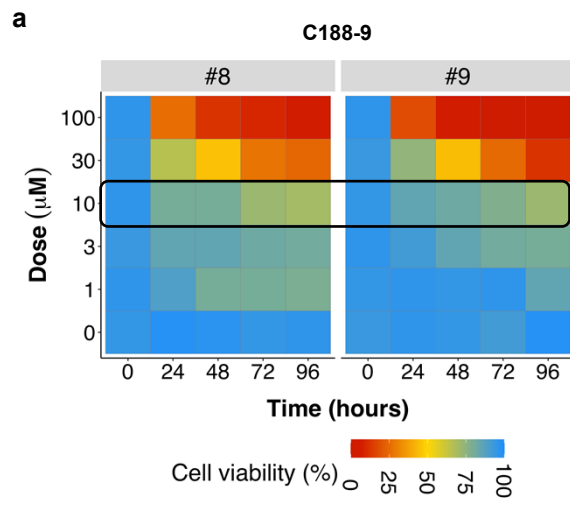
Supplementary Fig. 3. Adipokines down-regulate miR-200a improving clonogenic and invasive activity of CR-CSphCs

a, Box and whiskers plot showing cell growth of 8 different ASCs treated as indicated. Box and whiskers show min-to-max values, with line indicating the median value, and the connecting lines indicating the mean values of 8 independent experiments. Statistical significance was calculated using two-tailed paired nonparametric Mann–Whitney test. **b**, Top twenty significantly enriched gene sets from PANTHER (GO biological process annotation) (FDR p -value ≤ 0.05) identified through the analysis of differentially expressed genes in CR-CSphCs (#1, #8, #9, #21). **c**, Gating strategy to sort CD31⁻/CD34⁺/CD45⁻ ASCs used on the *in vitro* endothelial-differentiation assay presented on Fig. 3d. **d**, Tube formation assay analysis of Huvec cells exposed to vehicle (Medium), CM derived from CD44v6⁺ CR-CSCs (#1, #8, #9, #21), in presence or absence of VEGF neutralizing antibody, or VEGF for 16 hours. **e**, Boxplot of epithelial and markers expression in CMS2 cells treated as indicated for 48 hours. Box and whiskers show min-to-max values, with line indicating the mean value. **f**, Up- (red) and down- (blue) regulated signaling pathways, computed by GSEA, in CMS2 CR-CSphCs (#8, #9) treated with V-ASC conditioned medium. **g**, miR-200 family members expression in CMS2 CR-CSphCs (#8, #9) following treatment with V-ASC CM. **h**, miR-200a expression levels in CMS2 CR-CSphCs (#8, #9) treated as indicated. **i**, miR-200a expression levels in CMS2 (#8, #9) and CMS4 CR-CSphCs (#1, #21) transfected with antagomiR-200a or synthetic miR-200a, respectively. **j**, Invasion assay of CMS2 (#8, #9) and CMS4 (#1, #21) CR-CSphCs as indicated. **k**, miR-200a expression in CR-CSphCs (#1, #21) transduced with EV or miR-200a. **l**, ZEB2 expression levels in CR-CSphCs (#1, #21) transduced as indicated. **m**, Immunoblot analysis of ZEB2 in CMS4 CR-CSphCs (#1, #21) transduced as in (k). β -actin was used as loading control. One representative of 6 independent experiments is shown. Samples were run on the same gel and images were cropped only for the purpose of this figure. Source data are provided as a Source Data file. **n**, Colony forming assay of CMS2 CR-CSphCs transduced with empty vector (EV) or cl.2 miR-200a and treated as indicated, at 21 days. Data represent mean \pm S.D. of colony size performed in 4 independent experiments using 2 different CR-CSphC lines (#8, #9). n represents the number of colonies. Statistical significance was calculated using two-tailed nonparametric Mann–Whitney test. **o**, Number of invading CMS2 (#8, #9) and CMS4 (#1, #21) CR-CSphCs transduced as in (n) and treated as indicated. For (d, g-l and o) data are shown as mean \pm S.D. of 6 independent experiments. Statistical significance between 2 groups was determined by unpaired Student's t-test (2-tailed). **** $p \leq 0.0001$; * $p \leq 0.05$.

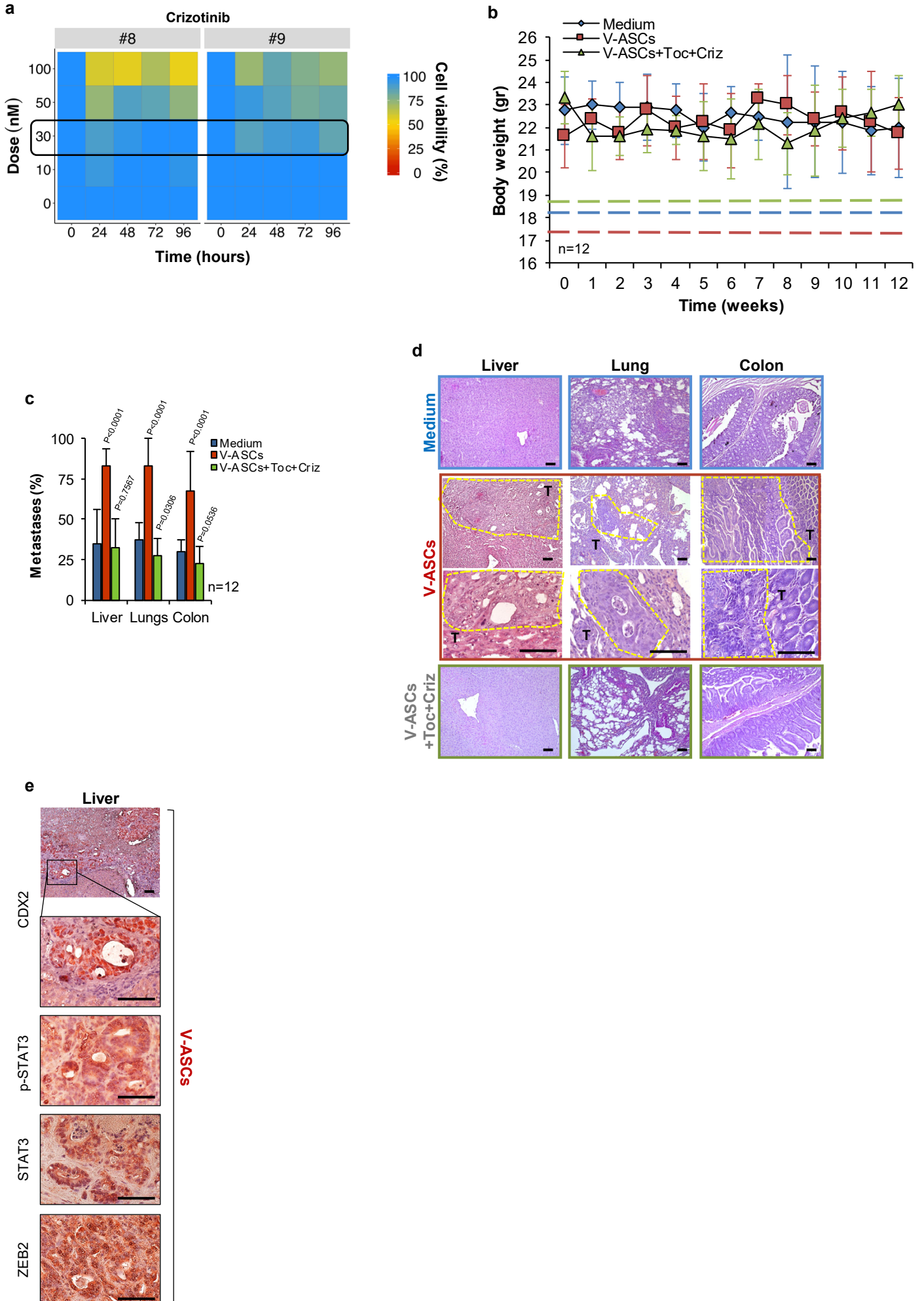


Supplementary Fig. 4. ZEB2 is crucial for CRC metastasis formation

a, ZEB2 expression in CMS2 CR-CSphCs (CSphC #8, #9) transduced with EV or ZEB2. *GAPDH* was used as housekeeping control gene. **b**, Immunoblot analysis of ZEB2 and vimentin expression in CR-CSphCs (CSphC #8, #9) transduced as indicated. β -actin was used as loading control. Samples were run on the same gel and images were cropped only for the purpose of this figure. Source data are provided as a Source Data file. **c**, Representative flow cytometry analysis of CD44v6 on CR-CSphCs transduced with empty vector (EV) or ZEB2. **d**, Immunohistochemical analysis of CD44v6 on CRC tissue with weak (1), moderate (2), and strong (3) staining intensity. Scale bars represent 100 μ m. CD44v6 score (Q score = percentage of positive cells (P) x intensity (I) in) CRC patients with healthy weight (n=28) and obesity (n=9). Box and whiskers show min-to-max values, with line indicating the mean value. **e**, *ZEB2* expression levels in CMS4 CR-CSphCs (CSphC #1, #21) transduced with inducible nonsilencing (ns) shRNA control, or ZEB2 shRNA, following 72 hours of exposure to doxycycline. *GAPDH* was used as housekeeping control gene. **f**, Immunoblot analysis of ZEB2 and vimentin in cells transduced as in (c). β -actin was used as loading control. Samples were run on the same gel and images were cropped only for the purpose of this figure. Source data are provided as a Source Data file. For (a-b and e-f) data represent mean \pm S.D. of 6 independent experiments. **g**, Immunofluorescence analysis of ZEB2 in RFP tagged CR-CSphCs (CSphC #1, #21) transduced as indicated. Scale bars, 40 μ m. One representative of 6 independent experiments is shown. **h**, Heatmap of EMT-related genes in CMS4 CR-CSphCs (CSphC #1, #21) transduced as indicated. Data are mean of 3 independent experiments. **i**, Whole body *in vivo* imaging analysis of mice (n=6) intrasplenically injected with CMS4 CR-CSphCs (CSphC #1, #21) transduced as indicated, at 8 weeks after splenectomy. Spleen was removed 30 minutes after cell injection. Red dotted line indicates the area of photons quantification. (*right panel*) Luciferase signal measured as photons per second that leave a square centimeter of tissue and radiate into a solid angle of one steradian (ph/s/cm²/sr). One representative of 6 independent experiments is shown. Statistical significance between 2 groups was determined by unpaired Student's t-test (2-tailed).



Supplementary Fig. 5. STAT-3 is activated in the proximity of VAT in CRC patients with obesity
a, Heatmap matrix of CMS2 CR-CSphC (CSphC #8, 9) viability following treatment with dose-escalation of STAT3 inhibitor (C188-9), at the indicated time points. Black boxes indicate the selected concentration for *in vitro* studies.

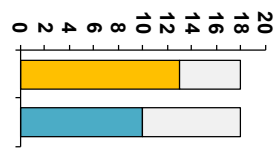


Supplementary Fig. 6. IL-6R and c-Met blockade prevents the metastasis formation of CR-CSphCs induced by VAT.

a, Heatmap matrix of CMS2 CR-CSphC (CSphC #8, 9) viability following treatment with dose-escalation of crizotinib, at the indicated time points. Black boxes indicate the selected concentration for *in vitro* studies. **b**, Kinetics of body weight variation in mice following intrasplenic injection of LUC-GFP CMS2 CR-CSphCs (#8, 9) alone (Medium) or co-injected with V-ASCs, at the indicated time points. Mice were treated i.p. with tocilizumab (Toc) and crizotinib (Criz). Dotted lines represent the maximum tolerated reduction in body weight, measured as 80% of basal weight of mice belonging to each treatment group. Data are mean of 12 independent experiments in mice treated as indicated. **c**, Metastasis formation in mice treated as indicated, 9 weeks after treatment suspension. **d**, H&E analysis of liver, lung and colon metastatic lesions derived from mice treated as indicated. Scale bars, 200 μ m. T: tumor. **e**, Representative immunohistochemical analysis of CDX2, p-STAT3, STAT3, and ZEB2 in paraffin-embedded sections of tumor xenograft specimens of CRC liver metastasis in mice intrasplenically co-injected with CR-CSphCs and V-ASCs. Scale bars, 100 μ m. For (d-e) one representative of 12 independent experiments is shown. Statistical significance between 2 groups was determined by unpaired Student's t-test (2-tailed).

Supplementary Table 1. Human primary ASC cell lines

ASC #	2	3	4	5	6	7	8	9	10	11	12	13	14	16	17	18	20	21
Subcutaneous								N/A	N/A	N/A	N/A					N/A		
Visceral	N/A		N/A			N/A						N/A		N/A	N/A		N/A	N/A
BMI	43	25	25	28	24	25	21	26	24	61	N/A	21	30	N/A	30	20	23	24



Supplementary Table 3. Primer sequences and source.

Gene Symbol	Primer sequence/Catalog #	Source
<i>NGF</i>	Cat. # PPH00205F	Qiagen
<i>BDNF</i>	Cat. # PPH00569F	Qiagen
<i>NTF3</i>	Cat. # PPH00687A	Qiagen
<i>NTF4</i>	Cat. # PPH01123A	Qiagen
<i>ZEB1</i>	Cat. # PPH01922A	Qiagen
<i>ZEB2</i>	Cat. # PPH09021B	Qiagen
<i>CDX2</i>	Fwd: 5-TTCACTACAGTCGCTACATCACC-3 Rev: 5-TTGTTGATTTTCCTCCTCTTGC-3	Metabion
<i>E-CADHERIN</i>	Fwd: 5-TGGAGGAATTCTTGCTTTGC-3 Rev: 5-CGCTCCTCCGAAGAAAC-3	Metabion
<i>CXCR4</i>	Fwd: 5-AGCATGACGGACAAGTACAGG-3 Rev: 5-GATGAAGTCGGGAATAGTCAGC-3	Metabion
<i>FRMD6</i>	Fwd: 5-GGACACTCTGGGTTGATTGTG-3 Rev: 5-TGTGTCGATCAGTGGAGGTC-3	Metabion
<i>N-CADHERIN</i>	Fwd: 5-ACAGTGGCCACCTACAAAGG-3 Rev: 5-CCGAGATGGGGTTGATAATG-3	Metabion
<i>SLUG</i>	Fwd: 5-GGTCAAGAAGCATTCAACG-3 Rev: 5-CACAGTGATGGGGCTGTATG-3	Metabion
<i>SNAIL</i>	Fwd: 5-GGGAATTCTATGCCGCGCTCTTTCCTCGTC-3 Rev: 5-GGGGATCCTCAGCGGGGACATCCTGAGCAG-3	Metabion
<i>TWIST</i>	Fwd: 5-GGCATCACTATGGACTTTCTCTATT-3 Rev: 5-GGCCAGTTTGATCCCAGTATT-3	Metabion
<i>VIMENTIN</i>	Fwd: 5-TTCCTGGGCTACGACCATAC-3 Rev: 5-TGTGCTCCATCAAGCAATTC-3	Metabion
<i>GAPDH</i>	Fwd: 5-GCT TCG CTC TCT GCT CCT CCT GT-3 Rev: 5-TAC GAC CAA ATC CGT TGA CTC CG-3	Metabion

4. CONCLUSIONS

Despite significant efforts have been made in improving cancer patients' outcome, the survival of CRC patients is still poor. Chemo-resistance is one of the main hurdles in cancer therapy and CSCs play a crucial role in this event. For this reason, they are subject of intense research work that aims at better understanding of its behavior and at the development of efficacious targeted therapies. Promising strategies for the cancer treatment include: the targeting of CSCs-specific features, using small molecule inhibitors, epigenetic therapies, the targeting of CSC microenvironment and the induction of a differentiated state.

The deregulation of different epigenetic pathways affects gene expression patterns correlated with cell proliferation and survival. In addition, various epigenetic alterations regulate the maintenance of CSCs. The lysine methyltransferase SETD8 and the DNA methyltransferase 1 have a critical role in different tumours. Nevertheless, the role of SETD8 in CRC is incompletely understood and it has not been intensively studied. Their inhibition could be an effective approach to the CSCs targeting. However, the limited *in vivo* stability of the DNMT1 inhibitor decitabine, represents a strong limitation for its administration. We showed the effectiveness of the use of UNC0379, an inhibitor of SETD8, in tumour treatment and in CSCs targeting.

Proteins belonging to the bone morphogenetic protein family (BMP) have the ability to promote the differentiation of CSCs. Among these, we have identified a variant of BMP7 characterized by improved stability and solubility (BMP7v), which sensitizes CRC and CSCs to chemotherapy and recapitulate a gene expression profile related to cell differentiation. Furthermore, we have shown that treatment with BMP7v makes CSCs also sensitive to targeted therapies (**Chapter 1**). Moreover, in recent years, scientific research has focused on the various mechanisms responsible for the development of resistance to therapies, including the genetic heterogeneity and the activation of alternative survival signaling pathways. The EGFR is the main target identified in the treatment of CRC. The treatment with anti-EGFR antibodies combined to chemotherapy is currently the most effective therapy for metastatic CRC RAS wt. However, the therapeutic response is temporary and limited to a small number of patients. Activation of alternative signaling pathways downstream or parallel to MAPK pathway is involved in the inefficacy of anti-EGFR treatment. We have shown that CSCs CD44v6 positive, express high levels of HER2 and are resistant to therapy with cetuximab, a monoclonal antibody directed against EGFR. CSCs CD44v6⁺ exhibit activation of the PI3K signaling pathway, which is associated with transcriptional regulation of ERBB2 in CSCs CD44v6⁺. The targeting of HER2, MEK and PI3K determines the cell death of CSCs and the

regression of tumors resistant to anti-EGFR therapy, including those with the mutation in KRAS and PIK3CA. Furthermore, this combinatorial treatment is able to induce cell death of CR-CSCs and tumor regression, even in presence of cytokines released by tumor-associated fibroblasts (**Chapter 2**). Furthermore, CSCs show a higher expression of the MAPK p38 α and are dependent on its kinase activity. We have shown that the p38 α inhibitor ralimetinib causes increased sensitization of CSCs to chemotherapeutic agents commonly used for the treatment of CRC, and exhibits a synthetic lethality effect when used in combination with the MEK inhibitor, trametinib. The protein p38 α represents a further example of a targeted treatment for CSCs (**Chapter 3**).

In recent years, there has been a growing interest in the use of natural compounds in the treatment of tumors. This interest is mainly derived from their availability and their low toxicity. Alkaloids have represented a very important source for the development of compounds with therapeutic purposes. Among these, particular interest was given to nortopsentin, whose analogues showed a great anti-proliferative activity against different human tumor cell lines.

We evaluated the biological activity of the neosynthetic alkaloid NORA234 in the treatment of CR-CSCs. NORA234 causes an initial reduction in the proliferation and clonogenic potential of CSCs, followed by an adaptive response that selects resistant clones that express high levels of CD44v6 and have a constitutive activation of the Wnt signaling pathway. Furthermore, NORA234 causes genotoxic stress, cell cycle arrest in the G2-M phase and activation of CHK1 (Checkpoint kinase 1), promoting DNA damage repair in CSCs. The combination of NORA234 and rabusertib, the CHK1 inhibitor, induces the death of both CD44v6⁻ and CD44v6⁺ (**Chapter 4**). We also evaluated the anticancer properties of natural flavonoids, polymethoxyflavones and prenylflavonoids, extracted from *Citrus sinensis* and *Humulus lupulus*, respectively. The fractions of the natural extracts, individually and in combination, reduced the cellular vitality of CSCs and improved the efficacy of chemotherapy with 5-Fluorouracil and oxaliplatin. Furthermore, the combination of the two extracts resulted in a reduction of the expression of the marker CD44v6 and in the inhibition of the Wnt signaling pathway (**Chapter 5**).

Another promising therapeutic strategy for CSCs eradication is the targeting of the tumor microenvironment. The interaction of CSCs with this tumor niche is essential for the growth, maintenance and differentiation of CSCs. The tumor microenvironment associated with obesity is a strong risk factor for cancer progression. We have shown that IL-6 and HGF produced by stromal cells of tumor visceral adipose tissue promote the expansion of the compartment of metastatic colorectal cancer cells (CD44v6⁺), which in turn secrete neurotrophins that recruit adipose stem cells within the tumor mass. We have shown that fat-derived factors promote metastatic dissemination. Finally, we have observed that the paracrine effect of visceral adipose tissue induces

a transition in the gene expression profile of CSCs from an epithelial type subtype (consensus molecular subtype, CMS2) to a mesenchymal subtype (CMS4). Therefore, the targeting of the factors produced by fat in obese patients with CRC could represent a therapeutic strategy to prevent metastatic disease (**Chapter 6**).

5. REFERENCES

- AMADO, R. G., WOLF, M., PEETERS, M., VAN CUTSEM, E., SIENA, S., FREEMAN, D. J., JUAN, T., SIKORSKI, R., SUGGS, S., RADINSKY, R., PATTERSON, S. D. & CHANG, D. D. 2008. Wild-type KRAS is required for panitumumab efficacy in patients with metastatic colorectal cancer. *J Clin Oncol*, 26, 1626-34.
- AVGUSTINOVA, A. & BENITAH, S. A. 2016. The epigenetics of tumour initiation: cancer stem cells and their chromatin. *Curr Opin Genet Dev*, 36, 8-15.
- BARKER, N., RIDGWAY, R. A., VAN ES, J. H., VAN DE WETERING, M., BEGTHEL, H., VAN DEN BORN, M., DANENBERG, E., CLARKE, A. R., SANSOM, O. J. & CLEVERS, H. 2009. Crypt stem cells as the cells-of-origin of intestinal cancer. *Nature*, 457, 608-11.
- BARKER, N., VAN ES, J. H., KUIPERS, J., KUJALA, P., VAN DEN BORN, M., COZIJNSEN, M., HAEGEBARTH, A., KORVING, J., BEGTHEL, H., PETERS, P. J. & CLEVERS, H. 2007. Identification of stem cells in small intestine and colon by marker gene Lgr5. *Nature*, 449, 1003-7.
- BAYLIN, S. B. & JONES, P. A. 2011. A decade of exploring the cancer epigenome - biological and translational implications. *Nat Rev Cancer*, 11, 726-34.
- BENSON, A. B., VENOOK, A. P., AL-HAWARY, M. M., ARAIN, M. A., CHEN, Y. J., CIOMBOR, K. K., COHEN, S., COOPER, H. S., DEMING, D., FARKAS, L., GARRIDO-LAGUNA, I., GREM, J. L., GUNN, A., HECHT, J. R., HOFFE, S., HUBBARD, J., HUNT, S., JOHUNG, K. L., KIRILCUK, N., KRISHNAMURTHI, S., MESSERSMITH, W. A., MEYERHARDT, J., MILLER, E. D., MULCAHY, M. F., NURKIN, S., OVERMAN, M. J., PARIKH, A., PATEL, H., PEDERSEN, K., SALTZ, L., SCHNEIDER, C., SHIBATA, D., SKIBBER, J. M., SOFOCLEOUS, C. T., STOFFEL, E. M., STOTSKY-HIMELFARB, E., WILLETT, C. G., GREGORY, K. M. & GURSKI, L. A. 2021. Colon Cancer, Version 2.2021, NCCN Clinical Practice Guidelines in Oncology. *J Natl Compr Canc Netw*, 19, 329-359.
- BERLIN, J., BENDELL, J. C., HART, L. L., FIRDAUS, I., GORE, I., HERMANN, R. C., MULCAHY, M. F., ZALUPSKI, M. M., MACKAY, H. M., YAUCH, R. L., GRAHAM, R. A., BRAY, G. L. & LOW, J. A. 2013. A randomized phase II trial of vismodegib versus placebo with FOLFOX or FOLFIRI and bevacizumab in patients with previously untreated metastatic colorectal cancer. *Clin Cancer Res*, 19, 258-67.
- BERTOTTI, A., PAPP, E., JONES, S., ADLEFF, V., ANAGNOSTOU, V., LUPO, B., SAUSEN, M., PHALLEN, J., HRUBAN, C. A., TOKHEIM, C., NIKNAFS, N., NESSELBUSH, M., LYTLE, K., SASSI, F., COTTINO, F., MIGLIARDI, G., ZANELLA, E. R., RIBERO, D., RUSSOLILLO, N., MELLANO, A., MURATORE, A., PARALUPPI, G., SALIZZONI, M., MARSONI, S., KRAGH, M., LANTTO, J., CASSINGENA, A., LI, Q. K., KARCHIN, R., SCHARPF, R., SARTORE-BIANCHI, A., SIENA, S., DIAZ, L. A., JR., TRUSOLINO, L. & VELCULESCU, V. E. 2015. The genomic landscape of response to EGFR blockade in colorectal cancer. *Nature*, 526, 263-7.
- BHASKARAN, K., DOS-SANTOS-SILVA, I., LEON, D. A., DOUGLAS, I. J. & SMEETH, L. 2018. Association of BMI with overall and cause-specific mortality: a population-based cohort study of 3.6 million adults in the UK. *Lancet Diabetes Endocrinol*, 6, 944-953.
- BLANPAIN, C., HORSLEY, V. & FUCHS, E. 2007. Epithelial stem cells: turning over new leaves. *Cell*, 128, 445-58.
- BOLAND, C. R. & GOEL, A. 2010. Microsatellite instability in colorectal cancer. *Gastroenterology*, 138, 2073-2087 e3.
- BONNET, D. & DICK, J. E. 1997. Human acute myeloid leukemia is organized as a hierarchy that originates from a primitive hematopoietic cell. *Nat Med*, 3, 730-7.
- BUROCK, S., DAUM, S., KEILHOLZ, U., NEUMANN, K., WALTHER, W. & STEIN, U. 2018. Phase II trial to investigate the safety and efficacy of orally applied niclosamide in patients with metachronous or synchronous metastases of a colorectal cancer progressing after therapy: the NIKOLO trial. *BMC Cancer*, 18, 297.
- CACHEUX, W., LIEVRE, A., RICHON, S., VACHER, S., EL ALAM, E., BRIAUX, A., EL BOTTY, R., MARIANI, P., BUECHER, B., SCHNITZLER, A., BARBAZAN, J., ROMAN-ROMAN, S., BIECHE, I. & DANGLES-MARIE, V. 2019. Interaction between IGF2-PI3K axis and cancer-associated-fibroblasts promotes anal squamous carcinogenesis. *Int J Cancer*, 145, 1852-1859.

- CANCER GENOME ATLAS, N. 2012. Comprehensive molecular characterization of human colon and rectal cancer. *Nature*, 487, 330-7.
- CARBONE, A. 2020. Cancer Classification at the Crossroads. *Cancers (Basel)*, 12.
- CEDAR, H. & BERGMAN, Y. 2009. Linking DNA methylation and histone modification: patterns and paradigms. *Nat Rev Genet*, 10, 295-304.
- CHANG, W. W. & LEBLOND, C. P. 1971. Renewal of the epithelium in the descending colon of the mouse. I. Presence of three cell populations: vacuolated-columnar, mucous and argentaffin. *Am J Anat*, 131, 73-99.
- CHEN, D., JI, X., HARRIS, M. A., FENG, J. Q., KARSENTY, G., CELESTE, A. J., ROSEN, V., MUNDY, G. R. & HARRIS, S. E. 1998. Differential roles for bone morphogenetic protein (BMP) receptor type IB and IA in differentiation and specification of mesenchymal precursor cells to osteoblast and adipocyte lineages. *J Cell Biol*, 142, 295-305.
- CLARA, J. A., MONGE, C., YANG, Y. & TAKEBE, N. 2020. Targeting signalling pathways and the immune microenvironment of cancer stem cells - a clinical update. *Nat Rev Clin Oncol*, 17, 204-232.
- CLEVERS, H. 2006. Wnt/beta-catenin signaling in development and disease. *Cell*, 127, 469-80.
- COLLINS, A. T., BERRY, P. A., HYDE, C., STOWER, M. J. & MAITLAND, N. J. 2005. Prospective identification of tumorigenic prostate cancer stem cells. *Cancer Res*, 65, 10946-51.
- COLYN, L., BARCENA-VARELA, M., ALVAREZ-SOLA, G., LATASA, M. U., URIARTE, I., SANTAMARIA, E., HERRANZ, J. M., SANTOS-LASO, A., ARECHEDERRA, M., RUIZ DE GAUNA, M., ASPICHUETA, P., CANALE, M., CASADEI-GARDINI, A., FRANCESCONI, M., CAROTTI, S., MORINI, S., NELSON, L. J., IRABURU, M. J., CHEN, C., SANGRO, B., MARIN, J. J. G., MARTINEZ-CHANTAR, M. L., BANALES, J. M., ARNES-BENITO, R., HUCH, M., PATINO, J. M., DAR, A. A., NOSRATI, M., OYARZABAL, J., PROSPER, F., URMAN, J., CUBERO, F. J., TRAUTWEIN, C., BERASAIN, C., FERNANDEZ-BARRENA, M. G. & AVILA, M. A. 2021. Dual Targeting of G9a and DNA Methyltransferase-1 for the Treatment of Experimental Cholangiocarcinoma. *Hepatology*, 73, 2380-2396.
- COOKE, T., REEVES, J., LANIGAN, A. & STANTON, P. 2001. HER2 as a prognostic and predictive marker for breast cancer. *Ann Oncol*, 12 Suppl 1, S23-8.
- CORCORAN, R. B., ANDRE, T., ATREYA, C. E., SCHELLENS, J. H. M., YOSHINO, T., BENDELL, J. C., HOLLEBECQUE, A., MCCREE, A. J., SIENA, S., MIDDLETON, G., MURO, K., GORDON, M. S., TABERNERO, J., YAEGER, R., O'DWYER, P. J., HUMBLET, Y., DE VOS, F., JUNG, A. S., BRASE, J. C., JAEGER, S., BETTINGER, S., MOOKERJEE, B., RANGWALA, F. & VAN CUTSEM, E. 2018. Combined BRAF, EGFR, and MEK Inhibition in Patients with BRAF(V600E)-Mutant Colorectal Cancer. *Cancer Discov*, 8, 428-443.
- CORCORAN, R. B., EBI, H., TURKE, A. B., COFFEE, E. M., NISHINO, M., COGDILL, A. P., BROWN, R. D., DELLA PELLE, P., DIAS-SANTAGATA, D., HUNG, K. E., FLAHERTY, K. T., PIRIS, A., WARGO, J. A., SETTLEMAN, J., MINO-KENUDSON, M. & ENGELMAN, J. A. 2012. EGFR-mediated re-activation of MAPK signaling contributes to insensitivity of BRAF mutant colorectal cancers to RAF inhibition with vemurafenib. *Cancer Discov*, 2, 227-35.
- CORTESE, I., MURANSKI, P., ENOSE-AKAHATA, Y., HA, S. K., SMITH, B., MONACO, M., RYSCHKEWITSCH, C., MAJOR, E. O., OHAYON, J., SCHINDLER, M. K., BECK, E., REOMA, L. B., JACOBSON, S., REICH, D. S. & NATH, A. 2019. Pembrolizumab Treatment for Progressive Multifocal Leukoencephalopathy. *N Engl J Med*, 380, 1597-1605.
- DALERBA, P., DYLLA, S. J., PARK, I. K., LIU, R., WANG, X., CHO, R. W., HOEY, T., GURNEY, A., HUANG, E. H., SIMEONE, D. M., SHELTON, A. A., PARMIANI, G., CASTELLI, C. & CLARKE, M. F. 2007. Phenotypic characterization of human colorectal cancer stem cells. *Proc Natl Acad Sci U S A*, 104, 10158-63.
- DAVIES, H., BIGNELL, G. R., COX, C., STEPHENS, P., EDKINS, S., CLEGG, S., TEAGUE, J., WOFFENDIN, H., GARNETT, M. J., BOTTOMLEY, W., DAVIS, N., DICKS, E., EWING, R., FLOYD, Y., GRAY, K., HALL, S., HAWES, R., HUGHES, J., KOSMIDOU, V., MENZIES, A., MOULD, C., PARKER, A., STEVENS, C., WATT, S., HOOPER, S., WILSON, R., JAYATILAKE, H., GUSTERSON, B. A., COOPER, C., SHIPLEY, J., HARGRAVE, D., PRITCHARD-JONES, K., MAITLAND, N., CHENEVIX-TRENCH, G., RIGGINS, G. J., BIGNER, D. D., PALMIERI, G., COSSU, A., FLANAGAN, A., NICHOLSON, A., HO, J. W., LEUNG, S. Y., YUEN, S. T., WEBER, B. L., SEIGLER, H. F., DARROW, T. L., PATERSON, H., MARAIS, R., MARSHALL, C. J.,

- WOOSTER, R., STRATTON, M. R. & FUTREAL, P. A. 2002. Mutations of the BRAF gene in human cancer. *Nature*, 417, 949-54.
- DERRIEN, T., JOHNSON, R., BUSSOTTI, G., TANZER, A., DJEBALI, S., TILGNER, H., GUERNEC, G., MARTIN, D., MERKEL, A., KNOWLES, D. G., LAGARDE, J., VEERAVALLI, L., RUAN, X., RUAN, Y., LASSMANN, T., CARNINCI, P., BROWN, J. B., LIPOVICH, L., GONZALEZ, J. M., THOMAS, M., DAVIS, C. A., SHIEKHATTAR, R., GINGERAS, T. R., HUBBARD, T. J., NOTREDAME, C., HARROW, J. & GUIGO, R. 2012. The GENCODE v7 catalog of human long noncoding RNAs: analysis of their gene structure, evolution, and expression. *Genome Res*, 22, 1775-89.
- DOUILLARD, J. Y., OLINER, K. S., SIENA, S., TABERNERO, J., BURKES, R., BARUGEL, M., HUMBLET, Y., BODOKY, G., CUNNINGHAM, D., JASSEM, J., RIVERA, F., KOCAKOVA, I., RUFF, P., BLASINSKA-MORAWIEC, M., SMAKAL, M., CANON, J. L., ROTHER, M., WILLIAMS, R., RONG, A., WIEZOREK, J., SIDHU, R. & PATTERSON, S. D. 2013. Panitumumab-FOLFOX4 treatment and RAS mutations in colorectal cancer. *N Engl J Med*, 369, 1023-34.
- DOW, L. E., O'ROURKE, K. P., SIMON, J., TSCHAHARGANEH, D. F., VAN ES, J. H., CLEVERS, H. & LOWE, S. W. 2015. Apc Restoration Promotes Cellular Differentiation and Reestablishes Crypt Homeostasis in Colorectal Cancer. *Cell*, 161, 1539-1552.
- DU, L., WANG, H., HE, L., ZHANG, J., NI, B., WANG, X., JIN, H., CAHUZAC, N., MEHRPOUR, M., LU, Y. & CHEN, Q. 2008. CD44 is of functional importance for colorectal cancer stem cells. *Clin Cancer Res*, 14, 6751-60.
- ERAMO, A., LOTTI, F., SETTE, G., PILOZZI, E., BIFFONI, M., DI VIRGILIO, A., CONTICELLO, C., RUCO, L., PESCHLE, C. & DE MARIA, R. 2008. Identification and expansion of the tumorigenic lung cancer stem cell population. *Cell Death Differ*, 15, 504-14.
- ESTELLER, M. 2007. Cancer epigenomics: DNA methylomes and histone-modification maps. *Nat Rev Genet*, 8, 286-98.
- FANG, J., FENG, Q., KETEL, C. S., WANG, H., CAO, R., XIA, L., ERDJUMENT-BROMAGE, H., TEMPST, P., SIMON, J. A. & ZHANG, Y. 2002. Purification and functional characterization of SET8, a nucleosomal histone H4-lysine 20-specific methyltransferase. *Curr Biol*, 12, 1086-99.
- FEARON, E. R. 2011. Molecular genetics of colorectal cancer. *Annu Rev Pathol*, 6, 479-507.
- FENG, J., ZHOU, Y., CAMPBELL, S. L., LE, T., LI, E., SWEATT, J. D., SILVA, A. J. & FAN, G. 2010. Dnmt1 and Dnmt3a maintain DNA methylation and regulate synaptic function in adult forebrain neurons. *Nat Neurosci*, 13, 423-30.
- FENG, K. C., GUO, Y. L., LIU, Y., DAI, H. R., WANG, Y., LV, H. Y., HUANG, J. H., YANG, Q. M. & HAN, W. D. 2017. Cocktail treatment with EGFR-specific and CD133-specific chimeric antigen receptor-modified T cells in a patient with advanced cholangiocarcinoma. *J Hematol Oncol*, 10, 4.
- FITZGERALD, A. A. & WEINER, L. M. 2020. The role of fibroblast activation protein in health and malignancy. *Cancer Metastasis Rev*, 39, 783-803.
- FLEMING, N. I., JORISSEN, R. N., MOURADOV, D., CHRISTIE, M., SAKTHIANANDESWAREN, A., PALMIERI, M., DAY, F., LI, S., TSUI, C., LIPTON, L., DESAI, J., JONES, I. T., MCLAUGHLIN, S., WARD, R. L., HAWKINS, N. J., RUSZKIEWICZ, A. R., MOORE, J., ZHU, H. J., MARIADASON, J. M., BURGESS, A. W., BUSAM, D., ZHAO, Q., STRAUSBERG, R. L., GIBBS, P. & SIEBER, O. M. 2013. SMAD2, SMAD3 and SMAD4 mutations in colorectal cancer. *Cancer Res*, 73, 725-35.
- FRIEDMAN, J. M., LIANG, G., LIU, C. C., WOLFF, E. M., TSAI, Y. C., YE, W., ZHOU, X. & JONES, P. A. 2009. The putative tumor suppressor microRNA-101 modulates the cancer epigenome by repressing the polycomb group protein EZH2. *Cancer Res*, 69, 2623-9.
- FUJIWARA, Y., IGUCHI, H., YAMAMOTO, N., HAYAMA, M., NII, M., UEDA, S., KOMURO, K., SUGIMOTO, M., VLAHOVIC, G. & KOZUKI, T. 2019. Tolerability and efficacy of durvalumab in Japanese patients with advanced solid tumors. *Cancer Sci*, 110, 1715-1723.
- GIACCHETTI, S., PERPOINT, B., ZIDANI, R., LE BAIL, N., FAGGIUOLO, R., FOCAN, C., CHOLLET, P., LLORY, J. F., LETOURNEAU, Y., COUDERT, B., BERTHEAULT-CVITKOVIC, F., LARREGAIN-FOURNIER, D., LE ROL, A., WALTER, S., ADAM, R., MISSET, J. L. & LEVI, F. 2000. Phase III multicenter randomized trial of oxaliplatin added to chronomodulated fluorouracil-leucovorin as first-line treatment of metastatic colorectal cancer. *J Clin Oncol*, 18, 136-47.
- GOLL, M. G. & BESTOR, T. H. 2005. Eukaryotic cytosine methyltransferases. *Annu Rev Biochem*, 74, 481-514.

- GOMEZ-PUERTO, M. C., IYENGAR, P. V., GARCIA DE VINUESA, A., TEN DIJKE, P. & SANCHEZ-DUFFHUES, G. 2019. Bone morphogenetic protein receptor signal transduction in human disease. *J Pathol*, 247, 9-20.
- HANAHAN, D. & COUSSENS, L. M. 2012. Accessories to the crime: functions of cells recruited to the tumor microenvironment. *Cancer Cell*, 21, 309-22.
- HANAHAN, D. & WEINBERG, R. A. 2000. The hallmarks of cancer. *Cell*, 100, 57-70.
- HANAHAN, D. & WEINBERG, R. A. 2011. Hallmarks of cancer: the next generation. *Cell*, 144, 646-74.
- HATA, K., OKANO, M., LEI, H. & LI, E. 2002. Dnmt3L cooperates with the Dnmt3 family of de novo DNA methyltransferases to establish maternal imprints in mice. *Development*, 129, 1983-93.
- HE, L. & HANNON, G. J. 2004. MicroRNAs: small RNAs with a big role in gene regulation. *Nat Rev Genet*, 5, 522-31.
- HE, X. C., ZHANG, J., TONG, W. G., TAWFIK, O., ROSS, J., SCOVILLE, D. H., TIAN, Q., ZENG, X., HE, X., WIEDEMANN, L. M., MISHINA, Y. & LI, L. 2004. BMP signaling inhibits intestinal stem cell self-renewal through suppression of Wnt-beta-catenin signaling. *Nat Genet*, 36, 1117-21.
- HEISS, M. M., MURAWA, P., KORALEWSKI, P., KUTARSKA, E., KOLESNIK, O. O., IVANCHENKO, V. V., DUDNICHENKO, A. S., ALEKNAVICIENE, B., RAZBADAUSKAS, A., GORE, M., GANEA-MOTAN, E., CIULEANU, T., WIMBERGER, P., SCHMITTEL, A., SCHMALFELDT, B., BURGESS, A., BOKEMEYER, C., LINDHOFER, H., LAHR, A. & PARSONS, S. L. 2010. The trifunctional antibody catumaxomab for the treatment of malignant ascites due to epithelial cancer: Results of a prospective randomized phase II/III trial. *Int J Cancer*, 127, 2209-21.
- HERMANN, P. C., HUBER, S. L., HERRLER, T., AICHER, A., ELLWART, J. W., GUBA, M., BRUNS, C. J. & HEESCHEN, C. 2007. Distinct populations of cancer stem cells determine tumor growth and metastatic activity in human pancreatic cancer. *Cell Stem Cell*, 1, 313-23.
- HERVIOU, L., OVEJERO, S., IZARD, F., KARMOUS-GADACHA, O., GOURZONES, C., BELLANGER, C., DE SMEDT, E., MA, A., VINCENT, L., CARTRON, G., JIN, J., DE BRUYNE, E., GRIMAUD, C., JULIEN, E. & MOREAUX, J. 2021. Targeting the methyltransferase SETD8 impairs tumor cell survival and overcomes drug resistance independently of p53 status in multiple myeloma. *Clin Epigenetics*, 13, 174.
- HODI, F. S., O'DAY, S. J., MCDERMOTT, D. F., WEBER, R. W., SOSMAN, J. A., HAANEN, J. B., GONZALEZ, R., ROBERT, C., SCHADENDORF, D., HASSEL, J. C., AKERLEY, W., VAN DEN EERTWEGH, A. J., LUTZKY, J., LORIGAN, P., VAUBEL, J. M., LINETTE, G. P., HOGG, D., OTTENSMEIER, C. H., LEBBE, C., PESCHEL, C., QUIRT, I., CLARK, J. I., WOLCHOK, J. D., WEBER, J. S., TIAN, J., YELLIN, M. J., NICHOL, G. M., HOOS, A. & URBA, W. J. 2010. Improved survival with ipilimumab in patients with metastatic melanoma. *N Engl J Med*, 363, 711-23.
- HUANG, E. H., HYNES, M. J., ZHANG, T., GINESTIER, C., DONTU, G., APPELMAN, H., FIELDS, J. Z., WICHA, M. S. & BOMAN, B. M. 2009. Aldehyde dehydrogenase 1 is a marker for normal and malignant human colonic stem cells (SC) and tracks SC overpopulation during colon tumorigenesis. *Cancer Res*, 69, 3382-9.
- INGOLD HEPPNER, B., BEHRENS, H. M., BALSCHUN, K., HAAG, J., KRUGER, S., BECKER, T. & ROCKEN, C. 2014. HER2/neu testing in primary colorectal carcinoma. *Br J Cancer*, 111, 1977-84.
- ISSA, J. P. 2004. CpG island methylator phenotype in cancer. *Nat Rev Cancer*, 4, 988-93.
- JAIR, K. W., BACHMAN, K. E., SUZUKI, H., TING, A. H., RHEE, I., YEN, R. W., BAYLIN, S. B. & SCHUEBEL, K. E. 2006. De novo CpG island methylation in human cancer cells. *Cancer Res*, 66, 682-92.
- JONES, P. A. & BAYLIN, S. B. 2002. The fundamental role of epigenetic events in cancer. *Nat Rev Genet*, 3, 415-28.
- KAMINSKAS, E., FARRELL, A., ABRAHAM, S., BAIRD, A., HSIEH, L. S., LEE, S. L., LEIGHTON, J. K., PATEL, H., RAHMAN, A., SRIDHARA, R., WANG, Y. C., PAZDUR, R. & FDA 2005. Approval summary: azacitidine for treatment of myelodysplastic syndrome subtypes. *Clin Cancer Res*, 11, 3604-8.
- KARAPETIS, C. S., KHAMBATA-FORD, S., JONKER, D. J., O'CALLAGHAN, C. J., TU, D., TEBBUTT, N. C., SIMES, R. J., CHALCHAL, H., SHAPIRO, J. D., ROBITAILLE, S., PRICE, T. J., SHEPHERD, L., AU, H. J., LANGER, C., MOORE, M. J. & ZALCBERG, J. R. 2008. K-ras mutations and benefit from cetuximab in advanced colorectal cancer. *N Engl J Med*, 359, 1757-65.

- KO, J. H., UM, J. Y., LEE, S. G., YANG, W. M., SETHI, G. & AHN, K. S. 2019. Conditioned media from adipocytes promote proliferation, migration, and invasion in melanoma and colorectal cancer cells. *J Cell Physiol*, 234, 18249-18261.
- KODACH, L. L., WIERCINSKA, E., DE MIRANDA, N. F., BLEUMING, S. A., MUSLER, A. R., PEPPELENBOSCH, M. P., DEKKER, E., VAN DEN BRINK, G. R., VAN NOESEL, C. J., MORREAU, H., HOMMES, D. W., TEN DIJKE, P., OFFERHAUS, G. J. & HARDWICK, J. C. 2008. The bone morphogenetic protein pathway is inactivated in the majority of sporadic colorectal cancers. *Gastroenterology*, 134, 1332-41.
- KOPETZ, S., DESAI, J., CHAN, E., HECHT, J. R., O'DWYER, P. J., MARU, D., MORRIS, V., JANKU, F., DASARI, A., CHUNG, W., ISSA, J. P., GIBBS, P., JAMES, B., POWIS, G., NOLOP, K. B., BHATTACHARYA, S. & SALTZ, L. 2015. Phase II Pilot Study of Vemurafenib in Patients With Metastatic BRAF-Mutated Colorectal Cancer. *J Clin Oncol*, 33, 4032-8.
- KOSINSKI, C., LI, V. S., CHAN, A. S., ZHANG, J., HO, C., TSUI, W. Y., CHAN, T. L., MIFFLIN, R. C., POWELL, D. W., YUEN, S. T., LEUNG, S. Y. & CHEN, X. 2007. Gene expression patterns of human colon tops and basal crypts and BMP antagonists as intestinal stem cell niche factors. *Proc Natl Acad Sci U S A*, 104, 15418-23.
- KOUZARIDES, T. 2007. Chromatin modifications and their function. *Cell*, 128, 693-705.
- LAPIDOT, T., SIRARD, C., VORMOOR, J., MURDOCH, B., HOANG, T., CACERES-CORTES, J., MINDEN, M., PATERSON, B., CALIGIURI, M. A. & DICK, J. E. 1994. A cell initiating human acute myeloid leukaemia after transplantation into SCID mice. *Nature*, 367, 645-8.
- LEE, S. H., CHEN, T. Y., DHAR, S. S., GU, B., CHEN, K., KIM, Y. Z., LI, W. & LEE, M. G. 2016. A feedback loop comprising PRMT7 and miR-24-2 interplays with Oct4, Nanog, Klf4 and c-Myc to regulate stemness. *Nucleic Acids Res*, 44, 10603-10618.
- LI, Z., NIE, F., WANG, S. & LI, L. 2011. Histone H4 Lys 20 monomethylation by histone methylase SET8 mediates Wnt target gene activation. *Proc Natl Acad Sci U S A*, 108, 3116-23.
- LIU, M., QIN, Y., HU, Q., LIU, W., JI, S., XU, W., FAN, G., YE, Z., ZHANG, Z., XU, X., YU, X. & ZHUO, Q. 2021. SETD8 potentiates constitutive ERK1/2 activation via epigenetically silencing DUSP10 expression in pancreatic cancer. *Cancer Lett*, 499, 265-278.
- MA, J., SUN, X., WANG, Y., CHEN, B., QIAN, L. & WANG, Y. 2019. Fibroblast-derived CXCL12 regulates PTEN expression and is associated with the proliferation and invasion of colon cancer cells via PI3k/Akt signaling. *Cell Commun Signal*, 17, 119.
- MASSAGUE, J. 2008. TGFbeta in Cancer. *Cell*, 134, 215-30.
- MCMILLAN, R. & MATSUI, W. 2012. Molecular pathways: the hedgehog signaling pathway in cancer. *Clin Cancer Res*, 18, 4883-8.
- MEINDL-BEINKER, N. M., BETGE, J., GUTTING, T., BURGERMEISTER, E., BELLE, S., ZHAN, T., SCHULTE, N., MAENZ, M., EBERT, M. P. & HAERTEL, N. 2019. A multicenter open-label phase II trial to evaluate nivolumab and ipilimumab for 2nd line therapy in elderly patients with advanced esophageal squamous cell cancer (RAMONA). *BMC Cancer*, 19, 231.
- MENG, W., WU, Y., HE, X., LIU, C., GAO, Q., GE, L., WU, L., LIU, Y., GUO, Y., LI, X., LIU, Y., CHEN, S., KONG, X., LIANG, Z. & ZHOU, H. 2014. A systems biology approach identifies effective tumor-stroma common targets for oral squamous cell carcinoma. *Cancer Res*, 74, 2306-15.
- MERCHANT, A. A. & MATSUI, W. 2010. Targeting Hedgehog--a cancer stem cell pathway. *Clin Cancer Res*, 16, 3130-40.
- MIGDEN, M. R., RISCHIN, D., SCHMULTS, C. D., GUMINSKI, A., HAUSCHILD, A., LEWIS, K. D., CHUNG, C. H., HERNANDEZ-AYA, L., LIM, A. M., CHANG, A. L. S., RABINOWITS, G., THAI, A. A., DUNN, L. A., HUGHES, B. G. M., KHUSHALANI, N. I., MODI, B., SCHADENDORF, D., GAO, B., SEEBACH, F., LI, S., LI, J., MATHIAS, M., BOOTH, J., MOHAN, K., STANKEVICH, E., BABIKER, H. M., BRANA, I., GIL-MARTIN, M., HOMSI, J., JOHNSON, M. L., MORENO, V., NIU, J., OWONIKOKO, T. K., PAPADOPOULOS, K. P., YANCOPOULOS, G. D., LOWY, I. & FURY, M. G. 2018. PD-1 Blockade with Cemiplimab in Advanced Cutaneous Squamous-Cell Carcinoma. *N Engl J Med*, 379, 341-351.
- MOTZER, R. J., PENKOV, K., HAANEN, J., RINI, B., ALBIGES, L., CAMPBELL, M. T., VENUGOPAL, B., KOLLMANNBERGER, C., NEGRIER, S., UEMURA, M., LEE, J. L., VASILIEV, A., MILLER, W. H., JR., GURNEY, H., SCHMIDINGER, M., LARKIN, J., ATKINS, M. B., BEDKE, J., ALEKSEEV, B., WANG, J., MARIANI, M., ROBBINS, P. B., CHUDNOVSKY, A., FOWST, C., HARIHARAN, S., HUANG, B., DI PIETRO,

- A. & CHOUEIRI, T. K. 2019. Avelumab plus Axitinib versus Sunitinib for Advanced Renal-Cell Carcinoma. *N Engl J Med*, 380, 1103-1115.
- NEPALI, K. & LIOU, J. P. 2021. Recent developments in epigenetic cancer therapeutics: clinical advancement and emerging trends. *J Biomed Sci*, 28, 27.
- NG, E. K., TSANG, W. P., NG, S. S., JIN, H. C., YU, J., LI, J. J., ROCKEN, C., EBERT, M. P., KWOK, T. T. & SUNG, J. J. 2009. MicroRNA-143 targets DNA methyltransferases 3A in colorectal cancer. *Br J Cancer*, 101, 699-706.
- O'BRIEN, C. A., POLLETT, A., GALLINGER, S. & DICK, J. E. 2007. A human colon cancer cell capable of initiating tumour growth in immunodeficient mice. *Nature*, 445, 106-10.
- ODA, H., OKAMOTO, I., MURPHY, N., CHU, J., PRICE, S. M., SHEN, M. M., TORRES-PADILLA, M. E., HEARD, E. & REINBERG, D. 2009. Monomethylation of histone H4-lysine 20 is involved in chromosome structure and stability and is essential for mouse development. *Mol Cell Biol*, 29, 2278-95.
- OKANO, M., BELL, D. W., HABER, D. A. & LI, E. 1999. DNA methyltransferases Dnmt3a and Dnmt3b are essential for de novo methylation and mammalian development. *Cell*, 99, 247-57.
- PARK, J., EUHUS, D. M. & SCHERER, P. E. 2011. Paracrine and endocrine effects of adipose tissue on cancer development and progression. *Endocr Rev*, 32, 550-70.
- PARK, S. Y., KIM, J. Y., CHOI, J. H., KIM, J. H., LEE, C. J., SINGH, P., SARKAR, S., BAEK, J. H. & NAM, J. S. 2019. Inhibition of LEF1-Mediated DCLK1 by Niclosamide Attenuates Colorectal Cancer Stemness. *Clin Cancer Res*, 25, 1415-1429.
- PLAKS, V., KONG, N. & WERB, Z. 2015. The cancer stem cell niche: how essential is the niche in regulating stemness of tumor cells? *Cell Stem Cell*, 16, 225-38.
- POWELL, S. M., ZILZ, N., BEAZER-BARCLAY, Y., BRYAN, T. M., HAMILTON, S. R., THIBODEAU, S. N., VOGELSTEIN, B. & KINZLER, K. W. 1992. APC mutations occur early during colorectal tumorigenesis. *Nature*, 359, 235-7.
- PRAHALLAD, A., SUN, C., HUANG, S., DI NICOLANTONIO, F., SALAZAR, R., ZECCHIN, D., BEIJERSBERGEN, R. L., BARDELLI, A. & BERNARDS, R. 2012. Unresponsiveness of colon cancer to BRAF(V600E) inhibition through feedback activation of EGFR. *Nature*, 483, 100-3.
- PRINCE, M. E., SIVANANDAN, R., KACZOROWSKI, A., WOLF, G. T., KAPLAN, M. J., DALERBA, P., WEISSMAN, I. L., CLARKE, M. F. & AILLES, L. E. 2007. Identification of a subpopulation of cells with cancer stem cell properties in head and neck squamous cell carcinoma. *Proc Natl Acad Sci U S A*, 104, 973-8.
- QUAIL, D. F. & DANNENBERG, A. J. 2019. The obese adipose tissue microenvironment in cancer development and progression. *Nat Rev Endocrinol*, 15, 139-154.
- RICCI-VITIANI, L., LOMBARDI, D. G., PILOZZI, E., BIFFONI, M., TODARO, M., PESCHLE, C. & DE MARIA, R. 2007. Identification and expansion of human colon-cancer-initiating cells. *Nature*, 445, 111-5.
- ROSEN, E. D. & SPIEGELMAN, B. M. 2014. What we talk about when we talk about fat. *Cell*, 156, 20-44.
- RUAN, H., BU, L., HU, Q., CHENG, H., LU, W. & GU, Z. 2019. Strategies of Combination Drug Delivery for Immune Checkpoint Blockades. *Adv Healthc Mater*, 8, e1801099.
- SAKAMURI, D., GLITZA, I. C., BETANCOURT CUELLAR, S. L., SUBBIAH, V., FU, S., TSIMBERIDOU, A. M., WHELER, J. J., HONG, D. S., NAING, A., FALCHOOK, G. S., FANALE, M. A., CABANILLAS, M. E. & JANKU, F. 2018. Phase I Dose-Escalation Study of Anti-CTLA-4 Antibody Ipilimumab and Lenalidomide in Patients with Advanced Cancers. *Mol Cancer Ther*, 17, 671-676.
- SAMUELS, Y., WANG, Z., BARDELLI, A., SILLIMAN, N., PTAK, J., SZABO, S., YAN, H., GAZDAR, A., POWELL, S. M., RIGGINS, G. J., WILLSON, J. K., MARKOWITZ, S., KINZLER, K. W., VOGELSTEIN, B. & VELCULESCU, V. E. 2004. High frequency of mutations of the PIK3CA gene in human cancers. *Science*, 304, 554.
- SANGIORGI, E. & CAPECCHI, M. R. 2008. Bmi1 is expressed in vivo in intestinal stem cells. *Nat Genet*, 40, 915-20.
- SARTORE-BIANCHI, A., TRUSOLINO, L., MARTINO, C., BENCARDINO, K., LONARDI, S., BERGAMO, F., ZAGONEL, V., LEONE, F., DEPETRIS, I., MARTINELLI, E., TROIANI, T., CIARDIELLO, F., RACCA, P., BERTOTTI, A., SIRAVEGNA, G., TORRI, V., AMATU, A., GHEZZI, S., MARRAPESE, G., PALMERI, L., VALTORTA, E., CASSINGENA, A., LAURICELLA, C., VANZULLI, A., REGGE, D., VERONESE, S., COMOGLIO, P. M., BARDELLI, A., MARSONI, S. & SIENA, S. 2016. Dual-targeted therapy with trastuzumab and lapatinib in treatment-refractory, KRAS codon 12/13 wild-type, HER2-positive

metastatic colorectal cancer (HERACLES): a proof-of-concept, multicentre, open-label, phase 2 trial. *Lancet Oncol*, 17, 738-746.

- SATO, T., VRIES, R. G., SNIPPERT, H. J., VAN DE WETERING, M., BARKER, N., STANGE, D. E., VAN ES, J. H., ABO, A., KUJALA, P., PETERS, P. J. & CLEVERS, H. 2009. Single Lgr5 stem cells build crypt-villus structures in vitro without a mesenchymal niche. *Nature*, 459, 262-5.
- SCHATTON, T., MURPHY, G. F., FRANK, N. Y., YAMAURA, K., WAAGA-GASSER, A. M., GASSER, M., ZHAN, Q., JORDAN, S., DUNCAN, L. M., WEISHAUPT, C., FUHLBRIGGE, R. C., KUPPER, T. S., SAYEGH, M. H. & FRANK, M. H. 2008. Identification of cells initiating human melanomas. *Nature*, 451, 345-9.
- SCHMIDT, M., SCHEULEN, M. E., DITTRICH, C., OBRIST, P., MARSCHNER, N., DIRIX, L., SCHMIDT, M., RUTTINGER, D., SCHULER, M., REINHARDT, C. & AWADA, A. 2010. An open-label, randomized phase II study of adecatumumab, a fully human anti-EpCAM antibody, as monotherapy in patients with metastatic breast cancer. *Ann Oncol*, 21, 275-282.
- SHEN, L., TOYOTA, M., KONDO, Y., LIN, E., ZHANG, L., GUO, Y., HERNANDEZ, N. S., CHEN, X., AHMED, S., KONISHI, K., HAMILTON, S. R. & ISSA, J. P. 2007. Integrated genetic and epigenetic analysis identifies three different subclasses of colon cancer. *Proc Natl Acad Sci U S A*, 104, 18654-9.
- SHI, X., KACHIRSKAIA, I., YAMAGUCHI, H., WEST, L. E., WEN, H., WANG, E. W., DUTTA, S., APPELLA, E. & GOZANI, O. 2007. Modulation of p53 function by SET8-mediated methylation at lysine 382. *Mol Cell*, 27, 636-46.
- SHUKLA, S. & MEERAN, S. M. 2014. Epigenetics of cancer stem cells: Pathways and therapeutics. *Biochim Biophys Acta*, 1840, 3494-3502.
- SOSMAN, J. A., KIM, K. B., SCHUCHTER, L., GONZALEZ, R., PAVLICK, A. C., WEBER, J. S., MCARTHUR, G. A., HUTSON, T. E., MOSCHOS, S. J., FLAHERTY, K. T., HERSEY, P., KEFFORD, R., LAWRENCE, D., PUZANOV, I., LEWIS, K. D., AMARAVADI, R. K., CHMIELOWSKI, B., LAWRENCE, H. J., SHYR, Y., YE, F., LI, J., NOLOP, K. B., LEE, R. J., JOE, A. K. & RIBAS, A. 2012. Survival in BRAF V600-mutant advanced melanoma treated with vemurafenib. *N Engl J Med*, 366, 707-14.
- SULLIVAN, R. J., HAMID, O., GONZALEZ, R., INFANTE, J. R., PATEL, M. R., HODI, F. S., LEWIS, K. D., TAWBI, H. A., HERNANDEZ, G., WONGCHENKO, M. J., CHANG, Y., ROBERTS, L., BALLINGER, M., YAN, Y., CHA, E. & HWU, P. 2019. Atezolizumab plus cobimetinib and vemurafenib in BRAF-mutated melanoma patients. *Nat Med*, 25, 929-935.
- SUNG, H., FERLAY, J., SIEGEL, R. L., LAVERSANNE, M., SOERJOMATARAM, I., JEMAL, A. & BRAY, F. 2021. Global Cancer Statistics 2020: GLOBOCAN Estimates of Incidence and Mortality Worldwide for 36 Cancers in 185 Countries. *CA Cancer J Clin*, 71, 209-249.
- TAKAWA, M., CHO, H. S., HAYAMI, S., TOYOKAWA, G., KOGURE, M., YAMANE, Y., IWAI, Y., MAEJIMA, K., UEDA, K., MASUDA, A., DOHMAE, N., FIELD, H. I., TSUNODA, T., KOBAYASHI, T., AKASU, T., SUGIYAMA, M., OHNUMA, S., ATOMI, Y., PONDER, B. A., NAKAMURA, Y. & HAMAMOTO, R. 2012. Histone lysine methyltransferase SETD8 promotes carcinogenesis by deregulating PCNA expression. *Cancer Res*, 72, 3217-27.
- TARDAT, M., MURR, R., HERCEG, Z., SARDET, C. & JULIEN, E. 2007. PR-Set7-dependent lysine methylation ensures genome replication and stability through S phase. *J Cell Biol*, 179, 1413-26.
- TODARO, M., ALEA, M. P., DI STEFANO, A. B., CAMMARERI, P., VERMEULEN, L., IOVINO, F., TRIPODO, C., RUSSO, A., GULOTTA, G., MEDEMA, J. P. & STASSI, G. 2007. Colon cancer stem cells dictate tumor growth and resist cell death by production of interleukin-4. *Cell Stem Cell*, 1, 389-402.
- TODARO, M., GAGGIANESI, M., CATALANO, V., BENFANTE, A., IOVINO, F., BIFFONI, M., APUZZO, T., SPERDUTI, I., VOLPE, S., COCORULLO, G., GULOTTA, G., DIELI, F., DE MARIA, R. & STASSI, G. 2014. CD44v6 is a marker of constitutive and reprogrammed cancer stem cells driving colon cancer metastasis. *Cell Stem Cell*, 14, 342-56.
- TOLCHER, A. W., MESSERSMITH, W. A., MIKULSKI, S. M., PAPADOPOULOS, K. P., KWAK, E. L., GIBBON, D. G., PATNAIK, A., FALCHOOK, G. S., DASARI, A., SHAPIRO, G. I., BOYLAN, J. F., XU, Z. X., WANG, K., KOEHLER, A., SONG, J., MIDDLETON, S. A., DEUTSCH, J., DEMARIO, M., KURZROCK, R. & WHELER, J. J. 2012. Phase I study of RO4929097, a gamma secretase inhibitor of Notch signaling, in patients with refractory metastatic or locally advanced solid tumors. *J Clin Oncol*, 30, 2348-53.

- TRAN, B., KOPETZ, S., TIE, J., GIBBS, P., JIANG, Z. Q., LIEU, C. H., AGARWAL, A., MARU, D. M., SIEBER, O. & DESAI, J. 2011. Impact of BRAF mutation and microsatellite instability on the pattern of metastatic spread and prognosis in metastatic colorectal cancer. *Cancer*, 117, 4623-32.
- URUSHIBARA, S., TSUBOTA, T., ASAI, R., AZUMI, J., ASHIDA, K., FUJIWARA, Y. & SHIOTA, G. 2017. WNT/beta-Catenin Signaling Inhibitor IC-2 Suppresses Sphere Formation and Sensitizes Colorectal Cancer Cells to 5-Fluorouracil. *Anticancer Res*, 37, 4085-4091.
- VALKENBURG, K. C., DE GROOT, A. E. & PIENTA, K. J. 2018. Targeting the tumour stroma to improve cancer therapy. *Nat Rev Clin Oncol*, 15, 366-381.
- VALTORTA, E., MARTINO, C., SARTORE-BIANCHI, A., PENAULT-LLOORCA, F., VIALE, G., RISIO, M., RUGGE, M., GRIGIONI, W., BENCARDINO, K., LONARDI, S., ZAGONEL, V., LEONE, F., NOE, J., CIARDIELLO, F., PINTO, C., LABIANCA, R., MOSCONI, S., GRAIFF, C., APRILE, G., FRAU, B., GARUFI, C., LOUPAKIS, F., RACCA, P., TONINI, G., LAURICELLA, C., VERONESE, S., TRUINI, M., SIENA, S., MARSONI, S. & GAMBACORTA, M. 2015. Assessment of a HER2 scoring system for colorectal cancer: results from a validation study. *Mod Pathol*, 28, 1481-91.
- VAN CUTSEM, E., KOHNE, C. H., LANG, I., FOLPRECHT, G., NOWACKI, M. P., CASCINU, S., SHCHEPOTIN, I., MAUREL, J., CUNNINGHAM, D., TEJPAR, S., SCHLICHTING, M., ZUBEL, A., CELIK, I., ROUGIER, P. & CIARDIELLO, F. 2011. Cetuximab plus irinotecan, fluorouracil, and leucovorin as first-line treatment for metastatic colorectal cancer: updated analysis of overall survival according to tumor KRAS and BRAF mutation status. *J Clin Oncol*, 29, 2011-9.
- VAN VLERKEN, L. E., KIEFER, C. M., MOREHOUSE, C., LI, Y., GROVES, C., WILSON, S. D., YAO, Y., HOLLINGSWORTH, R. E. & HURT, E. M. 2013. EZH2 is required for breast and pancreatic cancer stem cell maintenance and can be used as a functional cancer stem cell reporter. *Stem Cells Transl Med*, 2, 43-52.
- VEDELD, H. M., SKOTHEIM, R. I., LOTHE, R. A. & LIND, G. E. 2014. The recently suggested intestinal cancer stem cell marker DCLK1 is an epigenetic biomarker for colorectal cancer. *Epigenetics*, 9, 346-50.
- VESCHI, V., LIU, Z., VOSS, T. C., OZBUN, L., GRYDER, B., YAN, C., HU, Y., MA, A., JIN, J., MAZUR, S. J., LAM, N., SOUZA, B. K., GIANNINI, G., HAGER, G. L., ARROWSMITH, C. H., KHAN, J., APPELLA, E. & THIELE, C. J. 2017. Epigenetic siRNA and Chemical Screens Identify SETD8 Inhibition as a Therapeutic Strategy for p53 Activation in High-Risk Neuroblastoma. *Cancer Cell*, 31, 50-63.
- VEY, N., DELAUNAY, J., MARTINELLI, G., FIEDLER, W., RAFFOUX, E., PREBET, T., GOMEZ-ROCA, C., PAPAYANNIDIS, C., KEBENKO, M., PASCHKA, P., CHRISTEN, R., GUARIN, E., BROSKE, A. M., BAEHNER, M., BREWSTER, M., WALZ, A. C., MICHELIN, F., RUNZA, V., MERESSE, V. & RECHER, C. 2016. Phase I clinical study of RG7356, an anti-CD44 humanized antibody, in patients with acute myeloid leukemia. *Oncotarget*, 7, 32532-42.
- VOGELSTEIN, B., FEARON, E. R., HAMILTON, S. R., KERN, S. E., PREISINGER, A. C., LEPPERT, M., NAKAMURA, Y., WHITE, R., SMITS, A. M. & BOS, J. L. 1988. Genetic alterations during colorectal-tumor development. *N Engl J Med*, 319, 525-32.
- VOGELSTEIN, B., LANE, D. & LEVINE, A. J. 2000. Surfing the p53 network. *Nature*, 408, 307-10.
- WEISENBERGER, D. J., SIEGMUND, K. D., CAMPAN, M., YOUNG, J., LONG, T. I., FAASSE, M. A., KANG, G. H., WIDSCHWENDTER, M., WEENER, D., BUCHANAN, D., KOH, H., SIMMS, L., BARKER, M., LEGGETT, B., LEVINE, J., KIM, M., FRENCH, A. J., THIBODEAU, S. N., JASS, J., HAILE, R. & LAIRD, P. W. 2006. CpG island methylator phenotype underlies sporadic microsatellite instability and is tightly associated with BRAF mutation in colorectal cancer. *Nat Genet*, 38, 787-93.
- WONG, K. K. 2020. DNMT1 as a therapeutic target in pancreatic cancer: mechanisms and clinical implications. *Cell Oncol (Dordr)*, 43, 779-792.
- WONG, K. K. 2021. DNMT1: A key drug target in triple-negative breast cancer. *Semin Cancer Biol*, 72, 198-213.
- WU, C., HU, S., CHENG, J., WANG, G. & TAO, K. 2017. Smoothed antagonist GDC-0449 (Vismodegib) inhibits proliferation and triggers apoptosis in colon cancer cell lines. *Exp Ther Med*, 13, 2529-2536.
- WU, F., YANG, J., LIU, J., WANG, Y., MU, J., ZENG, Q., DENG, S. & ZHOU, H. 2021. Signaling pathways in cancer-associated fibroblasts and targeted therapy for cancer. *Signal Transduct Target Ther*, 6, 218.
- WU, S., RHEE, K. J., ALBESIANO, E., RABIZADEH, S., WU, X., YEN, H. R., HUSO, D. L., BRANCATI, F. L., WICK, E., MCALLISTER, F., HOUSSEAU, F., PARDOLL, D. M. & SEARS, C. L. 2009. A human colonic commensal

- promotes colon tumorigenesis via activation of T helper type 17 T cell responses. *Nat Med*, 15, 1016-22.
- WU, S., WANG, W., KONG, X., CONGDON, L. M., YOKOMORI, K., KIRSCHNER, M. W. & RICE, J. C. 2010. Dynamic regulation of the PR-Set7 histone methyltransferase is required for normal cell cycle progression. *Genes Dev*, 24, 2531-42.
- WU, X., LUO, F., LI, J., ZHONG, X. & LIU, K. 2016. Tankyrase 1 inhibitor XAV939 increases chemosensitivity in colon cancer cell lines via inhibition of the Wnt signaling pathway. *Int J Oncol*, 48, 1333-40.
- YAGI, K., AKAGI, K., HAYASHI, H., NAGAE, G., TSUJI, S., ISAGAWA, T., MIDORIKAWA, Y., NISHIMURA, Y., SAKAMOTO, H., SETO, Y., ABURATANI, H. & KANEDA, A. 2010. Three DNA methylation epigenotypes in human colorectal cancer. *Clin Cancer Res*, 16, 21-33.
- YAO, Q., CHEN, Y. & ZHOU, X. 2019. The roles of microRNAs in epigenetic regulation. *Curr Opin Chem Biol*, 51, 11-17.
- YI, J. M., TSAI, H. C., GLOCKNER, S. C., LIN, S., OHM, J. E., EASWARAN, H., JAMES, C. D., COSTELLO, J. F., RIGGINS, G., EBERHART, C. G., LATERRA, J., VESCOVI, A. L., AHUJA, N., HERMAN, J. G., SCHUEBEL, K. E. & BAYLIN, S. B. 2008. Abnormal DNA methylation of CD133 in colorectal and glioblastoma tumors. *Cancer Res*, 68, 8094-103.
- YONESAKA, K., ZEJNULLAHU, K., OKAMOTO, I., SATOH, T., CAPPUZZO, F., SOUGLAKOS, J., ERCAN, D., ROGERS, A., RONCALLI, M., TAKEDA, M., FUJISAKA, Y., PHILIPS, J., SHIMIZU, T., MAENISHI, O., CHO, Y., SUN, J., DESTRO, A., TAIRA, K., TAKEDA, K., OKABE, T., SWANSON, J., ITOH, H., TAKADA, M., LIFSHITS, E., OKUNO, K., ENGELMAN, J. A., SHIVDASANI, R. A., NISHIO, K., FUKUOKA, M., VARELLA-GARCIA, M., NAKAGAWA, K. & JANNE, P. A. 2011. Activation of ERBB2 signaling causes resistance to the EGFR-directed therapeutic antibody cetuximab. *Sci Transl Med*, 3, 99ra86.
- YOO, C. B., JEONG, S., EGGER, G., LIANG, G., PHIASIVONGSA, P., TANG, C., REDKAR, S. & JONES, P. A. 2007. Delivery of 5-aza-2'-deoxycytidine to cells using oligodeoxynucleotides. *Cancer Res*, 67, 6400-8.
- ZHANG, R., QI, F., SHAO, S., LI, G. & FENG, Y. 2019. Human colorectal cancer-derived carcinoma associated fibroblasts promote CD44-mediated adhesion of colorectal cancer cells to endothelial cells by secretion of HGF. *Cancer Cell Int*, 19, 192.
- ZHOU, Z., ZHOU, Q., WU, X., XU, S., HU, X., TAO, X., LI, B., PENG, J., LI, D., SHEN, L., CAO, Y. & YANG, L. 2020. VCAM-1 secreted from cancer-associated fibroblasts enhances the growth and invasion of lung cancer cells through AKT and MAPK signaling. *Cancer Lett*, 473, 62-73.